Tectonic Controls on Carbonate Reservoir Development on the Pelagian Platform, Central Mediterranean

Barnaby Richard Philps

A thesis
submitted for the degree of
Doctor of Philosophy

Department of Earth Sciences & Engineering
Royal School of Mines
Imperial College,
London

2001



Tectonic Controls on Carbonate Reservoir Development on the Pelagian Platform, Central Mediterranean

The Pelagian Platform forms a distinct structural element on the North African continental margin. It is bounded by several major fault zones; the North-South Axis, the Gafsa-Jerrafa Fault Zone and the Malta-Medina Escarpments. Internally, it is characterised by a complicated framework of shallow shelves and intervening fault-controlled basins. The Gabes-Tripoli Basin, within which the Miskar and Hasdrubal Gas Condensate Fields are located, is situated on it's south-western margin. This basin formed during the late Mesozoic as a transtensional pull-apart feature within the dextral Gafsa-Medina Shear Zone. Strike-slip tectonic processes on the Pelagian Platform are thought to have accommodated much of the movement between Africa and Europe from the Mesozoic to the present day. This model provides a mechanism by which to alleviate the spatial overlap problems between the Adriatic promontory and the European continental margin in structural restorations.

The internal structure of the Gabes-Tripoli Basin is characterised by a pervasive system of approximately NW-SE trending extensional to oblique-slip faults, which trend sub-parallel to the basin axis. This fault system has produced horst and graben topography in the Mesozoic and Tertiary sequence. The NNE-SSW trending Kerkennah and Amilcar Highs, in the western part of the basin, are interpreted to have formed during the late-middle Cretaceous by transpression along pre-existing basement lineaments. The evolution of the basin was characterised by episodes of extension and tectonic subsidence, associated with increased activity on the Gafsa-Medina Shear Zone. These phases were occasionally interrupted by periods of inversion.

The structure and evolution of the Miskar and Hasdrubal Fields reflect the main tectonic events that have affected the Gabes-Tripoli Basin. The tectonic fabric of each reservoir is dominated by stylolites and fractures, which according to well test data exert a significant influence on reservoir performance. Two styles of stylolite have been identified in each reservoir: 1) Aggregate stylolites, and 2) Intergranular stylolites. Aggregate stylolites are divided into: i) High amplitude 'sutured' stylolites, and ii) Low amplitude 'non-sutured' stylolites. High amplitude stylolites developed in packstone-grainstone fabrics, whereas low amplitude stylolites formed in mudstone-wackestone fabrics. Most stylolites are bedding-parallel structures that developed in response to overburden pressure. Aggregate stylolites developed along bed boundaries where there is a variation in composition between lithogical units. Consequently, stylolite frequency appears to be directly related to bedding surface distribution. Fractures within the Miskar and Hasdrubal reservoirs may be classified into, 1) Sub-vertical Mode I fractures that initiate at the peaks and troughs of stylolite seams and are the result of the overburden stress (i.e. STA-fractures), and 2) Sub-vertical to moderately dipping Mode II and III fractures that are associated with seismic-scale faults in this transtensional setting. All fractures tend to parallel the main orientation of seismic-scale faults (~NW-SE). Fracture frequency appears to increase with both stylolite abundance and proximity to faulting. In Hasdrubal, a relationship exists between core-derived fracture intensity and proximity to seismic-scale faulting.

Stylolitisation and fracturing occurred at multiple stages in the burial history of each reservoir. Initial compaction and dewatering caused grain microfracturing in packstone-grainstone fabrics. Following lithification, stylolites developed during periods of basin subsidence. Stylolite growth was accompanied by stylolite-associated fracture development. These vertical Mode I fractures formed perpendicular to the main extension direction (~NE-SW). Active extension in the basin was also accommodated by NW-SE extensional fault growth. These fault systems generated their own fracture associations. During successive phases of extension, stylolite- and fault-related fractures were periodically reactivated and extended. Numerous inversion events also reactivated early STA- and fault-related fractures, and also caused stylolites to crack open to form sub-horizontal fractures.

Fractures within the Hasdrubal and Miskar reservoirs contribute to enhance reservoir flow. This effect is particularly apparent in the direction parallel to the main fracture trend. Based on the current study, the Miskar and Hasdrubal Fields are classed as Type III reservoirs, whereby matrix porosity supplies the bulk of the hydrocarbon storage capacity and fractures significantly enhance production rates.

Acknowledgements

Firstly, I would like to thank the BG Group for their assistance in conceiving and funding the project. At BG I would like to thank David Beckett in particular, for his invaluable input, support and patience throughout the course of the thesis, Peter Ellis for his insightful discussions on fractured reservoir characterisation, Paul Wright for his knowledge on carbonate sedimentology, and all other members of asset teams who have helped out with those problems and questions that periodically arose.

At Imperial College, I would like to thank my two supervisors, John Cosgrove and Howard Johnson for their advice throughout the thesis, Lidia Lonergan for her invaluable discussions and Richard Jolly for his knowledge of fractured reservoir analysis, and the research opportunity that he later gave to me at Golder Associates. Thank you also to all other members of staff that have helped me out along the way, and made my stay at Imperial College a highly memorable one.

At Cambridge University, I would like to thank Nicky White for allowing me to use his strain rate inversion software, and in addition Paul Faulkner and Paul Wheeler for their input and assistance in it's use.

Finally, I would like to thank my family and friends. Mamie, thank you for getting me started with the project, and for your continuous support. Mum, Dad and Oliver thanks for everything. All my friends at Imperial College and elsewhere including in no particular order Marcus, Clarky, Parky, Gypsy, John, Chris, Lisa, Gareth, Gary, Mad, Paul x2, Matt, Simon x2, Jim, Natasha, Salim, George, Mohammed, Lena, Delphine, Mellisa, Johanna and all those that I may have forgotten. To all of the above and those not mentioned we have had some memorable times.

Table of Contents

Chapter 1
Introduction **1**

1.1. Aim & Overview 1
1.2. Project Methodology & Limitations 1
1.2.1. Methodology 1
1.2.2. Limitations 4
1.3. Location of the study area 4
1.4. Previous work in the study area 5

Chapter 2
Tectonic Setting of the Pelagian Platform in the Central Mediterranean **7**

2.1. Introduction 7
2.2. Mediterranean Tectonics - a review 9
2.2.1. Introduction 9
2.2.2. The Opening of the Western Neo-Tethys 10
2.2.3. Adria - Microplate or Promontory? 13
2.2.4. The Closure of the Neo-Tethys 14
2.3. Geological Framework of the Pelagian Platform 22
2.3.1. Introduction 22
2.3.2. Bathymetry 22
2.3.3. Crustal Structure & Seismicity 23
2.3.4. Tectono-Stratigraphic Framework 27
2.4. Tectonic Evolution of the Pelagian Platform 34
2.4.1. Upper Triassic to Early Cretaceous Evolution 34
2.4.2. Early Cretaceous to Early Eocene Evolution 35
2.4.3. Early Eocene to Late Miocene Evolution 37
2.4.4. Late Miocene to Present Day Evolution 39

Chapter 3
Structure & Evolution of the Gulf of Gabes **41**

3.1. Introduction 41
3.2. Previous Work 42
3.3. Location 43

3.4. Data Acquisition 43
3.5. Lithostratigraphic Framework 44
3.5.1. Introduction 44
3.5.2. Triassic Stratigraphy 44
3.5.3. Jurassic Stratigraphy 44
3.5.4. Cretaceous Stratigraphy 46
3.5.5. Tertiary Stratigraphy 55
3.6. Structural Framework of the Gulf of Gabes 64
3.6.1. Introduction 64
3.6.2. Seismic Stratigraphy 64
3.6.3. Principal Structural Elements 67
3.7. Subsidence History of the Gulf of Gabes 93
3.7.1. Introduction 93
3.7.2. Extension and Subsidence 93
3.7.3. Preliminary Subsidence Modelling Procedures 96
3.7.4. Strain Rate Inversion Theory 100
3.7.5. Data Utilised 103
3.7.6. Results & Discussion 104
3.8. Tectonic Evolution of the Gulf of Gabes 113
3.8.1. Introduction 113
3.8.2. Upper Triassic (Rhaetian)-Lower Cretaceous (Barremian) 113
3.8.3. Lower Cretaceous (Aptian) to Upper Eocene (Priabonian) 114
3.8.4. Oligocene (Rupelian) to Present Day 120

Chapter 4
Evaluating Fractured Reservoirs: Fundamental Concepts 123

4.1. Introduction 123
4.2. Principals of Fractured Reservoir Evaluation 124
4.2.1. Fracture Definition 125
4.2.2. Brittle Failure Criteria 125
4.2.3. Natural Fracture Classification 127
4.2.4. Controls on Tectonic & Regional Fracture Development 131
4.2.5. Influence of Fractures on Reservoir Performance 133
4.2.6. Classification of Fractured Reservoirs 140
4.3. Stylolite Definition & Classification 141
4.3.1. Influence of Stylolites on Reservoir Performance 143

Chapter 5
Sampling & Analysis of Fractured Reservoirs 145

5.1. Introduction 145
5.2. Detection of Naturally Fractured Reservoirs 145
5.2.1. Direct Detection Methods 145
5.2.2. Indirect Detection Methods 147
5.3. Sampling Fracture Systems 147
5.3.1. Core & Outcrop Sampling Strategies 147
5.3.2. Natural & Induced Fracture Determination in Core 150
5.3.3. Oriented Core Analysis 155
5.3.4. Structural Terminology 156
5.3.5. Sampling Bias in Linear (1D) Scanline Surveys 156
5.3.6. Sampling & Interpretation of Image Logs 159
5.4. Data Analysis & Presentation 163
5.4.1. Fracture Orientation 164
5.4.2. Fracture Length & Height 166
5.4.3. Fracture Frequency 167
5.4.4. Fracture Spacing 168

Chapter 6
Structural Analysis of the Miskar Gas Condensate Field 178

6.1. Introduction 178
6.2. Location & Field History 179
6.3. Database 180
6.4. Local Structure & Reservoir Stratigraphy 180
6.4.1. Introduction 180
6.4.2. Structure 180
6.4.3. Reservoir Stratigraphy 181
6.4.4. Depositional Setting of the R1 Superior & Inferior Reservoirs 189
6.5. Seismic Stratigraphy & Structure 190
6.5.1. Introduction 190
6.5.2. Seismic Stratigraphic Framework 190
6.5.3. Seismic Structure 190
6.5.4. Structural Evolution of the Miskar Field 202
6.6. Structural Analysis of the Miskar A-3, -6, -7, -9, -10 & -11 Cores 209
6.6.1. Introduction 209

6.6.2. Core Quality & Study Limitations 210
6.6.3. Core Observations 211
6.6.4. Discussion of Core Observations 241
6.6.5. Sequence of Fracturing in the Miskar Reservoirs 247
6.6.6. Influence on Reservoir Performance 250

Chapter 7
Structural Analysis of the Hasdrubal Gas Condensate Accumulation 252

7.1. Introduction 252
7.2. Location & Field History 253
7.3. Database 253
7.4. Local Structure & Reservoir Stratigraphy 254
7.4.1. Introduction 254
7.4.2. Structure 254
7.4.3. Reservoir Stratigraphy 254
7.4.4. Regional Depositional Setting of the Metlaoui Group 260
7.5. Seismic Stratigraphy & Structure 264
7.5.1. Introduction 264
7.5.2. Seismic Stratigraphy 264
7.5.3. Seismic Structure 265
7.5.4. Structural Evolution of the Hasdrubal Field 268
7.6. Structural Analysis of the Hasdrubal -2, -3 & -4 Cores 270
7.6.1. Introduction 270
7.6.2. Core Quality & Study Limitations 271
7.6.3. Core Observations 271
7.7. Analysis of CAST & FMS Image Logs from the Hasdrubal -2 & -3 wells 292
7.7.1. Introduction 292
7.7.2. Data Quality & Study Limitations 292
7.7.3. Image Log Interpretation 293
7.7.4. Comparison of Core & Image Log Observations 299
7.8. Discussion of Core & Image Log Observations 302
7.8.1. Stylolites 302
7.8.2. Fractures 304
7.8.3. Sequence of Fracturing in the Hasdrubal Reservoir 311
7.8.4. Influence on Reservoir Performance 314

Chapter 8
Fault-Related Reservoir Fracturing in Hasdrubal: Outcrop Analogues 316

8.1. Introduction 316
8.2. Scope & Previous Work.....316
8.2.1. Introduction 316
8.2.2. Sampling Fracture Populations from Subsurface Data 317
8.3. Outcrop Analogue Identification 319
8.4. Fracture Classification & Sampling at Outcrop 319
8.5. Outcrop Analogue Studies in Malta.....321
8.5.1. Introduction 321
8.5.2. Stratigraphy 321
8.5.3. Structure 326
8.5.4. Observations Along The Maghlaq Fault System.....327
8.5.5. Observations from Selected Quarries.....339
8.6. Summary & Discussion of Observations 345

Chapter 9
Discussion & Conclusions 351
9.1. Introduction 351
9.2. Regional Setting of the Pelagian Platform 351
9.3. Structure & Evolution of the Gulf of Gabes.....352
9.4. Tectonic Controls on Reservoir Development 353
9.5. Influence on Reservoir Performance.....357
9.6. Implications for Field Development.....359
9.7. Further Work 360

References 361

Appendices

Enclosures

List of Figures

Fig. 1.1. Location map of the Central Mediterranean 2

Fig. 1.2. Location map of the Miskar and Hasdrubal Gas Condensate Fields 3

Fig. 2.1. Tectonic map of the Mediterranean basin and Black Sea 8

Fig. 2.2. (a) Position of Africa with respect to Europe from 175Ma to the Present Day. (b) Flow lines depicting the path of Africa's motion for 3 points on the present day African coastline 10

Fig. 2.3. Flow lines showing the relative motion of Europe, Iberia and Africa with respect to North America from the Early Jurassic to the Present Day 11

Fig. 2.4. Reassembly of the principal continental masses in (a) the Triassic (220 ± 20Ma) showing the position of the Paleo-Tethys (after Smith et al., 1973), and (b) the Late Triassic to Early Jurassic showing the opening of the Neo-Tethys 12

Fig. 2.5. Location of the two Paleo-Tethys and Neo-Tethys suture zones 13

Fig. 2.6. The development of the Neo-Tethys at 150Ma 14

Fig. 2.7. Plate tectonic reconstructions from the Early Jurassic to the Eocene illustrating the relative motion of North America, Africa and Europe 15

Fig. 2.8. Diagram illustrating back-arc extension caused by subduction roll-back ..17

Fig. 2.9. Kinematic reconstructions depicting the evolution of the western and central Mediterranean region 19

Fig. 2.10. Tectonic map of the Central Mediterranean 21

Fig. 2.11. Bathymetry of the region encompassing the Pelagian Platform 23

Fig. 2.12. Free-air gravity map of the Pelagian Platform 24

Fig. 2.13. Line drawing of seismic profile MS-19, and the respective Bouger and Residual Gravity data over the Straits of Sicily Rift Zone 25

Fig. 2.14. Simplified magnetic anomaly map of the Pelagian Platform 25

Fig. 2.15. Seismicity on the Pelagian Platform since May 1981 26

Fig. 2.16. Tectonic map of the Pelagian Platform 27

Fig. 2.17. Comparative Mesozoic and Tertiary stratigraphy of offshore Tunisia, offshore western Libya, the Maltese Islands and the Hyblean Plateau 29

Fig. 2.18. Tectonic map of the Hyblean-Maltese Shelf 30

Fig. 2.19. Evolution of the Pelagian Platform 38

Fig. 2.20. Evolution of the Straits of Sicily Rift Zone 40

Fig. 3.1. Location map of the Gulf of Gabes region on the Pelagian Platform 43

Fig. 3.2. Seismic and well base map 45

Fig. 3.3. Lithostratigraphic Correlation 47

Fig. 3.4. Isopach map of the Valanginian and Hauterivian showing sediment thickness variations in the Meloussi, Boudinar and Lower and Middle M'Cherga Formations 48

Fig. 3.5. Isopach and facies map of the Barremian and Lower Aptian showing sediment thickness variations in the lower units of the Gafsa Group 49

Fig. 3.6. Isopach and facies map of the Aptian showing sediment thickness variations in the Serdj and Orbata Formations 50

Fig. 3.7. Isopach map of the Albian showing sediment thickness variations in the lower part of the Fahdene Formation 51

Fig. 3.8. Isopach and facies map of the Cenomanian showing sediment thickness variations in the upper part of the Fahdene Formation 52

Fig. 3.9. Isopach and facies map of the Cenomanian - Middle Turonian showing sediment thickness variation in the Bireno, Annaba and Bahloul Formations 53

Fig. 3.10. Isopach and facies map of the Campanian to Maastrichtian showing sediment thickness variations in the Abiod Formation 54

Fig. 3.11. Distribution of the Aleg Formation over the Gulf of Gabes 56

Fig. 3.12. Distribution of the Abiod Formation over the Gulf of Gabes 57

Fig. 3.13. Distribution of the Metlaoui Group over the Gulf of Gabes 58

Fig. 3.14. Isopach map of the Ypresian showing sediment thickness variations in the Metlaoui Group 59

Fig.3.15. Isopach map of the Lutetian to Priabonian showing sediment thickness variations in the Cherahil Formation and it's lateral equivalents 61

Fig. 3.16. Isopach map of the Oligocene and Lower Miocene showing sediment thickness variations in the Fortuna Sandstone Formation and it's lateral equivalents 62

Fig. 3.17. Isopach map of the Middle and Upper Miocene showing sediment thickness variations in the Oum Douil Group 63

Fig. 3.18. Principals of seismic stratigraphic analysis 65

Fig. 3.19. Principal structural elements in the Gulf of Gabes region 68

Fig. 3.20. WSW-ENE trending cross-section west of the North-South Axis 69

Fig. 3.21. Seismic lines CTWT-92-106 & 106A with respective line illustration showing a regional NNW-SSE section across the Gulf of Gabes 71

Fig. 3.22. Seismic lines CTWT-92-108 & 108A with respective line illustration showing a NW-SE section across the Kerkennah High 72

Fig. 3.23. Seismic line CTWT-92-102 with a respective line illustration showing a NW-SE section across the western margin of the Gabes-Tripoli Basin.....73

Fig. 3.24. Seismic line CTWT-92-101 with a respective line illustration showing a NE-SE section across Medina & Lampedusa Plateaux 74

Fig. 3.25. Seismic line CTWT-92-103 with a respective line illustration showing a NW-SE section from the Medina Plateax into the Gabes-Tripoli Basin.....75

Fig. 3.26. Top Bireno TWT Structure Map across the Gulf of Gabes 77

Fig. 3.27. Top Abiod TWT Structure Map across the Gulf of Gabes 78

Fig. 3.28. Top Metlaoui TWT Structure Map across the Gulf of Gabes.....79

Fig. 3.29. Top Renieche TWT Structure Map across the Gulf of Gabes 80

Fig. 3.30. Isopach map of the Aleg Formation across the Gulf of Gabes.....82

Fig. 3.31. Isopach map of the Abiod Formation across the Gulf of Gabes 83

Fig. 3.32. Isopach map of the El Haria/Tselja Formations across the Gulf of Gabes..84

Fig. 3.33. Isopach map of the Metlaoui Group across the Gulf of Gabes 85

Fig. 3.34. Isopach map of the Cherahil Formation across the Gulf of Gabes.....86

Fig. 3.35. Isopach map of the Salammbo Formation across the Gulf of Gabes 87

Fig. 3.36. Isopach map of the Miocene-Present Day across the Gulf of Gabes 88

Fig. 3.37. WNW-ESE stratigraphic correlation across the Gulf of Gabes 89

Fig. 3.38. NE-SW stratigraphic correlation across the Gulf of Gabes 90

Fig. 3.39. Schematic illustration showing the structural development of the Kerkennah High from the Turonian/Maastrichtian 91

Fig. 3.40. Configuration and thermal profile of the lithosphere and asthenosphere before, during, and after uniform (instantaneous) stretching.....94

Fig. 3.41. Time-dependent stretching model of Jarvis & McKenzie (1980).....96

Fig. 3.42. Comparison of the influence of using the Harland et al. (1989) and Gradstein et al. (1994) timescales on backstripped subsidence data 97

Fig. 3.43. Backstripping errors associated with varying lithologies in subsidence data from the Miskar A-1 well 99

Fig. 3.44. An example of strain rate inversion from the Schio Central stratigraphic section, Dolomites, northern Italy 103

Fig. 3.45. Best-fit water-loaded subsidence curves for the 32 wells analysed in the study, together with their respective strain rate models..... 106

Fig. 3.46. Relationship between extension and igneous activity on the Pelagian Platform in the Mesozoic and Cenozoic..... 107

Fig. 3.47. Isopach map of volcanics within the Aleg Formation 108

Fig. 3.48. Isopach map of volcanics within the Abiod Formation..... 109

Fig. 3.49. Decompacted geohistory plots for selected boreholes in central Tunisia. 112

Fig. 3.50. Sequential restoration showing the structural evolution of the Gulf of Gabes area..... 117

Fig. 3.51. Mechanism for the development of the Gabes-Tripoli Basin 119

Fig. 3.52. Mechanism for the development of the Kasserine Island 120

Fig. 3.53. Block diagram to illustrate the postulated geometry of structures in Central and Northern Tunisia 121

Fig. 4.1. Location map of the Hasdrubal and Miskar Gas Condensate Fields 124

Fig. 4.2. Relationships between effective principal stresses 125

Fig. 4.3. Schematic diagram illustrating the three fundamental modes of fracture 126

Fig. 4.4. Composite Griffith and Navier-Coulomb failure envelopes and Mohr circle construction 127

Fig. 4.5. Relationship between stress states, the fault and fracture orientations derived from those stress states 128

Fig. 4.6. A generalisation of dominant fold-related fracture sets 129

Fig. 4.7. Schematic diagram illustrating the major features of stratabound and non-stratabound regional joint systems 130

Fig. 4.8. Plot of bed thickness versus fracture spacing 132

Fig. 4.9. Direct effect of fracture morphology on whole-core permeability 136

Fig. 4.10. Plots showing fracture porosity as a function of fracture width and fracture spacing, and fracture permeability as a function of fracture width and spacing 139

Fig. 4.11. Effect of fracture and matrix interaction on whole core permeability 140

Fig. 4.12. Classification of stylolites according to geometry 142

Fig. 4.13. Classification of stylolites in relation to bedding plane 142

Fig. 4.14. Classification of stylolite seams based on the relative percentage of clay material and 'structurally resistive' elements 143

Fig. 5.1. Sampling techniques used in core analysis 148

Fig. 5.2. Sampling techniques used in field outcrop analysis 150

Fig. 5.3. Series of schematic diagrams illustrating the principal characteristics of natural fractures 152

Fig. 5.4. Series of schematic diagrams illustrating the principal characteristics of drilling, coring and handling induced fractures 153

Fig. 5.5. Plan view showing the angular configuration of principal and secondary scribe lines on an oriented core 155

Fig. 5.6. Scanlines through a single set of persistent, parallel joints..... 156

Fig. 5.7. Effect of trace length bias caused by scanline sampling..... 159

Fig. 5.8. CAST and FMS image logging tools..... 160

Fig. 5.9. Acoustic and resistivity borehole images 162

Fig. 5.10. Schematic diagram showing showing borehole breakout and induced fracture generation in an arbitrary well-bore 163

Fig. 5.11. (a) Rose diagram for fracture dip direction, (b) Histogram of fracture dip angle for the same dataset 164

Fig. 5.12. Diagram illustrating the principal of hemispherical projection techniques 165

Fig. 5.13. Schematic plot showing the cumulative frequency distribution of fracture length for three examples 166

Fig. 5.14. Models of subsurface fractures and their interaction with boreholes..... 169

Fig. 5.15. Schematic diagram of fractured core, lacking regular, mechanically significant layering..... 172

Fig. 5.16. Spatial and dimensional relationships that relate fracture geometry and fracture porosity in a reservoir when the borehole axis is not parallel to the fractures..... 173

Fig. 5.17. Schematic diagram showing an idealised homogeneous, fractured reservoir, which forms the basis of the AFS (Average Fracture Spacing) method .. 176

Fig. 6.1. Location of the Miskar Gas Field..... 179

Fig. 6.2. Depth structure map of the Top R1 Inferior Member (Aleg Formation) over the Miskar structure 181

Fig. 6.3. Main reservoir stratigraphy in the Miskar Gas Condensate Field..... 182

Fig. 6.4. An interval of core from the R1 Superior Member within Miskar -6..... 184

Fig. 6.5. An interval of core from the R1 Inferior Member within Miskar -6..... 185

Fig. 6.6. An interval of core from the Bireno Member within Miskar -6..... 187

Fig. 6.7. An interval of core from the Abiod Formation within Miskar -6 188

Fig. 6.8. Schematic depositional model of the R1 Superior and Inferior members of the Aleg Formation over the Miskar area 189

Fig. 6.9. E-W Arbitrary seismic line over the Miskar structure and interpreted line drawing showing the main seismic sequences identified across the area 193

Fig. 6.10. E-W Arbitrary seismic line over the Miskar structure and interpreted line drawing showing the main structural elements present 194

Fig. 6.11. Seismic line 1800 over the Miskar structure and interpreted line drawing showing the main structural elements present 195

Fig. 6.12. Depth structure map of the top Abiod Formation over the Miskar area.. 197

Fig. 6.13. Depth structure map of the top R1 Inferior Member illustrating the en-echelon nature of faulting..... 199

Fig. 6.14. Mechanism for the development of en-echelon extensional faults within the cover sequence above a 'basement' wrench fault..... 200

Fig. 6.15. Blow-up of area within the Arbitrary seismic line shown in Figure 6.10 illustrating the internal disposition of reflection events in the Upper Cretaceous succession 203

Fig. 6.16. Sequential restoration of the Miskar structure showing the main tectonic phases that have affected the area during the Mesozoic and Tertiary..... 205

Fig. 6.17. Fault propagation in the cover sequence above a sinistral strike-slip 'basement' wrench fault 207

Fig. 6.18. Miskar A-3. Stylolite and Fracture Frequency versus depth..... 212

Fig. 6.19. Schematic diagram illustrating the minimum amount of material removed by stylolitisation 216

Fig. 6.20. Miskar A-3. Apparent fracture frequency versus depth..... 217

Fig. 6.21. Cumulative frequency distribution of fracture height within the cored intervals in the Miskar A-3 well 221

Fig. 6.22. Miskar A-6. Stylolite and Fracture Frequency versus depth..... 224

Fig. 6.23. Miskar A-6. Apparent fracture frequency versus depth 225

Fig. 6.24. Cumulative frequency distribution of fracture height within the cored intervals in the Miskar A-6 well 227

Fig. 6.25. Miskar A-7. Stylolite and Fracture Frequency versus depth 228

Fig. 6.26. Miskar A-7. Apparent fracture frequency versus depth 230

Fig. 6.27. Miskar A-9. Stylolite and Fracture Frequency versus depth 231

Fig. 6.28. Miskar A-9. Apparent fracture frequency versus depth 232

Fig. 6.29. Miskar A-10. Stylolite and Fracture Frequency versus depth 234

Fig. 6.30. Miskar A-10. Apparent fracture frequency versus depth 235

Fig. 6.31. Miskar A-11. Stylolite and Fracture Frequency versus depth 238

Fig. 6.32. Miskar A-11. Apparent fracture frequency versus depth 240

Fig. 6.33. Sequential restoration of the main phase of fracturing in the primary reservoir intervals within the Miskar Gas Condensate Field 248

Fig. 7.1. Location of the Hasdrubal Gas Condensate Field 253

Fig. 7.2. Two-way-time (TWT) structure map of the Top Metlaoui Group 255

Fig. 7.3. Reservoir stratigraphy in the Hasdrubal Gas Condensate Field 256

Fig. 7.4. Schematic palaeogeography and depositional model for the Metlaoui Group in and around the Hasdrubal Field 261

Fig. 7.5. The El Garia facies belt around Hasdrubal, showing a series of small structurally controlled embayments 263

Fig. 7.6. Arbitrary seismic line across the Hasdrubal Gas Condensate Field 266

Fig. 7.7. A comparison of two-way-time (TWT) maps for a) the Top Metlaoui (Lower Eocene) and b) the Top Melquart (Miocene) intervals 268

Fig. 7.8. Sequential restoration of the Hasdrubal Structure showing the main tectonic phases that have affected the area during the Mesozoic and Tertiary 269

Fig. 7.9. Hasdrubal -2. Stylolite and Fracture Frequency versus depth 273

Fig. 7.10. Hasdrubal -2. Fracture frequency versus depth 275

Fig. 7.11. Cumulative frequency distribution of fracture height within the cored intervals in the Hasdrubal -2 well 276

Fig. 7.12. Hasdrubal -3. Stylolite and Fracture Frequency versus depth 277

Fig. 7.13. Hasdrubal -3. Fracture frequency versus depth 278

Fig. 7.14. Cumulative frequency distribution of fracture height within the cored intervals in the Hasdrubal -3 well 279

Fig. 7.15. Hasdrubal -4. Stylolite and Fracture Frequency versus depth 281

Fig. 7.16. Hasdrubal -4. Fracture frequency versus depth 285

Fig. 7.17. Cumulative frequency distribution of fracture height within the cored intervals in the Hasdrubal -4 well 290

Fig. 7.18. Rose diagrams of fracture orientation within the El Garia Formation, and the Compact Micrite Member 290

Fig. 7.19. Fracture dip and strike versus depth within the upper part of the El Garia Formation 291

Fig. 7.20. Bedding dip azimuth vector plot for Hasdrubal –2 294

Fig. 7.21. Typical stylolitised bed boundary and associated high amplitude fractures within Hasdrubal –2 294

Fig. 7.22. Low amplitude fractures imaged over the interval 2998m to 3000m in Hasdrubal –2 295

Fig. 7.23. Bedding dip azimuth vector plot for Hasdrubal –3 297

Fig. 7.24. Resistive fractures imaged by FMS in Hasdrubal –3 298

Fig. 7.25. Conductive fractures imaged by FMS in Hasdrubal –3 299

Fig. 7.26. Stylolite-associated fractures imaged by FMS in Hasdrubal –3 300

Fig. 7.27. Comparison of stylolite and fracture frequencies from the image and core log analyses 301

Fig. 7.28. Stylolite and fracture frequencies in Hasdrubal –4 306

Fig. 7.29. Depth structure map of the top Metaloui Formation over the Hasdrubal Gas Accumulation 308

Fig. 7.30. Series of plots showing the relationship between fracture intensity and proximity to seismic-scale faulting 309

Fig. 7.31. (a) Plot of $\delta^{13}C$ versus $\delta^{18}O$ for diagenitic calcites from Hasdrubal -2, -3 and -4. (b) Plot of $\delta^{13}C$ versus $\delta^{18}O$ for the various types of calcite in Hasdrubal –4 310

Fig. 7.32. Burial History curve for the El Garia Fm. in Hasdrubal –4 311

Fig. 7.33. Sequential restoration showing the main phases of fracturing in the primary reservoir interval in the Hasdrubal Gas Condensate Field 313

Fig. 8.1. Comparison of top Reservoir seismic scale displacement data with well displacement data 318

Fig. 8.2. Sample fracture log used in the field 320

Fig. 8.3. Geological Map of Malta 322

Fig. 8.4. Stratigraphy of the Maltese Islands 323

Fig. 8.5. Geological map of the Maghlaq Fault System, on the southern coast of Malta 328

Fig. 8.6. Summary of observations made along the Maghlaq Fault System .....Enc. 4

Fig. 8.7. TWT Structure map of the top Metlaoui Formation 331

Fig. 8.8. Location map showing the Ghar Lapsi Fault Zone at Ras Hanzir 333

Fig. 8.9. Ras Hanzir: Field illustration summarising the style and intensity of sub-seismic scale deformation associated with the Ghar Lapsi Fault .....Enc. 5

Fig. 8.10. Location map showing the Ras il-Hamrija Fault west of Wied Babu 334

Fig. 8.11. Wied Babu: Field illustration of the style and intensity of sub-seismic scale deformation associated with the Ras il-Hamrija Fault.....Enc. 5

Fig. 8.12. Log-log plots showing the spacing distributions of small and intermediate-scale faults and fractures along the three scanlines at Wied Maghlaq..... 336

Fig. 8.13. Location map showing the Blue Grotto Fault..... 337

Fig. 8.14. Blue Grotto: Field illustration of the style and intensity of sub-seismic scale deformation associated with the Blue Grotto Fault .....Enc. 5

Fig. 8.15. Location map showing the Il-Hnejja and Wied iz-Zurreiq Faults at the northern end of Wied iz-Zurreiq 338

Fig. 8.16. Wied iz-Zurreiq: Field illustration of the style and intensity of sub-seismic scale deformation associated with the Il-Hnejja Fault .....Enc. 5

Fig. 8.17. Location map of the Ix-Xaqqa Quarry 339

Fig. 8.18. Ix-Xaqqa Quarry: Field illustration of footwall fracturing associated with the main fault zone to the south of the quarry .....Enc. 6

Fig. 8.19. Ix-Xaqqa Quarry: Field illustration of hangingwall deformation associated with the Ix Xaqqa Fault .....Enc. 6

Fig. 8.20. Location map of the Lapsi Quarry 341

Fig. 8.21. Lapsi Quarry: Field illustration showing the nature of deformation associated with the intermediate structures in Plate 8.9 .....Enc. 7

Fig. 8.22. Location map of the Naxxar Gap Quarries 342

Fig. 8.23. Naxxar Gap Quarries: Field illustration showing the nature of deformation associated with the Naxxar and Misrah Faults .....Enc. 8

Fig. 8.24. Naxxar Gap Quarries: Field illustration of the main fault in the western part of the quarry .....Enc. 8

Fig. 8.25. Naxxar Gap Quarries: Field illustration of the style and intensity of fracturing associated with the Misrah Fault .....Enc. 8

Fig. 8.26. Location map of the Attard Quarries 344

Fig. 8.27. Attard Quarries: Study Area A – Field illustration of fracturing associated with the intermediate scale structure in Plate 8.20 .....Enc. 9

Fig. 8.28. Attard Quarries: Study Area B – Field illustration of fracturing associated with the Incita Fault .....Enc. 9

Fig. 8.29. Summary of the relationship between seismic and sub-seismic scale fault and fracture distributions at outcrop along the Maghlaq Fault System ... 346

Fig. 8.30. Minimum size of deformation zones associated with seismic scale-scale faults along the Maghlaq fault System 347

Fig. 8.31. Top reservoir depth structure map over the Hasdrubal area, showing the extent of deformation associated with seismic-scale faults of varying displacement 350

Fig. 9.1. Simplified tectonic map of the Pelagian Platform, showing the role of strike-slip deformation in the development of the Gabes-Tripoli Basin and the Straits of Sicily Rift Zone 352

Fig. 9.2. Main tectonic phases affecting the Gabes-Tripoli Basin and hence the Miskar and Hasdrubal reservoirs 354

Fig. 9.3. Schematic diagram showing optimum wellbore approach angles to intersect an extensional fault zone within the Hasdrubal reservoir 359

List of Plates

Plate 6.1. Miskar A-3: 3661.95m 213

Plate 6.2. Miskar A-3: 3318.00m 213

Plate 6.3. Miskar A-3: 3358.98m 214

Plate 6.4. Miskar A-3: Micro-stylolitisation within the Abiod Formation 214

Plate 6.5. Miskar A-3: 3308.48m 215

Plate 6.6. Miskar A-3: Calcite-filled vugs within the Abiod Formation 215

Plate 6.7. Miskar A-3: 3647.68m 219

Plate 6.8. Miskar A-3: 3307.60m 219

Plate 6.9. Miksar A-3: 3730.00m 221

Plate 6.10. Miskar A-6: 5022.90m 221

Plate 6.11. Miskar A-6: 5072.37m 224

Plate 6.12. Miskar A-6: 5102.02m 224

Plate 6.13. Miskar A-6: 5077.25m 226

Plate 6.14. Miskar A-6: 4888.70m 226

Plate 6.15. Miskar A-9: 3888.25m 233

Plate 6.16. Miskar A-10: 4654.25m 233

Plate 6.17. Miskar A-10: 4648.50m 236

Plate 6.18. Miskar A-10: 4666.40m 236

Plate 6.19. Miskar A-11: 4852.30m 239

Plate 6.20. Miskar A-11: 4641.10m 239

Plate 7.1. Hasdrubal -4: 3037.42m 256

Plate 7.2. Hasdrubal -4: 3037.42m 256

Plate 7.3. Hasdrubal -4: 3032.50m 257

Plate 7.4. Hasdrubal -4: 3011.75m 257

Plate 7.5. Hasdrubal -4: 2966.00m....260

Plate 7.6. Hasdrubal -4: 2986.50m....260

Plate 7.7. Hasdrubal -2: 2422.80m....274

Plate 7.8. Hasdrubal -2: 2968.91m....274

Plate 7.9. Hasdrubal -4: 3036.45m....282

Plate 7.10. Hasdrubal -4: 2991.80m....282

Plate 7.11. Hasdrubal -4: 3011.00m....283

Plate 7.12. Hasdrubal -4: 3029.00m....283

Plate 7.13. Hasdrubal -4: 2998.75m....284

Plate 7.14. Hasdrubal -4: 3030.00m....284

Plate 7.15. Hasdrubal -4: 3000.70m....286

Plate 7.16. Hasdrubal -4: 3036.35m....286

Plate 7.17. Hasdrubal -4: 3015.50m....286

Plate 7.18. Hasdrubal -4: 3001.46m....286

Plate 7.19. Hasdrubal -4: 3021.60m....287

Plate 7.20. Hasdrubal -4: 2989.50m....287

Plate 7.21. Hasdrubal -4: 2989.25m....288

Plate 7.22. Hasdrubal -4: 3005.00m....288

Plate 7.23. Hasdrubal -4: 3024.00m....289

Plate 7.24. Hasdrubal -4: 3005.00m....289

Plate. 8.1. Ras il-Hamrija: Well-exposed fault segment within the Maghlaq Fault System....330

Plate. 8.2. Ras il-Hamrij: Fresh slickensides indicate almost pure dip-slip displacements 330

Plate 8.3. Ras Hanzir: 2-3m wide zone of fault gouge immediately adjacent to the main Ghar Lapsi fault....330

Plate 8.4. Ras il-Hamrija: Well-exposed fault segment within the Maghlaq Fault System cutting an older fault trace that is associated with the Victoria Lines Fault System 330

Plate 8.5. Ras Hanzir: Overview of the hangingwall deformation zone associated with the Ghar Lapsi Fault ..... Enc. 5

Plate 8.6. Wied Babu: Overview of the hangingwall deformation zone associated with the Ras il-Hamrija Fault ..... Enc. 5

Plate 8.7. Blue Grotto: Overview of the hangingwall deformation zone associated with the Blue Grotto Fault ..... Enc. 5

Plate 8.8. Wied iz-Zurreiq: Overview of the hangingwall deformation zone associated with the Il-Hnejja Fault ..... Enc. 5

Plate 8.9. Overview of the Ix-Xaqqh Quarry showing the location of study areas Enc. 6

Plate 8.10. Ix-Xaqqa Quarry: Photo-montage of footwall fracturing associated with the main fault zone to the south ..... Enc. 6

Plate 8.11. Ix-Xaqqa Quarry: Photo-montage of hangingwall deformation associated with the Ix-Xaqqa Fault ..... Enc. 6

Plate 8.12. Lapsi Quarry: Overview of Quarry ..... Enc. 7

Plate 8.13. Lapsi Quarry: Overview of deformation associated with intermediate-scale structures within the Maghlaq Fault System ..... Enc. 7

Plate 8.14. Naxxar Gap Quarries: Overview of the western part of the quarry showing the location of Study Area A ..... Enc. 8

Plate 8.15. Naxxar Gap Quarries: Overview of the eastern part of the quarry showing the Misrah Fault ..... Enc. 8

Plate 8.16. Naxxar Gap Quarries: Overview of the eastern part of the quarry showing the Misrah Fault ..... Enc. 8

Plate 8.17 Naxxar Gap Quarries: Photomontage of Study Area A showing the nature of deformation within the footwall section of the Victoria Lines Fault ..... Enc. 8

Plate 8.18 Naxxar Gap Quarries: Enlarged view of area indicated in Plate 8.17 showing the main fault zone in the western part of the quarry ..... Enc. 8

Plate 8.19 Overview of Study Area B ..... Enc. 8

Plate 8.20 Attard Quarries: Overview of Study Area A ..... Enc. 9

Plate 8.21 Attard Quarries: Overview of Study Area B ..... Enc. 9

List of Tables

Table 3.1. Seismic stratigraphic framework of the Gulf of Gabes region 66

Table 3.2. Definitions and values of model parameters 95

Table 3.3. Parameters used for sediment decompaction. 98

Table 4.1. Angular relationships between fracture type and principal stress 127

Table 4.2. Fracture sets associated with folding 129

Table 4.3. Main controls on fracture intensity 131

Table 4.4. Published natural fracture widths 138

Table 4.5. Published experimental fracture widths 138

Table 4.6. Fractured reservoir classification scheme 140

Table 5.1. Detection of natural fractures by variations in geophysical log response ...146

Table 5.2. Structural terminology used in the report 156

Table 6.1. Data available for wells Miskar A-1 to A-11. 180

Table 6.2. Seismic stratigraphic framework for the Miskar and Hasdrubal areas 191

Table 6.3. Cored intervals in Miskar wells under analysis 210

Table 6.4. Measured depths to lithostratigraphic unit tops. 210

Table 6.5. Cored intervals in Miskar A-3 211

Table 6.6. Stylolite frequency and spacing in Miskar A-3 213

Table 6.7. Material removed through pressure solution in Miskar A-3 217

Table 6.8. Apparent fracture frequency and spacing in Miskar A-3 220

Table 6.9. Distribution of fracture type, and nature of fracture fill in Miskar A-3 222

Table 6.10. Cored intervals in Miskar A-6 223

Table 6.11. Stylolite frequency and spacing in Miskar A-6 223

Table 6.12. Material removed through pressure solution in Miskar A-3. 225

Table 6.13. Apparent fracture frequency and spacing in Miskar A-6 226

Table 6.14. Distribution of fracture type, and nature of fracture fill in Miskar A-6.....228

Table 6.15. Stylolite frequency and spacing in Miskar A-7 229

Table 6.16. Material removed by pressure solution in Miskar A-7 229

Table 6.17. Apparent fracture frequency and spacing in Miskar A-7 229

Table 6.18. Distribution of fracture type, and nature of fracture fill in Miskar A-7.....230

Table 6.19. Stylolite frequency and spacing in Miskar A-9 231

Table 6.20. Material removed by pressure solution in Miskar A-9 231

Table 6.21. Apparent fracture frequency and spacing in Miskar A-9 232

Table 6.22. Distribution of fracture type, and nature of fracture fill in Miskar A-9.....233

Table 6.23. Cored intervals in Miskar A-10 234

Table 6.24. Stylolite frequency and spacing in Miskar A-10 234

Table 6.25. Material removed through pressure solution in Miskar A-10 235

Table 6.26. Apparent fracture frequency and spacing in Miskar A-10 236

Table 6.27. Distribution of fracture type and nature of fracture fill in Miskar A-10.....236

Table 6.28. Cored intervals in Miskar A-11 237

Table 6.29. Stylolite frequency and spacing in Miskar A-11 238

Table 6.30. Material removed through pressure solution in Miskar A-11 239

Table 6.31. Apparent fracture frequency and spacing in Miskar A-11 239

Table 6.32. Distribution of fracture type and nature of fracture fill in Miskar A-11.....240

Table 6.33. Comparison of stylolite frequencies and material removed in each well....243

Table 6.34. Comparison of fracture frequencies and spacing in each well 246

Table 7.1. Data available for wells Hasdrubal -1 to –4 254

Table 7.2. Cored intervals in Hasdrubal wells under analysis.....270

Table 7.3. Lithostratigraphic tops in Hasdrubal wells.....270

Table 7.4. CAST and FMS image log runs in Hasdrubal -2 & -3 271

Table 7.5. Cored intervals in Hasdrubal –2.....272

Table 7.6. Stylolite frequency and spacing in Hasdrubal –2.....272

Table 7.7. Material removed through pressure solution in Hasdrubal –2.....273

Table 7.8. Apparent fracture frequency and spacing in Hasdrubal –2.....275

Table 7.9. Distribution of fracture type, and nature of fracture fill in Hasdrubal –2...276

Table 7.10. Cored intervals in Hasdrubal –3.....277

Table 7.11. Stylolite frequency and spacing in Hasdrubal –3.....277

Table 7.12. Material removed through pressure solution in Hasdrubal –3.....278

Table 7.13. Apparent fracture frequency and spacing in Hasdrubal –3.....278

Table 7.14. Distribution of fracture type, and nature of fracture fill in Hasdrubal –3...280

Table 7.15. Cored intervals in Hasdrubal –4.....280

Table 7.16. Stylolite frequency and spacing in Hasdrubal –4.....281

Table 7.17. Material removed through pressure solution in Hasdrubal –4.....283

Table 7.18. Apparent fracture frequency and spacing in Hasdrubal –4.....285

Table 7.19. Distribution of fracture type, and nature of fracture fill in Hasdrubal –4...285

Table 7.20: Summary of structural dip zonation in Hasdrubal –2.....293

Table 7.21. Fracture statistics in Hasdrubal –2.....296

Table 7.22. Borehole breakout and induced fracture statistics for Hasdrubal – 2.....296

Table 7.23. Fracture statistics in Hasdrubal –3.....297

Table 7.24. Induced fracture statistics for Hasdrubal –3.....299

Table 7.25. Comparison of measured stylolite frequencies from image and core data .300

Table 7.26. Comparison of measured fracture frequencies from image and core data..301

Table 7.27. Comparison of stylolite frequencies and material removed in each well....303

Table 7.28. Comparison of fracture frequencies and spacing in each well.....306

Table 7.29. Comparison of fracture frequencies and spacing in each well.....311

Table 8.1. Classification of faults and fractures measured at outcrop.....319

Table 8.2. .Comparison of average 2nd order fault spacing distributions for subsurface structures in the Hasdrubal Accumulation and exposed structures in the Maghlaq Fault System 332

Table 8.3. Summary of sub-seismic scale fracture spacing along three scanlines in the hangingwall of the Ras il-Hamrija Fault 335

Table 8.4. Summary of sub-seismic scale fracture spacing along two scanlines in the hangingwall section of the Il-Hnejja Fault 338

Table 8.5. Summary of the relationship between seismic and sub-seismic scale faulting and fracturing on the Maghlaq fault System 341

Table 8.6. Summary of small/intermediate-scale fracture spacing associated with the Misrah Fault Zone.....343

Table 8.7. Summary of small-scale fracture spacing along two scanlines adjacent to the main fault plane observed in Study Area A 344

Table 8.8. Spatial distribution of seismic and sub-seismic scale faulting and fracturing in the Maghlaq System. 345

Chapter 1

Introduction

1.1. Aim & Overview

The structural configuration of the Pelagian Platform in the Central Mediterranean region (**Fig. 1.1**) reflects a complex tectonic history involving both intraplate extension and plate margin deformation processes. To date, the controls of these tectonic processes on the structural development of the region are poorly constrained due, partly due to a lack of scientific attention in recent years. The aim of this thesis is to investigate the structure and evolution of the southern margin of the Pelagian Platform (i.e. the Gulf of Gabes region), and to examine the tectonic controls on the structural development of two of the principal carbonate reservoirs within the region. A better understanding of the processes that have caused fracturing within these carbonate reservoirs will provide a critical tool for planning well position and orientation in exploration and field development, and should also increase the accuracy in prediction of well performance and yield.

1.2. Project Methodology & Limitations

1.2.1. Methodology

The first part of the study commenced with a comprehensive review of Western and Central Mediterranean tectonics, undertaken in order to place the Pelagian Platform in it's proper regional context, and to establish the main structural processes that have affected the Mesozoic to Present Day evolution of the Central Mediterranean region. This review resulted in a synthesis, which was integrated with subsequent studies on the main structure, stratigraphy and evolution of the Pelagian Platform. After the

regional framework was established, a detailed study of the Gulf of Gabes area (which includes the Gabes-Tripoli Basin) was undertaken. Regional seismic profiles were interpreted and used to construct two-way-time (TWT) structure maps for important seismic events. These data were then integrated with regional lithostratigraphic correlations and isopach maps of sediment thickness, which were produced from available well logs. Finally, the inverse strain rate modelling procedure of White (1993; 1994) was used to model the subsidence histories for a number of wells. The combination of these analyses allowed a detailed synthesis of the tectonic and depositional evolution of the study area.

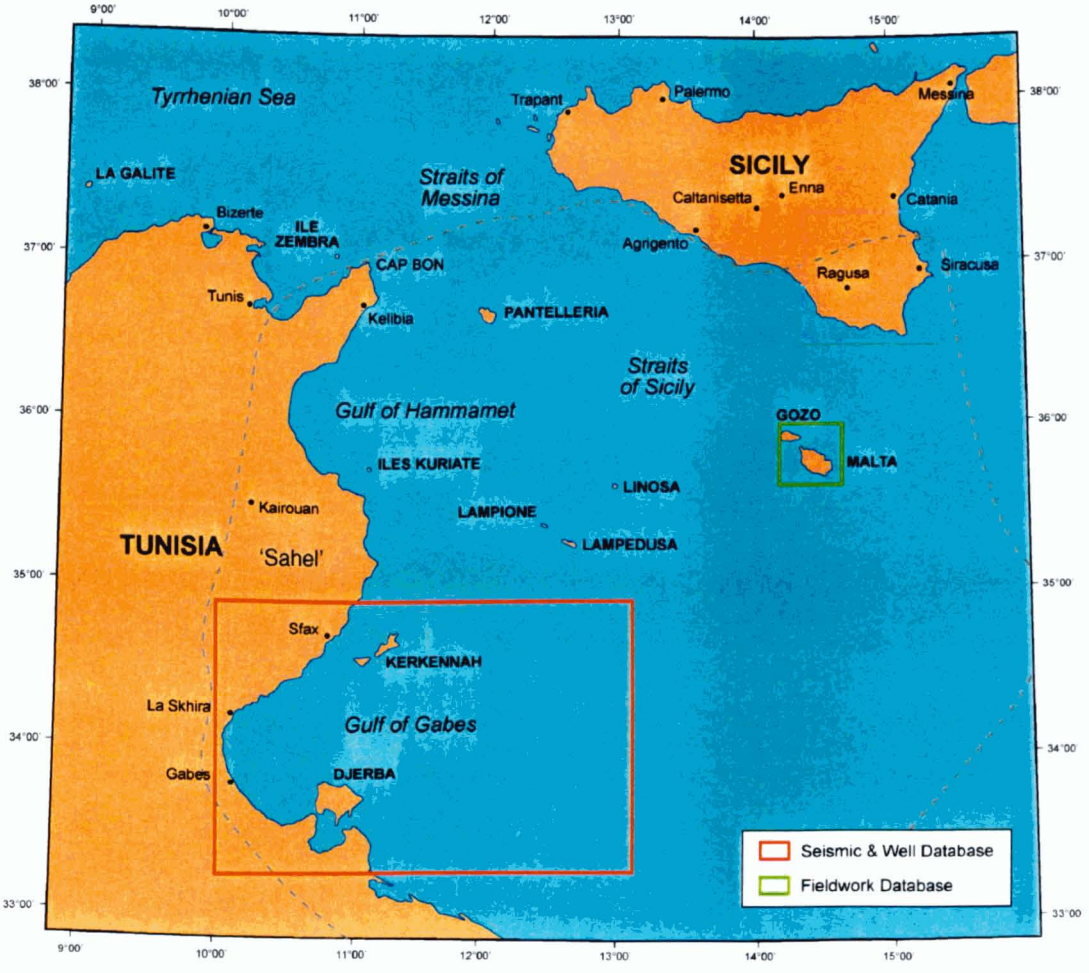

Fig. 1.1. Location map of the Central Mediterranean showing the extent of the Pelagian Platform (i.e. the area inside the dashed line). The Gulf of Gabes is located in the south-western margin of the platform area.

The second part of the project concentrated on the regional and local tectonic controls on fracture development within carbonates at a reservoir scale. Two discoveries, owned and operated by the BG Group, were utilised in this study (i.e. the Hasdrubal and Miskar Gas Fields) (**Fig. 1.2**). They were chosen because well test data indicated that reservoir-scale fracturing might be contributing significantly to hydrocarbon flow rates.

Detailed analyses of seismic, core and FMI/CAST images were conducted for each area and integrated into working structural models. In addition to this, a particular aim of this exercise was to attempt to develop predictive models for the distribution and configuration of fracture systems and hierarchical structures associated with seismic-scale faults. In order to achieve this, core analyses were integrated with fieldwork studies from appropriate outcrop analogues in the Maltese Islands. Finally, the fracture data from one of the discoveries (Hasdrubal) was incorporated into a fracture simulation package (FracMan) in an attempt to build a three dimensional fracture model of the principal reservoir interval. This is presented in Appendix D. In presenting these studies this thesis has been sub-divided into two main sections:

1. Tectonic controls on the structure, and kinematic evolution, of the Gulf of Gabes region;

2. Tectonic controls on the structural development of selected carbonate reservoirs on the Pelagian Platform; case studies of the Miskar and Hasdrubal Gas Fields.

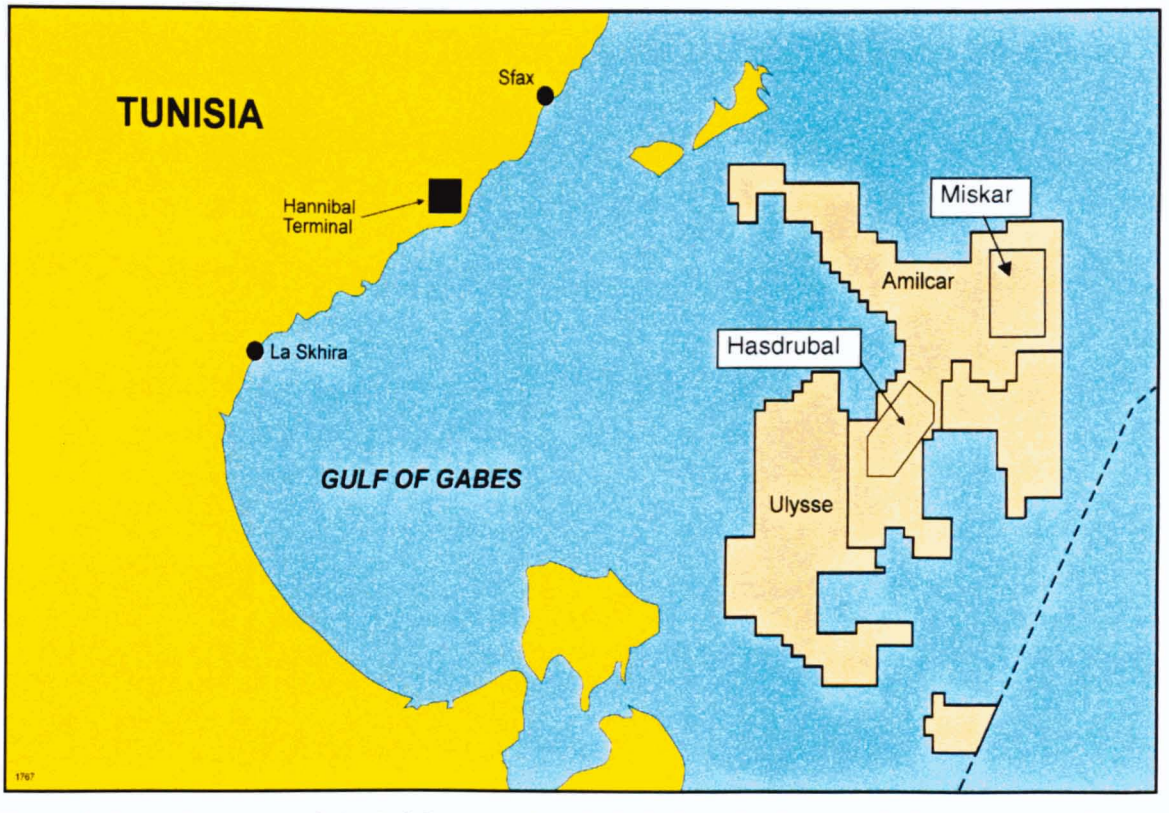

Fig. 1.2. Location map of the Miskar and Hasdrubal Gas Condensate Fields in the Amilcar Concession, Gulf of Gabes, offshore Tunisia.

1.2.2. Limitations

The BG Group provided access to as much of the relevant data that was available. Recent high resolution seismic and well data was available over the two gas condensate fields, allowed detailed field analyses to be undertaken. Unfortunately, regional profiles over the Gabes-Tripoli Basin more difficult to access, and therefore best use had to be made of the available lines.

Cored intervals from the Miskar and Hasdrubal Fields were analysed wherever possible but unfortunately, due to drilling and handling, certain reservoir zones were missing or reduced to rubble. This precluded detailed structural evaluation. In addition, the majority of these wells were not oriented, and therefore it was impossible to obtain accurate orientation data.

Fieldwork studies were initially aimed at the onshore region of Tunisia (Sahel). However, a reconnaissance trip to eastern Tunisia at the beginning of the project identified that there was very limited outcrop on the Tunisian 'Sahel', and that it would be more advantageous to concentrate on other regions. The Maltese Islands were eventually selected after a short reconnaissance trip, because they provided the closest tectonic analogues within comparable lithologies to subsurface structures within the Gulf of Gabes region.

1.3. Location of the Study Area

The Pelagian Platform is located on the northern margin of the African Plate within the Central Mediterranean region (33^0-37^0 Lat. and 10^0-16^0 Long.) (**Fig. 1.1**). It extends from southeastern Sicily in the north, down to the Libyan coastline in the south and incorporates the onshore Sahel region of eastern Tunisia. Most of the region is covered by shallow sea, the only outcropping portions occur in SE Sicily (Hyblean Plateau), the Maltese and Pelagian Islands, and the Sahel region of Tunisia.

The Gulf of Gabes region, including the Gabes-Tripoli Basin is located at the southern margin of the Pelagian Platform (33^0-35^0 Lat. and 10^0-15^0 Long.). The Miskar and Hasdrubal Gas Fields described in Chapters 6 and 7 are located in the western part of this basin, just north of the main depocentre.

1.4. Previous Work in the Study Area

The geology and evolution of the Mediterranean region has been studied extensively over the past century. The generally accepted theory is that the evolution of this area has been controlled by the relative motion of Africa with respect to Europe throughout the Mesozoic and Tertiary (Neumayr, 1885; Suess, 1893; 1901; Smith, 1971; Smith & Woodcook, 1982; Dewey et al., 1973, 1989; Biju-Duval et al., 1977; Hsü, 1977; Channel et al., 1979; Sengor, 1979; Dercourt et al., 1986; Savostin et al., 1986).

Numerous plate tectonic models have been derived for the Mediterranean based on quantitative kinematic analyses on poles of rotation (Smith, 1971), magnetic anomaly lineations (Pitman & Talwani, 1972; Dewey et al, 1973; 1989) hotspot tracks (Morgan, 1981, 1983; Cavallin & Tornaghi, 1986), and qualitative analyses of faunal and floral data (Channell et al., 1979; Hsü, 1977; Dercourt et al., 1986). In addition, a number of workers have detailed the regional geology of various parts of the Mediterranean system from the Atlantic to the Pamirs, through extensive fieldwork studies.

A large concentration of the aforementioned work has been undertaken in the Western Mediterranean region. In contrast to this, detailed studies in the Central Mediterranean region are relatively sparse. Morelli et al. (1975), Finetti (1982) and Jongsma et al. (1985) outline the principal structural domains within the Central Mediterranean area through the use of gravity, magnetic and seismic data. Burollet et al. (1978), Salaj (1978) and Boccaletti et al. (1990) present regional overviews of the main geology of the Pelagian Platform, with particular reference to the stratigraphy of the region. Ben-Avraham et al. (1987), Westaway (1990), Ben-Avraham & Grasso (1991) and Ben-Avraham et al. (1995) present regional structural models for the evolution of specific, isolated segments of the Central Mediterranean region, but do not present integrated tectonic models for the entire area.

Smaller scale, area-specific investigations on the Pelagian Platform have mainly been undertaken in the onshore areas of SE Sicily and the Maltese/Pelagian Islands. Ghisetti & Vezzani (1980), Grasso et al. (1986; 1990), Cogan et al. (1989), Barrier (1992), Gardiner et al. (1995) and Torelli et al. (1998) among others, present accounts on the structure of these regions, based on fieldwork, seismic and well data, whereas Patacca et al. (1979), Pedley (1981; 1990), Pedley & Grasso (1991), Grasso & Lentini (1982) give details on the lithostratigraphy (N.B. the published structural models concerning

the evolution of southeast Sicily are controversial, and remain a subject of much debate). The geology of onshore eastern Tunisia, in contrast, is poorly documented. Anderson (1996) has nevertheless described the structure and evolution of the westernmost part of the Pelagian Platform in east-central Tunisia, based on fieldwork from the around the North-South Axis (refer to Chapter 2).

Literature on the geology of the offshore regions, and in particular the Gulf of Gabes (incorporating the western part of the Gabes-Tripoli Basin) is very scarce, and generally restricted to oil company reports and conference abstracts. The lithostratigraphy of these areas is mainly obtained from studies of onshore and offshore well data, and also from fieldwork in south-central Tunisia. Burollet (1956), Bishop (1975; 1985; 1988), Moody (1987), Bailey et al. (1989), Ben Ferjani et al. (1990), M'Rabat et al. (1995) provides the most comprehensive lithostratigraphic account of the offshore Gulf of Gabes region. The structure of this region is barely documented. Hammuda et al. (1992), Anketell, (1992) and El Ghoul, (1992) briefly outline the geology of the Gabes-Tripoli Basin, but mainly concentrate on the Libyan (eastern) part of the basin where stratigraphic nomenclatures differ.

Prior to the initiation of this dissertation, analyses on the structure and stratigraphy of the Hasdrubal and Miskar Gas Condensate Fields were limited. Studies generally had consisted of seismic interpretation, which involved the mapping of the main reservoir horizons and the construction of TWT and depth structure maps, together with core studies aimed at identifying zonation (i.e. layering) within these reservoirs (Braithwaite, 1998). As a consequence, available literature for both fields is limited and confined to oil company reports.

Chapter 2

Tectonic Setting of the Pelagian Platform in the Mediterranean

2.1. Introduction

In order to understand the tectonic processes controlling the structural evolution of the Gulf of Gabes, and in particular the Gabes-Tripoli Basin (which incorporates the Hasdrubal and Miskar Gas Fields), the study area must first be considered in its regional context during every stage of its development. Section 2.2 will discuss the Mesozoic and Tertiary evolution of the Central Mediterranean region, and identify the palaeo-position of the Pelagian Platform at each stage (**Fig. 2.1 (Enclosure 1)**). It will provide a regional discussion of:

- Timing of continental break-up, the ages and extent of tectonic activity, and the distribution of stress fields through time;
- Rates of drift of the African plate (with respect to North America and Europe) and the details of the eventual collision with Europe.

Section 2.3 will then summarise the geological framework of the Pelagian Platform, and establish the Gulf of Gabes within this setting. It will present accounts of:

- The bathymetry, crustal structure and recent seismicity within the region;
- The present-day tectono-stratigraphic framework of the area;

An integrated regional structural model is presented in Section 2.4 that attempts to summarise the main tectonic phases that have controlled the evolution of this region. This review should provide a broad framework for Chapter 3, which will use seismic and well data to discuss the structure and evolution of the Gulf of Gabes area.

CONTAINS PULLOUTS

2.2. Mediterranean Tectonics - a review

2.2.1. Introduction

In accordance with the kinematics of plate tectonics, that require the continuity of opening and closing of oceans, the idea of an Ancient Mediterranean ocean was first proposed by Neumayr (1883). He postulated the existence of an equatorial ocean separating a NeoArctic continent in the north from a Brazilian-Ethiopian continent in the south. Suess (1893) later named this ocean 'Tethys', and defined it as a Mesozoic feature north of Gondwanaland. Du Toit (1932) proposed a more precise description of Tethys, referring to it as an east-west trending intercontinental ocean separating the two supercontinents of Laurasia (in the north) from Gondwana (in the south). These early ideas still generally remain plausible today. However, the Tethyan ocean represents a mosaic of sub-basins that developed over the Palaeozoic/Mesozoic and a number of models have been advocated to explain their evolution.

Argand (1924) developed the early models of Neumayr (1883), which suggested that the complex geometries observed in the Mediterranean region were the result of continental drift and the rotation of microplates (**Fig. 2.1**). Evidence for such movements is given by the least squares fit of the circum-Atlantic continents (Bullard et al., 1965) which requires Africa to have occupied a different position relative to Europe in early Mesozoic time than it does today. Consequently conventional interpretations now relate the Late Triassic to present-day geological development of the Mediterranean region to the relative motion of Africa with respect to Europe, and to the complex interactions between intervening microplates (Smith, 1971; Dewey et al., 1973; Biju-Duval et al., 1977) (**Fig. 2.2a-b**). The existence of microplates is strongly supported by palaeomagnetic data, although their number, rigidity, rotations and displacements remain highly controversial.

In 1971, Smith proposed that the evolution of the African-European system could be reconstructed using its motions relative to the North American plate (**Fig. 2.3**). This became the basis for all subsequent kinematic plate tectonic models of the Mediterranean system from the early Mesozoic to the present-day. Numerous models have been derived based on quantitative kinematic analyses on; 1) poles of rotation (Smith, 1971), 2) well defined magnetic anomaly lineations in the north and central

Atlantic (Pitman & Talwani, 1972; Dewey et al., 1973, 1989) 3) hotspot tracks (Morgan, 1981, 1983; Cavallin & Tornaghi, 1986), and 4) qualitative analyses on faunal and floral data (Channell et al., 1979; Hsü, 1977; Dercourt et al., 1986).

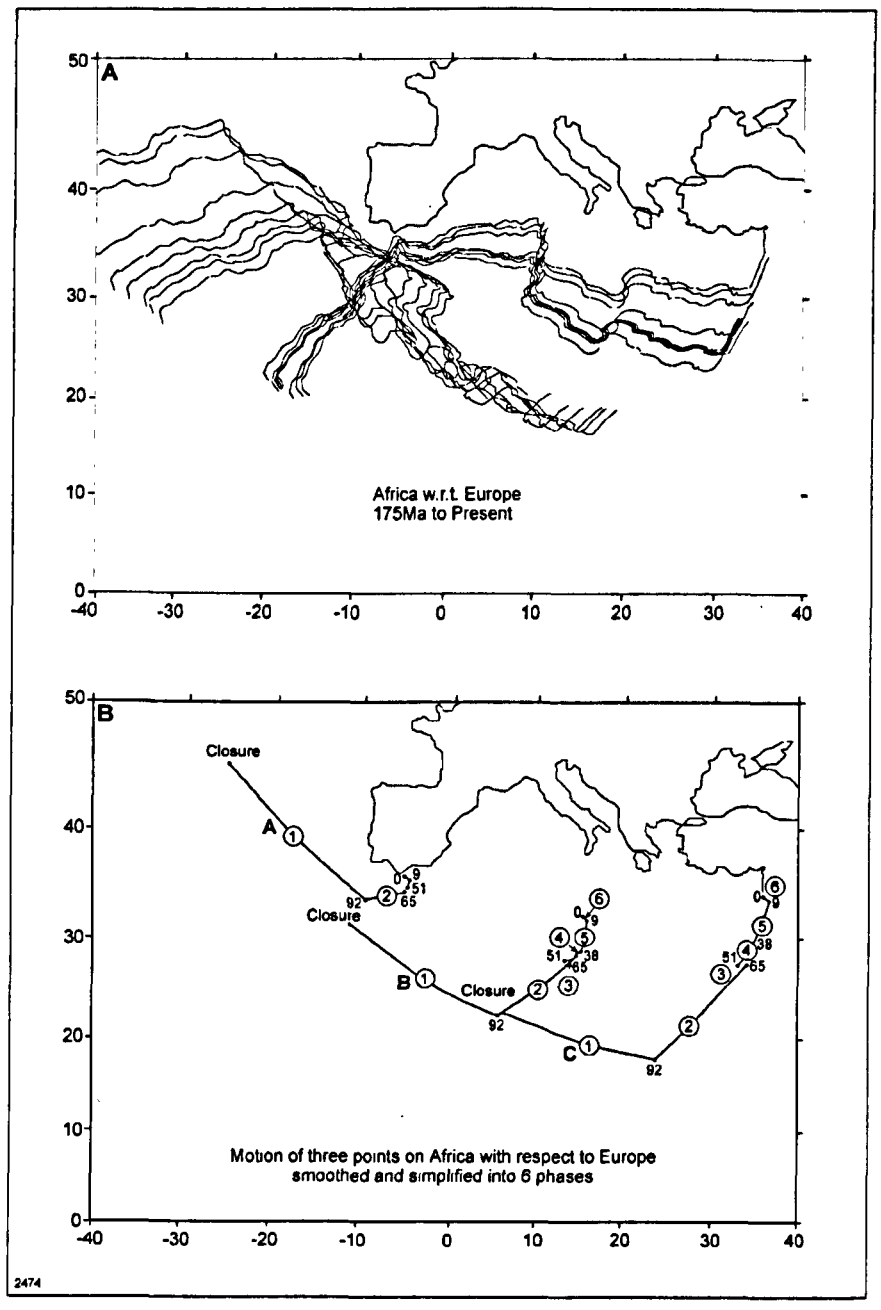

Fig. 2.2. (A) Position of Africa with respect to Europe from 175Ma to the present-day. (B) Flow lines depicting the path of Africa's motion for 3 points on the present-day African coastline (from Dewey et al., 1989)

2.2.2. The Opening of the Western Neo-Tethys

Prior to the late Triassic/early Jurassic the major continents were conjoined to form Pangea (Smith et al., 1981). Carey (1958) reconstructed Pangea, illustrating that during this time a wedge shaped 'Palaeotethys', opening to the east, separated Laurasia

from Gondwana (**Fig. 2.4a**). The initial fragmentation of western Pangea during the Middle to Late Triassic (Hsü & Bernoulli, 1975; Dewey et al., 1979) occurred by the gradual westward spreading of the 'Neo-Tethys' (Mesozoic Tethys), as the 'Palaeo-Tethys' (Palaeozoic Tethys) was slowly consumed along the Cimmerian and Indosinian suture (Hsü & Bernoulli, 1978) (**Figs. 2.4b & 2.5**).

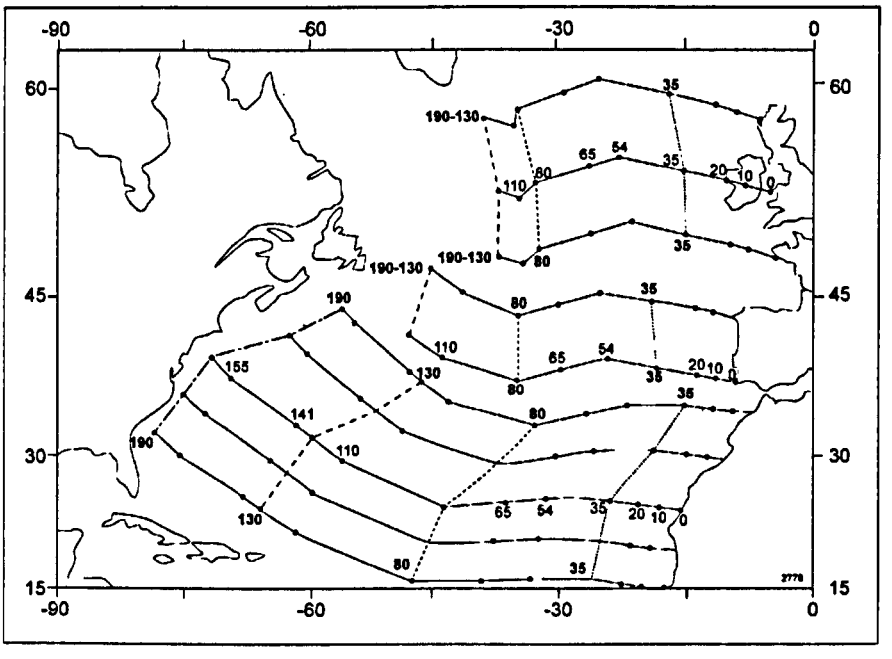

Fig. 2.3. Flow lines showing the relative motion of Europe, Iberia and Africa with respect to North America from the early Jurassic to the present-day (from Savostin et al., 1986)

McKenzie & Weiss (1975) and Sengor (1979a) proposed that the initial onset of Neo-Tethyan rifting was due to back-arc spreading processes associated with the subduction of the Palaeo-Tethyan sea floor. However Livermore & Smith (1985) and Coward & Dietrich (1989) propose that the Late Triassic (Rhatian-Norian) sinistral transtensive motion of Africa relative to Europe resulted in the development of rift basins across the Western Mediterranean area, most notably the early Piedmont-Ligurian Basin (**Fig. 2.6**). In both cases, the lack of evidence for the existence of lower Mesozoic oceanic crust tends to suggest that the Triassic period of Neotethyan continental rifting did not evolve into oceanic spreading (Channell et al., 1979).

It was not until the Liassic that renewed extension generated oceanic crust in the Piedmont-Ligurian Ocean causing the separation of Africa and Europe (Hayward & Hill, 1988). Livermore & Smith (1985) propose that the opening of this part of the Neo-Tethys actually induced the onset of NW-SE directed rifting in the central Atlantic between Africa and North America (**Fig. 2.3 & 2.7a**). This rift phase is

thought to have eventually culminated in oceanic spreading (i.e. post-rift phase) within the central Atlantic between ~173-180Ma (Dewey et al., 1989). As a consequence Africa separated from North America, simultaneously causing relative sinistral strike-slip motion between the African and European plates (Smith, 1971; Dewey et al., 1973). Livermore & Smith (1985) propose that this motion caused the gradual closure of the Piedmont-Ligurian Ocean (the western part of the Neo-Tethys), while others argue that spreading continued in the western Neo-Tethys until the Late Jurassic, despite the influence of high tensile stresses between Africa and North America.

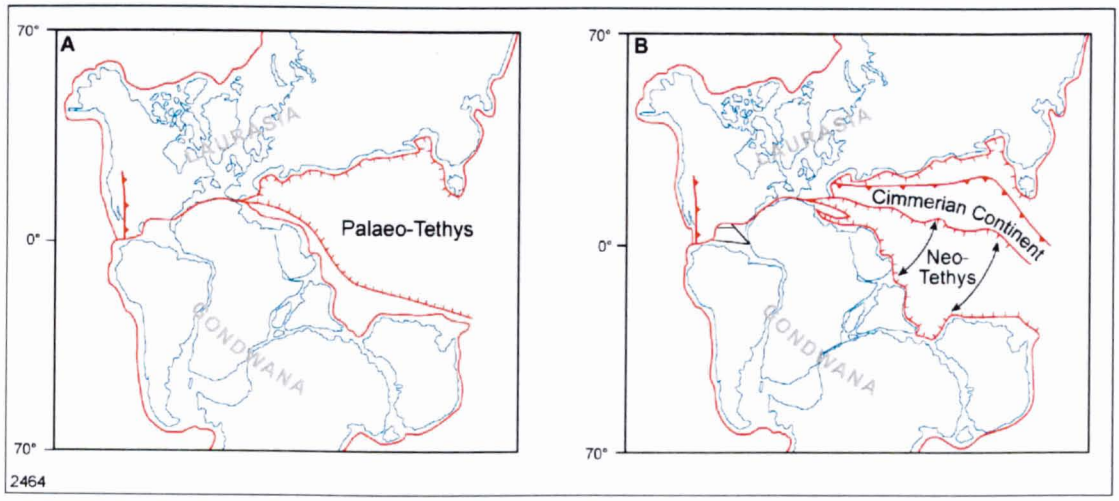

Fig. 2.4. Reassembly of the principal continental masses in (A) the Triassic (220 ± 20Ma) showing the position of the Palaeo-Tethys (after Smith et al., 1973), and (B) the late Triassic to early Jurassic showing the opening of the Neo-Tethys (modified after Sengor, 1979).

Early to Middle Jurassic (~180m.y. ago until 155m.y. ago) sea-floor spreading in the Neo-Tethys was characterised by slow, constant spreading rates that gradually increased towards the Late Jurassic, coinciding with a worldwide transgression (Savostin et al. 1986). In the Central Atlantic spreading rates decreased from the Late Jurassic (~150Ma) until the middle Cretaceous (~110Ma), and the Central Atlantic Ridge shifted eastward closer to Africa (Dewey et al., 1973) (**Fig. 2.7b-c**). During this episode (between the latest Jurassic and the earliest Cretaceous) increased tectonic activity within the entire Northwest European and Arctic-North Atlantic rift system (late Cimmerian Phase) was accompanied by significant crustal thinning, dispersed igneous activity and ophiolite obduction (Savostin et al., 1986). Dewey et al. (1989) suggest that the width of the Middle Jurassic (Callovian) Neo-Tethys was slightly smaller than the contemporaneous width of the Central Atlantic

2.2.3. Adria – Microplate or Promontory?

Considerable controversy remains over the origins and affinities of the Adria area. This area has been categorised variously as both a microplate and an extended promontory of the North African continental margin (**Fig. 2.7a**). It is important to attempt to obtain a clear understanding of this issue because it has a direct impact on Mesozoic and Tertiary evolution of the study area.

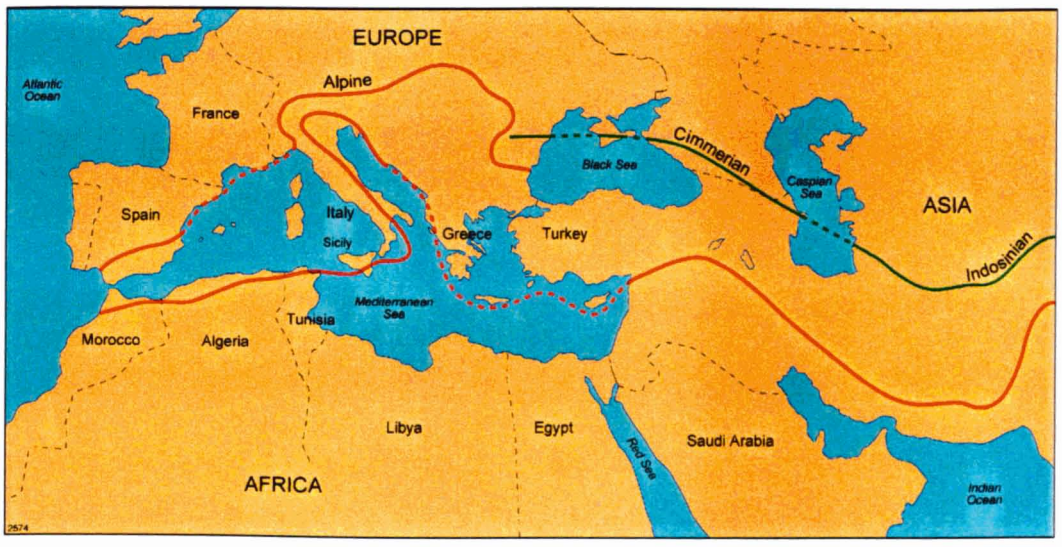

Fig. 2.5. Location of the two suture zones. The Palaeo-Tethys was eliminated by subduction along the Cimmerian-Indosinian suture zone. The Tethys disappeared through subduction and collision along the Alpine-Himilayan suture zone. Suture zones are defined by ophiolitic assemblages (modified after Hsü, 1971).

Various workers have argued on the basis of Rhatian facies associations that, during the Late Triassic, rifting on the North African continental margin led to the dispersal of the northern part of the African-Apulian plate (i.e. Adria) (Biju-Duval et al., 1977). These arguments are in accordance with the plate tectonic models of Dewey et al (1973) and Cavallin & Tornaghi (1986). In contrast, Channell et al. (1979) suggested that Adria has remained an extension of the African plate throughout the Mesozoic to the present-day. Laubscher & Bernoulli (1977) supported this idea proposing a continuity of continental crust from North Africa to Sicily and along the Italian peninsular to former Yugoslavia and Greece, without an oceanic connection across the promontory from the western to the eastern part of the Neotethys.

It was only recently that deep reflection seismic data confirmed that continental crust extends across northern Tunisia and along the Italian peninsula to Greece (refer to Section 2.3.3) (Boccaletti et al., 1987). This demonstrates that 'Adria' has remained a

promontory of the African Plate from the Mesozoic to the present-day and that the study area is underlain by thinned continental crust. Jongsma et al. (1985) show however, that there are large overlap problems between an Adriatic promontory and the European continental margin when Africa and Europe are restored back through the Tertiary and late Mesozoic. In order to alleviate the misfit, they propose that large strike-slip movements may have been accommodated within the Pelagian Platform and adjacent areas.

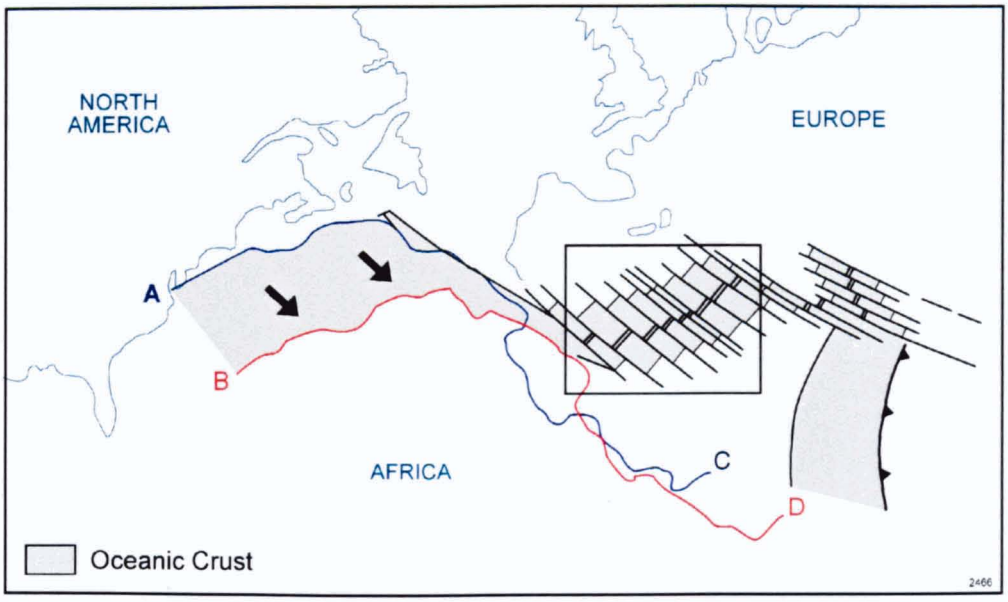

Fig. 2.6. The development of the Neo-Tethys at 150Ma (interpreted as a transform belt between the African and European continents): A-B indicates the positions of Africa at 175Ma and 150Ma (Livermore & Smith, 1985), C-D indicates the positions of Africa at 175Ma and 149.2Ma (Dewey et al., 1989) (after Coward & Dietrich, 1989).

2.2.4. The Closure of the Neo-Tethys

Dewey et al. (1989) propose that during the Aptian (~118Ma) the first oceanic crust had developed in the Bay of Biscay and in the North Atlantic (north of the Azores-Gibraltar fracture zone) creating the Iberian plate (**Fig. 2.7d**). The effect of the North Atlantic and Bay of Biscay opening (~118-110Ma) combined with the separation between South America and Africa (~110Ma) caused spreading rates in the Central Atlantic to increase by about three times (**Fig. 2.7e**). This in turn induced a spreading differential between the North and Central Atlantic, which is thought to have caused Africa's motion relative to Europe to change gradually to northeasterly directed compression (~118-84Ma) (Dewey et al., 1989) (**Fig. 2.7f**). As a result, strike-slip motion between Africa and Iberia on the transform plate boundary essentially ceased.

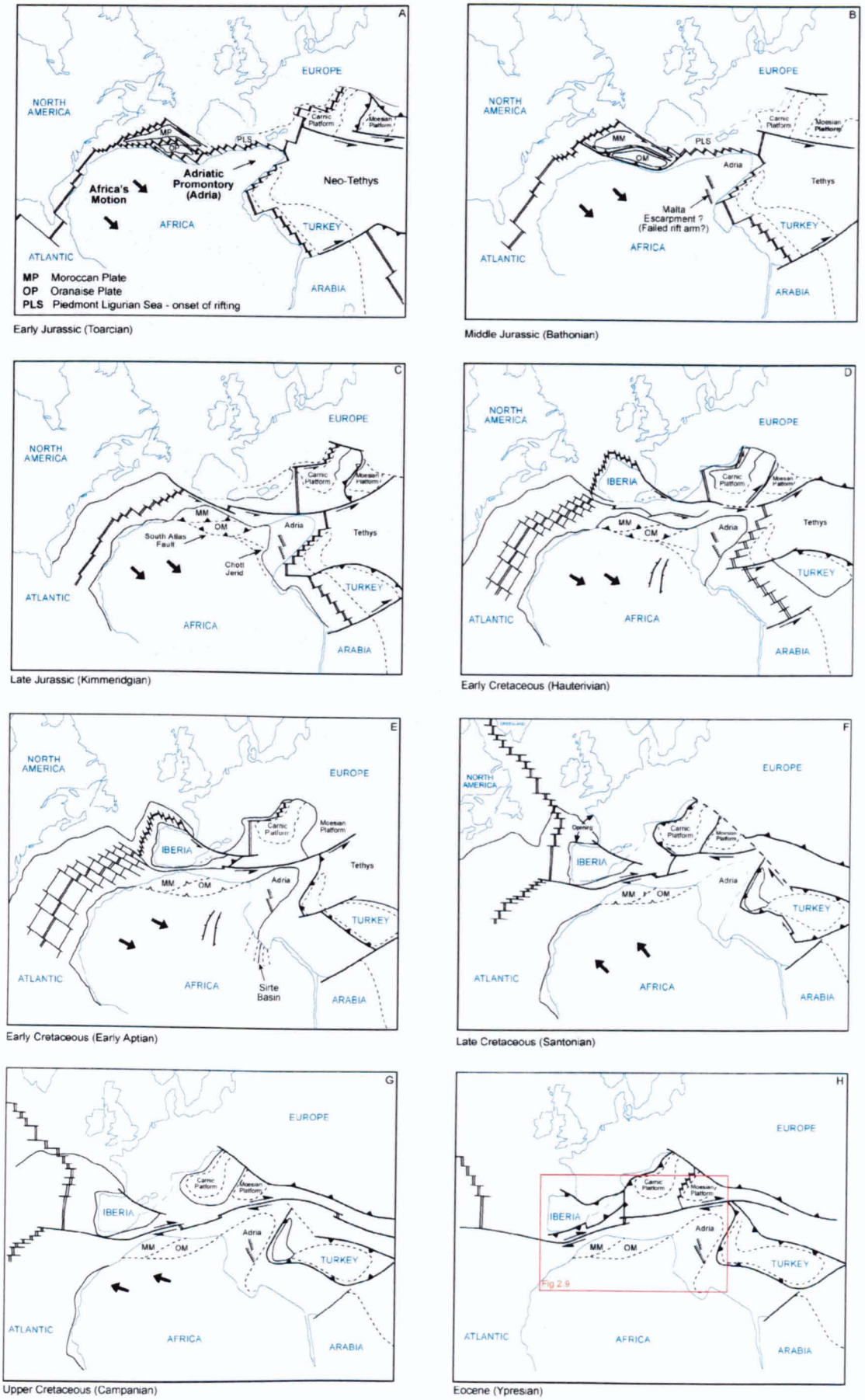

Fig. 2.7. Series of plate tectonic reconstructions from the Early Jurassic to the Eocene illustrating the relative motion of North America, Africa and Europe. Filled arrows show the relative motion of Africa with respect to Europe (modified after Dewey et al., 1973)

Initial Africa-Europe Plate Collision

The compressional regime throughout the Late Cretaceous caused the initiation of north to northwesterly dipping subduction zones beneath the southern margin of Europe where the western Neo-Tethyan ocean began to be consumed (Hill & Hayward, 1988). Closure of this ocean occurred perpendicular to the original E-W spreading direction, probably utilising one of the well developed ridge axis transform faults (probably in the Piedmont-Ligurian Sea) as a suitable zone of weakness for subduction nucleation (Abbatte et al., 1984). Northeasterly directed compression additionally induced the first stage of collision between the North African continental margin and the European continental margin leading to inversion of many basins along the African-Arabian Tethyan margin (e.g. Syrian Arc) (Guiraud, 1998). It also initiated various present-day thrust belts (e.g. the Tunisian and Saharan Atlas) and reactivated deep-seated E-W and N-S trending lineaments throughout the North African Tethyan margin (e.g. The North-South Axis of Central Tunisia). Dewey et al. (1973) and Channel et al. (1979) dated this initial collision at ~95Ma (Cenomanian), while Guiraud (1998) has subsequently proposed an age of approximately 85Ma (Santonian).

The northeasterly compression continued throughout the Late Cretaceous. Savostin et al. (1986) demonstrated utilising the model of Olivet et al. (1984) that at around 80Ma this compressive regime caused the relative motion of the European and African plates to switch to dextral strike-slip. The latest paths presented by Dewey et al. (1989) suggest that this transition in movement was essentially a very gradual process. Pitman & Talwani (1972) and Dewey et al. (1973) have proposed that about 1000km of dextral movement occurred from then until the present-day, associated with hundreds of kilometres of northward motion.

During the Campanian (66.7Ma), another change of relative motion between Africa and Europe occurred. A gradual increase in the dextral transcurrent component is thought to have caused a dramatic decrease in the rate of convergence between Africa and Europe (Channell et al., 1979; Cavallin & Tornaghi, 1986) (**Fig. 2.7g**). This correlates closely with a change in the orientation of the Charlie-Gibbs fracture zone, Thulean volcanism in the NE Atlantic as well as renewed subsidence in the North Sea (Ziegler, 1975).

During the Ypresian (55.7Ma) Africa resumed it's northward course, culminating in the resumption of tectonic activity at the plate margins (Meso-Alpine deformation-53Ma (Dewey et al., 1989)) (**Fig 2.7h**). This correlates well with initial opening in the Greenland-Norwegian Sea, and the gradual cessation of spreading in the Labrador Sea (Dewey et al., 1989). Meso-Alpine deformation continued uninterrupted into the Oligocene, as a result of persistent north-south compression. A magmatic arc developed on the overriding Eurasian plate, followed by widespread calc-alkaline volcanism in Sardinia and Calabria (which remained attached to Europe at that time) (Treves, 1984). It has been proposed that this tectonic activity was related to the onset of back arc extension within the European plate, which occurred either by the induction of secondary convection behind the subduction zone (Treves, 1984), by the delamination of the down-going continental lithosphere (Channell & Mareschal, 1992), or by subduction roll-back mechanisms (Lonergan & White, 1997). The latter of these mechanisms is favoured in this account (**Fig. 2.8**). The rifting between Southern France and the still attached Corsica-Sardinia-Calabria (CSC) block is thought to have begun around 30 Ma (Hill & Hayward, 1988), only a few million years after the initiation of Meso-Alpine collision (**Fig. 2.9a-b**).

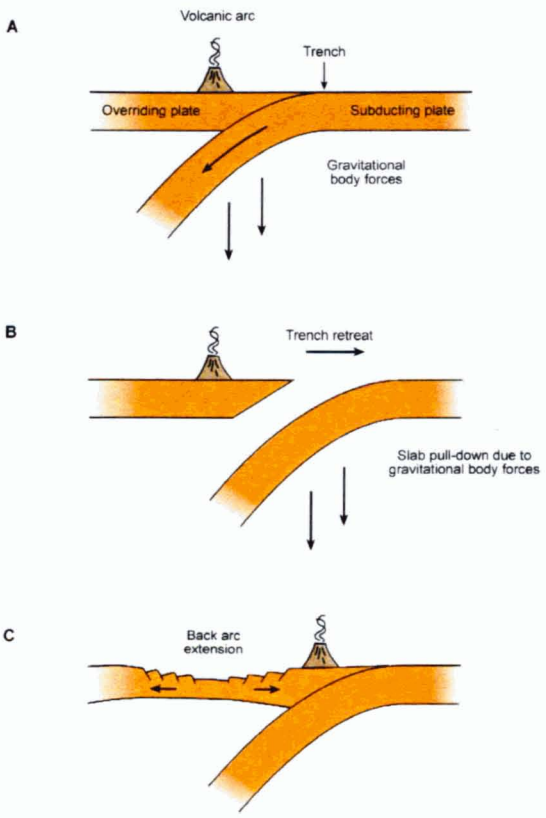

Fig. 2.8. Diagram illustrating back-arc extension caused by subduction roll-back (modified after Lonegan & White, 1997).

Formation of the Modern Balearic-Ligurian Basin

Progressive back-arc extension (due to subduction roll-back) within the southern European continent throughout the Oligocene eventually resulted in the formation of the first modern day Western Mediterranean Basin, the Balearic-Ligurian Sea (Hsu et al., 1979; Channell and Mareschal, 1989; Dewey et al., 1989) (**Fig. 2.9b**). Extension in the Balearic-Ligurian Sea caused the gradual counterclockwise rotation (~25^0-30^0) of the independent Corsica-Sardinia-Calabria (CSC) plate away from Europe (Treves, 1984; Keller, 1990) (**Fig. 2.9b-c**). It has been proposed that the initial rotation of Sardinia may have occurred independently of Corsica, which is an idea supported by data on their respective poles of rotation (Dewey et al., 1989). Cohen et al. (1980) demonstrate on the basis of magnetic lineations that the Petit Kabylie formed the southern extension of the CSC plate during the late Oligocene and Early Miocene. They subsequently termed it the Corsica-Sardinia-Petit Kabylie (CSPK) microplate.

Alpine Collision

The exact age of collision between the CSPK microplate and the northern sector of Western Adria is controversial (**Fig. 2.9b-c**). Hill & Hayward (1988) suggest that initial collision occurred in the latest Oligocene (~25Ma), while Cohen et al., (1980) propose an age of ~14Ma- 16Ma (Serravallian/Langhian). Nevertheless, collision resulted in the gradual accretion of a 12 km thick orogenic wedge (consisting of the stacked sedimentary/ophiolitic nappes of the present-day Northern Apennines) onto the thinned continental crust of the Adriatic promontory's passive margin.

The progressive counter-clockwise rotation of the CSPK microplate throughout the Early Miocene allowed continental collision to extend southwards, leading to more intense deformation in the Central and Southern Apennines (Hill & Hayward, 1988; Dewey et al., 1989; Keller, 1990) (**Fig. 2.9b-c**). The rotation of the CSPK microplate ended in the Middle Miocene (dated according to palaeomagnetic data at ~18-19Ma by Dewey et al., 1989), when Apenninic deformation became entirely controlled by the strike-slip N-NNE/S-SSW convergence between Africa and Eurasia (Hill & Hayward, 1988) (**Fig. 2.9c**). This led to intense shortening in the growing mountain belt between 18-10Ma, while the Alpine chain was being eroded (Hill & Hayward, 1988). Cohen et al. (1980) propose that after the completion of CSPK rotation (~19Ma), spreading in the area west of the Straits of Sardinia caused the Petit Kabylie

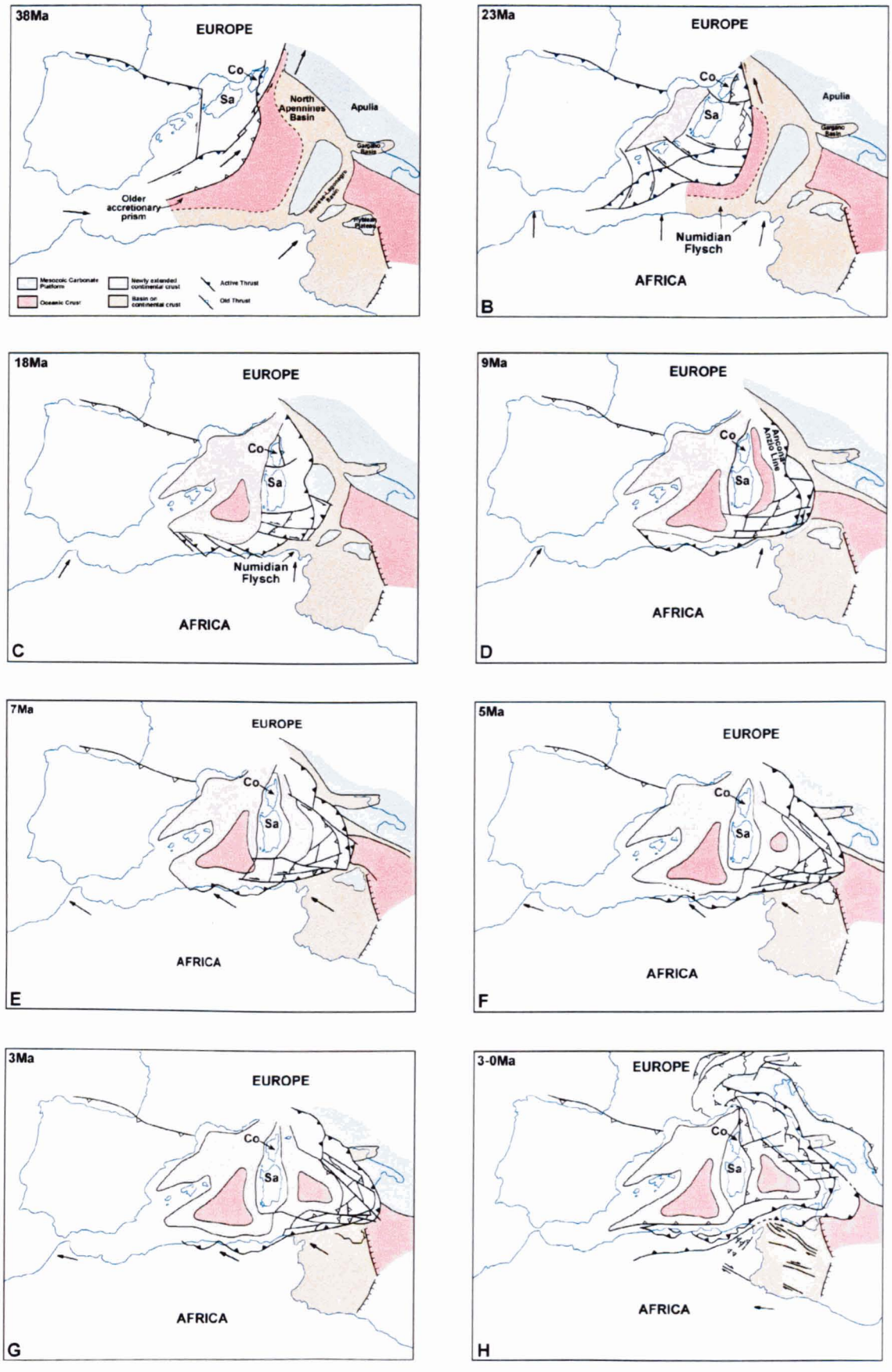

Fig. 2.9. Kinematic reconstructions depicting the evolution of the western and central Mediterranean region. The reconstructions show events occurring and the relations of tectonic events at A) 38Ma (Priabonian), B) 23Ma (Aquitanian), C) 18Ma (Burdigalian), D) 9Ma (Tortonian), E) 7Ma (Tortonian), F) 5Ma Zanclean, G) 3Ma (Piacenzian), and H) 3Ma to 0Ma (Piacenzian to Holocene) (modified after Dewey et al., 1989).

to move away from Sardinia to it's present-day position in eastern Algeria. The extensional regime in northern Tunisia and the compressional regime in eastern Algeria are both related to this Tortonian seafloor spreading.

Formation of the Modern Tyrrhenian Basin

Nappe emplacement and most Apenninic deformation had virtually ceased in the Late Miocene (Hill & Hayward, 1988), at which time the only remaining subduction zone had migrated to the southeastern sector of the Western Mediterranean (Lonergan & White, 1997) (**Fig. 2.9d**). During this time, persistent plate consumption led to the development of a volcanic arc on Calabrian continental crust, as the final areas of Neo-Tethys were being destroyed. It appears most likely that the originally N-NW dipping subduction zone which was involved in the back arc extension of the Balearic-Ligurian Sea also generated the Southern Tyrrhenian Sea during persistent roll-back (Lonergan & White, 1997). The initiation of rifting is usually considered as middle to late Miocene in age, postdating the collision of the Calabrian island arc with the Adriatic Promontory by a few million years (Hill & Hayward, 1988; Dewey et al., 1989; Channell & Mareschal, 1992).

The approximate Miocene-Pliocene boundary was marked by a final change in Africa's motion relative to Europe, to a general NNW-NW direction (present-day relative motion) (Dewey et al., 1989) (**Fig 2.9e-f**). These movements were joined in the early Pliocene by a component of counterclockwise rotation, eventually resulting in the emplacement of the Calabrian Arc onto both Sicily and the southwestern extremity of present-day Italy (Manzonni & Vigliotti, 1983). Continued extension along the Tyrrhenian rift system finally allowed the onset of sea floor spreading in the southeastern and central regions, and to the reactivation of former Apenninic thrusts as extensional faults (Hill & Hayward 1988). During the latest Miocene, Sicily also began a counterclockwise rotation, causing the onset of extension in the Sicily Channel and adjacent Pantelleria Graben (Hill & Hayward, 1988) (**Fig 2.9g-h**).

Figure 2.10 (Enclosures 2 & 3) illustrates the present-day tectonic configuration of the Central Mediterranean area. Robbins et al. (1992) and Ward (1994) suggest that the African plate is currently moving north-northwestwards at a rate of slightly less than 1 cm yr^{-1} towards Europe. Smith & Livermore (1985) postulate that complete closure of the Mediterranean will probably occur some 30-40Ma into the future.

CONTAINS PULLOUTS

2.3. Geological Framework of the Pelagian Platform

2.3.1. Introduction

The present-day reconstruction of the Central Mediterranean region shows the Pelagian Platform located between Latitudes 33°-37° and Longitudes 10°-16° on the northern margin of the African Plate (**Fig. 2.10**). It is bordered to the south by the Saharan Platform (a stable cratonic area) and to the north by the frontal part of the Sicilian segment of the Apenninic-Maghrebian thrust belt (Butler et al., 1995). In Tunisia it terminates abruptly against the North-South Axis, a major transfer zone that has been active throughout the Mesozoic and Tertiary. To the east it is bounded by the Malta Escarpment, which separates the platform area from the Ionian Sea.

The present-day configuration of the Pelagian Platform is represented by a complicated network of shallow shelves and intervening fault-controlled basins. This framework reflects a complex tectonic history involving both intraplate extension and plate margin deformation. To date, the controls on these tectonic processes remain poorly understood due, in part, to a concentration of research elsewhere. Nevertheless, this region has played an important role in the regional geodynamic and kinematic evolution of the North African continental margin. This section examines the tectono-stratigraphic framework of the region and provides a synthesis of the structural evolution of the area. It will also introduce the location of the main study area.

2.3.2. Bathymetry

Shallow seas cover the majority of the Pelagian Platform. The only outcropping portions occur in SE Sicily, Maltese and Pelagian Islands, and the onshore 'Sahel' region of Tunisia (**Fig. 2.11**). Bathymetric maps over the submerged portion show the presence of three main shelf areas that are separated from one another by a series of approximately NW-SE trending structural highs (Medina and Lampedusa Plateaux) and tectonic troughs (Pantelleria, Linosa, Malta and Medina graben). These are more clearly illustrated in **Figure 2.16**. In the southern part of the platform gentle eastward gradients characterise the Gulf of Gabes and the offshore regions of Libya.

The eastern margin of the Pelagian Platform is marked by a two steep escarpments (20^0-30^0), which have composite vertical displacements in excess of 3000m (Malta

and Medina Escarpments) (Grasso & Reuther, 1988) (**Fig. 2.11**). They separate continental crust of the platform area from sub-oceanic crust of the Ionian Sea (Makris & Stobbe, 1984; Ferrucci et al., 1991). These escarpments are separated from each other by a series of east-west trending seamounts that form the Medina Ridge.

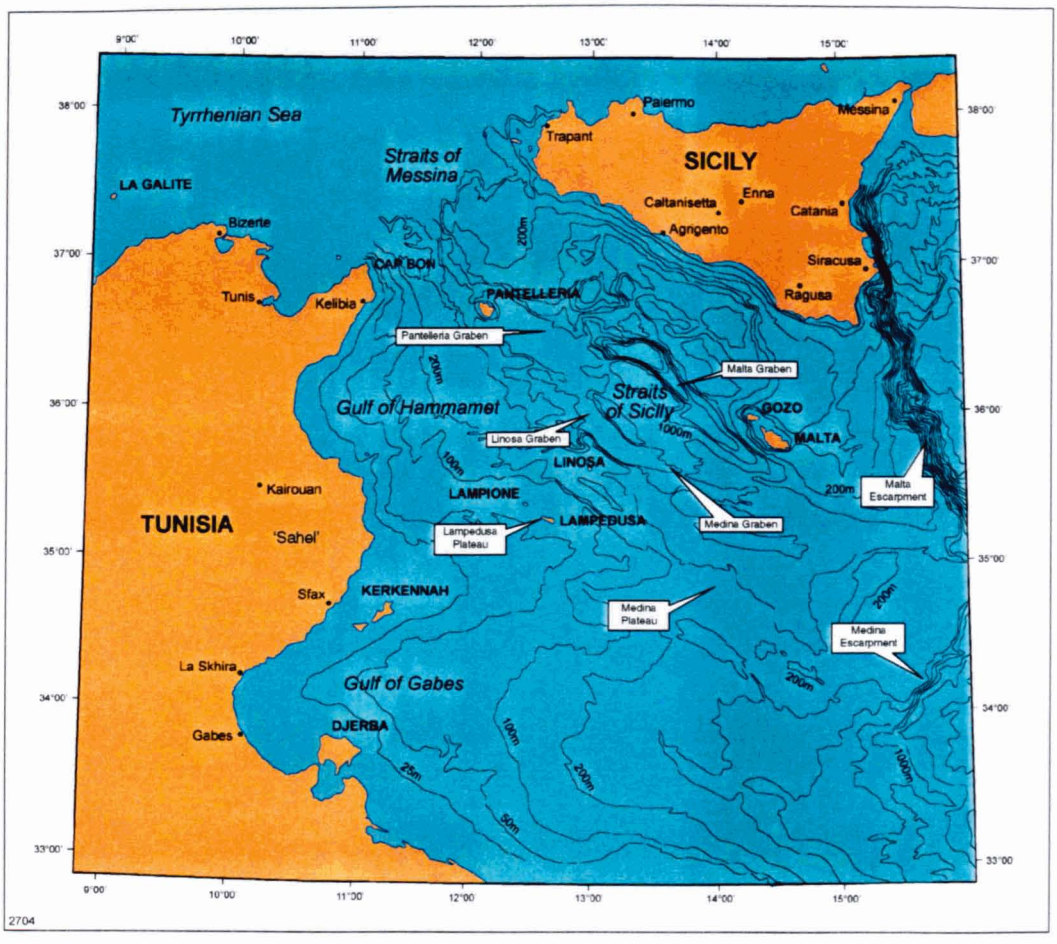

Fig. 2.11. Bathymetry of the region encompassing the Pelagian Platform (after IOC-UNESCO, 1981). Refer to Figure 1.1 for the boundaries to the Pelagian Platform.

2.3.3. Crustal Structure & Seismicity

Gravity

Free air and Bouger gravity fields over the Pelagian Platform generally show positive values near to zero and gentle gradients south of 35^0N (Morelli et al., 1975) (**Fig. 2.12**). In contrast anomalies of >50 mgal are common over the Straits of Sicily and the Malta and Medina Escarpments. Over the Pantelleria and Linosa graben, values of ~90 mgal are thought to be associated with volcanic intrusion and Late Miocene-Recent crustal stretching (Morelli et al., 1975; Jongsma et al., 1985; Grasso et al., 1990). Deep refraction seismic data supports this theory, indicating that the

continental crust on the Pelagian Platform thins from approximately 30-35km beneath central Tunisia and Sicily to 20km along this zone (Boccaletti et al., 1987) (**Fig. 2.13**).

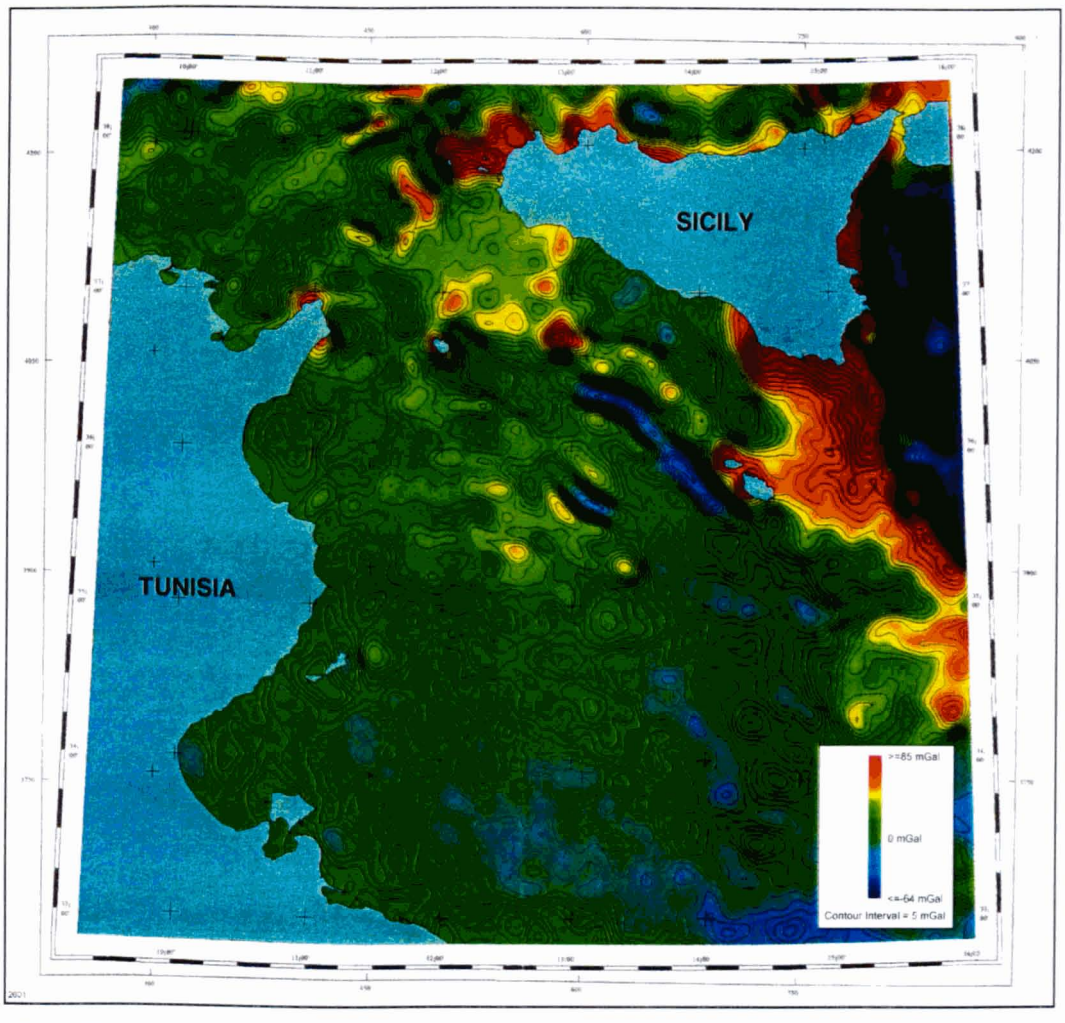

Fig. 2.12. Free-air gravity map of the Pelagian Platform. High anomalies are present along the Straits of Sicily Rift Zone (Pantelleria and Linosa Islands) and the Malta Escarpment (NPA & TREIC Report, 1997).

Magnetics

The total magnetic field over the area shows low amplitude, broad anomalies over the southwestern region of the Pelagian Platform (Morelli et al., 1975) (**Fig. 2.14**). In contrast high amplitude short wavelength anomalies are observed along the Malta Escarpment, Medina Plateau and over major volcanic edifices (i.e. the volcanic islands of Pantelleria and Linosa).

Heat Flow

Published heat flow measurements over the Pelagian Platform are sparse. The only one identified, located in the Linosa Trough gave a value of 50 mWm^{-2} (Erickson et

al., 1977). This value is slightly greater than the global normal (~42 mWm^{-2}), although it should be noted that it is uncorrected for the relatively high sedimentation rates in this trough (e.g. ~128 cm ka^{-1}) (Maldonado & Stanley, 1976).

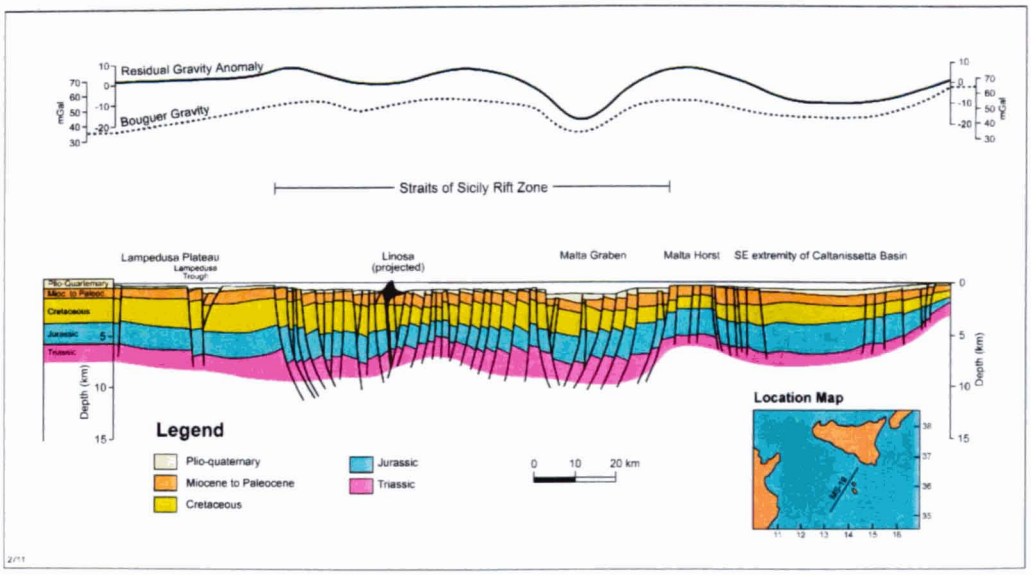

Fig. 2.13. Line drawing of seismic profile MS-19, and the respective Bouger and Residual Gravity data over the Straits of Sicily Rift Zone (after Finetti, 1985).

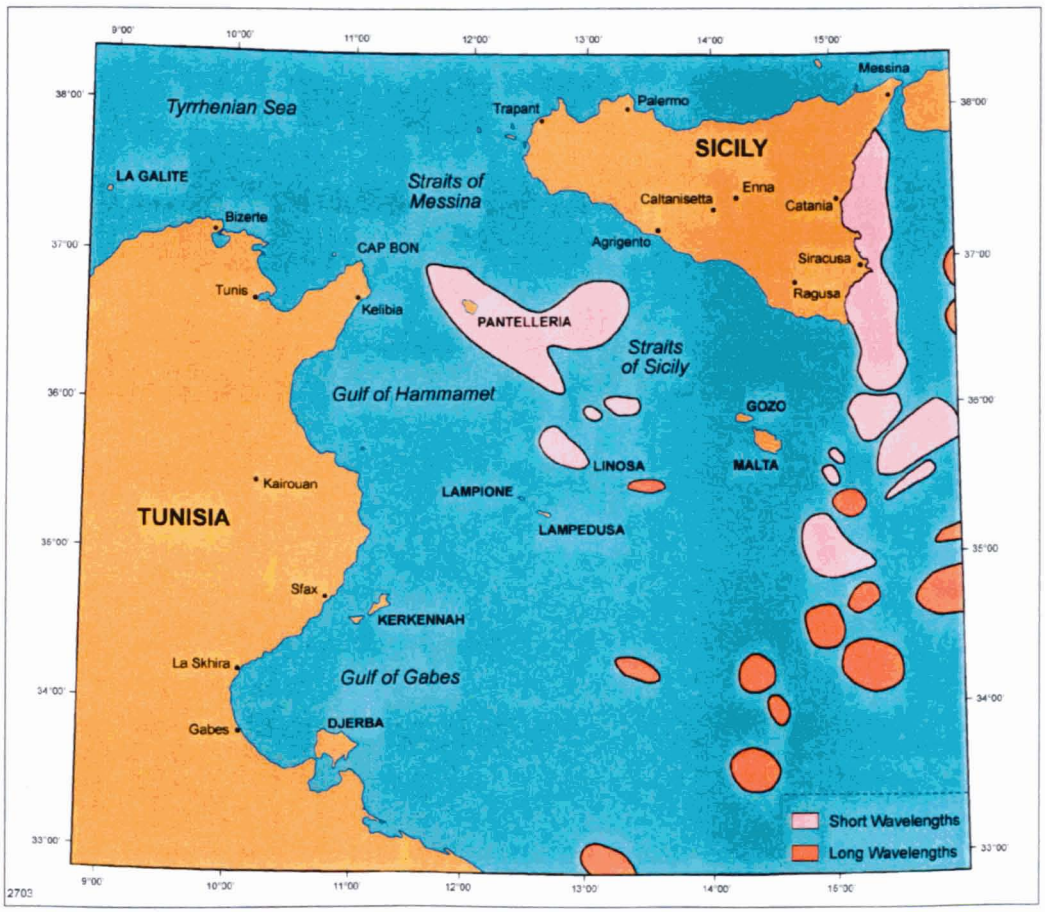

Fig. 2.14. Simplified magnetic anomaly map of the Pelagian Platform. Short wavelength anomalies characterise the Straits of Sicily Rift Zone and the Malta Escarpment. Long wavelength anomalies are present over the Medina Plateau (after Morelli et al., 1975).

Seismicity

In recent time (i.e. 1961–2000), the Pelagian Platform has experienced relatively few earthquakes (**Fig. 2.15**). Recorded magnitudes have ranged between 3.8 and 5.1, with no reliable focal depths recorded greater than 10km (Jongsma et al., 1985). This is an indication that the present deformation rate is relatively low and mainly in the upper part of the crust.

Jongsma et al. (1985) and Westaway (1990) have determined focal mechanisms for the larger earthquakes on the platform area, in particular, the Tripoli earthquake of 1974 (M_S 5.6). The focal mechanism proposed for this earthquake varies considerably between workers; Jongsma et al. (1985) advocated a reverse dextral oblique-slip mechanism, whereas Westaway (1990) proposed a normal dextral oblique-slip mechanism (**Fig 2.15**). The latter mechanism of Westaway (1990) is preferred as it is more consistent with the development of recent structures in the Tripoli region.

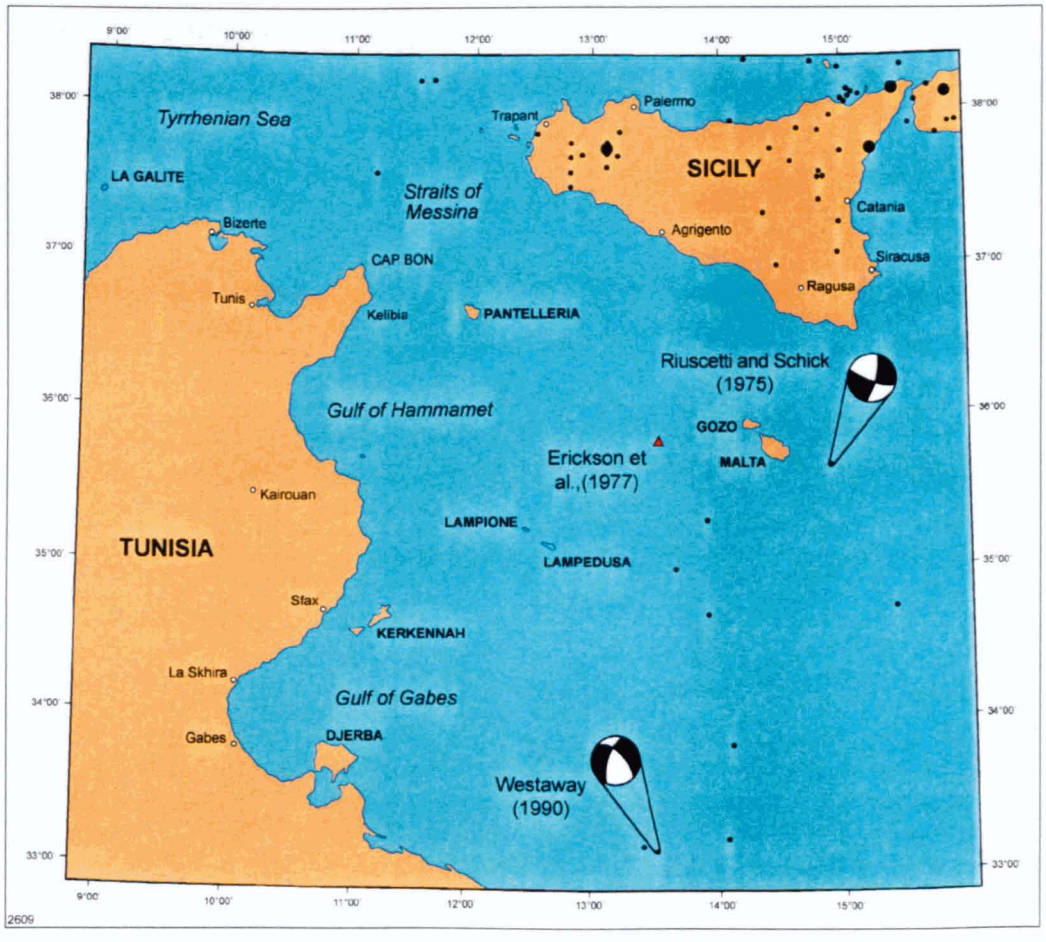

Fig. 2.15. Seismicity on the Pelagian Platform since May 1981. Small and large black (filled) circles show the location of earthquake foci for depths of 0-50km and 50-200km respectively. The filled red triangle represents the location of the heat-flow station of Erickson (1977). Fault plane solutions are given for two earthquakes, offshore Malta and offshore Libya (modified after Jongsma et al., 1985)

2.3.4. Tectono-Stratigraphic Framework

The bathymetric, gravity and magnetic maps presented in the following section illustrate that the Pelagian Platform may be sub-divided into distinct geological domains (**Fig 2.16**). In summary, three main shelves are distinguished based on the 200m bathymetric contour interval:

- **The Hyblean-Maltese Shelf** – which extends from Malta into the onshore region of south-east Sicily (i.e. the Hyblean Plateau);
- **The Tunisian Shelf** – which extends offshore eastern Tunisia down to Libya, and contains the Tunisian 'Sahel', it's onshore extension. The Gulf of Gabes region straddles the eastern side of the Tunisian Shelf;
- **The Adventure Shelf** - a smaller shelf area located in the offshore region of southwestern Sicily.

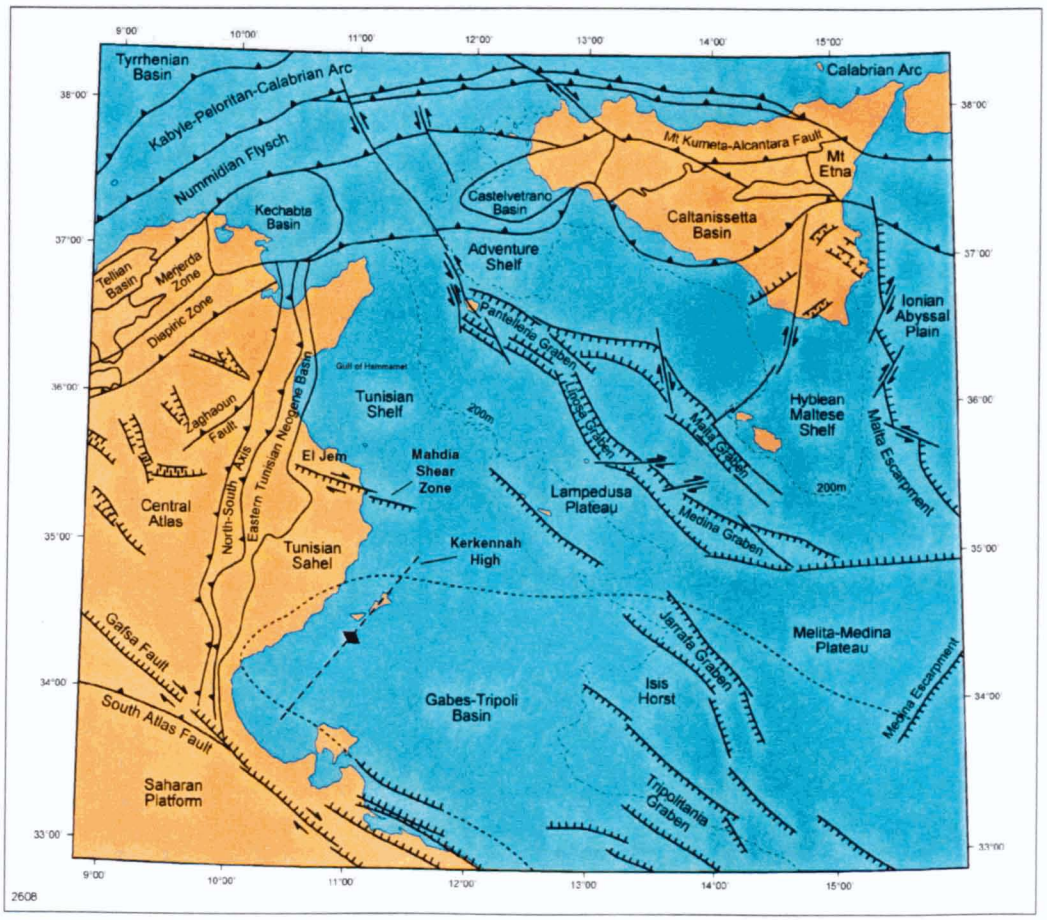

Fig. 2.16. Simplified tectonic map of the Pelagian Platform showing the main geological elements (compiled from numerous sources, including Bishop (1975, 1988), Boccaletti et al. (1983; 1987, 1988), Burollet et al. (1978), Burollet (1991), Cello (1987), Dercourt et al. (1975), Grasso et al. (1990), Finetti (1985), Jongsma et al. (1985), Monaco & Tortorici (1996), Reuther (1990), Reuther et al. (1993) Beckett, (2000) and Yellin-Dror et al. (1997).

These shelves are separated from one another by a series of approximately NW-SE trending structural highs (plateaux) and tectonic depressions:

- **The Medina & Lampedusa Plateaux** – located offshore Central Tunisia, south of the Straits of Sicily;
- **The Pantelleria, Malta, Linosa & Medina Graben** – located in the Straits of Sicily. Together, these graben form the Straits of Sicily Rift Zone.

In addition, within the southern sector of the Pelagian Platform, bathymetric maps delineate a large basin that provides the area of interest this thesis:

- **The Gabes-Tripoli Basin** – which extends from the North-South Axis in the west, across the Eastern Tunisian Shelf into the Libyan offshore, terminating at the Medina Escarpment.

A brief overview of the geology of each of these structural domains is given below. **Figure 2.17** provides a detailed lithostratigraphic correlation for the entire region based on fieldwork and well data from the three main shelf areas.

Hyblean-Maltese Shelf

The Hyblean-Maltese Shelf is located on the northeastern portion of the Pelagian Platform, covering an area of approximately 17,000 km^2 (**Fig. 2.16**). It consists of the emergent Hyblean Plateau that constitutes southeastern Sicily, and its southern offshore extension, which continues as far as the Maltese Islands. It is bounded to the east by the N-S Malta Escarpment and to the west by the NNE-SSW oriented Margi and Comiso Faults (Pedley and Grasso, 1991), which are oblique to the main trend of the Maghrebian Chain. In the north and northwest it is bordered by frontal Gela thrust.

Finetti (1982) has shown from seismic, gravity and well data that it consists of an approximately 8.8km thick succession of Permo-Triassic to Quaternary platform carbonates and intercalated volcanics, underlain by crystalline basement (N.B. depth to Moho is ~23km) (**Fig. 2.17**). The late Cenozoic succession progressively thins from west to east and from north to south, due to regional uplift in the Pleistocene (Bianca et al., *in press*). This uplift is characterised on the emergent parts of the Hyblean Plateau by the occurrence of several orders of middle to late Quaternary marine terraces and palaeostrandlines (Di Grande & Raimondo, 1982).

CONTAINS PULLOUTS

Structurally, the Hyblean-Maltese Shelf has been mainly affected by extension and strike-slip movements (Ghisetti & Vezzani, 1980), although minor thrusting and folding does occur. On the Hyblean Plateau, NE-SW and ENE-WSW trending normal faults predominate, forming small asymmetric horst and graben parallel to the Gela-Catania Foredeep (e.g. the Marina di Ragusa Graben system) (Barrier, 1992) (**Fig. 2.18**). In the western part of the Hyblean Plateau, the NNE-SSW trending Scicli Fault forms a major shear zone dissecting the entire shelf area. Secondary NNW-SSE and NW-SE faults are present on the eastern margin of the platform area, associated with the Malta Escarpment (Torelli et al., 1998). On the Maltese Islands however, WNW-ESE and NE-SW faulting reflects a complex history of Late Miocene crustal stretching in the Straits of Sicily.

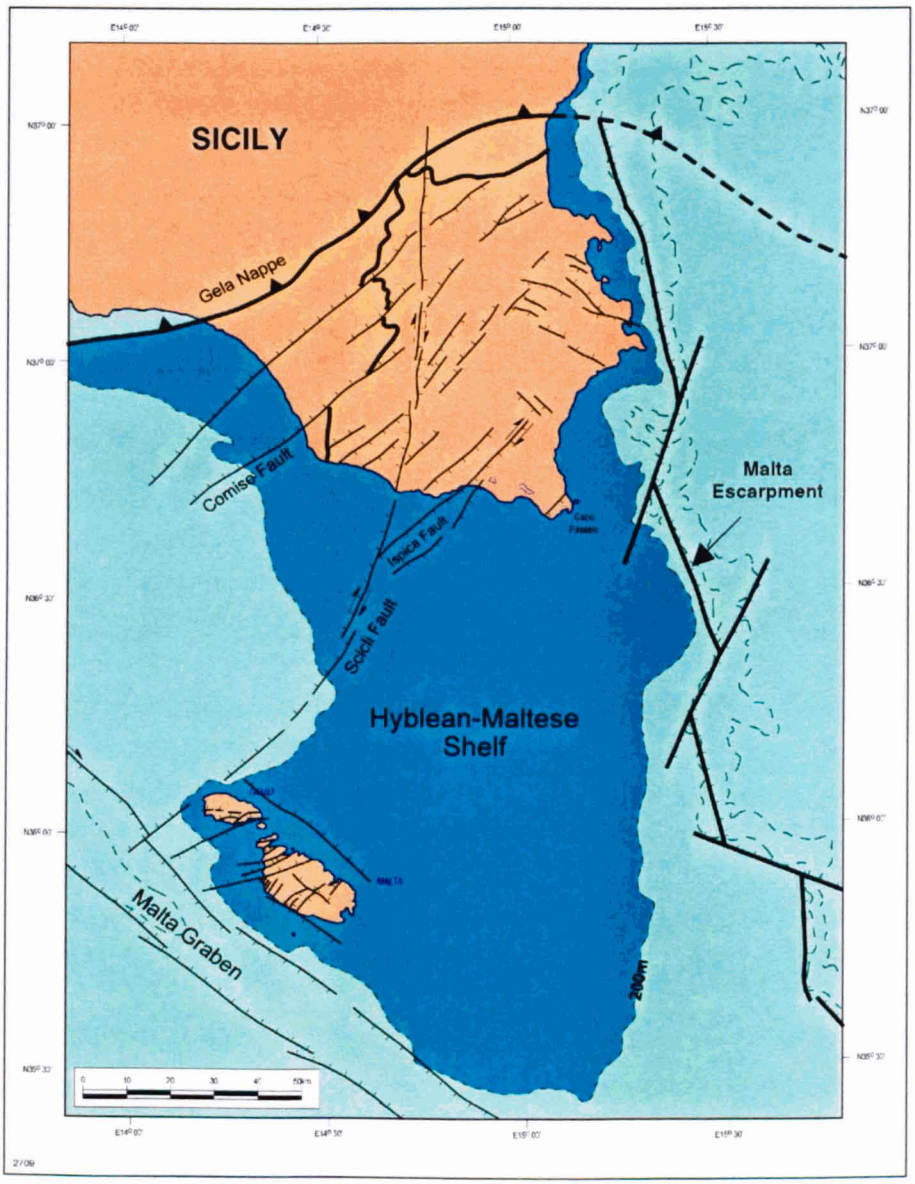

Fig. 2.18. Tectonic map of the Hyblean-Maltese Shelf, showing the main styles of faulting (compiled from Finetti (1985), Grasso et al. (1990) and Pedley (1990).

The Tunisian Shelf

The Tunisian Shelf consists of the onshore 'Sahel' region of Tunisia, east of the North-South Axis and extends offshore incorporating the Djerba and Kerkennah islands located in the Gulf of Gabes, and also the Pelagian Islands of Lampedusa and Lampione (**Fig. 2.16**). Ben Ferjani et al. (1990) and Torelli et al. (1995) estimate that it consists of an approximately 6 to 6.5km thick succession dominated by Triassic to present-day platform carbonates (**Fig. 2.17**). Camion (1991) suggests that the original early Mesozoic platform margin ran approximately NW-SE across central Tunisia, in agreement with the facies maps of Salaj (1978). Shallow water carbonate deposition was generally restricted to the southern and central parts of the present-day shelf area, whereas deep-water basinal deposition occurred to the northeast (i.e. Gulf of Hammamet). The age of the underlying basement is poorly constrained, although Precambrian granites and metamorphic schists have been drilled in southern Tunisia (N.B. depth to Moho is between 25-35km) (Burollet, 1991).

The present-day structure of the Tunisian Shelf is extremely varied. In the northern areas (i.e. the Cap Bon Peninsula and the Gulf of Hammamet) adjacent to the frontal zones of the Alpine thrust front, reverse and strike-slip fault geometries are common. Thrusts identified in the Gulf of Hammamet strike approximately NE-SW, parallel to the main trend of folding (e.g. Sidi Abderrahman anticline) (Ben Ferjani et al., 1990). Messaoudi & Hamouda (1994) have shown that parts of the Gulf of Hammamet have been partially inverted along pre-existing extensional faults. Further offshore to the east, NW-SE trending Plio-Pleistocene extensional faults are evident, related to extension in the Straits of Sicily.

In the central parts of the Tunisian Shelf (i.e. the Mahdia and El Jem regions) large N-S trending sinistral shear zones are apparent, associated with the North-South Axis (e.g. the El Jem Shear Zone (EJSZ)) (Bedir et al. 1992). These structures are accompanied by broad E-W trending dextral shear zones, in particular the Mahdia Shear Zone (MSZ) (Bedir et al. 1992) (**Fig. 2.16**). Transtensional and transpressional movements on these two fault systems throughout the Mesozoic and Tertiary controlled the subsidence history of this area. The significance of the MSZ is discussed in Section 2.3.5.

To the south of this zone, the Tunisian Shelf is dominated by NW-SE extensional faulting. N-S structures are also present and show evidence of inversion (e.g. Miskar Gas Field). The NNE-SSW trending Kerkennah Arch (or Kerkennah Plateau) located in the western part of the Gulf of Gabes is important in that it influenced sedimentation throughout the Mesozoic and Tertiary. The western part of the Gabes-Tripoli Basin straddles the southern margin of the Tunisian Shelf. This basin formed during the Late Triassic as a result of Tethyan rifting and became the main depocentre for sedimentation during the Mesozoic and early Tertiary. In the southern part of the Gulf of Gabes, halokenisis is evident with the presence of large Triassic salt walls piercing the Mesozoic and Cenozoic succession (e.g. in the vicinity of Djerba Island) (Burollet, 1991).

The Adventure Shelf

The Adventure Shelf, located offshore south-western Sicily is bounded to the east by the Caltanissetta Basin, the north by the frontal part of the Appeninic-Maghrebian thrust belt and to the south by the Straits of Sicily Rift Zone (**Fig. 2.16**). It consists of a sedimentary succession similar to that on the Hyblean-Maltese Shelf. The eastern margin is characterised by a broad transpressive sinistral shear zone with associated NNE-SSW trending thrusts and strike-slip faults (Antonelli et al., 1988; Argani et al., 1987). Gravity data shows that this fault zone can be traced offshore to the northwestern end of the Malta graben (Morelli et al., 1975) (**Fig. 2.12**). Reuther et al., (1993) indicate that the northeast-southwest extension of the Malta Graben is accommodated by sinistral strike-slip movement along this fault zone. Thrusting and strike-slip faulting is evident along the northern margin of the Adventure Shelf adjacent to the frontal segment of the Maghrebian chain. In the south, NW-SE extensional structures dominate, trending parallel to the system of graben that form the Straits of Sicily Rift Zone (Finetti, 1982).

The Straits of Sicily Rift Zone

The Straits of Sicily Rift Zone (SSRZ) is located c. 200km south of the frontal Apennine-Maghrebian thrusts in between Sicily and Tunisia (Pedley and Grasso, 1991) (**Fig. 2.16**). As previously mentioned, it is comprised of a series of NW-SE trending graben (i.e. The Pantelleria, Linosa, Malta and Medina Graben), which

formed during a phase of Late Miocene crustal extension (Cello et al., 1985; Reuther and Eisbacher, 1985; Boccaletti et al., 1987).

Bathymetric maps clearly define a series of roughly E-W and N-S trending lineaments within this zone, which are cut by a later system of NW-SE trending faults (Reuther et al., 1993). These younger NW-SE faults form the master bounding faults to the post-Late Miocene graben. Estimated composite normal displacements on these faults range between 500m in the Pantelleria Graben to approximately 1000m in the Malta graben (Winnock, 1981). The graben are generally filled with Late Miocene-Pleistocene turbidites between 1000-2000m thick in the Pantelleria and Linosa graben (Maldonado and Stanley, 1977; Boccaletti et al., 1987). In addition, these graben host volcanics of predominantly alkaline composition, ranging in age from 274,000BP to the present-day (Mahood and Hildreth, 1983). Typical volcanic suites are exposed on the islands of Pantelleria and Linosa (Reuther and Eisbacher, 1985).

The eastward termination of the Straits of Sicily Rift Zone is marked by a series of seamounts that make up the Medina Ridge (Finetti, 1985; Jongsma, 1991; Anketell, 1992) (**Fig. 2.16**). This zone of complex deformation separates the Malta and Medina Escarpments. It is characterised by a series of NE-SW trending folds and reverse faults, which are thought to represent the continuation of the SSRZ dextral strike-slip zone into the Ionian Sea (Jongsma et al., 1985).

The Lampedusa and Medina Plateaux

The Lampedusa and Medina Plateaux are located south of the Straits of Sicily Rift Zone and north of the Gabes-Tripoli Basin (**Fig. 2.16**). They represent regional structural highs that have existed since at least the Cretaceous (Finetti, 1982). Structurally, they are dissected by numerous NW-SE trending extensional faults, common to the eastern part of the Pelagian Platform. Both areas are affected by extensive volcanic activity, the Medina Plateau characterised by several prominent magnetic anomalies (Morelli et al., 1975) (**Fig. 2.14**).

The Gabes-Tripoli Basin

The Gabes-Tripoli Basin (GTB) (Finetti, 1985), otherwise known as the Gabes-Tarãbulus Basin (Hammuda et al., 1992) or the Sabratah Basin (Anketell, 1992) is located on the southern part of the Pelagian Platform (Anketell, 1992) (**Fig. 2.16**). It

extends from the North-South Axis in the west, across the Tunisian Shelf into the Libyan offshore where it terminates at the Medina Escarpment (El Ghoul, 1992; Hammuda et al. 1992). It is bounded to the south by the Gafsa-Jarrafa Fault Zone (GJFZ), which also forms the southernmost limit to the Pelagian Platform (Burollet, 1978).

The basin itself is elongate (~500km in length and ~250km wide), trending approximately WNW-ESE. It contains a succession of platform carbonates and basinal shales up to 11km thick in the deepest part (McCrossan et al., 1989). Anketell (1992) suggests that its development is coeval with the formation of the adjacent Sirte Basin in Libya. Structurally, the Gabes-Tripoli Basin is characterised by a system of approximately NW-SE trending extensional faults, sub-parallel to the basin axis (Anketell, 1992). These faults form a series of graben that vary in length from a few to several hundred kilometres (Hammuda et al., 1992).

2.4. Tectonic Evolution of the Pelagian Platform

The following section provides a brief synthesis of the key tectonic phases that have affected the Pelagian Platform, and offers mechanisms for the formation of individual structural elements (e.g. the Straits of Sicily Rift Zone).

2.4.1. Late Triassic to Early Cretaceous Evolution

In the Late Triassic and Middle to Late Jurassic the Pelagian Platform was subjected to rifting associated with the westward spreading of the Neo-Tethys (Ouali, 1985). Geophysical evidence (Boccaletti et al., 1988) indicates that the depth to the base of the crust decreases across the Pelagian Platform in an ENE direction, towards Late Jurassic age oceanic or highly attenuated continental lithosphere in the Ionian Sea (Dewey et al., 1973; Finetti, 1982). This suggests an approximately ENE extension direction. It created a series of N-S trending extensional faults and E-W transfer zones above earlier basement lineaments across the Pelagian Platform. The most important of these N-S structures developed along the lines of the present-day North-South Axis and the Malta and Medina Escarpments (**Fig 2.19a**). The E-W trending Mahdia Shear Zone (MSZ) in east-central Tunisia and the Gafsa-Jarrafa Fault Zone (GJFZ) may represent remnants of these early transfer zones.

During this tectonic phase extensive shallow-water carbonate platforms developed on the North African continental margin. Shelf carbonates were deposited throughout central and southern Tunisia and on the much of the eastern margin of the present-day Hyblean-Maltese Shelf (HMS) (**Fig. 2.17**). The western limit of the platform area on the HMS during the Late Triassic was defined by a large N-S fault zone related to the Malta Escarpment. In Tunisia, the North-South Axis exerted considerable control on sedimentation throughout the Late Triassic to Early Jurassic (Salaj, 1978). This is illustrated by the large thickness and facies variations in the stratigraphic record across Tunisia. Zaier et al. (1998) suggest that the first halokinetic movements occurred in the Early Jurassic.

In the Middle Jurassic a large basin (the Tunisian Trough) began to develop in northern Tunisia in response to the opening of the Piedmont-Ligurian Sea (Burollet, 1978) (**Fig. 2.19a**). It was bounded to the southeast by the Zaghouan-Ressas structural belt and to the northeast and southwest by major NW-SE transfer zones that were associated with the rifting (Morgan et al., 1998) (**Fig.2.19a**). Pelagic sediment input into this basin was minimal throughout the Middle and Late Jurassic.

2.4.2. Early Cretaceous to Early Eocene Evolution

In the Early Cretaceous the Tunisian Trough expanded to include the northern part of the present-day Tunisian Shelf area (**Fig. 2.19b**). The pattern of sedimentation became strongly influenced by the introduction of terrigenous material from the southern part of the present-day Tunisian Shelf (i.e. Kasserine Island) (Salaj, 1978). Elsewhere carbonate platforms on the African margin continued to prograde northwards throughout the Early Cretaceous reaching maximum northward extents at the end of the Barremian-Aptian.

During the Barremian the North African continental margin was subjected to a period of approximately N-S extension. (Guiraud, 1998). This created a system of E-W and WNW-ESE trending faults across the platform area and also reactivated older basement lineaments, in particular the Gafsa-Jarrafa Fault Zone, (located on the southern limit of the Pelagian Platform) (**Fig. 2.19b**). Dip-slip movements on this fault zone caused the onset of subsidence and extension within the Gabes-Tripoli Basin (GTB).

Within the Aptian interval a fundamental change occurred in the relative motion of Africa with respect to Europe. The onset of sea-floor spreading in the North Atlantic caused Africa's motion to shift to northeastward compression (Dewey et al., 1989). As a consequence, the relative motion of the European and African plates switched to dextral strike-slip. Jongsma et al. (1985) demonstrate that this change also induced a component of dextral strike-slip movement on many WNW-ESE to E-W trending faults on the Pelagian Platform (e.g. the Gafsa-Jarrafa Fault Zone (GJFZ)). Dextral movements on these faults are thought to have controlled the Late Cretaceous to present-day subsidence history of the GTB (Anketell, 1992) (**Fig. 2.19c**). A detailed discussion of the development of this basin is presented in Chapter 3.

Throughout the Late Cretaceous most of the Pelagian Platform was covered by shallow-water carbonate platform sequences. The development of these carbonate platforms was controlled principally by NW-SE trending extensional fault systems. This is illustrated by the Late Cretaceous platform margin in Tunisia that trends approximately NW-SE (Camion, 1991). On the Hyblean-Maltese Shelf the distribution of platform carbonates was still largely controlled by an active N-S trending fault zone.

As previously mentioned, maximum progradation of these platform areas was attained in the late Aptian, before partial drowning during the Albian and Cenomanian transgressions prevailed. Camion (1991) suggests that during the middle Turonian an abrupt increase in subsidence rates, related to increased extension caused a complete drowning of the pre-existing platforms over most of the North African continental margin (**Fig. 2.19d**). This increase in subsidence was accompanied by an increase in tectonic activity on the North-South Axis. The widespread thickness and facies variations that characterise the Upper Cretaceous stratigraphy of Tunisia support this theory. Salaj (1978) also gives evidence of localised volcanic activity along this zone during this time.

Deformation during the Santonian is associated with a period of compression that caused widespread inversion throughout North Africa. It is believed to be related to a slight shift in the motion of Africa relative to Europe to a more northerly trend that may have induced NW-SE compression (Anketell, 1992). During this period major dextral strike-slip displacements took place along the GMSZ, causing significant

subsidence in the parts of the GTB, most notably along the Jerrafa and Tripolitania graben and uplift in others. Anketell & Ghellali (1991) suggest that dextral shear along the GJFZ, was translated eastwards along the North Cyrenaican Fault Zone, ultimately causing inversion in northern Cyrenaica.

During the Campanian, a relative increase in the dextral transcurrent stress component caused a dramatic decrease in the rate of convergence between Africa and Europe. This led to increased extension and subsidence in the GTB and the adjacent Sirte Basin. Flooding of the Tethyan Sea onto the North African continental margin throughout this extensional phase led to the deposition of deeper water sediments throughout the Pelagian Platform (e.g. Abiod Formation). Continued deep-water sedimentation is also characteristic of the Palaeocene (Zaier, 1998).

2.4.3. Early Eocene to Late Miocene Evolution

The early Eocene period was characterised by progradation of a NW-SE trending carbonate shelf that extended across south-central Tunisia into the offshore regions of the Gulf of Gabes and SE into Libya (Moody, 1987). During this period, continued movements along the GMSZ led to progressive NE-SW extension and subsidence in the GTB and adjacent areas (Anketell, 1992). Fault activity appears to significantly influence the depositional geometry of early Eocene carbonates in this area.

Within northern Tunisia a NE-SW trending foreland basin and forebulge system began to develop in response to SE directed thrust loading in the Straits of Sardinia during the middle Eocene (**Fig. 2.19e**) (Anderson, 1991). The zone of emergence described by Salaj (1978) between Le Kef-Mateur (N. Tunisia) and western Sicily is interpreted as a forebulge related with the foreland basin. This high area remained a prominent structural feature throughout the Eocene and Oligocene. On the present-day Hyblean-Maltese Shelf area, deeper water conditions prevailed with the deposition of pelagic limestones and marls over the region (i.e. the Amerillo Formation).

The end of the Eocene was marked across much of the African margin by a marine transgression that drowned much of the pre-existing platform area in southern Tunisia. From the Oligocene period, pelagic deposition characterised most of the western part of the Pelagian Platform. In Tunisia the Eocene foreland basin and forebulge system continued to migrate southeastwards.

CONTAINS PULLOUTS

During the Middle Miocene the Corsica-Sardinia-Petit-Kabylie (CSPK) microplate finally collided with the North African continental margin. This led to emplacement of allochthonous 'Numidian' thrust sheets in the Tellian Atlas of northern Tunisia (Anderson, 1991) (**Fig. 2.19f**). It also caused widespread inversion throughout the northern part of the Pelagian Platform (e.g. along the North-South Axis and within the Gulf of Hammamet). Most nappe emplacement had ended by the Late Miocene. Following collision, the CSPK microplate rotated westwards progressively away from Sardinia (Cohen et al., 1980). This event caused extension throughout Tunisia during the Tortonian, creating a series of pull-apart basins that were subsequently filled with Late Miocene and Plio-Pleistocene sediments (**Fig. 2.16**). Anderson (1991) demonstrates that the North-South Axis was reactivated as a sinistral strike-slip fault zone after the Middle Miocene.

2.4.4. Late Miocene to Present-Day Evolution

Within the Late Miocene a change in the regional stress field is thought to have caused the development of the NW-SE trending Pantelleria, Malta, Linosa and Medina Graben (**Fig. 2.19g**). Jongsma et al. (1987) suggest that a shift to SE-NW directed convergence in the Late Miocene induced dextral and sinistral strike-slip movements on large pre-existing E-W and N-S trending faults in the Straits of Sicily. This effectively created a zone of NE-SW extension where a series of NW-SE trending composite pull-apart graben developed (**Fig. 2.20**). Grasso & Reuther (1988) on the other hand propose that the Straits of Sicily Rift formed as a large pull-apart structure associated with the NNE-SSW trending Scicli wrench zone in SE Sicily (**Fig. 2.18**). Dart et al. (1993) argue against such models with fieldwork data from the Maltese Islands, which provide little evidence of strike-slip deformation (a pre-requisite of each model). Fault slip data from the study of Dart et al. (1993) alternatively shows an approximately N-S extension axis. This supports the model of Argnani (1990), which proposes N-S orientated foreland extension in the region of the Straits of Sicily Rift that is coeval and causally related to back-arc extension in the Tyrrhenian Sea, and compression in the Apennine-Maghrebian thrust belt.

Grasso et al. (1990) demonstrate that maximum subsidence within these pull-apart graben was attained during the Pliocene and Early Pleistocene. Continuity of activity until the present-day is supported by recent seismic data, which shows large

displacements in young unconsolidated Late Pleistocene-Holocene sea-floor sediments (Grasso et al., 1990). Reuther et al. (1993) have estimated that during the last 1Ma horizontal displacements along the master faults to the main graben have been in the order of 1 mm yr^{-1}. They have also calculated that the maximum displacement on many of these E-W and NNW-SSE trending strike-slip transfer zones is approximately 2-3km.

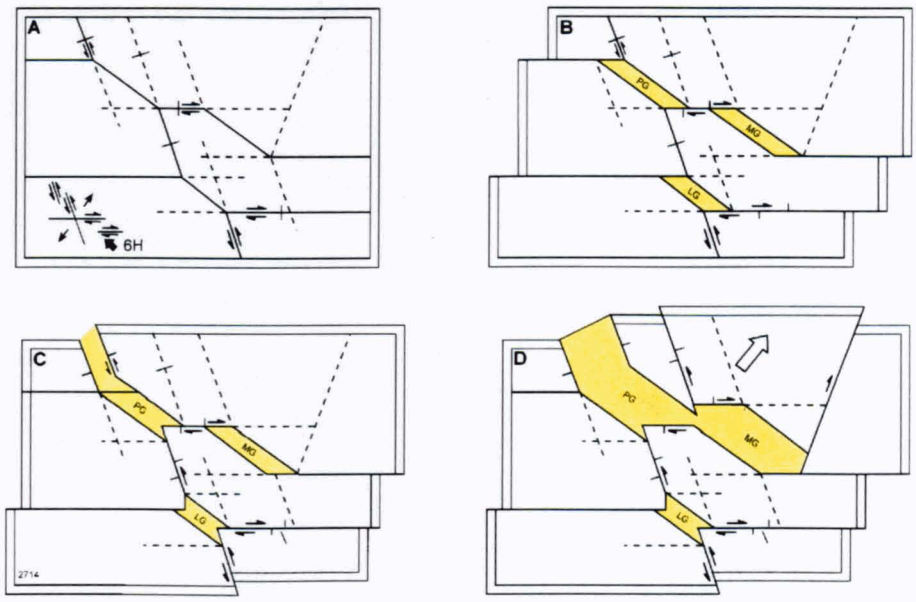

Fig. 2.20. Schematic illustration showing the evolution of the Straits of Sicily Rift Zone (SSRZ). A) Pre-existing fracture pattern and potential fault geometry between Sicily and Tunisia before movements. Inset shows the orientation of Late Miocene to recent maximum horizontal stress (σ_H); B) Activation of E-W striking faults by dextral movements: formation of NW-SE pull-aparts; C) E-W dextral and NNW-SSE sinistral movements create composite pull-apart graben; D) Composite pull-aparts and transverse basins induce NE-SW oriented crustal extension and the reactivation of faults perpendicular to the spreading axis (i.e. the Scicli Fault) (from Reuther et al., 1993)

The Medina Ridge, which separates the Malta and Medina Escarpments also developed during this period. Anketell and Ghellali (1991) propose that these seamounts formed as a dextral strike-slip trailing contractional fan (**Fig. 2.16**).

Chapter 3

Structure & Evolution of the Gulf of Gabes

3.1. Introduction

This chapter will discuss the structure and evolution of the Gulf of Gabes, where the Miskar and Hasdrubal Gas Condensate Fields are situated. This area incorporates the western part of the Gabes-Tripoli Basin. A detailed knowledge of the tectonic processes affecting the Gulf of Gabes is essential in order to attempt to fully understand the controls on fracture development at the reservoir scale within these two Fields.

A variety of integrated techniques were used to construct a detailed tectono-stratigraphic framework for the Gulf of Gabes region, and these are discussed in this chapter. Sections 3.2, 3.3 and 3.4 will establish the study area in its regional setting, discuss previous work and outline the dataset utilised. Section 3.5 will summarise the main lithostratigraphy of the area. An attempt is also made to correlate sequences into the eastern (Libyan) part of the Gabes-Tripoli Basin where a different stratigraphic nomenclature is used.

Section 3.6 uses seismic and well data as the basis for a discussion of the structure of the Gulf of Gabes region. Regional seismic profiles have been interpreted and used to construct two-way-time (TWT) structure maps for important seismic events. These data are integrated with regional lithostratigraphic correlations and isopach maps of sediment thickness, which were produced from available well logs across the study area.

Section 3.7 uses the inverse modelling procedure of White (1993; 1994) to model the strain rate variation through time, and hence the subsidence history of a number of

wells across the Gulf of Gabes. These studies are used to construct a regional tectonic model (Section 3.8), which attempts to summarise the extent and timing of the main tectonic events that have contributed to the evolution of the Gulf of Gabes area.

Comprehensive structural studies on the Miskar and Hasdrubal Fields have contributed significantly to the understanding of the tectonic controls on the evolution of the Gulf of Gabes area. Consequently, throughout this chapter, the reader is often advised to consult Chapters 6 and 7, which detail these analyses individually.

3.2. Previous Work

Much of the previous work undertaken on the Gulf of Gabes is unpublished, and has been undertaken by one or two oil companies. Reports by BG Group and precursor companies have been used as a basis for this study. However, these reports are largely concerned with regional and detailed sedimentology and stratigraphy. This is due, in part, to the perception that the principal challenges in developing the hydrocarbon potential of the area were sedimentological in nature

The geology of the offshore Gulf of Gabes region is very poorly documented, and generally restricted to oil company reports that are of limited use. Sedimentological studies generally overshadow structural analyses. This is due, in part, to an abundance of available sedimentary outcrop analogues in onshore Tunisia (N.B. the structural style of the regions in onshore Tunisia where there is good outcrop differs significantly to that offshore). Burollet (1956), Bishop (1975, 1985, 1988), Beckett (1998), Salaj (1978), Moody (1987), Ben Ferjani et al. (1990) and M'Rabat et al. (1995) provide the most detailed accounts of the lithostratigraphy within this region. The integration of these studies (presented in Section 3.5) provides a comprehensive lithostratigraphic framework for the area.

Anketell (1995), Hammuda et al. (1992) and El Ghoul (1992) give brief accounts on the structure and evolution of the Gabes-Tripoli Basin. These studies although useful, tend to concentrate on the eastern (i.e. Libyan) part of the basin. Anderson (1995) and Bedir et al. (1992) have analysed the structural style and subsidence history of the onshore 'Sahel' region, northwest of the Gulf of Gabes. Their results have been integrated into this study. Apart from these few published analyses the only other documented material on this interesting and important area is within oil company

reports. As a consequence, the results of this structural study will provide an important framework for future studies.

3.3. Location

As previously mentioned in Chapter 2, the Gulf of Gabes is located at the southern margin of the Pelagian Platform between Latitudes 33°-35° and Longitudes 10°-16° (**Fig. 3.1**). It is bounded to the south by the Gafsa-Jerrafa Fault Zone (GJFZ), and to the north by the Medina-Lampedusa Plateaux. The Gabes-Tripoli Basin straddles the eastern margin of the Gulf of Gabes, extending across the Libyan offshore to the Medina Escarpment. The Miskar and Hasdrubal Gas Fields analysed in Chapters 6 and 7 are located in the western part of this basin, just north of the main depocentre.

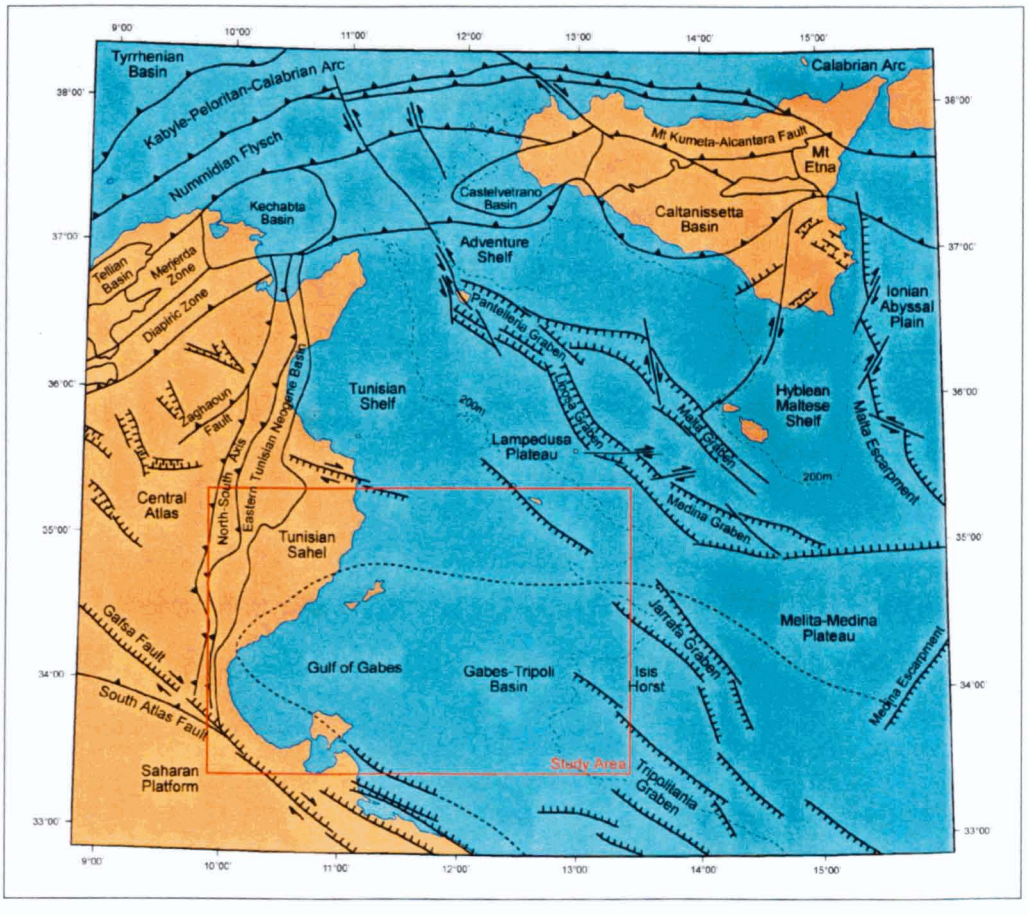

Fig. 3.1. Location map of the Gulf of Gabes region on the Pelagian Platform

3.4. Data Acquisition

Seismic reflection and well data form the basis of this study. These data were acquired through the BG TVP, Tunisia and Italy offices. Where available, non-proprietary sources were also utilised. **Figure 3.2** shows the main data presented in this study.

3.5. Lithostratigraphic Framework

3.5.1. Introduction

The deepest wells drilled in the Gulf of Gabes area penetrate platform carbonates of the Upper Jurassic Nara Formation (Riccio Sud -1, Remo -1) (Torelli et al., 1995). The stratigraphy below this can be inferred from wells to the south, that intersect most of the Palaeozoic succession. This section summarises the Triassic to present-day stratigraphy and palaeogeography of the Gulf of Gabes region, incorporating the western (i.e. Tunisian) part of the Gabes-Tripoli Basin. BG's in-house stratigraphic correlations are used to compare the stratigraphy of the Gulf of Gabes with the adjacent Libyan offshore (**Fig. 3.3**).

3.5.2. Triassic Stratigraphy

In southern Tunisia the main focus of Tethyan extensional tectonics during the Triassic, was concentrated on the Jerrafa region (i.e. the Chott Fejej, on the northern margin of the Saharan Platform) where a series of WNW-SE faults, downthrown to the NNE have thick deposits of Triassic sediments in their hangingwall sections (Burollet et al., 1978). The Gafsa-Jerrafa Fault Zone, located at the southern margin of the Gulf of Gabes was active during this episode. In the Gabes-Tripoli Basin, the Triassic stratigraphy is poorly constrained. However, onshore studies indicate that the Triassic in the Gulf of Gabes is probably composed of shallow marine carbonates and marly shales, corresponding to the Bir El Jaja, Ouled Chebbi, Tagi, Azizia and Bu Sceba Formations. The upper part of the Triassic consists of thick evaporites representing the Bir Al Ghanem Formation (Ben Ferjani et al., 1990).

3.5.3. Jurassic Stratigraphy

The Jurassic of the Gulf of Gabes consists of the Lower, Middle and Upper Nara Formations and the basal section of the Sidi Khalif Formation.

Lower Nara Formation (Hettangian-Toarcian): This unit consists of a lower sequence of shallow water dolomitic limestones with occasional interbedded evaporites that grade up into marly limestones and shales. These lithofacies are indicative of deposition within a lagoonal/tidal flat environment. This formation passes transitionally up into the Middle Nara Formation.

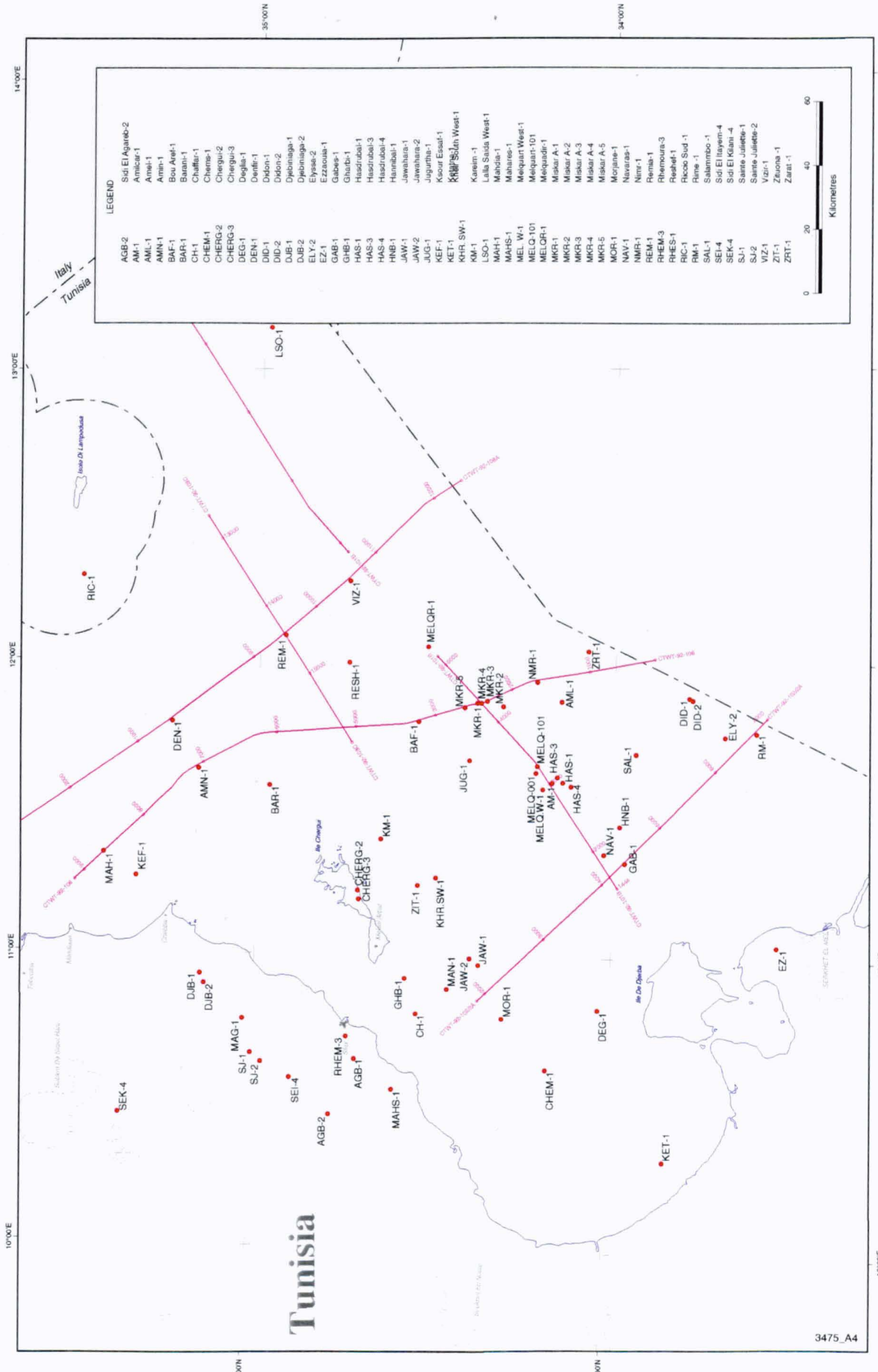

Fig. 3.2. Seismic and Well Base Map across the Gulf of Gabes.

Middle Nara Formation (Aalenian-Callovian): This interval is composed of a lower unit of fossiliferous limestones and shales that grade up into a sequence of shallow marine oolitic limestones and interbedded evaporites. This lithology is up to 1000m thick in wells at the southern margin of the Gabes-Tripoli Basin (e.g. Guellala –1) indicating strong tectonic subsidence during this period (Salaj, 1978).

Upper Nara Formation (Oxfordian-Tithonian): The Upper Nara Formation lies conformably on the Middle Nara Formation. It consists of a sequence of massive marine dolomitic limestones characterised in the lower unit by the Ammonitico Rosso Member. In the western part of the Gulf of Gabes it passes transitionally up into the Sidi Khalif Formation, whereas to the south (in the Chott Fejej) it grades into the continental Asfer Formation (Ben Ferjani et al., 1990).

3.5.4. Cretaceous Stratigraphy

The Cretaceous section of the Gulf of Gabes is well understood due to the abundance of wells penetrating through this interval. A more detailed lithological account can therefore be given. The isopach maps in **Figures 3.4-3.10** show sediment thickness variations for various intervals throughout the Cretaceous sequence. Where possible, facies boundaries are superimposed onto these maps.

Sidi Khalif Formation (Tithonian-Berrasian): The Upper Jurassic Nara Formation consists of a lower sequence of hemi-pelagic marly wackestones and packstones, and an upper sequence of interbedded sandy shales and limestones that rapidly grade up into the Meloussi Formation (M'Rabat et al., 1995). It has a highly variable thickness (200m to >1000m). M'Rabat et al. (1995) suggest that it was deposited in an open marine environment with episodic siliciclastic input.

Meloussi Formation (Hauterivian-Barremian): This unit consists of a sequence of interbedded sandstones, bioclastic/oolitic dolomites, dolomitic limestones, quartzites and green clays (Burollet, 1956). This formation has a thickness of ~400m in onshore Tunisia, reducing significantly along the North-South Axis. In central and southern Tunisia, the Meloussi Formation corresponds to a deltaic wedge with alternations of delta front sand progradation and marine carbonate transgressions (M'Rabat et al., 1995). North of Kasserine, subsidence was active and more marine conditions developed, as evidenced by the transition to the open marine M'Cherga Formation.

CONTAINS PULLOUTS

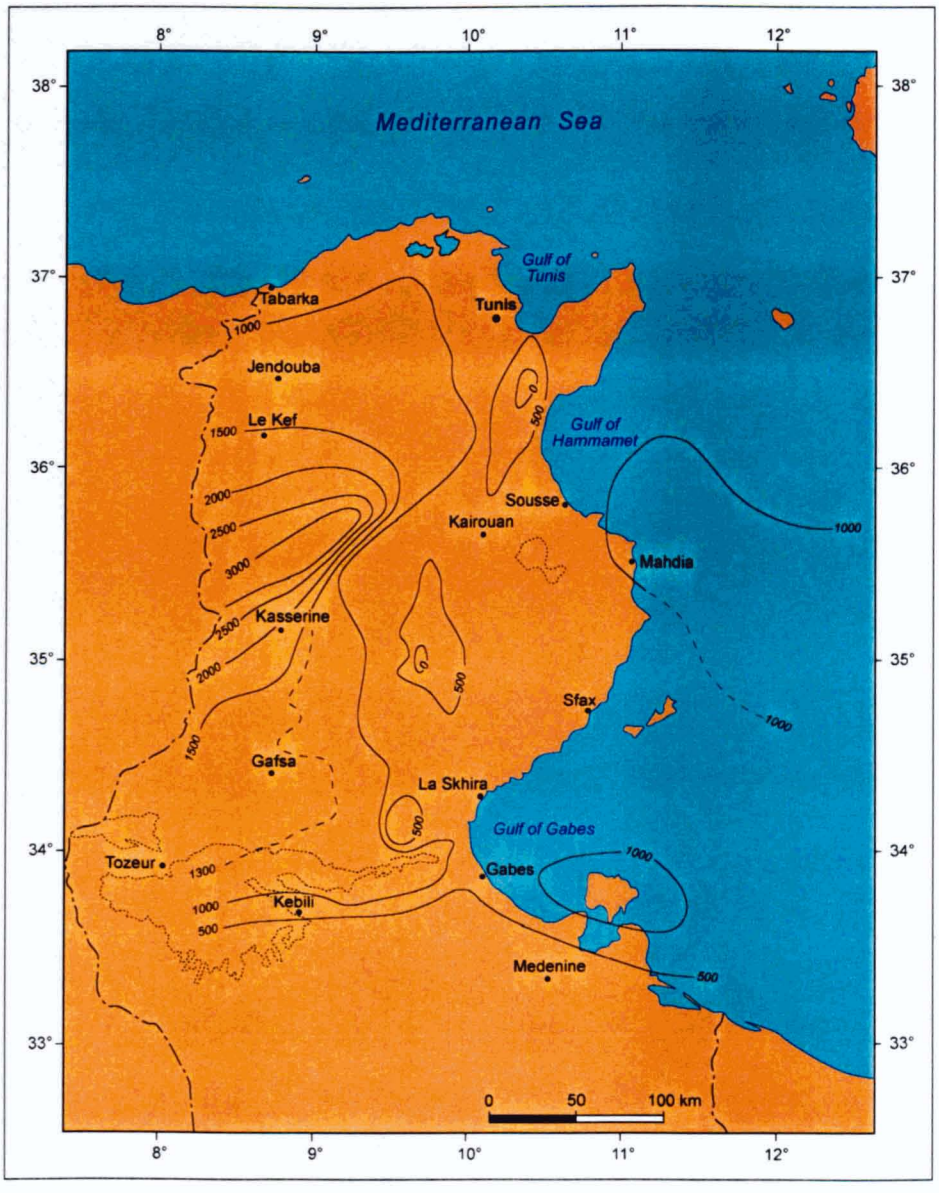

Fig. 3.4. Isopach map of the Valanginian and Hauterivian showing sediment thickness variations in the Meloussi, Boudinar and Lower and Middle M'Cherga Formations (modified after Ben Ferjani et al., 1990).

Bou Hedma Formation (Barremian): This unit consists of interbedded shales, sands, dolomitic limestones and evaporites (gypsum) (Burollet, 1956). It ranges considerably in thickness throughout offshore eastern Tunisia (60-880m). M'Rabat et al. (1995) suggest that these lithologies correspond to deposition on an internal shelf, with localised tidal flats and sabkhas. The Bou Hedma Formation is replaced to the northeast of the Gulf of Gabes by the open marine M'Cherga Formation.

Sidi Aich Formation (Aptian): This unit, approximately 100-250m thick consists of a sequence of fine-grained, well-sorted sandstones, which contain rare thin carbonate and clay interbeds (Burollet, 1956). M'Rabat et al. (1995) suggest that it was deposited in a

shallow marine sub-tidal environment. The Sidi Aich Formation grades northeastward into the open marine facies of the M'Cherga Formation (this is seen in the Gulf of Hammamet).

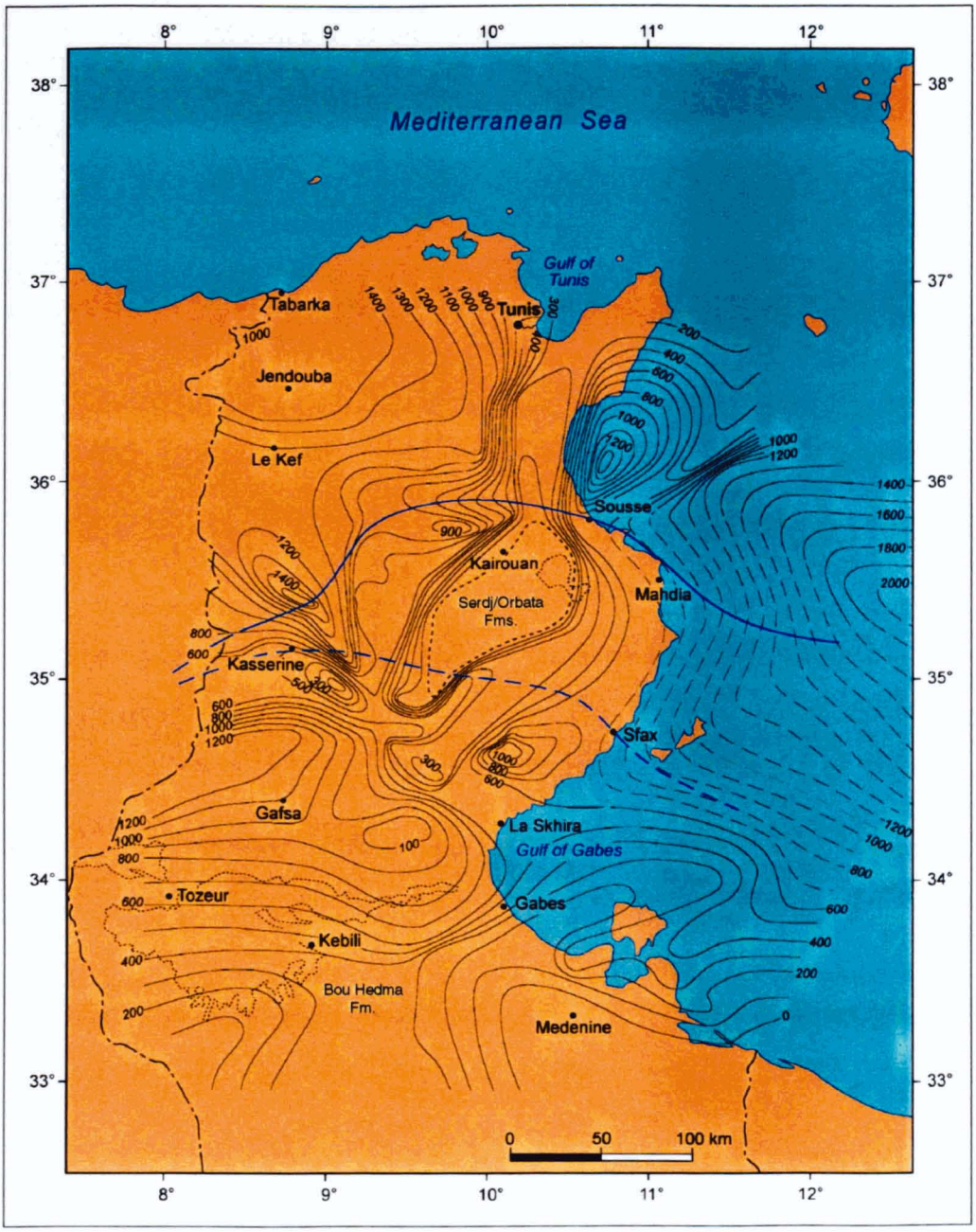

Fig. 3.5. Isopach and facies map of the Barremian and Aptian showing sediment thickness variations in the lower Formations of the Gafsa Group. The dashed blue line shows the northern limit of the Bou Hedma Formation. The solid blue line shows the northern limit of the Serdj and Orbata Formations (modified after Ben Ferjani et al., 1990).

Serdj Formation (Aptian): This unit is composed of a lower succession of bioclastic limestones and interbedded marls, and an upper sequence of rudistic bioherms

(Burollet, 1956). Several wells in the Gabes-Tripoli Basin have penetrated up to 1000m of the Serdj Formation. M'Rabat et al., (1995) suggest that this formation corresponds to deposition on a shallow marine carbonate platform, open to the north and east. Rudist bioherms were locally developed where suitable conditions existed (D. Beckett, pers. comm., 2001).

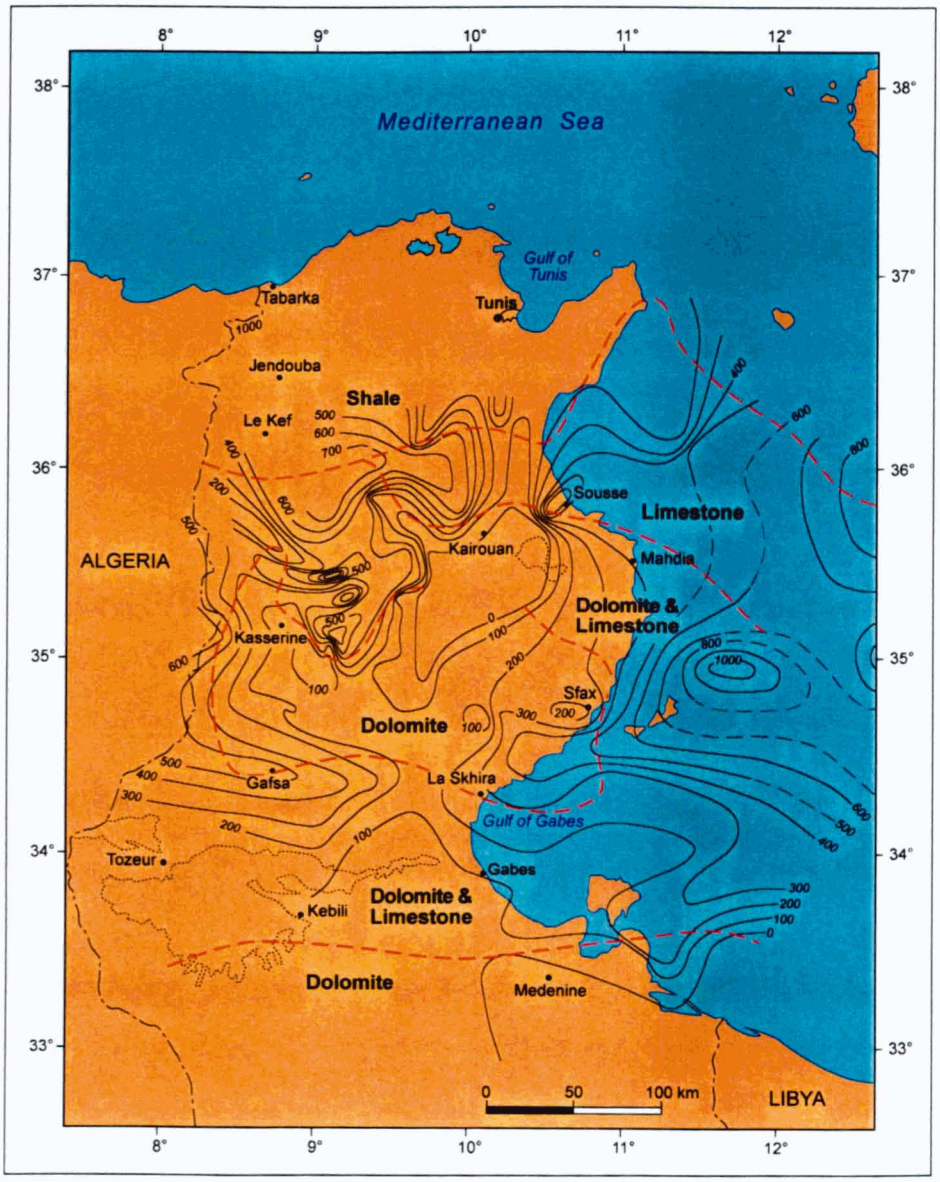

Fig. 3.6. Isopach and facies map of the Aptian showing sediment thickness variations in the Serdj and Orbata Formations. The dashed red lines show the limits of the various facies tracts (modified after Ben Ferjani et al., 1990).

Hameina Formation (Aptian): This unit consists of black and green shales with interbedded sandstones, dolomites and bioclastic wackestones (~300m thick) (Burollet, 1956). However in the basinal areas where the Serdj carbonates are replaced by the M'Cherga shales, the limit between the Hameima and M'Cherga Formations is variable; in the deeper zones, all of the Hameina Formation is replaced by the upper

horizons of the M'Cherga Formation (M'Rabat et al., 1995). M'Rabat et al. (1995) suggest that the onshore portion of this unit relates to deposition on an intermediate outer shelf environment, whereas the offshore sequence represents deeper (more open marine conditions) into which there was the occasional influx of siliclastic turbidites.

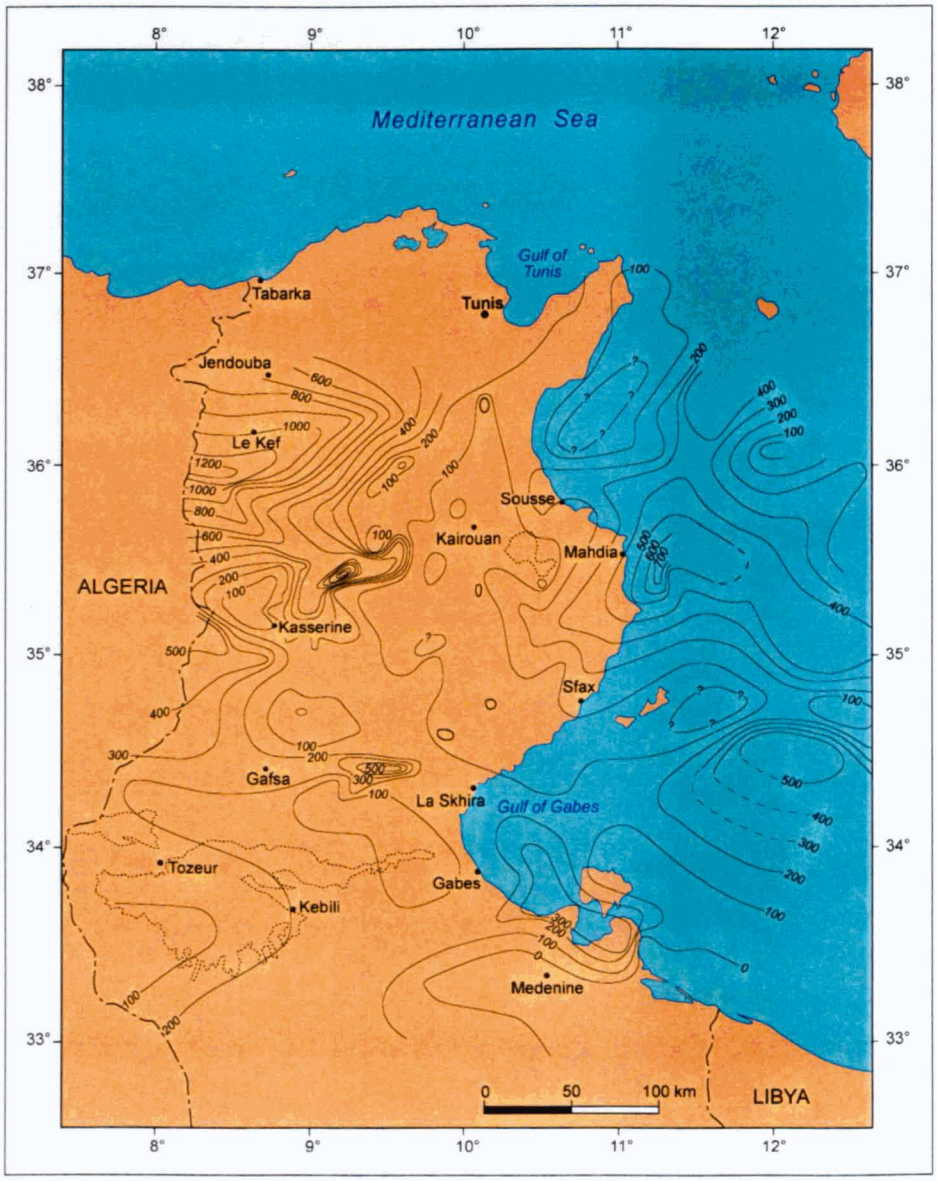

Fig. 3.7. Isopach map of the Albian showing sediment thickness variations in the lower part of the Fahdene Formation (modified after Ben Ferjani et al., 1990).

Fahdene Formation (Aptian-Cenomanian) (Seismic Sequence 1 (SS-1))(Table 3.1): This unit consists of a thick (1211m thick in Teboulba -1) sequence of dark grey to black shales and marls with occasional interbedded argillaceous limestones (Burollet, 1956). In basinal areas the lower boundary with the Hameina Formation is progressive (Rabat et al., 1995). On paleohighs however, the lower boundary is generally represented by a major unconformity. It records deposition in an open marine

environment (Rabat et al., 1995), and is the equivalent of the Zebbag Formation, which corresponds to the internal carbonate shelf in south central Tunisia.

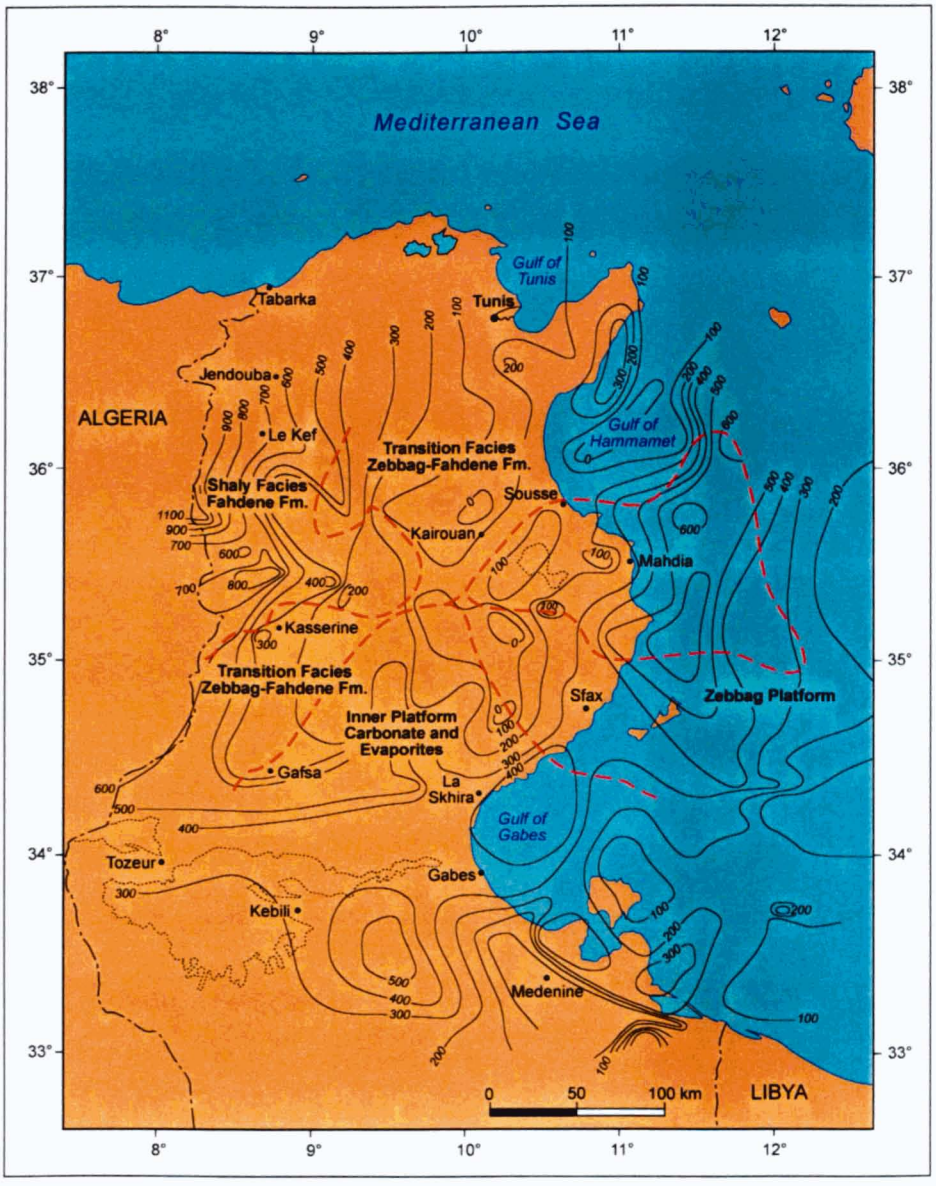

Fig. 3.8. Isopach and facies map of the Cenomanian showing sediment thickness variations in the upper part of the Fahdene Formation (modified after Ben Ferjani et al., 1990).

Bahloul Formation (Cenomanian)(SS-2): This unit consists of thin laminated black to dark grey argillaceous limestones rich in organic matter (up to 14% TOC), interbedded with a thin marls and shales (0-50m thick) (Burollet, 1956). The lower boundary is sharp forming a local unconformity in many areas. Rabat et al. (1995) propose that this formation was deposited in a relatively deep marine, anoxic environment. It is proven as one of the best source-prone intervals in Tunisia, forming the source for hydrocarbons in the Upper Cretaceous Abiod and Aleg reservoirs (Bishop, 1988).

Annaba Formation (Turonian)(SS-3)(Table 3.1): This unit consists of dark grey shales and marls with interbedded bioclastic wackestones in the upper part of the sequence (0-

120m thick) (Burollet, 1956). M'Rabat et al. (1995) suggest that it was deposited in a deep-water outer shelf or mid-outer ramp setting.



Fig. 3.9. Isopach and facies map of the Cenomanian to Turonian showing sediment thickness variations in the Bireno, Annaba and Bahloul Formations (modified after Ben Ferjani et al., 1990).

Aleg Formation (Turonian to Campanian)(SS-3 to SS-7): The Aleg Formation may be sub-divided into six Members; 1) Upper Aleg Member (SS-7), 2) Upper Aleg Carbonate Member (SS-6), 3) R-1 Superior Member (SS-5), 4) R-1 Inferior Member (SS-5), 5) Lower Aleg Member (SS-4), and 6) Bireno Member (SS-3) (Cook & Wright, 1998) (Table 3.1). The lithological details of each of these members will be described comprehensively in Chapter 6. In general however, it consists of i) a lower section of peloidal wackestones overlain by shales, ii) a middle section of bioclastic packstones and wackestones and iii) an upper section of massive carbonates and shales. **Figure 3.11** shows the distribution of the Bireno Member of the Aleg Formation in the Gulf of

Gabes region. Cook & Wright (1998) suggest that it was deposited in a mid to outer ramp environment.

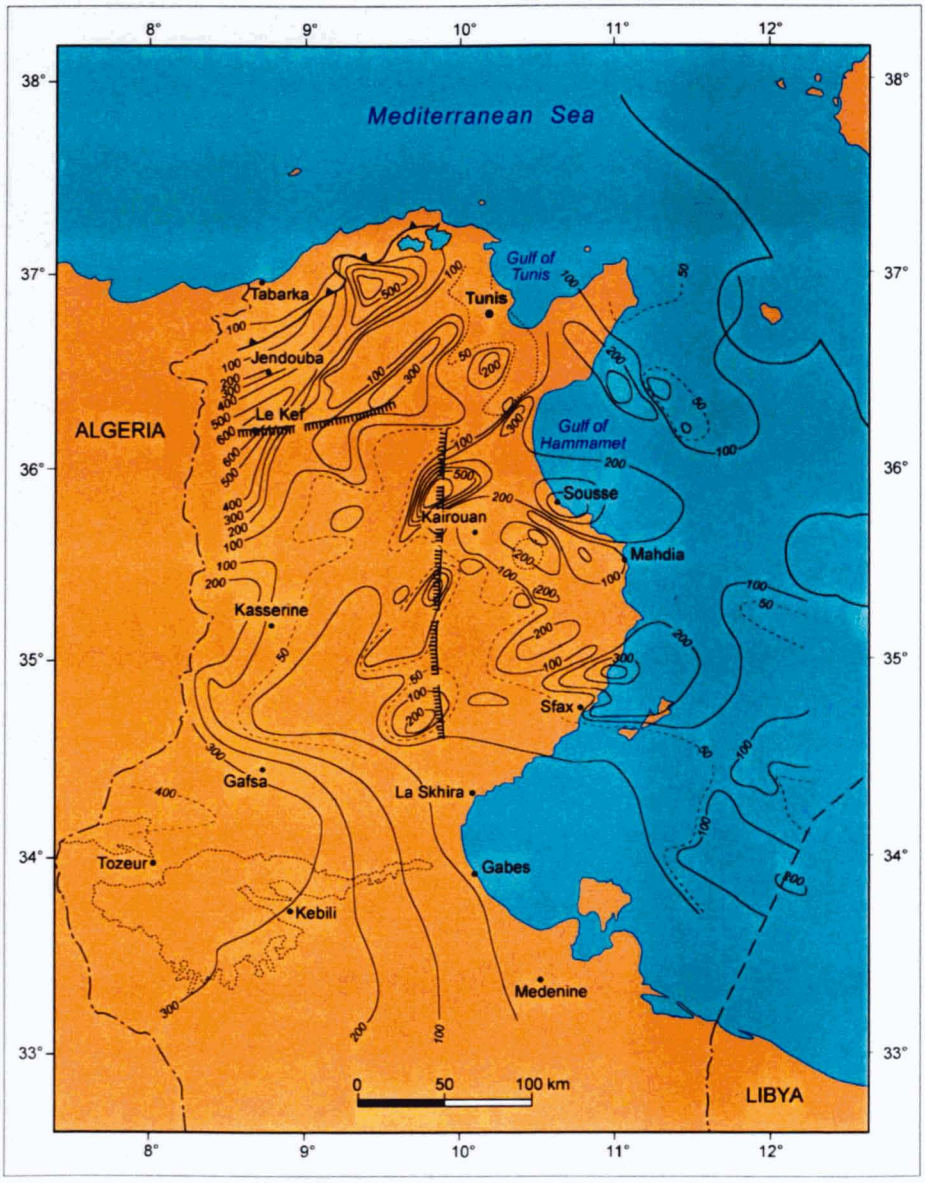

Fig. 3.10. Isopach and facies map of the Campanian to Maastrichtian showing sediment thickness variations in the Abiod Formation (modified after Ben Ferjani et al., 1990).

Abiod Formation (Campanian to Maastrichtian)(SS-8): The Abiod Formation unconformably overlies the Aleg Formation (Burollet, 1956). It is very fine-grained, and is composed of foraminiferal-nannofossil chalk. It is between 200-400m thick on the Pelagian Shelf. The biota described from the Abiod consists mostly of coccoliths and planktonic forams with minor amounts of bivalve, echinoderm and ostracod debris. Bioturbation features are common in some intervals, but only *Zoophycos* and *Chondrites* trace fossils are identifiable. This biota is consistent with deposition in an offshore, low energy, outer ramp environment (Cook & Wright, 1998). Locally the transition between the Abiod Formation and the Upper Maastrichtian El Haria

Formation is sharp, marked by an unconformity. The Abiod Formation is the main exploration target in the onshore Sidi El Kilani Field, and a secondary target in the Miskar Gas Field. The distribution of the Abiod Formation in the Gulf of Gabes area is shown in **Figure 3.12.**

3.5.5. Tertiary Stratigraphy

El Haria Formation (Maastrichtian-Thanetian)(SS-9): This unit consists of a thick sequence of shales, with thin interbedded limestone intervals at the base (300-600m thick) (Burollet, 1956). The basal contact with the Abiod Formation is marked by an unconformity. M'Rabat et al. (1995) suggest that it was deposited in an open marine environment with abundant planktonic foraminifera. Around the 'Kasserine Island' and the North-South Axis it is shallower and rich in benthonic foraminifera.

Tselja Formation (Thanetian-Ypresian)(SS-9)(Table 3.1): This unit consists of bioclastic packstones and wackestones, with thinly interbedded shales and evaporites. It represents the shallow water equivalent of the Chouabine Formation (D. Beckett, pers. comm., 2001), and passes transitionally into the Ain Merhotta and El Garia Formations of the Metlaoui Group.

The Metlaoui Group (Ypresian-Lutetian)

The Metlaoui Group (SS-10) has been extensively studied over the last 30 years due to its source and reservoir potential. Previous studies demonstrate that it was deposited on a northeast dipping carbonate shelf across central Tunisia and the Gulf of Gabes region. Moody (1987) demonstrated through fieldwork studies that it is represented by a series of shoreline-parallel facies tracts that have irregular margins (**Fig. 3.13**). Moving basinward, these facies tracts consist of 1) the Faid Formation, 2) the Ain Merhotta Formation, 3) the El Garia Formation, the 4) the Ousselat Formation, 5) the Bou Dabbous Formation and 6) the Chouabine Formation. The Compact Micrite Member forms the upper transgressive unit to the Metlaoui Group. Beckett (1998) and Racey et al. (2001) have recently revised the early model of Moody (1987), and consequently this will be used in further discussions. **Figure 3.14** shows sediment thickness variations during the Ypresian.

Faid Formation (Ypresian)(SS-10): This unit consists of variable thicknesses of dolomitic mudstones with interbedded evaporites. It represent deposition on the uppermost inshore reaches of the ramp system within a sabkha/tidal flat environment

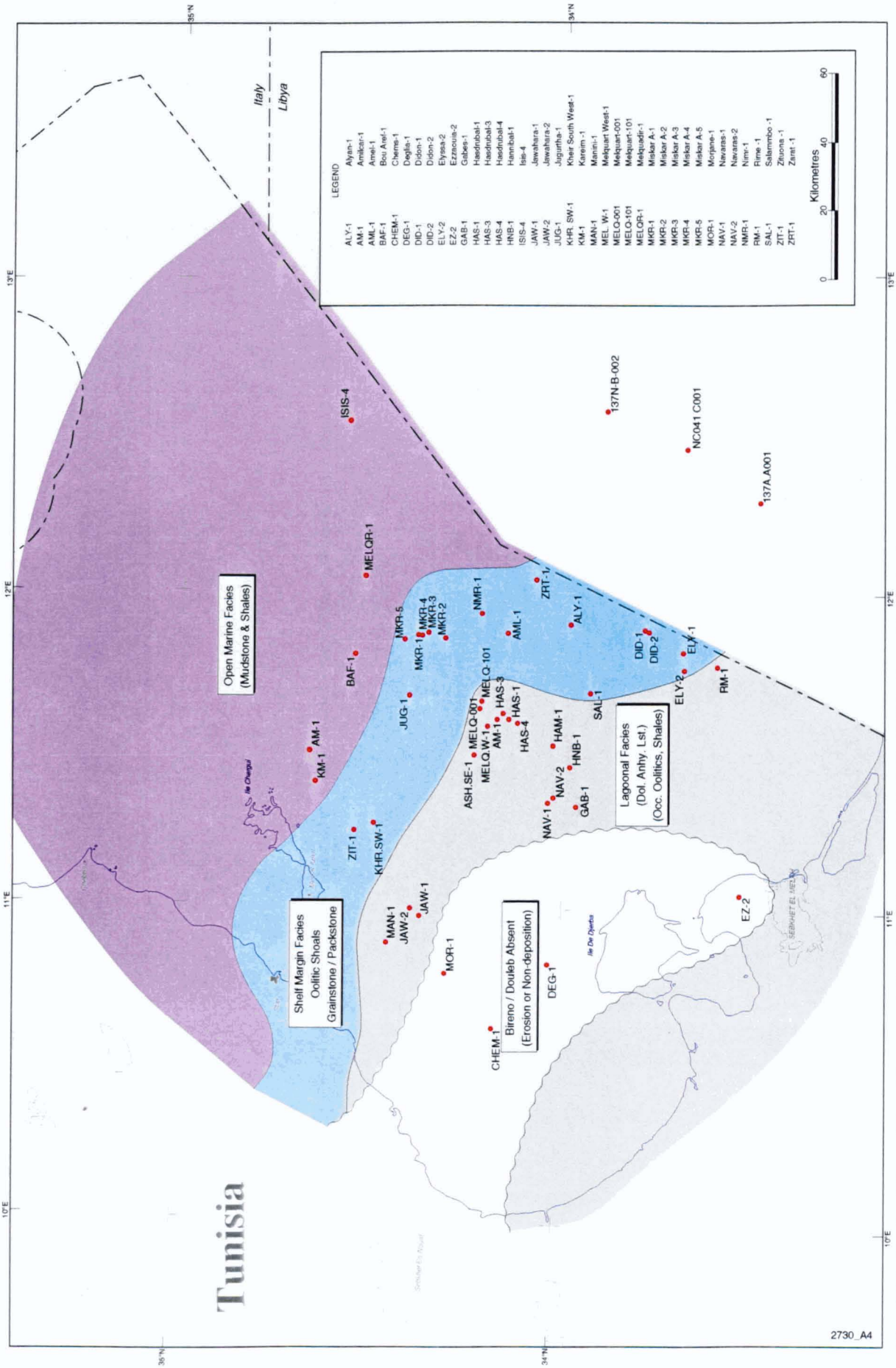

Fig. 3.11. Facies Map of the Bireno and Douleb Members (SS-2/3) (Mid - Late Turonian) across the Gulf of Gabes.

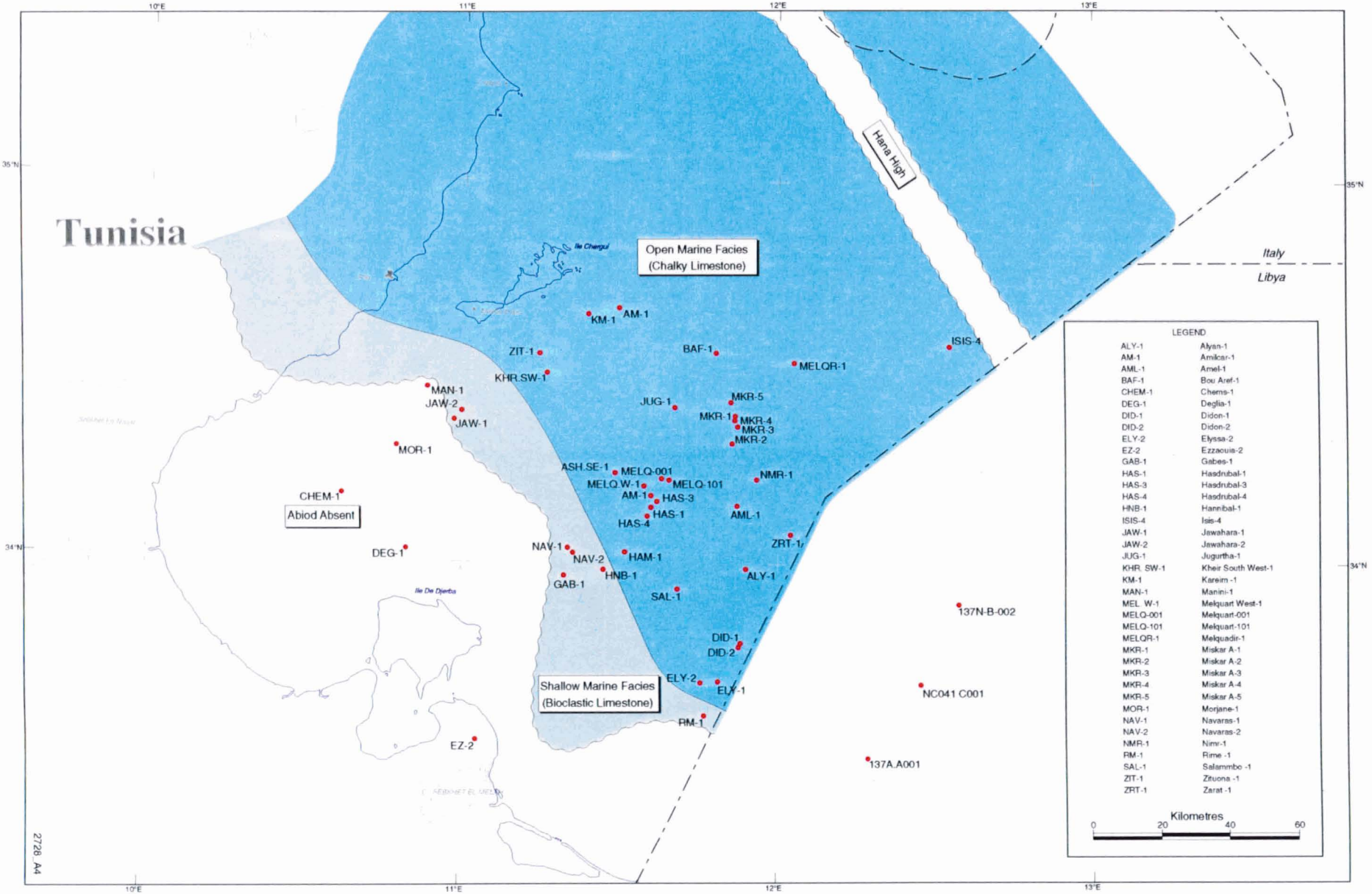

Fig. 3.12. Facies Map of the Abiod Formation (SS-8) (Early Campanian - Early Maastrichtian) across the Gulf of Gabes.

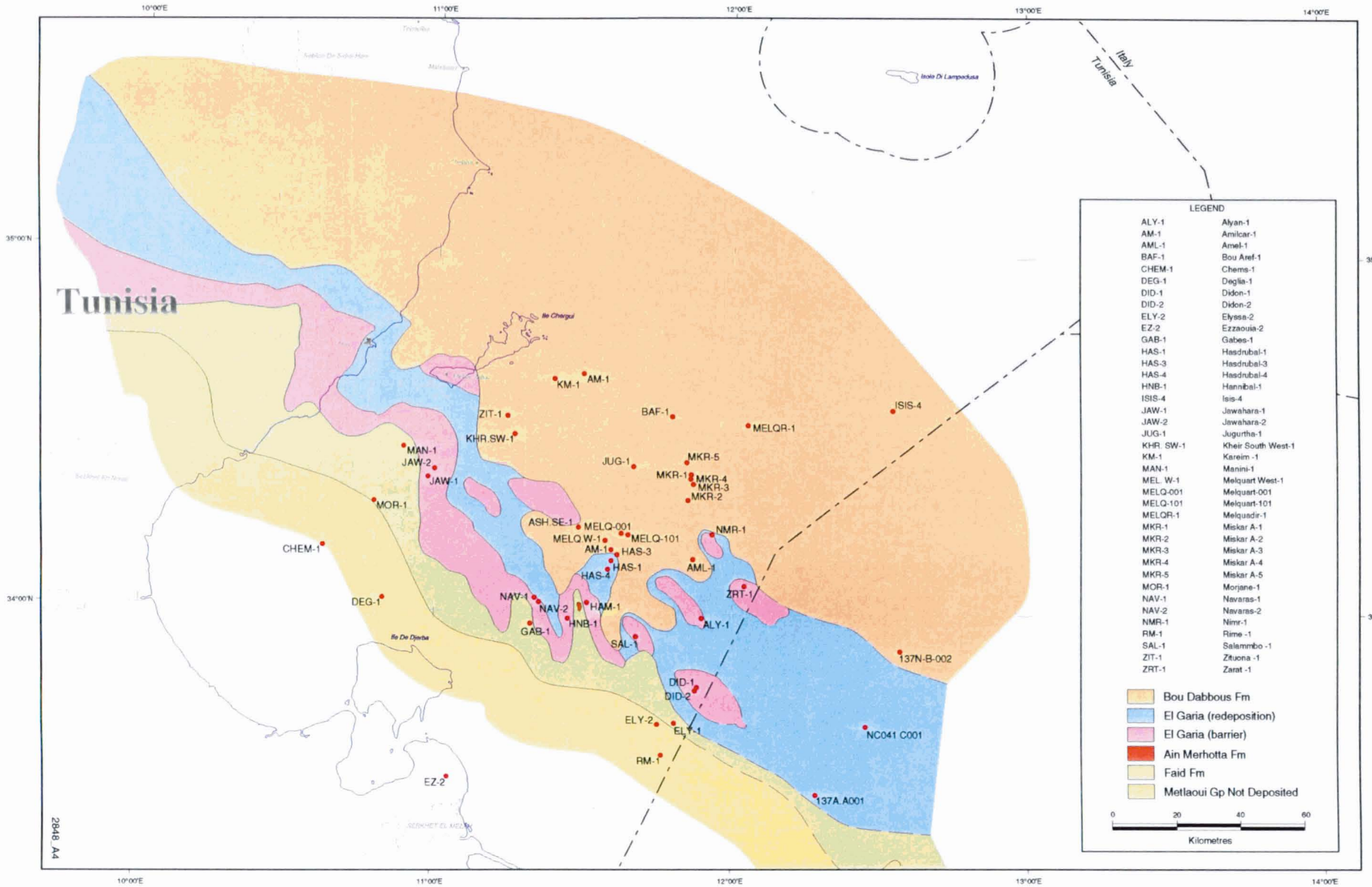

Fig. 3.13. Facies Map of the Metlaoui Group (SS-10) (Early Ypresian - Early Lutetian) across the Gulf of Gabes. (Modified after Beckett, 2000)

(Loucks et al., 1998). It is locally developed on tectonic highs (i.e. fault blocks) in the more distal parts of the Gabes-Tripoli Basin.

Ain Merhotta Formation (Ypresian)(SS-10): Onshore studies from Central Tunisia demonstrate that the Ain Merhotta Formation consists of micritic mudstones interbedded with wackestones and packstones rich in Milliolids, red algae and gastropods (Moody, 1987). It is approximately 100m thick, and represents deposition within a restricted back-bank lagoon in an inner ramp environment (Beckett 1998).



Fig. 3.14. Isopach map of the Ypresian showing sediment thickness variations in the Metlaoui Group (modified after Ben Ferjani et al., 1990).

El Garia Formation (Ypresian)(SS-10): This unit forms the main reservoir interval in the onshore Sidi El Itayem and the offshore Ashtart and Hasdrubal Fields. It consists of a sequence of nummultic wackestones, packstones and grainstones. Maximum

thicknesses are attained onshore at Djebel Cherahil (160m thick) (Moody, 1987). Moody (1987) and Bailey et al. (1989) subdivided the El Garia Formation into two distinct facies tracts within the mid-ramp environment; a landward zone occupied by high-energy shoal facies, and a basinward zone of low relief nummulitic banks. This classification has been revised and is presented in more detail in Chapter 7.

Ousselat Formation (Ypresian)(SS-10): This unit which consists of nummulithoclastic packstones and grainstones interbedded with thin coralline beds (Moody & Grant, 1989) has only been observed in Central Tunisia, and is not recognised in the Gulf of Gabes. Loucks et al. (1998) interpret it as a deep-water, outer ramp deposit composed of the sediment derived from the mid-ramp El Garia facies tract, which has been transported down-slope by storm suspension and turbidity currents.

Bou Dabbous Formation (Ypresian)(SS-10): This unit forms the principal source of hydrocarbons for the El Garia Formation. It is composed of fine-grained globigerinid-rich packstones and wackestones intercalated with rare packstone deposits containing nummulitic debris. Loucks et al. (1998), Bailey et al. (1989) and Racey et al. (2001) suggest that it was deposited within an open marine environment.

Chouabine Formation (Thanetian- Ypresian)(SS-10): This unit consists of a thick sequence of phosphatic calcareous mudstones containing frequent nummulites, nummuloclastics and gastropods. A deep-water origin is invoked due to the high mud and phosphatic content, moderate bioturbation and the presence of a deep-water biota. Some workers interpret it as a transgressive unit at the base of the Metlaoui Group (Beckett, 1998; Racey et al., 2001). It passes upwards into the globigerinid-rich facies of the Bou Dabbous Formation, the offshore equivalent of the El Garia Formation.

Compact Micrite Member (Lutetian)(SS-10): This unit is comprised of calcareous mudstones that show varying degrees of lamination. It is interpreted to have been deposited during a transgressional phase, following the deposition of the El Garia Formation (Beckett, 1998).

Cherahil Formation (Bartonian-Priabonian)(SS-11): This unit conformably overlies the Metlaoui Group. It consists of a thick lower sequence of interbedded mudstones and foraminiferal wackestones (Cherahil 'A' Member), a thin middle sequence of nummulitic grainstones (Reineche Member) and a thick upper sequence of interbedded mudstones and foraminiferal wackestones (Cherahil 'B' Member).

Ben Ferjani et al. (1990) suggest that this unit represents deposition on a mid-shelf environment during a widespread marine transgression throughout the Late Eocene. To the northeast of the Gulf of Gabes it grades laterally into the progressively more open marine facies tracts of the Souar and Halk El Menzel Formations. The top of the Cherahil Formation is marked by a regional unconformity throughout the Gulf of Gabes. The isopach map in **Figure 3.15** shows sediment thickness variations across Tunisia during the Lutetian and Priabonian.

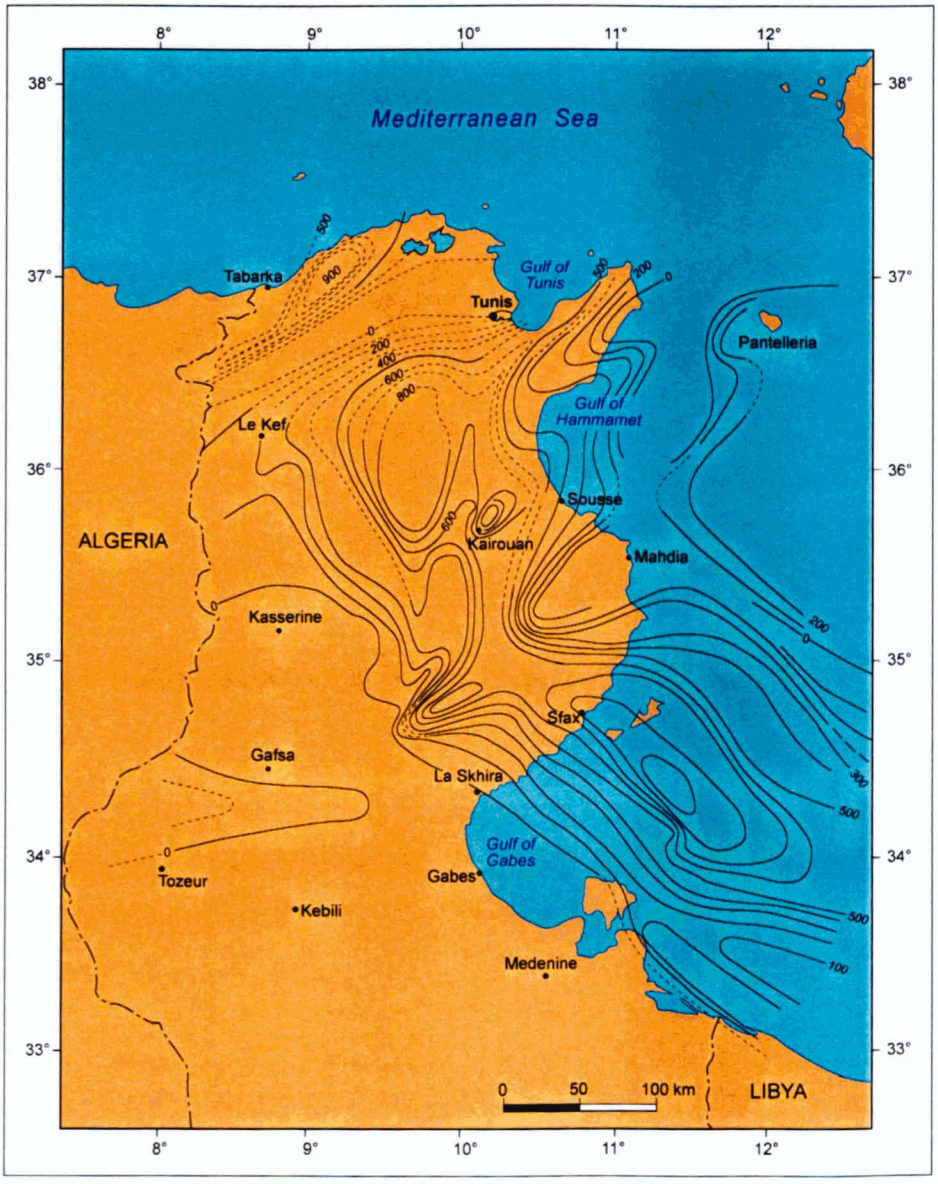

Fig. 3.15. Isopach map of the Lutetian to Priabonian showing sediment thickness variations in the Cherahil Formation and its lateral equivalents (modified after Ben Ferjani et al., 1990).

Salammbo Formation (Rupelian-Burdigalian)(SS-12): This unit was first defined by Fournie (1978), after the completion of the Salammbo -1 well. It can be subdivided into two units; 1) a lower unit consisting of a basal nummulitic packstone package (Vascus

Member) (~3m thick) followed by a thick sequence of calcareous shales rich in globigerina, and, 2) an upper unit of interbedded argillaceous micrites, biomicrites, and globigerinid-rich shales. Ben Ferjani et al. (1990) suggest that this unit was deposited under open marine basinal conditions. In the north of the Gulf of Gabes the Salammbo Formation grades laterally into the shallow water Fortuna Formation. **Figure 3.16** shows sediment thickness across Tunisia during the Oligocene and Early Miocene.

Ain Grab Formation (Langhian)(SS-13): This thin unit consists of interbedded bioclastic limestones and calcareous shales (Burollet, 1956). Ben Ferjani et al. (1990) suggest that it corresponds to the onset of the main Miocene transgression that occurred after the first phases of Atlassic compression.

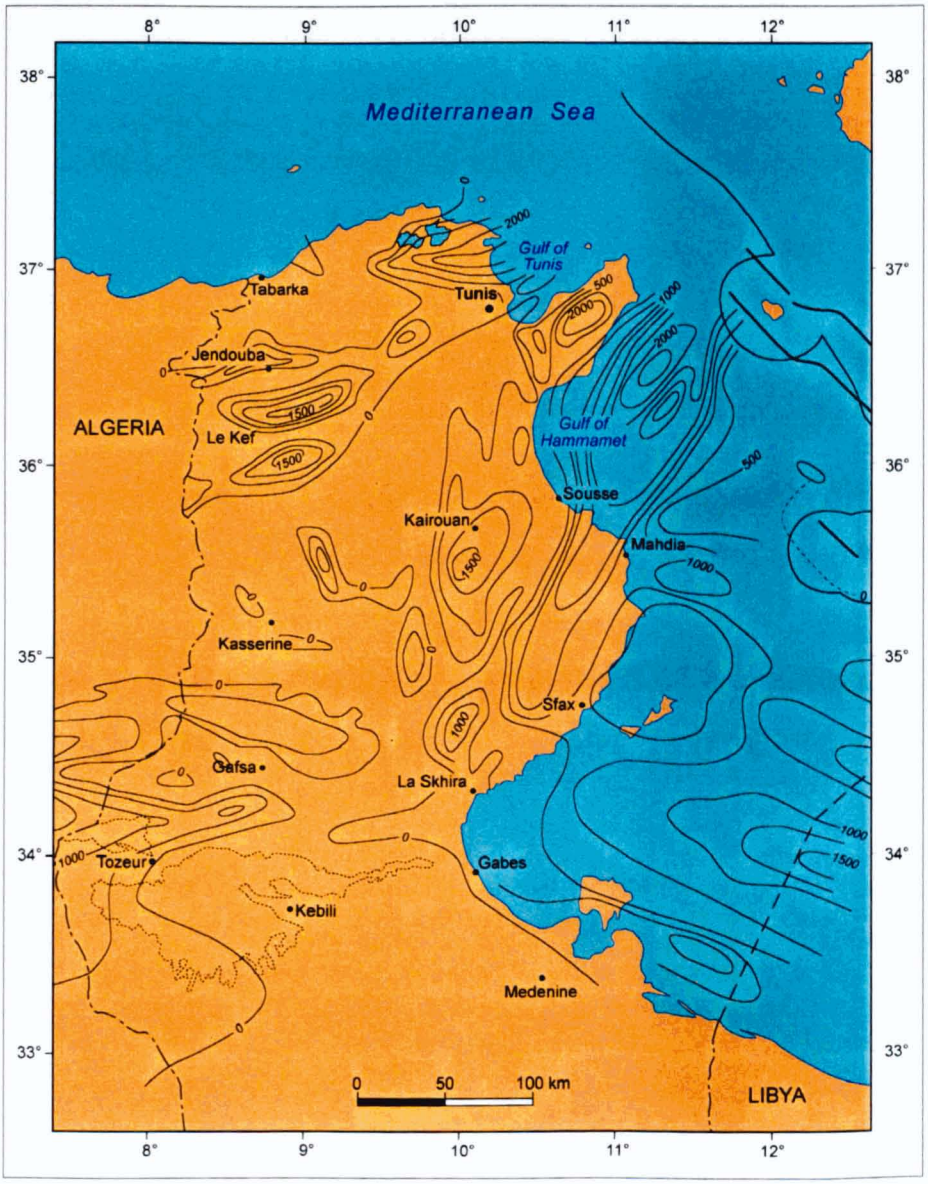

Fig. 3.16. Isopach map of the Oligocene and Early Miocene showing sediment thickness variations in the Fortuna Sandstone Formation and its lateral equivalents (modified after Ben Ferjani et al., 1990).

The Oum Douil Group (Langhian-Messinian)

Burollet (1956) first defined the middle to Upper Miocene Oum Douil Group. It consists of an upward shallowing sequence comprising the Mahmoud, Beglia, Melquart and Oued Bel Khadim Formations: **Figure 3.17** shows sediment thickness variations across Tunisia during the Middle and Late Miocene.

Mahmoud Formation (Langhian)(SS-14): This unit forms the lower member of the Oum Douil Group within the Gabes-Tripoli Basin. It consists of dark grey to green shales interbedded with occasional glauconite rich, bioclastic wackestones and packstones (Burollet, 1956). The top of the Mahmoud Formation is truncated by a regional unconformity. Ben Ferjani et al. (1990) suggest that it was deposited under open marine conditions.

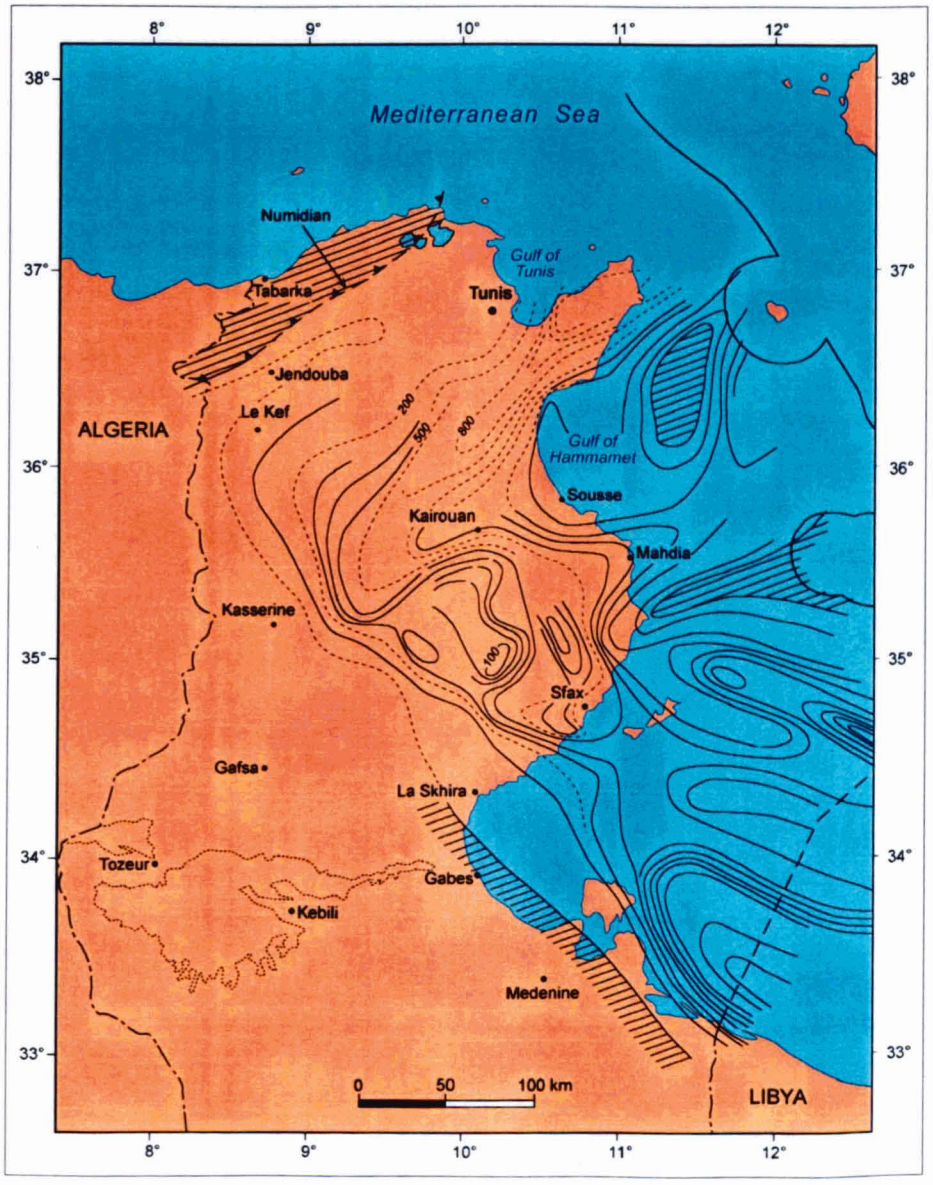

Fig. 3.17. Isopach map of the Middle and Late Miocene showing sediment thickness variations in the Oum Douil Group (modified after Ben Ferjani et al., 1990).

Beglia Formation (Serravallian-Tortonian)(SS-15): The Beglia Formation is comprised of interbedded thick coarse-grained sandstones, shales and bioclastic limestones (Burollet, 1956). Within the Gulf of Hammamet, the Beglia Formation passes laterally into the turbiditic Birsa Formation.

Melquart Formation (Tortonian-Messinian)(SS-16): This unit forms the lateral equivalent of the Segui Formation in the north (Burollet, 1956). It consists of interbedded shales and bioclastic wackestones that were deposited in a relatively shallow marine mid-ramp environment (Ben Ferjani et al., 1990).

Oued Bel Khadim Formation (Messinian)(SS-17): This unit, which forms the upper member to the Oum Douil Group, consists of a terrigenous sequence of interbedded shales, sands and evaporites (Burollet, 1956). These facies are indicative of deposition in a lacustrine and/or lagoonal environment. The top of the Oued bel Khadim Formation is marked by a regional unconformity.

Raf Raf Formation (Zanclean-Piacenzian)(SS-17): This unit unconformably overlies the Oum Douil Group. It consists of a lower conglomeratic unit, and an upper thick shale sequence, rich in planktonic foraminifera (Burollet, 1956). Ben Ferjani et al. (1990) suggest that it relates to a transgressional phase in the Early Pliocene.

3.6. Structural Framework of the Gulf of Gabes

3.6.1. Introduction

Regional seismic reflection profiles and 3D seismic data from the Amilcar, Miskar and Ulysse concessions were used to constrain the seismic stratigraphy, structural framework and evolution of the Gulf of Gabes, and in particular, the Gabes-Tripoli Basin (**Fig. 3.1**). The observations from seismic are integrated with isopach maps, regional stratigraphic correlations (based on available well data), and the results of the subsidence modelling procedure described in Section 3.7 (N.B. The following sections provide only a broad framework of the area; more detailed accounts on the structure and evolution of the Miskar and Hasdrubal Fields are provided in Chapters 6 and 7).

3.6.2. Seismic Stratigraphy

The integration of reasonable quality regional profiles and high resolution, 3D seismic data from the Hasdrubal and Miskar Fields has allowed the construction of a seismic

stratigraphic framework over the area (Table 3.1). This framework is consistently referred to throughout the thesis (Chapters 6 & 7).

Principles of Seismic Stratigraphic Analysis

Seismic stratigraphy involves the subdivision of seismic sections into sequences of reflections that are interpreted as the seismic expression of genetically related sedimentary sequences (Keary & Brooks, 1991). The principles behind seismic sequence analysis are two-fold:

- Reflections are taken to define chrono-stratigraphical units, since the types of rock interface that produce reflections are stratal surfaces and unconformities; by contrast, the boundaries of diachronous lithological units tend to be transitional and often do not produce reflections.
- Genetically related sedimentary sequences are defined as sequences that consist of a set of concordant strata that exhibit discordance with underlying and overlying sequences (i.e. they are typically bounded by angular unconformities variously representing onlap, downlap, toplap or erosion) **(Fig. 3.18a-b)**.

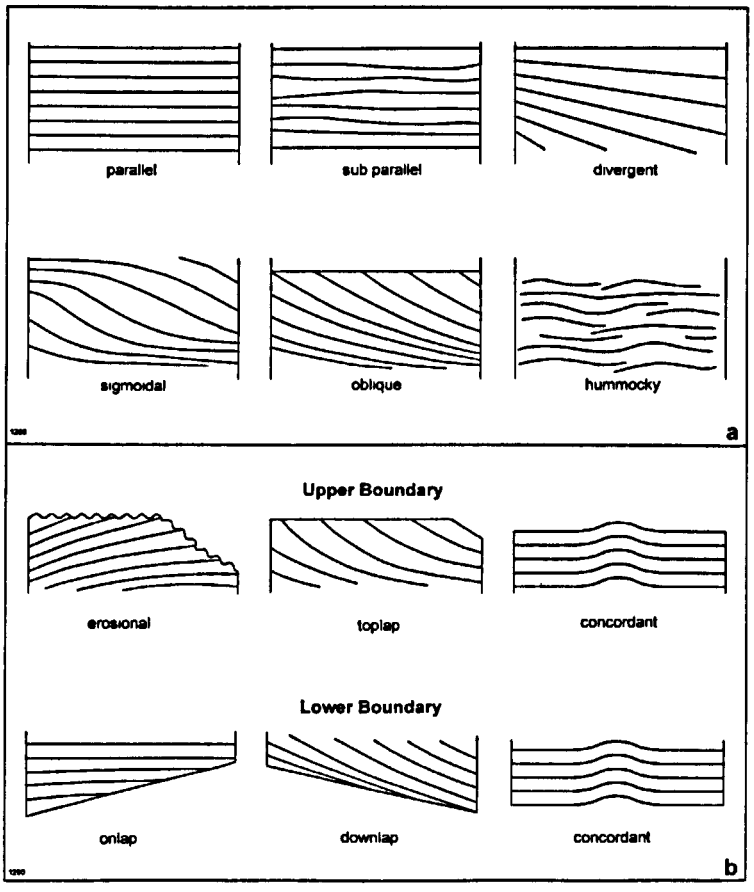

Fig. 3.18. Principles of seismic stratigraphic analysis. a) Various internal bedforms within sedimentary sequences. b) Different types of geological boundary defining sequences (from Keary & Brooks, 1991).

Sequence Number	System/Series Rank	Stratigraphy	Seismic Sequence Characteristics							
			Geological Boundary		Internal Character					Tectonic Control
			Lower	Upper	PA	SP	DIV	SIG	OBL	HUM	
SS-1	Upper Cretaceous	Upper Fahdene Fm.	Onlap	Concordant	✔						
SS-2	Upper Cretaceous	Bahloul/Lower Aleg Mbr.	Onlap	Erosional			✔				✔✔
SS-3	Upper Cretaceous	Bireno Mbr. (Aleg)	Onlap	Concordant		✔(?)	✔(?)				✔
SS-4	Upper Cretaceous	Low. Aleg Shale Mbr. (Aleg)	Concordant	Concordant	✔						
SS-5	Upper Cretaceous	R1 Sup./Inf. Mbr. (Aleg)	Concordant	Concordant		✔					✔
SS-6	Upper Cretaceous	Aleg Carbonate Mbr. (Aleg)	Concordant	Concordant		✔					✔
SS-7	Upper Cretaceous	Up. Aleg Shale Mbr. (Aleg)	Onlap	Erosional			✔				✔✔✔
SS-8	Upper Cretaceous	Abiod Fm.	Onlap	Erosional			✔				✔✔
SS-9	Palaeocene	El Haria/Tselja/Chouabine Fm.	Onlap	Erosional	✔						
SS-10	Eocene	Metlaoui Gp.	Onlap	Concordant		✔					✔
SS-11	Eocene	Cherahil Fm.	Concordant	Erosional		✔(?)	✔(?)				✔✔
SS-12	Oligocene/Miocene	Salammbo Fm.	Onlap	Erosional	✔						
SS-13	Middle Miocene	Ain Grab Fm.	On lap	Erosional	✔						
SS-14	Middle Miocene	Mahmoud Fm.	Onlap	Erosional		✔(?)	✔(?)				✔✔
SS-15	Upper Miocene	Beglia Fm.	Onlap	Erosional		✔(?)	✔(?)				✔
SS-16	Upper Miocene	Melquart Fm.	Onlap	Concordant		✔(?)	✔(?)				✔
SS-17	Upper Miocene/Present	O Bel Khadim/Present	Concordant	N/A	✔(?)						✔

Table 3.1. Seismic stratigraphic framework for the Gulf of Gabes area, based on regional seismic profiles and high resolution 3D seismic data from the Hasdrubal and Miskar Fields (N.B. not all the sequences are indicated on the regional seismic profiles presented in Figures 3.21 to 3.25, due to the poorer data quality. Number of ✔'s shows the degree of tectonic control on sedimentation.

Seismic Stratigraphic Framework of the Gulf of Gabes

Seventeen seismic sequences, bounded by relatively well-defined sequence boundaries have been interpreted in the Gulf of Gabes region, from regional profiles and high resolution 3D seismic data (Table 3.1). Due to data quality only 12 sequences are shown on the seismic lines in **Figures 3.21-3.25**. These sequences are differentiated into syn- and post-rift sequences based on their internal character and the nature of their upper and lower boundaries with adjacent sequences.

In general, seismic data quality is generally good in the Tertiary section above the Maastrichtian unconformity and can be correlated with confidence. However, below this event, the stratigraphy consists primarily of carbonate rocks that have similar seismic velocities. The lack of pronounced velocity contrast between stratigraphic intervals in this section consequently leads to a reduction in data resolution.

Two-way-time (TWT) structure maps over the Gulf of Gabes area have been constructed for four seismic horizons; 1) Top R1 Superior Member (Aleg Formation), 2) Top Abiod Formation, 3) Top El Garia Formation (Metlaoui Group) and 4) Top Reineche Member (Cherahil Formation). The R1 Superior Member, the El Garia Formation, and, to a lesser extent, the Reineche Member constitute the principal reservoir intervals in the region.

3.6.3. Principal Structural Elements

Seismic and well log analyses show that the present-day Gulf of Gabes region is composed of four principal structural elements: 1) The Kerkennah High, 2) The Jerrafa-Djerba High, 3) The Medina-Lampedusa Plateaux and 4) The Gabes-Tripoli Basin (**Fig. 3.19**). The whole area is characterised by a pervasive system of approximately NW-SE trending extensional faults that have been periodically active since at least the middle Cretaceous (refer to Section 3.7). **Figure 3.20** presents a WSW-ENE trending cross-section from just west of the North-South Axis into the Gulf of Gabes area. It illustrates the thinned nature of continental crust below the Pelagian Platform.

Kerkennah High

The Kerkennah High (Kerkennah Arch) is located in the near-shore regions of the Gulf of Gabes (**Fig 3.19**). It extends from the Jerrafa-Djerba High in the south to the Medina-Lampedusa Plateaux in the north, and encompasses the Kerkennah islands.

Seismic lines CTWT-92-106/106A (**Fig. 3.21**), CTWT-92-108/108A (**Fig. 3.22**), and CTWT-92-102/2A (**Fig. 3.23**), together with the TWT structure maps in **Figures 3.26-3.29** show the seismic expression of this feature. It represents a broad NNE-SSW trending high (orthogonal to the present-day structural grain), which separates two basinal regions to the SE and NW (i.e. the 'Sfax' Basin and the Gabes-Tripoli Basin). Late Jurassic to present-day NW-SE trending extensional faults dissect the area.

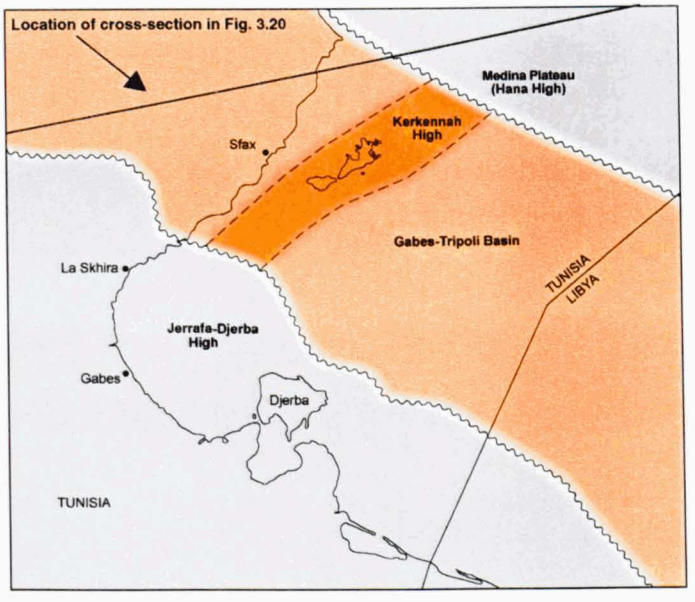

Fig. 3.19. Principal structural elements in the Gulf of Gabes region showing the location of the Gabes-Tripoli Basin, the Medina Plateau, the Kerkennah High and Jerrafa-Djerba High.

Seismic lines CTWT-92-106/106A (**Fig. 3.21**) and CTWT-92-108/108A (**Fig. 3.22**), together with the isopach maps and regional correlation presented in **Figures 3.30-3.37** illustrate the control that the Kerkennah High has exerted on sedimentation throughout the Mesozoic and Tertiary. **Figure 3.34** shows some inconsistencies compared to the other isopach maps presented and thus must be treated with caution. In this map the Kerkennah High does not appear to exert much control on sedimentation. This disagrees with the seismic data available, and shows that where there is a lack of well control (as in this case) it is imperative to use any other available data to hand to construct these maps. It is apparent that during the Early Cretaceous, this zone had little affect on deposition, shown by the constant thickness of the Lower Cretaceous succession (**Figs. 3.21-3.22**). During the Cenomanian however, the area appears to have been established as a palaeo-high separating two sub-basins. The Upper Cretaceous to Middle Miocene section onlaps gently onto the Kerkennah High, and is significantly reduced on the crest of the structure. To the north, much of the Palaeocene and Eocene section is totally absent.

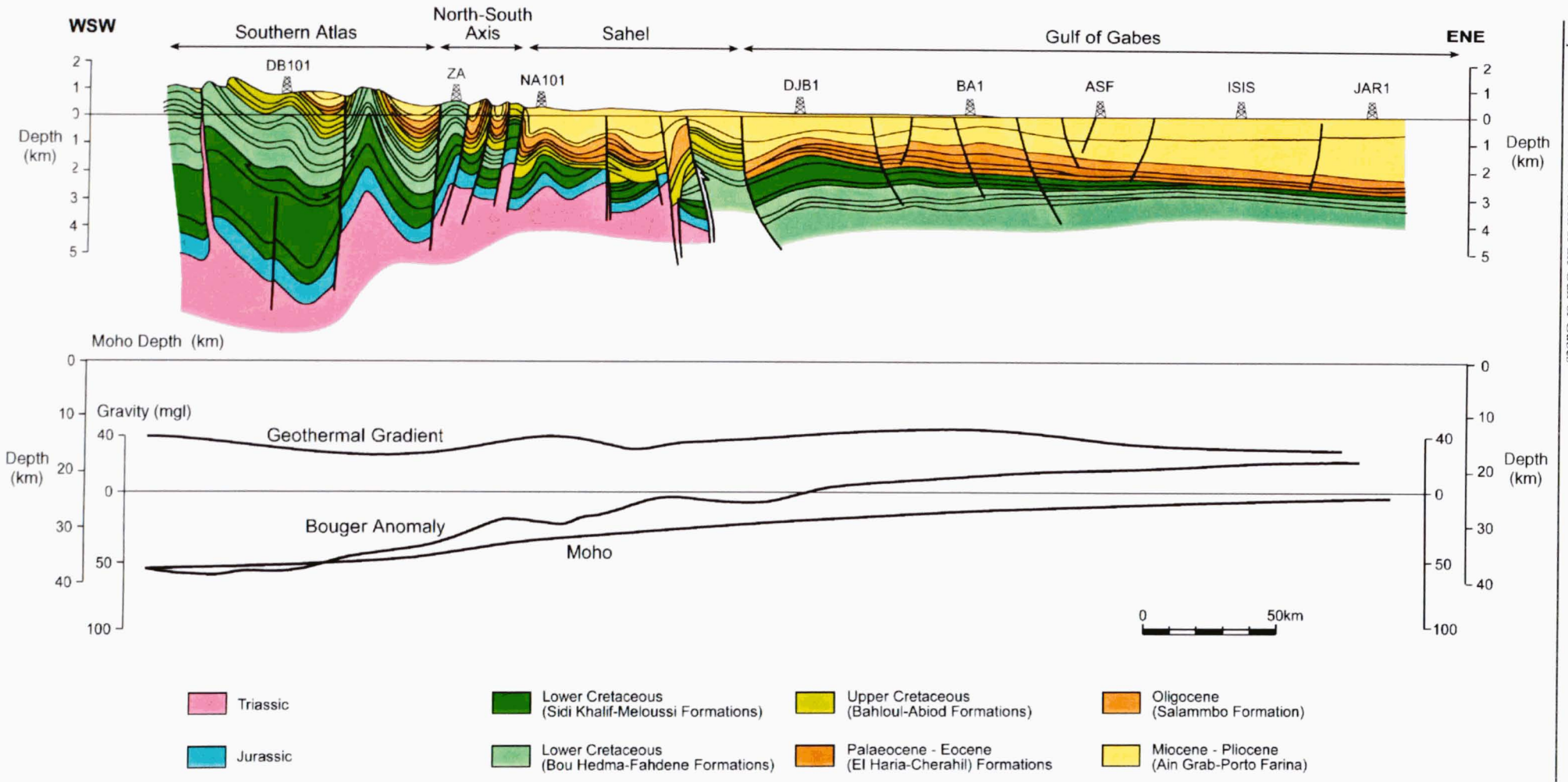

Fig. 3.20. WSW-ENE trending cross-section from just west of the North-South Axis into the Gulf of Gabes area (from Ben Ferjani et al. 1990).

It is postulated in this study that the present-day Kerkennah High overlies an older basement lineament, which may have been created during Neo-Tethyan rifting or an older tectonic event. Subsequent movements on the structure, particularly in the Late Cretaceous caused uplift along this NNE-SSW trending zone. As a consequence, it became an area of non-deposition and/or erosion. A series of reconstructions are given in **Figure 3.39** to illustrate the evolution of this area from the Albian to present-day.

To the north, the Kerkennah High terminates abruptly against a steeply dipping, ESE-WNW trending fault zone that is characterised by large vertical displacements throwing down to the NNE (>950m at Middle Miocene level) (**Figs. 3.21-3.22**)). Strong evidence to suggest that this structure has been active throughout the Mesozoic and Tertiary is provided by the thickening of hangingwall sediments adjacent to the main fault zone, in particular within the Middle Miocene to present-day section. Folding within the Lower Jurassic to Palaeocene hangingwall succession may be the product of halokinesis and/or localised transpression. Arguments to support both mechanisms are valid, and it is probably a combination of the two that has caused the complex structural and stratigraphic geometries observed (**Fig. 3.21**). The proposed model suggests that the onset of salt movement commenced during the deposition of the Lower Fahdene Formation in the late Aptian. Migration continued into the Palaeocene, and was accompanied by intermittent pulses of dextral transpression (i.e. during the Santonian and Maastrichtian) (refer to Chapters 6 and 7). A major unconformity occurs in the hangingwall section above the El Haria Formation (SS-9). Over the crest of the salt dome the entire Eocene to Lower Miocene sequence is absent. There is no evidence of folding in the Middle Miocene to present-day sequence suggesting a cessation in salt movement and compression. However, the strong tilting and the large thickness variations within this succession suggest active extension and fault block rotation during this period.

The presence of this ESE-WNW trending fault zone (at the northern limit of the Kerkennah High) probably represents the offshore extension of the Mahdia Shear Zone (MSZ), which was discussed in Section 2.3.4. Bedir et al. (1992) demonstrate that the onshore portion of this fault zone is characterised by dextral strike-slip movements. This sense of shear is probably translated offshore, although the lack of available seismic data in this study precludes any direct determination. The significance of this zone will be discussed in more detail in Section 3.8.

CONTAINS PULLOUTS

Jerrafa-Djerba High

The WNW-ESE trending Jerrafa-Djerba High is located on the southern margin of the Gulf of Gabes (**Fig. 3.19**). It is bounded to the north by the Gafsa-Jarrafa Fault Zone, and extends across southern Tunisia incorporating the northern part of the Saharan Platform. The regional correlation provided in **Figure 3.38** illustrates the transition from this area into the Gabes-Tripoli Basin to the north. Thin continental sands, lagoonal dolomites and evaporitic sequences dominate this region (Bishop, 1975), in contrast to the thick, basinal deposits characterised in the Gabes-Tripoli Basin. During much of the Mesozoic and Tertiary it has remained an area of non-deposition and/or erosion, as evidenced by numerous stratigraphic omissions from the sedimentary record (Ezz -2 well (**Fig. 3.38**)). TWT structure and isopach maps over the Gulf of Gabes show the nature of sedimentation across the Gafsa-Jarrafa Fault Zone, from the Jerrafa-Djerba High into the Gabes-Tripoli Basin (**Figs. 3.26-3.36**).

Medina-Lampedusa Plateaux

As discussed in Section 2.3.4, the WNW-ESE trending Medina and Lampedusa Plateaux form the northern boundaries to the Gabes-Tripoli Basin (**Fig. 3.19**). Seismic lines CTWT-92-101 (**Fig. 3.24**) and CTWT-92-103C (**Fig. 3.25**) show the seismic expression of the Medina Plateau and its transition into the Gabes-Tripoli Basin. This transition is characterised by a series of faulted steps downthrowing to the southwest.

Structurally, the Medina Plateau is cut by numerous NW-SE trending faults, which show evidence of extensional and possibly oblique-slip displacements (**Figs. 3.24-3.25**). The southern margin is defined by an extremely steep, SW-dipping fault zone which downthrows to the northeast. Composite vertical displacements on this zone exceed 700m at top Jurassic level. However, most movement appears to be relatively recent (i.e. Late Miocene to present-day). In the hangingwall section, a broad, open anticline has been developed immediately adjacent to the main fault plane. In many ways this fault zone is similar to that interpreted at the northwestern end of lines CTWT-92-106/106A (which is believed to represent an extension of the dextral Mahdia Shear Zone). It may therefore be postulated that an approximately WNW-ESE trending dextral shear zone exists along the southern margin of the Medina and Lampedusa Plateaux, which links to the Mahdia Shear Zone in onshore Tunisia. This feature is termed the Mahdia-Medina Shear Zone (MMSZ).

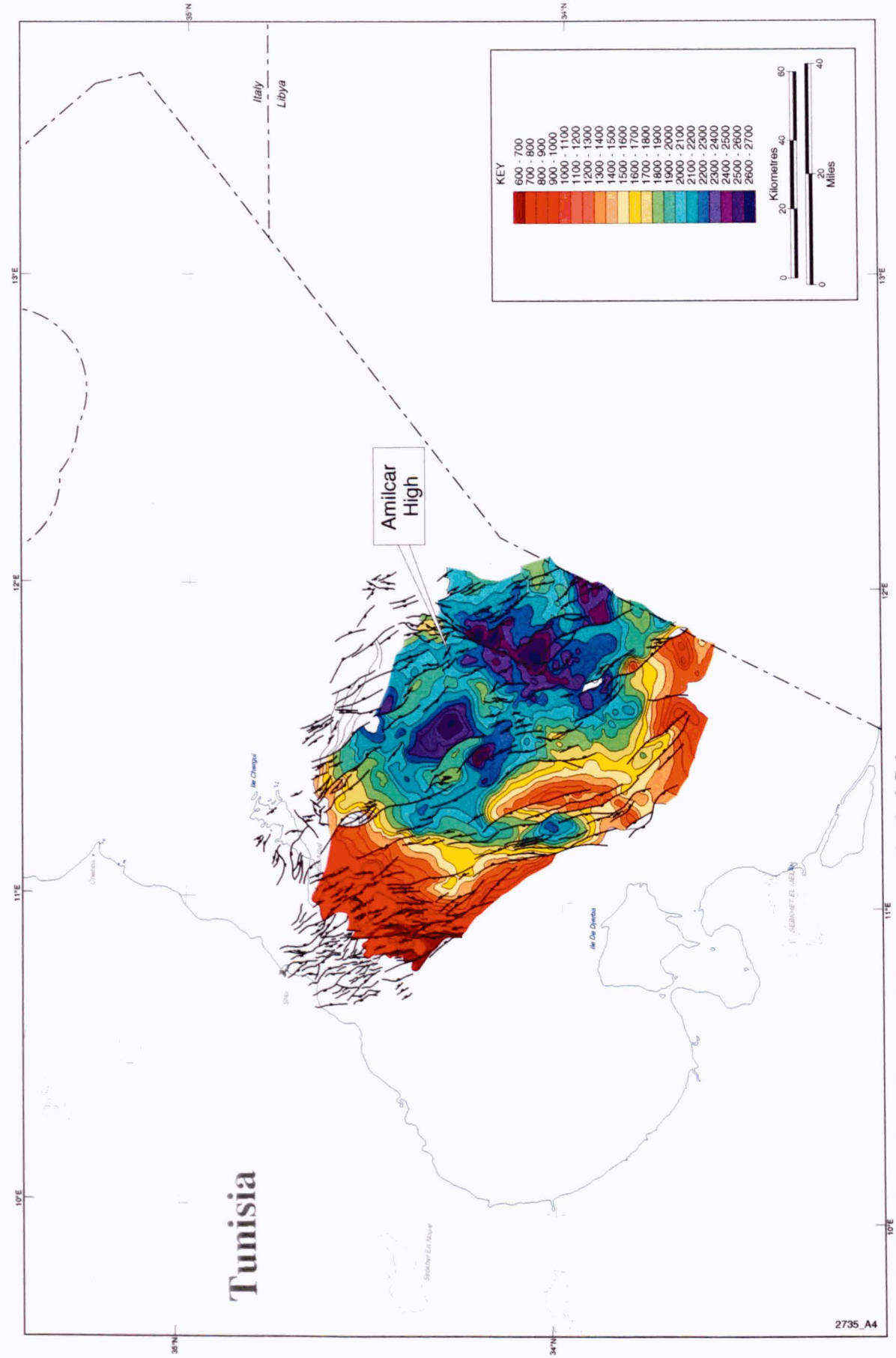

Fig. 3.26. Top Bireno TWT Structure Map across the Gulf of Gabes.

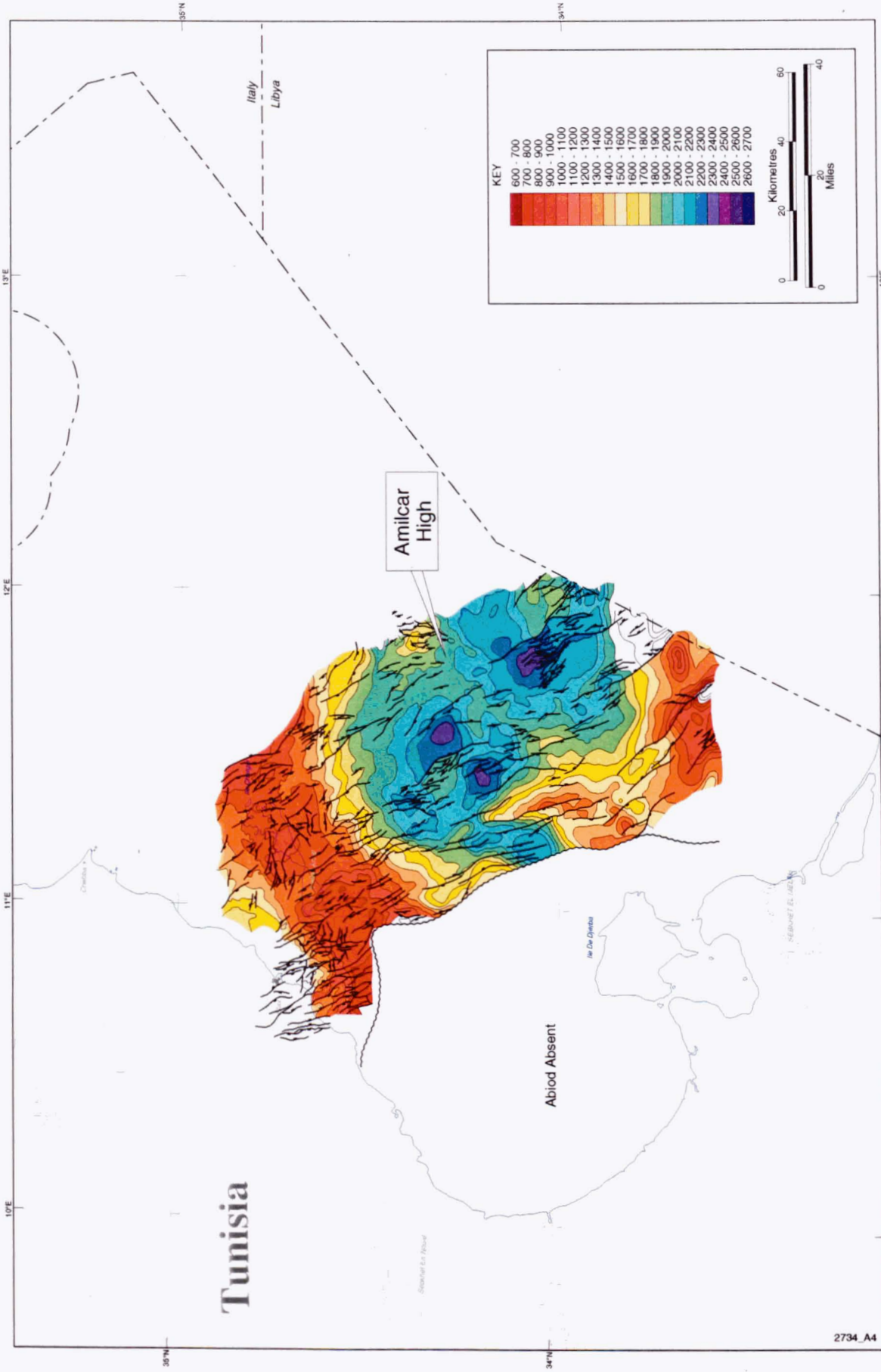

Fig. 3.27. Top Abiod TWT Structure Map across the Gulf of Gabes.

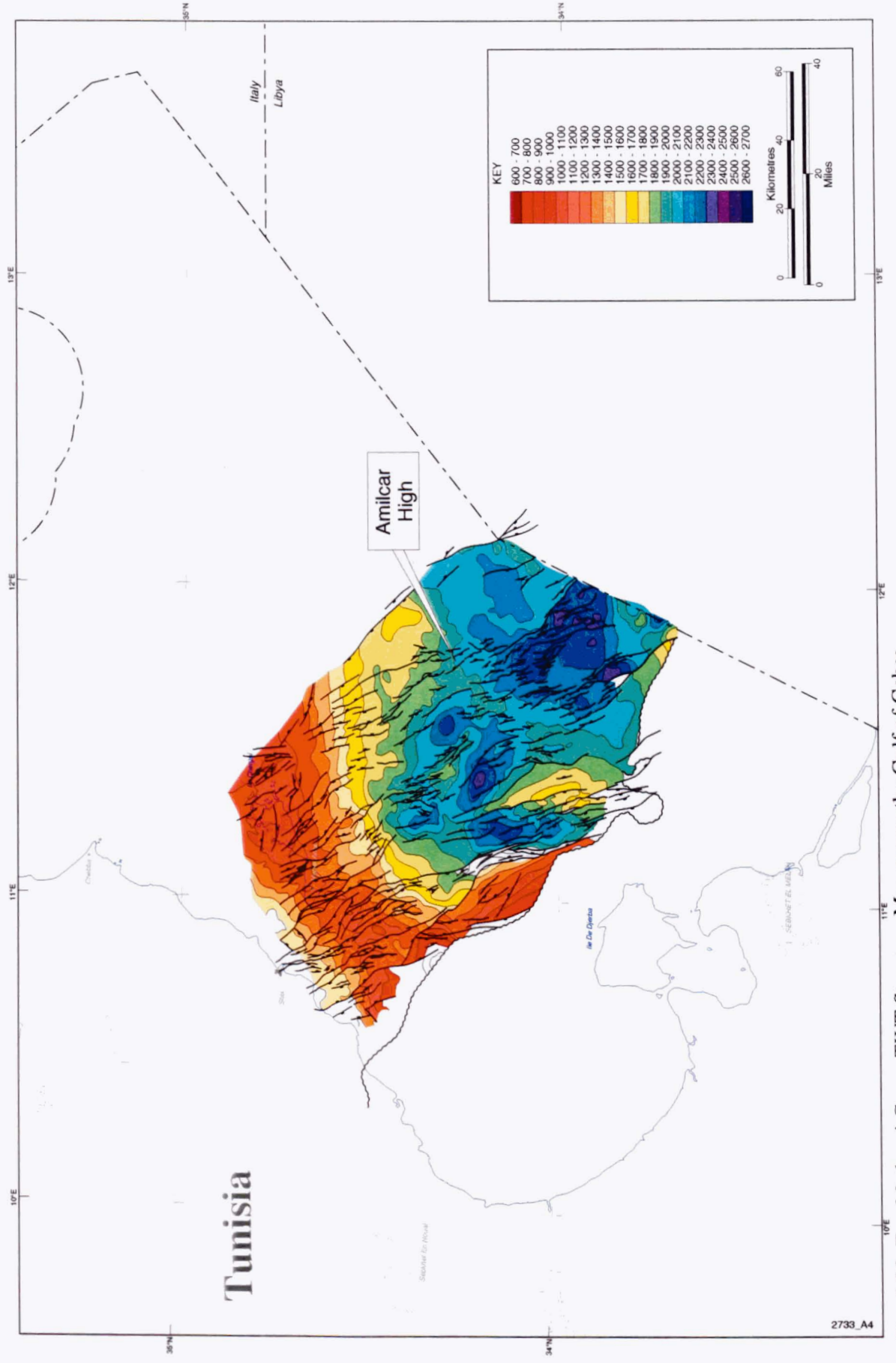

Fig. 3.28. Top Metlaoui Group TWT Structure Map across the Gulf of Gabes.

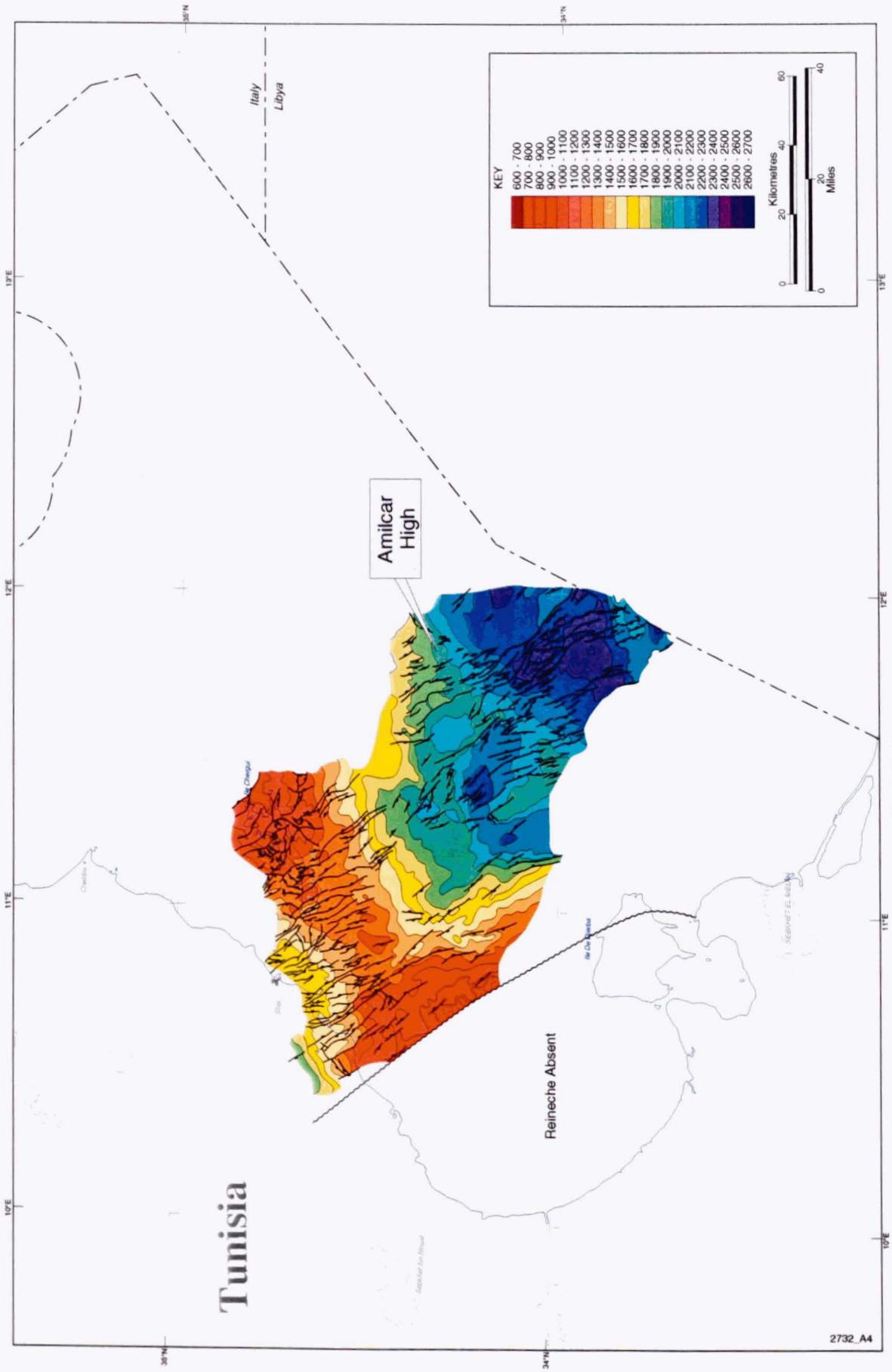

Fig. 3.29. Top Reineche TWT Structure Map across the Gulf of Gabes.

Seismic lines CTWT-92-101 (**Fig. 3.24**) and CTWT-92-103 (**Fig. 3.25**), together with the isopach maps and regional correlation given in **Figures 3.30-3.36**, and **3.38** show the nature of sedimentation from the Medina and Lampedusa Plateaux in the north into the Gabes-Tripoli Basin in the south. The thick Upper Cretaceous sediments that characterise the Gabes-Tripoli Basin to the south, thin and gently onlap onto this basin-bounding high.

Gabes-Tripoli Basin

As previously discussed in Chapter 2, the Gabes-Tripoli Basin is located south of the Medina and Lampedusa Plateaux and north of the Jerrafa-Djerba High (**Fig. 3.19**). Seismic lines CTWT-92-101, CTWT-92-102 and CTWT-92-106 (**Figs. 3.21, 3.23 & 3.24**), together with the TWT structure maps given in **Figures 3.26-3.29** display the geometry of the western (Tunisian) part of the basin. It is elongate in form, trending approximately WNW-ESE, and consists of a thick Mesozoic and Tertiary sequence of carbonates and shales. The basin depocentre runs just south of the Hasdrubal Gas Field (**Figs. 3.30-3.38**). The southern boundary with the Jerrafa-Djerba High is represented by the Gafsa-Jarrafa Fault Zone, which has composite vertical displacements in excess of ca. 4000m (Bishop, 1975) (**Fig. 3.38**).

Structurally, the western part of the Gabes-Tripoli Basin is characterised by a pervasive system of roughly NW-SE trending extensional faults, sub-parallel to the basin axis (**Figs. 3.26-3.29**). These faults produce a horst-and-graben topography within the Mesozoic to present-day succession; the largest features include the Jerrafa and Tripolitana Graben and additionally the Isis Horst. The Jerrafa Graben is clearly defined on line CTWT-92-101 (between shotpoints 8500 and 9500) (**Fig. 3.24**). It contains a thick Upper Cretaceous to present-day sequence, indicating tectonic activity throughout the period (N.B. a considerable amount of Middle Miocene to present-day movement is apparent). Observations from seismic and landsat image data illustrate that most of the extensional faulting in the Gabes-Tripoli Basin is oblique to the WNW-ESE trending Gafsa-Jarrafa Fault Zone (GJFZ), and the proposed Mahdia-Medina Shear Zone (MMSZ). These geometries are in agreement with the model proposed by Anketell (1995), which suggests that the Gabes-Tripoli Basin was formed as a pull-apart feature above a large dextral shear zone; the limits of which are formed by the JGFZ and the MMSZ (refer to Section 3.8 for a discussion).

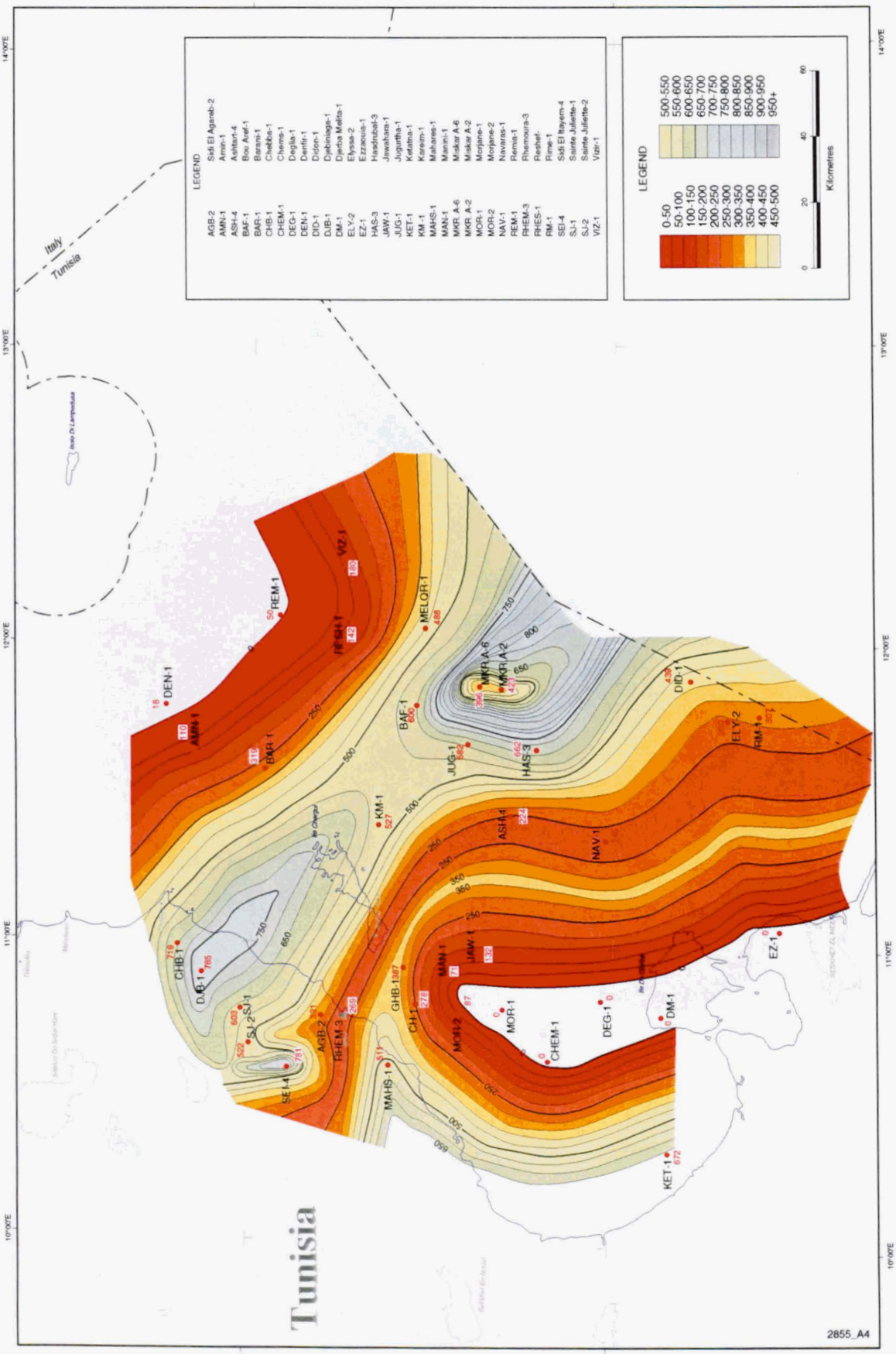

Fig. 3.30. Isopach Map of the Aleg Formation (SS-2 to 7) (derived from well data).

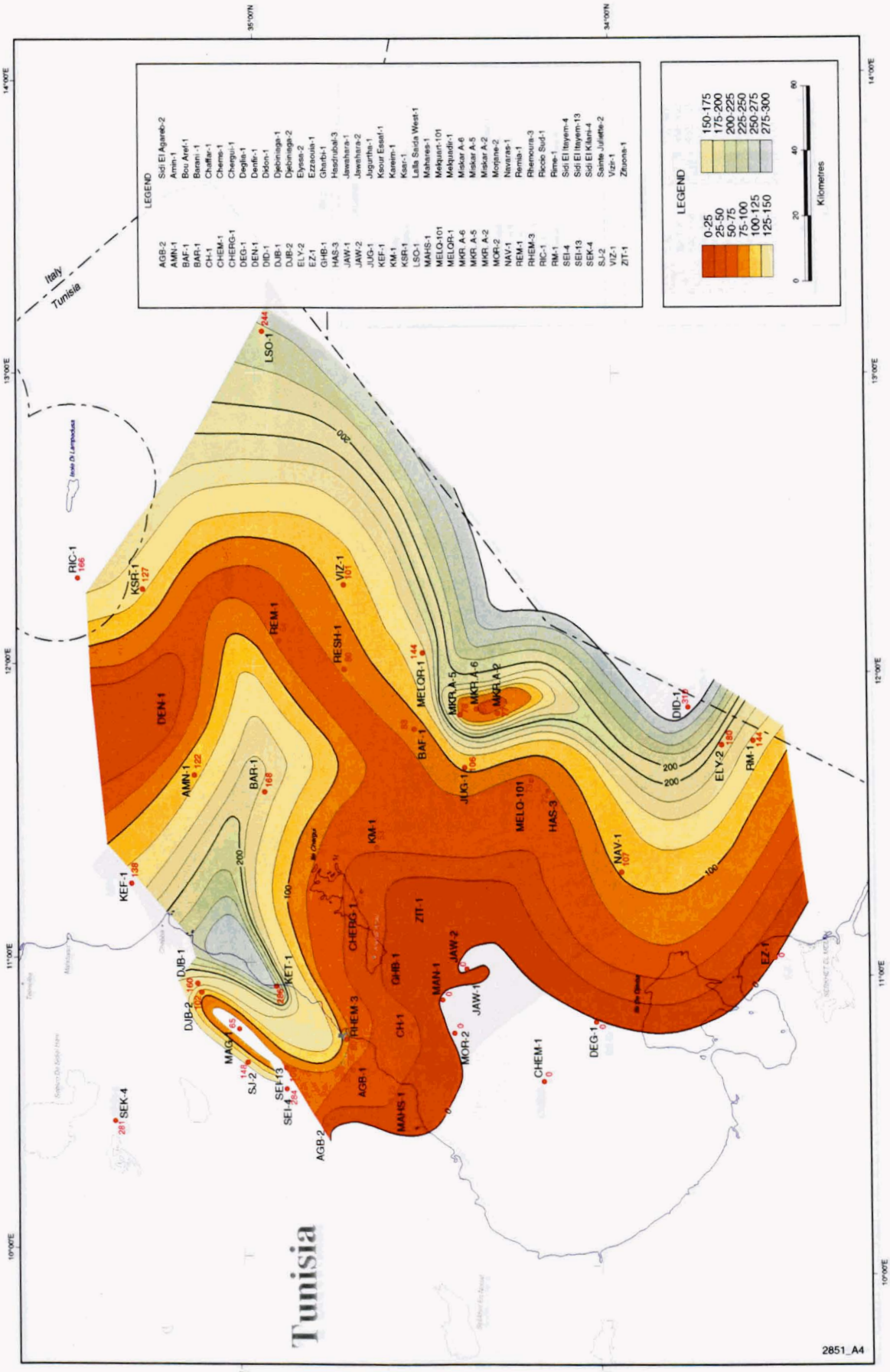

Fig. 3.31. Isopach Map of the Abiod Formation (SS-8) (derived from well data).

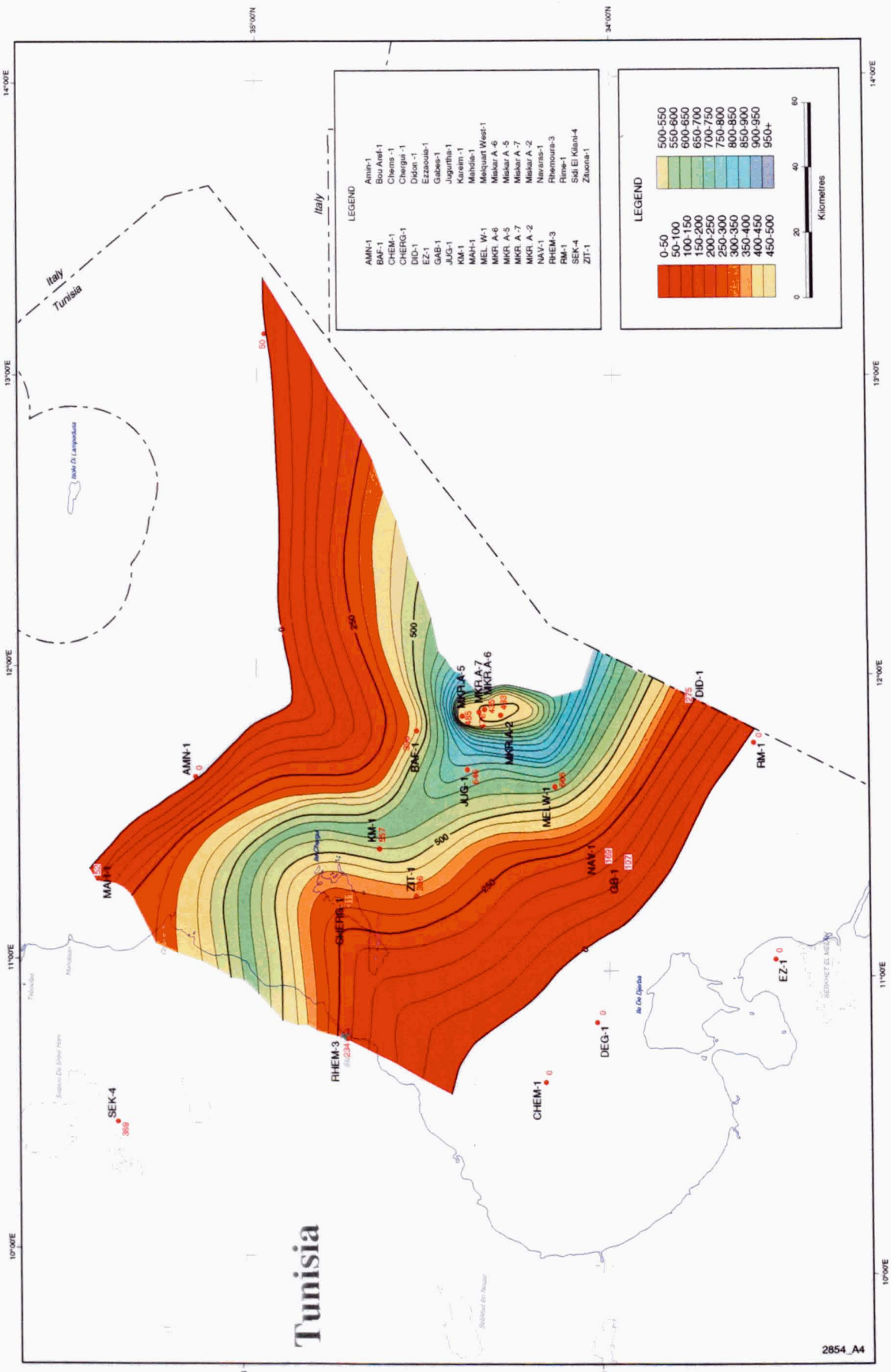

Fig. 3.32. Isopach Map of the El Haria / Tjelja Formations (derived from well data).

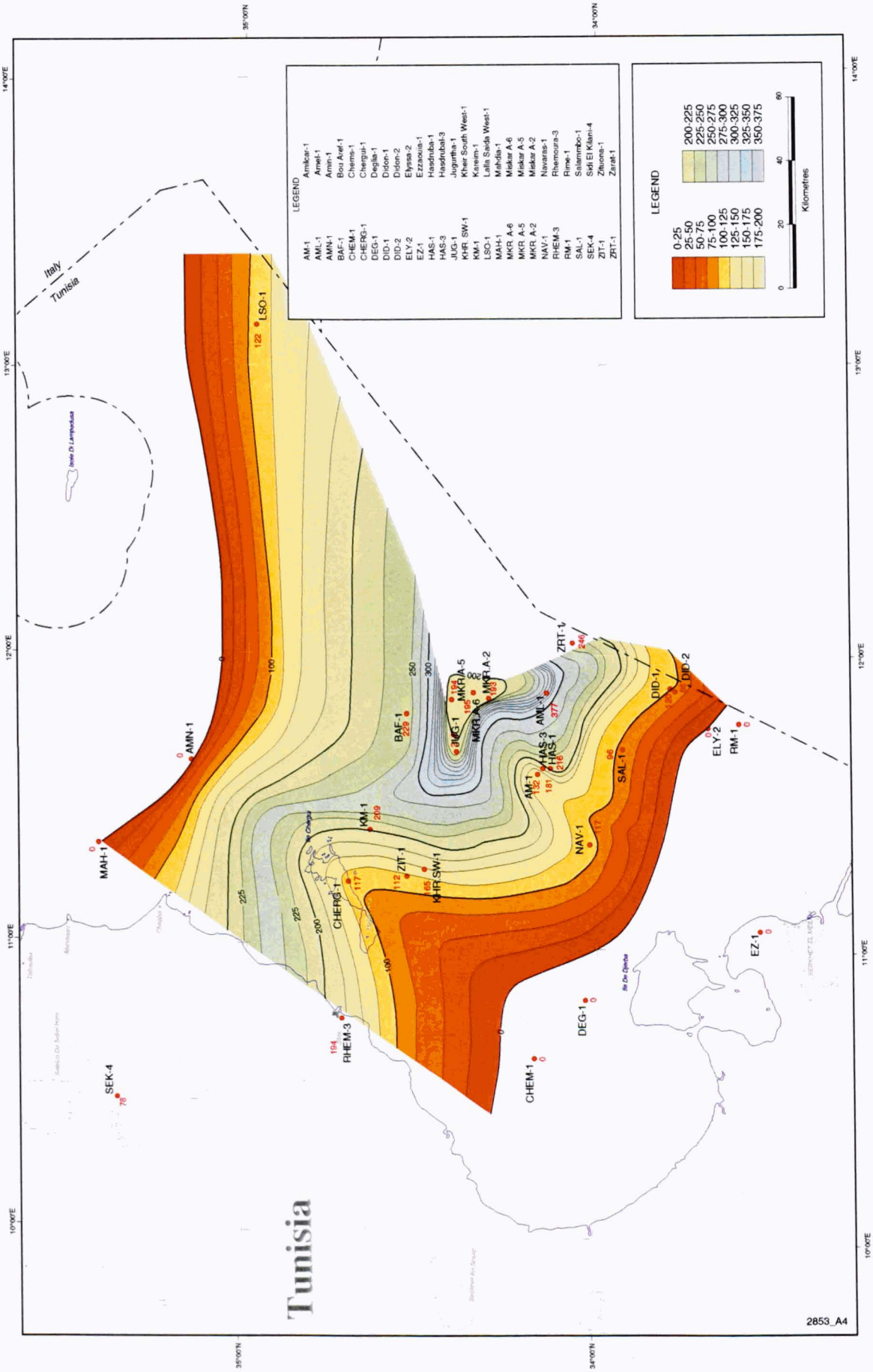

Fig. 3.33. Isopach map of the Metlaoui Group (SS-10) (derived from well data).

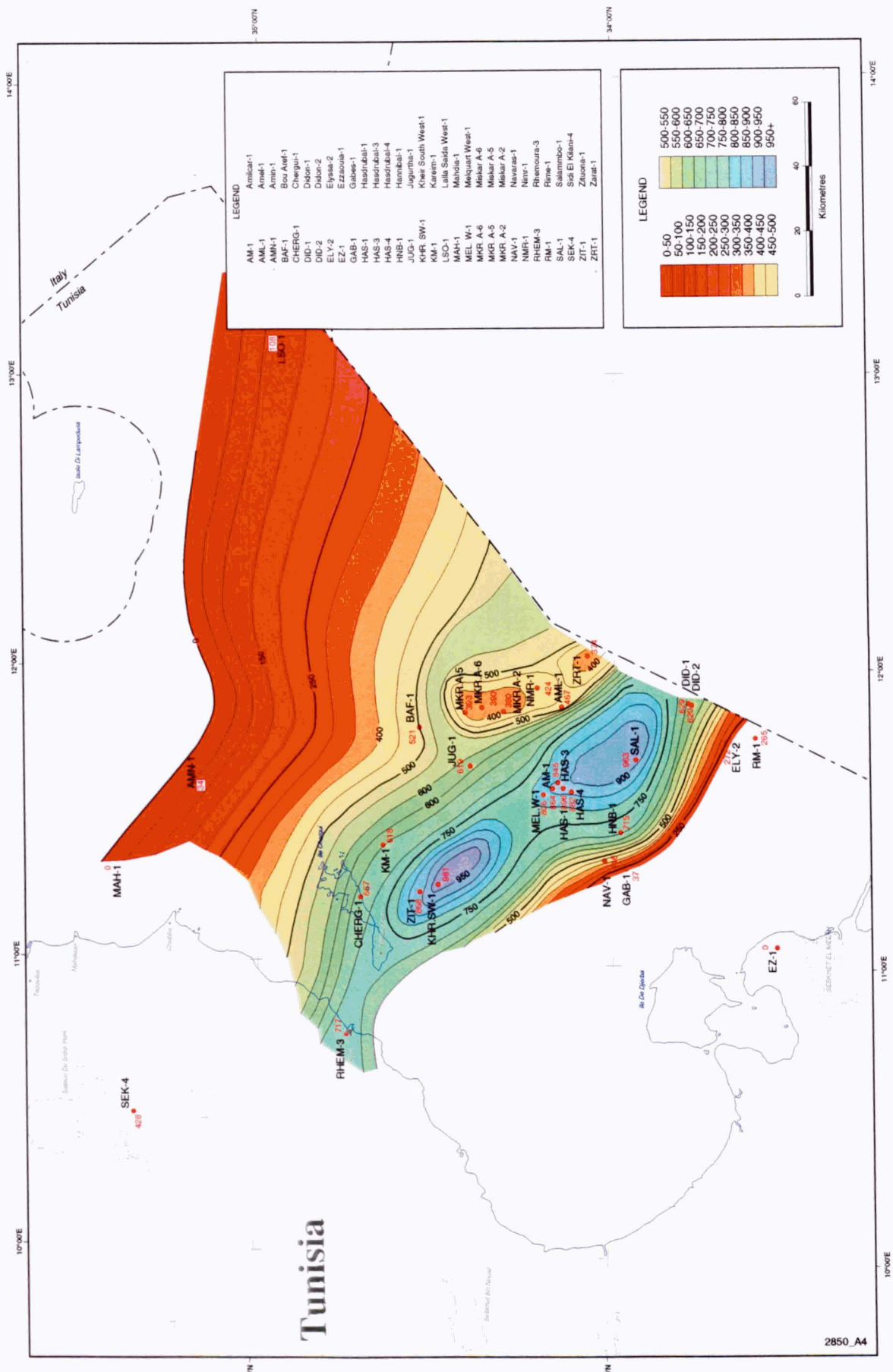

Fig. 3.34. Isopach Map of the Cherahil Formation (derived from well data).

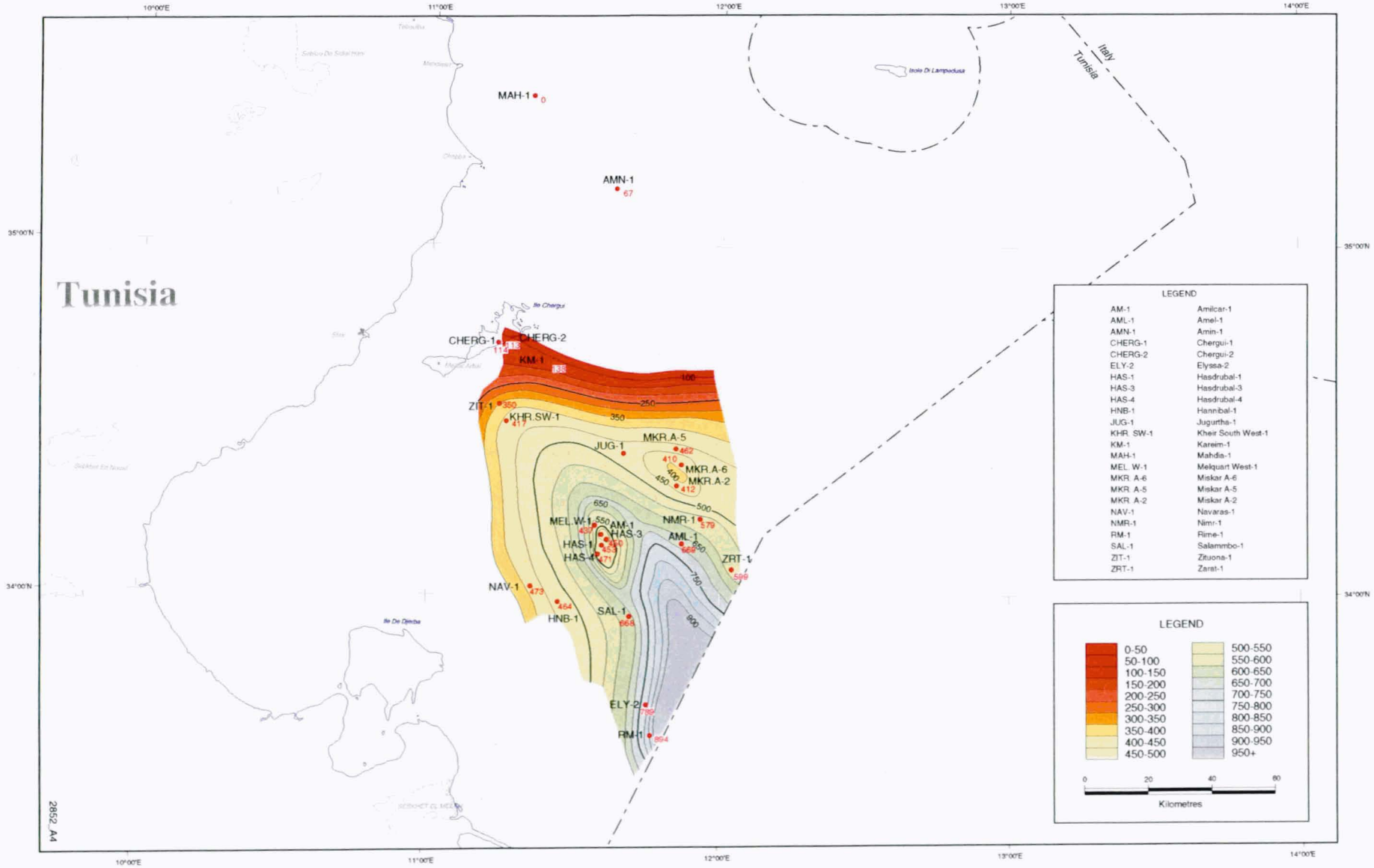

Fig. 3.35. Isopach Map of the Salammbo Formation (SS-12) (derived from well data).

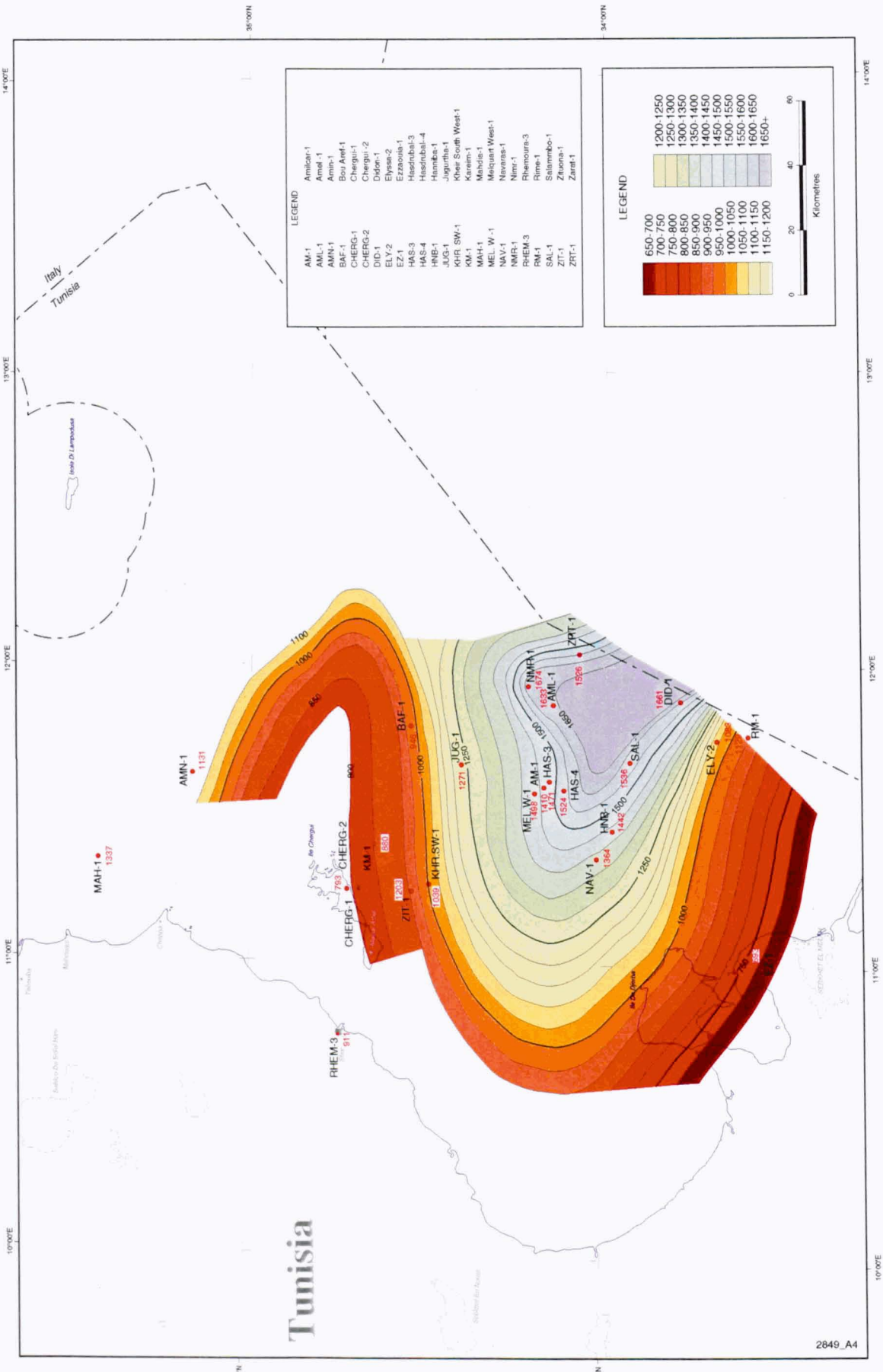

Fig. 3.36. Isopach Map of the Miocene to Present Day Section (SS-13 to 17) (derived from well data).

CONTAINS PULLOUTS

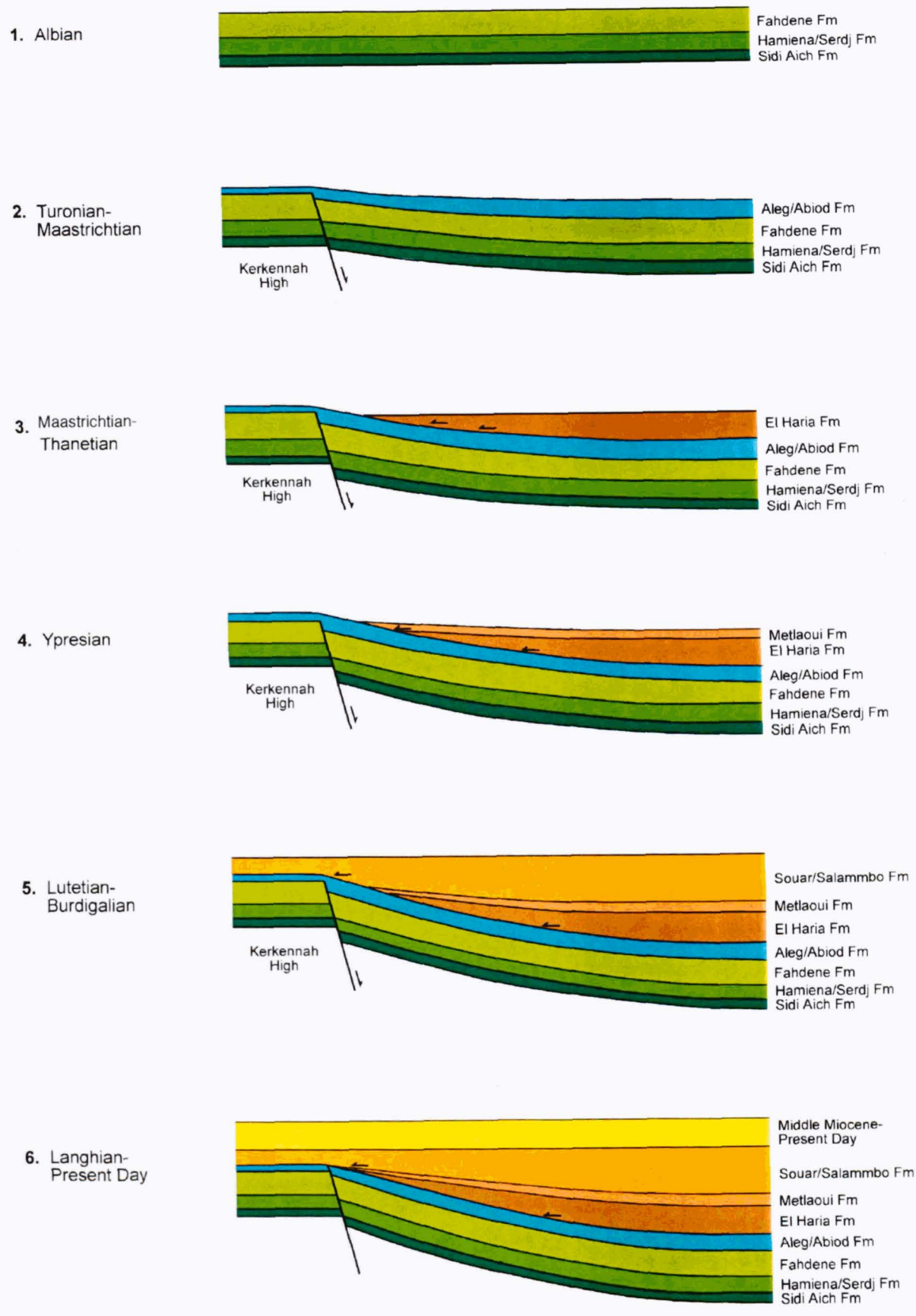

Fig. 3.39. Schematic illustration showing the structural development of the Kerkennah High from the Turonian/Maastrichtian. Note the effect of the Kerkennah High on sedimentation.

Within the central part of the Gulf of Gabes, an approximately NNE-SSW trending ridge has been delineated, orthogonal to the basin axis. This structural high, termed as the 'Amilcar High', extends from the Vizir -1 well in the northeast to the Gabes -1 well in the southwest, and incorporates the Miskar and Hasdrubal Gas Fields (**Figs. 3.26-3.29**). It essentially divides the western part of the Gabes-Tripoli Basin into two separate sub-basins located to the NW and SE (**Figs. 3.21-3.23**). The eastern bounding fault to the Amilcar High is well expressed on **Figure 3.26.** Detailed analyses of 3D seismic data illustrate that this zone has undergone several phases of transtension and transpression. The evolution of the Amilcar High, and its impact on the development of the Miskar and Hasdrubal structures is discussed in more detail in Chapters 6 and 7. Therefore only a brief summary is provided in this section.

It is postulated that the Amilcar High, like the Kerkennah High, is underlain by a series of NNE-SSW trending Late Triassic lineaments, created during Neo-Tethyan rifting. 3D seismic analyses show that a rejuvenation of NE-SW extension in the Late Cretaceous reactivated these early structures in transtension, essentially creating a NNE-SSW trending palaeo-high, orthogonal to the basin axis. Intermittent phases of ~NW-SE compression are recorded along the Amilcar High, indicated by the partial inversion of the eastern half graben; the main phases occurred in the Santonian and late Maastrichtian. It appears to have remained a palaeo-high until at least the late Eocene. En-echelon fault configurations within the Upper Cretaceous to Upper Eocene succession show that strike-slip movements on these early NNE-SSW trending structures have, in part, controlled fault development in the cover sequence.

Faulting in the Upper Cretaceous to present-day sequence

Four principal levels (or tiers) of NW-SE to NNW-SSE faults have been identified in the Upper Cretaceous to present-day succession across the Gulf of Gabes, from high-resolution 3D seismic data. These are discussed in detail in Chapters 6 and 7. On 2D regional seismic data, only two fault systems can be identified due to the poorer resolution of the data (**Figs. 3.21-3.25**). These two fault systems overlie, and are apparently influenced by oblique-slip movements on the older NNE-SSW structures. The lower level of extensional faults, extend from the Cenomanian Aleg Formation (SS-3 to 7) into the Priabonian, where they terminate at the Oligocene unconformity. The upper system of extensional faults extend through the Langhian to present-day

section. Many of the faults in the lower 'tier' are seen to propagate into upper levels, where they commonly link with faults in the upper tier through 'soft-linkage'.

3.7. Subsidence History of the Gulf of Gabes

3.7.1. Introduction

Stratigraphic borehole data can be used to determine the subsidence history of an area (White, 1993, 1994). In this section, inverse strain rate modelling procedures are used to determine the Mesozoic and Tertiary subsidence histories of 33 wells in the Gulf of Gabes region. Sections 3.7.2, 3.7.3 and 3.7.4 summarise the theory and methodology of the procedure. Section 3.7.5 presents the results of the study and attempts to integrate the main conclusions with observations from seismic and well data. It will also compare the results with the analysis of Anderson (1991), which was conducted in the onshore Sahel region to the north of the Gulf of Gabes (**Fig. 3.1**).

3.7.2. Extension and Subsidence

Uniform Extension

Models of lithospheric extension account for observations of subsidence, crustal thinning, upper crustal faulting, enhanced heat flow, and magmatism in sedimentary basins worldwide. In these models, divergent passive margins form due to thinning of the lithosphere. This thinning is accommodated in the upper crust by normal faulting, and by plastic creep in the lower crust and lithospheric mantle (McKenzie, 1978a). The stretching factor, β, is used to measure the amount of crustal thinning. Often, the amount of lithospheric stretching is less than that required to initiate seafloor spreading and intra-continental basins result. These models have been tested successfully in areas such as the North Sea (Sclater & Christie, 1980; Barton & Wood, 1984), the east coast margin of the United States (Watts & Steckler, 1989), and the currently active Aegean region (McKenzie, 1978a).

Instantaneous Extension

The uniform stretching model of McKenzie (1978b) attempts to quantify the thermal response of the lithosphere to uniform stretching (**Fig 3.40**). Vertical crustal movements are calculated assuming instantaneous stretching, local (Airy) isostasy, and

depth-invariant extension with depth. The asthenosphere will rise passively following instantaneous stretching of the lithosphere. As the temperature throughout the lithosphere remains fixed, the geothermal gradient and the surface heat flow will increase. Crustal thinning is accompanied, in the stretched surface zone, by fault controlled subsidence, provided that the initial crustal thickness is >~17km for a 125km thick lithosphere (Table 3.2). Subsequent conductive cooling of asthenosphere leads to a density increase, which in turn promotes a phase of thermal (post-rift) subsidence. This thermal subsidence occurs according to an exponential decay function, whereby lithosphere 125 km thick is close to thermal equilibrium ~60Ma after extension.

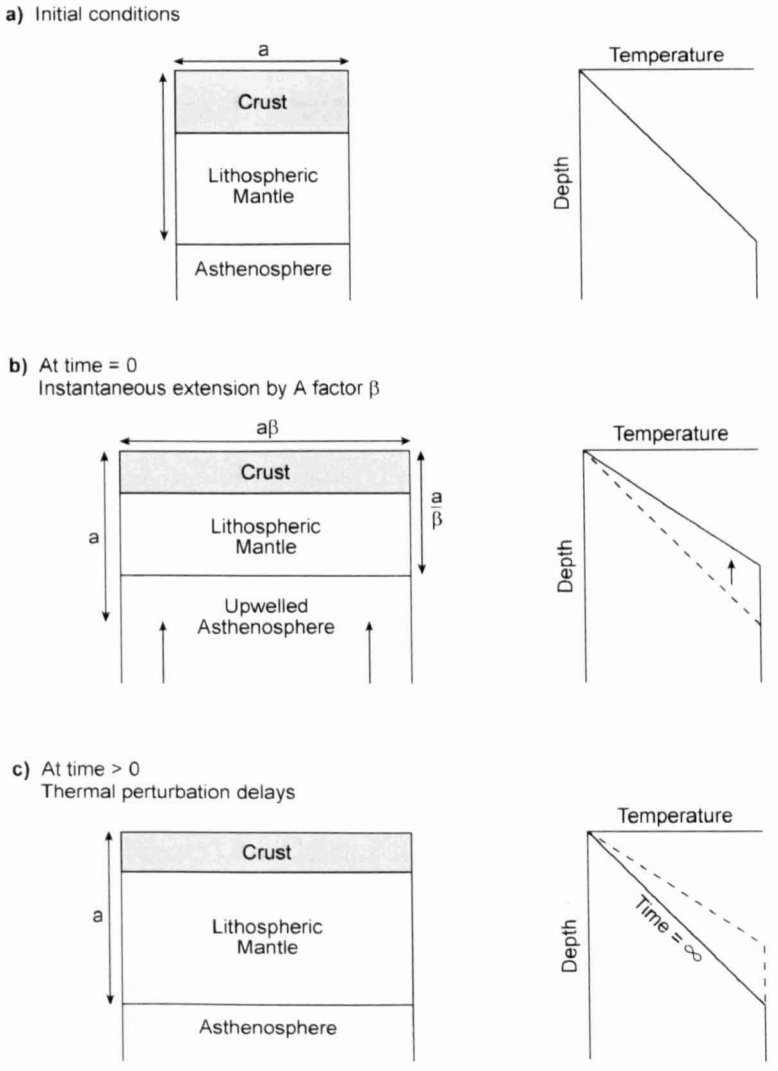

Fig. 3.40. Configuration (left) and thermal profile (right) of the lithosphere and asthenosphere before, during, and after uniform (instantaneous) stretching. A section of the lithosphere is stretched by a factor β causing upwelling of the asthenosphere. The thermal perturbation will decay according to an exponential decay function. After approximately 60 Myr the lithosphere will become close to thermal equilibrium (from McKenzie, 1978b).

Parameter	Definition	Value	Units
A	Lithospheric thickness	125	km
t_c	Pre-rift crustal thickness	35	km
τ_e	Lithospheric elastic thickness		km
S_w	Water loaded subsidence		km
S_s	Total column subsidence		km
S_e	Thickness of sediment removed by erosion		km
β	Stretching factor		
$\dot{\varepsilon}$	Strain rate		s^{-1}
t	Time		s
T	Temperature		°C
T_1	Temperature at base lithosphere	1333	°C
u	Horizontal velocity		km s^{-1}
v	Vertical velocity		km s^{-1}
x	Horizontal coordinate		km
z	Vertical coordinate		km
α	Lithospheric thermal expansion coefficient	3.28×10^{-5}	$°C^{-1}$
κ	Thermal diffusivity of the lithosphere	8.04×10^{-7}	$m^2 s^{-1}$
τ	Thermal decay time of lithosphere	62.8	Ma
ρ_m	Density of mantle	3.33	g cm^{-3}
ρ_a	Density of asthenosphere	3.20	g cm^{-3}
ρ_c	Density of crust	2.80	g cm^{-3}
ρ_s	Density of sediment		g cm^{-3}
ρ_w	Density of seawater	1.03	g cm^{-3}
λ	Compaction decay length		km
ϕ	Sediment porosity		

Table 3.2. Definitions and values of model parameters used in this chapter. Ga^{-1} units are also used for strain rate in this dissertation, where $Ga^{-1} = 3.16 \times 10^{16}$ s^{-1}.

Finite Duration Extension

The instantaneous stretching model assumes infinite strain rates and is generally only valid where rift periods are <20Ma (Jarvis & McKenzie, 1980). A more advanced model allows for simultaneous upwards advection of heat and conductive cooling of the upwelling lithosphere (Jarvis & McKenzie, 1980). This finite-duration extension model assumes a constant strain rate during rifting and allows the rate of lateral removal of lithospheric material and upwelling lithosphere to be calculated (**Fig. 3.41**). The temporal evolution of the lithospheric thermal pertubation (caused by extension during and after stretching) can be obtained by the heat flow equation (Jarvis & McKenzie, 1980);

$$\frac{\partial T}{\partial t} = \kappa \frac{\partial^2 T}{\partial z^2} - \dot{\varepsilon}(a - z)\frac{\partial T}{\partial z} \qquad (3.1)$$

where T is the temperature, t is the time, κ is the thermal diffusivity, a is lithospheric thickness, z is distance measured from the base of the lithosphere at $z = a$, and $\dot{\varepsilon}$ is vertical strain rate. $\dot{\varepsilon}$ can be defined as

$$\dot{\varepsilon} = \frac{\partial u}{\partial x} = -\frac{\partial v}{\partial z} \tag{3.2}$$

therefore,

$$v(z) = \dot{\varepsilon}(a - z) \tag{3.3}$$

Where $v(z)$ and $u(z)$ are the vertical and horizontal velocity respectively. The strain rate is equal vertically and horizontally to converse area. White (1993, 1994) shows that where the data are well constrained, it is possible to determine variations in 1D strain rate during rifting.

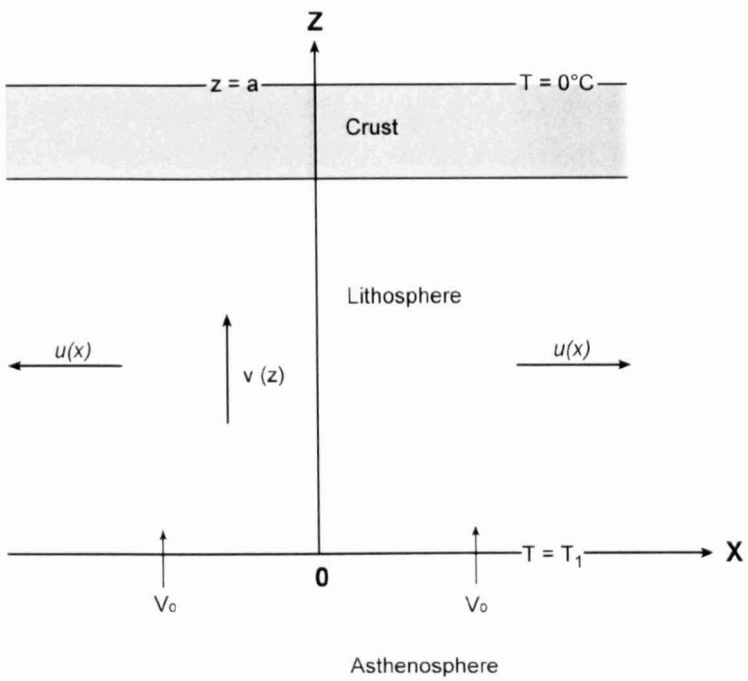

Fig. 3.41. Time-dependent stretching model. The asthenosphere upwells across the surface z = 0 to replace the crust and mantle lithosphere which stretches with horizontal velocity $u(x)$. Vertical velocity, $v(z)$, varies linearly with z from V_0 at z = 0 to 0 at z = a. The surface z = 0 is maintained at the asthenospheric temperature ($T = T_1$), while the upper surface, z = a is maintained at $T = 0^0$C (from Jarvis & McKenzie, 1980).

3.7.3. Preliminary Subsidence Modelling Procedures

Borehole data provides depth, age, lithological and biostratigraphical information. These data are limited by the depth of the well itself, and the quality and abundance of fossil assemblages present. In order to quantify, analyse, and compare rifting, both

within and between basins, several methods must be employed before any modelling of extension can be undertaken.

Timescale correlation

All biostratigraphic well log data have been correlated with the Gradstein et al. (1995) and Berggren et al. (1995) timescales for the Mesozoic and Cenozoic respectively. These timescales are generally acknowledged to represent the most recent and reliable geological age data, and are used widely throughout industry and academia. It has been shown that use of previous timescales (e.g. Harland et al., 1990) has only very minor effects on the shape of subsidence curves or the stretching factor, β, extracted from them (Rowley, 1998) (**Fig. 3.42**).

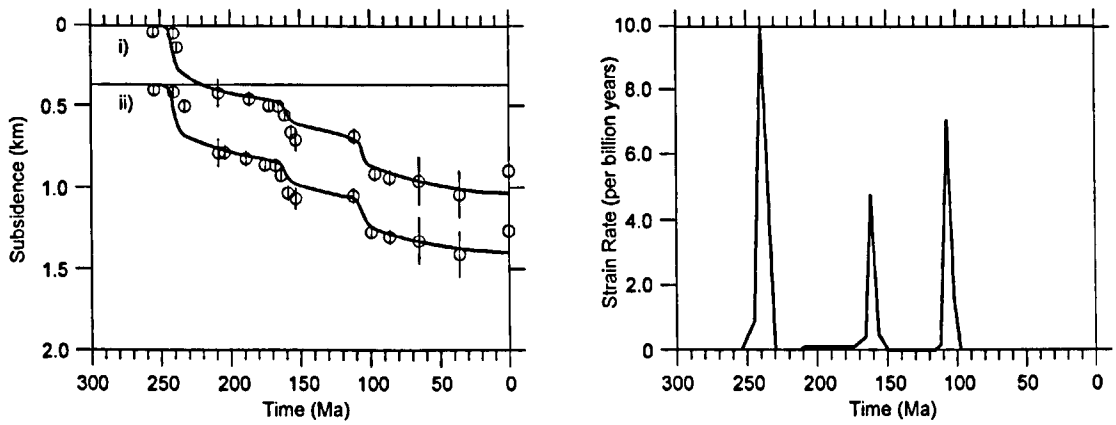

Fig. 3.42. Comparison of the influence of using the Harland et al. (1989) and Gradstein et al. (1995) timescales on backstripped subsidence data. (a) shows two subsidence curves with backstripped subsidence data using i) Harland et al. (1990) timescale and ii) Gradstein et al. (1995) timescale. Solid black line represents the best fitting theoretical subsidence curve for the backstipped data modelled with the Harland et al. (1990) timescale (i), which is also an excellent fit for (ii). (b) Corresponding strain rate curve for the theoretical subsidence curve (from Wheeler, 2000).

Errors often occur in the assignment of absolute ages to lithostratigraphical units due to poor biostratigraphy. However, as the duration of the majority of the subsidence events investigated in this study are greater than the errors associated with the dating of these units, the effects on subsidence are relatively minor.

Backstripping

A combined method of sediment decompaction and conversion to water-loaded subsidence (backstripping) has been utilised in this study (Steckler & Watts, 1978; Sclater & Christie, 1980). This method allows the extraction of tectonic subsidence by

correcting for the effects of sediment loading and palaeobathymetry. Decompaction involves the calculation of the density of any one sediment layer at any time in the past, and hence enables the restoration of the stratigraphic column at that time. The average solid grain density, ρ_{sg}, surface porosity, ϕ_o, and compaction decay length, λ, of any such layer are calculated using weighted means of values assigned to basic lithologies (Table 3.3).

Lithology	ρ_{sg} (g cm^{-3})	ϕ_o	λ (km)
Shale	2.70	0.60	2.00
Sandstone	2.65	0.50	2.50
Limestone	2.70	0.40	1.00
Chalk	2.70	0.55	2.20
Basalt	3.00	0.10	2.50
Dolomite	2.86	0.20	3.00
Anhydrite	2.96	0.40	0.50
Salt	2.16	0.20	0.75

Table 3.3. Parameters used for sediment decompaction (Sclater & Christie, 1980). ρ_{sg} is the solid grain density, ϕ_o is the surface porosity, and λ is the compaction decay length. Errors associated with the effects of varying the parameters of Table 3.2 on the resulting subsidence are small (~100m) (Gallagher, 1989).

Assuming an exponential relationship between porosity, ϕ, and depth, z, with ϕ_o being the surface porosity and λ the compaction decay length (e.g. Sclater & Christie, 1980) then

$$\phi = \phi_o \exp\left(\frac{-z}{\lambda}\right) \tag{3.4}$$

As such it is possible to calculate the average density of any layer, ρ_s, at any given time from

$$\rho_s = \bar{\phi}\rho_w + (1-\bar{\phi})\rho_{sg} \tag{3.5}$$

where ρ_w is the density of sea-water (1.03g cm^{-3}), and $\bar{\phi}$ is the average porosity of that layer at that time. The mean sediment density of the section $\bar{\rho}_s$ is hence given by

$$\bar{\rho}_s = \sum_{i=1}^{n}\left[\frac{\bar{\phi}_i\rho_w + (1-\bar{\phi}_i)\rho_{sg_i}}{S_s}\right]z_i \tag{3.6}$$

Where at any one time and for any layer i, n is the total number of layers, S_s, is the total (decompacted) column thickness, z_i is the thickness of the ith layer. In order to convert

sediment-loaded to water loaded subsidence, Airy isostasy is assumed. This assumption requires that the lithosphere has no strength (i.e. elastic thickness, $\tau_e = 0$), and that any point on the lithosphere is affected only by the load directly above it. The water-loaded subsidence, S_w, can hence be calculated

$$S_w = S_s\left(\frac{\rho_m - \overline{\rho}_s}{\rho_m - \rho_w}\right) - \Delta_{SL}\left(\frac{\rho_m}{\rho_m - \rho_w}\right) + Wd \qquad (3.7)$$

where ρ_m is the density of the lithospheric mantle, Δ_{SL} is the difference in height of the palaeo-sea level from that of the present-day, Wd is the depth of the sediments beneath sea-level at their time of deposition.

Errors associated with the backstripping method could result from uncertainties in lithologies, in palaeobathymetries, and/or in palaeo-sea level. **Figure 3.43** shows the effects on backstripping of assuming uniform lithologies for data from the Miskar A-1 well in the Gulf of Gabes. The errors associated with assuming all sandstone and shale are relatively minor, while those associated with limestone and basalt are more pronounced.

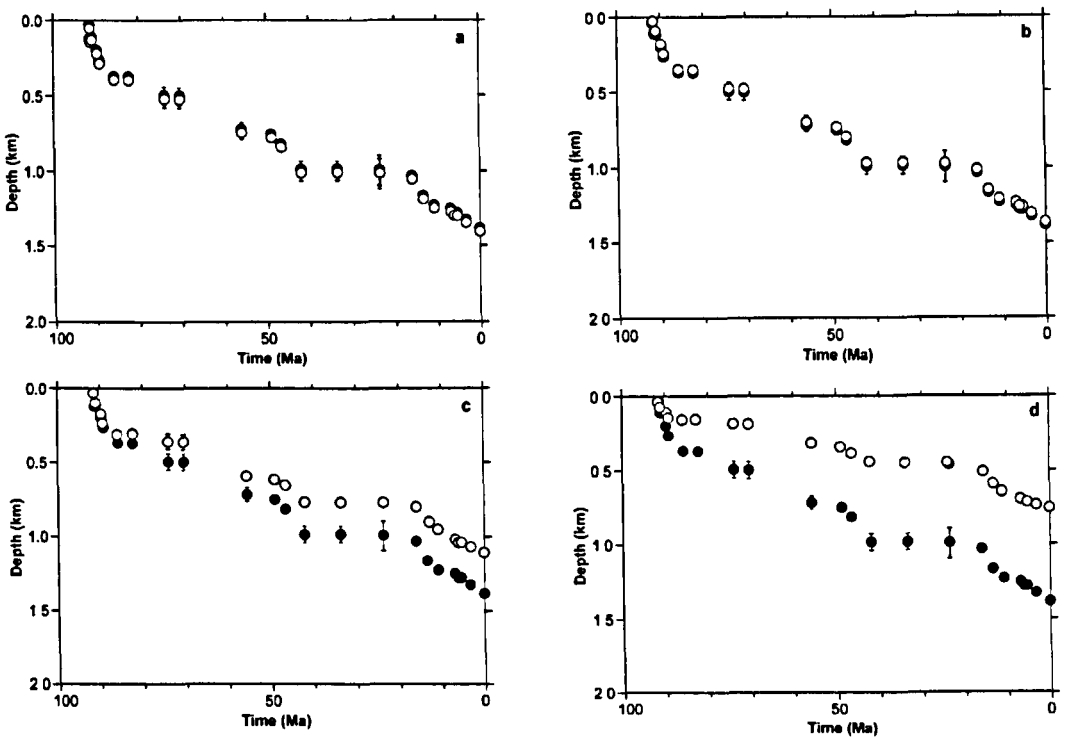

Fig. 3.43. Backstripping errors associated with varying lithologies. Subsidence data from the Miskar A-1 well, Gabes-Tripoli Basin, offshore Tunisia. Vertical error bars represent palaeobathymetry errors and black circles are backstripped data with lithologies derived from well logs. Unfilled circles are where a uniform lithology throughout the section has been assumed upon backstripping, where lithologies are; (a) 100% shale, (b) 100% sandstone, (c) 100% limestone, and (d) 100% basalt.

Ignoring the depth of deposition (or palaeobathymetry) of any sedimentary unit can lead to undue significance being placed on otherwise insignificant changes in subsidence rate (Barton & Wood, 1984). As such, palaeo-water depth estimation is potentially one of the largest sources of error in any tectonic subsidence analysis. In this study (White, 1993, 1994) maximum and minimum palaeo-water depth bounds are presented as vertical error bars on tectonic subsidence data. The palaeo-water depth values used in this study were all obtained from Beckett (1998). In most cases such error bars are small (<200m). Sea-level corrections have been shown to have little effect on β factors for extensional modelling (Wooler et al., 1992).

3.7.4. Strain Rate Inversion Theory

Subsidence patterns within extensional sedimentary basins provide a record of vertical motion over time, and so should also contain information concerning the vertical component of strain rate. Assuming pure shear extension with no depth dependant stretching, then the horizontal strain rate will be related to vertical subsidence. Therefore, if lithospheric strain rate is allowed to vary as rifting in a basin proceeds, then any documented changes in the rate of syn-rift subsidence can be explained (White, 1993; 1994). Based on these premises, and where high quality subsidence data are available with good bathymetric control, the potential exists to extract information about the strain rate variation through time (White 1993; 1994).

Total strain (stretching factorβ) is an integral of the strain rate over the period of rifting

$$\beta = \exp\left(\int_0^{\Delta t} \dot{\varepsilon}(t) dt \right) \tag{3.8}$$

where $\dot{\varepsilon}(t)$ is the vertical strain rate and Δt is the duration of stretching. Water-loaded subsidence as a function of time, $S(t)$, can be written as a function of β so that;

$$S(t) = A(1 - \frac{1}{\beta}) - BQ(t) \tag{3.9}$$

where,

$$A = t_c \frac{(\rho_m - \rho_c)}{(\rho_a - \rho_w)} \tag{3.10}$$

$$B = \frac{\alpha \rho_m}{(\rho_a - \rho_w)} \tag{3.11}$$

t_c is the pre-rift crustal thickness and α is the lithospheric thermal expansion coefficient (**Table 3.2**). The difference between the perturbed temperature of the lithosphere as a function of depth and time, $T(z,t)$, and the equilibrium temperature structure of the lithosphere, $T(z, \infty)$, is given by;

$$Q(t) = \int_0^a [T(z,t) - T(z,\infty)]dz \tag{3.12}$$

Where a is lithospheric thickness and z is the distance measured from the base of the lithosphere. $T(z,t)$ is approximated by using finite difference techniques to solve the 1D heat flow equation (Equation 3.1).

The strain rate distribution through time can be expressed in terms of the water-loaded subsidence by rearranging Equations 3.8 and 3.9 to give,

$$\dot{\varepsilon}(t) = \frac{d}{dt}\left\{\ln\left(\frac{A}{A - S(t) - BQ(t)}\right)\right\} \tag{3.13}$$

$\dot{\varepsilon}(t)$ can thus, subject to errors, be obtained without any prior knowledge of the duration of lithospheric extension.

Strain Rate Inversion: Direct Search Method

To solve the strain rate inverse problem, White (1993; 1994) concluded that, as the observed subsidence data involved are discrete and noisy, the best approach involved solving the forward modelling problem many times. This is undertaken until the difference between the observed and theoretical subsidence is minimised. This difference (or data misfit) is calculated using the least squares (L_2 norm) method. Data misfit, ϕ, is given by;

$$\phi = \frac{1}{N}\sum_{i=1}^{N}\left[\frac{s_i^o - s_i^p}{\sigma_i}\right]^2 \tag{3.14}$$

where s_i^o and s_i^p are the observed and predicted subsidence, N is the number of observed subsidence data, and σ_i is the standard deviation for the ith data point.

Given the observed data, the aim of any inversion procedure is to find the model (or set of model parameters) that best explains these observations, thus yielding the minimum value of misfit ϕ. In this problem the data consists of a series of subsidence points at specific intervals in time. These data will always contain errors, σ_i, and it is unlikely

that the misfit will equal zero (i.e. for the predicted data values to exactly match the observed). By weighting each data misfit by independent Gaussian errors associated with them (Equation 3.14), the more precise data will have more influence than the data with large errors in determining the misfit. Using the White (1993; 1994) model, the strain rate as a function of time, $\dot{\varepsilon}(t)$, is first parameterised by using M discrete values, $\dot{\varepsilon}_K$, at time intervals, δt, of 5-10 Ma. The interpolation between each time-step using a cube spline method (Press et al., 1989) then provides a value for $\dot{\varepsilon}(t)$. The inversion is established by imposing additional independent smoothing functions on $\dot{\varepsilon}(t)$. This is accomplished through the introduction of an *ad hoc* trial function, H, which is equal to the data misfit, ϕ, plus three additional smoothing terms, so that;

$$H = \left\{ \frac{1}{N} \sum_{i=1}^{N} \left[\frac{s_i^o - s_i^p}{\sigma_i} \right]^2 \right\}^{1/2}$$

$$+ W_1 \left[\frac{1}{M-1} \sum_{K=2}^{M} \left(\frac{\dot{\varepsilon}_K - \dot{\varepsilon}_{K-1}}{\delta t} \right)^2 \right]^{1/2}$$

$$+ W_2 \left[\frac{1}{M} \sum_{K=1}^{M} (\dot{\varepsilon}''_K)^2 \right]^{1/2}$$

$$+ \frac{W_3}{M} \sum_{K=1}^{M} |\log(\dot{\varepsilon}_K)| \qquad (3.15)$$

where W_1, W_2, and W_3 are separate weighting coefficients, and values of $\dot{\varepsilon}''_K$ are estimates of the second derivative of $\dot{\varepsilon}$ generated by cubic spline interpolation. The second and third terms cause $\dot{\varepsilon}(t)$ to be smoother. The fourth term tends to infinity as any value of $\dot{\varepsilon}_K$ approaches zero.

A multi-dimensional direct search scheme (Powell's algorithm (Press et al., 1989)) is then utilised in order to minimise the trial function, H, by the systematic variation of $\dot{\varepsilon}(t)$ alone. The algorithm exploits a series of line minimisations, thereby precluding the need to sample the entire model space. Linear dependence is generally avoided by a change of direction when a minimum is reached. This change of direction is related to an average of the previous set of directions, minus the direction in which the function made its largest decrease (Press et al., 1992).

White (1993, 1994) demonstrates through the use of this model a series of good fits to both synthetic and actual subsidence data for the Dolomites area of northern Italy (**Fig. 3.44**). The model has since proven extremely useful in forming the basis of subsidence and strain rate analyses of a large number of regions world-wide (Hall, 1995; Bellingham, 1999; Wheeler, 2000; Faulkner, 2000).

The method is not infallible. One debate surrounds the 'spikey' nature of the modelled strain rate solutions and the *ad hoc* nature of the smoothing employed within the trial function H (P. Faulkner, pers. Comm., 2000). The three smoothing factors (W_1, W_2 and W_3) acting in H are an integral part of the inversion scheme and, as such, any strain rate solution will be influenced by them. These factors are, however, varied independently of the algorithm itself, and as such their influence is both complex and indirect.

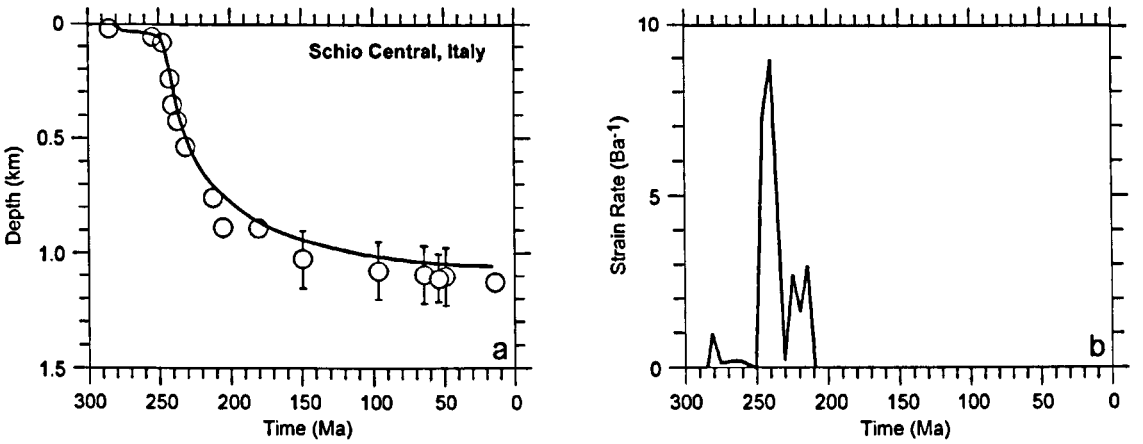

Fig. 3.44. An example of strain rate inversion from the Schio Central stratigraphic section, Dolomites, northern Italy. (a) Circles represent water-loaded subsidence data; vertical bars are two standard deviations of palaeobathymetric errors; solid line is the best-fit subsidence curve calculated from final strain rate distribution. (b) Linearly interpolated final strain rate distribution obtained by inversion at 5 Myr sampling intervals and corresponding to the best-fit subsidence curve of (a) (White, 1994).

3.7.5. Data Utilised

Thirty-two wells have been modelled using the 1D strain rate inversion procedure of White (1993; 1994) (**Fig. 3.2**). Most of these wells penetrate the Upper Cretaceous succession, with the majority terminating in the Aleg, Serdj and Fahdene Formations. Only the Rime -1 well penetrates part of the Jurassic Upper Nara Formation. This therefore precludes an analysis of Late Triassic to Middle Jurassic rifting. The analysis of Anderson (1991), undertaken in the Kairouan area to the northwest, is used to partially constrain the Early Jurassic subsidence history of this region (Section 3.8).

However, caution must be applied to these data, due to the fact that very few of these wells provide information on the thickness of the Nara Formation.

3.7.6. Results & Discussion

Water-loaded subsidence curves for all the wells analysed, together with their respective strain rate models are illustrated in **Figure 3.45**. These data show a main phase of tectonic subsidence in the Late Cretaceous between the late Albian to late Coniacian (~100 Ma-85 Ma). An examination of seismic data from the Gulf of Gabes suggests that this event is related to normal faulting, and hence crustal extension (**Fig. 3.21**). The extrusion of sub-aqueous basalts, observed in a number of wells in the Gulf of Gabes coincides with the timing of this fault activity (e.g. Miskar A-6, Jugurtha -1). These observations are in agreement with the work of Finetti (1982), which illustrates the relationship between extension and igneous activity on the Pelagian Platform throughout the Mesozoic and Cenozoic (**Fig. 3.46**). The maps of volcanic presence/thickness which are given in **Figures 3.47** and **3.48** show that sub-aqueous basalts occur in approximately NW-SE trending zones, parallel to the main Late Cretaceous faulting in the area.

The isopach map of the Aleg Formation (SS-3 to 7) illustrated in **Figure 3.30** shows the variation of Turonian to Coniacian sediment thickness over the Gulf of Gabes area. It delineates two basinal areas where sedimentation rates were high (i.e. the Sfax and Gabes-Tripoli Basins). These areas are characterised by up to 900m of Turonian to Coniacian sediments. The reduction in sediment thickness, along an approximately NNE-SSW trending zone between these two basinal areas suggests that initial uplift of the Kerkennah High occurred prior to the Late Cretaceous. Thinning of the Aleg Formation onto the Medina and Lampedusa Plateaux to the northeast shows that these areas were also established palaeo-highs at this time. In addition, in the Gabes-Tripoli Basin, the reduction in sediment thickness on to the crest of the Miskar horst indicates pre-Turonian activity on the present-day Amilcar High.

The 1D subsidence analyses provide β values for this main extensional event, ranging from 1.04-1.23. Evidence from the 1D modelling consistently suggests an ~85 Ma age of termination of active extension in the Gulf of Gabes. This age is in agreement with the subsidence analyses of Anderson (1991), which were conducted on wells located in the onshore 'Sahel' region of Tunisia (**Fig. 3.49**).

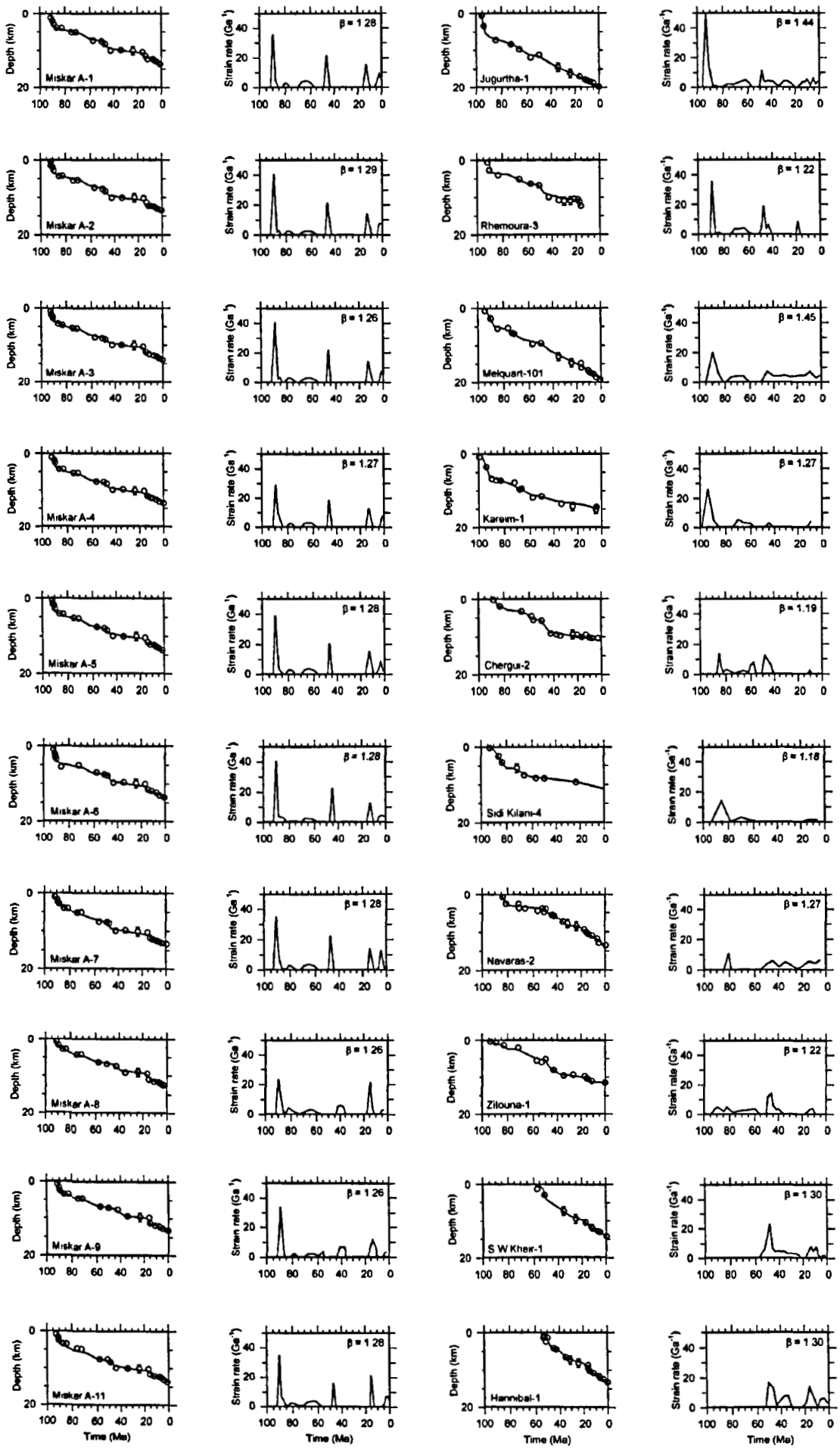
Depth (km)
Strain rate (Ga⁻¹)
Miskar A-1
β = 1.28
Jugurtha-1
β = 1.44
Miskar A-2
β = 1.29
Rhemoura-3
β = 1.22
Miskar A-3
β = 1.26
Melquart-101
β = 1.45
Miskar A-4
β = 1.27
Karem-1
β = 1.27
Miskar A-5
β = 1.28
Chergui-2
β = 1.19
Miskar A-6
β = 1.28
Sidi Kilani-4
β = 1.18
Miskar A-7
β = 1.28
Navaras-2
β = 1.27
Miskar A-8
β = 1.26
Zitouna-1
β = 1.22
Miskar A-9
β = 1.26
S W Kheir-1
β = 1.30
Miskar A-11
β = 1.28
Hannibal-1
β = 1.30
Time (Ma)

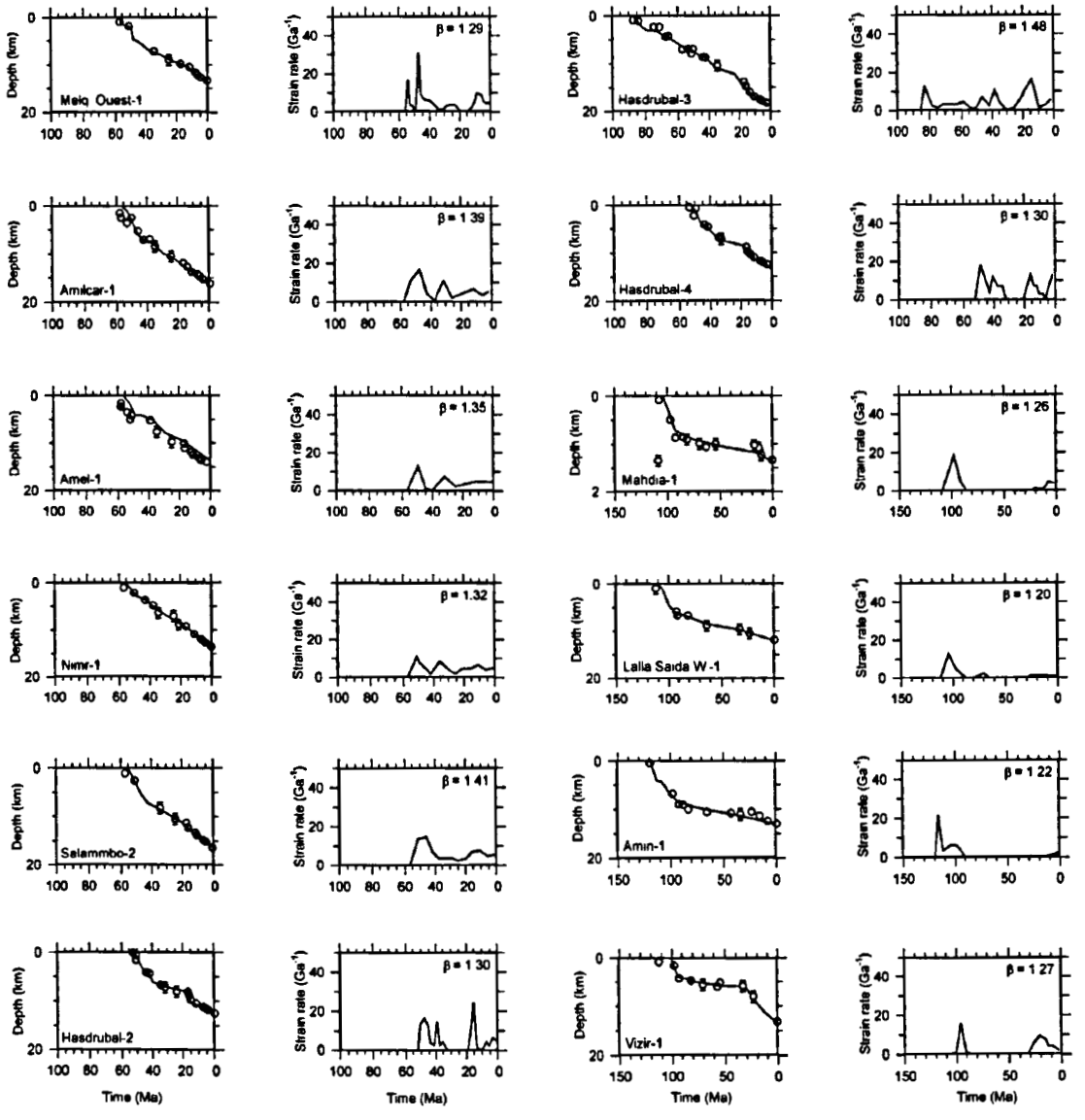

Fig. 3.45. Best fit water-loaded subsidence curves for the 32 wells analysed in the study, together with their respective strain rate models. The linearly interpolated final strain rate distributions are obtained by inversion at 5-10 Myr sampling intervals.

Subsidence curves show that following this extensional event, the area underwent a period of uplift and erosion, and/or non-deposition during the late Coniacian and Santonian. Across much of the western part of the Pelagian Platform, including the study area, the top of the Aleg Formation is truncated, particularly on palaeo-highs such as Miskar (refer to Chapter 6). After this short-lived episode, the entire area was subjected to a period of relatively uneven thermal subsidence throughout the Campanian and early Maastrichtian (i.e. during the deposition of the Abiod Formation (SS-8)). Localised extensional fault activity may have continued in a subdued fashion throughout this period. The isopach map of the Abiod Formation illustrated in **Figure 3.31** shows a similar pattern of sediment thickness to the Aleg Formation. The Sfax and

Gabes-Tripoli-Misurata Basins are located to the NW and SE respectively of the increasingly dominant Kerkennah High. In the south of the Gulf of Gabes, the Jerrafa-Djerba High appears to exert more control on sedimentation than it did during the deposition of the Aleg Formation (SS-3 to 7).

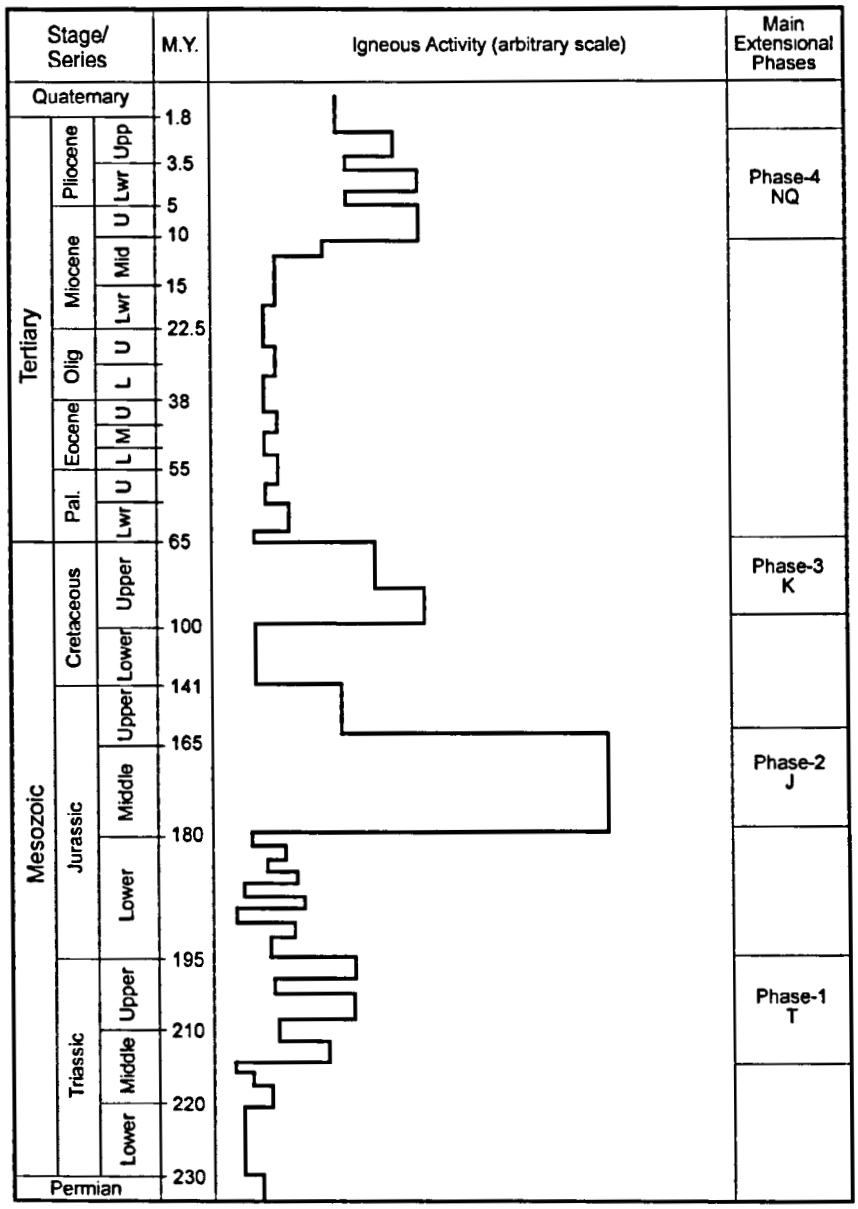

Fig. 3.46. Relationship between extension and igneous activity on the Pelagian Platform in the Mesozoic and Cenozoic (from Finetti, 1982).

Another period of uplift and associated erosion/non-deposition occurred in the late Maastrichtian and Thanetian (**Figs. 3.45**). It is believed to correspond to a phase of ESE-WNW directed compression, which partially inverted pre-existing NW-SE trending extensional faults, in particular the eastern bounding half-graben to the Miskar Structure (Chapter 6). Over much of the Gulf of Gabes, the Abiod Formation is significantly eroded or absent.

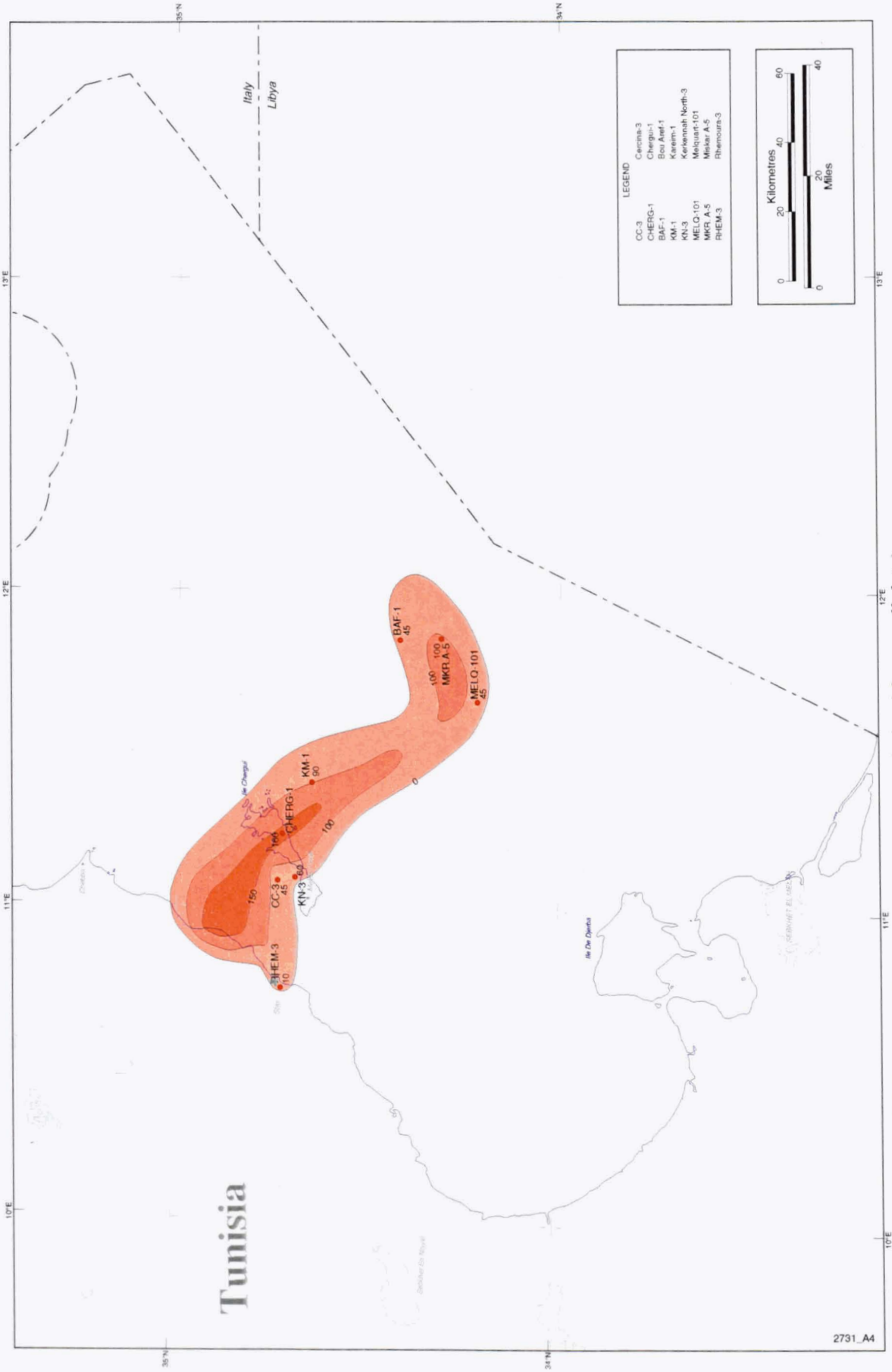

Fig. 3.47. Isopach Map of Volcanics within the Aleg Formation (derived from well data).

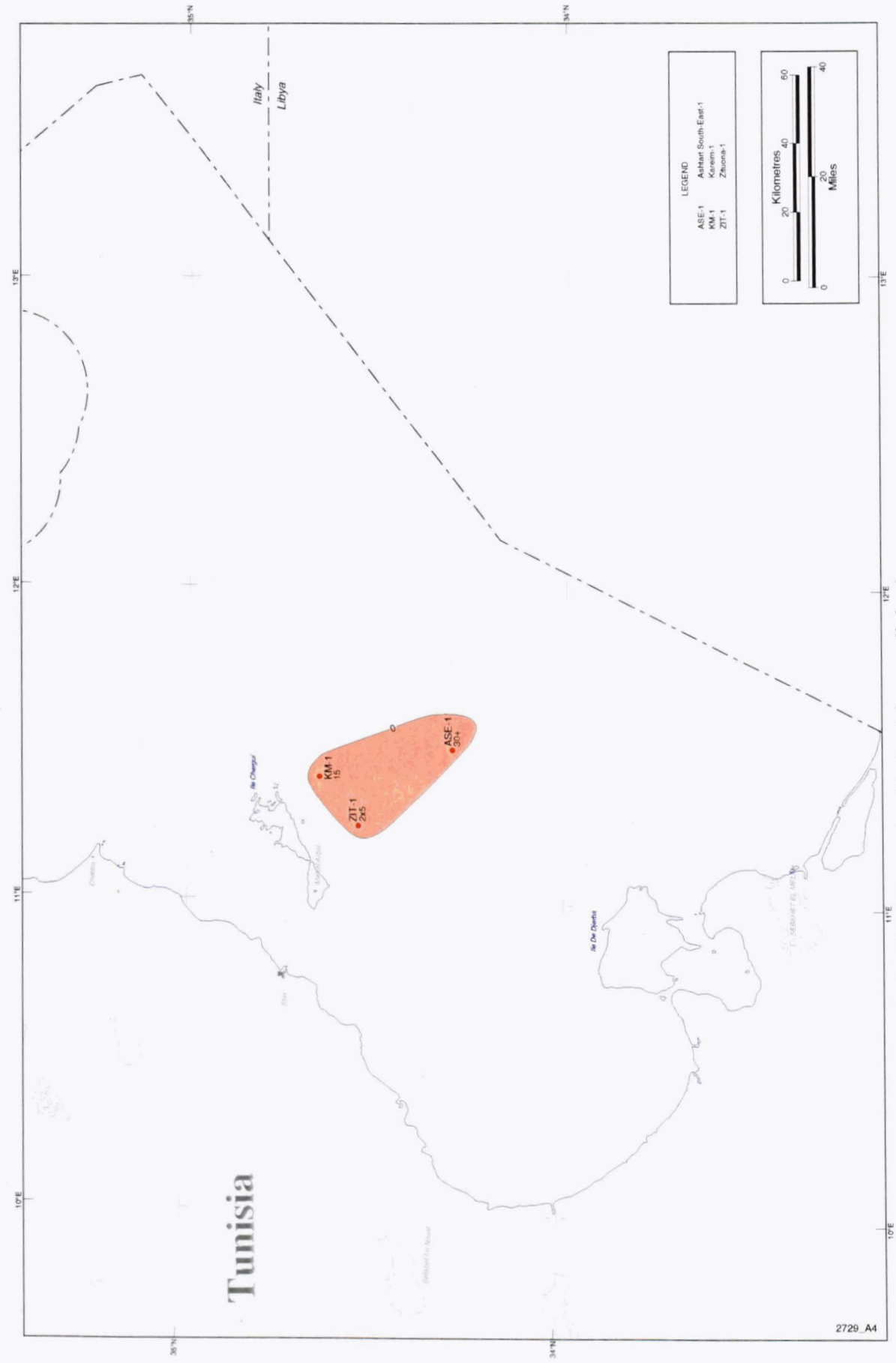

Fig. 3.48. Isopach Map of Volcanics in the Abiod Formation (derived from well data).

Following this episode, the Gulf of Gabes entered a period of tectonic quiescence and thermal subsidence. The isopach map presented in **Figure 3.32** shows the thickness distribution of the Maastrichtian to Thanetian El Haria Formation (SS-9). The impact of the Jerrafa-Djerba High and Medina/Lampedusa Plateaux on sedimentation throughout this period is clearly evident. This is also the case for the Kerkennah High, which separates the Sfax and Gabes-Tripoli Basins. Even thermal subsidence continued into the Ypresian during the deposition of the Metlaoui Group (SS-10)(**Fig. 3.45**). Localised fault activity is evident in the Gulf of Gabes throughout this period, in particular along the zone forming the present-day Amilcar High (Chapters 6 and 7).

At approximately 48 Ma, the Gulf of Gabes experienced a second phase of tectonic subsidence, marked by extensional fault generation and the reactivation of earlier structures. No volcanics are associated with this event (**Fig. 3.45**). The thickness distribution of the Lutetian to Priabonian Cherahil Formation (SS-11) is illustrated in **Figure 3.34**. It demonstrates the influence of the NE-SW trending Amilcar High on sedimentation throughout this period. The control of the Kerkennah High is less apparent. Three separate sub-basins are indicated within the Gabes-Tripoli Basin. These contain thick (>900m) Upper Eocene sediment accumulations. In the north and south of the Gulf of Gabes, the Cherahil Formation onlaps gently onto the Medina/Lampedusa Plateaux and the Jerrafa-Djerba High respectively.

The timing of this extensional event appears to coincide with the onset of NW-SE oriented compression in northern Tunisia, and could therefore be attributed to thrust loading (in the Straits of Sardinia) causing flexural subsidence in the Gulf of Gabes area. The isopach maps provided by Anderson (1991) for this period show approximately NE-SW thickness trends on the onshore 'Sahel' region to the north. These data hence support a model of lithospheric flexure accompanied by the creation of a NE-SW trending foreland basin and flexural bulge system. This model appears to be valid in northern and central Tunisia where isopach maps show NE-SW trending thickness variations. However in the Gulf of Gabes region, isopach maps do not show this trend. An alternative explanation demonstrates that NW-SE directed compression could have induced dextral movements on the pre-existing WNW-ESE trending Gafsa-Jarrafa and Mahdia-Medina fault zones. These movements may have caused the observed extension and subsidence in the Gabes-Tripoli Basin.

Strain rate models provide β values for this extensional event, ranging from 1.02-1.22. An age of ~40 Ma is given for the termination of active tectonic subsidence. A comparison with the geohistory plots of Anderson (1991) show a very consistent age for this event (**Fig. 3.49**).

Following this event, a phase of tectonic quiescence and thermal subsidence prevailed throughout the Gulf of Gabes (**Fig. 3.45**). This was accompanied by minor episodes of uplift and associated erosion/non-deposition that produced a series of local unconformities; the unconformity at the top of the Cherahil Formation (SS-11) is the most widely recognised of these events. On the Miskar and Hasdrubal Structures, the entire Bartonian and Priabonian sections are missing (Chapters 6 and 7). Seismic data shows many of the Ypresian to Lutetian faults terminating at the Eocene unconformity (**Figs. 3.21-3.25**).

Subsidence curves show that this phase of quiescence gave way to a third phase of tectonic subsidence and extension in the Middle to Late Miocene (~16 Ma). This period of extension continued until at least ~10 Ma, although it can be argued that active extension has occurred up to the present-day (shown on subsidence plots by two very close strain rate peaks) (**Fig. 3.45**). It was accompanied by the generation of a new system of approximately NW-SE trending extensional faults that have a slightly different orientation from the underlying Ypresian to Lutetian system (refer to Chapters 6 and 7). Strain rate models give β values for this Middle Miocene to present-day phase of tectonic subsidence of between 1.02 and 1.15. These models show close agreement with the work of Anderson (1991). The isopach map provided in **Figure 3.36** shows sediment thickness distribution for the Miocene to present-day succession in the Gulf of Gabes. It delineates a western high area, controlled by uplift on the Kerkennah High, from the Gabes-Tripoli Basin to the east. The initial timing of this event coincides with the onset of thrust emplacement in northern Tunisia, which could have caused flexural subsidence. This is followed closely by the start of rifting in Straits of Sicily (ca. late Tortonian). The geohistory plots of Anderson (1991) clearly show a differentiation in tectonic style across the North-South Axis from the Middle Miocene to present-day. On the western side of this fault zone significant uplift is associated with thrusting (**Fig. 3.49a-b**). In contrast, on the eastern side (i.e. the 'Sahel') active extension is associated with foreland basin development (**Fig. 3.49c-i**)

CONTAINS PULLOUTS

3.8. Tectonic Evolution of the Gulf of Gabes

3.8.1. Introduction

The tectonic evolution of the Gulf of Gabes region consists of a complex interplay of tectonic processes. These are discussed in the following section. **Figure 3.50** consists of a series of reconstructions illustrating the development of the area throughout the Mesozoic and Tertiary.

3.8.2. Late Triassic (Rhaetian)-Early Cretaceous (Barremian)

The Late Triassic to Early Cretaceous evolution of the Gulf of Gabes region is poorly constrained due, in part, to the low resolution of seismic data below the Maastrichtian unconformity and the lack of wells penetrating this section. Nevertheless, it is inferred from regional analyses (Chapter 2), that the study area underwent significant tectonic subsidence during the Late Triassic and Late Jurassic to Early Cretaceous periods (**Fig. 3.46**). These phases of approximately ENE-directed lithospheric extension are attributed to rifting caused by the westward spreading of the Neo-Tethys (N.B. the Gulf of Gabes is located on the southern margin of the Neo-Tethys Ocean). Subsidence within the Gulf of Gabes during this period was probably controlled by faults generated above basement lineaments (i.e. the postulated North-South Axis basement faults, the E-W trending Mahdia Shear Zone structures, and the WNW-ESE oriented basement structures underlying the Gafsa-Jerrafa Fault Zone). The latter faults controlled the location of the Jurassic-Early Cretaceous Tethyan basin margin, marking the transition from the continental sediments of the Saharan Platform in the south (i.e. Asfer Formation), into the basinal sediments of the of the Tethyan Realm to the north (i.e. Sidi Kalif Formation in the Gabes-Tripoli Basin). The exact nature of displacement on these faults is unclear, although given the ENE-directed extension direction (active throughout this period) it is inferred that they were characterised by oblique-slip movements (Anderson, 1991).

During the Late Jurassic and Early Cretaceous, extensive shallow-water carbonate platforms developed across many parts of the Southern Tethyan basin margin. Within the Gulf of Gabes, rapid deposition was synchronous with tectonic subsidence. Thick Upper Jurassic and Lower Cretaceous syn-rift sequences are located in the hangingwall section of the WNW-ESE trending Gafsa-Jerrafa Fault Zone (**Fig. 3.38**). To the west of

the Gulf of Gabes on the Sahel of Central Tunisia, a large N-S trending area (i.e. Kairoaun Island) became elevated during the Early Cretaceous (Barremian-early Aptian) (**Fig. 3.5**). Anderson (1991) presents a review of the theoretical mechanisms capable of producing such uplift during this stage of basin evolution.

It is postulated that the main phase of rifting on the Pelagian Platform ceased during the Early Cretaceous, probably in the Hauterivian to Barremian. Following this, the area entered a phase of thermal subsidence. It is shown in the following discussion that this phase of thermal subsidence in the Gulf of Gabes area was interrupted throughout the Late Cretaceous and Cenozoic by intermittent periods of localised tectonic subsidence and crustal extension (rifting) caused by strike-slip deformation and accompanied by pull-apart basin development (e.g. the Gabes-Tripoli Basin). These tectonic phases are clearly identified on the subsidence curves presented in Section 3.7, and are discussed in more detail in the following section.

3.8.2. Early Cretaceous (Aptian) to Late Eocene (Priabonian)

As previously mentioned, it has been shown that during the late Aptian the relative motion of the European and African plates gradually switched to dextral strike-slip (Dewey et al., 1989). This effectively induced a component of dextral strike-slip movement on to pre-existing E-W and WNW-ESE trending lineaments within the Gulf of Gabes, most notably along the Gafsa-Jerrafa and the postulated Mahdia-Medina Fault Zones (Jongsma et al., 1985; Anketell, 1995). These two fault systems bound a broad WNW-ESE trending dextral shear zone incorporating the Gulf of Gabes and Libyan offshore (Gafsa-Medina Shear Zone (GMSZ)). **Figure 3.51** presents the mechanism proposed for the Mesozoic and Cenozoic development of the Gabes-Tripoli Basin. These reconstructions show that it probably developed as large pull-apart basin above the Gafsa-Medina Shear Zone. The observed obliquity between the NW-SE to NNW-SSE trending basin faults and the bounding Gafsa-Jerrafa and Mahdia-Medina Fault Zones supports this model. A late Albian age is proposed for the initiation of tectonic subsidence in the basin, as illustrated on the subsidence curves in Section 3.7. Recent earthquake data demonstrate that this dextral tectonic regime is still currently active in the Gulf of Gabes (Westaway, 1995; 1990) (**Fig 2.15**).

Throughout the Aptian and early Albian (i.e. prior to the initiation of tectonic subsidence in the Gabes-Tripoli Basin) sedimentation rates were low. This is

demonstrated on seismic profiles given in Section 3.6, which show only minor thickness variations in the Serdj, Hameina and Fahdene Formations (SS-1). Elsewhere on the North African continental margin, carbonate platform development attained its maximum northward progradation during this period (i.e. in the late Aptian).

The onset of uplift of the NNE-SSW trending Kerkennah High on the western margin of the Gulf of Gabes is poorly constrained, although seismic data tends to suggest a middle to late Albian age. This is based on the various onlapping relationships of the Cenomanian and Turonian sequence onto this zone (**Fig. 3.21-3.22**). It should be noted that an earlier age of onset cannot be eliminated. The exact mechanism for the uplift is not fully understood. One mechanism suggests that the high could have formed in response to Triassic salt migration and doming along an approximately NNE-SSW trending zone (presumably utilising an earlier basement lineament). An alternative model considers that the dextral movements along the Gafsa-Medina Shear Zone (in the late Aptian) could have reactivated an earlier NNE-SSW trending lineament, thus causing a zone of uplift. Continued uplift of this area occurred into the Middle Miocene. This is shown on seismic by the upwardly tilting nature of the onlapping Upper Cretaceous to Middle Miocene sequence onto the high.

During the late Albian and Coniacian, dextral movement on the Gafsa-Medina Shear Zone caused the onset of NE-SW extension and tectonic subsidence within the Gabes-Tripoli Basin (refer to text above) (**Fig. 3.51**). This event coincided with a widespread late Albian to early Cenomanian marine transgression, which effectively drowned the pre-existing platform areas to the west of the basin (Camion, 1991). During this period, rapid sedimentation of the Bahloul and Aleg Formations (SS-3 to 7) occurred in the developing basinal areas. **Figure 3.11** illustrates the facies distribution of the Aleg Formation in the Gulf of Gabes. Several NW-SE trending systems tracts are identified that parallel the Early Cretaceous passive margin. The isopach map of the Aleg Formation presented in Section 3.6 (**Fig. 3.30**) clearly delineates the Gabes-Tripoli Basin from the Kerkennah High during this time. It also indicates that the Amilcar High within the Gabes-Tripoli Basin had become an established palaeo-high during this period. The development of this zone is thought to be controlled by the reactivation (in sinistral transtension) of a series of pre-existing NNE-SSW trending basement lineaments in response to dextral shear along the Gafsa-Medina Shear Zone (**Fig. 3.50**). Thick growth sequences associated with vertical displacements on these NNE-SSW

trending structures are particularly evident in the eastern bounding half-graben to the Miskar horst (Chapter 6). Strain rate models give stretching values (β) between 1.04 and 1.23 for this episode.

Following the deposition of the Aleg Formation, the Gulf of Gabes was subjected to a period of NNW-SSE compression at the end of the Coniacian, which continued into the Santonian. This was related to a change in the relative motion of Africa relative to Europe (Anketell, 1995). This caused widespread uplift and erosion/non-deposition across the study area, in particular on fault highs (e.g. Hasdrubal, Miskar etc.), together with partial inversion of small half grabens. As a consequence, the top of the Aleg Formation is represented by an unconformity over the majority of the study area.

During the early Campanian, a relative increase in the dextral strike-slip component on the Gafsa-Medina Shear Zone caused a rejuvenation of NE-SW extension in the Gabes-Tripoli Basin. Although apparent on seismic data (which shows a system of extensional growth faults developed in the Abiod Formation), this phase of tectonic subsidence is hardly evident in the strain rate models presented in Section 3.7 (**Fig. 3.45**). This could be because the duration of the event is less than the sample interval employed in the inversion procedure. The deposition of the Abiod Formation (SS-8) in the Campanian to Maastrichtian was accompanied by a major marine transgression, evident across the entire North African continental margin (Camion, 1991) (**Fig. 3.12**). Throughout this period the Kerkennah High continued to be elevated with respect to adjacent areas.

Towards the end of the Maastrichtian, the Pelagian Platform experienced another period of approximately WNW-ESE directed compression. This event reactivated and partially inverted many pre-existing Albian to Maastrichtian faults in the Gulf of Gabes, causing uplift and erosion of the top of Abiod Formation. The eastern half-graben to the Miskar Horst became inverted during this episode (Chapter 6). Compression continued throughout the early deposition of the El Haria Formation (Maastrichtian-Thanetian). Complex onlapping relationships observed in this sequence,are due to the coeval nature of ongoing deposition and compression. Within the Gabes-Tripoli Basin the El Haria Formation attains a thickness in excess of 800m. To the west of the Kerkennah High it thins towards the North-South Axis. This is consistent with the emergence of the Kasserine Island at this time (Anderson, 1991).

CONTAINS PULLOUTS

During the late Thanetian, compression ceased, and the area entered a phase of tectonic quiescence and thermal subsidence. This continued into the Ypresian during the deposition of the Metlaoui Group (SS-10). The facies map illustrated in **Figure 3.13** shows a system of NW-SE trending facies belts across the Gulf of Gabes area that straddle the western part of the Gabes-Tripoli Basin. Localised extensional fault activity may have continued in a subdued fashion throughout this period, in particular along the Amilcar High. The isopach map of the Metlaoui Group across the study area, illustrates fault control on sedimentation along this zone, most notably over the Miskar and Hasdrubal structures (**Fig. 3.33**). The top of the Metlaoui Group is marked by a widespread marine transgression, represented by the deposition of the Compact Micrite Member (Lutetian).

Following the deposition of the Compact Micrite Member, the Gulf of Gabes experienced a phase of rejuvenated extension and tectonic subsidence that continued into the middle Bartonian (~40 Ma). Strain rate models give stretching values (β) between 1.02 and 1.22 for this episode. It is marked by extensional fault generation (coeval with the deposition of the Cherahil Formation (SS-11)), together with the reactivation of earlier Late Cretaceous fault systems. Various models have been proposed to explain this event (Section 3.7). The most likely postulates that NW-SE directed compression (due to the onset of thrust emplacement in the Straits of Sardinia) induced dextral movements on the Gafsa-Medina Shear Zone. These movements would have effectively caused the observed extension and subsidence across the study area, in particular within the Gabes-Tripoli Basin. Consequently, the increased sedimentation rates are indicative of this period, particularly in the basinal areas (**Fig. 3.34**). In onshore Central Tunisia, NE-SW trending sediment thickness variations in the Cherahil Formation (Anderson, 1991) are attributed to the development of a foreland basin and flexural bulge caused by thrust loading in the Straits of Sardinia. The 'Kasserine Island', located in Central Tunisia is interpreted to have resulted through the constructive interference of the NE-SW flexural bulge (related to thrust loading) and the original NW-SE passive margin (Ben Ferjani et al., 1990) (**Fig. 3.52**). Anderson (1991) infers that the middle to late Eocene transgression across the 'Kasserine Island' could be the result of fore-bulge collapse as the thrust front and foreland basin migrated further to the southeast. Uplift of the Kerkennah High continued to occur throughout this episode.

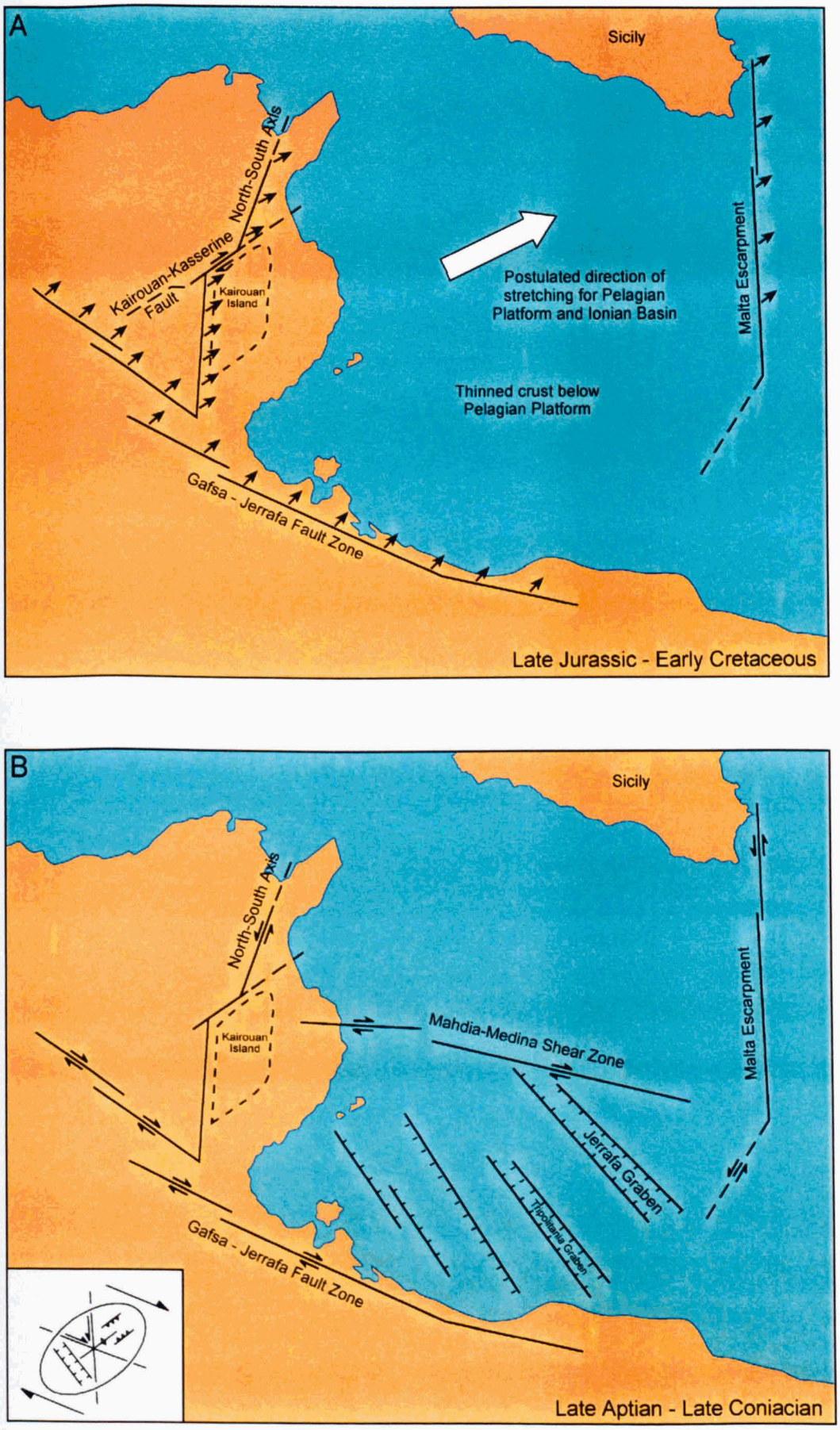

Fig. 3.51. Mechanism for the development of the Gabes-Tripoli Basin. A) Late Jurassic-Early Cretaceous, B) Late Aptian - Late Coniacian.

At approximately 40 Ma, tectonic subsidence in the Gabes-Tripoli Basin appears to have ceased, giving way to even thermal subsidence throughout the deposition of the upper part of the Cherahil Formation (i.e. Cherahil B Member). This phase of quiescence was interrupted at the end of the Eocene by a period of uplift and erosion/non-deposition. On structural highs, the entire Bartonian to Priabonian section is missing (i.e. Hasdrubal and Miskar). Seismic data illustrates the termination of the Lutetian-Bartonian fault system against this unconformity.

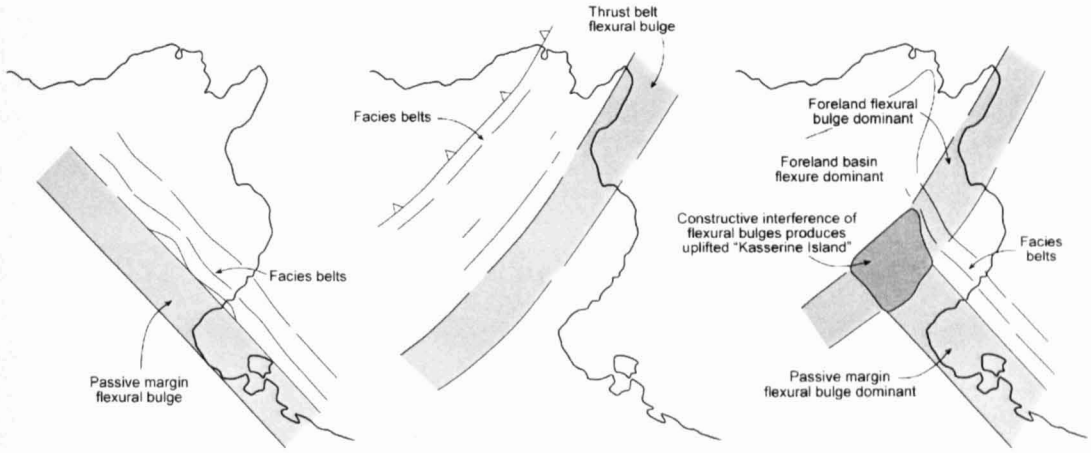

Fig. 3.52. Mechanism for the development of the Kasserine Island through constructive interference between the NW-SE trending North African passive margin and the NE-SW trending flexural bulge associated with thrust loading in the northwest (from Anderson, 1991).

3.8.3. Oligocene (Rupelian) to Present-Day

Even thermal subsidence across the Gulf of Gabes characterised the Oligocene and Early Miocene, and was accompanied by the deposition of the shaley Salammbo Formation (SS-12). This phase of quiescence (with that in the late Eocene) suggests that thrust propagation essentially ceased during these periods, causing a cessation in activity along the Gafsa-Medina Shear Zone, and hence tectonic subsidence in the Gabes-Tripoli Basin. This argument is supported by the work of Anderson (1991), which shows a relatively stationary flexural bulge throughout this period.

At approximately 16 Ma, thrust emplacement commenced in northern Tunisia (Hill & Hayward, 1988; Dewey et al., 1989). Anderson (1991) shows the postulated geometry of structures in central and northern Tunisia from this event (**Fig. 3.53**). NW-SE compression caused dextral reactivation on the Gafsa-Medina Shear Zone, thus inducing extension and subsidence in the Gabes-Tripoli Basin (**Fig. 3.45**).

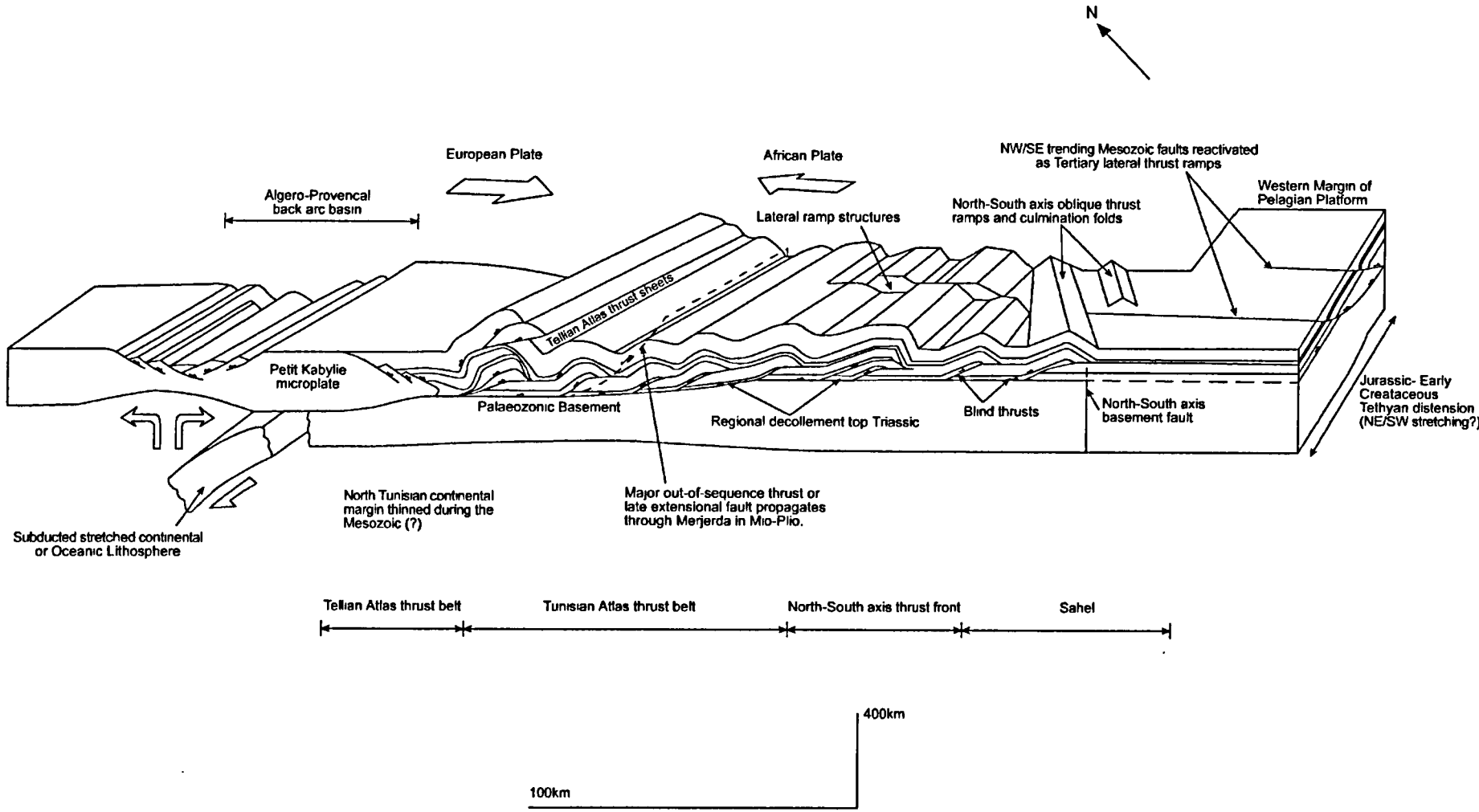

Fig. 3.53. Block diagram to illustrate the postulated geometry of structures in Central and Northern Tunisia (from Anderson, 1991)

Seismic data shows the development of a WNW-ESE fault system within the Ain Grab to present-day succession. TWT structure maps show that it has a slightly different trend to the lower fault sets (Chapter 6 and 7). Middle Miocene sedimentation rates associated with this event are high. Thrust belt propagation continued throughout the Late Miocene, as indicated on palaeogeographic maps by the southeastward migration of the associated foreland basin and fore-bulge system. It is apparent from seismic data and the isopach maps illustrated in Section 3.6 that during the Middle Miocene, uplift on the Kerkennah High essentially ceased (**Figs. 3.21-3.23**). The cause of this event is unknown.

Shortly after final thrust emplacement in the Late Miocene, crustal extension commenced in the Straits of Sicily. This event, which created the Pantelleria, Linosa, Malta and Medina Graben, is related to the rotation of the Petite-Kabylie westwards, progressively away from Sardinia (Cohen et al., 1980). Various models referring to the evolution of the Straits of Sicily Rift Zone are given in Chapter 2. Grasso et al. (1990) illustrate that maximum subsidence during this phase was attained during the Pliocene and Early Pleistocene. Seismic sections over the Gulf of Gabes support this model as the Jerrafa and Tripolitania grabens contain a thick Plio-Pleistocene sequence (**Figs. 3.24-3.255**). It is concluded that the broad Middle Miocene to present-day peak on strain rate models can therefore be attributed to a combination of Middle to Late Miocene thrust emplacement and Late Miocene to present-day crustal extension in the Straits of Sicily (**Fig. 3.45**). The closely spaced nature of the events precludes differentiation into two separate episodes on most subsidence curves. Strain rate models give stretching values (β) between 1.02 and 1.15 for this period of Late Miocene to present-day tectonic subsidence.

Chapter 4

Evaluating Fractured Reservoirs: Fundamental Concepts

4.1. Introduction

As a consequence of their tendency towards early lithification, carbonate rocks are particularly susceptible to brittle deformation by fracturing at multiple stages throughout their burial history. Where fractures are present in a reservoir interval, the contrast between fracture and rock matrix properties causes highly heterogeneous permeability fields, which result in complex saturation distributions. Efficient production of such reservoirs therefore requires a good understanding of the mechanisms controlling fracture development and the distribution of fracture systems they produce.

This section of the thesis examines the tectonic controls on fracture development and reservoir architecture within two carbonate reservoirs on the Pelagian Platform. These are the Hasdrubal and Miskar Gas Fields, which are owned and operated by the BG Group (**Fig. 4.1**). They were chosen because well test and core data demonstrated that reservoir-scale fracturing had an important effect on hydrocarbon flow rates, a phenomenon that was poorly understood in these reservoirs (Hasdrubal Plan of Development Report, 1998). Detailed analyses of seismic, core and FMI/CAST images were conducted in each asset and integrated into working structural models. In addition, analysed fracture data from the Hasdrubal Field was incorporated into a fracture simulation package (FracMan) in an attempt to build a three-dimensional fracture model of the principal reservoir interval. Finally, a particular aim of this exercise was to develop predictive models for the distribution and configuration of fracture systems and hierarchical structures associated with seismic-scale faults. In

order to achieve this, core analyses were integrated with fieldwork studies from appropriate outcrop analogues in Malta (No outcrop analogues were available in Tunisia).

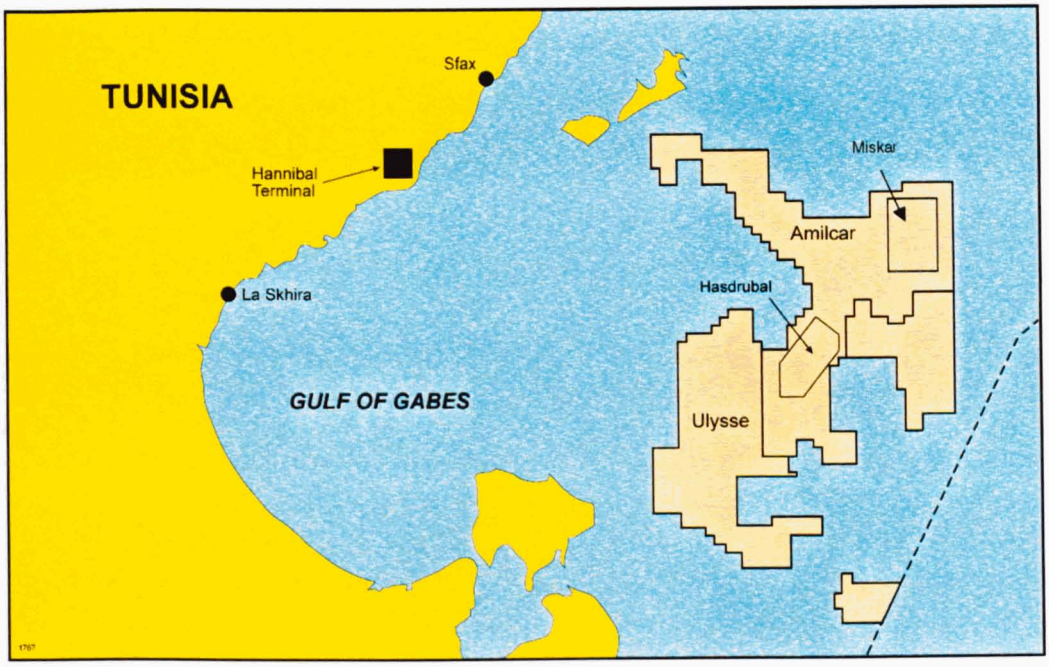

Fig. 4.1. Location map of the Hasdrubal and Miskar Gas Condensate Fields in the Gulf of Gabes region.

This chapter introduces the main principles of fractured reservoir characterisation, focusing briefly on the fundamentals of fracture mechanics. It will also discuss the various schemes with which to classify natural fracture systems, and review the influence of these systems on fluid flow. Chapter 5 will then provide an overview of the sampling and analytical techniques used in fractured reservoir characterisation. Methods of fracture detection are discussed, together with the various sampling and analytical strategies that are employed in this study. An account of sampling bias is also presented.

4.2. Principles of Fractured Reservoir Evaluation

'Fractured reservoirs are very complicated and difficult to evaluate. Effective evaluation and prediction in these reservoirs require an early recognition of the role of the natural fracture system present and a systematic approach to the gathering and analysis of pertinent data' (Nelson, 1985; 2001).

The following review follows the procedure of Nelson (1985, 2001). It briefly presents the critical attributes that must be evaluated to quantify fractured reservoirs in a logical,

workable sequence commencing with a discussion of fracture mechanics and natural fracture origin, through to the presentation of a generalised classification scheme applicable to all fractured reservoirs.

4.2.1. Fracture Definition

'A fracture may be defined as a discrete break within a rock mass across which cohesion is lost or reduced' (Griggs & Handin, 1960).

4.2.2. Brittle Failure Criteria

When a brittle isotropic rock is loaded to failure the resultant fractures that form are orientated with respect to the three principal stress axes (i.e. $\sigma_1 > \sigma_2 > \sigma_3$) (Price & Cosgrove, 1990) (**Fig. 4.2**). In general the mode of failure is related to the value of the least principal stress (σ_3), the magnitude of differential stress ($\sigma_1 - \sigma_3$), and the tensile strength of the rock (T). Three classes of failure are generally distinguished; 1) Tensile failure: characterised by Mode I fractures (i.e. extensional fractures) (**Fig. 4.3a**), 2) Shear failure: characterised by Mode II and III fractures which represent 'in-plane' and 'anti-plane' shear failure respectively (i.e. shear fractures) (**Fig. 4.3b-c**), and 3) Hybrid tensile/shear failure: characterised by mixed-mode fractures (Mode IV fractures) (i.e. extensional/shear fractures).

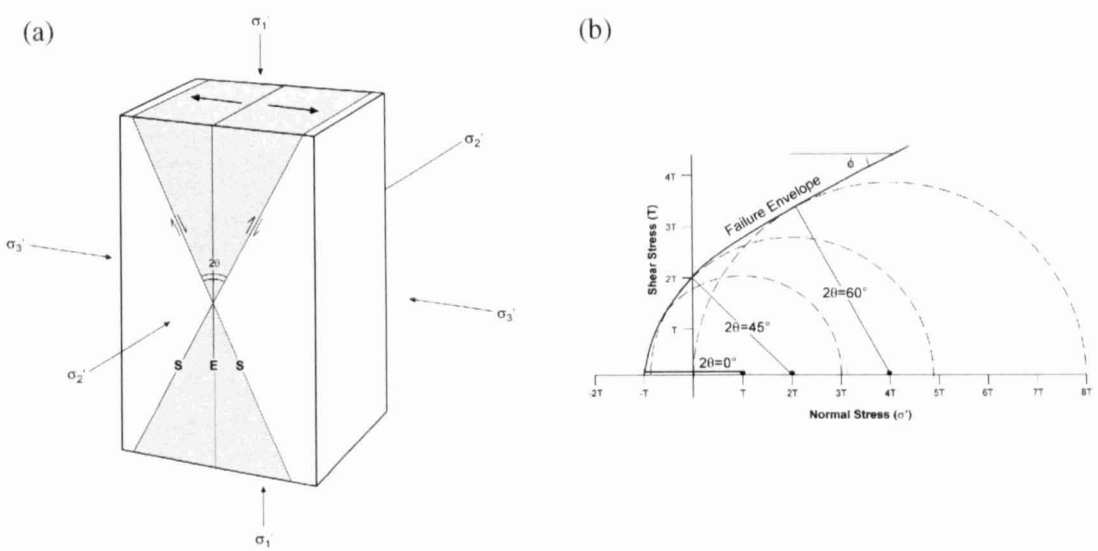

Fig. 4.2. (a) Block diagram showing relationships between effective principal stresses ($\sigma'_1 > \sigma'_2 > \sigma'_3$) and an extension fracture (E) and conjugate shear fractures (S) developed in a mechanically isotropic brittle rock. Stipple indicates the quadrants within which hybrid fractures form. (b) Composite failure envelope and Mohr circles constructed for $2\theta = 0$, 45 and 60^0. T, is the tensile strength, and ϕ, is the angle of internal friction (from Hancock 1985).

Tensile failure occurs when the least principal stress, σ_3, attains a sufficient magnitude to overcome the inherent resistance of the rock to fail in tension (i.e. when $\sigma_3 > T$). Griffith (1925), proved that providing $\sigma_1 \neq \sigma_3$ and $(3\sigma_1 + \sigma_3) > 0$, the tensile stresses around the tip of a flaw reach the critical stress (resulting in failure) when:

$$\tau^2 + 4T\sigma_n - 4T^2 = 0 \qquad (4.1)$$

where τ is the shear stress and σ_n is the normal stress acting on the flaw. Murrell (1958) expressed this non-linear relationship graphically as a Mohr envelope, and demonstrated that when the differential stress $(\sigma_1 - \sigma_3) < 4T$, tensile failure results (**Fig. 4.4**). Mode I fractures formed under this condition will initiate perpendicular to the least principal stress (i.e. σ_3), and propagate in the σ_1/σ_2 plane.

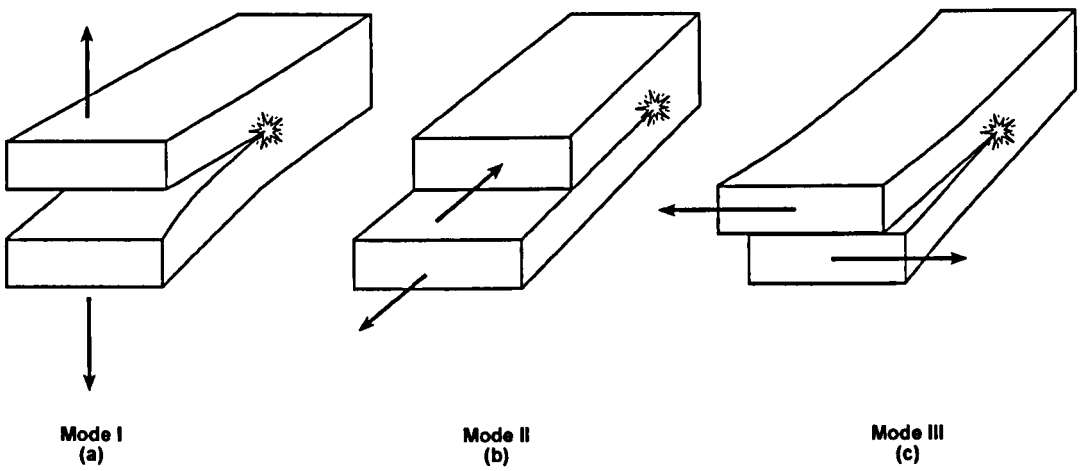

Fig. 4.3. Schematic diagram illustrating the three fundamental modes of fracture. (a) Mode I, tensile or opening mode, (b) Mode II, in-plane shear or sliding mode, (c) Mode III, anti-plane shear or tearing mode (modified after Lawn & Wilshaw, 1975).

Shear failure will occur along any surface when the shear stress acting in that plane is sufficiently large to overcome both the frictional resistance to sliding (Amonton's Law),

$$\tau = \sigma_n \tan \phi_r \qquad (4.2)$$

and the cohesive strength of the material, C_0,

$$\tau = C_0 + \sigma_n \tan \phi_r \qquad (4.3)$$

This linear relationship known as the Navier-Coulomb criteria for shear failure, plots as 'straight line' envelope on a Mohr construction (**Fig. 4.4**). Solving Equation 4.3 demonstrates that pure shear failure occurs when the differential stress $(\sigma_1 - \sigma_3) > 8T$ (Phillips, 1972; Hancock, 1985; Engelder, 1993; Dunne & Hancock, 1994).

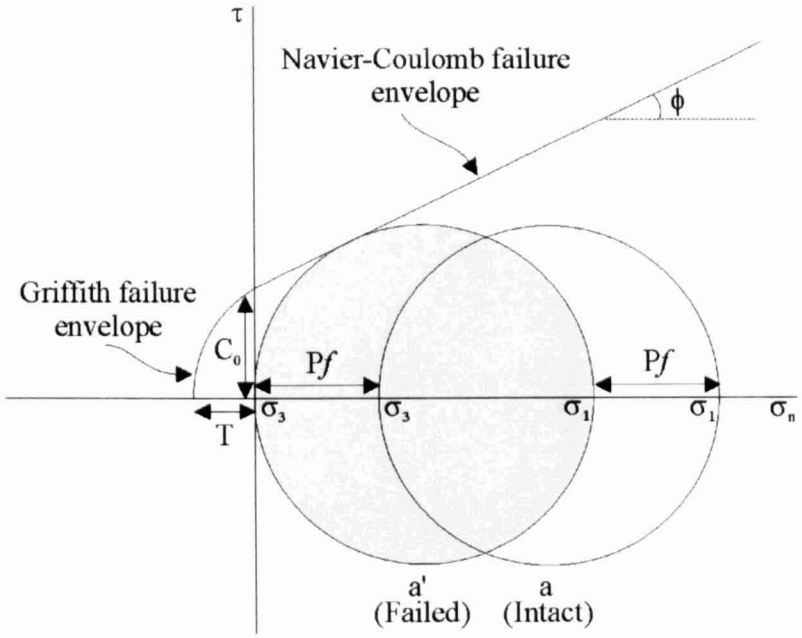

Fig. 4.4. Composite Griffith and Navier-Coulomb failure envelopes and Mohr circle construction illustrating how an increase in pore fluid pressure may move a rock that was in a stable stress field into an unstable stress field (from Cosgrove, 1992).

The Griffith criterion for tensile failure and the Navier-Coulomb criteria for shear failure represent end members of the failure criterion. However the continuum between these two criteria where the differential stress (σ_1 - σ_3) = 4T - 8T, represent conditions favourable for the development of mixed-mode fractures (Price & Cosgrove, 1990). Angular relationships between fractures and the principal stresses at failure may be quantified, and are shown in **Table 4.1**. The dihedral angle represents the angle between a theoretical conjugate fracture set, about the maximum principal stress axis, σ_1.

Fracture Class	Failure Mode	σ_1–σ_3	Dihedral Angle (2θ)
Mode I	Tensile	<4T	0^0
Mode IV	Tensile-Shear	4T-8T	$1\text{-}45^0$
Mode II & III	Shear	>8T	$>45^0$

Table 4.1. Generic classification scheme illustrating the angular relationships between fracture mode and the principal stresses at failure

4.2.3. Natural Fracture Classification

According to Nelson (1985, 2001) natural fractures may be classified into two distinct categories; i) Tectonic fractures and ii) Regional fractures.

Tectonic Fractures

Stearns (1968b) demonstrates that tectonic fractures are associated with faulting and folding. Fractures associated with faulting may be assigned to the same stress state that caused the fault. Therefore the majority of fractures within the vicinity of a fault are Mode II/III fractures parallel or conjugate to the fault plane (**Fig. 4.5**). Mode I fractures may also be present, bisecting the acute angle between the conjugate set. Stearns (1968b) argues that the intensity of fracturing associated with faulting appears to be a function of lithology, distance from the fault plane, amount of displacement along the fault, total strain in the rock mass, depth of burial, and fault type (i.e. thrust, growth, etc.).

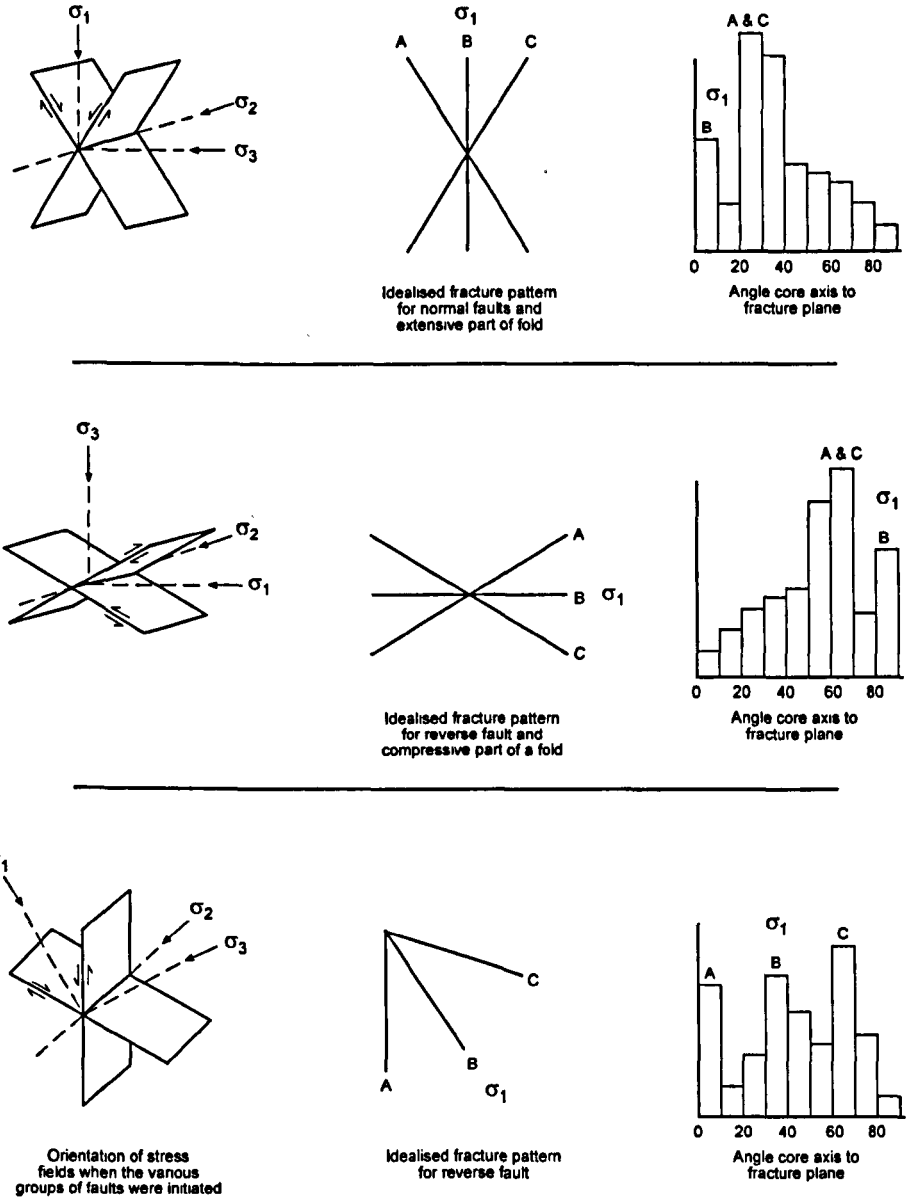

Fig. 4.5. Relationship between stress states, the fault and fracture orientations derived from those stress states, and the resultant dip histograms subsequently obtained from core analyses (from Price, 1966; Friedman, 1969).

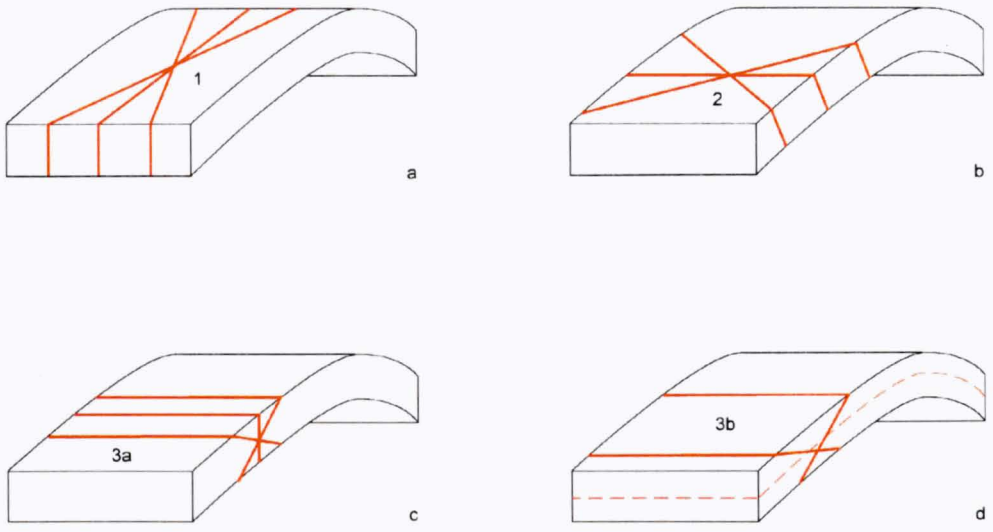

Fig. 4.6. A generalisation of dominant fold-related fracture sets (from Stearns, 1967b).

Fractures that are associated with folding do not form correlative to the stress state that created the folding, but result from the stresses generated through the bending of layers. Stearns (1964, 1967) and Norris (1966) demonstrated that five distinct fracture patterns may be associated with folds which relate to the relative configuration of principal stresses at formation (**Table 4.2**) (**Fig. 4.6**). Four of these patterns consist of two Mode II/III fracture sets, and an accompanying Mode I fracture set bisecting the acute angle between the conjugates. The fifth is related to bedding plane slip. The relative position and intensity of these patterns varies according to the geometry and origin of the fold. McQuillan (1974) suggests that fracture intensity generally increases within regions where the rate-of-change-of-dip is greatest (i.e. the hinge regions).

Set	σ_1	σ_2	σ_3
I *	Parallel to dip direction Parallel to bedding	Perpendicular to bedding	Parallel to bedding
II *	Perpendicular to dip direction Parallel to bedding	Perpendicular to bedding	Parallel to bedding
III	Perpendicular to bedding Parallel to dip direction	Parallel to bedding strike Parallel to bedding strike	Parallel to dip direction Perpendicular to bedding
IV	Parallel to bedding	Parallel to bedding strike	Perpendicular to bedding
V	At an angle to bedding (dihedral angle)	Parallel to bedding strike	At an angle to bedding (90^0 – dihedral angle)

Table 4.2. Fracture sets associated with folding. * Most predictable fracture sets.

Regional Fractures

Regional fractures, otherwise referred to as 'joints' form predominantly perpendicular to bedding, display little to no evidence of shear (i.e. Mode I fractures) and are characterised by a marked consistency in orientation (Engelder & Geiser, 1980). They are commonly developed in orthogonal sets and often form layer-bound fracture systems which change strike within different formations (Price, 1966; Stearns, 1968a) **(Fig. 4.7a)**.

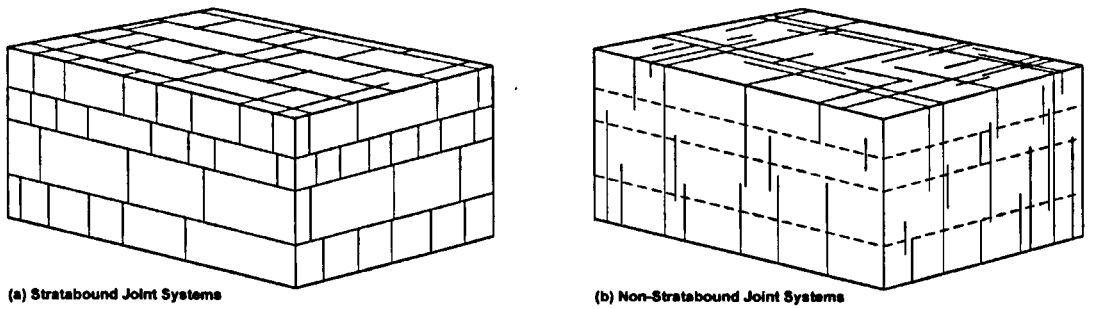

Fig. 4.7. Schematic diagram illustrating the major features of (a) stratabound and (b) non-stratabound regional joint systems. In stratabound systems, joints are largely confined to individual beds, their size is limited to a narrow range, and spacing is regular. In non-stratabound cases, joint sizes cover a wider range, fractures cross-cut bedding and spacing tends to be clustered (from Odling et al. 1999).

The origin of regional fractures is still in many respects an enigma. Price (1974) modelled the development of orthogonal fracture sets by considering the evolution of an idealised, hypothetical basin. He suggested that the two orthogonal orientations parallel the long and short axes of the basin in which they form, and are the product of sequential subsidence, uplift, and exhumation. Supporting studies have been reported by Narr & Currie (1982) and Das Gupta & Currie (1983).

Engelder (1985) also supports this model of 'joint' development, concluding that based on the timing of joint propagation during the history of burial, lithification, deformation, and denudation of a sedimentary sequence within a basin, four types of joints may be distinguished; i) tectonic, ii) hydraulic, iii) unloading and iv) release. Tectonic joints form at depth, prior to uplift, in response to the combined effect of abnormal fluid pressures generated during tectonic compaction, and by the action of tectonic stresses (N.B. Tectonic stresses are usually horizontal components of the in situ stress field which are a deviation from the reference state as a consequence of natural processes on all scales (Engelder, 1993)). Hydraulic joints also form at depth but in response to high fluid pressures caused by sedimentary compaction. Unloading

joints form near the surface as a response to thermal contraction accompanying uplift and erosion (Price, 1959). Their orientation is controlled by the residual or contemporary tectonic stress fields at the time of their formation. Hancock & Engelder (1989) termed unloading joints that have propagated in a relatively unchanged stress field until the present day as neotectonic joints. Release joints form under the same conditions. However their development is controlled by the nature of the rock fabric.

It is generally believed that tectonic fractures enhance the productivity of a reservoir while regional fractures provide the connectivity (McPhail, 1998).

4.2.4. Controls on Tectonic & Regional Fracture Development

It is widely recognised that a number of parameters control tectonic and regional fracture development. Variations in bulk rock composition, grain size, porosity, bed thickness and structural position principally control fracture distribution and intensity within a given rock mass (Stearns, 1968b) (**Table 4.3**). Price (1966), Stearns & Friedman (1972) and others demonstrate that differences in composition, grain size and porosity affect the strength of rocks, therefore causing variations in fracture intensity. The exact influence of these parameters however, has not been fully quantified.

Controlling Parameter	Effect on Fracture Intensity
Composition	↑ brittle components → ↑ fracture intensity
Grain Size	↓ grain size → ↑ fracture intensity
Porosity	↓ porosity → ↑ fracture intensity
Bed Thickness	↓ bed thickness → ↑ fracture intensity
Structural Position	↑ strain → ↑ fracture intensity ↑ rate of change of dip → ↑ fracture intensity

Table 4.3. Main controls on fracture intensity. ↑ - Increase. ↓ - Decrease.

Hobbs (1967), Ladiera & Price (1981) and others demonstrate that bed thickness influences fracture spacing within 'stratabound' systems (i.e. sequences where there is little mechanical coupling between adjacent lithological layers) (Odling et al., 1999) (**Fig. 4.7a**). As a general rule fracture spacing increases with an increase in layer

thickness. However the exact quantitative relationship between the two is still uncertain, although it is generally accepted that spacing relationships are linear in layers <1.5m thick (Ladiera & Price, 1981; Huang & Angelier, 1989; Narr & Suppe, 1991) **(Fig. 4.8)**.

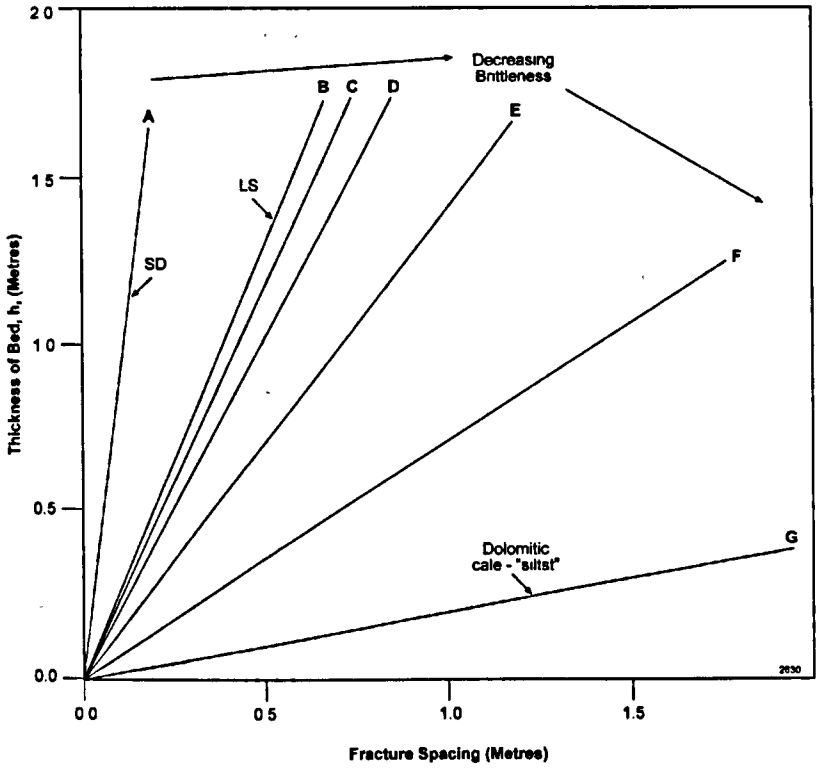

Fig. 4.8. Bed thickness vs fracture spacing. Data is from (A) Nelson (1985); (B, D, E) McQuillan (1973); (C, F) Bogdanov (1947); (G) Sowers (1970). In all but curve (A), symbols are not data points but slope construction points from the original published data (from Nelson, 2001).

Price (1966) first suggested that proximity to local structure influenced fracture distribution based on the assumption that fracture intensity is associated to strain. It can be shown experimentally that an increase in strain results in increased fracture intensities within a given rock volume. Two common methods incorporating the total strain approach can be used to predict fracture intensity with structural position:

- The determination of stress/strain distributions from geological maps and cross-sections can be combined with structural studies from seismic, core and outcrop data to predict fracture intensity associated with local structure;
- Determination of fracture intensity can also be made using the radius-of-curvature or rate-of-change-of-dip approach. This assumes that flexure-related fracturing is most intense where the rate-of-change of dip or curvature is at a maximum.

It is important to note that to date there are no widely accepted generic models to explain fracture intensity relationships associated with different types of structure (i.e. strike-slip fault, extensional faults, folds etc.). This is due in part, to the 'unique' nature of most fractured reservoirs, and the complex interplay of all the other parameters.

4.2.5. Influence of Fractures on Reservoir Performance

The physical character of fractures within a given reservoir volume is controlled by their mode of origin, the mechanical properties of the host rock and by sub-surface diagenesis. These factors combine to develop features that will cause an increase or decrease in reservoir porosity and permeability (Nelson, 2001). A quantitative evaluation of fracture permeability and porosity is therefore essential in the evaluation of a naturally fractured reservoir.

Fracture Permeability

Darcy (1856) presented the first quantitative description of fluid flow through porous media. He demonstrated that laminar, compressible, single phase Newtonian flow (Q) in a continuous, homogeneous, porous material is given by,

$$Q = KA\frac{dh}{dl} \tag{4.4}$$

where K is the hydraulic conductivity, A is the cross-sectional area and dh/dl is the head gradient. Hydraulic conductivity (K) is given by,

$$K = k\left(\frac{\rho g}{\mu}\right) \tag{4.5}$$

where k is the intrinsic permeability ($k = Nd^2$), ρ is the fluid density, g is the acceleration of gravity, μ is the fluid viscosity, N is a dimensionless coefficient characteristic of the medium and d is the average constitutive grain diameter of the rock (Hubbert, 1940).

Darcy's equation (Equation 4.4) is valid in porous media containing no fractures. However, Huitt (1955) and Lamb (1957) among others show that in a fractured system Nd^2 cannot be defined for flow in the fractures themselves. As a consequence, the parallel-plate theory of flow was developed to model flow in fracture systems. This theory assumes that flow occurs between two smooth parallel plates separated by a distance, e, where,

$$\frac{Q}{A} = \frac{e^3}{12S}\frac{dh}{dl}\cdot\frac{\rho g}{\mu} \tag{4.6}$$

where S is the fracture spacing. This equation is valid for single-phase, Newtonian, laminar flow in planar fractures with small overall changes in width, e. A combination of Equations 4.4 and 4.6 gives the total flow (i.e. Darcy's Equation for the intact-rock portion of the system, and the parallel-plate theory for fractures) (Parsons, 1966),

$$k_{fr} = k_r + \frac{e^3 \cos^2 \alpha}{12S} \tag{4.7}$$

and

$$k_f = \frac{e^2}{12}\cdot\frac{\rho g}{\mu} \tag{4.8}$$

where k_{fr} is the permeability of the fracture plus intact-rock system, k_f is the permeability of the fracture, k_r is the permeability of the intact-rock and α is the angle between the axis of the pressure gradient and the fracture planes.

Equation 4.8 assumes that flow is laminar between smooth, non-moving, parallel plates, that fluid flow across any fracture/matrix surface does not alter the flow of either system, and that the fractures are homogeneous with respect to orientation, width and spacing. The assumption of laminar flow is valid for low fluid flow rates and surface roughness. However, where subsurface flow rates are fast, equations for turbulent flow need to be utilised. Equation 4.8 also assumes that 'fluid flow across the fracture/matrix surface will not alter the flow of either system'. This is a reasonable assumption in reservoirs which have either very high or very low matrix permeabilities, whereby cross-flow between the fracture and matrix systems becomes non-existent. However, in cases where intermediate matrix permeabilities are encountered, cross-flow becomes more important. Barenblatt et al. (1960) among others have attempted to quantify cross-flow in such systems. These equations are complicated and beyond the scope of this review.

Fracture Porosity

Fracture porosity, like matrix porosity is the percentage of a particular void volume in a rock mass compared to its total volume. The two basic relationships to calculate fracture porosity and matrix porosity are given in Equations 4.9 and 4.10.

$$\phi_r = \frac{V_p}{V_b} \times 100 \tag{4.9}$$

$$\phi_f = \frac{e}{D+e} \times 100 \tag{4.10}$$

where ϕ_r is the matrix porosity, ϕ_f is the fracture porosity, V_p is the volume of pores (other than fractures), V_b is the bulk volume, D is the average spacing between parallel fractures and e average effective width of fractures. Nelson (2001) shows by analysis of these two equations that fracture porosity (ϕ_f) is scale-dependent, whereas matrix porosity (ϕ_r) is not. This because ϕ_f has a spacing term built into its calculation (Equation 4.10).

Fracture porosity, although generally much smaller than matrix porosity, tends to have a much greater effect on permeability, because of the interconnected nature of most fracture systems. Small increases in fracture porosity will have a marked effect on permeability parallel to the fracture. The effect of fracture porosity on permeability varies with depth (i.e. compressibility). Nelson (2001) shows that fractures compress more readily than the matrix in which they occur, thus leading to a decrease in fracture permeability. This effect is greatest in brittle rocks.

Fracture porosity determinations can be made from 1) Core analysis, 2) k_f/ϕ_f relationships, 3) Field determinations, 4) Logs and 5) Multiple well tests. These methods, however, usually give different values of ϕ_f because they are based on slightly different data

Properties controlling Fracture Porosity and Permeability

It has been shown in the preceding discussion that fracture porosity and permeability is affected by the attributes of the fracture system itself. Principal factors controlling fracture porosity and permeability include, 1) Fracture morphology, 2) Fracture width, 3) Fracture intensity and 4) Fracture and matrix porosity communication.

Fracture Morphology

Fracture morphology in a reservoir interval is principally determined from core. Nelson (1985) demonstrates that there are four basic types of natural fracture plane morphology; 1) Open fractures, 2) Deformed fractures, 3) Mineral-filled fractures and 4) Vuggy fractures.

Open fractures possess no diagenetic material filling the width between the walls of the fracture. In such cases, the fracture permeability is a function of fracture width, the in-situ effective stress component normal to the fracture plane, and the roughness and contact area of the fracture walls. Open fractures tend to increase 'in-plane' permeability. The effect on fluid flow perpendicular to the fracture plane is negligible (**Fig. 4.9a-b**).

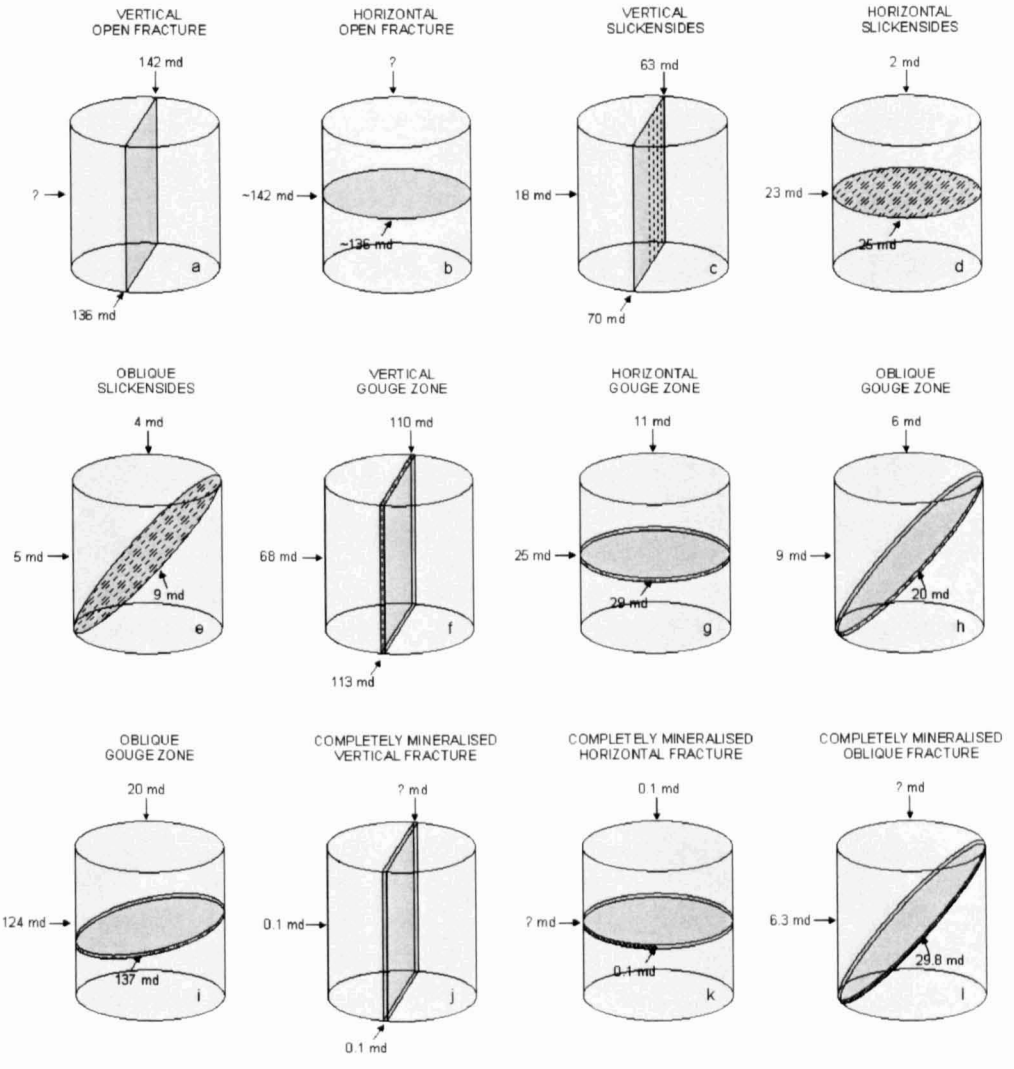

Fig. 4.9. Direct effect of fracture morphology on whole-core permeability. (a) Vertical open fracture, (b) Horizontal open fracture, (c) Vertical fracture with slickensides, (d) Horizontal fracture with slickensides, (e) Moderately dipping fracture with slickensides, (f) Vertical fracture filled with gouge, (g) Horizontal fracture filled with gouge, (h) Moderately dipping fracture filled with gouge, (i) Gently dipping fracture filled with gouge, (j) Completely mineralised vertical fracture, (k) Completely mineralised horizontal fracture, and (l) Completely mineralised moderately dipping fracture (modified after Nelson, 2001).

Deformed fractures are those features that have been altered after their initiation. Nelson (2001) considers two types of deformed fracture; 1) Gouge-filled fractures and 2) Slickensided fractures. Gouge-filled fractures are the product of cataclasis or

granulation, associated with shear movements on a fracture plane. Granulation or cataclastic zones reduce porosity, grain size, sorting and therefore the permeability of the fracture zone, thus having an adverse effect on reservoir performance. Laboratory experiments demonstrate that the reduction in permeability occurs perpendicular to the fracture or gouge zone (Nelson, 2001) (**Fig. 4.9c-e**). Gouge-filled fractures are more commonly found in high porosity siliciclastic rocks. Slickensided fractures develop in response to cataclasis and/or grain melting and recrystallisation. The result is a decrease in permeability perpendicular to the fracture wall. In some cases a permeability increase is observed along the fracture plane due to the mismatch of smooth fracture walls (**Fig. 4.9f-i**).

Mineral-filled fractures are filled with secondary or diagenetic mineralisation (i.e. quartz, calcite etc.). The effect of mineralisation on fracture permeability is controlled by the completeness of filling and the diagenetic history of the material. Generally, completely filled fractures are permeability barriers, whilst partially filled fractures in the form of vug development or intergranular porosity can give a measurable increase in permeability (**Fig. 4.9j-l**). In some cases incomplete mineral fill in fractures can create the principal reservoir quality.

Vuggy fractures are not essentially a true fracture morphology, but a matrix alteration surrounding the fracture (Nelson, 2001). This vuggy porosity is developed along fracture planes due to dissolution processes. Vugs develop along and adjacent to the fractures and are more or less restricted to a narrow zone surrounding the fracture itself. Vuggy fractures without diagenetic alteration of the vug walls should, as in open fractures, increase reservoir permeability parallel to the fracture, and have little permeability effect across the fracture.

Fracture Width

Accurate estimates of fracture width from the subsurface are extremely difficult to obtain, particularly in cases where the fracture system is uncemented. Nelson (2001) presents published data from a number of workers showing fracture width values for natural and experimentally derived fracture systems (**Tables 4.4 & 4.5**). Measurements of natural fracture width have been taken at relatively shallow depths (several hundred metres) (**Table 4.4**), whereas experimental fracture widths were recorded under simulated conditions (in excess of 3000m) for a variety of rock types (**Table 4.5**). A comparison of these results shows that fracture width decreases with increased depth.

Workers	Fracture Widths (cm)
Noorishad et al. (1971)	3.0×10^{-2}
Ohnishi & Goodman (1974)	$1.3\text{-}2.5 \times 10^{-2}$
Sharp et al. (1972)	$1.0\text{-}5.0 \times 10^{-2}$
Snow (1968a)	5.0×10^{-3}
Snow (1968b)	$0.5\text{-}1.5 \times 10^{-2}$
Van Golf-Racht (1982)	$1.0\text{-}4.0 \times 10^{-3}$
Wilson & Witherspoon (1970)	2.5×10^{-2}

Table 4.4. Published natural fracture widths (taken from Nelson, 2001).

Rock Type	Fracture Widths (cm)
Medium to Coarse Sandstone	10^{-2}
Fine to Medium Sandstone	10^{-3}
Crystalline Limestone	10^{-3}
Siltstone	10^{-4}
Shale	10^{-5}
Chalk	$10^{-5} - 10^{-6}$

Table 4.5. Published experimental fracture widths (taken from Nelson, 2001).

Fracture Intensity

Along with fracture width, fracture intensity is the other important quantitative parameter necessary to predict fracture porosity and permeability in a reservoir. Fracture intensity within a given rock mass has been quantified by many workers in terms of fracture frequency (Priest, 1993) and fracture spacing (Narr, 1996). Unlike fracture width, which is difficult to observe directly, fracture frequency and spacing can be directly quantified through core, borehole and outcrop data. Nelson (2001) demonstrates that variations in fracture spacing can have a dramatic effect on both fracture porosity and permeability (**Fig. 4.10a-b**). The various methods adopted for the sampling and calculation of fracture frequency and spacing is discussed in detail in Chapter 5.

Fracture & Matrix Porosity Communication

Reservoirs in which fractures play a significant role in both the production and storage of reserves must be treated as 'dual-porosity' systems (i.e. one system in the matrix and one in the fractures). In many cases, flow communication in dual-porosity systems is good (i.e. uninhibited cross-flow), whereby the matrix and fracture systems respond to

the overall fluid pressure gradient as well as directly to each other. However, occasionally adverse fracture/matrix interactions can present significant production and evaluation problems (e.g. consider a case of a reservoir with poor communication between a highly permeable fracture system and a highly porous matrix system) (i.e. inhibited cross-flow) (Nelson, 2001).

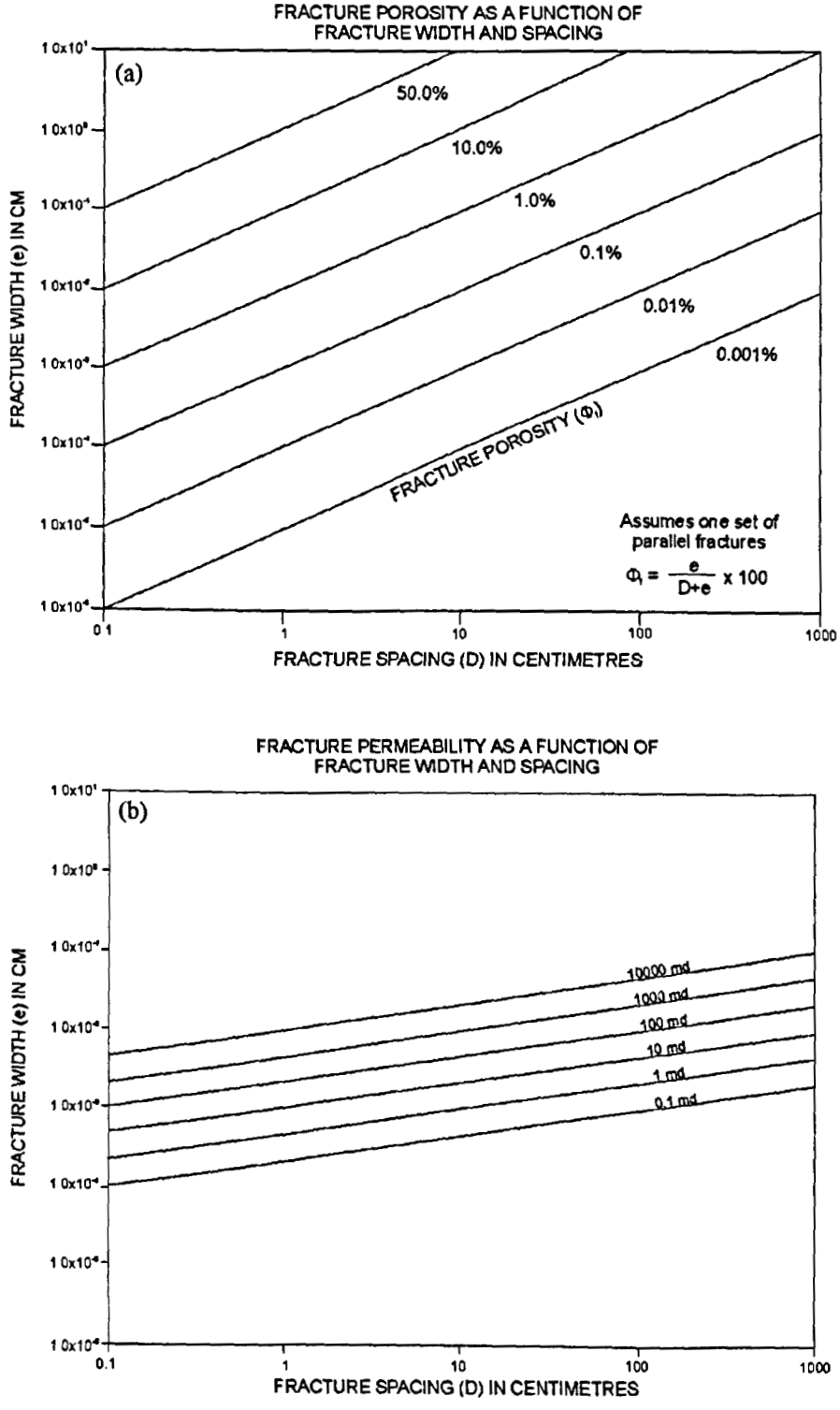

Fig. 4.10. (a) Fracture porosity as a function of fracture width and fracture spacing, (b) Fracture permeability as a function of fracture width and spacing (from Nelson, 2001).

Quantification of fracture/matrix interaction is difficult. Estimates are normally given from thin-section analyses, which are based on determining the effect of the geometry of the fracture/matrix interface on both porosity and directional permeability. **Figure 4.11** shows the effect of fracture/matrix interaction on whole-core permeability.

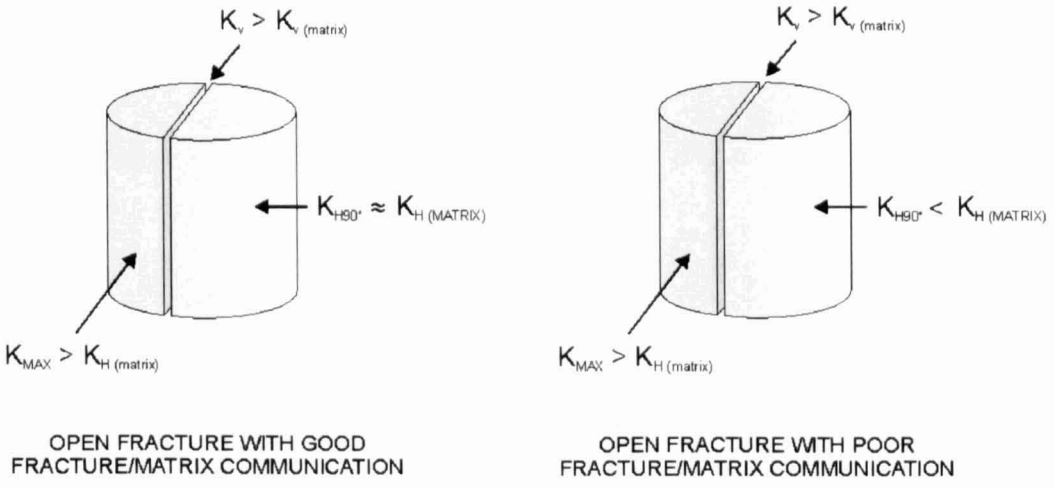

Fig. 4.11. Effect of fracture and matrix interaction on whole core permeability (from Nelson, 2001).

4.2.6. Classification of Fractured Reservoirs

Once the origin, distribution and reservoir properties of the fracture system(s) within a reservoir volume have been determined, the reservoir can be classified. Nelson (2001) expands on the scheme of Hubbert & Willis (1955) to classify fractured reservoirs according to the positive effects that fracture systems have on overall reservoir quality (**Table 4.6**).

Reservoir Type	Influence of Fractures on Reservoir Quality
Type I	Fractures provide the essential reservoir porosity and permeability
Type II	Fractures provide the essential reservoir permeability
Type III	Fractures partially assist permeability in an producible reservoir
Type IV	Fractures provide no additional porosity/permeability but create anisotropy

Table 4.6. Fractured reservoir classification scheme (from Nelson, 2001).

The first three types describe positive reservoir attributes of the fracture system. The fourth, however, describes those reservoirs in which fractures are important not for the reservoir quality they impart, but for the inherent flow anisotropy and reservoir partitioning they create.

4.3. Stylolite Definition & Classification

It will become apparent in the course of core analysis of the Miskar and Hasdrubal accumulations that stylolitisation also has an important effect on reservoir performance. Consequently, it is necessary to define and classify stylolites. Park & Schot (1968), originally defined stylolites in relation to the rock grain fabric, stating that 'any departure from a bedding seam, usually marked by a layer of insoluble material could be called a stylolite'. They differentiated between two scales of stylolites: 1) aggregate stylolites and 2) intergranular stylolites.

- Aggregate stylolites: where the amplitude is greater than the grain diameter of the rock.
- Intergranular stylolites: where the amplitude is smaller than the grain diameter of the rock.

The processes taking place at single intergranular boundaries are basically different from those taking place in an aggregate (Park & Schot, 1968). At simple grain boundaries, the stress-strain relationships and also the solution relationships are a function of the two neighbouring grains only. The crystallographic orientation of the grains, their angle and amount of contact, the interface-energy per unit area of contact and the capillarity relationships will influence the resulting interlacing boundaries. In contrast, aggregate stylolite geometries are dependant on the aggregate fabric relations, pressure, solution effects, porosity, permeability, and rate and duration of stylolitisation, and not on the crystallographic orientation or, and the contact relationships between the individual grains alone.

Several classification schemes have been proposed for stylolite description. Park & Schot (1968) classified stylolites according to the two-dimensional geometry expressed by the seam. They differentiated stylolites into six geometric types (**Fig. 4.12**), stating that gradational transitions may exist between the various types, in particular between types 1 and 2. In addition, they have also differentiated between different types of stylolites on the basis of their relation to sedimentary bedding (**Fig. 4.13**). Wanless (1979) on the other hand, categorised them on the basis of the presence and degree of suturing of the seam material (**Fig. 4.14**). Through his studies, he managed to illustrate the relationship different stylolite types with regard to the various percentages of clay and 'mechanically resistive' (e.g. bioclastic debris) material present, within a given

rock mass. It was shown that where there is only minor clay material present within a rock mass that contains many 'structurally resistive' elements (i.e. shell debris), high amplitude, 'sutured' stylolites will develop (Wanless, 1979) (**Fig. 4.14**). In contrast, a rock mass containing a high proportion of clay material and few 'structurally resistive' elements will become the host to low amplitude 'non-sutured' stylolites (Wanless, 1979) (**Fig. 4.14**). The scheme of Wanless (1979) is incorporated into the core studies of the Hasdrubal and Miskar Fields.

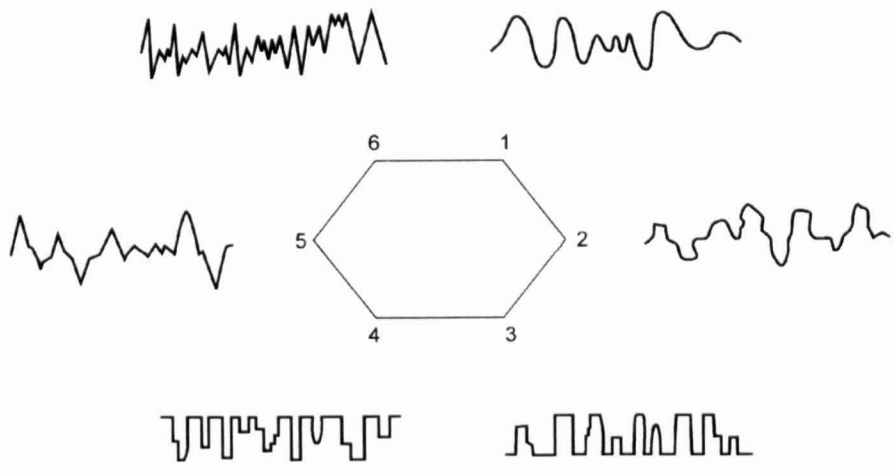

Fig. 4.12. Classification of stylolites according to geometry. 1) Simple or primitive wave-like type, 2) Sutured type, 3) Up-peak type, 4) Down-peak type, 5) Sharp peak type (tapered and pointed) and 6) Seismogram type (after Park & Schott, 1968).

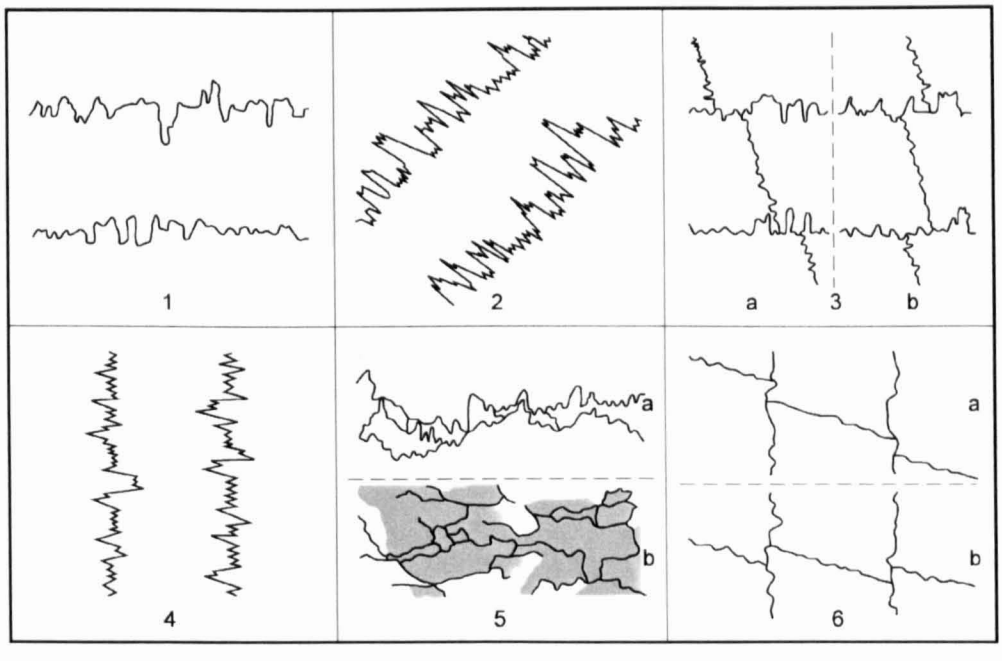

Fig. 4.13. Classification of stylolites in relation to bedding plane. 1) Horizontal stylolites, 2) Inclined stylolites, 3) Horizontal-inclined (vertical) cross-cutting stylolites, 4) Vertical stylolites, 5) Interconnecting network stylolites, and 6) Vertical-inclined (horizontal) cross-cutting stylolites (after Park & Schott, 1968).

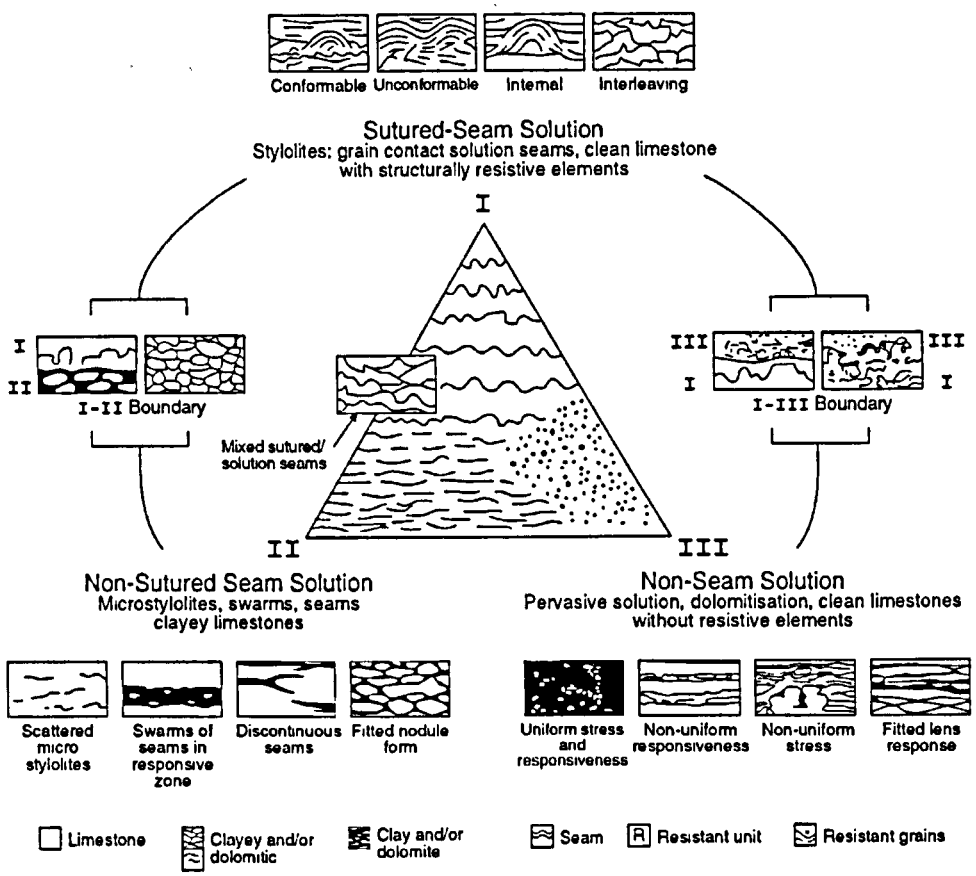

Fig. 4.14. Classification of stylolite seams based on the relative percentage of clay material and 'structurally resistive' elements present within a given rock mass (after Wanless, 1979).

4.3.1. Influence of Stylolites on Reservoir Performance

Nelson (2001) suggests that in general, the major effect of a stylolite in a reservoir is the creation of a highly directional, narrow zone of reduced porosity and permeability. In this sense these features may be treated in the same way as tectonic gouge-filled fractures in reservoir analysis.

Many workers associate stylolites with lower porosity sections of core (Dunnington, 1967). These relatively low-porosity zones may be original or due to pre-stylolitisation diagenesis and, therefore, and therefore localise stylolitisation by causing stress concentrations. The remainder of these low-porosity zones may be post-stylolitisation or syn-stylolitisation and due to local precipitation of pressure-dissolved material (Nelson, 2001). As a consequence of the lower porosity zones (surrounding stylolites) and the presence of fine-grained seam material, stylolite zones have a much reduced permeability compared to the adjacent undeformed rock. This permeability reduction is greater perpendicular to the stylolite seam than parallel to it.

In some instances, stylolites actually enhance reservoir permeability. This can occur in reservoirs where stylolite seams have been cracked open by later stage tectonic events. In such cases the stylolites act as conduits to fluid flow. For example, in a reservoir which has a relatively 'layer-cake' succession, re-cracked bedding-parallel stylolites will cause a marked increase in K_H.

Chapter 5

Sampling & Analysis of Fractured Reservoirs

5.1. Introduction

This chapter summarises the various sampling and analytical techniques that are used in the dissertation. An overview of the principal methods of detecting natural fractures in hydrocarbon reservoirs is outlined in Section 5.2. Section 5.3 introduces the various sampling strategies used in Chapters 6, 7 and 8, and provides a discussion of sampling bias for a number of these techniques. Finally, data analysis and presentation techniques are reviewed, together with the procedures to calculate fracture spacing in core (Section 5.4).

5.2. Detection of Naturally Fractured Reservoirs

Various direct and indirect methods may be used to determine the presence of natural and induced fractures within a reservoir interval. Direct detection methods allow measurement of a number of parameters including fracture dip and orientation, size and aperture etc. Indirect methods however, provide none of the quantitative fracture data required to evaluate a fractured reservoir.

5.2.1. Direct Detection Methods

- Drill cuttings: Fractures may be detected in drilled samples. However, their absence does not necessarily preclude their presence in the subsurface. This method is incapable of providing fracture orientation data.
- Core analyses: Structural core logging provides the best method for detecting natural fractures within a zone of interest, provided fracturing is not so intense as

to reduce core recovery. Careful analysis can provide details on fracture dip and orientation (if core is oriented), intensity, rock strength, rock fabric and fracture-matrix flow interaction.

- Image log analyses: Image logs provide a downhole view of fracturing within the reservoir interval. Two particular tools are used in this study; 1) the micro-resistivity based Formation Micro-Scanner (FMS) (Schlumberger, 1992) and 2) the Circumferential Acoustic Scanning Tool (CAST) (Halliburton, 1995). Such tools compliment core studies in that they can give direct information on hole size and bedding and additionally fracture orientations.
- Impression Packers: Impression packers are bladders coated with a soft pliable material. Unpressurised packers are lowered into the zone of interest in the well and then pressurised. As the soft coating is pressed against the surface of the wellbore, it conforms to the rugosity of the hole, including fractures. Subsequent observation of the packer coating gives an idea of the physical character of the wellbore. This technique is used almost exclusively in the detection of hydraulic fractures. It has limited use in the detection of natural fractures because these fracture systems may not cut the mudcake.

Geophysical Logs	Log Response to Fracturing
Sonic Logs	Reduction in P-wave & S-wave amplitudes. Effect on P-waves is small compared to the effect on S-waves. Shales also produce large reductions in S-wave amplitudes, so its application is limited to 'shale-free' formations (**Fig. 5.1a**).
Caliper Logs	Rugose or elliptical wellbore geometries indicate that the hole may have caved in due to the presence of natural fractures. Caution must be applied in interpreting rugose geometries because they can also be caused by borehole breakouts or induced fractures (**Fig. 5.1b**).
Resistivity Logs	Increase in resistivity on the Dual Induction Laterolog (which reads horizontal conductivity) compared to vertically focused or spherically focused short reading tools in the presence vertical fractures filled with low resistivity mud filtrate (**Fig. 5.1c**).
Dipmeter Micro-Resistivity Log	Micro-resistivity separation: As the sonde on the tool rotates, moving upwards in the presence of a mud filtrate-invaded vertical fracture, one of the pads could intersect the fracture while the adjacent pad would not causing a separation in micro-resistivity (**Fig. 5.1d**).
Density Log Compensation Tool	Assumes that for a constant lithology borehole roughness is associated to fracturing. Therefore as the density compensation curve detects roughness, it will detect fractures (**Fig. 5.1e**).

Table 5.1. Detection of natural fractures through variations in geophysical log response (Mc Phail, 1995).

5.2.2. Indirect Detection Methods

- Drill reports: A loss of circulation within the wellbore, recorded on a well report or mudlog is generally the first indication that a reservoir interval is fractured.
- Geophysical log evaluation: Most geophysical logs react abnormally to the presence of fractures in a reservoir interval. **Table 5.1** illustrates the various effects that fractures have on log response for a number of geophysical tools.
- Flow or well test evaluation: An integrated analysis of pressure build up, pressure draw-down and Drill Stem Test (DST) data with established conceptual dual-porosity models can aid determination of fracture presence. However the procedures are often quite involved and a complete discussion of testing techniques is beyond the scope of this thesis.

5.3. Sampling Fracture Systems

In order to evaluate a fractured reservoir, geometrical properties such as orientation, dip, frequency, spacing and size require quantification. In this thesis fractures were sampled in core (Hasdrubal -2, -3, & -4; Miskar -3, -6, -8, -9, -10, & -11), from image logs (Hasdrubal -2 & -3) and at outcrop (Malta and SE Sicily). Varying sampling strategies were employed to suit the type of analysis required, details of which are given below.

5.3.1. Core & Outcrop Sampling Strategies

Nelson (1985) and Priest (1993) provide good accounts of the different measurement systems that may be utilised to obtain fracture properties based on varying sampling strategies in core and at outcrop.

- Core Analyses: are used to gain a direct insight into subsurface fracturing (i.e. within hydrocarbon reservoirs, nuclear repositories etc.). Structural studies of core data are often integrated with borehole imaging techniques, and also mechanical and fluid flow test results.
- Surface Outcrop Analyses: are often used to indirectly predict/estimate subsurface fracturing. In this thesis studies on appropriate outcrop analogues have been conducted to gain an insight into potential sub-seismic scale fracture distributions in the Miskar and Hasdrubal Fields.

Two principal sampling techniques have been adopted to analyse fracture distributions in core and at outcrop (Attewell & Farmer, 1976; Rives et al., 1992; Priest, 1993; Wu & Pollard, 1995): 1) Scanline sampling and 2) Window sampling. These two sampling techniques can be used for either analysis.

Scanline Sampling

Scanline sampling techniques provide a one-dimensional, linear survey across an area of interest (e.g. an exposed rock face or a cored interval). Conventional scanline sampling along a cored interval involves attaching a measuring tape along the centre of the core, in order to form a 'scanline' down the core length with increments that correspond to depth. The depth of the intersection between the scanline and each structural feature (e.g. fracture, stylolite, shear band etc.), and its dip and dip direction (if the core is oriented) is then recorded, along with various other observations and measurements (e.g. fracture type, length, aperture, fill, displacement etc.) (**Fig. 5.1a**).

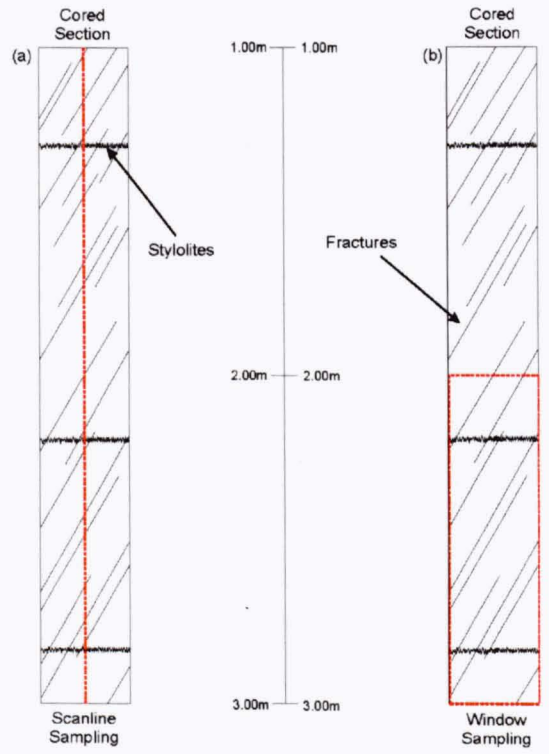

Fig. 5.1. Sampling techniques used in core analysis. (a) Scanline sampling and, (b) Window sampling along an interval of core.

The scanline sampling methodology at an exposed rock face is the same. However, it is recommended that a clean, approximately planar rock face (representative of the whole exposure), which is relatively large compared to the size and spacing of the fractures

present be selected. Priest (1993) considers that such a rock face should contain between 150 - 350 fractures, of which 50% must have at least one end visible. Scanlines (i.e. measuring tapes) are then oriented on the rock face in various configurations dependent on the type of analysis required (**Fig 5.2a**). For instance if there are numerous sets of fractures present, it may be constructive to separate out each individual set, and place scanlines perpendicular to the strikes of the various populations. This technique would provide a quantitative analysis of the fracture frequency and spacing of individual sets. However if the relative fracture frequency and spacing of the bulk rock mass is required a scanline at a random orientation is used. Subsequent scanlines should be set up on rock faces approximately at right angles to the first to minimise orientation sampling bias. It is often useful to position the start of each scanline at a discontinuity. This leads to more accurate fracture spacing determinations.

Scanline sampling is extremely useful in that it provides a fast and efficient way to gather and manipulate fracture data. However, an inherent problem associated with this form of sampling is that large biases are introduced, in particular with respect to the orientation and size of fractures. Section 5.3.3 provides a review of the biases associated with various sampling strategies, and presents ways in which to correct for these discrepancies.

Window Sampling

Conventional window sampling provides a two-dimensional areal analysis of fracture distribution within a specified area of rock (Phal, 1981). In core analyses all fractures are logged within a particular area of core (i.e. every 1m interval). Depth to the centre of each fracture is recorded along with dip and orientation (if the core is oriented), fracture type, length and aperture etc (**Fig. 5.1b**).

At an exposed rock face this technique remains virtually unchanged. Phal (1981) shows that this method principally involves constructing a square (as large as possible to minimise sampling bias) on a clean rock face from measuring tapes (**Fig. 5.2b**). Each side length should intersect between 30 and 100 discontinuities (Priest, 1993). If viable a second or even third window (of equal dimensions) should be set up on adjacent orthogonal faces. Phal (1981) proposed that three classes of fractures should be measured: 1) Fractures which are totally contained in the window (i.e. where both tips

terminate in the window), 2) Fractures which intersect the edge of the window, but still have one trace tip terminating in the window, and 3) Fractures which intersect the edge of the window, and have no ends terminating in the window.

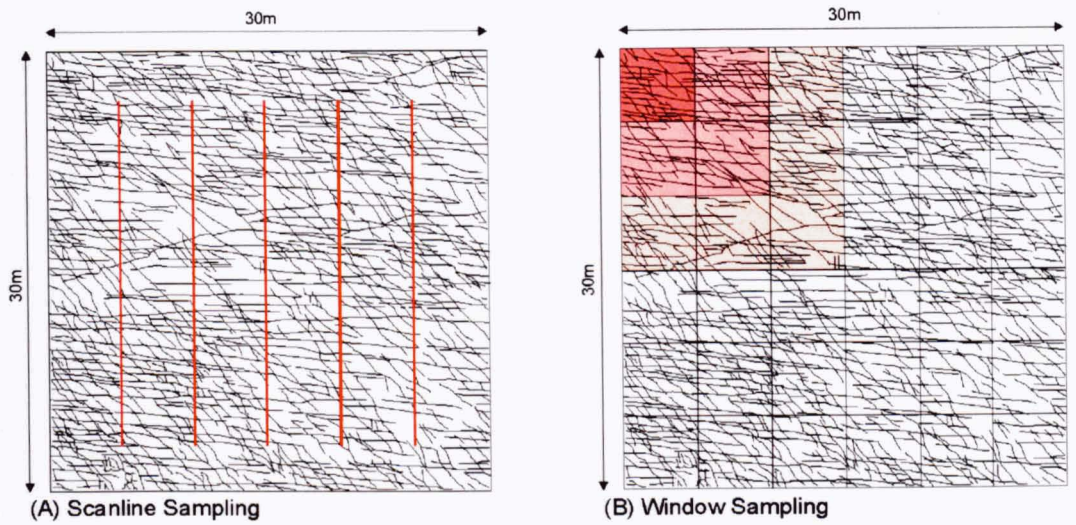

Fig. 5.2. Sampling techniques used in field outcrop analysis. (a) Scanline sampling and, (b) Window sampling on a fractured surface.

This technique has advantages over linear scanline sampling in that it reduces the sampling bias for orientation and size. However, as rock faces are of finite extent a bias is still imposed due to curtailment of fractures (N.B. Curtailment is when the full extent of the fracture is lost due to the limited outcrop extent. Therefore the fracture is assigned a value of the maximum observable length that can be seen). A quicker but less effective approach to this method may be adopted by photographing outcrop faces (photographic window sampling), and then arbitrarily placing sample windows on the images, from which classes of fractures can be analysed. Certain problems with this technique include lack of information on fracture orientation, frequency and surface geometry, and, additionally, distortion caused by perspective

Other novel concepts which have been proposed for sampling fracture populations include ground probing radar, seismo-acoustic holography (Sattarov et al., 1990), laser techniques (Ord & Cheung, 1991), and extended photographic methods (Tsoutrelis et al., 1990) which can estimate fracture orientation, size, spacing and surface geometry. These techniques are beyond the scope of this work and therefore are not discussed.

5.3.2. Natural & Induced Fracture Determination in Core

It is essential when sampling a volume of rock to differentiate between natural and induced fracture systems. A failure to adhere to this rule will lead to biased estimates of

fracture frequency and fracture spacing. The following sets of conditions indicate that associated fractures in core may have been induced naturally:

- Polished and slickenlined fracture faces in well-lithified rock usually are a clear indicator of natural fracture origin (**Fig. 5.3a**). However, polished surfaces, perpendicular to the core axis accompanied by curved slickenlines, can be induced during the coring process (**Fig. 5.4a**).
- Marker bed offsets along faults that have not lost cohesion indicate a natural fracture even though the fault surface in this case is not visible (**Fig. 5.3b**). Such faults may have developed in soft sediments prior to lithification.
- Secondary mineral growths on the walls of fractures clearly indicate that the fractures were naturally induced (**Fig. 5.3c**).
- Scribe grooved fractures and conchoidal chips that originate at the scribe knife and that carve (hook) abruptly into a nearby fracture indicate a natural origin (**Fig. 5.3d**). However, drilling induced fractures that originate before the bit, or any fracture that developed before the scribe, can also show this scribe-chip relationship.
- Natural fracture faces that are parallel or sub-parallel to the core axis may be cut by small conchoidal chips at the fracture-core margin intersection (**Fig. 5.3e**). These chips are located preferentially along the right-hand edge of the fracture face when the face is held toward the observer with the down-core direction pointing downward. The chips are formed by the plucking action of the drill bit rotating clockwise. Drilling induced fractures originating before the bit may also show chipped right-hand margins.
- Planar or curviplanar fractures that do not curve (hook) abruptly toward core margins may have a natural origin. Again, however, drilling induced fractures also may not hook toward core margins (**Fig. 5.3f**).
- Pressure solution features on a fracture surface are a clear indication of an initial fracture that has been subjected subsequently to compression (**Fig. 5.3g**). This indicates a natural origin for such fractures.
- Fracture surface structures (i.e. plume components) that are oversized with respect to the size of the core, as well as plume components that do not show symmetrical correlation with core geometry, are characteristic of natural fractures (**Fig. 5.3h-i**).

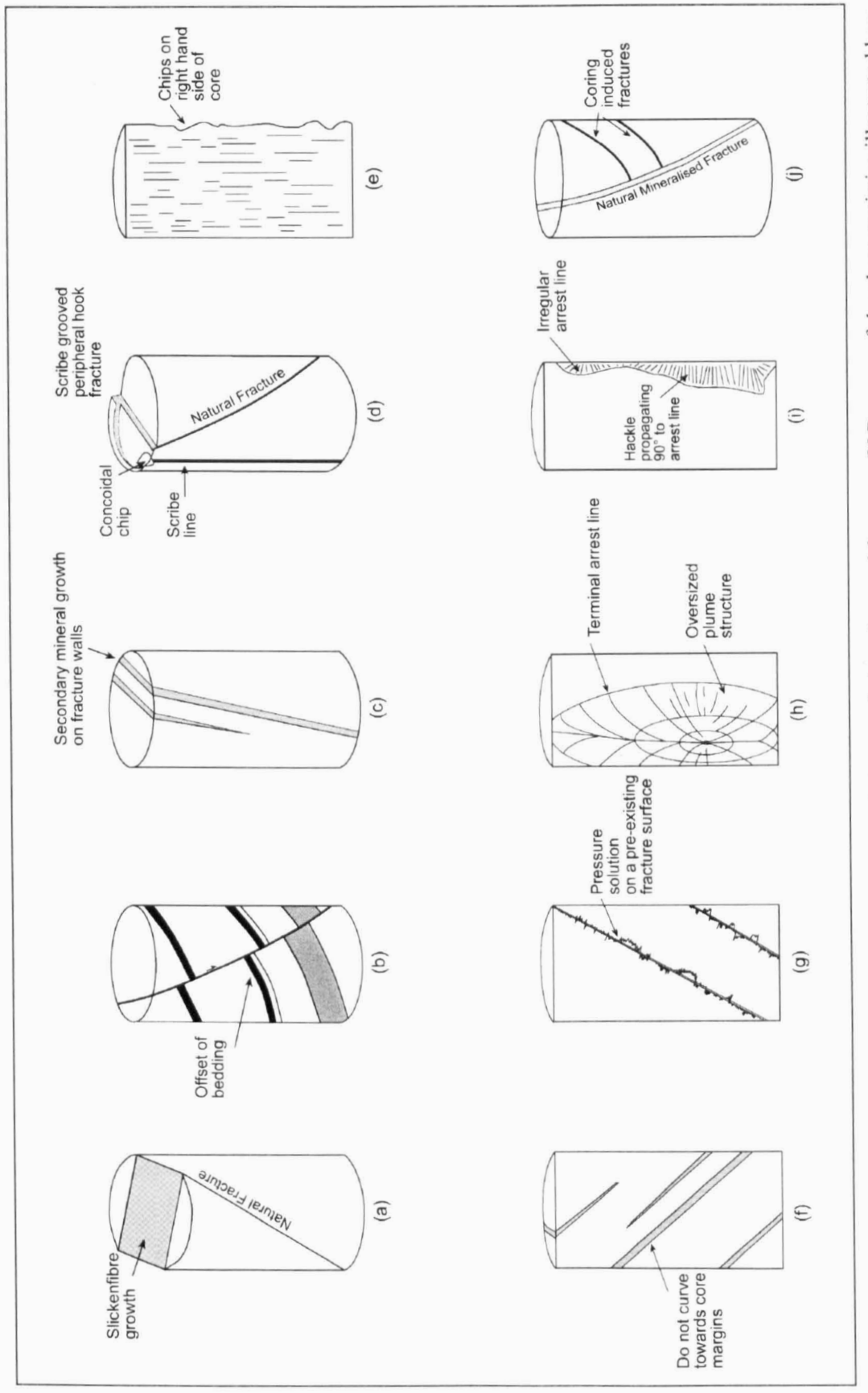

Fig. 5.3. Series of schematic diagrams illustrating the principal characteristics of natural fractures (N.B. some of the characteristics illustrated here can also be indicative of induced fractures (e.g. Fig. 5.3e & f)).

- Natural fractures may be abutted by drilling- or coring-induced fractures, and drilling-induced fractures may be abutted by coring- or handling-induced fractures (**Fig. 5.3j**).

Induced Fracture Determination in Core

The unique characteristics of induced fractures are primarily based upon distinct geometrical relationships between core parameters and fracture surface structures (i.e. plume components), fracture trace morphology and, in some cases, fracture frequency. However, several distinguishing features listed in the following section may be present on both drilling-induced and natural fractures.

Characteristics of Drilling-induced Fractures

- Drilling-induced fractures and surface structures that developed before the advancing bit, and are subsequently captured by coring commonly show unique geometrical relationships with core parameters. For example, plume axes on numerous fractures of the same type have a constant orientation with the core.
- Drilling-induced fracture surfaces commonly show a unique orientation within a core. For example, petal-centreline fractures always curve into the core and propagate downward in the vicinity of the core centre (**Fig. 5.4a**).

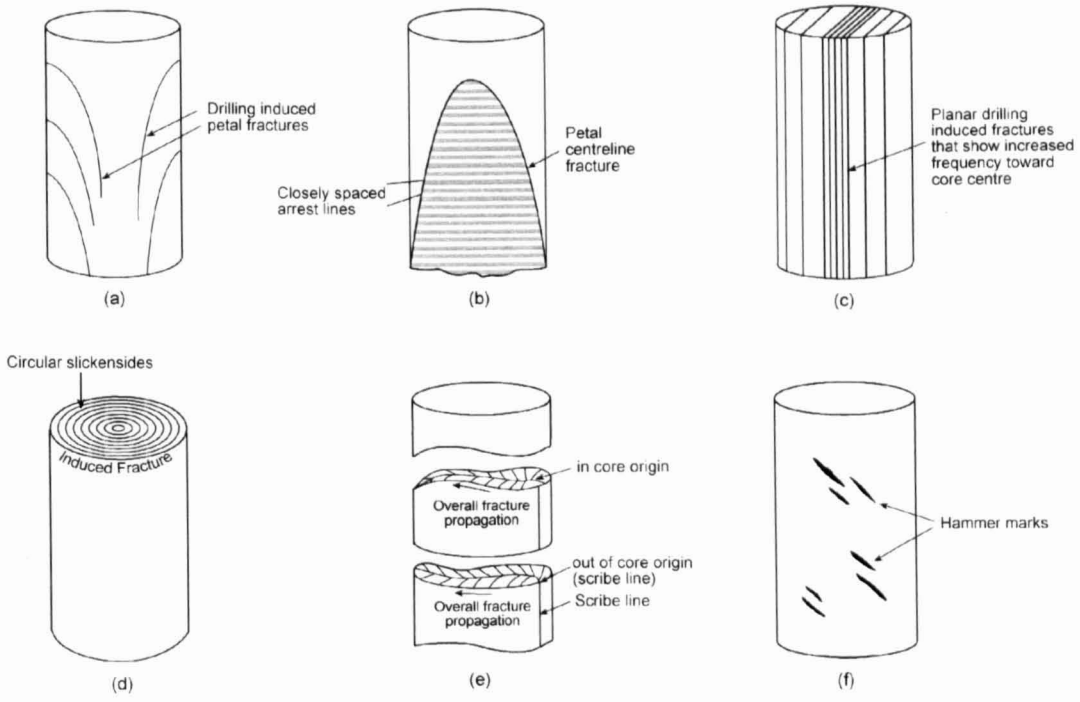

Fig. 5.4. Series of schematic diagrams illustrating the principal characteristics of drilling, coring and handling induced fractures.

- Closely spaced arrest lines that are convex downcore are common on petal-centreline fractures (**Fig. 5.4b**).
- Drilling induced fractures that are closely spaced and sub-parallel to the core axis have an increased frequency toward the core centre (**Fig. 5.4c**).
- Drilling induced fractures may be chipped along their right-hand margin. This is due to the plucking action of the clockwise rotating drill bit. This characteristic, by itself, is not definitive, as natural fractures may also show margin chips (**Fig. 5.3e**).
- Drilling induced fractures will be chipped by passage of the scribe knife, as will any fracture that developed prior to knife passage.
- The cored portion of any drilling induced fracture generally does not contain the fracture origin.

Characteristics of Coring-induced Fractures

- Coring-induced fractures always contain the fracture origin because they are initiated behind the bit.
- Polished surfaces, perpendicular to the core axis, accompanied by curved slickenlines, can be induced during the coring process (**Fig. 5.4d**).
- Hackle plume components on coring-induced fractures curve to meet the core boundary, or a pre-existing fracture surface orthogonally (**Fig. 5.4e**).
- Arrest lines on coring induced fractures curve and attempt to meet the core boundary, or a pre-existing fracture surface tangentially (**Fig. 5.4e**).
- Inclusion or twist hackle may become coarser, and hackle steps may increase uniformly in relief toward core margins or pre-existing fractures.
- Coring-induced fractures may hook abruptly toward the core margin or a pre-existing fracture (**Fig. 5.4j**).

Characteristics of Handling-induced Fractures

- An origin location is present on all handling-induced fractures. However, origins may be obscure, especially on fractures cutting coarse-grained rock.
- Hammer marks on the surface of the core at or near the fracture origin strongly suggest an induced fracture. Hackle traces typically radiate from these hammer marks (**Fig. 5.4f**).

- A fracture lacking any drilling mud on its surface suggests that the fracture formed sometime after the coring process. Although the mud can be washed from a core, seldom is it cleaned sufficiently that no mud remains on the fracture surface.
- Overly damaged core stored in new boxes may indicate rough handling at some point in the core's history.
- Handling induced desiccation fractures show a distinct symmetry to core margins, and the largest fracture bounded core segment is commonly at the core centre.

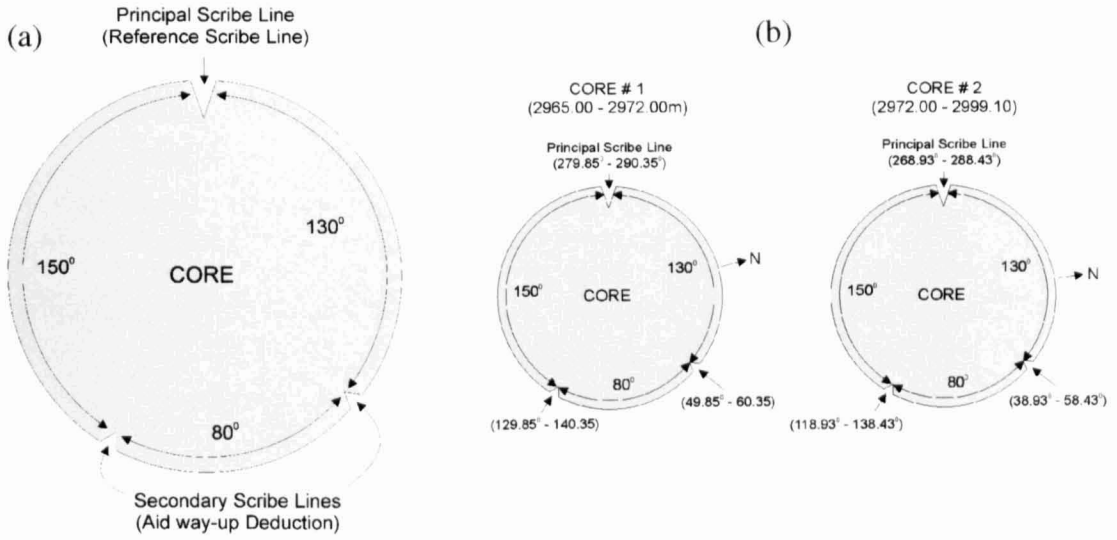

Fig. 5.5. (a) Plan view showing the angular configuration of principal and secondary scribe lines on an oriented core. (b) Scribe line data for Cores 1 and 2 in Hasdrubal –4 (N.B. these values have been corrected for declination (magnetic to true = 0.71).

5.3.3. Oriented Core Analysis

Orientation data from cores is invaluable in fractured reservoir evaluation. An oriented core generally has three distinct grooves (or scribe lines) on its surface, which run down the length of the core (**Fig. 5.5a**). The deepest groove, which is known as the Principal Scribe Line is used as a reference, whilst the two other shallower grooves (termed Secondary Scribe Lines) aid way-up deduction of the core. The standard angular configuration of scribe lines on oriented core is shown in **Figure 5.5a**. Apparent fracture orientation measurements are taken with reference to the Principal Scribe Line (of which the precise orientation is known). Thereafter, true fracture orientations can be calculated. The dip of discontinuities within oriented core can also be taken, but may need to be corrected for any deviation of the well about the vertical. **Figure 5.5b** gives an example of scribe line data for cores 1 and 2 in Hasdrubal -4.

5.3.4. Structural Terminology

As a consequence of the numerous and confusing classification schemes used in the literature to define structural features, it has been necessary to adopt one particular classification scheme in this study (Table 5.2).

Terminology	Definition
Natural Fracture	A fracture that has been formed by compactional or tectonic processes.
Induced Fracture	A fracture that has been induced through coring and/or handling.
Mode I Fracture	A discrete break within a rock mass that exhibits opening displacements.
Mode II Fracture	A discrete break within a rock mass which exhibits shearing displacements.
Mode III Fracture	A discrete break in a rock mass which exhibits both opening & shearing.
Compactional Stylolite	A pressure solution seam that formed by compactional processes.
Tectonic Stylolite	A pressure solution seam that formed by tectonic processes.

Table 5.2. Structural terminology used in the report

5.3.5. Sampling Bias in Linear (1D) Scanline Surveys

Orientation Correction: 'Terzaghi Correction'

Although the linear sampling regime of the scanline survey produces an objective sampling strategy in core and at outcrop it does introduce an orientation sampling bias (Terzaghi, 1965; La Point & Hudson, 1985). **Figure 5.6** shows the influence of scanline orientation on fracture frequency, where three scanlines of different orientation are shown traversing a single set of parallel fracture traces.

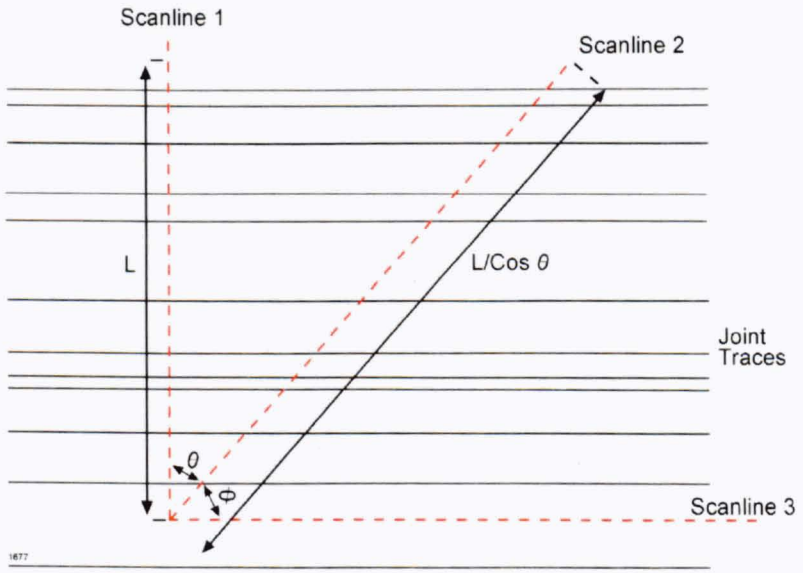

Fig. 5.6. Scanlines through a single set of persistent, parallel joints. Maximum frequency is encountered along scanline 1; a lower value will be intersected along scanline 2; and the lowest value of zero will be found along scanline 3 (from La Point & Hudson, 1985).

Clearly, maximum frequency is encountered along scanline 1, normal to the fracture traces; a lower value will be intersected along scanline 2, at an angle θ to scanline 1; and the lowest value of zero will be found along scanline 3, parallel to the joint set. Statistical techniques are routinely used to correct for this sampling bias, the most common being the geometrical correction which is based on the observed angle between the sampling line and the normal to a particular fracture (Terzaghi, 1965) (**Fig. 5.6b**).

Consider a single planar fracture with a normal of trend/plunge α_n/β_n and a surface area A. The probability, P_s, that a randomly located long scanline of trend/plunge α_s/β_s will intersect, and therefore sample, this fracture is directly proportional to the area, A, of the fracture projected on to a plane normal to the scanline direction. Hence,

$$P_s \propto A_s \tag{5.1}$$

But,
$$A_s = A\cos\delta \tag{5.2}$$

Where δ is the acute angle between the fracture normal and the sampling line, so that,

$$P_s \propto A\cos\delta \tag{5.3}$$

The angle δ can be determined either graphically from a hemispherical projection, by vector algebra methods or from the following expression,

$$\cos\delta = |\cos(\alpha_n - \alpha_s)\cos\beta_n\cos\beta_s + \sin\beta_n\sin\beta_s| \tag{5.4}$$

The absolute value function in Equation 5.4 ensures that the angle δ is always acute; this property is important in subsequent analysis. The highest probability of intersection, P_{sm}, occurs when $\delta = 0$ and $A_s = A$. The lowest probability of intersection is zero; this occurs when $\delta = 90^0$ and $A_s = 0$. Any scanline sample will, therefore be biased to contain a lower proportion of those fractures that happen to have a higher value of δ. This reduced proportion can be expressed by the ratio:

$$\frac{P_s}{P_{sm}} = \cos\delta \tag{5.5}$$

This reduced sample size at the higher values of δ can be compensated for by assigning a higher weighting to those fractures that are sampled. A fracture with a normal trend/plunge, α_n/β_n sampled by a scanline of trend/plunge α_s/β_s is assigned a weighting w given by,

$$w = \frac{1}{\cos\delta} \qquad \delta < 90^0 \qquad (5.6)$$

For a large sample size this weighting will serve to balance the orientation sampling bias introduced by linear sampling. However, when δ approaches 90^0, w becomes very large, to the extent that a single data point could dominate the distribution pattern. In such cases, great care must be exercised when interpreting data.

Although valid in some cases, a principal limitation with the Terzaghi correction is that it assumes an equal distribution of fractures in a rock mass. This however, is unrealistic in most geological cases, particularly in the case of faults, which show natural clustering (Cowie et al., 1993). La Pointe & Hudson (1985) have since suggested using geostatistical variogram analyses to allow for inhomogeneous fracture patterns.

It will become evident in later discussions that the sampling bias discussed here is a major factor in the determination of fracture frequency and spacing estimates within the Hasdrubal and Miskar reservoirs. This is due to the fact that the core axis (i.e. the 1D scanline) is sub-parallel to the majority of fractures present in the respective reservoir intervals. Probabilistic and algebraic methods to resolve this problem are discussed in section 5.4.3.

Trace Length Correction

One method of measuring fracture trace lengths is to follow a fracture in both directions from its intersection with a scanline. The total length measured (i.e. the sum of the two 'semi-trace' lengths) is the length of that particular fracture trace. From the measurements of all such fractures that intersect a scanline, a histogram can be compiled to indicate their statistical length distribution. This technique is directly valid in homogeneous systems where fracture length remains constant. However, more often than not, fracture trace lengths vary within a given sample area (La Point & Hudson, 1985). Consequently, a scanline passing through a single inhomogeneous fracture set is more likely to intersect longer fractures, thus introducing a trace length bias into the measured distribution. Priest & Hudson (1981) show that the relation between the observed distribution of trace lengths $g(l)$, along the scanline and the expected distribution of trace lengths, $f(l)$, in the array is given as,

$$g(l) = \frac{lf(l)}{\bar{l}} \qquad (5.7)$$

where $g(l)$ and $f(l)$ are probability density functions. l is the observed trace length, and $\bar{l}$ is the unbiased mean trace length.

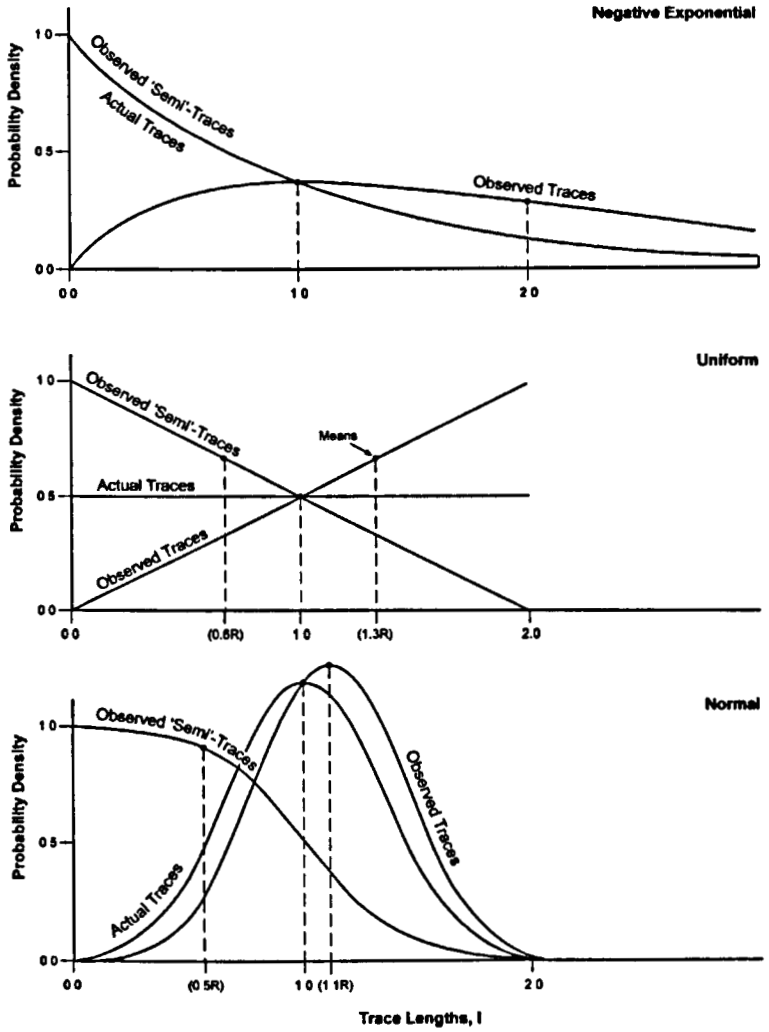

Fig. 5.7. Effect of trace length bias caused by scanline sampling (refer to text for details) (from La Pointe & Hudson, 1985).

Figure 5.7 illustrates the effect of trace length bias caused by scanline sampling, where the relationship given in Equation 5.7 has been plotted for three illustrative distributions of trace length. In all cases, the observed traces have a higher density of longer trace lengths. For more detailed reviews of the effects of censored trace length measurements the reader is referred to Priest & Hudson (1981).

5.3.6. Sampling & Interpretation of Image Logs

Tools & Processing Procedures

Image logs from the Circumferential Acoustic Scanning Tool (CAST) and the Formation Micro-Scanner (FMS) were utilised in this study for the Hasdrubal -2 and -3

wells respectively. These tools use different techniques to provide high resolution images of the borehole wall within a reservoir zone.

- Circumferential Acoustic Scanning Tool (CAST) (**Fig. 5.8a**): The Circumferential Acoustic Scanning Tool (CAST) is an ultrasonic acoustic televiewer that records variations in acoustic impedance (amplitude) and borehole size (transit time) (Halliburton, 1995). It provides a 360^0 coverage of the borehole wall. The transducer in the sonde revolves at several hundred revolutions per minute, each time recording 200 acoustic echoes of the borehole wall. The resolution of this tool is not as good as that of the Formation Micro-Scanner; ca. 3 cm for most structural features. However, unlike the FMS tool, it can be used in oil-based muds.

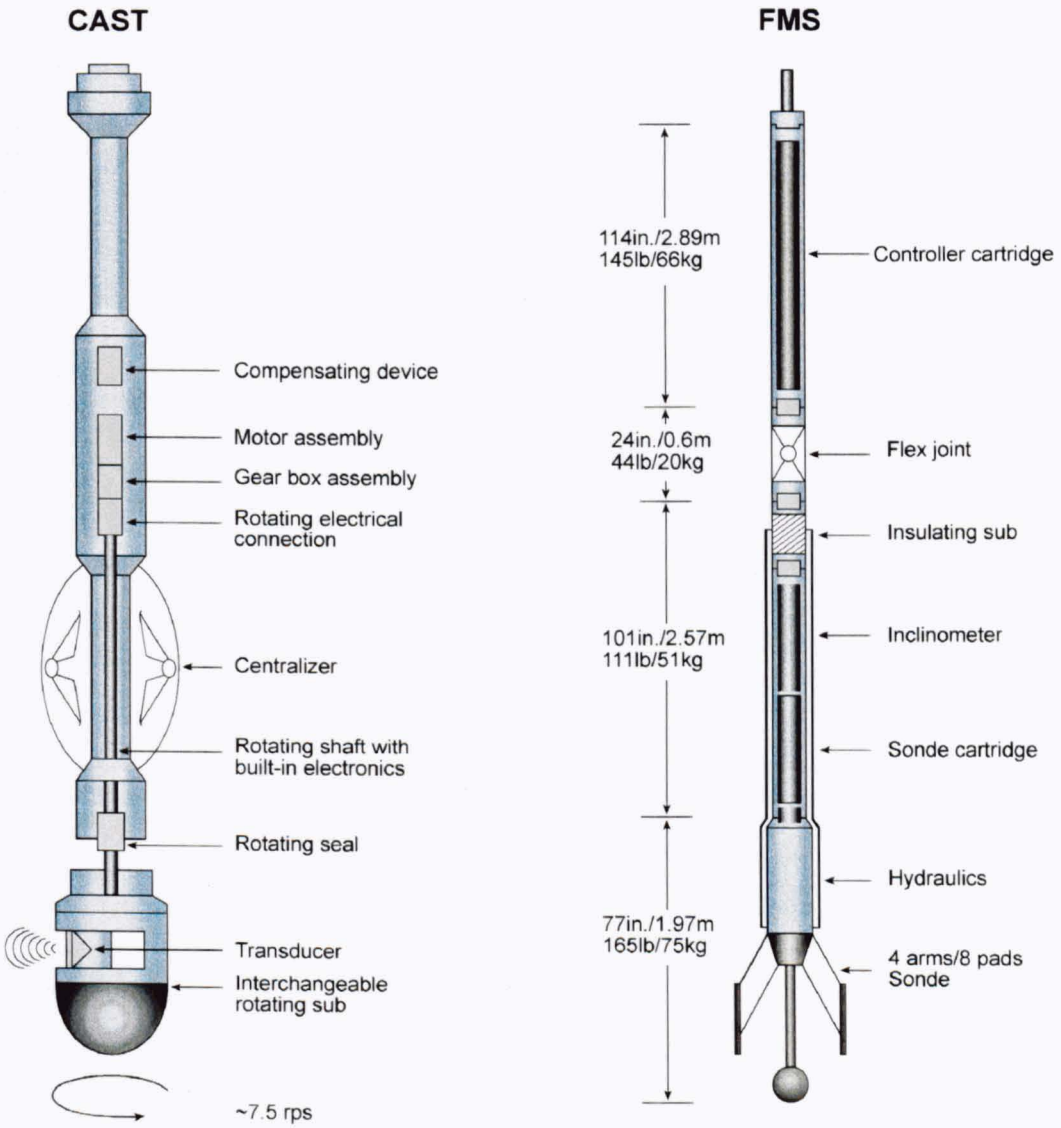

Fig. 5.8. CAST and FMS image logging tools (from Halliburton and Schlumberger brochures, 1995 & 1999 respectively).

- Formation Micro-Scanner (FMS) (**Fig. 5.8b**): Formation Micro-Scanner data from Hasdrubal -3 was acquired using a Formation Micro-Imager tool in pad only mode. This is standard procedure in regions where a full suite of downhole tools is not available to the logging company. The Formation Micro-Imager (FMI) is a micro-resistivity imaging device with an array of 24 measuring electrodes on each of four orthogonal pads, with similar arrays on laterally offset flaps attached to each pad. The electrodes are 0.2 inch in diameter and are spaced in two rows 0.15 inch apart, giving resistivity traces with a very high lateral and vertical sampling (0.15 inch vertical, 0.15 inch lateral sampling). Structural resolution is generally moderate to good but depends on the resistivity contrast (bedding resolution can be ca. 1 cm, whereas fracture resolution can be on the sub mm scale). The main limitation with the device is that it cannot be used in oil-based muds, due to the poor signal in high resistivity zones (e.g. oil or gas saturated reservoir intervals).

CAST data from Hasdrubal -2 required no pre-processing. However, FMI data from Hasdrubal -3 required magnetic declination correction (0.54^0 E), accelerometer-based speed correction and depth matching to openhole logs (e.g. gamma ray log). Once these procedures had been completed normal and dynamic normalised, false colour images were generated and interpreted.

Interpretation Procedures

Z&S Recall software was used in this study to manually pick structural features. The main advantage of this manual pick technique is that each feature may be classified into a category (e.g. bedding, fractures, stylolites etc.), and that only the results in which the interpreter has confidence are used for structural interpretation. Another advantage of manual dip picking is the ability to measure and orient discordant surfaces such as fractures and faults, which are unlikely to be generated by standard interval correlation techniques. In this study, interpretation focussed on structural dip determination, fault and fracture characterisation and in-situ stress determination

Structural Dip Determination

Structural dip is best identified from well-bedded intervals, which are assumed to be originally horizontally stratified (i.e. shales and parallel-bedded sandstones or carbonates) (**Fig. 5.9a**). In Hasdrubal -2 and -3, structural dip was examined using vertical dip trend analysis and by carrying out statistical analysis of stereoplots.

Fracture Characterisation

The CAST and FMS tools image fractures in the borehole wall when an acoustic or electrical contrast exists between fracture fill and the wallrock (**Fig. 5.9b**). The maximum resolution of the tools vary with contrast in rock properties, fracture width and the intrinsic controls set by the sampling rate and logging speed. Fractures identified from CAST and FMI images should always be calibrated to core observations wherever possible.

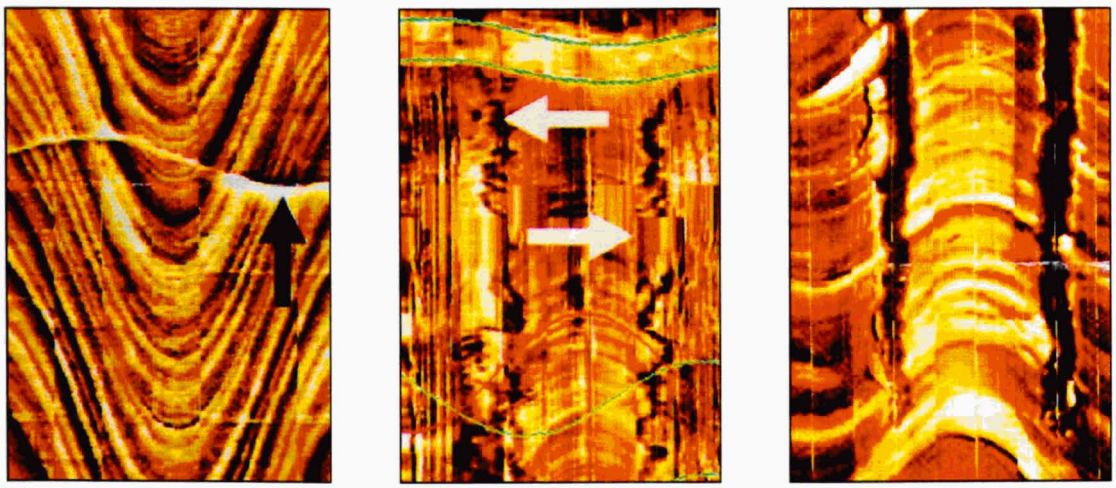

Fig. 5.9. Acoustic and resistivity borehole images. (a) Well bedded sandstone-shale sequence cut by a resistive fracture (shallow sinusoid), (b) Resistive fracture (interpreted in green) cross cutting bedding (interpreted in red) and (c) Borehole breakout shown by vertical dark patches on opposite sides of the borehole (from Lofts & Bourke, 1999).

Borehole Breakouts & Induced Fractures: In-Situ Stress Determination

Boreholes are subjected to in-situ gravitational, tectonic and residual stresses. In most cases, the axis of the highest stress magnitude is the overburden stress (σ_V), and two further principal stress axes lie in a horizontal plane (σ_h and σ_H), their relative orientations and magnitudes relating to present-day or residual tectonic stress fields. In-situ stresses are balanced prior to drilling as rock grains and cement provide a reactive force against compression. However, drilling of a borehole generates a free surface that focuses stresses into its vicinity and may cause borehole breakout and/or induced tensile fractures. The orientation of these features and an understanding of the susceptibility of their host rock to each mode of failure allows the orientation and relative magnitude of present-day in-situ stresses to be assessed (Barton et al., 1997).

Borehole breakouts are recognised from image logs as vertical dark (acoustic: low amplitude, high transit time; resistivity: conductive, defocused) patches, commonly

occurring on the opposite sides of the borehole (**Fig. 5.9c**). They develop if the boundary tangential stresses exceed the effective strength of the rock, causing localised compressive shear fracturing of the borehole wall in the direction of the least compressive stress (σ_h) (**Fig 5.10a**). Drilling-induced tensile fractures are recognised from borehole images as regular arrays of fractures (acoustic: low amplitude, high transit time; resistivity: conductive) on opposite sides of the borehole wall (**Fig. 5.9b-c**). They develop when mud pressures within the borehole exceed the tensile strength of the borehole wall and propagate in the direction of the maximum horizontal stress (σ_H) (**Fig. 5.10b**).

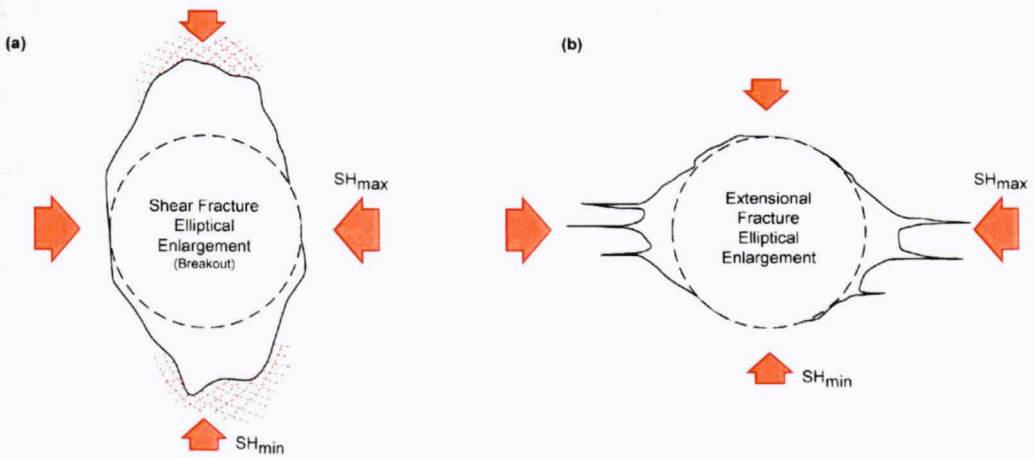

Fig. 5.10. Schematic diagram showing a plan view a well-bore. The orientation of borehole elongation relative to the directions of the principal horizontal stresses is shown for (a) borehole breakout and (b) induced fracture generation (from Mc Phail, 1995).

Constraints on Image log Interpretation: Artefacts

It is essential to differentiate between natural fractures, induced fractured and artefacts (that are associated with the CAST and FMS image logs) prior to any quantitative analysis. Common artefacts include 1) vertical and spiral banding (CAST), 2) vertical stripes (tool marks) created in soft rock zones or where there is a thick mudcake (CAST) and tool stick and pull affects (FMS). For a more detailed review of the various artefacts caused by acoustic and resistivity borehole imaging devices the reader is referred to Lofts & Bourke (1999).

5.4. Data Analysis & Presentation

Information from core and outcrop provided the principal data source for statistical analysis. The utility of studies of image log interpretations from Hasdrubal -2 and -3

was partially constrained by the inadequate resolution of structural features on processed images. As a consequence, these data were mainly used to validate and QC the core interpretation, together with providing information on the present day stress field (i.e. from borehole breakout and induced fracture development). Statistical analyses were undertaken to provide information on 1) Fracture orientation, 2) Fracture Length and Height, 3) Fracture frequency and 4) Fracture spacing.

5.4.1. Fracture Orientation

One of simplest forms of graphical representation of fracture orientation is the rose diagram (Attewell & Farmer, 1976) (**Fig. 5.11a**).

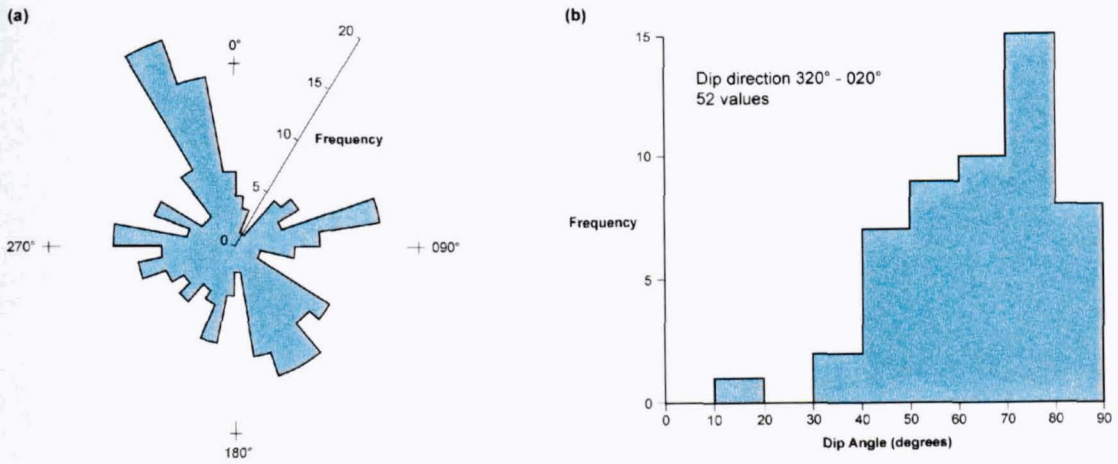

Fig. 5.11. (a) Rose diagram for fracture dip direction, (b) Histogram of fracture dip angle for the same dataset (from Priest, 1993).

This approach is particularly suited to cases where most of the fractures have angles of dip in excess of about 60^0. In such cases dip direction data are of primary significance and can be plotted on a circular histogram divided into convenient class intervals (e.g. 5^0, 10^0, 15^0) depending on the sample size. The results are plotted as wedges that have a radial extent that is proportional to the frequency in each class interval. This frequency can be expressed either as a raw number, as a proportion or as a percentage of the total sample size. The disadvantage of rose diagrams however, is that they contain no information on dip angle. This can be overcome to some extent by plotting a dip histogram of dip angle (**Fig. 5.11b**).

Stereographic or hemispherical projection methods form the basis of representing three-dimensional orientation data in two dimensions. The basic principal of hemispherical projection is that the orientation of a line in three-dimensional space is

uniquely represented by the position of a point within a circular projection of radius R (**Fig. 5.12**).

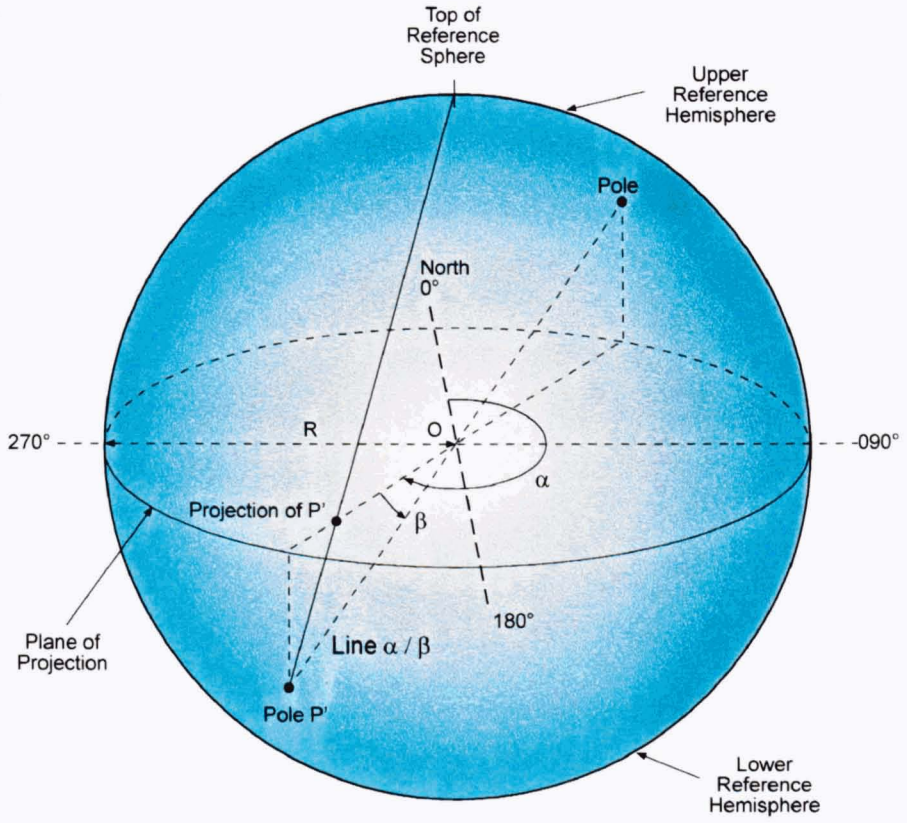

Fig. 5.12. Diagram illustrating the principal of hemispherical projection techniques. The reference sphere intersected by a line α and plunge β to define the point (or pole) P' and it's projection (from Priest, 1993).

The perimeter of this projection area is associated with the circle of geographical azimuth directions as that the radius on which the point plots is given directly by the trend direction, α, of the line that it represents. The radial distance, r, of the point from the centre of the projection circle is a function of the plunge, β, of the line that it represents, subject to the boundary conditions that r = 0 when $\beta = 90^0$ and r = R when β = 0. The form of the functional relation between r and β depends on the projection method adopted. Two of the most common projection methods utilise an imaginary hemisphere of radius R positioned below the plane of projection so that its circular face forms the projection circle. The first of these methods termed the lower hemisphere equal angle projection, gives rise to the following relation between r and β

$$r = R \tan \frac{90^0 - \beta}{2} \qquad (5.8)$$

The second method, termed the lower hemisphere equal area projection gives the following relation,

$$r = R\sqrt{2}\cos\frac{90^0 + \beta}{2} \tag{5.9}$$

A full discussion of the properties and relative merits of these two methods of projection is given by Priest (1993).

5.4.2. Fracture Length & Height

Fracture length populations are plotted as normalised cumulative frequency distributions, $N(l)$ (number of fractures with length greater or equal to length, l, per square kilometre). When logarithmic axes are used, a straight line indicates that the length distribution is power-law with an exponent, a, given by the slope of the graph,

$$N(l) \alpha l^{-a}$$

Power-law length distributions are often referred to as 'self-similar' and their exponents as 'fractal dimensions' (**Fig. 5.13**). Odling et al. (1999) define self-similar systems as those systems where visualisations at different scales are indistinguishable. Given a random set of lines in two-dimensional space, self-similarity is possible when the cumulative length distribution exponent, $a = 2$. When the exponent, a, is different from 2.0, the length populations lack either short fractures ($a < 2$) or long fractures ($a > 2$).

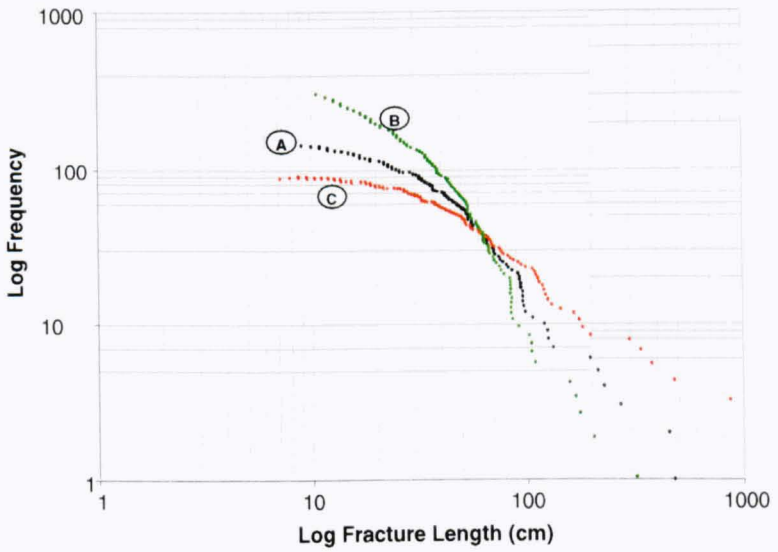

Fig. 5.13. Schematic plot showing the cumulative frequency distribution of fracture length for three examples. The length distributions of the fractures in each example show a straight line segment indicative of a power-law distribution. (A) shows a power-law distribution with an exponent of 2.0, (B) shows a power-law distribution with an exponent that is greater than 2.0, and (C) shows a power-law distribution with an exponent that is less than 2.0.

5.4.3. Fracture Frequency

Fracture frequency is one of the most fundamental measures of the degree of fracturing within a rock mass. Frequency can be expressed in terms of the number of fractures that are observed or predicted to occur in a unit volume, a unit area or a unit length of a sample from a given rock mass.

Linear Frequency

The simplest and most commonly used measure of fracture frequency is the linear frequency λ defined as the average number of fractures intersected by a unit length of sampling line. Linear frequency can be applied to all fractures or to a single set. It has already been shown that if the linear frequency along a line constructed normal to a set of parallel planar fractures is λ, then the observed frequency λ_s along a sampling line that makes an acute angle δ to the set normal is given by,

$$\lambda_s = \lambda \cos\delta \tag{5.10}$$

It is necessary to stipulate that the angle δ is acute since λ_s must always be positive. If there are D parallel planar fracture sets, the total frequency λ_s along the sampling line is given by the sum of the frequency components as follows.

$$\lambda_s = \sum_{i=1}^{D} \lambda_i \cos\delta_i \qquad \left(-90^0 \le \delta_i \le 90^0\right) \tag{5.11}$$

where δ_i is the acute angle between the sampling line and the normal to the ith set, λ_i is the frequency along the normal to the ith fracture set. If the sampling line has a trend α_s and a plunge β_s, and the mean normal to the ith fracture set has a trend α_{ni} and plunge β_{ni} then using Equation 5.4 without taking the absolute value,

$$\cos\delta_i = \cos(\alpha_s - \alpha_{ni})\cos\beta_s \cos\beta_{ni} + \sin\beta_s \sin\beta_{ni} \tag{5.12}$$

Fracture frequency data is generally expressed graphically on various types of histogram. In this dissertation different frequency histograms are used to show fracture intensity variations with depth (in the cored intervals in Hasdrubal and Miskar), and proximity to seismic and sub-seismic scale faults at outcrop . It is important to mention however, that many difficulties are associated with predicting fracture frequency and spacing in the Hasdrubal and Miskar reservoirs. These difficulties are due to the nature of sampling, whereby the core axis in most wells is sub-parallel to dominant fracture system. Consequently, as previously discussed (Section 5.3.3) large orientation biases

are introduced into fracture distributions, to the extent that use of the Terzaghi correction factor becomes limited and even obsolete. Alternative methods to determine fracture intensity in such cases are discussed in detail in the following section.

5.4.4. Fracture Spacing

Fracture spacing is defined as the distance between a pair of fractures measured along a line of specified location and orientation. It is linked to the reciprocal of fracture frequency,

$$\text{Spacing } (S) = \frac{1}{\lambda} \tag{5.13}$$

At outcrop, fracture spacing within a given rock mass can be quantified without too much difficulty, due to the relative control on scanline positioning (i.e. preferentially oriented perpendicular to fracturing). This is the case also in near-surface civil engineering projects (e.g. tunnels, shafts, dams, etc.) where boreholes of various angular relationships with respect to the fractures are relatively common (Priest, 1993) **(Fig. 5.14a)**.

In the deep subsurface, however, where boreholes are more often than not parallel or sub-parallel to subsurface fracture sets, this technique encounters difficulties related to the introduction of the orientation sampling bias previously discussed (Section 5.3.3) **(Fig. 5.14b)**. In such cases where the borehole is at a small angle to the plane of a particular fracture set (e.g. Hasdrubal and Miskar) the application of the Terzaghi correction factor (to alleviate the problem) becomes inadequate (Lacazette, 1991; Lorenz & Hill, 1994; Narr, 1996). As a consequence, new methods have had to be devised to determine sub-surface fracture intensity. The following account provides a review of the alternative methods to determine fracture spacing in such systems, and describes in detail the most appropriate technique for calculating fracture spacing in the Hasdrubal and Miskar Accumulations.

Probabilistic Methods

An alternative method to the scanline approach has been developed based on the probabilities of borehole fracture intersections, and is designed for use with data from deep wells. This approach differs from 1D (one-dimensional) scanline methods in that it treats core as a true 3D sample of rock (Narr, 1996). The methods usefulness is not restricted by the orientation-dependent limitations that affect scanline interpretations.

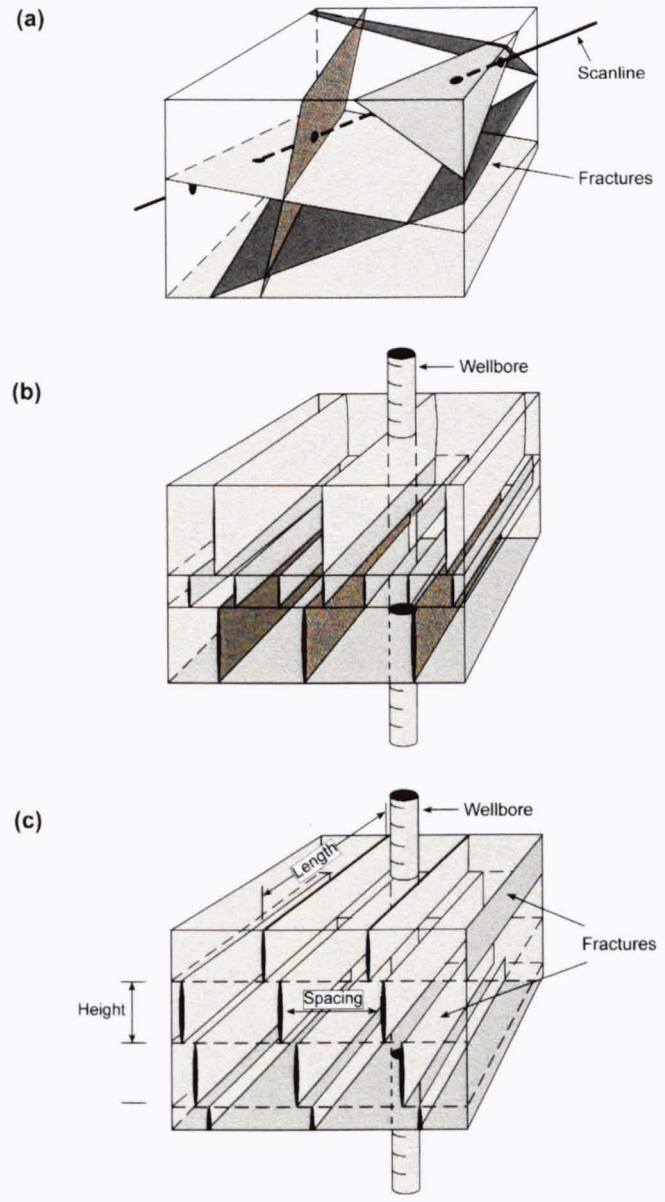

Fig. 5.14. Models of subsurface fracture systems and their interaction with boreholes. (a) Scanline passing through randomly oriented fractures, (b) Borehole of finite diameter passing through mechanically layered strata where fracture spacing is proportional to layer thickness and (c) Borehole of finite diameter passing through rock volume with set of uniformly distributed fractures having equal spacing and height (from Narr, 1996).

The geological model used within the probabilistic method outlined below views subsurface fracture systems as the buried equivalents of the joint systems common to outcrop (Narr & Lerche, 1984; Lerche & Narr, 1986; Aguilera, 1988; Narr, 1991). This equivalence is widely recognised (Drummond, 1964; Narr & Currie, 1982; Narr & Lerche, 1984; Nelson, 1985; Lorenz et al., 1991). These subsurface fracture or 'joint' systems are thus classified (for the purpose of this model) as sets of systematically spaced, parallel, bedding-normal discontinuities which exhibit little or no offset (Narr & Lerche, 1984).

Fracture Spacing Index (FSI) Methodology

The Fracture Spacing Index (FSI) methodology of Narr & Lerche (1984) and Narr (1991) is based on the theory that where mechanical layering is well developed (as in a stratigraphic succession with layers of different mechanical strengths), the spacing of fractures is directly proportional to layer thickness (Ladiera & Price, 1981; Narr & Lerche, 1984; Huang & Angelier, 1989; Narr, 1991) (**Fig. 5.14b**). From this empirical relationship, it is therefore possible to use data on bed thickness and 'joint-like' fracture incidence in core to compute the density of fractures for a series of beds in which other geological factors (i.e. lithology, structural position etc.) are relatively invariant. The method therefore expresses the density of fractures as the ratio of fractured-layer thickness $(T)^3$ to median fracture spacing (S), which is known as the Fracture-Spacing Index (FSI):

$$FSI = \frac{T}{S} \tag{5.14}$$

The probabilistic FSI approach has proved to be a useful analytical tool for predicting fracture densities in certain geological scenarios. However it has got several drawbacks, most notably, that not every stratigraphic sequence exhibits a spacing-thickness relationship (Ladiera & Price, 1981; Hanks et al., 1994). In addition, the FSI methodology relates to the presence of mechanical inter-stratification. However, if strata are thick bedded or massive, they may lack mechanical contrast across great thickness, or have highly variable mechanical surfaces, such as stylolites. In such situations the FSI method cannot be used.

The FSI method may also be difficult to apply even where it is appropriate because of the imperative it places on accurately interpreting mechanical layer boundaries in core. Recognising mechanical layer boundaries in core requires great care. Contemporary wireline logs are no substitute for core in identifying mechanical layer boundaries. If cores are unavailable, the FSI method cannot be accurately used.

Algebraic Methods

Average Fracture Spacing (AFS) Methodology

As a consequence of the problems encountered in using the FSI method, Narr (1996) subsequently proposed a new approach to eradicate the previous uncertainties. This new technique was termed the 'average fracture spacing' method (AFS). The method

treats borehole data as a true 3D sample of the reservoir (as does the FSI method). However, the AFS method relaxes several constraints specific to the FSI method, most notably that it requires no assumptions about fracture spacing-layer thickness relationships. It can therefore be used in lithologies that contain no well-developed mechanical layering. Moreover, it is easily used with conventional quantitative core descriptions and borehole imaging logs.

This technique proves to be particularly useful in examining subsurface fracture spacing in both Hasdrubal and Miskar, where most of the fractures identified in the cores are sub-parallel/parallel to the core axis, and where the differentiation of individual mechanical layers is particularly difficult.

Geological Model

The method presented by Narr (1996) uses the average height of fractures and their frequency of incidence, as measured in core or wireline image logs, to estimate the average spacing of fractures. It should be emphasised that, like the FSI approach, this model is dependant on the fact that subsurface fracture systems modelled have the fundamental characteristics of joints (i.e. fractures occur in an array with parallel fractures to form a set, fractures are perpendicular to bedding). The presence of mechanical boundaries is unimportant in this model.

The core or image log is assumed to contain a representative sampling of fractures. If more than one fracture set is present, then each set must be must be evaluated separately. Generally, average fracture spacing should be evaluated separately for each lithology in a well.

Mathematical Model

The basis of the Average Fracture Spacing (AFS) method is to equate fracture porosity measured in core with fracture porosity defined for the reservoir, which leads to average fracture spacing. Fracture porosity ϕ_f in core is:

$$\phi_f = \frac{Void\ space\ in\ fractures}{Total\ core\ volume}$$

$$\phi_f = \frac{\sum_{i=1}^{n} A_i H_i L_i}{W_c H_c L_c} \qquad (5.15)$$

where A_i = aperture, H_i = height, L_i = length of fractures contained in the core, n is the total number of fractures in the core, W_c = width, H_c = height, and L_c = length of the core (**Fig. 5.15**). Core width W_c is the diameter perpendicular to the fracture planes. Height H_c is the long dimension, measured parallel to the core axis, which is the dimension conventionally referred to as length. Length L_c is the core diameter parallel to the fractures. It is assumed that because fractures are long relative to the core diameter, the length of any fracture sampled by the core will almost certainly be at least as long as the core diameter; therefore, within the volume of the core we assume that $L_i = L_c$. This allows the cancellation of the length dimensions in Equation 5.15.

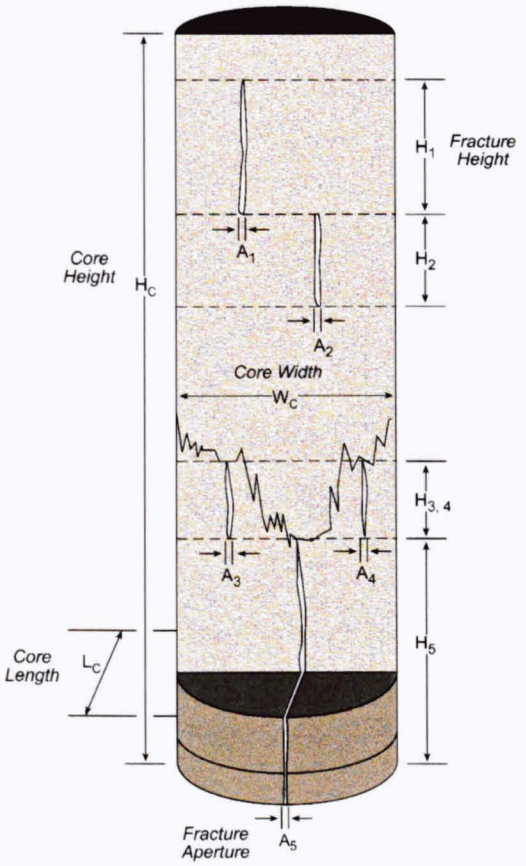

Fig. 5.15. Schematic diagram of fractured core, lacking regular, mechanically significant layering (from Narr, 1996).

It is important to clarify that although an actual subsurface fracture set might be similar to that shown in **Figure 5.14**, the AFS methodology considers a model in which fractures are described by their average spacing, S_{av}, average fracture height, H_{av}, average fracture length, L_{av}, and average aperture, A_{av} (**Fig. 5.15**). Within a finite volume of subsurface reservoir of height, H_r, width, W_r, and Length, L_r, containing n_f fractures (**Fig. 5.16**), fracture porosity is,

$$\phi_f = \frac{Void\ space\ in\ fractures}{Total\ core\ volume}$$

$$\phi_f = \frac{n_f A_{av} H_{av} L_{av}}{W_r H_r L_r} \tag{5.16}$$

If it assumed that fracture length is greater than the length of the selected reservoir volume, then the length terms cancel (an alternative way to think of fracture length is that individual fractures may be of less length than L_r, but as any individual fracture terminates in the length direction, a different fracture within the rock volume is terminating from the opposite direction, so that along any line normal to the fractures in the volume, the fracture porosity is constant).

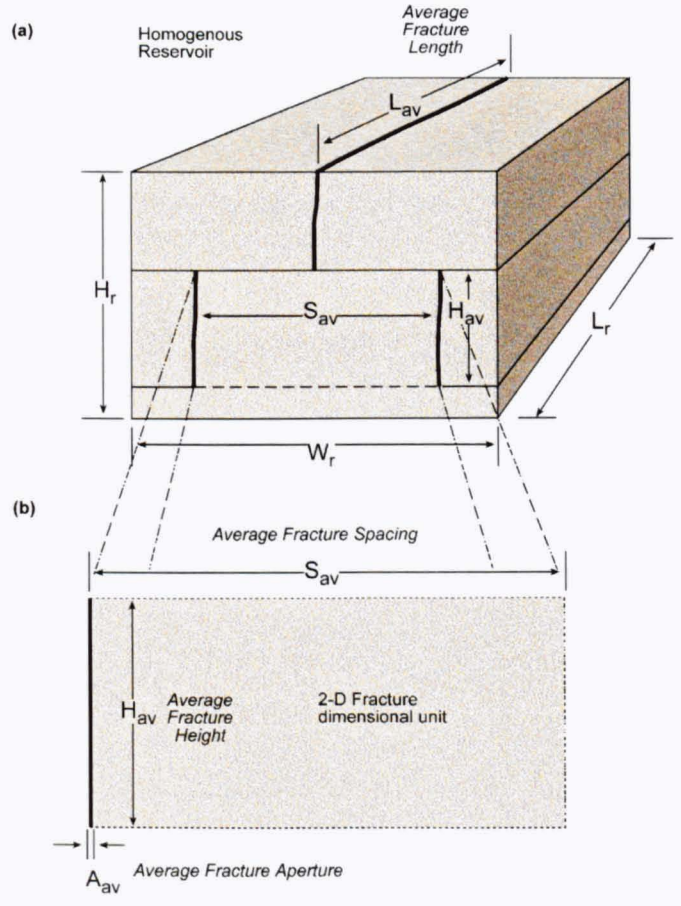

Fig. 5.16. Spatial and dimensional relationships that relate fracture geometry and fracture porosity in a reservoir when the borehole axis is not parallel to the fractures (from Narr, 1996).

By considering a volume of reservoir equal to the average height and spacing of one fracture (i.e. n_f =1, W_r = S_{av}, and H_r = H_{av}) (**Fig. 5.16**), Equation 5.16 is further simplified to,

$$\phi_f = \frac{A_{av}}{S_{av}} \tag{5.17}$$

Equation 5.17 can be equated to Equation 5.15, and solved for average fracture spacing,

$$S_{av} = \frac{A_{av} W_c H_c}{\sum_{i=1}^{n} A_i H_i} \tag{5.18}$$

This is the principal formula for average spacing of fractures in the subsurface. With the common exception of aperture, the parameters in this equation are available from conventional core or borehole images.

Reliable fracture apertures are notoriously very difficult to obtain in core (Howard & Nolen-Hoeksema, 1990) and are generally indeterminate from contemporary borehole imaging logs. Therefore when apertures are poorly known, an average aperture can substitute for individual values of A_i, thereby reducing Equation 5.18 to,

$$S_{av} = \frac{A_{av} W_c H_c}{\sum_{i=1}^{n} A_{av} H_i} = \frac{W_c H_c}{\sum_{i=1}^{n} H_i} \tag{5.19}$$

$$S_{av} = \frac{Core\ Diameter\ x\ Core\ Height}{Summed\ Fracture\ Height\ in\ Core}$$

Within a well, different rock types should be tested individually to investigate lithology-dependant variations in fracture spacing.

AFS Methodology for use in Wells of Arbitrary Orientation

The preceding discussion has been concerned with conventional cores that are oriented parallel or sub-parallel to subsurface fracture sets. However, average fracture spacing (AFS) can be computed with data from boreholes of arbitrary orientation relative to fracture sets and bedding. This proves particularly useful in estimating average fracture spacing in certain Miskar cores where the well is deviated at ~25^0 to the vertical. The methodology is discussed below.

Considering the idealistic case (as in most of the Miskar wells) where the majority of fractures of average height, H_{av}, are aligned vertically and show a horizontal spacing, S_{av} (**Fig. 5.17**). If a core of width W_c cuts this reservoir at angle β from the plane of the fractures, the effective spacing of fractures along the core is S_β. Consider the 2D case

of deviation toward a direction perpendicular to the fracture set. By describing the height of the core in terms of average fracture spacing along the core, $H_c = nS_{\beta av}$, the fracture porosity identified in the core is,

$$\phi_f = \frac{\sum_{i=1}^{n} A_i H_i}{nS_{\beta av} W_c} \tag{5.20}$$

By substituting $H_i = W_c / \sin\beta$ and $S_{\beta av} = S_{av} / \sin\beta$, fracture porosity can be simplified to,

$$\phi_f = \frac{\sum_{i=1}^{n} A_i (W_c / \sin\beta)}{nW_c (S_{av} / \sin\beta)}$$

$$\phi_f = \frac{\sum_{i=1}^{n} A_i}{nS_{av}}$$

$$\phi_f = \frac{A_{av}}{S_{av}} \tag{5.21}$$

This result equates to Equation 5.17, which describes the fracture porosity of the reservoir model. Hence it is possible to rearrange this equation and substitute for fracture porosity to describe reservoir fracture porosity in terms of fracture parameters observed in core of arbitrary orientation with respect to a subsurface fracture system.

$$S_{av} = \frac{A_{av}}{\phi_f} = \frac{A_{av}}{\left(\frac{\sum_{i=1}^{n} A_i H_p}{W_c H_c} \right)}$$

$$S_{av} = \frac{A_{av} W_c H_c}{\sum_{i=1}^{n} A_i H_p} \tag{5.22}$$

Equation 5.22 is identical to Equation 5.18, except that partial fracture height, H_p, is used instead of individual fracture height, H_i. If average fracture apertures were used, Equation 5.22 would be reduced to a form identical to Equation 5.19.

The principal complication introduced when the borehole is not parallel to fractures is an inability to determine the true height, H_i, of any fracture whose upper and lower

termination falls outside the confines of the core (or borehole image). Consequently the maximum measurable fracture height, H_p, is determined by the width of the core and the angle between the core and the fracture β: $H_p = Wc/\sin\beta$ (**Fig. 5.17**). If the angle β is not in a plane normal to bedding, then the apparent fracture height is less than this maximum, which has the effect of limiting the height of fractures, H_i, in the computation of average fracture spacing. However, this consideration is offset by the increase in number of fractures intersected, n. Therefore, as long as a sufficient length of fractured unit is sampled to obtain a representative sample, fracture porosity (the basis of the AFS method) is independent of core orientation.

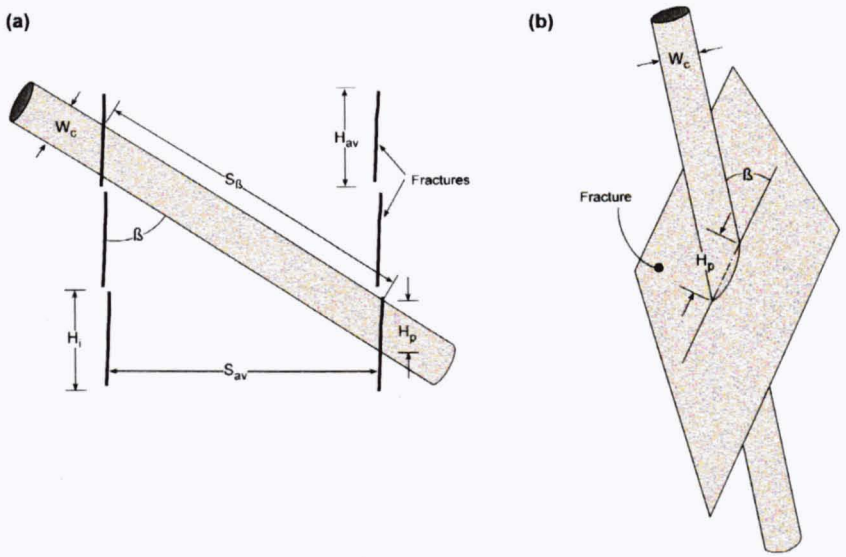

Fig. 5.17. Schematic diagram showing an idealised homogeneous, fractured reservoir which forms the basis of the AFS (Average Fracture Spacing) method. (a) Depiction of idealised reservoir volume, (b) two-dimensional fracture unit (from Narr, 1996).

The only special consideration when the borehole is not parallel to the fractures is that the height (or partial height, Hp) of the fractures must be measured parallel to the fracture surface in the plane that contains the angle β: H_p in **Figure 5.17**, and substituted for H_i in Equations 5.17 or 5.18.

Narr (1996) has used the AFS methodology on a number of carbonate and siliciclastic case studies to demonstrate the validity of the technique. Average fracture spacing estimates were calculated for a number of vertical wells and compared with direct spacing measurements from near-horizontal wells in the same areas. Results from the AFS method generally show good agreement with observed spacing in near-horizontal wells, particularly as the length of core sample analysed increases. Consequently this

technique has been used to determine fracture spacing in the Hasdrubal and Miskar Fields (Chapters 6 & 7).

Chapter 6

Structural Analysis of the Miskar Gas Condensate Field

6.1. Introduction

This chapter examines the controls on fracture development within the principal reservoir intervals in the Miskar Gas Condensate Field. An understanding of the nature and distribution of the fracture systems present will provide a useful aid in field development.

A number of separate analyses have been integrated in this study in order to gain an understanding of the processes controlling fracture development at the reservoir scale. Sections 6.2, 6.3 and 6.4 locate the Miskar Gas Field, present details on the exploration history of the acreage, and introduce the main structure and reservoir stratigraphy in the Field. Section 6.5 presents an interpretation of 3D seismic data over the area and establishes the overall structure and evolution of the Field. This is particularly important in that it provides an understanding of the stress history of the main reservoir intervals present.

Section 6.6 summarises the results from the structural analysis of the Miskar A-3, A-6, A-7, A-9, A-10 and A-11 cores. Qualitative structural descriptions are provided detailing the nature and style of fracturing in the principal reservoir zones, together with quantitative estimates of fracture spacing, frequency and length (refer to Chapter 5). Unfortunately, the lack of oriented core for all the wells analysed precludes a study of fracture set orientation. The results from each of these analyses have been incorporated into a working structural model illustrating the various stages of fracture development within the Field (6.6.5). Finally, a discussion of the influence that fracturing exerts on reservoir performance is presented in Section 6.6.6.

6.2. Location & Field History

The Miskar Gas Field is located within the Miskar Production Concession, approximately 110km ESE of Sfax, in the western part of the Gabes-Tripoli Basin (**Fig. 6.1**).

The field was discovered in 1974 by Elf Aquitaine with the Miskar -1 well. Gas condensate flowed from the Upper Cretaceous Aleg Formation in the Douleb (R-1 Superior/Inferior intervals) and Bireno Members. Subsequently, 4 additional appraisal wells were drilled between 1975 to 1979; the Miskar -3 and -4 wells encountered additional hydrocarbons in the Abiod Formation. Elf relinquished the block in 1984.

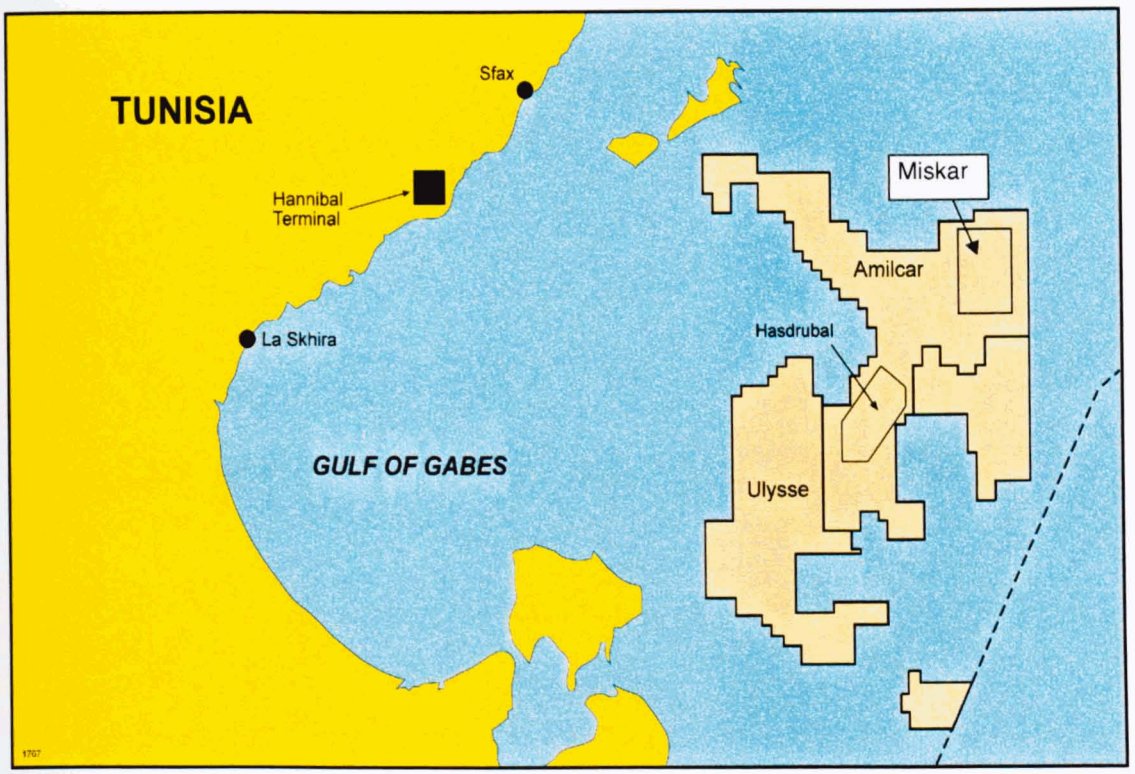

Fig. 6.1: Location of the Miskar Gas Field

In 1988 BG Tunisia Ltd. (BGT) signed the Amilcar Exploration Concession Agreement with Enterprise Tunisienne D'Activities Petroliers (ETAP). An extensive appraisal study was initiated, which included a 3D seismic survey in 1989, and an additional appraisal well (Miskar -6) in 1990. Development of the field began in 1993 (Miskar A-1). Since then, a further ten wells have been drilled on the structure (Miskar A-2 to A-11) (Cores from these development wells form the basis of this study). Gas Condensate is transported via pipeline to the Hannibal processing plant in Sfax.

6.3. Database

The current database that was available for use in this study includes a 3D seismic grid over the Miskar acreage, together with composite well logs, well reports and core from selected wells. The data available for each well is given in Table 6.1.

Well Name	Composite Log	Core Report	Core
Miskar A-1	✔	✔	
Miskar A-2	✔	✔	
Miskar A-3	✔	✔	✔
Miskar A-4	✔	✔	
Miskar A-5	✔	✔	
Miskar A-6	✔	✔	✔
Miskar A-7	✔	✔	✔
Miskar A-8	✔	✔	
Miskar A-9	✔	✔	✔
Miskar A-10	✔	✔	✔
Miskar A-11	✔	✔	✔

Table 6.1. Data available for wells Miskar A-1 to A-11.

6.4. Local Structure & Reservoir Stratigraphy

6.4.1. Introduction

A discussion of the local structure and reservoir stratigraphy of the Miskar Gas Condensate Field is presented in the following section. This will provide a broad framework for the rest of the chapter.

6.4.2. Structure

The Miskar structure is a north-south trending horst block that plunges to the south (**Fig. 6.2**). It is bounded to the east and west by two major fault zones with variable relief. These fault zones exhibit complex geometries with evidence of extension, inversion and oblique-slip. The central portion of the horst is further faulted with NNW-SSE to WNW-ESE trending extensional to oblique-slip faults dividing the field into north and south compartments. These two main compartments are sub-divided further by minor N-S trending faults.

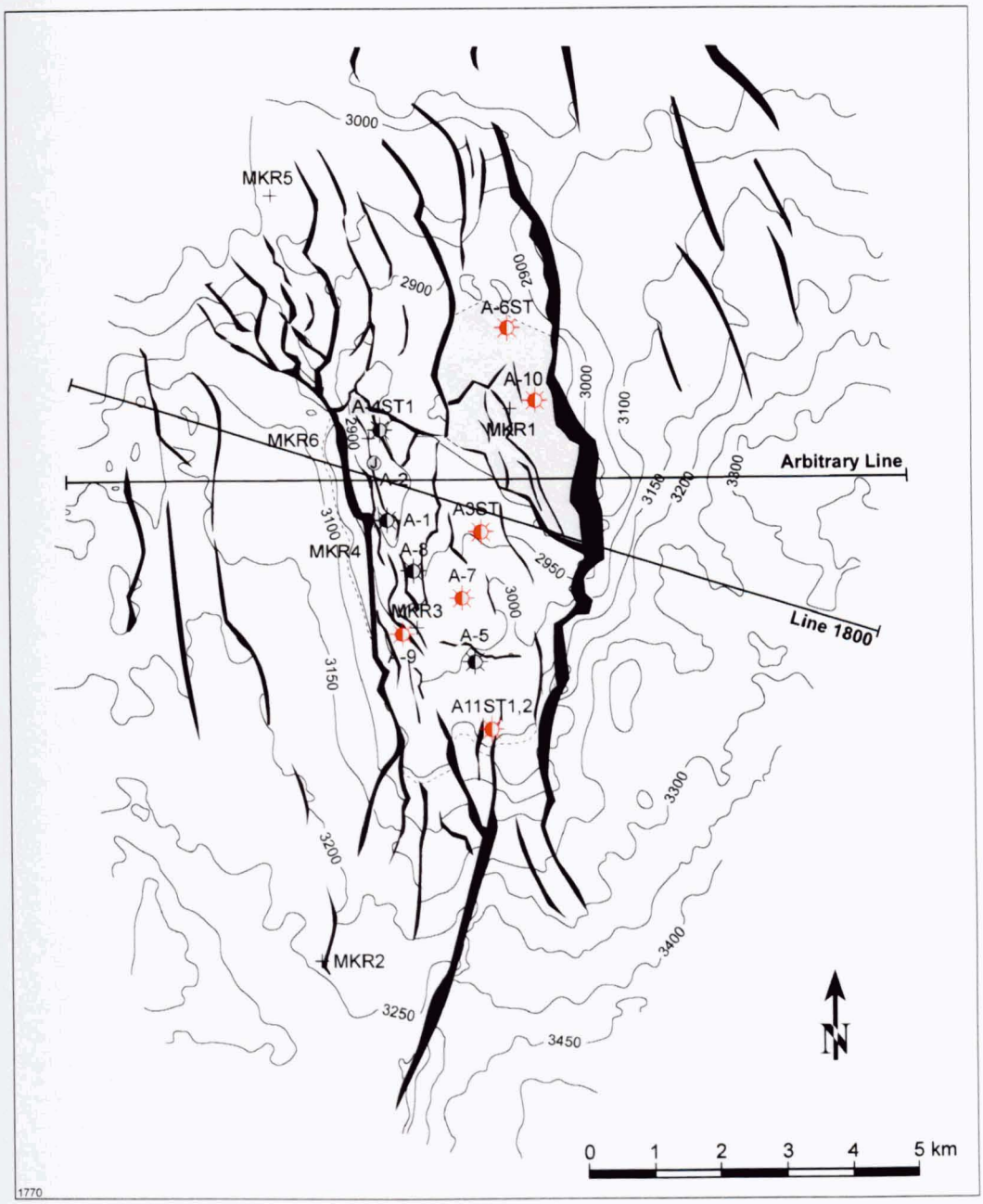

Fig. 6.2. Depth structure map of the Top R1 Inferior Member (Aleg Formation) over the Miskar structure. Data presented in this study is shown.

6.4.3. Reservoir Stratigraphy

The reservoir interval in the Miskar Gas Condensate Field is confined to the Upper Cretaceous Aleg and Abiod Formations (**Fig. 6.3**). Proven hydrocarbons have been encountered at three separate stratigraphic horizons:

- The R1 Superior/Inferior Members of the Aleg Formation;
- The Bireno Member of the Aleg Formation;
- The Abiod Formation.

Aleg Formation (early Turonian to early Campanian)

The Aleg Formation in the Miskar Field is sub-divided into 6 separate members; 1) The Upper Aleg Member, 2) The Carbonate Marker, 3) The R-1 Superior Member, 4) The R-1 Inferior Member, 5) The Lower Aleg Member and 6) The Bireno Member (Cook & Wright, 1998) (**Fig. 6.3**).

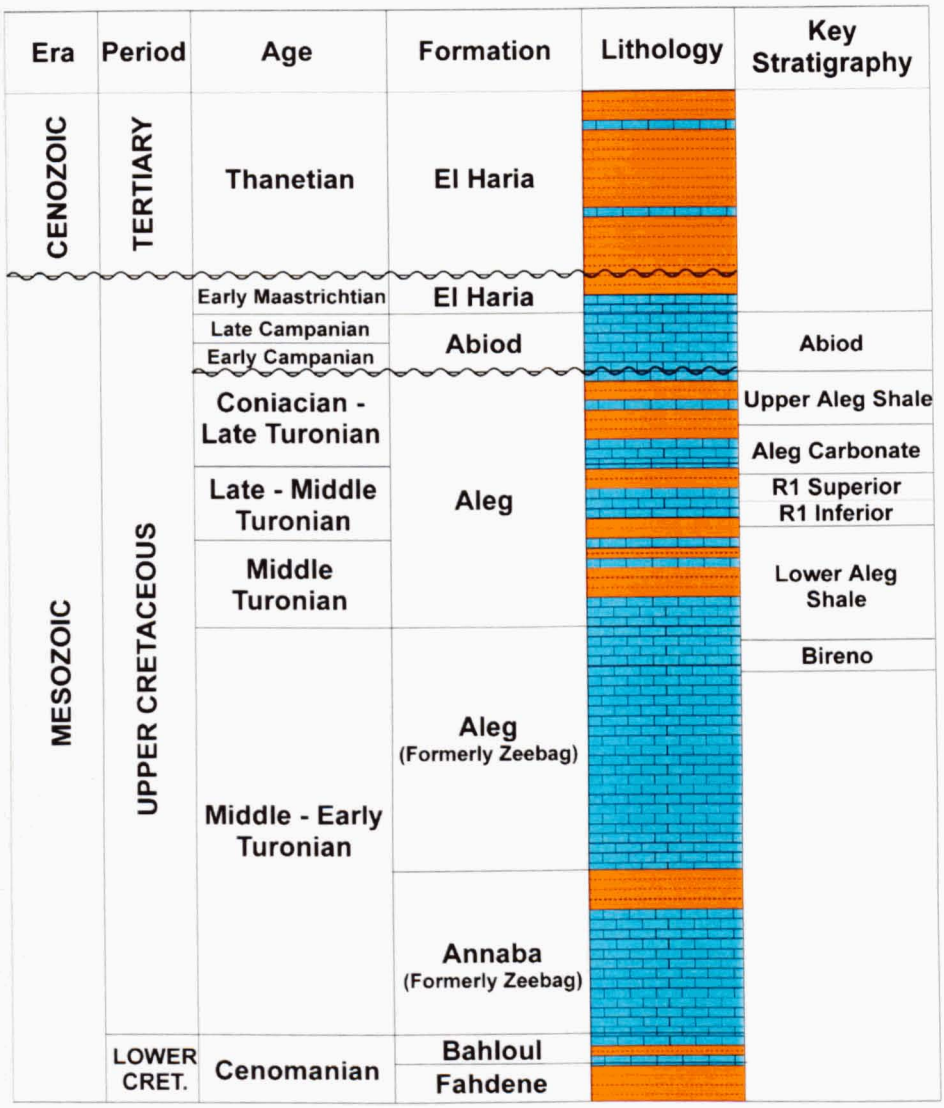

Fig.6.3. Main reservoir stratigraphy in the Miskar Gas Condensate Field (from Cook & Wright, 1998).

Upper Aleg Member (Coniacian)

The Upper Aleg Member consists of an upper unit of extensively bioturbated argillaceous packstones composed of variable amounts of fine to coarse skeletal debris and forams within a dominantly cryptocrystalline to microcrystalline matrix. This upper unit grades down into flaser bedded mudstones. The upper unit subsequently passes down into a lower sequence of non-fissile calcareous claystones, through into a

non-calcareous claystone base. These lithofacies are indicative of deposition within a deep-water outer shelf or mid to outer ramp environment (Cook & Wright, 1998).

Aleg Carbonate Member (late Turonian-early Coniacian)

The Upper Turonian to Lower Coniacian Aleg Carbonate Member consists of argillaceous limestones and interbedded claystones. The argillaceous limestones occasionally grade into wackestones and consist of a microcrystalline to rarely cryptocrystalline matrix containing forams, skeletal debris and traces of nodular pyrite burrow infill. No visible porosity is observed in this interval. These lithofacies represent deposition in a low energy mid to outer ramp setting (Cook & Wright, 1998).

R-1 Superior Member (late Turonian)

The R-1 Superior Member is the equivalent of the upper part of the Douleb Member of the Aleg Formation, found in onshore central Tunisia. It is on average 68m thick over the Miskar structure. The boundary between the R-1 Superior and R-1 Inferior intervals is located within a lagoonal-evaporitic sequence that caps the main R-1 Inferior sequence. The unit consists of argillaceous and silty, nodular and shelly lime mudstones and wackestones (**Fig. 6.4**). Hardgrounds occur at a number of levels and pyrite is common. Interbedded within this main lithofacies are packstones-wackestones with fine peloidal and skeletal fragments, mainly of echinoderms, molluscs, forams and calcispheres.

This lithofacies is interpreted to have been deposited in a mid to outer ramp environment; the interbedded packstones-wackestones may represent storm reworked intervals (Cook & Wright, 1998). Reservoir quality is fair in this unit, with a net/gross of ~28%. Porosities are generally low; the best are developed within the interbedded pack-wackestones where values are <15%. Matrix permeabilities are also very low.

Basaltic subaqueous volcanic rocks are also present in the R-1 Superior interval, located in the north of the Miskar field in Miskar-1, Miskar A-10 and Miskar A-6st. Above the volcanic flows, volcaniclastic breccias, probably deposited as subaqueous debris flows, and mixed volcaniclastic-carbonate rocks occur. Within the Miskar-2 well to the south of the Field, 145m of volcaniclastics occur within the basal section of the R-1 Superior reservoir. The extrusion of these volcanics is related to the active rifting, which has been noted on the Pelagian Platform from the middle to late Cretaceous (Finetti, 1982;).

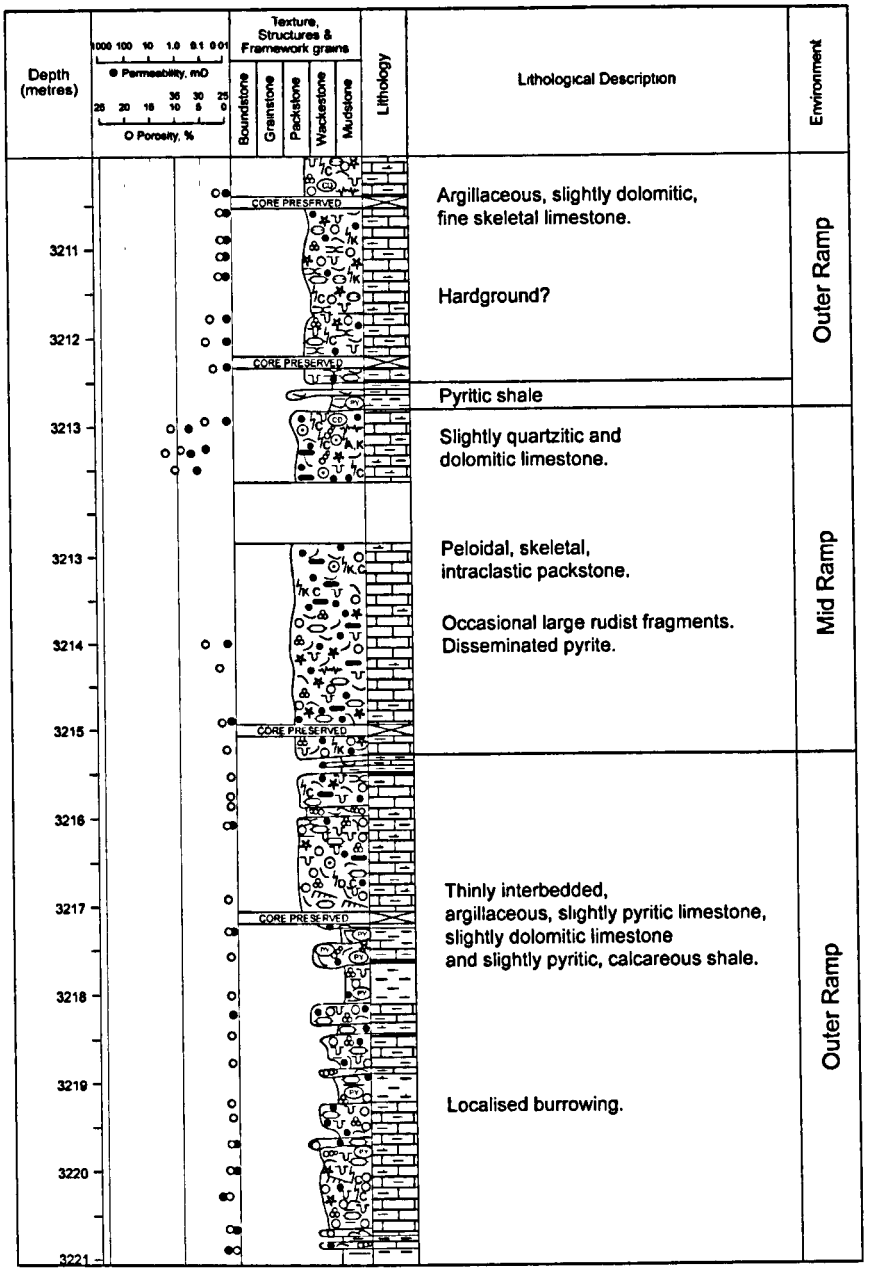

Fig. 6.4. An interval of core from the R1 Superior Member within Miskar -6 (from Cook & Wright, 1998) (refer to Fig. 6.7 for a key).

R-1 Inferior Member (late Turonian)

The R-1 Inferior Member represents the equivalent of the lower part of the Douleb Member of the Aleg Formation observed in onshore Tunisia. It is on average 26m thick over the Miskar structure, and is thickest in the northeast of the field, where it reaches 34m.

The R-1 Inferior Member consists of an upward coarsening sequence, commencing with offshore bioclastic packstones and wackestones with peloidal and echinoderm fragments, benthic forams and calcispheres (**Fig. 6.5**). This grades up into similar beds that also contain coarse rudist debris which are followed by rudist floatstones and

rudstones, with *in situ* rudists in muddy matrices. This is overlain by further wackestones and packstones containing coarse rudist debris. Locally overlying these beds are cross-stratified rudist grainstones and planar laminated grainstones. This marks the top of the coarsening-upwards sequence. These grainstones are capped by laminated grainstones, stromatolites, sabka evaporites and dolomites. These are interbedded with wackestones/packstones containing algae, miliolids and serpulids.

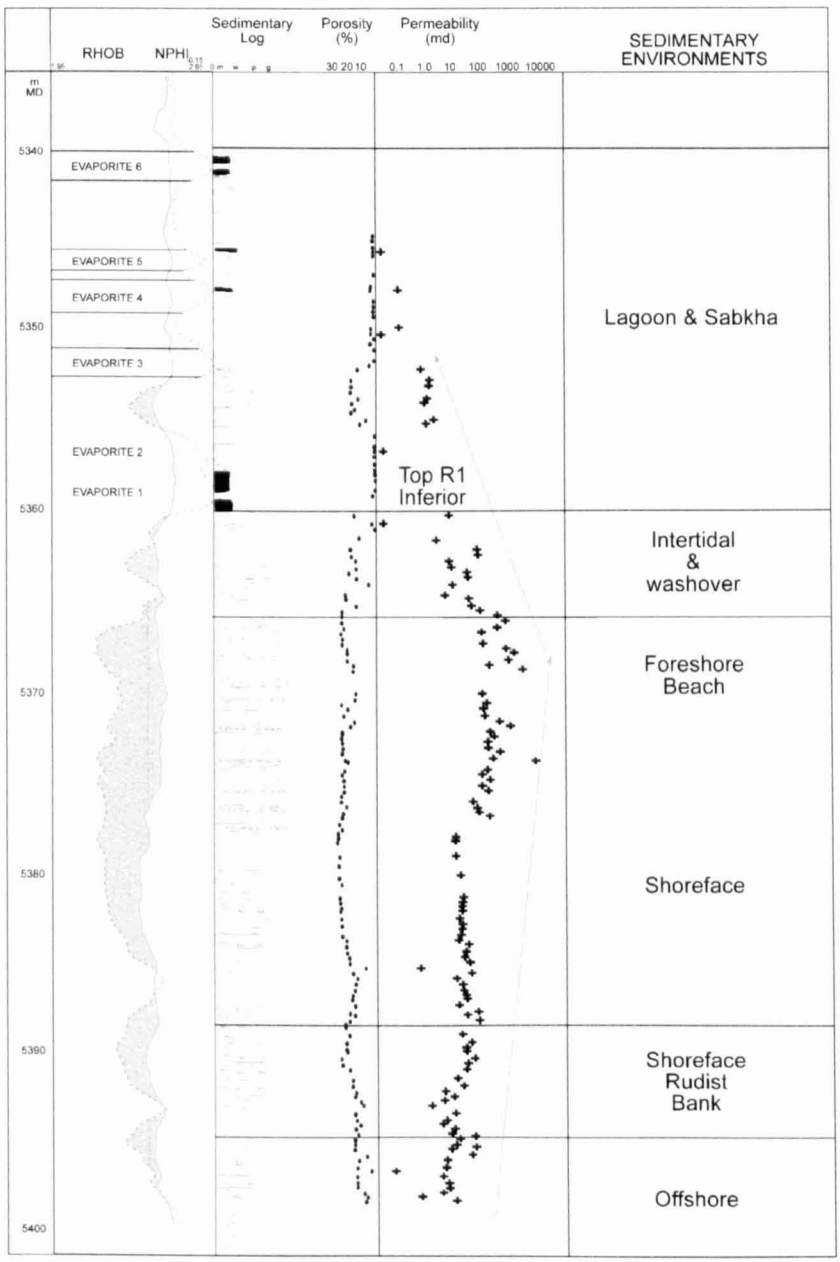

Fig. 6.5. An interval of core from the R1 Inferior Member within Miskar -6 (from Cook & Wright, 1998) (refer to Fig. 6.7 for a key)

The coarsening upwards sequence is interpreted to have been deposited in an offshore mid-ramp setting which shallowed through a rudist bank located in a lower shore-face environment, surrounded by storm reworked debris up through a shore-face

environment, into a beach (Cook & Wright, 1998). Above this, conditions shallowed, from intertidal to supratidal, allowing evaporites to develop. Lagoons developed behind the grainstone shoals.

Reservoir quality in the R-1 Inferior Member is generally fair to very good, with an average net/gross of 87%. In the upper shoreface grainstones porosities attain 25% and permeabilities range between 10-1000mD (Cook & Wright, 1998). In this lithofacies, intergranular porosities are high and early meteoric cementation has only partially occluded porosity. Mouldic porosity is present and dolomitisation has also increased porosity and permeability in many units. In the more muddy lithofacies, such as the rudist bank and flanks, the porosity is mainly microporosity within the matrix, which gives rise to high porosity (seldom exceeding 15%) but low permeability (<50mD).

Lower Aleg Member (middle Turonian)

The Lower Aleg Shale Member rests unconformably on the Bireno Member. Its thickness is relatively uniform across the Miskar area, averaging approximately 100m to 120m. It consists of interbedded grey/brown argillaceous mudstones-wackestones and marls that are rich in shell debris (i.e. rudists (?) and planktonic foraminifera). These lithofacies and biota are indicative of deposition in an open marine, deep-water mid to outer ramp environment (Cook & Wright, 1998).

Bireno Member (early-middle Turonian)

The Bireno Member (formerly Upper Zebbag) is a minor contributor to the gas-in-place in the Miskar Field. It has an average thickness of 39m over the Miskar structure, and consists of calcispheric, peloidal wackestones and packstones with varying amounts of bioturbation (**Fig. 6.6**). Observed biota include abundant calcispheres, common peloids and occasional planktonic foraminifera, together with echinoderm fragments and ostracods.

These lithofacies and biota are indicative of a deeper-water outer shelf or a middle to outer ramp setting, suggesting that the Bireno reservoir in the Miskar field is an offshore equivalent of the onshore Bireno Member in south-central Tunisia. Reservoir quality is moderate to good. Porosity is dominantly in the form of intergranular microporosity, and reaches up to 27%. Permeabilities are generally low (<10mD). These values are reduced further as the reservoir becomes more argillaceous and bioturbated.

Abiod Formation (early Campanian to early Maastrichtian)

The Abiod Formation unconformably overlies the Aleg Formation and forms the upper reservoir interval in the Miskar Field. It averages 69m thick on the structure, and is hydrocarbon bearing throughout. Off-structure, the Abiod Formation thickens significantly (e.g. 110m at Miskar-2 and up to 257m in Miskar-5). Substantial erosion of the Abiod Formation is evident on the northern compartmentalised fault block (Cook & Wright, 1998).

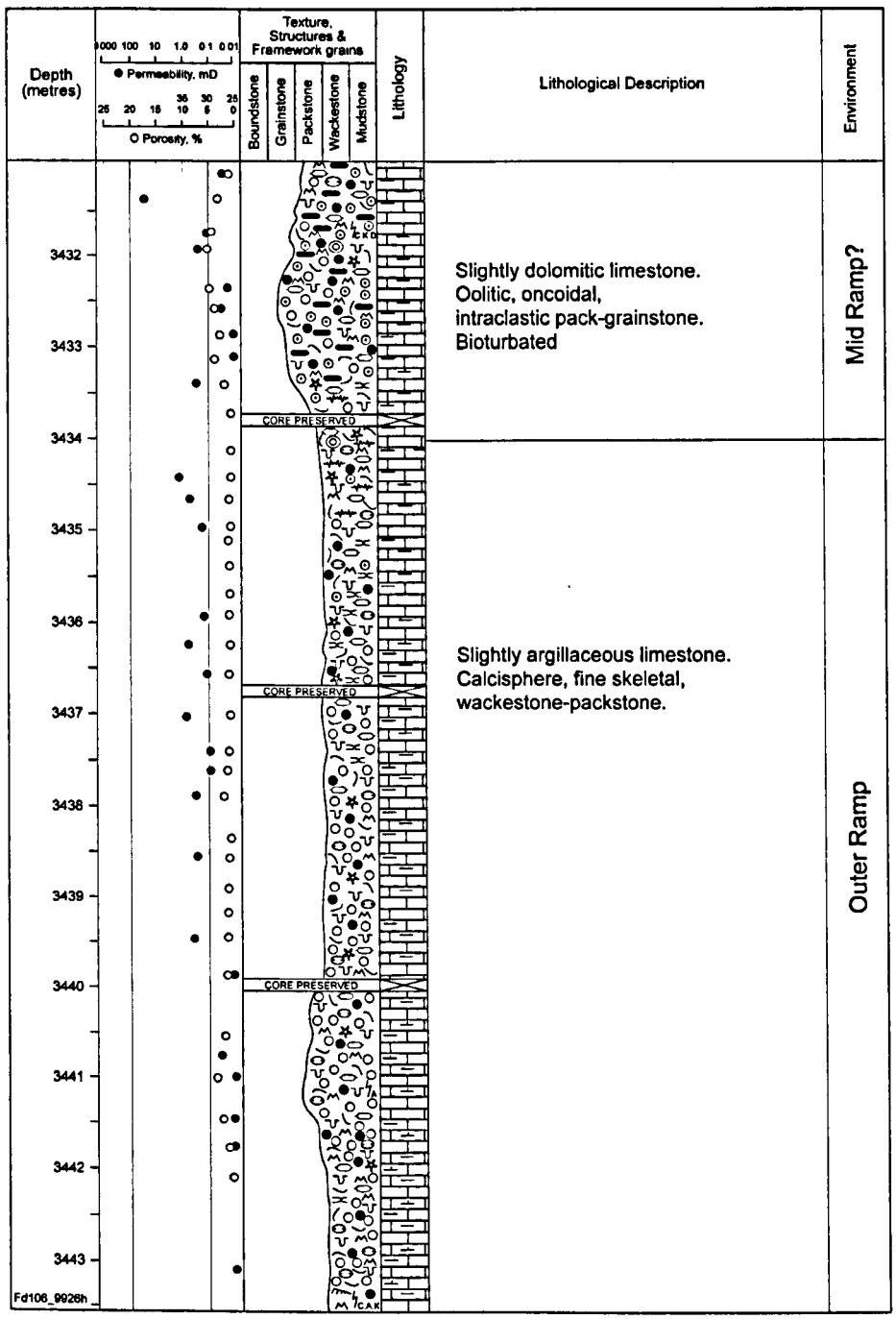

Fig. 6.6. An interval of core from the Bireno Member within Miskar -6 (from Cook & Wright, 1998) (refer to Fig. 6.7 for a key).

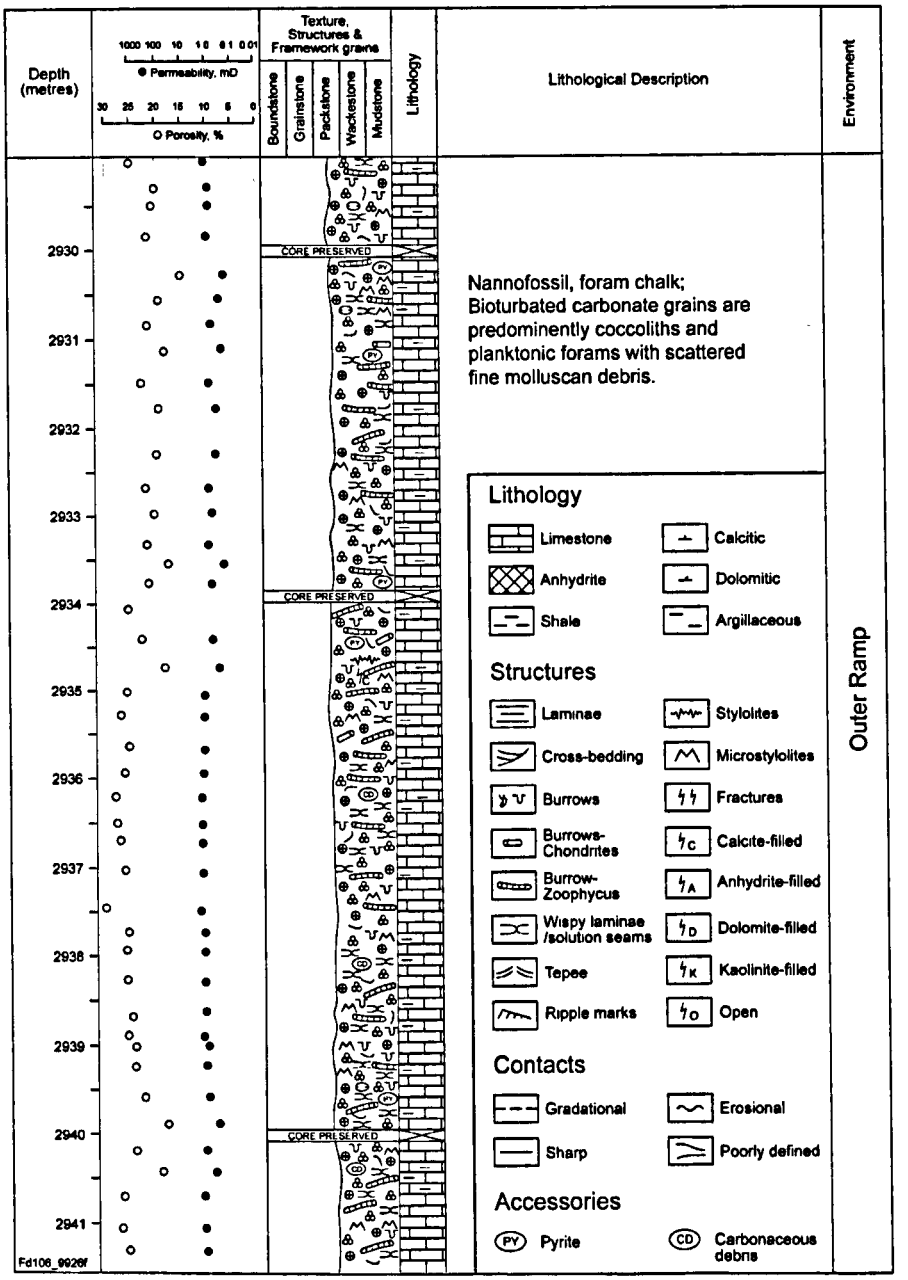

Fig. 6.7. An interval of core from the Abiod Formation within Miskar -6 (from Cook & Wright, 1998).

The Abiod Formation is very fine-grained, and is composed of foraminiferal-nannofossil chalk with wackestone to packstone textures (**Fig. 6.7**). The biota described from this unit consists mostly of coccoliths and planktonic forams with minor amounts of bivalve, echinoderm and ostracod debris. Bioturbation features are common in some intervals, but only *Zoophycos* and *Chondrites* trace fossils are identifiable. These biota are consistent with deposition in an offshore, low energy, outer ramp environment. Porosity is dominantly intergranular micro-porosity, and is relatively high, ranging between 8% and 32%. Permeabilities, however, are generally low, ranging between 0.01 to 7.5mD (Cook & Wright, 1998).

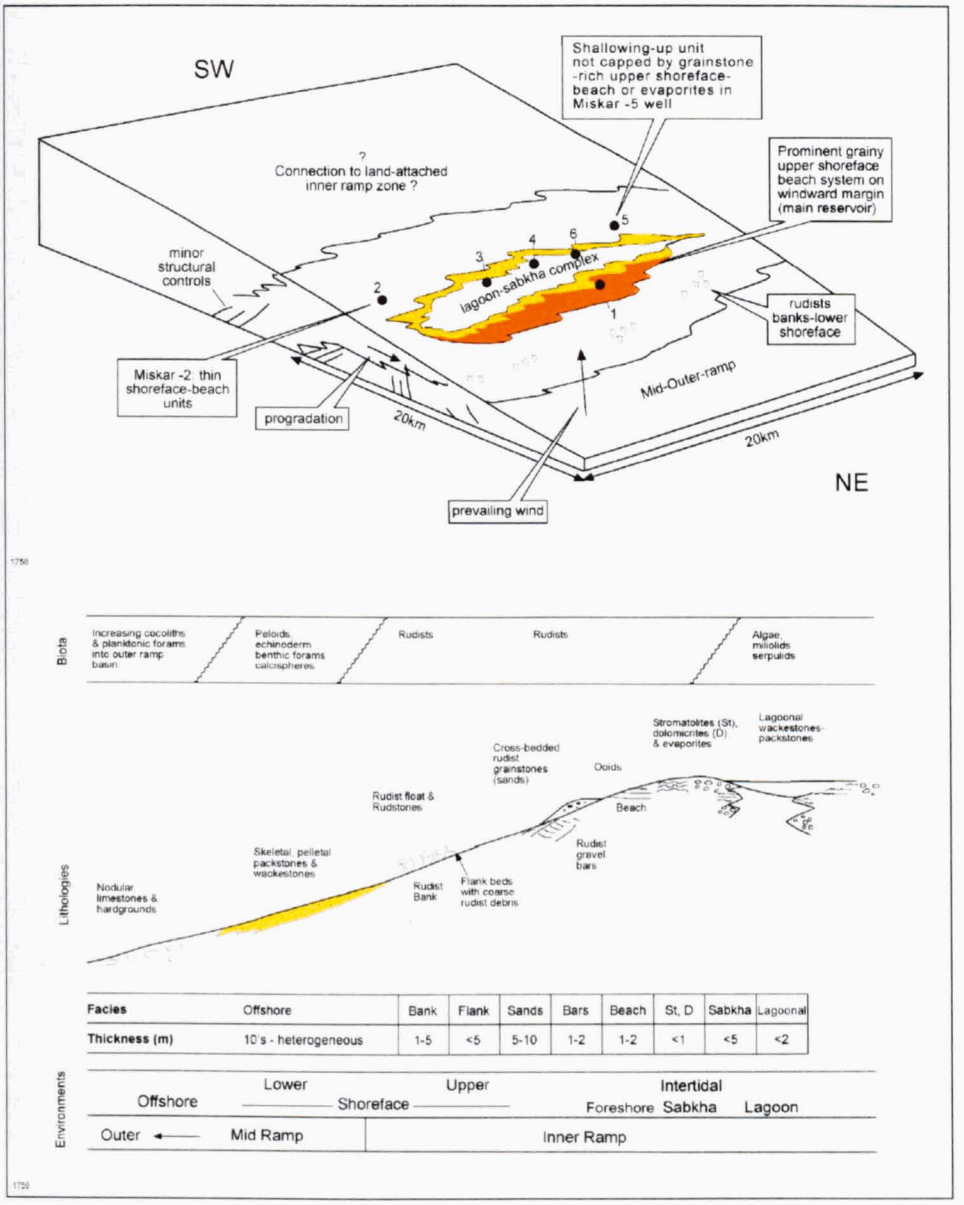

Fig. 6.8. Schematic depositional model of the R1 Superior and Inferior members of the Aleg Formation over the Miskar area (from Cook & Wright, 1998).

6.4.4. Depositional Setting of the R1 Superior & Inferior Reservoirs

The palaeogeographic maps presented in Chapter 3 (**Figs. 3.11 & 3.12**) show the facies distribution of the Upper Cretaceous Aleg and Abiod Formations across the Gulf of Gabes area. These maps delineate a series of approximately NW-SE trending facies tracts that parallel the earlier passive margin. During this period, the Miskar area was located in a mid to outer ramp setting. **Figure 6.8a-b** presents the proposed facies model for the main R1 Superior and Inferior reservoirs over the field. It shows that during this period the Miskar structure had become established as a palaeohigh. The R1 Superior and Inferior Members were deposited in a restricted lagoon-sabkha

complex in this mid ramp setting. The positions of the Miskar -1 to -6 appraisal wells are shown.

6.5. Seismic Stratigraphy & Structure

6.5.1. Introduction

LandMark™ software was utilised to interpret the Miskar 3D dataset. Every 20th line and 5th trace was interpreted on the 3D seismic grid. Horizons were then interpolated over the entire area, and faults were triangulated accordingly. Depth structure maps were constructed, and used in conjunction with seismic profiles to determine the main structural elements present, the timing of tectonic events and the influence of these tectonic processes on the depositional architecture of the main reservoir intervals.

6.5.2. Seismic Stratigraphic Framework

Seventeen seismic sequences have been interpreted in the Miskar dataset (Table 6.2). These were tied to zero-phase synthetic logs from available wells. They correspond to major stratigraphic intervals in the Gulf of Gabes (Section 3.5). The high seismic resolution below the Maastrichtian unconformity in the Miskar Gas Condensate Field allows the direct determination of all 17 sequences (**Fig 6.9**).

As previously discussed in Chapter 3, the Upper Cretaceous to present-day succession represents the post-rift thermal subsidence phase to the main episode of Late Jurassic and Early Cretaceous rifting. However, within the Gulf of Gabes this post-rift sequence is interrupted by numerous episodes of tectonic subsidence (causing fault generation and reactivation) that are associated with the development of the Gabes-Tripoli Basin. The phases of extension associated with this tectonic subsidence are characterised in the sedimentary succession by local thickening adjacent to active faults. Table 6.2 summarises the sequence stratigraphic framework for the area encompassing the Miskar and Hasdrubal Fields. **Figure 6.9** illustrates the main seismic sequences interpreted in the Miskar Field.

6.5.3. Seismic Structure

Seventy-two seismically resolvable faults were identified on the Miskar dataset. The geometry and timing of movement on these structures has been analysed through the interpretation of seismic profiles, and the construction of relevant depth structure maps.

Sequence Number	System/Series Rank	Stratigraphy	Seismic Sequence Characteristics							
			Geological Boundary		Internal Character						Tectonic Control
			Lower	Upper	PA	SP	DIV	SIG	OBL	HUM	
SS-1	Upper Cretaceous	Upper Fahdene Fm.	Onlap	Concordant	✔						
SS-2	Upper Cretaceous	Bahloul/Lower Aleg Mbr.	Onlap	Erosional			✔				✔✔
SS-3	Upper Cretaceous	Bireno Mbr. (Aleg)	Onlap	Concordant		✔(?)	✔(?)				✔
SS-4	Upper Cretaceous	Low. Aleg Shale Mbr. (Aleg)	Concordant	Concordant	✔						
SS-5	Upper Cretaceous	R1 Sup./Inf. Mbr. (Aleg)	Concordant	Concordant		✔					✔
SS-6	Upper Cretaceous	Aleg Carbonate Mbr. (Aleg)	Concordant	Concordant		✔					✔
SS-7	Upper Cretaceous	Up. Aleg Shale Mbr. (Aleg)	Onlap	Erosional			✔				✔✔✔
SS-8	Upper Cretaceous	Abiod Fm.	Onlap	Erosional			✔				✔✔
SS-9	Palaeocene	El Haria/Tselja/Chouabine Fm.	Onlap	Erosional	✔						
SS-10	Eocene	Metlaoui Gp.	Onlap	Concordant		✔					✔
SS-11	Eocene	Cherahil Fm.	Concordant	Erosional		✔(?)	✔(?)				✔✔
SS-12	Oligocene/Miocene	Salammbo Fm.	Onlap	Erosional	✔						
SS-13	Middle Miocene	Ain Grab Fm.	On lap	Erosional	✔						
SS-14	Middle Miocene	Mahmoud Fm.	Onlap	Erosional		✔(?)	✔(?)				✔✔
SS-15	Upper Miocene	Beglia Fm.	Onlap	Erosional		✔(?)	✔(?)				✔
SS-16	Upper Miocene	Melquart Fm.	Onlap	Concordant		✔(?)	✔(?)				✔
SS-17	Upper Miocene/Present	O Bel Khadim/Present	Concordant	N/A	✔(?)						✔

Table 6.2. Seismic stratigraphic framework for the Gulf of Gabes area, based on regional seismic profiles and high resolution 3D seismic data from the Hasdrubal and Miskar Fields. Number of ✔'s shows the degree of tectonic control on sedimentation.

Seismic Expression of Miskar Structure

As previously mentioned, the Miskar Field is located on an ~N-S trending horst block which is delineated by two approximately N-S trending fault zones (**Fig. 6.10**). These fault zones have variable relief, and exhibit complex geometries with evidence of extension, inversion and oblique slip movement. Within the horst block itself, numerous intra-horst faults divide the block into a series of compartments.

Western Fault Zone

The western bounding fault zone is expressed by a set of steeply dipping, kinked fault plane(s) that throw(s) down to the west (**Fig. 6.10**). It extends from at least the Upper Jurassic section to the Oligocene unconformity. Hangingwall displacements along this zone vary with depth; at Abiod level, displacements range between 50m and 200m, whereas at Bireno level displacements can exceed 700m. It is evident that this fault zone was highly active throughout the Late Cretaceous, due to the observed thickening of the Abiod Formation (*SS-8*) and particularly the Upper Aleg Shale Member of the Aleg Formation (*SS-7*) from the crest of the structure into the western bounding half-graben.

The present-day geometry of the fault zone is characterised in its lower portion by a steeply dipping concave-westward fault plane. This extends upwards to top Abiod level (*SS-8*) where it kinks sharply, and flattens out in the shaley El Haria Formation (*SS-9*). The fault zone then steepens upwards into the Bou Dabbous and Cherahil Formations where it commonly terminates against the Oligocene unconformity. The predominantly steeply dipping nature of this zone (particularly within the Cretaceous section) is indicative of a component of oblique-slip displacement. Evidence to support this is provided by folding of the Abiod to Cherahil Formations in the hangingwall block (immediately adjacent to the fault plane), which indicates Upper Eocene oblique transpression. This event is consistent with the observed unconformity located at the top of the Eocene. The Oligocene Salammbo Formation (*SS-12*) gently onlaps onto the folded beds of the Cherahil Formation (*SS-11*).

Eastern Fault Zone

The eastern bounding fault zone is more complex. It is expressed by steeply dipping, kinked fault planes that throw down to the east (**Fig. 6.10**). It extends from at least the Upper Jurassic section into the Mahmoud Formation (in the middle of the horst block).

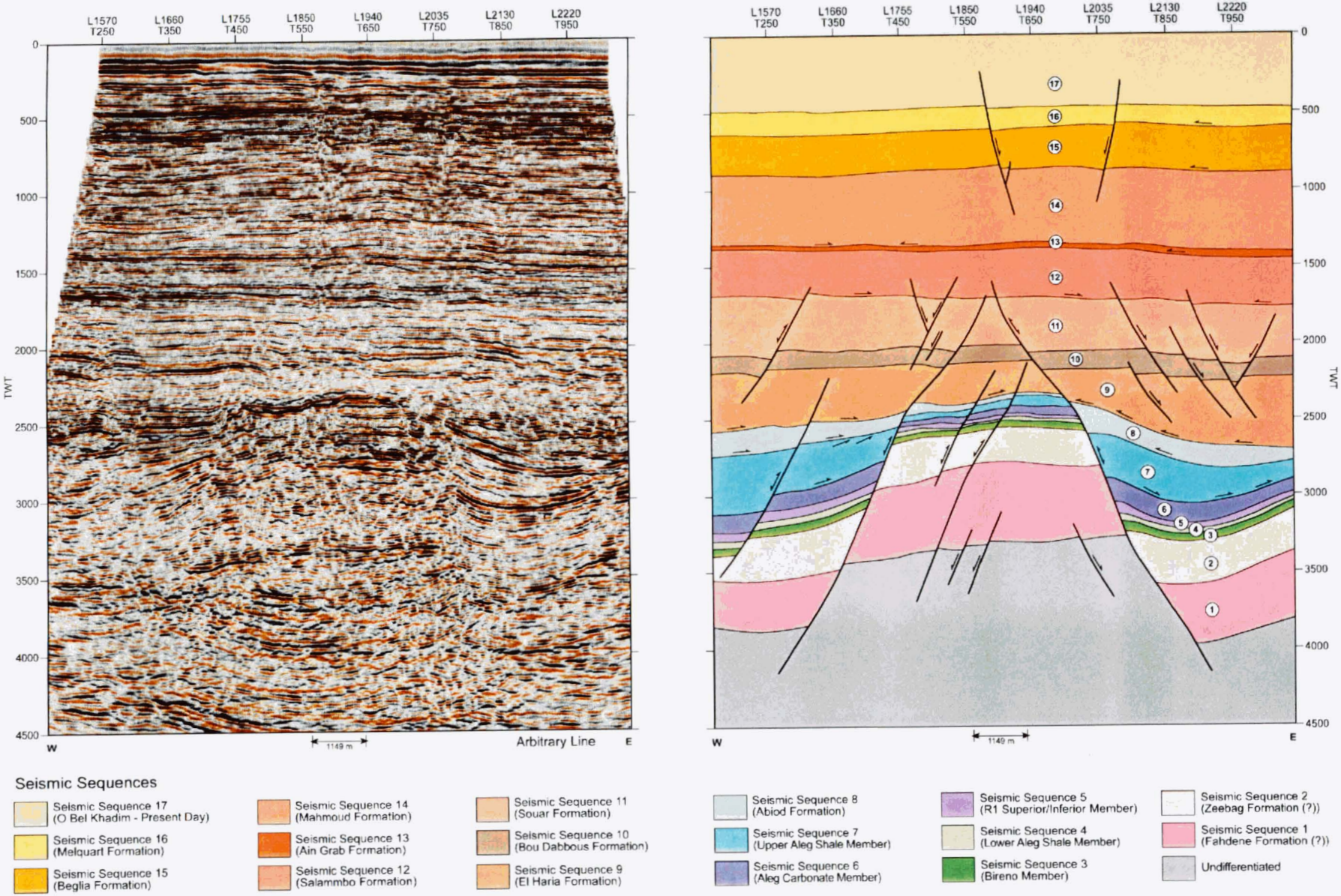

Fig. 6.9. E-W Arbitrary seismic line over the Miskar structure and interpreted line drawing showing the main seismic sequences identified across the area.

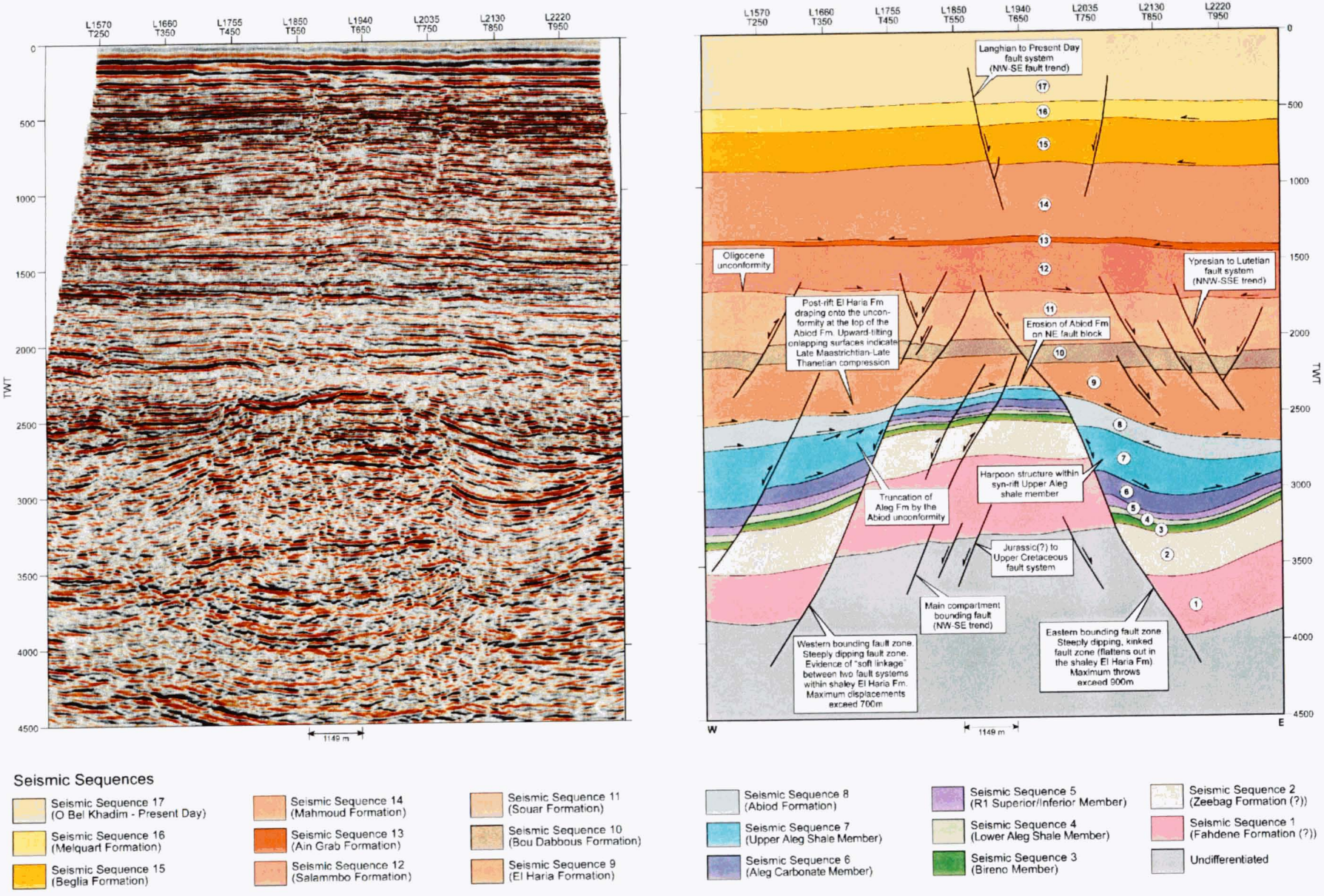

Fig. 6.10. E-W Arbitrary seismic line over the Miskar structure and interpreted line drawing showing the main structural elements present.

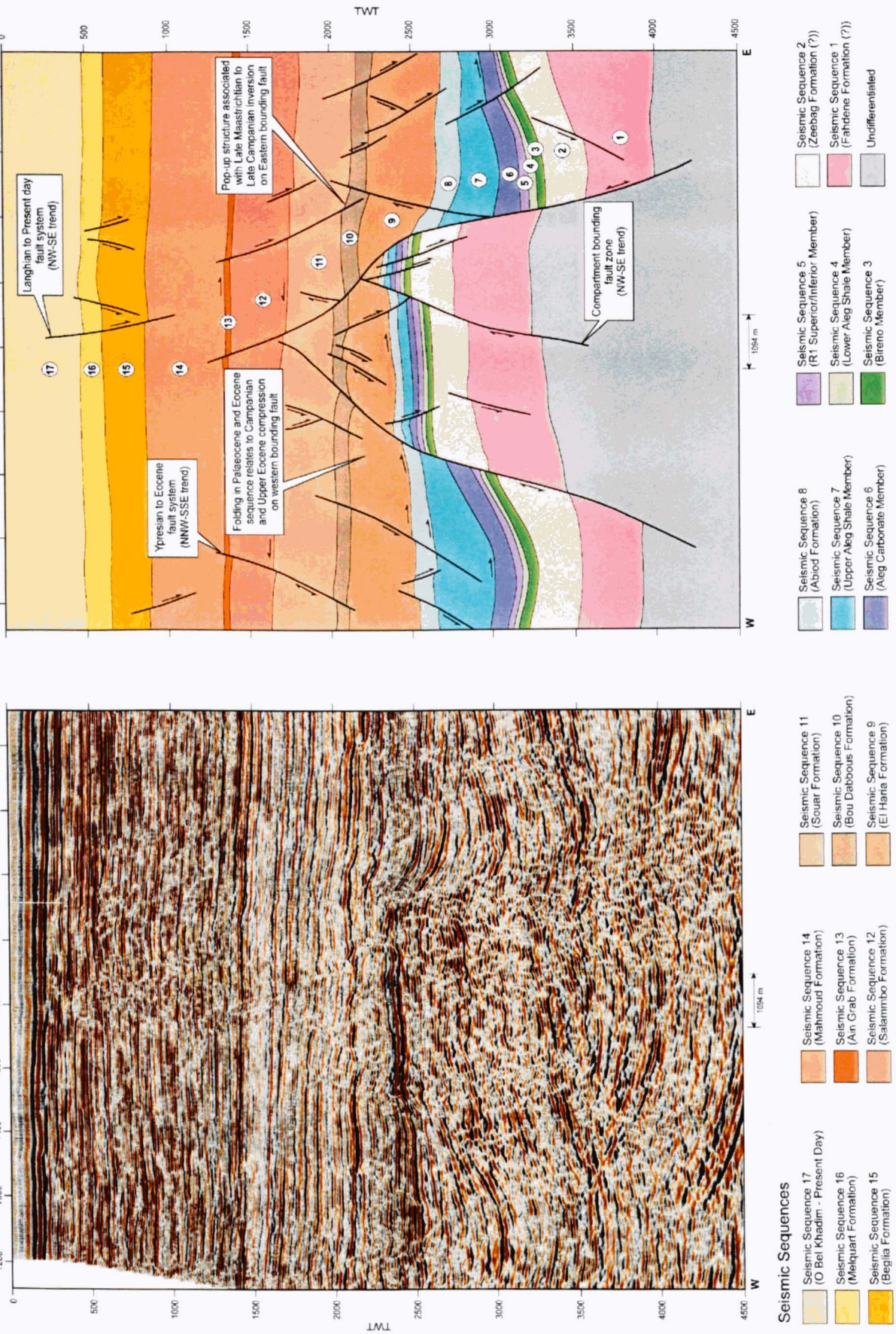

Fig. 611. Seismic line 1800 over the Miskar structure and interpreted line drawing showing the main structural elements present.

In general, hangingwall displacements vary with depth; at Abiod level throws range between 50m and 200m, whereas at Bireno level displacements can exceed 900m. Strong evidence to suggest that this fault zone was active throughout the Late Cretaceous is provided by the observed thickening of the Upper Aleg Shale Member of the Aleg Formation and Abiod Formation (*SS-7 & SS-8*) from the crest of the structure into the eastern bounding half graben. This thickening is particularly apparent within the hangingwall section immediately adjacent to the fault zone (N.B. this fault zone appears to have been more active during the Late Cretaceous than the western fault).

The present-day geometry of the fault zone is characterised in its lower portion by a steeply dipping fault plane with complex splay associations. This extends upwards to top Abiod level (*SS-8*) where the fault zone kinks sharply, and flattens out in the shaley El Haria Formation (*SS-9*). The zone then steepens upwards into the Bou Dabbous, Cherahil and Salammbo Formations (*SS-10, SS-11 & SS-12*) (N.B. The extension of the fault plane into the Salammbo Formation indicates late stage reactivation (late Tertiary)). An en-echelon system of 'harpoon' and 'pop-up' structures have been recognised in the hangingwall section of the fault zone (**Fig. 6.11**). These structures are thought to be associated with intermittent phases of sinistral transpression dating from the late Maastrichtian to the late Thanetian (N.B. the various onlapping relationships present within the El Haria Formation (*SS-9*) which are due to the gradual inversion of the eastern half-graben). Gentle folding in the Eocene succession is thought to relate to a separate transpressive phase at the end of that period.

Intra-Horst Faulting

The central portion of the Miskar horst block is cut by a two systems of smaller faults trending approximately NW-SE and N-S respectively. The most important of these faults, a NW-SE trending structure throwing down to the southwest (200m displacement) separates the horst into two main compartments (**Figs. 6.10-6.12**):

- A high northeastern compartment with considerable relief where the Abiod Formation is substantially to totally eroded;
- A lower southwestern compartment where the Abiod Formation is near complete.

This fault zone was particularly important during the Late Cretaceous to Palaeocene evolution of the Miskar Structure. Large sedimentary thickness variations within the Abiod Formation (*SS-8*) and lower parts of the El Haria Formation (*SS-9*) in the fault's

hangingwall section indicate that it was highly active during the Campanian and Maastrichtian. The relative difference in the amount of erosion of the Abiod Formation (*SS-8*) on the two compartmentalised blocks also supports the interpretation of a period of Maastrichtian tectonic activity (**Fig. 6.10**).

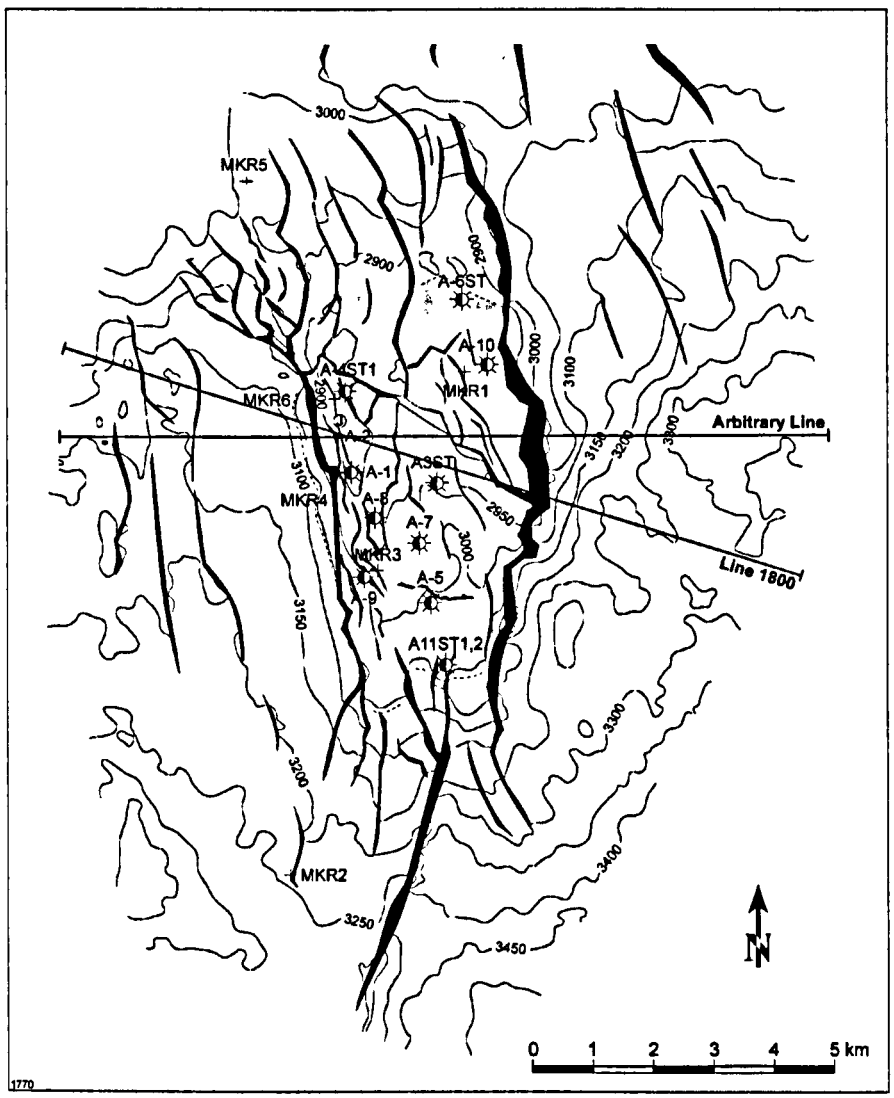

Fig. 6.12. Depth structure map of the top Abiod Formation over the Miskar area. The shaded region represents thinned and/or totally eroded Abiod Formation.

Sequence of Faulting in the Miskar Area

Detailed analysis of the seismic dataset has identified the presence of five major fault systems within the Miskar area ranging in age from at least the Jurassic to the present-day:

- Late Triassic (?) / Late Jurassic (?);
- Early (?) to late Turonian;
- Campanian to late Maastrichtian;

- Late Thanetian to Priabonian;
- Langhian to present-day.

The nature, timing and influence that these fault systems had on the depositional architecture of the Mesozoic and Tertiary sequence is discussed in the next section.

Late Triassic (?) / Late Jurassic (?) Fault System

This system of approximately N-S to NNE-SSW trending late Triassic (?) / late Jurassic (?) faults represents the oldest system of structures that can be interpreted from the seismic dataset. It is suggested that they formed initially as extensional faults above pre-existing basement lineaments, during a phase of Neo-Tethyan rifting. However, their present-day geometry suggest that they have subsequently been reactivated in both transtension or transpression at different stages through their evolution. Indeed, evidence suggests that these structures were intermittently reactivated in sinistral transtension (particularly in the Turonian), and then later in sinistral transpression during the late Campanian - late Maastrichtian and late Eocene.

These faults are identified on the Miskar dataset as the lowermost, steeper fault planes on the two horst-bounding faults (i.e. 4000-5000ms TWT)(N.B. they are not the lower angle planes that extend up into the Palaeocene and Tertiary section) (**Fig 6.10**). As previously discussed, these faults exhibit convex fault planes (out towards the hangingwall blocks), which are indicative of faults with oblique-slip displacements. Displacements on these faults are large (probably in excess of 1000m) For the purpose of this study these faults will be referred to as 'basement' structures.

Middle Cenomanian to Late Turonian Fault System

This pervasive system of approximately NW-SE trending faults was probably initiated during the middle Cenomanian to early Turonian (~2600ms-3200ms TWT). They extend up to the top of the Turonian where they generally terminate at the Abiod unconformity (~2400ms-2700ms TWT) (**Fig. 6.11**). The Abiod unconformity represents a period of regional uplift and erosion that occurred during Coniacian to Santonian times.

At Aleg level, this system of structures produces a complex horst and graben geometry. This is particularly clear in 2D seismic sections that extend into the bounding half-grabens. The lower parts of the Aleg Formation (i.e. the Bireno, Lower Aleg R1

Superior/Inferior and Aleg Carbonate Members) show only minor thickening associated with synsedimentary fault activity on these structures. This suggests that there was only minor tectonic activity during this period. However, the volcanics (sub-aqueous basalts) that are identified at the base of the R-1 Superior reservoir in the Miskar A-6 and A-10 cores suggest that the Miskar Structure was located on unstable crust during the early to middle Turonian (**Plate 6.15**). The extrusion of these volcanics probably occurred along the deep-seated ~N-S trending faults that underlie and effectively bound the structure. This volcanic event marks an episode of tectonic subsidence associated with the development of the Gabes-Tripoli Basin.

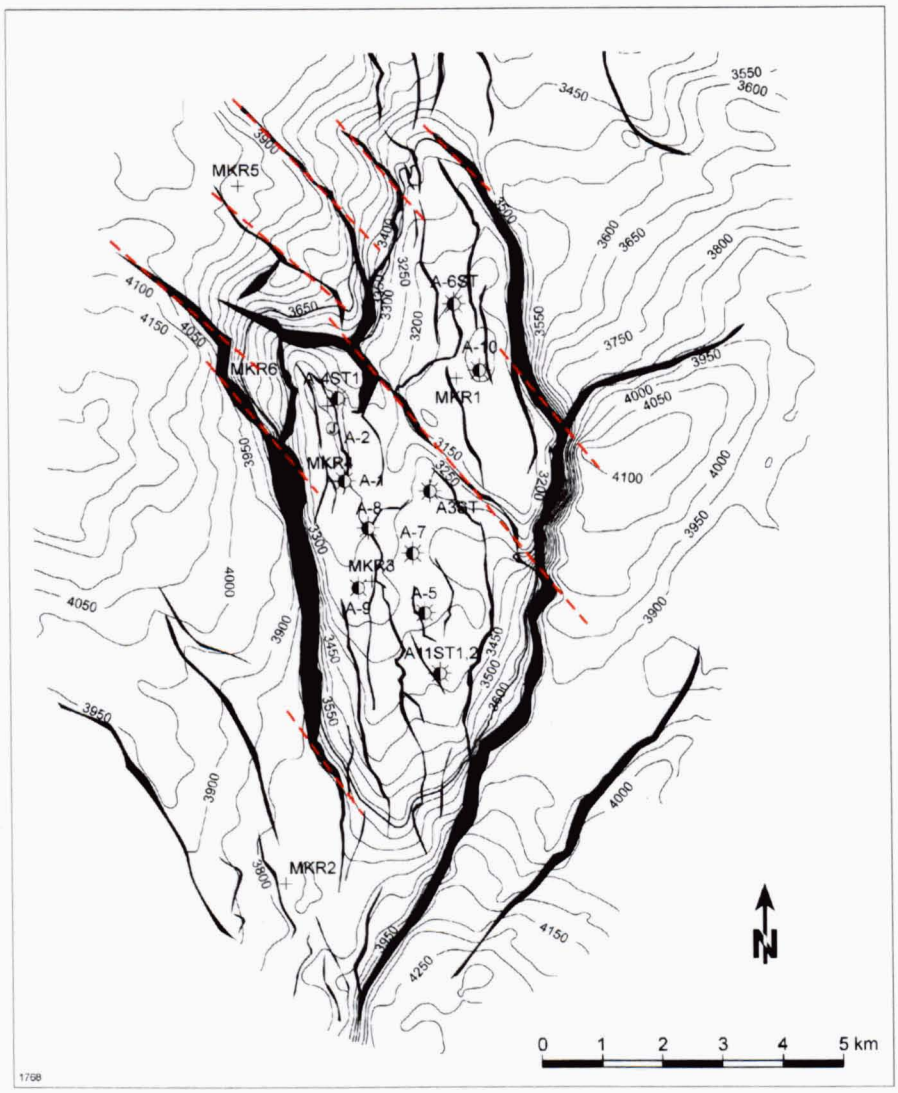

Fig. 6.13. Depth structure map of the top R1 Inferior Member illustrating the en-echelon nature of faulting.

The upper parts of the Aleg Formation (i.e. the Upper Aleg Member) show substantial thickening associated with movement on these structures. This is expressed as a series of seismic reflectors that are strongly divergent towards the main horst-bounding faults.

This period of late Turonian sedimentation is thought to correspond to increased tectonic subsidence in the Gabes-Tripoli Basin.

Depth structure maps across Miskar illustrate that this system of faults forms a subtle en-echelon configuration above the main NNE-SSW trending faults that bound the structure (**Fig. 6.13**). Their development appears to have been partially controlled by transtensional movement on the underlying N-S trending faults (as a result of reactivation) during a phase of approximately NNE-SSW directed extension associated with the development of the Gabes-Tripoli Basin (refer to Section 6.5.5) (**Fig. 6.14**).

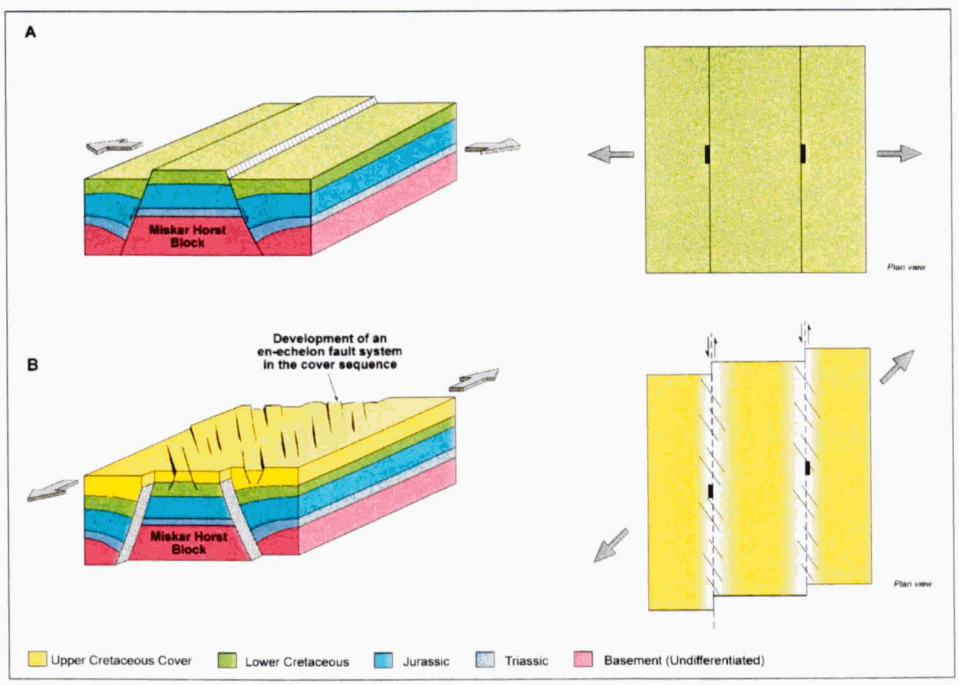

Fig. 6.14. Mechanism for the development of en-echelon extensional faults within the cover sequence above a 'basement' wrench fault.

Over the Miskar Structure, this system of faults is expressed on seismic sections as a series of steeply dipping convex-outward fault zones (**Fig. 6.10**). 'Harpoon' and 'pop-up' structures associated with transpression on these faults are clearly visible in the Aleg Formation, most notably adjacent to the eastern, horst-bounding fault zone (**Fig. 6.11**). These structures are thought to have formed during a phase of late Maastrichtian to late Thanetian ESE-WNW directed compression.

Campanian to Late Maastrichtian Fault System

This system of approximately NNE-SSW trending faults was initiated during the Campanian, after a period of regional uplift and erosion that had occurred throughout the late Coniacian and Santonian (**Fig. 6.10**). They formed in response to ENE-WSW

directed extension (prevalent throughout the deposition of the Abiod Formation (*SS-8*)), and mainly utilised pre-existing weaknesses developed from the earlier system of Turonian faults (refer to previous section). Many of these Campanian structures link up to the earlier system of faults directly, through 'dip-linkage' (N.B. that they have a slightly different trend to the earlier set). Maximum throws on this system are approximately 200m.

Depth structure maps over the area demonstrate, that, like the lower set of faults, the development of these structures was in part controlled by reactivation of the deep-seated NNE-SSW trending 'basement' faults underlying the horst block (**Fig. 6.14**). Seismic reflection profiles show large sediment thickness variations throughout the Abiod Formation adjacent to the main horst-bounding faults (Seismic reflectors diverge towards individual fault planes) (**Fig. 6.10**). This indicates that these structures had a strong control on deposition throughout this period of rejuvenated tectonic subsidence. The steeply dipping 'convex outward' fault plane geometries, and the nature of the 'harpoon' and 'pop-up' structures observed within the Abiod Formation suggest that these faults have been reactivated in transpression. As previously discussed in Chapter 3, this event appears to coincide with a phase of approximately ESE-WNW directed compression that commenced during the late Maastrichtian after the deposition of the Abiod Formation.

The fault that separates the horst block into two main compartments is associated with this Campanian to late Maastrichtian system. Seismic profiles across this fault zone show significant sedimentary thickening adjacent to the main fault, together with substantial erosion of the Abiod Formation, mainly on the higher northeastern fault block where it is substantially eroded or totally missing (Miskar A-6). These observations support an age of late Maastrichtian uplift and erosion.

Ypresian to Lutetian Fault System

Seismic profiles across the structure consistently demonstrate that the phase of ESE-WNW compression continued into the late (?) Thanetian. This is shown by 'upward' tilting on-lapping surfaces within the lower and middle parts of the El Haria Formation (**Fig. 6.15**). Towards the end of the Thanetian compression ceased, and a new period of relatively stable subsidence prevailed. During this period, fault activity is not evident. However, during the early to middle Eocene this stable regime gave way to a phase of

ENE-WSW extension. This led to the development of a system of approximately NNW-SSE faults (**Fig. 6.10**). These faults extend up into the Lutetian interval where they generally terminate against the Oligocene unconformity. Occasionally these structures pass across this unconformity, indicating a later stage of reactivation.

These faults are expressed on seismic profiles by moderately dipping planes that sole out in the shaley El Haria Formation. Displacements range between 30-200m. Some of these faults have utilised pre-existing weaknesses developed during the formation of earlier structures (e.g. the main horst bounding faults link through dip linkage) (**Fig. 6.10**). Only minor sedimentary thickness variations are apparent (in the Bou Dabbous and Cherahil Formations), indicating that active tectonics only had a minor control on deposition throughout this period. Gentle folding within the El Haria to Cherahil sequence is the product of both extension (producing small growth sequences) and also compression (which has partially inverted the strata adjacent to some faults). The end of the Eocene was characterised by a regional compressive event that caused uplift and sub-aerial erosion of the upper parts of the Cherahil Formation on many of the exposed tilted fault blocks (N.B. the Bartonian and Priabonian sections are missing on the crest of the Miskar structure) (**Fig. 6.10**).

Langhian to Present-Day Fault System

The approximately NW-SE trending Langhian to present-day system of extensional faults developed as a consequence to NE-SW directed extension that was associated with thrust emplacement in Northern Tunisia and/or the onset of rifting in the Straits of Sicily Rift Zone (N.B. they have a different orientation to the underlying fault set) (**Fig 6.10**).

Seismic profiles illustrate that this system of faults has moderate dips with only minor displacements (<100m). Small sedimentary thickness variations are apparent adjacent to some structures. Occasionally faults in this system link with faults in the lower set through 'dip linkage' (**Fig. 6.10**).

6.5.4. Structural Evolution of the Miskar Field

The structural evolution of the Miskar Gas Condensate Field closely traces the Mesozoic and Tertiary development of the Gabes-Tripoli Basin (explained in Section 3.8). A series of reconstructions are provided in **Figure 6.16** that summarise the development of the accumulation from the early Mesozoic to the present-day.

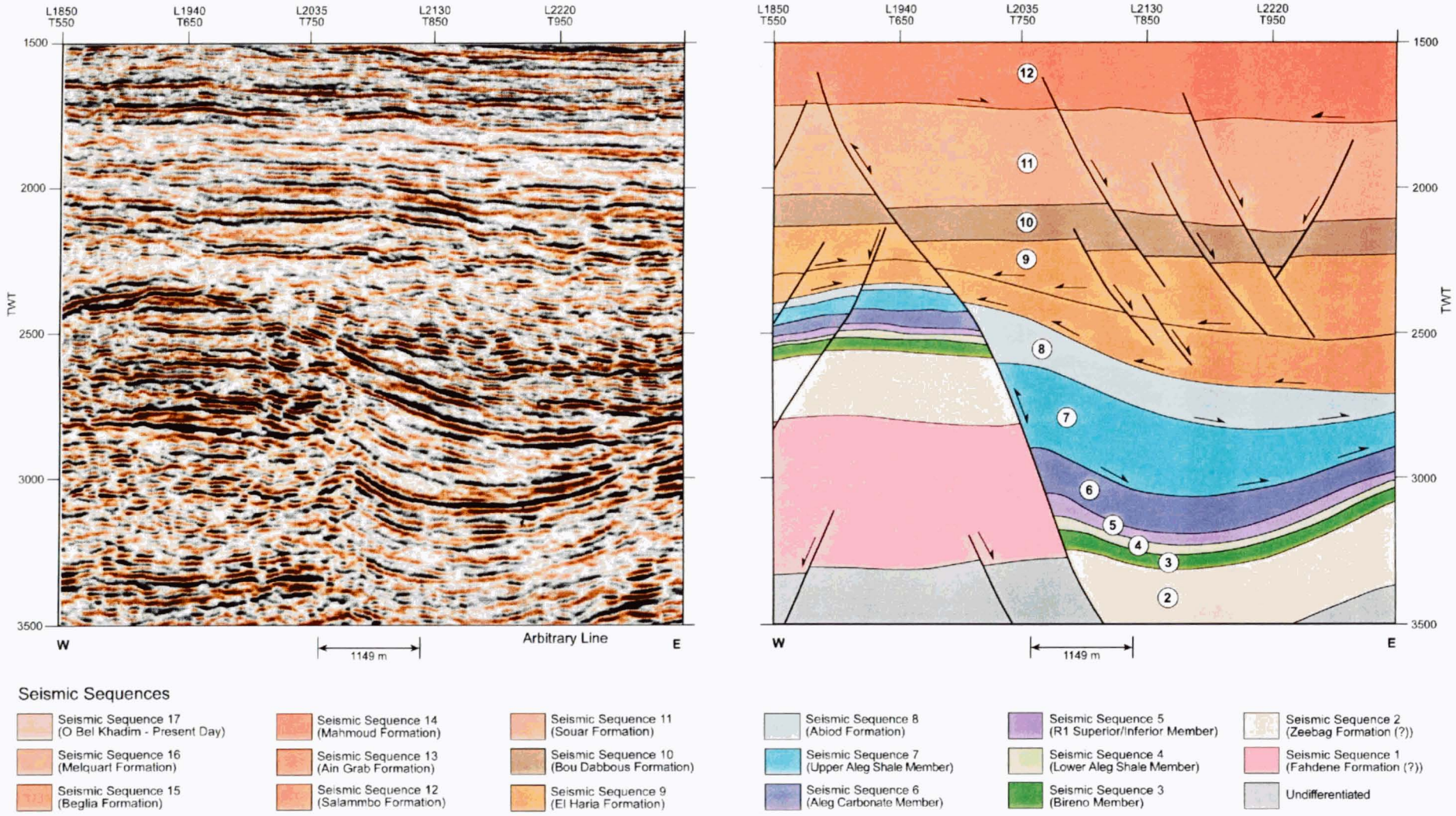

Fig. 6.15. Blow-up of area within the Arbitrary seismic line shown in Figure 6.10 illustrating the internal disposition of reflection events in the Upper Cretaceous succession

a) **Early Mesozoic E-W Extension**

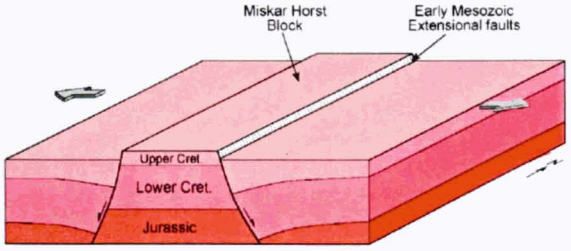

b) **Upper Cretaceous E-W Extension**

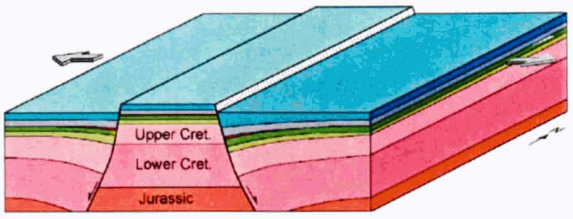

c) **NE-SW Extension**

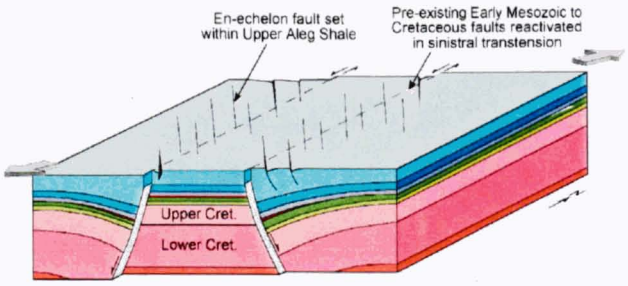

d) **Late Turonian to Late Santonian Uplift and Sub-aerial Erosion**

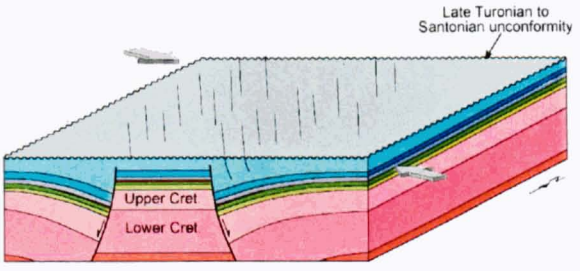

e) **Rejuvenation of ENE-WSW Extension**

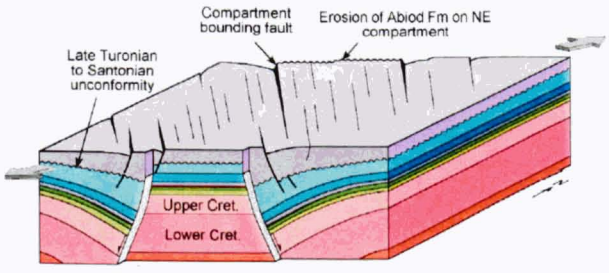

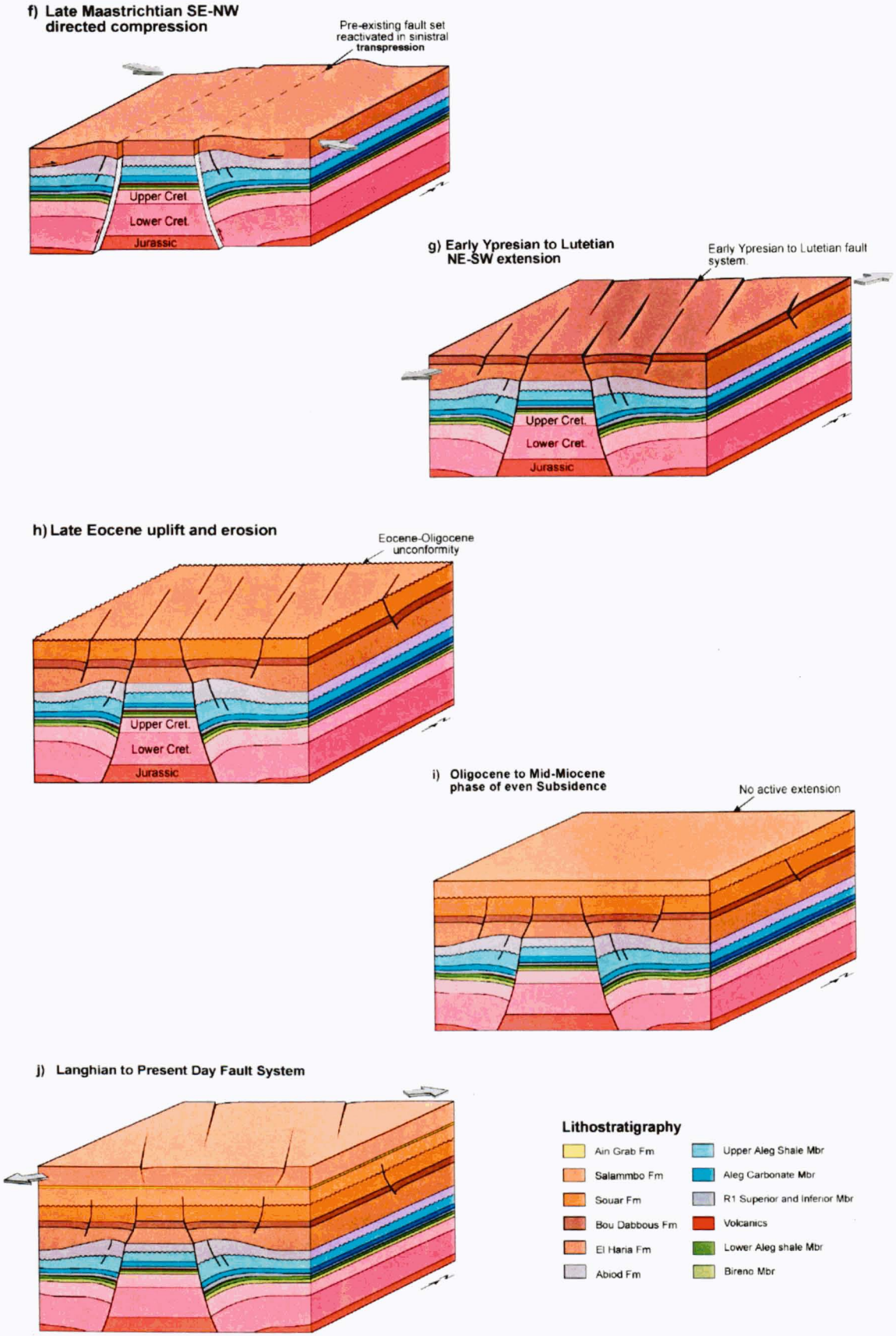

Fig. 6.16. Sequential restoration of the Miskar structure showing the main tectonic phases that have affected the area during the Mesozoic and Tertiary.

Late Triassic (Rhaetian) to Early Cretaceous (Aptian)

Available data demonstrates the presence of a system of roughly N-S to NNE-SSW trending deep-seated 'basement' structures that delineate the Miskar horst block. Regional studies suggest that these faults formed in response to crustal extension associated with Neo-Tethyan rifting in the Upper Triassic and Upper Jurassic-Lower Cretaceous (**Fig. 6.16a**).

Early Cretaceous (Aptian) to Late Palaeocene (Thanetian)

It has been established that during the Aptian, a change in the relative motion of Africa with respect to Europe (Dewey et al., 1989) caused dextral strike-slip movements on major E-W and WNW-ESE trending lineaments across the Gulf of Gabes region. This, in turn, caused the onset of NE-SW extension in the Gabes-Tripoli Basin during the latest Albian to Cenomanian. Intermittent periods of extension throughout the Late Cretaceous and Tertiary are observed in the Miskar area, the first being during the deposition of the upper parts of the Fahdene Formation and the Bahloul and Lower Aleg Formations (*SS-1 & SS-2*).

The deposition of the succeeding Bireno, Lower Aleg Shale, R1 Inferior/Superior and Aleg Carbonate Members of the Aleg Formation occurred during a phase of relative tectonic quiescence (**Fig. 6.16b**). Mild reactivation on the early N-S trending structures affected facies development of some of these sequences. Basalts within the lower parts of the R1 Superior Member (Miskar A-6 & A-10) indicate that the Miskar structure was located on unstable crust during the early to middle Turonian. The extrusion of these volcanics probably occurred along the deep-seated N-S trending faults that underlie the structure.

Following the deposition of the Aleg Carbonate Member (*SS-6*), the Miskar area experienced an intense period of approximately NE-SW extension, related to tectonic subsidence in the Gabes-Tripoli Basin (**Fig. 6.16c**). This is noted on seismic data by the rapid expansion of *SS-6* from the crest of the structure into the eastern and western half-grabens. It is believed that this phase of extension, which is identified on subsidence curves (**Fig. 3.35**), reactivated the underlying N-S to NNE-SSW trending 'basement' structures in sinistral transtension. This induced a shear couple within the cover sequence (i.e. the Upper Aleg Shale Member) above each reactivated fault trace. As a direct result, fault development in the Upper Aleg Shale Member was partially

controlled by transtensive movement on the pre-existing N-S trending structures (**Fig. 6.16c**) (N.B. this process was probably active during the deposition of *SS-1* and *SS-2*, although the poor seismic resolution at these levels precludes a direct determination). The en-echelon configuration of cover faults with respect to the underlying N-S trending structures supports this theory (**Fig. 6.14**).

The initiation and propagation of extensional faults in the cover sequence above 'basement' strike-slip zones is complex. Richard et al. (1991) demonstrates experimentally that increasing the amount of strike-slip movement on a 'basement' wrench fault causes the induced stress field in the overlying cover to rotate simultaneously (**Fig. 6.17**). Therefore, as a set of extensional faults develops above such a system, their propagation paths may rotate (or twist) accordingly with respect to the amount of strike-slip movement on the controlling fault. This process of 'out-of-plane' propagation (Lawn & Wilshaw, 1975) is believed to have occurred in the cover sequence above the two N-S/NNE-SSW trending basement lineaments in the Miskar structure.

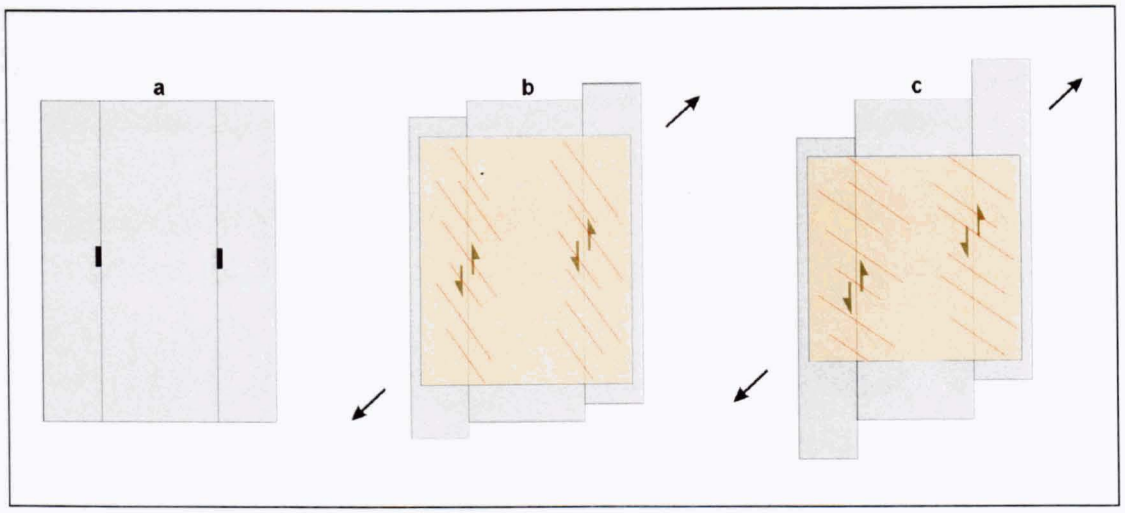

Fig. 6.17. Fault propagation in the cover sequence above a sinistral strike-slip 'basement' wrench fault. a) Pre-existing basement lineaments, b) Initiation of faults oblique to the initial basement structures, c) Propagation paths of faults rotate to accommodate increased strike-slip movement on basement structures.

The late Turonian to Santonian interval is characterised by a period of uplift and sub-aerial erosion that produced a regional unconformity at the top of the Aleg Formation (**Fig. 6.16d**). Following this, the Campanian to Maastrichtian period was characterised by the rejuvenation of NE-SW oriented extension (**Fig. 6.16e**). This was accompanied by a marine transgression and the deposition of the Abiod Formation. Many late Turonian faults were reactivated, propagating up into the Abiod Formation (N.B. the

slightly different fault trends on depth structure maps of the Aleg and Abiod Formations (**Figs. 6.10 & 6.11**)). Some of these Campanian structures link up to the earlier system of faults directly, through 'dip-linkage'. The en-echelon nature of faulting remains, indicating the control that the underlying N-S trending structures had on its development.

During this phase of extension the horst block was subdivided into two main compartments; 1) a northeastern compartment where the Abiod Formation is substantially/totally eroded, and 2) a southwestern compartment with a complete section of the Abiod Formation (**Fig. 6.16e**). Seismic sections across the fault zone (that separates these compartments) show moderate thickness variations within the Abiod Formation associated with fault activity (**Fig. 6.10**). It is believed that throughout much of this period sub-aerial erosion of the Abiod Formation deposited on the high block to the northeast was contemporaneous with deposition to the southwest.

Towards the end of deposition of the Abiod Formation, the Miskar area was subjected to a phase of SE-NW oriented compression, within the late Maastrichtian (**Fig. 6.16f**). This event, which continued into the late Thanetian, reactivated and partially inverted the pre-existing Turonian to Maastrichtian fault systems.

During this period, the eastern bounding fault zone was reactivated in sinistral transpression, causing the partial inversion of the eastern half-graben in the southern part of the field (**Fig. 6.16f**). Complex onlapping relationships are caused in the lower parts of the Palaeocene El Haria Formation by the coeval nature of ongoing deposition and SE-NW directed compression (**Fig. 6.15**). In the northern sector of this fault zone, compression was accommodated by strike-slip transfer, and therefore no inversion structures were generated. On the western fault zone only minor inversion of the western half-graben occurred.

During the late Thanetian, compression ceased, giving way to a period of relatively stable thermal subsidence (N.B. no active faulting is evident in the upper parts of the El Haria Formation). This continued into the early Ypresian during the deposition of the Bou Dabbous Formation (*SS-10*).

Eocene to Present-Day

At approximately 48Ma (**Fig 3.35**) the Miskar area experienced renewed tectonic subsidence associated with crustal extension in the Gabes-Tripoli Basin (**Fig. 6.16g**).

This event, which continued until the late Bartonian was accompanied by the development of a system of approximately NNW-SSE trending extensional faults that sole out in the El Haria Formation. Some of these features utilised pre-existing weaknesses developed during the formation of earlier structures. These faults pass up through the Cherahil Formation, where they terminate against the Oligocene unconformity (**Fig. 6.10**). This unconformity represents a regional compressive event that caused uplift and sub-aerial erosion of the Bartonian to Priabonian sections of the Cherahil Formation (**Fig. 6.16h**). Gentle folding in the El Haria to Cherahil sequence, particularly in the hanging-wall block of the western-bounding fault zone is thought to be due to partial inversion on this fault during this event. This episode is also thought to have tilted the Miskar horst down to the southeast.

The Oligocene Salammbo Formation onlaps gently onto the partially eroded fault blocks of the Cherahil Formation (**Fig. 6.10**). It was deposited during a period of relatively stable thermal subsidence, which continued into the Middle Miocene (**Fig. 6.16i**). No evidence of active faulting is associated with this period.

During the Langhian, the Miskar area experienced another period of fault-controlled subsidence. This event was accompanied by the initiation of NW-SE trending faults within the Mahmoud Formation (**Fig. 6.16j**). Activity on these structures is still apparent at the present-day. The timing of this activity coincides with the onset of thrust emplacement in northern Tunisia and later rifting in the Straits of Sicily (refer to Section 3.8 for a discussion).

6.6. Structural Analysis of the Miskar A-3, -6, -7, -9, -10 & -11 Cores.

6.6.1. Introduction

Comprehensive structural analyses of the available cored intervals from a number of Miskar wells were undertaken in order to ascertain the nature and distribution of fracturing in the principal reservoir zones. Table 6.3 lists the cored intervals analysed in each well, and **Figure 6.2** illustrates the position of each well in the Miskar Field. The results have been integrated with the field-scale seismic study (and the subsidence modelling analysis presented in Section 3.7), and provide an assessment of the sequence of fracturing in the accumulation.

Interval	A-3	A-6	A-7	A-9	A-10	A-11
El Haria Formation	✔		✔			
Abiod Formation	✔		✔			✔
Upper Aleg Member	✔					✔
Aleg Carbonate Member	✔					✔
R-1 Superior Member	✔	✔		✔		✔
R-1 Inferior Member	✔	✔		✔	✔	✔
Lower Aleg Member						
Bireno Member					✔	

Table 6.3. Cored intervals in Miskar wells under analysis.

All of the wells intersected the R1 Superior and Inferior reservoirs, with the exception of Miskar A-7. The Abiod reservoir was cored in the Miskar A-3, A-7 and A-11 wells. The lower Bireno reservoir has not been cored. Miskar A-3 and A-11 have the most complete section and are therefore the most useful. Table 6.4 summarises the formation top depths of each lithostratigraphic unit of importance for each well.

Interval	A-3	A-6	A-7	A-9	A-10	A-11
El Haria Formation	2741.0	3817.4	3014.0	3064.6	3396.3	3896.8
Abiod Formation	3306.8	Absent	3522.2	3557.8	3980.6	4797.6
Upper Aleg Member	3366.3	4522.0	3588.0	3609.5	4008.4	4899.3
Aleg Carbonate Member	3528.3	4731.5	3721.3	3734.9	4138.9	5101.2
R-1 Superior Member	3634.6	4866.7	3812.4	3828.5	4247.4	5251.6
R-1 Inferior Member	3695.2	5004.0	3884.6	3882.8	4353.9	5341.0
Lower Aleg Member	3750.0	5071.4	3906.0	3919.4	4406.6	5401.4
Bireno Member	3890.9	5274.0	3994.0		4579.4	5544.5

Table 6.4. Measured depths (m MD) to lithostratigraphic unit tops.

6.6.2. Core Quality & Study Limitations

All of the analysed cored intervals were slabbed and resinated. This aided handling and analysis. Core generally was of moderate to good quality, except along certain intervals where only rubble was observed. Rubble zones are commonly associated with drilling complications and/or fault zones.

A particular limitation in this analysis was the lack of oriented core. This precluded a direct determination of fracture and bedding orientation. Other limitations are associated with the deviation of the core axis relative to fracturing (i.e. most of the analysed cores trend sub-parallel to the fracture systems present). Consequently large

sampling biases are introduced. The implications of this have been discussed in Chapter 5, together with the most effective methods to alleviate the problem. The AFS method developed by Narr (1996) is used in this study to calculate fracture spacing.

6.6.3. Core Observations

Summaries of the core observations are given for each well in the following account. A detailed review of the structures present in Miskar A-3 is provided to introduce the nature of fracturing in the Miskar accumulation. Thereafter, brief accounts of the Miskar A-6, A-7, A-9, A-10 and A-11 cores are provided. Reference should be made to Appendix A for raw data collected from all wells.

Miskar A-3

Miskar A-3 is located within the southwestern compartment of the Miskar horst block, approximately 500m from the main NW-SE trending compartment bounding fault (**Fig. 6.2**). The well is near vertical within the Plio-Pleistocene section, but deviates to an angle of approximately 30^0 (from the vertical) in the main reservoir intervals. Nine cores were recovered during drilling. A listing of these is given in Table 6.5.

Core Number	Interval Depth (m)	Lithostratigraphic Unit	Recovery (%)
1	3305.5 – 3324.5	El Haria - Abiod	98.4
2	3324.5 – 3353.0	Abiod	97.2
3	3353.0 – 3381.0	Abiod - Upper Aleg Shale	99.6
4	3631.5 – 3659.4	Aleg Carbonate - R1 Sup.	97.0
5	3659.4 – 3687.3	R1 Superior	98.0
6	3687.3 – 3703.0	R1 Superior - R1 Inferior	97.7
7	3703.0 – 3728.0	Base R1 Inferior	49.5
8	3728.0 – 3743.0	Base R1 Inferior	100
9	3743.0 – 3750.5	Base R1 Inferior	95.0

Table 6.5. Cored intervals in Miskar A-3

Stylolites

A total of 118 aggregate stylolites were identified in Cores 1 - 9 within Miskar A-3 (**Fig. 6.18**). As previously discussed in Chapter 4, aggregate stylolites are defined as those stylolites that have greater amplitudes than the rock matrix (Park & Schott, 1968). The majority of these aggregate stylolites are horizontal compactional features that formed in response to overburden stress (σ_v). They tend to preferentially develop along bed boundaries where there is a distinct variation in the bulk rock composition

between two lithological units (**Plate 6.1**). Many of these structures appear to be laterally extensive, with the larger seams possibly extending over large areas (tens or even hundreds of metres). The development of such seams could have serious implications with regard to vertical communication within the reservoir (Nelson, 1985). However, if currently open, they may cause enhanced horizontal flow. Indeed, it has been observed that many of these stylolites contain partial dolomite and late calcite cements, suggesting that they may have cracked open at some point in their evolution. These events probably correspond to late phases of uplift and erosion. (i.e. unroofing).

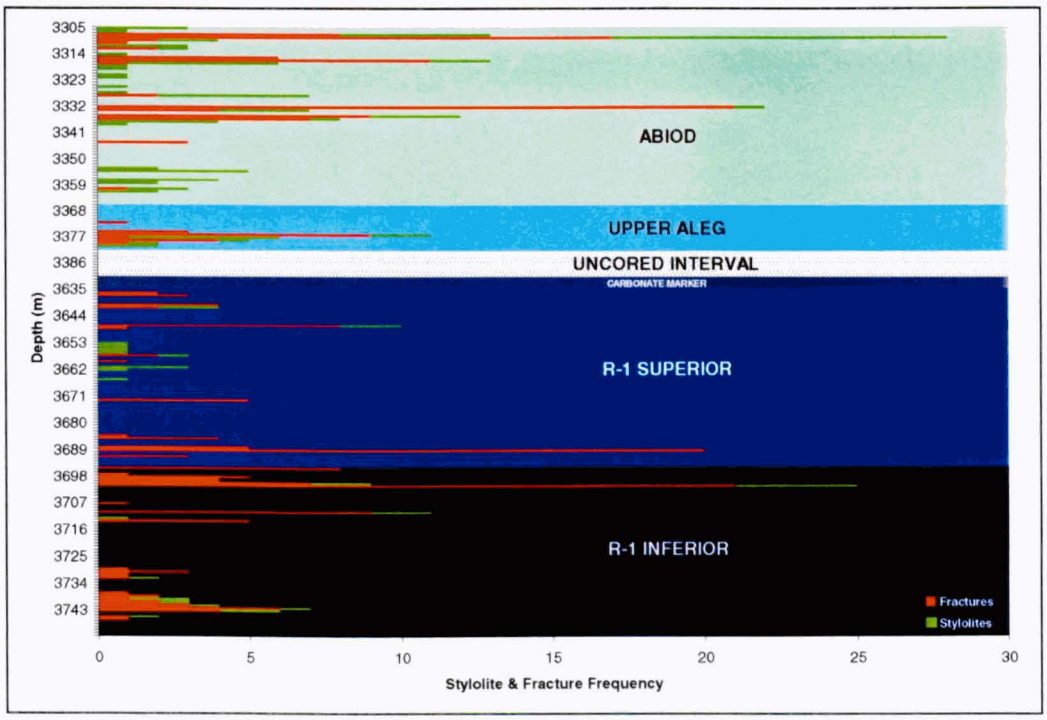

Fig. 6.18. Miskar A-3. Stylolite and Fracture Frequency versus depth

Two particular types of compactional aggregate stylolites are observed in the core:

- High amplitude, 'sutured' stylolites, which are highly irregular in form (**Plate 6.1**);
- Low amplitude 'non-sutured' (simple) stylolites that are highly regular in form (i.e. display good smooth sinusoidal geometries, and often contain pyrite) (**Plates 6.2 & 6.3**).

The difference in these two types of pressure solution seam may be attributed to development in different lithofacies. **Figure 6.18** indicates that compactional stylolites develop throughout the cored interval, most notably within the Abiod Formation, where stylolite frequencies attain maximum values of 11 stylolites/metre. Average stylolite frequencies within individual lithostratigraphic units are shown in Table 6.6.

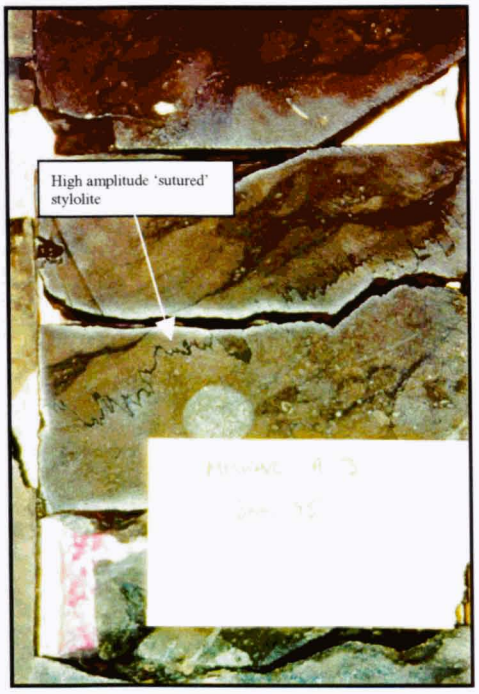

Plate 6.1: Miskar A-3: 3661.95m. High amplitude 'sutured' stylolite in the R1 Superior reservoir.

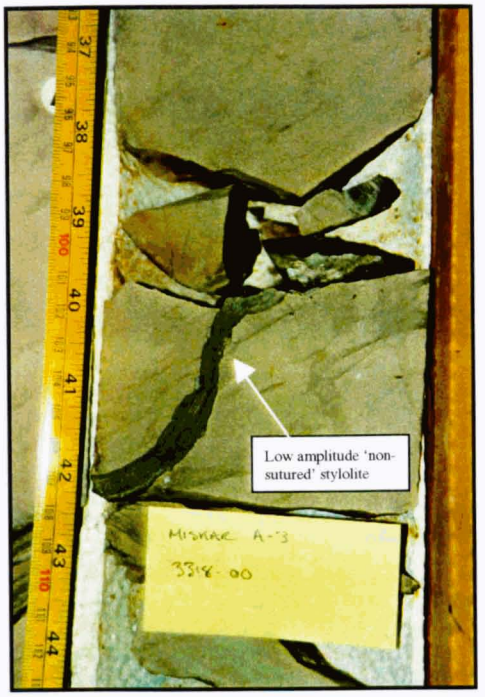

Plate 6.2. Miskar A-3: 3318.00m. Low amplitude 'non-sutured' stylolite in the Abiod Formation

Lithostratigraphic Unit	Number of Stylolites	Stylolite Freq/metre	Average Spacing (m)
Abiod Formation	75	1.26	0.80
Upper Aleg Member	11	0.71	1.41
Aleg Carbonate Member	0	0.00	0.00
R1 Superior Member	14	0.23	4.33
R1 Inferior Member	18	0.32	3.10
Total Core	118	0.61	1.65

Table 6.6. Stylolite frequency and spacing in each lithostratigraphic interval (Miskar A-3).

This table emphasises the preferential development of compactional aggregate stylolites within the Abiod Formation. The Upper Aleg Shale, R1 Superior and R1 Inferior intervals all contain stylolites but to a lesser extent. The Aleg Carbonate Member shows no record of stylolitisation, although only a small portion of this interval was cored.

Thin section analysis demonstrates that aggregate stylolites initially develop as intergranular stylolites at grain-grain contacts (**Plate 6.4**). Intergranular stylolites have been defined as those stylolites which have smaller amplitudes than the grain diameter of the host rock (Park & Schott, 1968). Intergranular stylolitisation on this scale is a pervasive feature throughout the cored intervals, particularly in wackestone-packstone facies. The development of these intergranular stylolites into larger scale aggregate stylolites occurs preferentially at certain horizons. These preferred sites were probably controlled by mechanical variations in the bulk rock composition between different

facies or sub-facies (i.e. at bed boundaries). The relative spacing of compactional aggregate stylolites may therefore be crudely related to the spacing of bed boundaries.



Plate 6.3. Miskar A-3: 3358.98m. Low amplitude 'non-sutured' stylolite seam in the Abiod Formation.

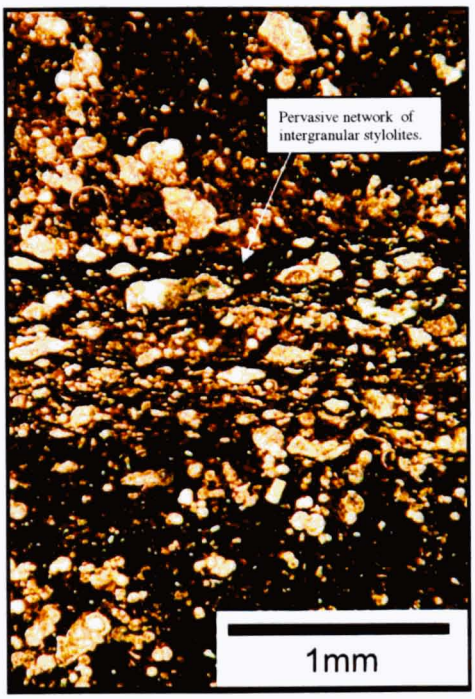

Plate 6.4. Pervasive network of intergranular stylolites in the Abiod Formation

It has already been mentioned in Chapter 4 that stylolite occurrence and geometry appears to be primarily controlled by both clay content and the percentage of structurally resistive elements (bioclastic debris) within a given host rock (refer to Section 4.3). Where there is only minor clay material present within a rock mass containing many structurally resistive elements (i.e. shell debris), high amplitude, sutured stylolites will be developed (Wanless, 1979). However, as clay content increases, inevitably the percentage of shell fragments within a given volume will decrease. This ultimately produces low amplitude, non-sutured stylolite seams (Wanless, 1979).

This theory appears to be consistent with the observations gained from the analysis of Miskar cores. In Miskar A-3 sutured stylolites were well developed in the R1 Superior and Inferior Members where a large percentage of bioclastic material in the form of peloid, echinoderm and mollusc fragments was present. However, in the chalky and slightly clayey Abiod Formation, low amplitude (simple) non-sutured stylolites tend to predominate.

Tectonic stylolites (i.e. pressure solution seams that have developed in response to tectonic compression) have also been identified in the cored interval (e.g. 3308.48-

3308.62m MD) (**Plate 6.5**). These features are developed at a high angle to the core axis (~80^0). They commonly crosscut and displace horizontal compactional stylolites indicating that they formed after the development of the compactional features (**Plate 6.5**). Unfortunately, the cored intervals are not oriented, so the exact orientation of these structures relative to a past tectonic episode cannot be directly determined. However, it is indicated through the use of seismic data that they probably formed in response to:

- A phase of SE-NW directed compression from the late Maastrichtian to late Thanetian, when the eastern horst-bounding fault was inverted in sinistral transpression;

- A phase of late Eocene compression that caused uplift and erosion of the Bartonian to Priabonian section of the Souar Formation.

These structures generally have lower amplitudes than the compactional features. This could suggest that the stresses exerted during the development of the compactional stylolites (i.e. σ_v) were longer lived than the compressional stresses that created the tectonic stylolites. This clearly is true when considering that overburden stress has acted throughout the subsidence history of individual lithological units. Core observations show that most tectonic stylolites are closed (i.e. they have not been cracked open after their formation) (**Plate 6.5**).

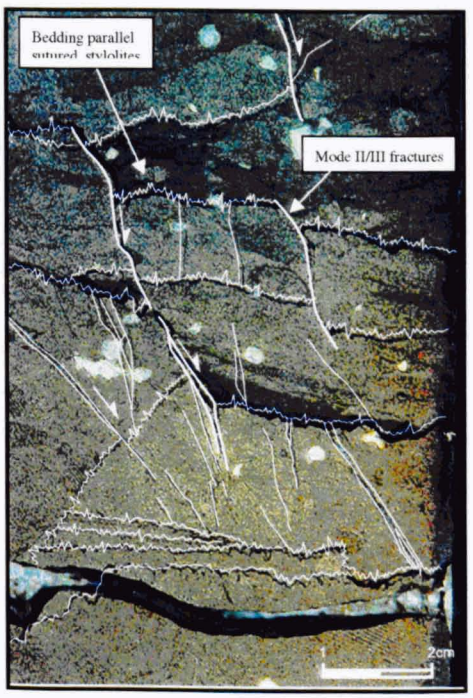

Plate 6.5. Miskar A-3: 3308.48m. Mode II/III fractures intersecting and displacing several stylolites within the Abiod Formation



Plate 6.6. Calcite-filled vugs within the Abiod Fm.)

It is evident from the analysis of the distance between dentae in each of these aggregate stylolite systems that a large amount of fluid must have been generated through the process of pressure solution. This is particularly apparent in the system of compactional stylolites that show that an average of 14.70mm (vertical distance between dentae) of material has been removed for each stylolite in the whole cored interval. Table 6.7 shows the material removed by aggregate stylolitisation within each lithostratigraphic unit. If these figures of removed material (by stylolitisation) are considered as proportion of the bulk rock volume (in 3D), it becomes apparent that a significant amount of the rock mass has gone into solution. For example a stylolite seam with circumferential area of $1000m^2$, and an average height between dentae (i.e. material loss) of 80mm, would yield a volume of $80m^3$ (**Fig. 6.19**). This is a minimum estimate of the amount of the total rock volume that has gone into solution, because the distance between stylolite dentae is also a minimum figure of the amount of material that has been lost.

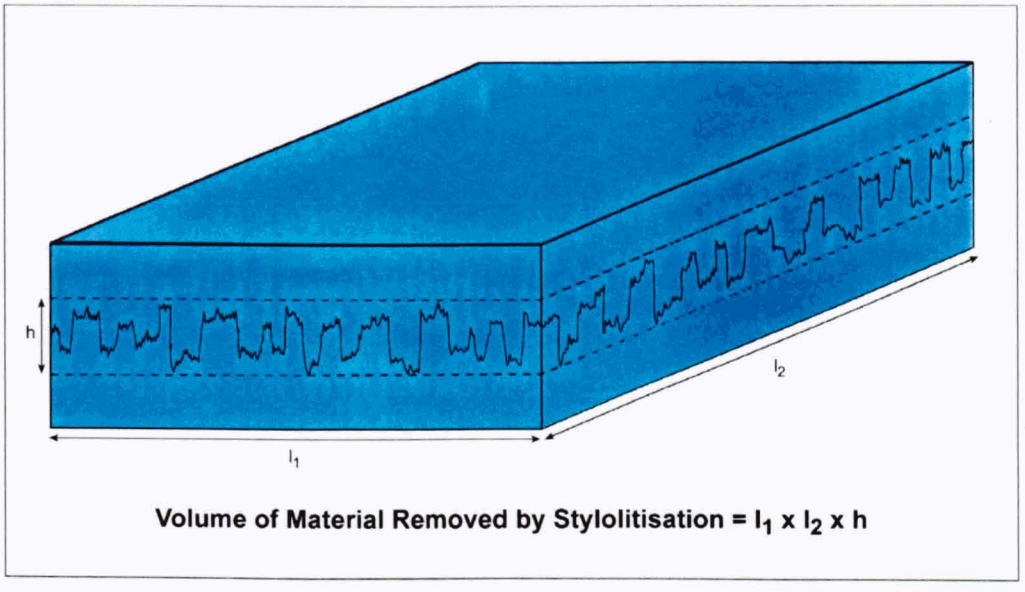

Fig. 6.19. Schematic diagram illustrating the minimum amount of material removed by stylolitisation

A proportion of the material in solution would have been reprecipitated in the surrounding matrix precluding porosity, while the rest would have been transported away from the immediate site of dissolution and may have been reprecipitated within the various fracture networks present. Evidence to suggest that these solutions would have been re-distributed in the surrounding rock matrix is provided by the presence of calcite filled vugs (**Plate 6.6**).

Lithostratigraphic Unit	Material Removed (mm)	Average Removed/Stylolite (mm)
Abiod Formation	489	6.52
Upper Aleg Member	65	5.91
Aleg Carbonate Member	0	0.00
R1 Superior Member	506	36.14
R1 Inferior Member	675	37.50
Total Core	1735	14.70

Table 6.7. Material removed through the process of pressure solution (mm) (Miskar A-3)

Fractures

A total of 263 fractures were identified within Cores 1 - 9 in Miskar A-3 (**Fig. 6.20**). A large proportion of these cored fractures are steeply dipping, sub-vertical to vertical Mode I fractures (i.e. fractures that have formed in extension) (**Plate 6.7**). These are accompanied by moderately dipping (e.g. 55^0-65^0) to sub-vertical Mode II and Mode III fractures (i.e. fractures that have formed in shear and shear/extension respectively) (**Plate 6.8**).

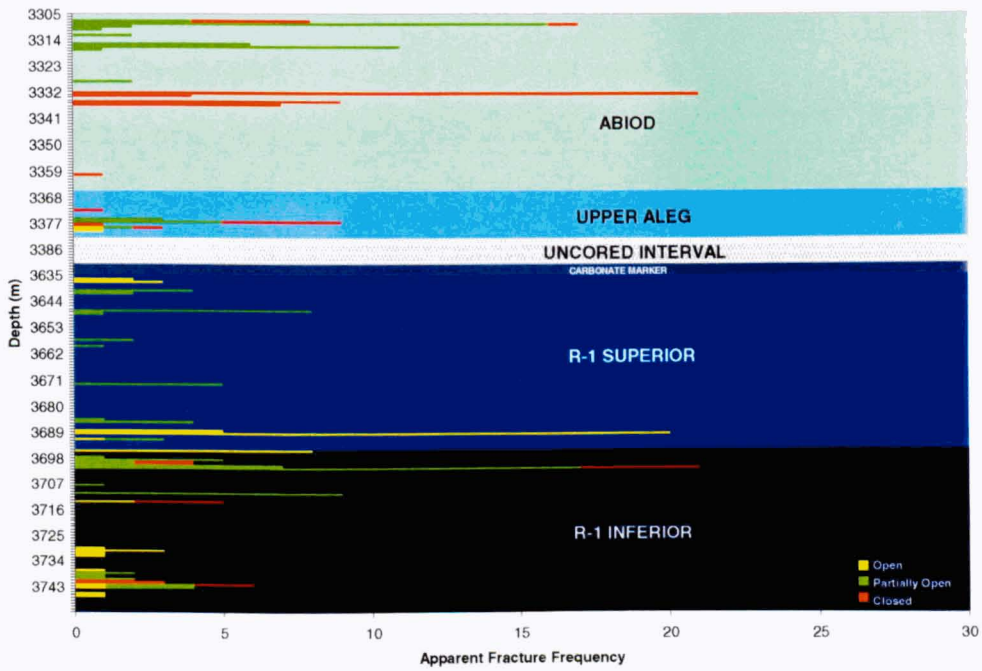

Fig. 6.20. Miskar A-3. Apparent fracture frequency versus depth

Mode I fractures are commonly observed to nucleate from the tips of stylolite dentae (**Plate 6.7**). This suggests that they initially developed contemporaneously with stylolitisation. In fact many of these fractures are generally filled with a zone of calcite cementation in the region immediately adjacent to the stylolite seam (**Plate 6.7**). These

zones commonly range between 50-150mm in length, and probably represent the first phases of calcite reprecipitation from the initial stages of pressure solution within the rock mass.

These Mode I fractures, termed 'stylolite-associated' fractures (STA fractures), often form the first in a series of sub-vertical, en-echelon Mode I fractures. These en-echelon fracture sets, which are usually partially filled with calcite cements, have formed in response to oblique extension during successive tectonic episodes. The nature of these long en-echelon systems (which can exceed 10m in length) are important in that they could exercise a significant influence on vertical permeability within the reservoir interval. In addition, their presence could result in vertical communication between different reservoir units. This phenomenon appears to be particularly apparent in the vicinity of the Miskar A-3 well, where well test data suggests vertical communication between the R1 Inferior and R1 Superior reservoir units.

Unfortunately, as previously mentioned, the cored intervals are not oriented, so the exact orientation of these stylolite-associated fractures cannot be accurately determined. However, an analysis of seismic data suggests that they are probably oriented approximately N-S to NW-SE, parallel to the main trend of the main seismic scale faults (**Fig. 6.2**).

Mode II and III fractures in the cored intervals in Miskar A-3 are less abundant, although important. They are generally characterised by moderately dipping fault planes (55^0-65^0) that have minor displacements and show evidence of both normal dip-slip and oblique-slip movements. They commonly form conjugate sets. **Plate 6.5** provides a good example of Mode II fractures intersecting and displacing a series of compactional stylolite seams (3308.48-3308.62m MD). In this example, throw on these fractures is normal dip-slip. Some of these Mode II fractures could have initially been Mode I fractures that have been reactivated. **Plate 6.7** shows a steeply dipping Mode III fracture intersecting and displacing a series of stylolite-associated fractures (3647.68-3648.00m MD). Slicken-fibre mineral growth on the fault plane indicates a sinistral oblique-slip displacement vector. The presence of calcite mineral growth on the fault plane suggests that calcite solutions were present in the rock system at the time of movement.



Plate 6.7. Miskar A-3: 3647.68m. Mode III fracture with slicken-fibre mineral growth showing sinistral oblique-slip.



Plate 6.8. Miskar A-3: 3307.60m. Calcite filled Mode II/III fractures within the Abiod Formation

The exact orientation of these Mode II and III fractures could not be evaluated, again due to the lack of oriented core. However, it is possible to infer from the seismic analysis that these different structures probably formed in response to:

- Mode II normal dip-slip fractures – NE-SW to ENE-WSW directed extension which has been active intermittently throughout the Late Cretaceous to present-day evolution of the area;
- Mode III sinistral (?) oblique-slip fractures – reactivation of pre-existing Mode II fractures during a phase of SE-NW directed transpression in the late Maastrichtian to late Thanetian.

Analysis of Mode II and III fractures demonstrates that many are partially to totally occluded by cements, reducing their potential as permeability conduits. Typical cements present include rhombic dolomite and late Fe-rich calcite cements. The calcite cements may be the reprecipitated product of stylolitisation.

Figure 6.20 and Table 6.8 show the relative distribution of all fractures within individual lithostratigraphic units, and the apparent fracture frequencies for these particular facies. Fracturing is common to all intervals, with the exception of the Aleg Carbonate Member, which was only partially cored. Fractures appear to be most abundant R1 Inferior interval up into the R1 Superior Member, where they then reduce in frequency throughout the Aleg Carbonate and Upper Aleg Shale Members. High

apparent fracture frequencies are observed in the Abiod Formation where frequencies attain maximum values of 21 fractures/metre. The abundance of fractures in the R1 Inferior, R1 Superior and Abiod intervals could either suggest that there is a lithological control on fracture development.

Lithostratigraphic Unit	No. of Fractures	App. Frac. Freq/metre	Fracture Spacing (m)
Abiod Formation	95	1.59	0.78
Upper Aleg Member	19	1.23	0.54
Aleg Carbonate Member	0	0.00	∞
R1 Superior Member	61	1.00	1.43
R1 Inferior Member	88	1.58	0.65
Total Core	263	1.35	0.84

Table 6.8. Apparent fracture frequency and average fracture spacing for each lithostratigraphic interval (Miskar A-3). Spacing values are based on average fracture apertures of 0.5mm.

It is obvious from the core observations given that most fractures are sub-parallel to the core axis. This therefore precludes a direct determination of fracture spacing (refer to Chapter 5 for a discussion). As a consequence, Narr's (1996) average fracture spacing (AFS) methodology has been used, in an attempt to obtain fracture spacing estimates for each Miskar well. A summary of this methodology is provided in Section 5.4.4. The average fracture spacing values shown in Table 6.8 for Miskar A-3 are based on average fracture apertures of 0.5mm (measured from calcite filled fractures in core). These data are highly consistent with apparent fracture frequency estimates for all lithostratigraphic intervals.

Although these values appear reasonable, it is apparent from core observations that significant undersampling of these fracture systems, particularly within the Abiod Formation is an inherent problem associated with the study. This is due to the fact that a large number fractures in the chalky lithofacies of the Abiod Formation appear to have closed and 'annealed' (after their development), thus making identification extremely difficult. Occasionally hydrocarbon staining and minor calcite cements located along 'annealed' fracture planes permit their identification **(Plate 6.9)**.

Known fracture heights (i.e. the length in the direction of dip) from all cored intervals in Miskar A-3 have been analysed to determine if the fracture height distribution is power-law over the entire cored section (refer to Section 5.4.2). Only fractures with visible terminations within the core area were analysed. Unfortunately, only a few fractures within each lithostratigraphic interval actually terminated in the core area.

This precluded a determination of fracture height distribution within individual lithofacies. It should be noted that large biases are introduced into this study because only fractures with terminations in the core area are utilised. Thus there tends to be a bias towards the shorter height distributions, because longer fractures more often than not terminate outside the core area.

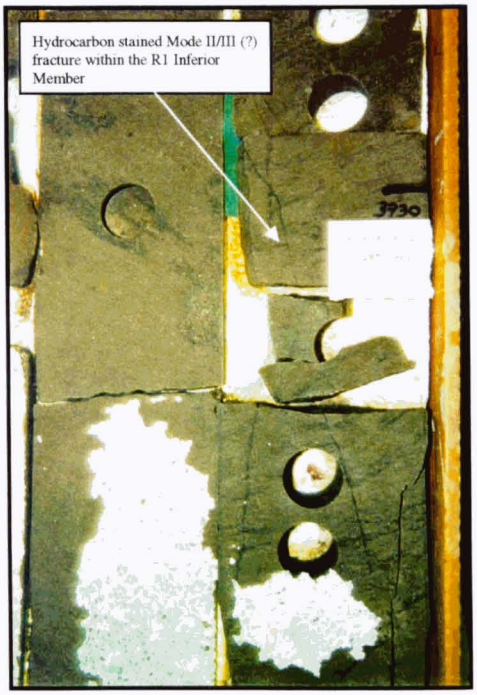

Plate 6.9. Miskar A-3: 3730.00m. Hydrocarbon stained Mode II/III (?) fracture in the R1 Inferior Member

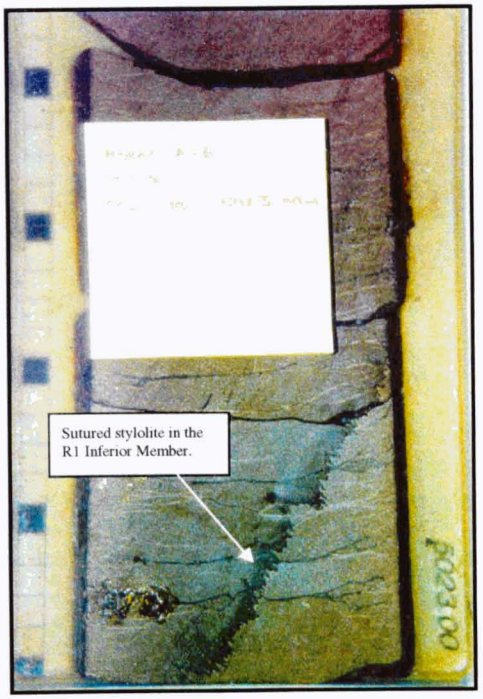

Plate 6.10. Miskar A-6: 5022.90m. Sutured bedding-parallel stylolite in the R1 Inferior Member.

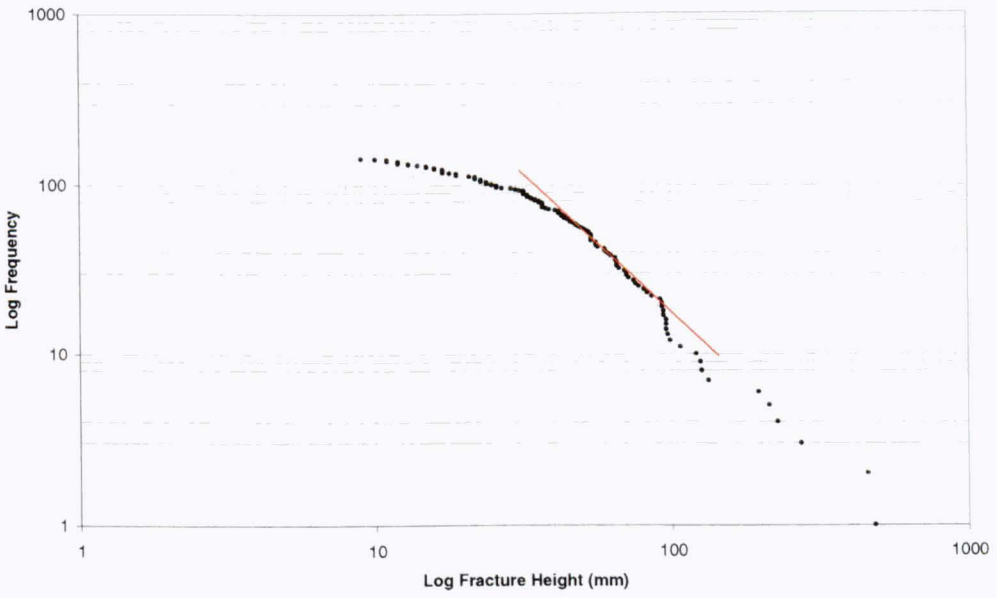

Fig. 6.21. Cumulative frequency distribution of fracture height within the cored intervals in the Miskar A-3 well.

The cumulative frequency distribution given in **Figure 6.21** shows a straight-line segment indicating a power-law height distribution over a scale range of 40-100 mm. The relatively small fracture heights observed, although highly biased are related to the en-echelon nature of fracturing, associated with stylolites. It is apparent from **Figure 6.21** that the power-law height distribution has upper and lower cut-offs, beyond which the power-law is not valid.

An examination of the nature and extent of cementation in fractures within Miskar A-3 has demonstrated that most cemented fractures occur in the Abiod Formation (Table 6.9). This could be attributed to the 'annealing' of fractures in this chalky lithofacies. Open fractures tend to dominate the R1 Inferior and lower parts of the R1 Superior reservoirs. Partially open fractures are distributed throughout the cored interval (**Fig. 6.20**).

Lithostratigraphic Unit	Fracture Type			Nature of Fracture Fill		
	I (STA)	I	II & III	CL	PO	OP
Abiod Formation	15	36	41	51%	49%	0%
Upper Aleg Member	1	11	6	39%	50%	11%
Aleg Carbonate Member	0	0	0	0%	0%	0%
R1 Superior Member	0	41	20	0%	49%	51%
R1 Inferior Member	19	56	17	15%	58%	27%
Total Core	35	144	84	26%	52%	22%

Table 6.9. Distribution of fracture type, and nature of fracture fill/cementation in Miskar A-3. Percentages are given for the amount of closed (CL), partially open (PO) and open (OP) fractures within each lithostratigraphic interval.

Miskar A-6

Miskar A-6 is located within the high northeastern compartment of the Miskar horst block, approximately 800m from the eastern horst-bounding fault zone (**Fig. 6.2**). The well is near vertical within the Plio-Pleistocene section, but deviates to an angle of approximately 55^0 (from the vertical) in the main reservoir intervals. Ten cores were recovered during drilling. An account of these is provided in Table 6.10.

All data has been corrected for the deviation in the well bore during drilling. A shorter account of the structural features present in Miskar A-6 is provided, because many of the features identified in Miskar A-3 are very similar to those observed in this well.

Core Number	Interval Depth (m)	Lithostratigraphic Unit	Recovery (%)
1	4877.7 – 4900.4	R1 Superior	98.5
2	4901.0 – 4926.8	R1 Superior	95.0
3	4928.0 – 4932.0	R1 Superior	90.0
4	4932.0 – 4942.0	R1 Superior	100.0
5	4954.0 – 4969.4	R1 Superior	100.0
6	4969.4 – 4996.0	R1 Superior	99.3
7	4996.0 – 5009.0	R1 Superior/R1 Inferior	97.3
8	5009.0 – 5026.0	R1 Inferior	98.5
9	5026.0 – 5053.5	R1 Inferior	99.6
10	5053.5 – 5081.3	R1 Inferior/Lower Aleg Shale	100.0

Table 6.10. Cored intervals in Miskar A-6

Stylolites

A total of 46 aggregate stylolites were identified in Cores 1 - 10 within Miskar A-6 (**Fig. 6.22**). Almost all of these stylolites are horizontal, compactional features that have preferentially developed along bed boundaries (**Plate 6.10**). They are often partially filled with dolomite and late calcite cements suggesting that they have cracked open at some period in their evolution (Macaulay et al., 2001) (**Plate 6.11**). Both high amplitude ('sutured') and low amplitude ('simple') compactional stylolites are identified in Miskar A-6, similar to those observations in Miskar A-3. The difference in morphology is thought to be facies controlled, the smoother seams preferentially developing in more clay-prone, finer grained fabrics.

Lithostratigraphic Unit	No. of Stylolites	Stylolite Freq/metre	Average Spacing (m)
R1 Superior Member	18	0.16	6.25
R1 Inferior Member	27	0.40	2.50
Lower Aleg Member	1	0.10	9.90
Total Core	46	0.24	4.13

Table 6.11. Stylolite frequency and stylolite spacing for each lithostratigraphic interval (Miskar A-6).

Figure 6.22 and Table 6.11 show the relative distribution of pressure solution seams in the cored intervals. Average stylolite frequencies suggest preferential development within the R1 Inferior and Abiod lithofacies. Only three stylolites have been recorded in the R1 Superior interval. This is different from that observed in Miskar A-3, and may be attributed to a slight change in the bulk rock composition.

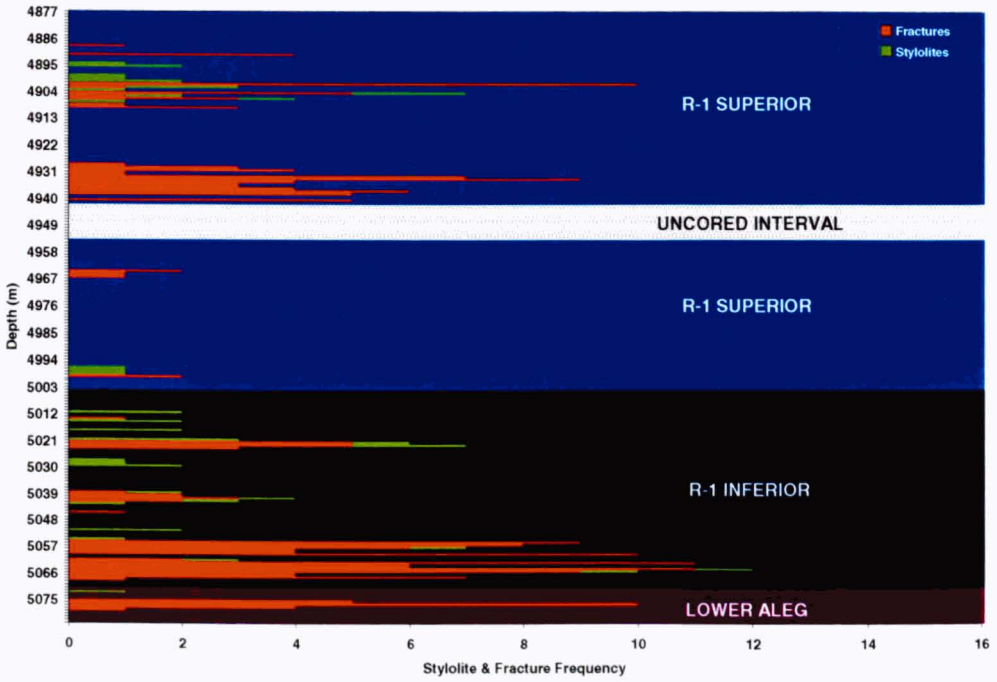

Fig. 6.22. Miskar A-6. Stylolite and Fracture Frequency versus depth

Tectonic stylolites have also been identified in the cored interval, but to a far lesser extent than Miskar A-3; only three tectonic stylolites were identified. They are developed at a high angle to the core wall (~80^0), and commonly intersect and displace horizontal compactional stylolites. They probably formed in response to the phases of compression that occurred during the late Maastrichtian to late Thanetian and Upper Eocene (refer to previous section for an explanation).

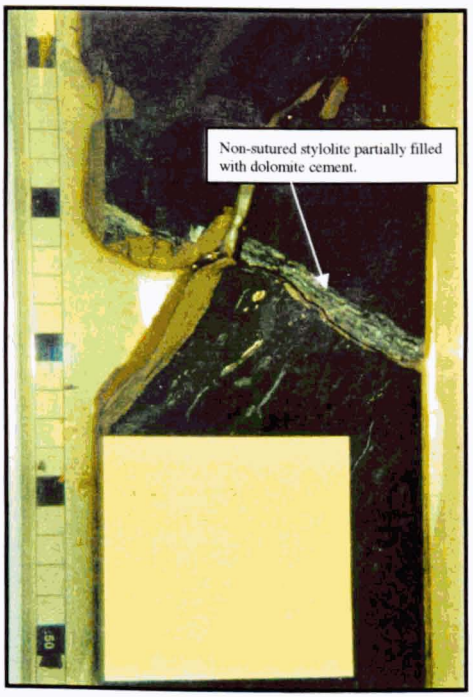

Plate 6.11. Miskar A-6: 5072.37m. Low amplitude 'non-sutured' stylolite partially filled with dolomite cement.

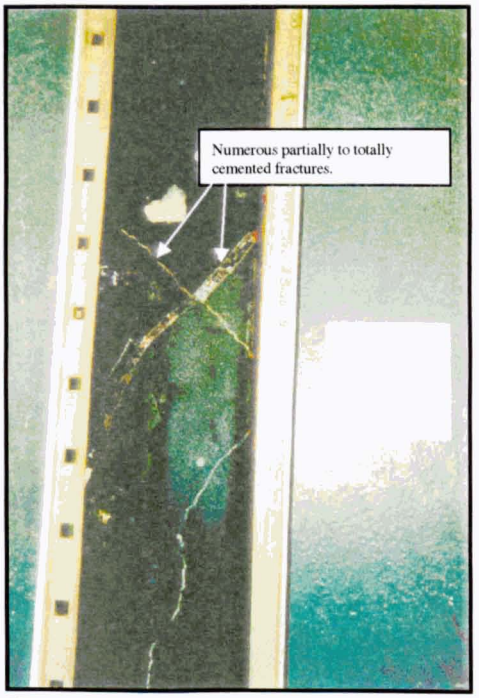

Plate 6.12.Miskar A-6: 5002.02m. Partially to totally filled fractures in the R1 Inferior Member.

Table 6.12 provides a minimum estimate of the amount of material that has been lost through the process of pressure solution, for each lithostratigraphic interval in Miskar A-6.

Lithostratigraphic Unit	Material Removed (mm)	Average Removed/Stylolite (mm)
R1 Superior Member	359	19.94
R1 Inferior Member	629	23.30
Lower Aleg Member	20	20.00
Total Core	1008	21.91

Table 6.12. Material removed through the process of pressure solution (mm) (Miskar A-3).

The material in solution has probably been re-precipitated in the surrounding matrix, particularly in vugs and along stylolite seams (4938.00-4939.00m MD), and also in the various fracture systems present (**Plates 6.11 & 6.12**). However, the only way to demonstrate this, is through laser isotope matching (D. Beckett, pers. comm., 2001).

Fractures

A total of 218 macro-fractures were identified within Cores 1 - 10 in Miskar A-6 (**Fig. 6.23**).

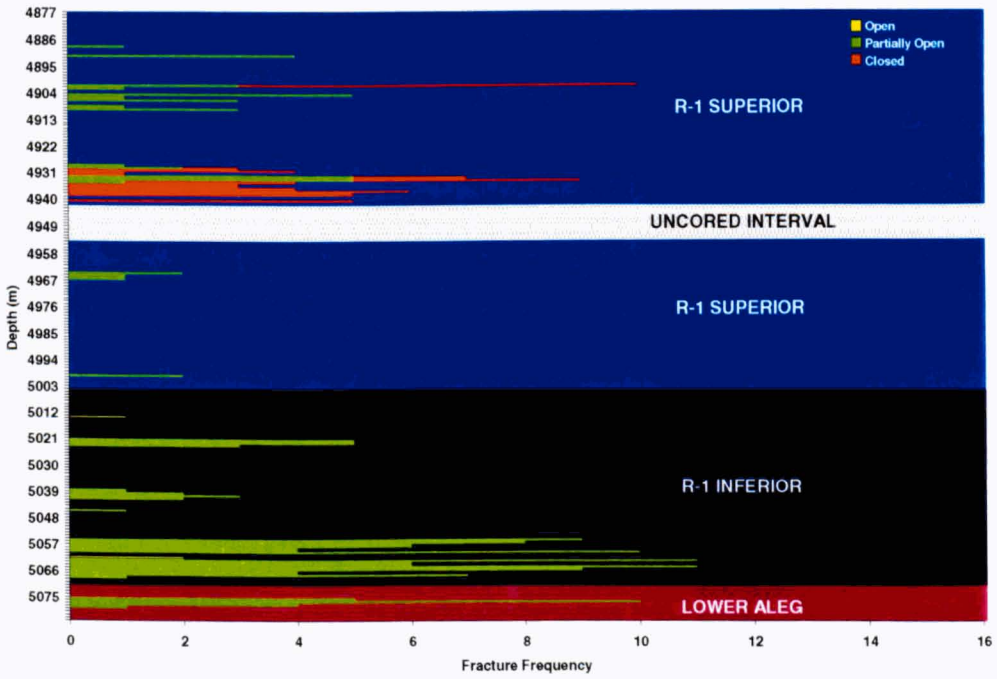

Fig. 6.23. Miskar A-6. Apparent fracture frequency versus depth

Most of these fractures are sub-vertical to vertical Mode I fractures, which form en-echelon systems that initially nucleated from the tips of stylolite dentae. They are

commonly partially to totally filled with calcite cements, which were probably reprecipitated from material derived during stylolitisation. An approximately N-S to NW-SE trend has been attributed to these structures based on seismic data.

Within Miskar A-6, these Mode I fractures are accompanied by moderately dipping Mode II fractures with normal dip-slip displacements. They are commonly identified in conjugate sets, and display infill cements of rhombic dolomite and calcite (**Plates 6.12 & 6.13**). A small fault zone was identified in Core No. 1 of Miskar A-6 (4888.70-4889.00) (**Plate 6.14**). This zone is characterised by intense brecciation and calcitisation. The relative trend of structures, such as these, probably parallels the main seismic scale faults in the Miskar structure.

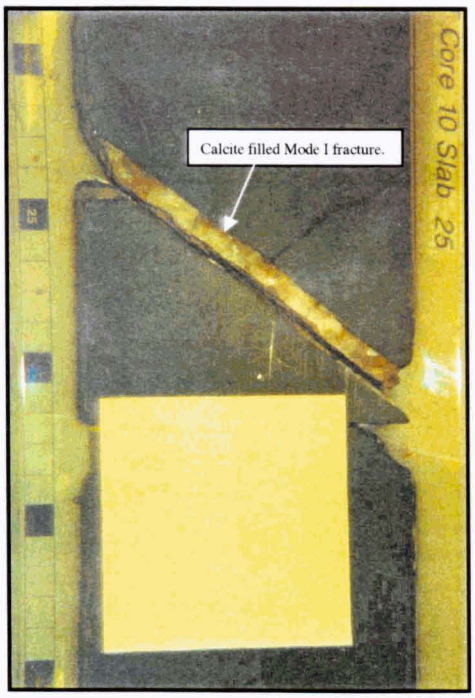

Plate 6.13. Miskar A-6: 5077.25m. Calcite filled Mode I fracture.

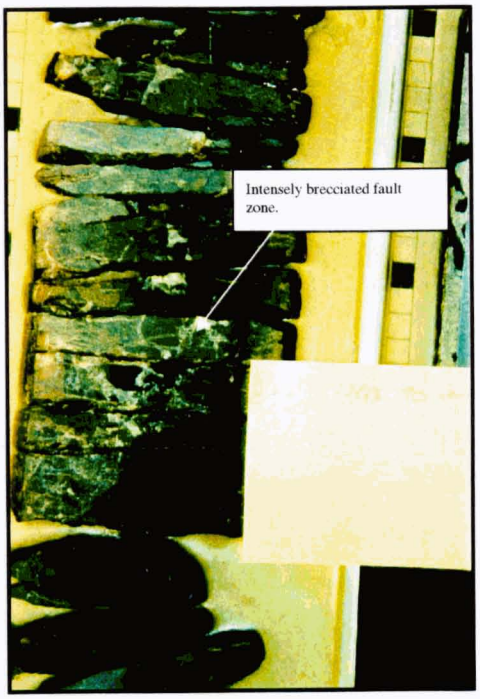

Plate 6.14. Miskar A-6: 4888.70m. Fault zone characterise by intense brecciation and calcite veining.

Lithostratigraphic Unit	No. of Fractures	App. Frac. Freq/metre	Fracture Spacing (m)
R1 Superior Member	87	0.77	1.15
R1 Inferior Member	112	1.66	0.57
Lower Aleg Member	19	1.92	0.41
Total Core	218	1.15	0.79

Table 6.13. Apparent fracture frequency and average fracture spacing for each lithostratigraphic interval (Miskar A-6). Spacing values are based on average fracture apertures of 0.5mm.

Figure 6.23 and Table 6.13 show the relative distribution of all fractures within individual lithostratigraphic units. It is clear that fracturing is preferentially developed

in the basal section of the R1 Inferior unit, where it then decreases up into the middle of the R1 Superior facies. Higher apparent fracture frequencies are evident in the upper portions of the R1 Superior interval. Average fracture spacing values (based on average fracture apertures of 0.5mm) are in close agreement with apparent fracture frequency values.

The cumulative frequency plot of fracture height shows a power-law distribution over a scale range of 60-120 mm (**Fig. 6.24**). This compares extremely well to the height distribution for the Miskar A-3 well.

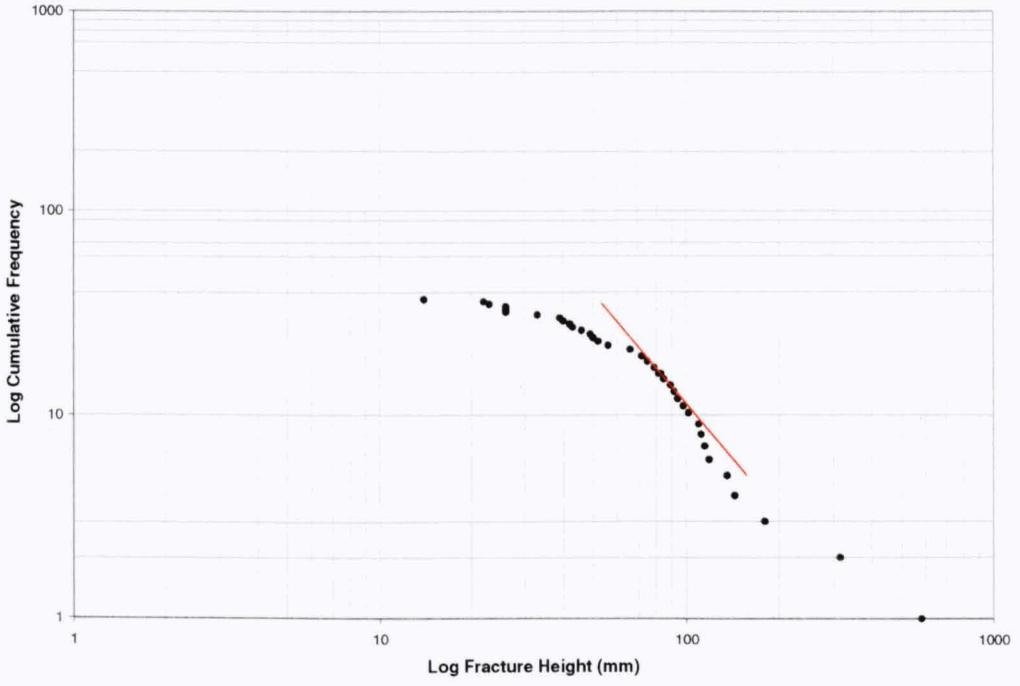

Fig. 6.24. Cumulative frequency distribution of fracture height within the cored intervals in the Miskar A-6 well

The nature and extent of cementation of fractures within Miskar A-6 is illustrated in Table 6.13. Closed fractures dominate the upper part of the R1 Superior Member. Partially open fractures occur throughout the cored interval, particularly in the lower part of the R1 Inferior Member and the upper part of the R1 Superior Member. No totally open fractures have been observed. Most fractures are Mode I types directly associated with stylolites, or in en-echelon sets leading from the main stylolite-associated fracture. It is important to note that a large proportion of the fractures present are either Mode II or III fractures. This is probably due to the close proximity of the well to large seismic-scale faults (**Fig. 6.2**).

Lithostratigraphic Unit	Fracture Type			Nature of Fracture Fill		
	I (STA)	I	II & III	CL	PO	OP
R1 Superior Member	4	22	55	52%	48%	0%
R1 Inferior Member	10	106	1	0%	97%	3%
Lower Aleg Member	0	20	0	0%	100%	0%
Total Core	14	148	56	21%	78%	1%

Table 6.14. Distribution of fracture type, and nature of fracture fill/cementation in Miskar A-6. Percentages are given for the amount of closed (CL), partially open (PO) and open (OP) fractures within each lithostratigraphic interval.

Miskar A-7

Miskar A-7 is located in the middle of the southwestern compartment of the Miskar horst block. It lies approximately 1500m from both the eastern horst-bounding fault zone and the main compartment-bounding fault (**Fig. 6.2**). The well is near vertical within the Plio-Pleistocene section, but deviates to an angle of approximately 5^0 (from the vertical) in the cored section. One core was recovered during drilling, through the El Haria-Abiod unconformity, between 3511.0m – 3538.9m (MD).

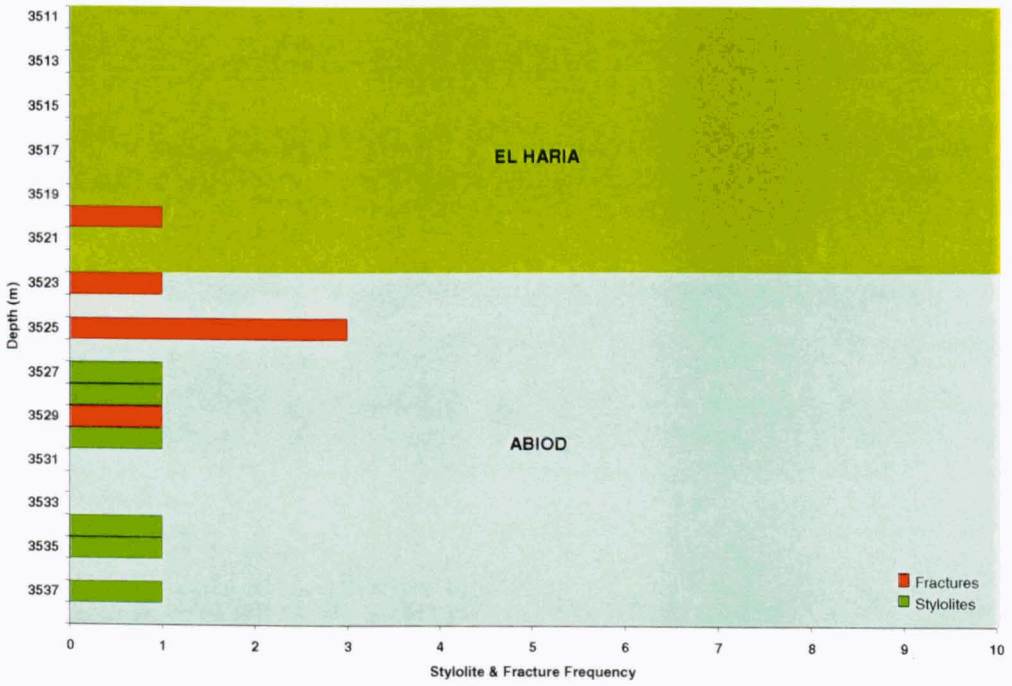

Fig. 6.25. Miskar A-7. Stylolite and Fracture Frequency versus depth

Stylolites

A total of only 6 aggregate stylolites were identified within Miskar A-7 (**Fig. 6.25**). They are all horizontal, compactional structures. Both high and low amplitude

compactional stylolite seams are recognised. Minor calcite and dolomite cements are apparent within these seams, together with pyrite mineralisation.

Figure 6.25 and Table 6.15 show the relative distribution of pressure solution seams in the cored interval. Table 6.16 provides a minimum estimate of the amount of material that has been lost through the process of pressure solution for each of the cored intervals in Miskar A-7.

Lithostratigraphic Unit	Number of Stylolites	Stylolite Freq/metre	Average Spacing (m)
El Haria Formation	0	0.00	>11.20
Abiod Formation	6	0.36	2.78
Total Core	6	0.22	4.65

Table 6.15. Stylolite frequency and spacing for each lithostratigraphic interval (Miskar A-7).

Lithostratigraphic Unit	Material Removed (mm)	Average Removed/Stylolite (mm)
El Haria Formation	0	0.00
Abiod Formation	171	28.5
Total Core	171	28.5

Table 6.16. Material removed by the process of pressure solution (mm) (Miskar A-7).

Fractures

Only six fractures were identified in the cored interval. Five of these were annealed, sub-vertical stylolite-associated fractures. It is noted that these fractures may be under-sampled in this core interval. **Figure 6.26** and Table 6.17 show the relative distribution of all fractures within the El Haria and Abiod Formations. The average spacing estimates shown in Table 6.17 are probably not a true representation of subsurface fracturing due to the short sample length.

Lithostratigraphic	No. of Fractures	App. Frac. Freq/metre	Fracture Spacing (m)
El Haria Formation	1	0.09	8.42
Abiod Formation	5	0.30	1.65
Total Core	6	0.22	2.43

Table 6.17. Apparent fracture frequency and average fracture spacing for each lithostratigraphic interval (Miskar A-7). Spacing values are based on average fracture apertures of 0.5mm.

The few observed structural features preclude a direct interpretation of fracture and stylolite distribution in this well. Table 6.18 shows the distribution of fracture type and

nature of fracture fill. However, this is also not very useful. A lack of data has not permitted an analysis of fracture height distribution.

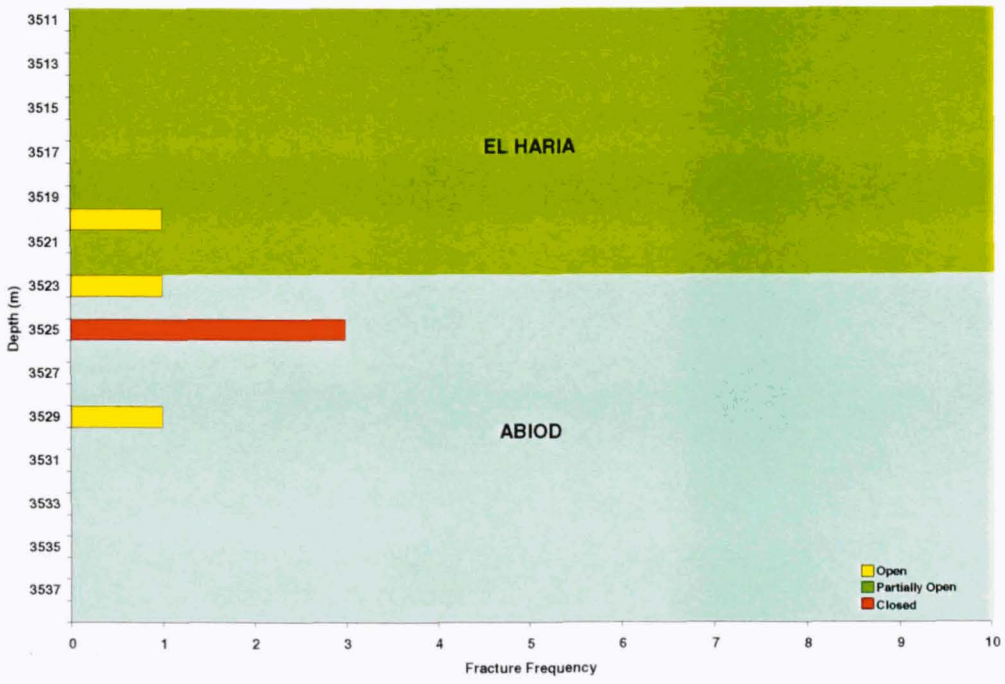

Fig. 6.26. Miskar A-7. Apparent fracture frequency versus depth

Lithostratigraphic Unit	Fracture Type			Nature of Fracture Fill		
	I (STA)	I	II & III	CL	PO	OP
El Haria Formation	0	1	0	0%	0%	100%
Abiod Formation	0	4	1	60%	0%	40%
Total Core	0	5	1	50%	0%	50%

Table 6.18. Distribution of fracture type, and nature of fracture fill/cementation in Miskar A-7. Percentages are given for the amount of closed (CL), partially open (PO) and open (OP) fractures within each lithostratigraphic interval.

Miskar A-9

Miskar A-9 is located in the southwestern compartment of the Miskar horst block, approximately 1000m from the western horst-bounding fault zone (**Fig. 6.2**). The well is near vertical within the Plio-Pleistocene section, but deviates to an angle of approximately 3^0 (from the vertical) in the cored section. One core was recovered during drilling, through the R1 Inferior and Superior reservoir intervals (3880.0m – 3917.0m MD).

Stylolites

A total of 5 compactional aggregate stylolites were identified in the cored interval, dominantly located in the R1 Inferior lithofacies (**Fig. 6.27** and Table 6.19). Both high and low amplitude compactional stylolite seams are recognised. Minor calcite and dolomite cements are apparent within these seams, together with pyrite mineralisation.

Lithostratigraphic Unit	Number of Stylolites	Stylolite Freq/metre	Average Spacing (m)
R1 Superior Member	0	0.00	>2.80
R1 Inferior Member	5	0.15	6.84
Total Core	5	0.14	7.40

Table 6.19. Stylolite frequency and spacing for each lithostratigraphic interval (Miskar A-9).

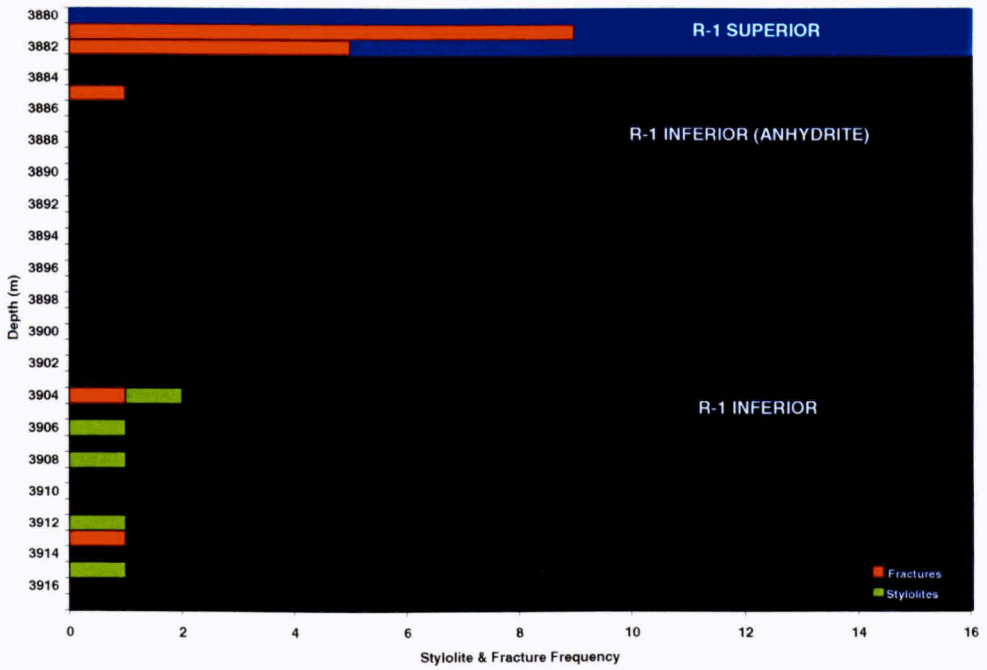

Fig. 6.27. Miskar A-9. Stylolite and Fracture Frequency versus depth

Table 6.20 provides a minimum estimate of the amount of material that has gone into solution through the process of stylolitisation for each of the cored intervals in Miskar A-9.

Lithostratigraphic Unit	Material Removed (mm)	Average Removed/Stylolite (mm)
R1 Superior	0	0
R1 Inferior	204	40.80
Total Core	204	40.80

Table 6.20. Material removed by the process of pressure solution (mm) (Miskar A-9).

Fractures

Seventeen fractures were recognised in the cored interval in Miskar A-9 (**Fig. 6.28**). The majority of these fractures were sub-vertical Mode I stylolite-associated fractures that form en-echelon configurations. They are generally partially to totally filled with dolomite and late calcite cements. **Figure 6.28** and Table 6.21 show the relative distribution of all fractures in the cored interval. These data show that fractures are developed preferentially in the R1 Superior Member, although the values are probably not representative of subsurface fracturing because of the short sample length.

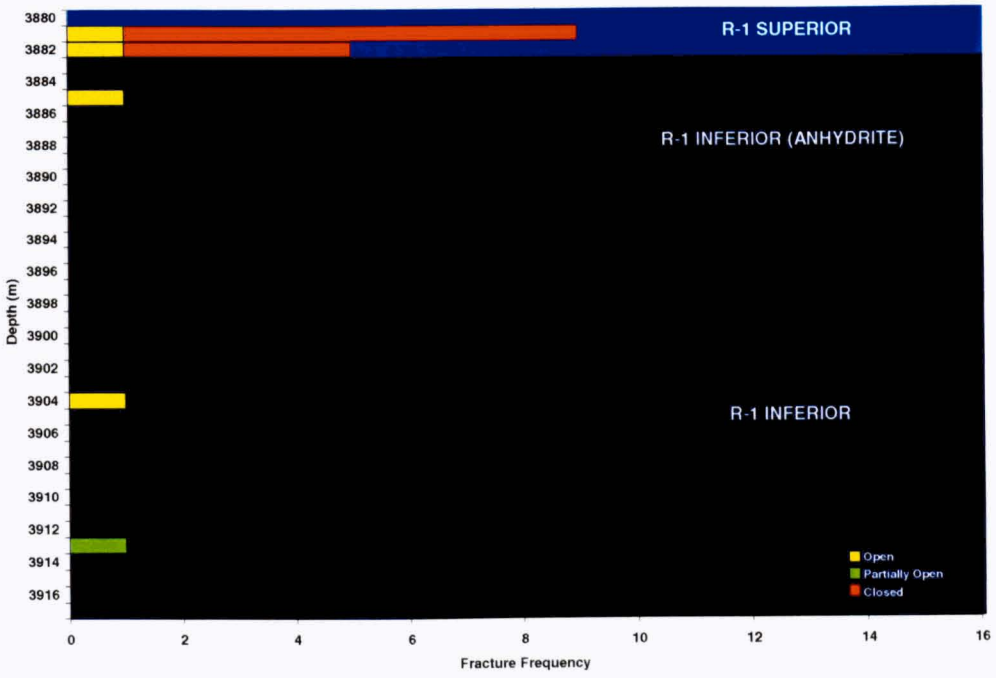

Fig. 6.28. Miskar A-9. Apparent fracture frequency versus depth

Lithostratigraphic Unit	No. of Fractures	App. Frac. Freq/metre	Fracture Spacing (m)
R1 Superior	14	5.00	0.24
R1 Inferior	3	0.09	5.94
Total Core	17	0.46	2.13

Table 6.21. Apparent fracture frequency and average fracture spacing for each litho-stratigraphic interval (Miskar A-9). Spacing values are based on average fracture apertures of 0.5mm.

Table 6.22 shows the distribution of fracture type and nature of cementation in the Miskar A-9 well. Most fractures observed are Mode I, stylolite-associated (STA) features or Mode I fractures forming en-echelon sets to the initial STA fracture. Closed fractures predominate particularly in the R1 Superior Member. An analysis of fracture height has not been undertaken due to the lack of available data.

Lithostratigraphic Unit	Fracture Type			Nature of Fracture Fill		
	I (STA)	I	II & III	CL	PO	OP
R1 Superior	0	15	0	86%	0%	14%
R1 Inferior	1	1	1	0%	0%	100%
Total Core	1	16	1	33%	0%	67%

Table 6.22. Distribution of fracture type, and nature of fracture fill/cementation in Miskar A-9. Percentages are given for the amount of closed (CL), partially open (PO) and open (OP) fractures within each lithostratigraphic interval.

Sub-aqueous basalts have been identified in Miskar A-9 (3888.10-3888.30m MD) (**Plate 6.15**). The presence of these indicates a period of Late Cretaceous tectonic subsidence related to a rift episode.



Plate 6.15. Miskar A-9: 3888.25m. Sub-aqueous basalt probably related to Late Cretaceous rifting

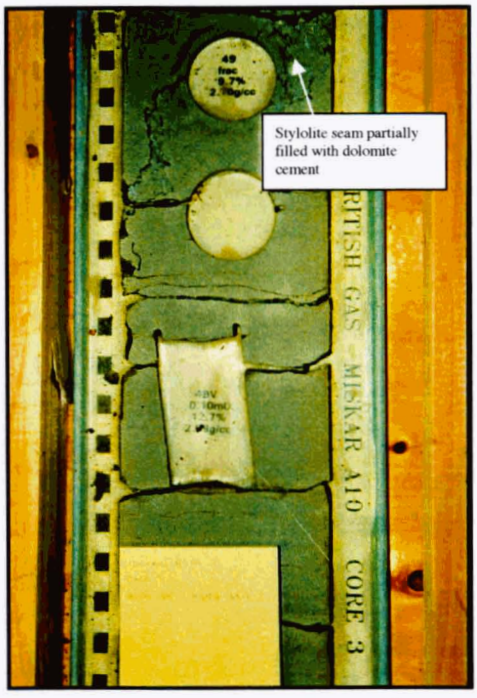

Plate 6.16. Miskar A-10: 4654.25m. High amplitude 'sutured' stylolites partially filled with dolomite cements.

Miskar A-10

Miskar A-10 is located in the middle of the northeastern compartment of the Miskar horst block, approximately 1200m between the eastern horst-bounding fault zone and the compartment-bounding fault respectively (**Fig. 6.2**). The well is near vertical within the Plio-Pleistocene section, but deviates to an angle of approximately 45^0 (from the vertical) in the cored section. Three cores were recovered during drilling. A listing of these is provided in Table 6.23.

Core Number	Interval Depth (m)	Lithostratigraphic Unit	Rec. (%)
1	4356.0 – 4389.0	R1 Inferior	100.0
2	4640.0 – 4645.0	Bireno	100.0
3	4645.0 – 4672.5	Bireno	100.0

Table 6.23. Cored intervals in Miskar A-10

Stylolites

A total of 21 aggregate stylolites were recognised in Miskar A-10 (**Fig. 6.29**). All of the stylolites were compactional features. Both high and low amplitude pressure solution seams are recognised. Minor calcite and dolomite cements are apparent within these seams, together with pyrite mineralisation (**Plate 6.16**).

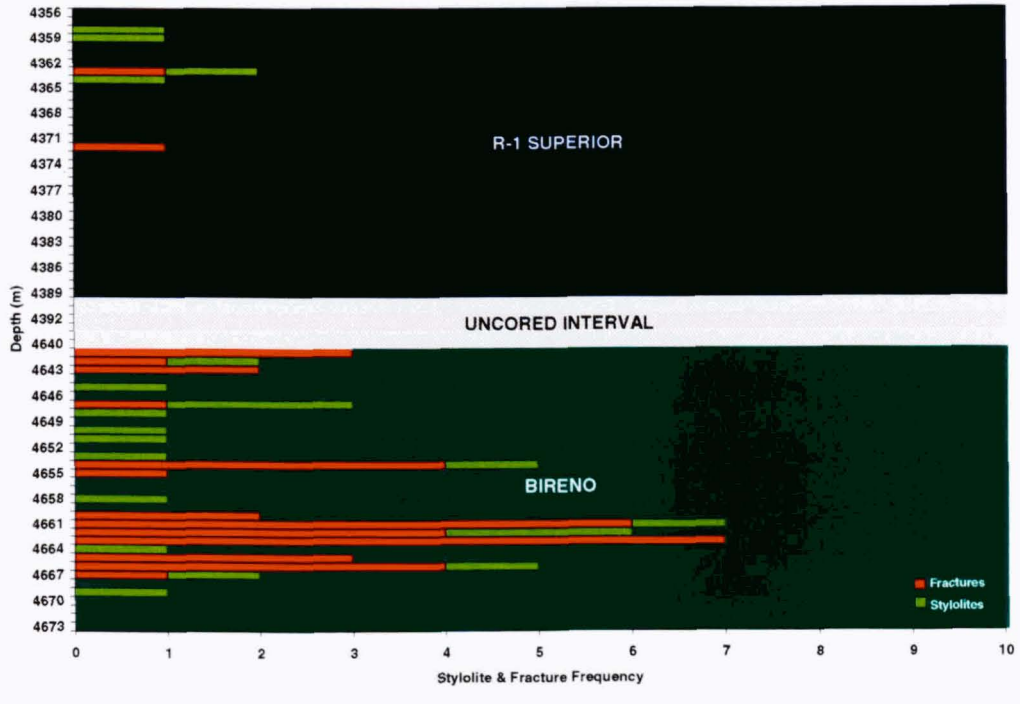

Fig. 6.29. Miskar A-10. Stylolite and Fracture Frequency versus depth

Figure 6.29 and Table 6.24 demonstrate that stylolites are preferentially developed within the Bireno reservoir interval. A total of 17 stylolites were identified in the Bireno interval with another 4 in the R-1 Superior Member.

Lithostratigraphic Unit	No. of Stylolites	Stylolite Freq/metre	Average Spacing (m)
R1 Inferior Member	4	0.12	8.25
Bireno Member	17	0.52	1.91
Total Core	21	0.32	3.10

Table 6.24. Stylolite frequency and spacing for each lithostratigraphic interval (Miskar A-10).

Table 6.25 provides a minimum estimate of the amount of material that has been lost through the process of pressure solution, for each of the cored intervals in Miskar A-10. The results presented in this table are consistent with other wells, and show that high amplitude stylolites are associated with these packstone/wackestone facies.

Lithostratigraphic Unit	Material Removed (mm)	Average Removed/Stylolite (mm)
R1 Inferior Member	80	20.00
Bireno Member	769	45.23
Total Core	849	40.43

Table 6.25. Material removed through the process of pressure solution (mm) (Miskar A-10).

Fractures

Forty-one fractures were recognised in the cored interval in Miskar A-10 (**Fig. 6.30**). The majority of these fractures were sub-vertical Mode I fractures associated with stylolites that form en-echelon configurations.

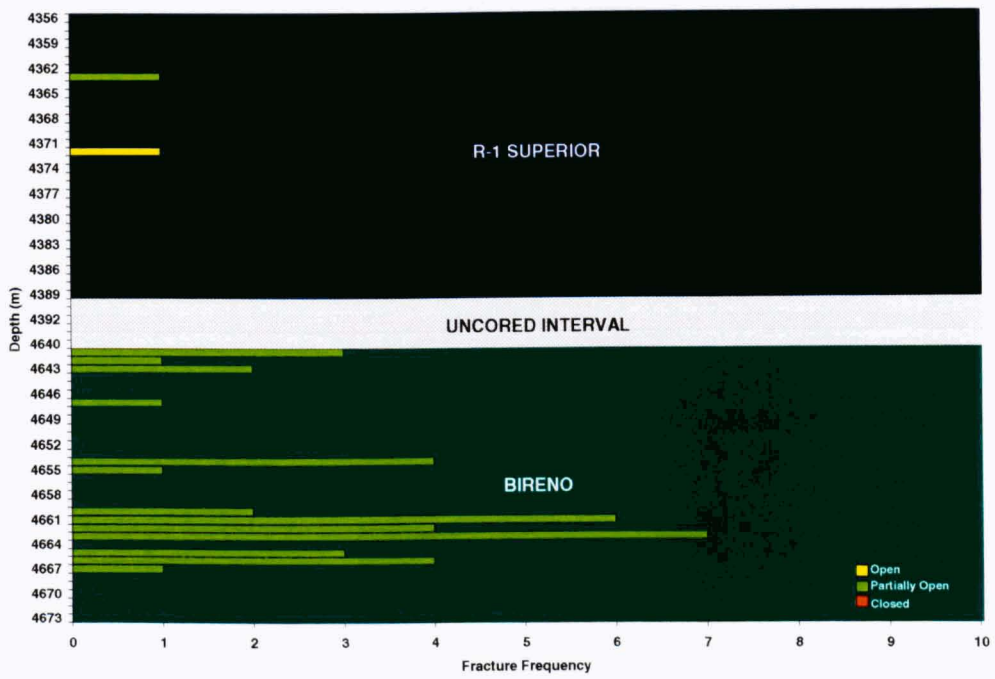

Fig. 6.30. Miskar A-10. Apparent fracture frequency versus depth

Plate 6.17 shows a good example of a compactional stylolite with a series of associated partially to totally filled fractures. These stylolite-associated fractures extend over long distances. **Plate 6.18** shows a system of these fractures. Note the close spacing of these features, which form a pervasive network in this portion of the cored interval. This part of the core provides a good representation of the real spacing of stylolite associated fractures, because it is deviated cored at a high angle to fracturing.

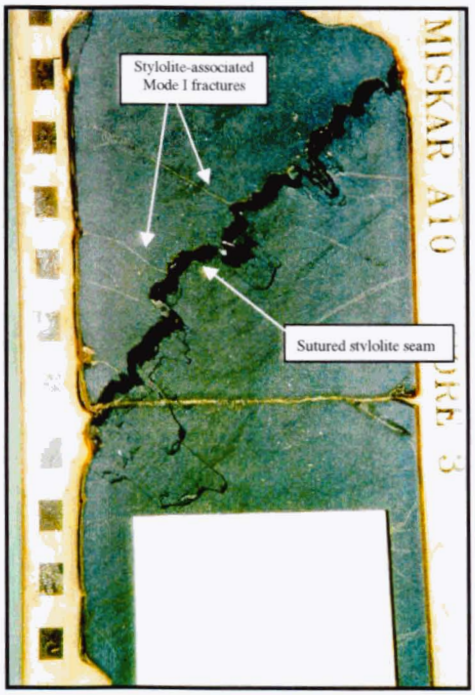

Plate 6.17. Miskar A-10: 4648.50m. Sutured stylolite with a series of associated partially to totally filled Mode I fractures.

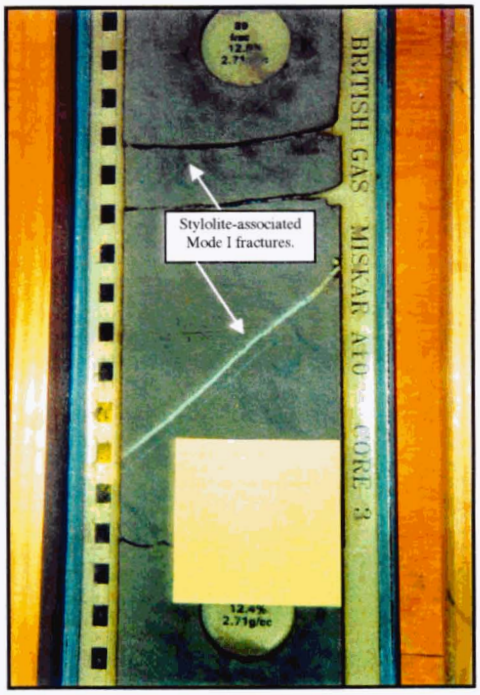

Plate 6.18. Miskar A-10: 4666.40m. Regularly spaced stylolite-associated fractures. Average spacing ~15-20cm.

Figure 6.30 and Table 6.26 show the relative distribution of all fractures within the cored interval. It is apparent that fractures preferentially develop in the Bireno Formation. Only two fractures were noted in the R1 Inferior Member. Again, these values may not be a true representation of subsurface fracturing.

Lithostratigraphic Unit	No. of Fractures	App. Frac. Freq/metre	Fracture Spacing (m)
R1 Inferior Member	2	0.06	12.2
Bireno Member	39	1.20	0.68
Total Core	41	0.63	1.29

Table 6.26. Apparent fracture frequency and average fracture spacing for each lithostratigraphic interval (Miskar A-10). Spacing values are based on average fracture apertures of 0.5mm.

Lithostratigraphic Unit	Fracture Type			Nature of Fracture Fill		
	I (STA)	I	II & III	CL	PO	OP
R1 Inferior Member	1	0	1	0%	49%	51%
Bireno Member	3	36	0	15%	58%	27%
Total Core	4	36	1	26%	52%	22%

Table 6.27. Distribution of fracture type and nature of fracture fill/cementation in Miskar A-10. Percentages are given for the amount of closed (CL), partially open (PO) and open (OP) fractures within each lithostratigraphic interval.

An examination of the nature and extent of cementation in fractures within Miskar A-10 shows a predominance of Mode I fractures that are associated with stylolites and STA fractures (Table 6.27). Almost all of the fractures observed are partially open. An analysis of fracture height has not been undertaken due to the lack of available data.

Miskar A-11

Miskar A-11 is located in the southern portion of the southwestern compartment of the Miskar horst block, approximately 1500m from the eastern horst-bounding fault zone (**Fig. 6.2**). The well is near vertical within the Plio-Pleistocene section, but deviates to an angle of approximately 45^0 (from the vertical) in the Abiod Formation, and ~25^0 in the R1 Superior and Inferior Members. Ten cores were recovered during drilling. A listing of these is provided in Table 6.28.

Core Number	Interval Depth (m)	Lithostratigraphic Unit	Recovery (%)
1	4851.0 – 4878.5	Abiod	100.0
2	4878.5 – 4906.3	Abiod/Upper Aleg Shale	100.0
3	5249.0 – 5270.8	Aleg Carbonate/R1 Superior	100.0
4	5270.8 – 5288.7	R1 Superior	100.0
5	5288.7 – 5307.5	R1 Superior	100.0
6	5307.5 – 5318.1	R1 Superior	100.0
7	5318.1 – 5331.9	R1 Superior	100.0
8	5331.9 – 5359.8	R1 Superior/R1 Inferior	100.0
9	5359.8 – 5387.5	R1 Inferior	100.0
10	5387.5 – 5400.0	R1 Inferior	100.0

Table 6.28. Cored intervals in Miskar A-11

Stylolites

A total of 133 aggregate stylolites were recognised in Miskar A-11 (**Fig. 6.31**). Of these, 129 are compactional features. Both 'sutured' high amplitude and 'simple' low amplitude seams are identified. Minor calcite and dolomite cements are apparent within these seams. The high number of stylolites identified with respect to other wells could be due to slight facies variations from other wells across the field.

Figure 6.31 and Table 6.29 demonstrate that stylolites are preferentially developed in the Abiod Formation. A total of 107 stylolites have been identified in the Abiod Formation with 5, 14 and 7 in the Upper Aleg, R1 Superior and R1 Inferior Members respectively.

Lithostratigraphic Unit	Number of Stylolites	Stylolite Freq/metre	Average Spacing (m)
Abiod Formation	107	2.22	0.45
Upper Aleg Member	5	1.40	0.71
Aleg Carbonate Member	0	0.00	0.00
R1 Superior Member	14	0.16	6.39
R1 Inferior Member	7	0.12	8.43
Total Core	133	0.64	1.55

Table 6.29. Stylolite frequency and spacing for each lithostratigraphic interval (Miskar A-11).

Five tectonic stylolites have been identified in the cored interval. They generally dip at approximately 50^0 and commonly intersect and displace horizontal compactional stylolites. **Plate 6.19** and shows a tectonic stylolite filled with pyrite which intersects and displaces a smooth compactional stylolite.

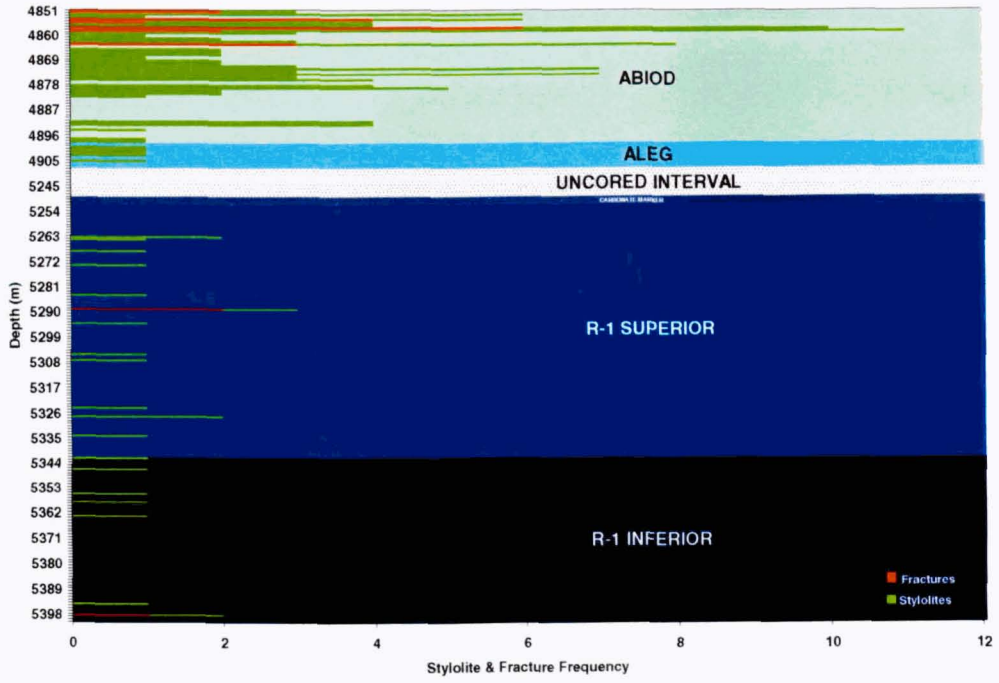

Fig. 6.31. Miskar A-11. Stylolite and Fracture Frequency versus depth

Table 6.30 provides a minimum estimate of the amount of material that has been lost through the process of pressure solution, for each of the cored intervals in Miskar A-6.

Fractures

Twenty-one fractures were identified in the cored intervals in Miskar A-11 (**Fig. 6.32**), although this small number is probably due to undersampling of annealed fractures. Most of the recognised fractures are Mode I stylolite-associated fractures that can form in en-echelon configurations (**Plate 6.20**). The remaining fractures present are steeply

dipping Mode II features that show minor normal displacements. A small fault zone was recognised at 5363.31 - 5263.51m (MD). Intense brecciation and calcitisation is associated with this zone.

Lithostratigraphic Unit	Material Removed (mm)	Average Removed/Stylolite
Abiod Formation	956	8.93
Upper Aleg Shale Member	5	1.00
Aleg Carbonate Member	0	0.00
R1 Superior Member	387	27.64
R1 Inferior Member	173	24.71
Total Core	1521	11.43

Table 6.30. Material removed through the process of pressure solution (mm) (Miskar A-11).



Plate 6.19. Miskar A-11: 4852.30m. Steeply dipping sutured tectonic stylolite intersecting and displacing a compactional stylolite.

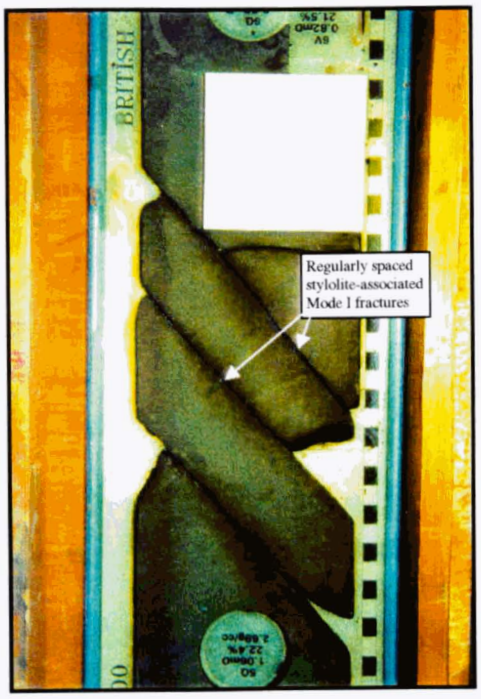

Plate 6.20. Miskar A-11: 4641.10m. Regularly spaced stylolite-associated Mode I fractures. Average spacing: 5-10cm.

Lithostratigraphic Unit	No. of Fractures	App. Frac. Freq/metre	Fracture Spacing (m)
Abiod Formation	18	0.37	3.13
Upper Aleg Member	0	0.00	>7.00
Aleg Carbonate Member	0	0.00	>2.60
R1 Superior Member	2	0.02	11.94
R1 Inferior Member	1	0.02	50.43
Total Core	21	0.10	8.56

Table 6.31. Apparent fracture frequency and average fracture spacing for each lithostratigraphic interval (Miskar A-11). Spacing values are based on average fracture apertures of 0.5mm.

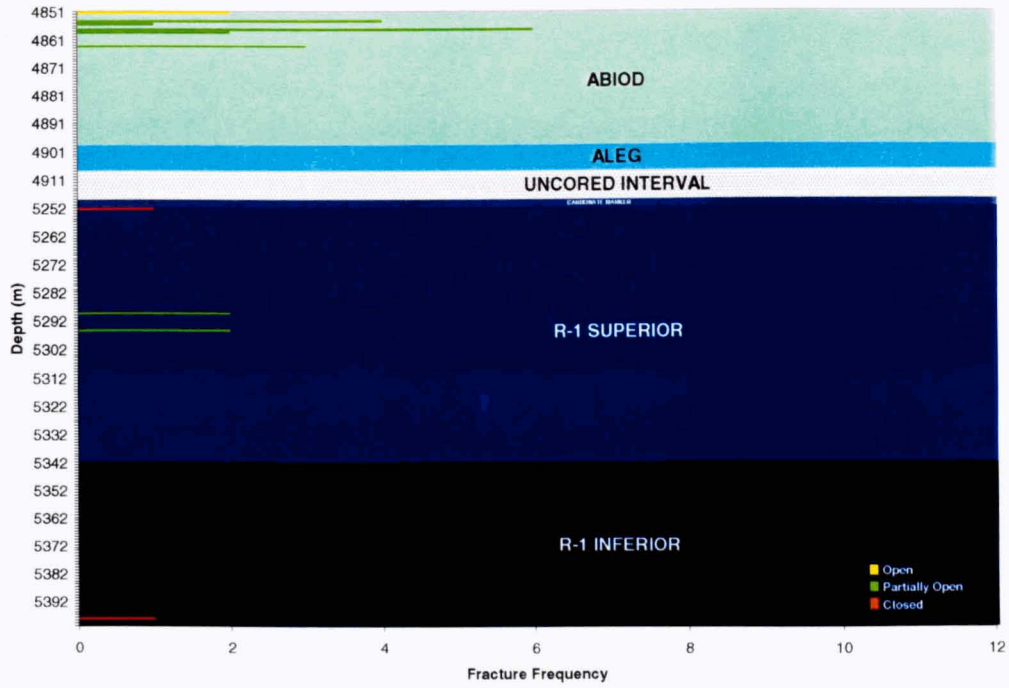

Fig. 6.32. Miskar A-11. Apparent fracture frequency versus depth

Figure 6.32 and Table 6.31 show the relative distribution of all fractures in the cored intervals. It is apparent that fractures are preferentially developed in the Abiod Formation (18 in total), with only a few developed in the R1 Superior and Inferior Members respectively. Miskar A-11 is a very interesting well in that it contains a significant number of stylolite seams, with very few associated fractures. This is indicated by spacing values that are unusually large within the main reservoir intervals (i.e. 11.94m and 50.43m in the R1 Superior and Inferior reservoirs respectively). This may be explained by the fact that Miskar A-11 is not in close proximity to any large, 'horst-bounding' faults, and consequently is less fractured than the other wells analysed which appear to be closer to major structures.

Lithostratigraphic Unit	Fracture Type			Nature of Fracture Fill		
	I (STA)	I	II & III	CL	PO	OP
Abiod Formation	14	2	0	0%	94%	6%
Upper Aleg Member	0	0	0	0%	0%	0%
Aleg Carbonate Member	0	0	0	0%	0%	0%
R1 Superior Member	2	2	0	0%	100%	0%
R1 Inferior Member	0	1	0	100%	0%	0%
Total Core	16	5	0	5%	90%	5%

Table 6.32. Distribution of fracture type, and nature of fracture fill/cementation in Miskar A-11. Percentages are given for the amount of closed (CL), partially open (PO) and open (OP) fractures within each lithostratigraphic interval.

Table 6.32 shows the distribution of fracture type, and the amount of cementation within fractures. The majority of fractures are Mode I stylolite-associated structures which tip off stylolite dentae. This observation is expected, owing to the high number of stylolite seams present. Most of these fractures are partially filled with calcite cements. An analysis of fracture height has been omitted due to the lack of available data.

6.6.4. Discussion of Core Observations

A discussion of the results obtained for each well is provided in the following section. Observations are compared between wells, and a model illustrating the proposed sequence of fracturing is presented. It must be stressed that although the calculated values may be representative of actual subsurface distributions, caution must be applied because the calculations for each well are based on measured data taken from different sample lengths (i.e. core intervals). Indeed, some of the sample lengths are too short to gain accurate distribution data (i.e. Miskar A-7 and A-9). In addition, along with other factors, the fracture distributions obtained from the cored intervals is in part, controlled by proximity to local structure (refer to Chapter 5). Hence, the higher fracture frequencies identified in certain wells could be attributed to local fault proximity (refer to following discussion).

Stylolites

Two types of stylolites have been identified through direct core observations and thin section analysis: 1) Aggregate stylolites and 2) Intergranular stylolites (refer to earlier text). The majority of aggregate stylolites observed in the core analysis are bedding-parallel, compactional stylolites that have formed in response to the overburden pressure (σ_v). They tend to develop preferentially along bed boundaries where there is a distinct variation in the bulk rock composition between two lithological units. Thin section analysis demonstrates that most aggregate stylolites develop as intergranular stylolites at grain-grain contacts.

Based on the classification of Wanless (1979), two particular types of aggregate stylolites have been recognised in the Miskar cores: 1) High amplitude 'sutured' stylolites and 2) Low amplitude 'non-sutured' stylolites, characterised by open sinusoidal geometries. Sutured stylolites tend to develop in coarse-grained, wackestone to packstone fabrics where there is only a small percentage of clay material, together

with a large amount of structurally resistive material (e.g. shell debris). This is the case for the R1 Superior and R1 Inferior Members. Non-sutured stylolites form in finer grained, more clay dominated fabrics where there is less shell debris (i.e. the Abiod Formation) (Table 6.33). Wanless (1979) proposes that gradational transitions may exist between these two types of stylolites. However, this is not apparent in this study. The columns or 'peaks and valleys' of aggregate stylolites generally parallel the maximum stress (σ_v) or strain during formation (Nelson, 1981).

Tectonic aggregate stylolites have also been identified in the cored intervals, in particular within Miskar A-3 and A-11. These seams, which are at a high angle to bedding are generally of the sutured type. Their amplitudes are almost always lower than those of the adjacent compactional structures. Within the Miskar cores they are commonly observed to cross-cut and displace the horizontal features, hence indicating that they formed after the development of the compactional features. The exact orientation of these structures relative to an original tectonic event is unknown, although it is suggested that they formed in response to either:

- A phase of SE-NW directed compression from the late Maastrichtian to late Thanetian, when the eastern horst-bounding fault was inverted in sinistral transpression;
- A phase of late Eocene compression that caused uplift and erosion of the Bartonian to Priabonian section of the Cherahil Formation.

The stylolites observed in the Miskar cores contain variable amounts of insoluble residue. This residue, which is generally fine-grained and dark, displays various amounts of foliation or fabric parallel to the stylolite. The accumulation of residue is usually thicker at the apex of the crests or valleys than along the vertical walls of the stylolite columns (**Plate 6.17**). The composition of the insoluble residue is variable, depending on the composition of the host rock. Most commonly, however, microgranular clay materials occur within the seam; this residue occurs as either one dark seam or as many semi-parallel sets of very thin seams. Clay residues are accompanied by small amounts of quartz, calcite, dolomite and occasional pyrite. Oil staining and late meteoric dolomitic cements (MacCaulay et al., 2001) along certain stylolites indicates that they have acted as migration pathways at some point in their development.

Average stylolite frequencies are generally fairly consistent in all the wells analysed (Table 6.33). Stylolite frequency is believed to crudely trace bedding, since most stylolites develop at boundaries between units of different bulk composition. The Abiod Formation contains a significant number of stylolites compared to other lithofacies, in particular within the Miskar A-3 and A-11 wells. This contributes to the slightly higher values that Miskar A-3 and A-11 show for the entire cored interval. The main reservoir units (i.e. the R1 Superior and R1 Inferior Members) show very consistent stylolite frequencies within all the wells analysed. These values are probably representative of actual subsurface distributions.

	Average Stylolite Frequency (Stylolites/m)						Average Amount Removed/Stylolite (mm)					
Lithostratigraphic Unit	**A-3**	**A-6**	**A-7**	**A-9**	**A-10**	**A-11**	**A-3**	**A-6**	**A-7**	**A-9**	**A-10**	**A-11**
El Haria Formation			0.00						0.00			
Abiod Formation	1.26		0.36			2.22	6.52		28.5			8.93
Upper Aleg Member	0.71					1.40	5.91					1.00
Aleg Carb. Member	0.00					0.00	0.00					0.00
R1 Superior Member	0.23	0.16		0.00		0.16	36.1	19.9		0.00		27.6
R1 Inferior Member	0.32	0.40		0.15	0.12	0.12	37.5	23.3		40.8	20.0	24.7
Lower Aleg Member		0.10						20.0				
Bireno Member					0.52						45.2	
Total Core	0.61	0.24	0.22	0.14	0.32	0.64	14.7	21.9	28.5	40.8	40.4	11.4

Table 6.33. Comparison of average stylolite frequencies, and the average amount of material removed within each lithostratigraphic interval for each well.

Minimum estimates of the material removed through the process of stylolitisation are also comparable in the cored intervals (Table 6.33). The R1 Superior and Inferior reservoir units consistently show higher stylolite amplitudes, indicating that a larger amount of material has been lost through pressure solution. As previously mentioned, these units, consisting of bioclastic packstones and wackestones (i.e. with high calcite contents) appear to favour high amplitude 'sutured' stylolite development. In contrast, the more clay rich finer-grained lithofacies (i.e. the Upper Aleg Shale Member and the Abiod Formation) favour lower amplitude 'non-sutured' stylolite formation (Wanless, 1979).

Origin of Stylolites

The pressure solution theory of Wagner (1913) is now widely recognised as the most plausible mechanism for the origin and formation of stylolites. The pressure solution

process essentially involves solution of the lattices or detrital grains around points and surfaces of contact between crystal lattices or mineral grains, where elastic strain and hence solubility are enhanced by 'unidirectional' pressure (e.g. the weight of the overburden) (Park & Schot, 1968). Solutions migrate away from these intergranular boundaries and are reprecipitated in regions of lower pressure or undersaturation (e.g. in the pore spaces between mineral grains and in vugs, cavities and fractures).

Stylolitisation in the Miskar reservoirs is a post-lithification process. As the main reservoirs were buried and compacted, dewatering occurred together with the elimination of unsupported pore space. Once lithified, the process of stylolitisation commenced preferentially along bed boundaries where there is a distinct variation in bulk rock composition between two lithological units. Stylolite amplitudes increased with progressive burial. The two-dimensional geometry of compactional and tectonic stylolites is interesting, in that most carbonaceous laminae of not planar, but are composed of a chains of discontinuous curved sections of arcs. This is suggestive of a shift in the pressure and consequent surface tensions along the stylolitic horizon with the process of stylolitisation; the process first dissolving at one point and then at another and continuing in this manner.

Factors Affecting Stylolitisation

It is apparent from the core analysis and the preceding discussion that a number factors affect stylolite development within the Miskar reservoir intervals. The most obvious control on stylolitisation is lithology, where the intensity and type of stylolites developed is intimately associated with the composition, shape (size, sorting and distribution) and packing of individual grains. This explains the difference in stylolite characteristics and intensity in the units cored in the Miskar wells. As already mentioned, low clay content, together with a large percentage of structurally resistive skeletal material within a host rock will cause the development of high amplitude, sutured stylolites, and vica versa. To date, the exact nature of this relationship has not been quantified.

Gilbert (1949) reviews the other factors that affect the process of stylolitisation. In summary, these include: 1) The general stress-strain conditions on the grains as conditioned by the degree of confinement of the pore fluid, 2) Depth (rate) of burial (pressure), 3) Partial modal volumes of the minerals involved, 4) Surface tension

effects, 5) Relative compressibility of liquid and solid phases, 6) Composition of the pore fluid, 7) Eh, pH and temperature, and 8) Mode and rate of neomorphism.

Fractures

The analysis of the cored intervals shows a predominance of sub-vertical Mode I extensional fractures. These are classed into two sub-sets: 1) Stylolite-associated (STA) fractures (i.e. those fractures that tip off stylolite dentae) and 2) En-echelon Mode I fractures sets that are intimately associated with the STA fractures. Stylolite-associated fractures are believed to develop contemporaneously with stylolitisation (i.e. during the diagenetic stage of burial (pre-lithification)). They are generally filled with a zone of calcite cementation in the region immediately adjacent to the stylolite seam (usually <300mm in length), which represents the first phase of calcite reprecipitation from the initial stages of pressure solution. The en-echelon sets of Mode I fractures that lead off from STA fractures are believed to have formed in response to stylolitisation and/or later phases of extension (N.B. the Gabes-Tripoli Basin in which the Miskar Field is situated has undergone successive phases of tectonic subsidence and extension from the Late Cretaceous to the present-day). They are generally partially to totally occluded by calcite cements. Occasionally, these fractures show evidence of normal and strike-slip displacements, in particular where they intersect and displace pre-existing stylolite seams.

Mode II and III fractures have also been identified in the cored intervals but to a lesser extent. They are generally moderately dipping features (55^0-65^0) that have minor displacements and show evidence of both normal dip-slip and oblique-slip movements. Many are totally occluded with calcite and late meteoric dolomite cements (MacCaulay et al., 2001). As previously discussed, the exact orientation of these fractures could not be evaluated, due to the lack of oriented core, although it is reasonable to infer from the seismic analysis that they probably formed in response to:

- Mode II normal dip-slip fractures – NE-SW to ENE-WSW directed extension which has been active intermittently throughout the Late Cretaceous to present-day evolution of the area;
- Mode III sinistral (?) oblique-slip fractures – reactivation of pre-existing Mode II fractures during a phase of SE-NW directed transpression in the Maastrichtian to Thanetian.

Apparent fracture frequency estimates indicate that Miskar A-3 and A-6 are more fractured that other wells (Table 6.34). Apparent fracture frequency values between the two wells are very consistent, particularly in the R1 Superior and R1Inferior intervals. Whole core frequencies are also comparable (Table 6.34). Values in the Miskar A-11 well are substantially lower.

	Apparent Fracture Frequency (Fractures/m)						Average Fracture Spacing (m)					
Lithostratigraphic Unit	A-3	A-6	A-7	A-9	A-10	A-11	A-3	A-6	A-7	A-9	A-10	A-11
El Haria Formation			0.09						8.42			
Abiod Formation	1.59		0.30			0.37	0.78		1.65			3.13
Upper Aleg Member	1.23					0.00	0.54					>7.0
Aleg Carb. Member	0.00					0.00						>2.6
R1 Superior Member	1.00	0.77		5.00		0.02	1.43	1.15		0.24		11.9
R1 Inferior Member	1.58	1.66		0.09	0.06	0.02	0.65	0.57		5.94	12.2	50.4
Lower Aleg Member		1.92						0.41				
Bireno Member					1.20						0.68	
Total Core	1.35	1.15	0.22	0.46	0.63	0.10	0.84	0.79	2.43	2.13	1.29	8.56

Table 6.34. Comparison of apparent fracture frequencies, and average fracture spacing values within each lithostratigraphic interval for each well.

Apparent fracture frequency values correlate particularly well with fracture spacing calculations (Table 6.34). This suggests that these two analyses give a relatively good representation of fracturing in the subsurface. The most consistent results are from the Miskar A-3 and A-6 wells. These wells show very similar spacing values in the main R1 Superior and R1 Inferior reservoir intervals (i.e. 1.43 (A-3) compared to 1.15 (A-6) in the R1 Superior interval, and 0.65 (A-3) compared to 0.57 (A-6) in the R1 Inferior interval). Spacing values for the whole core are also highly consistent (i.e. 0.84 (A-3) compared to 0.79 (A-6) respectively). These results, together with the highly comparable sample lengths (for the R1 Superior and Inferior intervals in each well) suggest that they are a good representation of subsurface fracture spacing. It should also be noted, that these two wells contain a high proportion of measured fractures, compared to the other wells. This could be a function of proximity to local structure. Both Miskar A-3 and A-6 were drilled adjacent to major structures which are likely to have large zones of fracturing associated with them (i.e. Miskar A-3 is located immediately adjacent to the main compartment bounding fault, whereas Miskar A-6 lies close to the eastern horst-bounding fault).

6.6.5. Sequence of Fracturing in the Miskar Reservoirs

The following discussion attempts to summarise the main stages of fracture development within the main Miskar reservoirs. A series of schematic block diagrams are also provided in order to illustrate the evolution of fracturing (**Fig. 6.33a-e**).

Throughout the Late Cretaceous the lower members of the Aleg Formation were deposited (i.e. the Bireno, Lower Aleg Shale, R1 Inferior/Superior and Aleg Carbonate Members) during a period of relative tectonic stability. Minor fault activity on pre-existing N-S trending lineaments influenced sedimentary deposition, and also caused minor N-S fracturing within newly deposited unlithified sediments (**Fig. 6.33a**).

As these sequences became buried and compacted internal micro-fracturing occurred within individual skeletal fragments in the Bireno and R1 Inferior/Superior Members. However, at a certain point early lithification processes, such as grain-grain compaction ceased and the process of stylolitisation commenced. The timing of this event (which is controlled by the factors given in Section 6.6.4) is difficult to determine, although it is plausible to suggest that compactional stylolites developed first within the lithified Bireno Member (**Fig. 6.33a**). These stylolites were developed preferentially along bed boundaries where there was a distinct variation in the bulk rock composition between two lithological units.

Fracturing associated with stylolitisation also occurred during this period. These 'stylolite-associated' fractures are observed to form approximately NW-SE trending en-echelon networks that tip off stylolite dentae. They are commonly filled with coarse, highly twinned calcite cements, which were principally derived from the matrix material. Stylolitisation is thought to have promoted induration by supplying cement.

Following the deposition of the Aleg Carbonate Member, the Miskar area experienced a period of approximately NE-SW extension associated with tectonic subsidence in the Gabes-Tripoli Basin. This phase of extension reactivated the underlying N-S trending 'basement' faults in sinistral transtension, and caused NW-SE oriented faulting in the Upper Aleg Shale Member. It is suggested in Section 6.5.4 that the development of this system of NW-SE trending structures was in part, controlled by transtensional movement on the underlying N-S structures. Reservoir scale fractures that developed during this phase of faulting trend approximately NW-SE (**Fig. 6.33b**). This event also reactivated many earlier N-S and NW-SE trending structures in sinistral transtension.

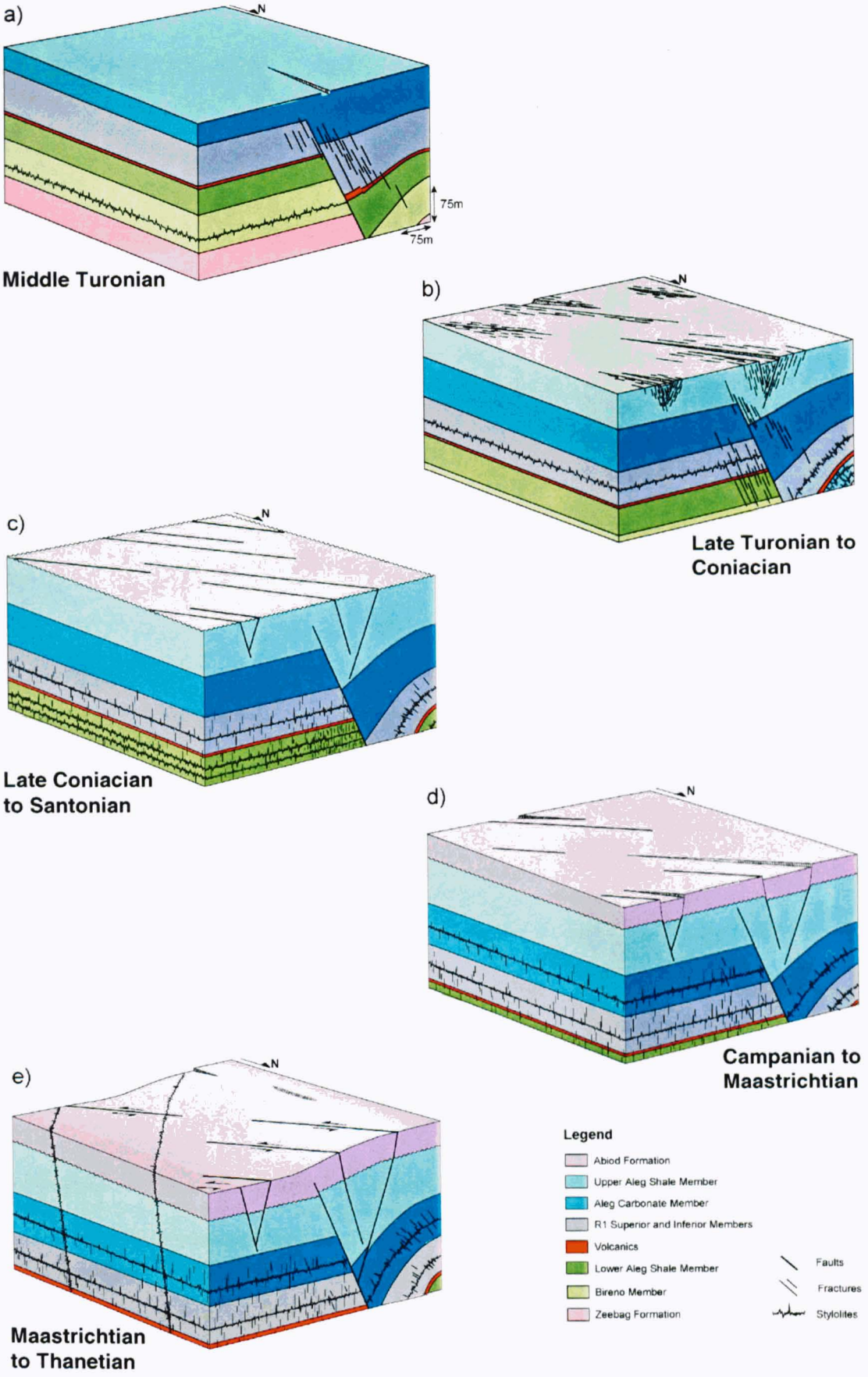

Fig. 6.33. Sequential restoration of the main phase of fracturing in the primary reservoir intervals within the Miskar Gas Condensate Field.

Throughout this phase of tectonic subsidence the process of stylolitisation continued (**Fig. 6.33b**). Stylolite amplitudes increased during progressive burial and diagenesis, as large volumes of calcite continued to be passed into solution. A large proportion of the solute was reprecipitated as calcite cement in the surrounding matrix, occluding porosity, whilst the remainder was transported away from the immediate site of dissolution and was reprecipitated within the various fracture systems and in other horizons.

The late Turonian to Santonian interval was characterised by a period of uplift and sub-aerial erosion that produced a regional unconformity at the top of the Aleg Formation. This period of 'unroofing' reactivated many pre-existing fractures (**Fig. 6.33c**), and may have caused some of the pre-existing stylolites to crack open and conduct fluids. Following this, the Campanian to Maastrichtian period was characterised by a rejuvenation of NE-SW oriented extension. This created a series of NW-SE trending extensional faults within the Abiod Formation (N.B. some of these faults occasionally link with reactivated late Turonian faults). Reservoir scale fractures associated with this tectonic period trend NW-SE, parallel to the main faults (**Fig. 6.33d**).

Towards the end of deposition of the Abiod Formation, the Miskar area was subjected to a phase of SE-NW oriented compression, during the late Maastrichtian. This event, which continued into the late Thanetian, reactivated the pre-existing Turonian to Maastrichtian fault systems in sinistral transpression (**Fig. 6.33e**). Flexuring associated with inversion on many of these structures caused extensional fracture development in the hinge regions of 'pop-up' and 'harpoon' structures (**Fig. 6.33e**). In addition, vertical tectonic stylolites developed, oriented perpendicular to the maximum compressive stress (i.e. σ_H).

Succeeding tectonic phases from the Palaeocene through to the present-day have probably also caused fracture development and reactivation in the main reservoir units. The influence of these events on the structural development of the main reservoir intervals is considered in more detail in Chapter 7, which focuses on fracture development in the lower Eocene El Garia Formation in the Hasdrubal Gas Condensate Accumulation.

6.6.6. Influence on Reservoir Performance

It is apparent from the preceding discussion that there are still uncertainties with regard to the nature and relative distribution of structural features in the main reservoir intervals in the Miskar Gas Condensate Field. This is mainly due to the small sample volume gained from core extraction.

Open and partially open Mode I fractures associated with stylolites form vertical to near vertical conduits to fluid flow throughout the reservoir. The connectivity of these fracture systems is unclear. On a vertical scale they form in en-echelon networks, with fractures ranging in size from the millimetre scale up to the metre scale. In the 2D core samples these fractures do not appear to be connected, although in three dimensions connectivity may be established, thus causing an increase in permeability in the direction parallel to the orientation of fracturing. It can be reasonably inferred from seismic data that most of these fractures trend approximately NW-SE, parallel to the main seismic-scale faults. The lateral extent (i.e. length) and connectivity of individual Mode I fractures is also unclear (due to the small diameter of the core), although if it is assumed that they are elliptical structures, height and length distributions should be similar.

Mode I fracture distributions appear to increase with proximity to local structure. Both Miskar A-3 and A-6 were drilled adjacent to major seismically resolvable faults. They consequently have a high number of observed Mode I fractures relative to other wells that were drilled further away from such structures. It is suggested that the strain along such fault zones was accommodated in part, by the reactivation of Mode I stylolite-associated fracture systems. In the vicinity of these faults, Mode I fractures are accompanied by NW-SE trending Mode II and III fractures associated with faulting. These laterally extensive structures are generally partially to totally filled with calcite and dolomite cements. Nevertheless, together with the Mode I fractures mentioned, they appear to be important conduits to flow. In the Miskar A-3, well test data suggests vertical communication between the R1 Inferior and R1 Superior reservoirs.

The high frequency of stylolites observed in the Miskar cores could have a marked influence on reservoir performance. If laterally extensive, they could affect large areas of the field. Their impact is two-fold; 1) If closed they act as major permeability barriers compartmentalising the reservoir, and 2) If open (which is the case for a number of the structures measured) they form major horizontal conduits to fluid flow.

A combination of extensive open stylolites, together with the associated systems of open to partially open Mode I fractures (if vertically and laterally connected), could contribute significantly to the reservoir performance. If this is the case, each of the Miskar reservoirs can be classified as a Type III reservoir, according to the scheme of Nelson (2001), whereby 'fractures partially assist permeability in an producible reservoir'. However, if unconnected it is more suitable to classify each reservoir interval as a Type IV reservoir (i.e. Fractures provide no additional porosity/ permeability but create anisotropy).

Chapter 7

Structural Analysis of the Hasdrubal Gas Condensate Accumulation

7.1. Introduction

This chapter presents the second field-specific case study incorporated in this thesis. It examines the controls on fracture development in the main reservoir intervals within the Hasdrubal Gas Condensate Accumulation, which lies immediately adjacent to the Miskar Field. The methodology used in this study is similar to that of Chapter 6.

Various analyses have been utilised to gain an understanding of the processes controlling fracture development at the reservoir scale. Sections 7.2, 7.3 and 7.4 locate the Hasdrubal Gas Condensate Accumulation, present details on the exploration history of the acreage, and introduce the main structure and reservoir stratigraphy. Section 7.5 utilises 3D seismic data over the area in order to establish the structural context and evolution of the accumulation.

Section 7.6 summarises the results from the analysis of the Hasdrubal -2, -3 and -4 cores. Structural core descriptions are presented, together with estimates of fracture spacing, frequency and length. Some oriented core was obtained during the drilling of Hasdrubal -4 allowing a determination of fracture and stylolite orientation. In addition, CAST and FMS image logs from the Hasdrubal -2 and -3 wells have been interpreted and incorporated into the study. The results of these analyses have been integrated into a 'working' fracture model showing the timing and sequence of fracturing in the main reservoir unit. Section 7.8.4 discusses the influence of fracturing on reservoir performance, and also make a comparison with the neighbouring Miskar Field.

7.2. Location & Field History

The Hasdrubal Gas Condensate Accumulation is located within the Amilcar Permit in the Gulf of Gabes, approximately 100km SE of Sfax (**Fig. 7.1**). It is 35km southwest of the Miskar Gas Condensate Field, and approximately 25km southeast of the Ashtart Oil Field, which produces from the same reservoir.

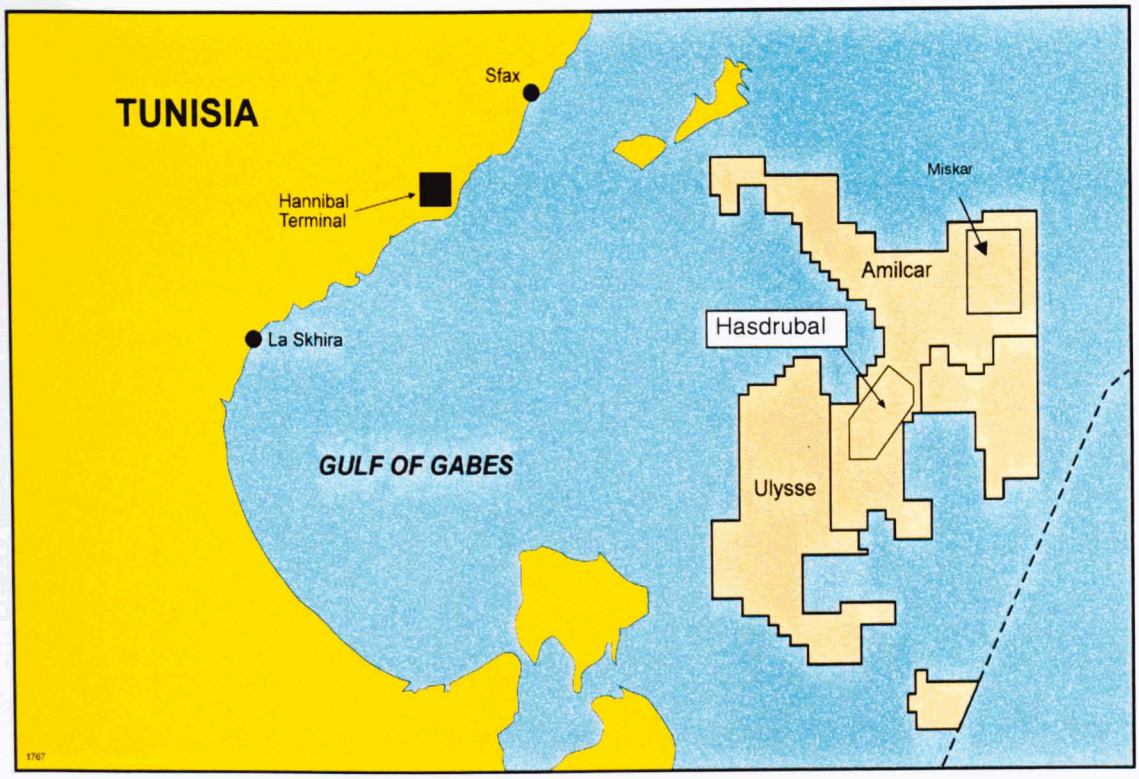

Fig. 7.1: Location of the Hasdrubal Gas Condensate Field.

The discovery well for the accumulation was drilled by Sofratep in 1975 (Hasdrubal – 1). Gas condensate flowed from the Ypresian El Garia Formation. Hydrocarbons were also encountered in the Upper Eocene Reineche Member of the Cherahil Formation, a secondary exploration target. The acreage was relinquished and acquired by the BG Group in 1993, and further drilling between 1994 and 1998 confirmed the potential of the discovery (Hasdrubal -2, -3 and -4). Development of the discovery is expected to commence in 2002.

7.3. Database

The database available for this study included a 3D seismic grid over the Hasdrubal acreage, together with composite well logs, well reports and core from selected wells.

Well Name	Composite Log	Core Report	Core
Hasdrubal –1	✔	✔	
Hasdrubal –2	✔	✔	✔
Hasdrubal –3	✔	✔	✔
Hasdrubal -4	✔	✔	✔

Table 7.1. Data available for wells Hasdrubal -1 to -4.

7.4. Local Structure & Reservoir Stratigraphy

7.4.1. Introduction

The following section documents the local structure and reservoir stratigraphy of the Hasdrubal accumulation. This will lead into Section 7.5, which will present a comprehensive overview of the main structure and evolution of the accumulation.

7.4.2. Structure

The Hasdrubal accumulation is located within a NNW-SSE trending horst block created between a system of 'left stepping' en echelon extensional to oblique slip faults (**Fig. 7.2**). It represents one of a series of highs that trend approximately NNE-SSW. The main horst block is cut by a series of small NNW-SSE trending seismically resolvable extensional faults, which have maximum throws of 30-100m.

7.4.3. Reservoir Stratigraphy

The primary reservoir stratigraphy in the Hasdrubal Accumulation belongs to the Metlaoui Group, which is dominantly Ypresian (early Eocene) in age (Bishop, 1985; Moody, 1987; Beckett, 1998; Racey et al., 2001) (**Fig. 7.3**). The Metlaoui Group consists of the Chouabine, Bou Dabbous, Ousselat, El Garia, Ain Merhotta and Faid Formations, and also the Compact Micrite Member. The El Garia Formation forms the primary reservoir, and is sourced by its offshore equivalent, the Bou Dabbous Formation. The sedimentology of the main constituents in the Metlaoui Group (identified in the cored intervals) is discussed below.

Chouabine Formation

The Chouabine Formation is present throughout the Hasdrubal area. It was extensively cored in Hasdrubal -2 and -3, with only the uppermost few metres cored in Hasdrubal -

1 and -4. The interval consists of phosphatic calcareous mudstones with nummulites, nummuloclastics, smaller benthonic foraminifera, miliolids, ostracods, bivalves and gastropods (**Plates 7.1 & 7.2**).

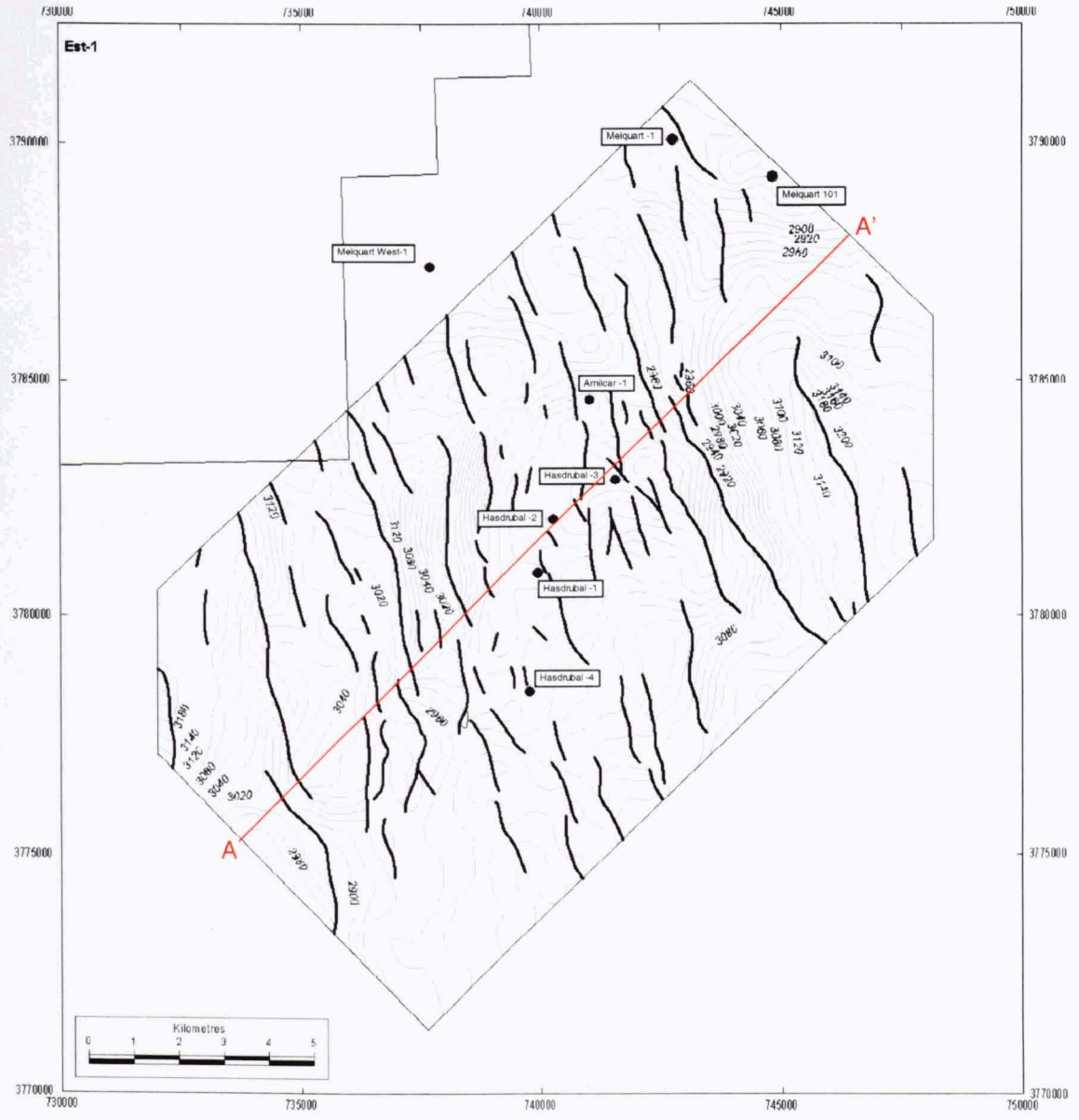

Fig. 7.2. Two-way-time (TWT) structure map of the Top Metlaoui Group. The red line shows the location of seismic line presented in Figure 7.6.

The mudstones show varying degrees of lamination and are often bioturbated. Fining-upwards units, characterised by grading from well bioturbated wackestones-packstones with clasts of phosphate, intraclasts (sometimes algally coated) and bioclastic debris (bivalve, echinoid, and nummulite) to poorly laminated mudstones are present (Braithwaite, 1998).. A well sorted, fairly homogeneous and partially dolomitised nummulitic bed (approximately 6m thick) has been observed within all the wells.

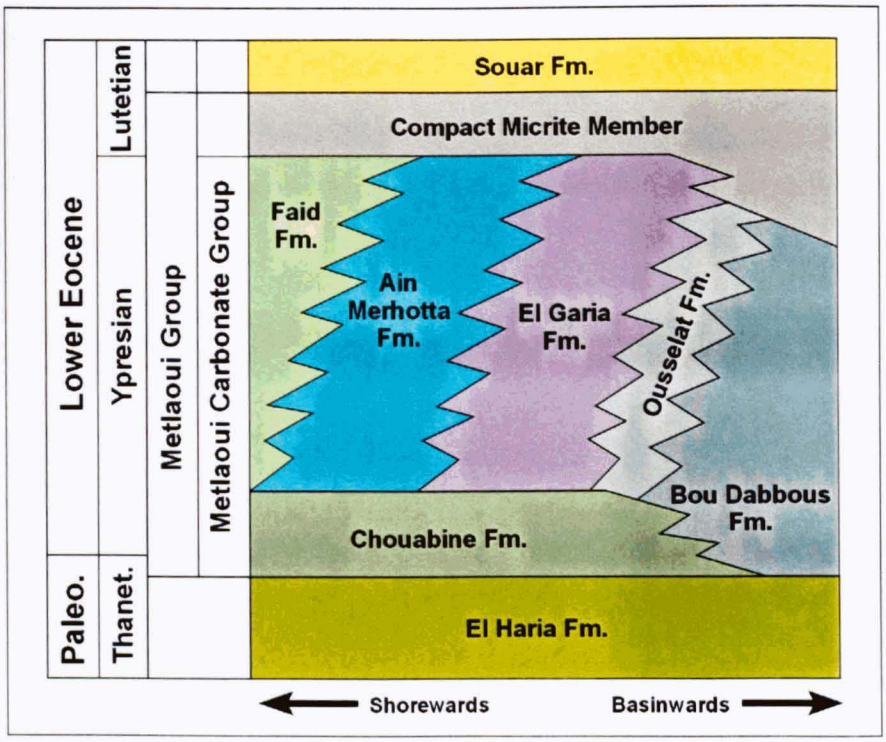

Fig. 7.3. Reservoir stratigraphy in the Hasdrubal Gas Condensate Field (after Moody, 1987).

A deep-water origin for the Chouabine Formation is invoked due to the high mud and phosphatic content, moderate bioturbation, low nummulite presence, intraclasts and the presence of a deep-water biota (Beckett, 1998). The thin fining upwards event beds and the main nummulitic interval may represent turbidite, tempestite or gravity flow deposits (Beckett, 1998).

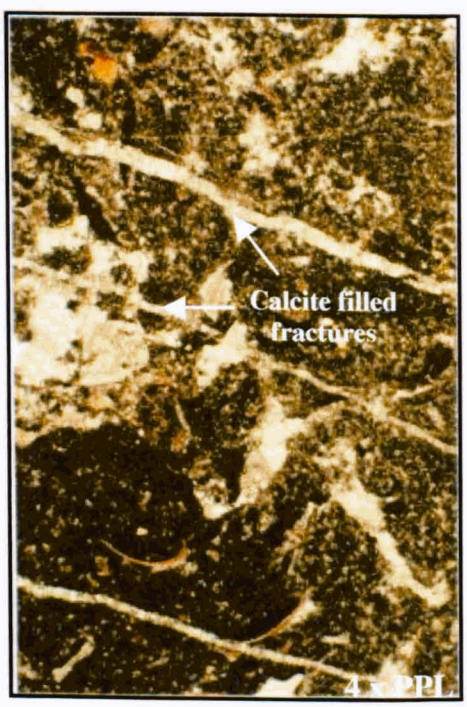

Plate 7.1. H4. Depth: 3037.42m MD. Calcite filled Mode I fractures in the Chouabine Formation.

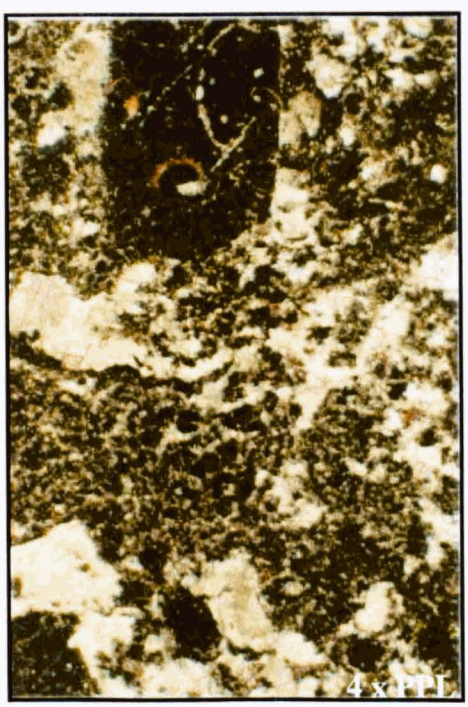

Plate 7.2. H4. Depth: 3037.42m MD. Chouabine Formation: Phosphatic, calcareous mudstone.

The thin-section photomicrographs in **Plates 7.1** and **7.2** show the Chouabine Formation consisting of peletic wackestones. Secondary pore spaces are filled with calcite and dolomite cements. **Plate 7.1** shows a series of calcite-filled fractures.

El Garia Formation

The El Garia Formation is present across most of the Hasdrubal area. It ranges between 40-60m in thickness on-structure, but thins and pinches out relatively rapidly basinward where it is replaced by its lateral equivalent, the Bou Dabbous Formation.

It consists of nummulitic wackestones/packstones, with occasionally rare grainstones. Core analysis has identified large variations in the dominance of A and B-form nummulites within the unit (Braithwaite, 1998). As a consequence, it has been divided into A-rich (A:B >10:1) and B-rich (A:B <9:1) and nummuloclastic intervals using the following assumptions: 1) A-form nummulites are <7mm in size (Aigner, 1985) and 2) An A:B ratio of 10:1 represents a life assemblage (Racey, 1994).

Additional bioclasts within the formation include *Discocyclina* sp., rare *Operculina* sp., bivalve and echinoid fragments and smaller benthonic foraminifera (Beckett, 1998). **Plate 7.3** shows a nummulitic packstone with A and B-form nummulites in an oil-stained matrix. **Plate 7.4** shows a nummulitic packstone with a highly porous, dolomitised matrix that contains large secondary pores filled with hydrocarbons.



Plate 7.3. H4. Depth: 3032.50m MD. El Garia Formation: B-form nummulites within an oil stained matrix.



Plate 7.4. H4. Depth: 3011.75m MD. El Garia Formation: Highly dolomitised nummultic packstone.

In general, the lower and upper thirds of the El Garia Formation contains more wackestone and packstone B-form nummulitic rich beds together with interbeds of broken nummulites and *Discocyclina* sp. (Braithwaite, 1998). The central portion of the El Garia Formation is relatively matrix poor, and is dominated by packstones and packstone-grainstones. A thin mudstone is present near the base of the A-form dominated interval in Hasdrubal -3. This is laminated and contains pyrite, phosphate and very rare thin-shelled bivalves. The top of the El Garia Formation in Hasdrubal -3 and -4 is thoroughly bioturbated and contains much phosphate and pyrite.

The most obvious sedimentary features observed within the core are bioturbation (*Thalassinoides* sp.) and thin coarsening and fining upwards units (Braithwaite, 1998). Coarsening upwards units are characterised by bedding parallel nummulites at the top of the unit. Fining upwards units are defined by bedding parallel nummulites at the base. Intervals of bedding parallel nummulites with a lack of interstitial matrix are commonly associated with high compaction and stylolite development. These units are either capped or based by nummulitic debris and micrite.

Dolomitisation is evident in the cores. The dolomitisation is most aggressive in the Hasdrubal -3 well and has partially-completely dissolved nummulitic tests in an interval between 2886.32 to 2887.85m. Dolomitisation appears to be most prevalent in originally more micritic facies, and tends to be most pervasive in a correlatable zone in the central parts of the reservoir in all the wells analysed (Braithwaite, 1998). Dolomite adds significantly to the porosity and permeability in all wells (Beckett, 1998). Visible porosity is dominantly intergranular (although this is not commonly effective unless the nummulites are fractured), with intergranular/crystalline, fracture and vuggy porosity also being identified.

Fining upwards units can be interpreted as event bed deposits with the nummuloclastic/micrite top representing fallout as the storm wanes and/or fair weather deposition resumes following storm activity (Beckett, 1998). The origin of the coarsening upwards cycles is less certain, but they may be formed by: 1) redistribution of nummulites by bioturbation following storm deposition, 2) the forced filling of open burrow networks during storm deposition (Tadesco & Wanless, 1991) or 3) small scale base level change. Other sedimentary structures indicative of physical reworking are evident in the Hasdrubal cores and include evidence of scoured or erosive contacts and broken nummulites (Braithwaite, 1998).

Biofabrics in the Hasdrubal cores, together with sedimentary structures such as lags and erosive contacts seem to imply that considerable physical reworking/transport of nummulite life assemblages has occurred (Beckett, 1998). Intervals of bedding parallel nummulites are interpreted as the most winnowed ('high energy'). This has resulted in significant textural modification from a supposed original mud substrate. However, A-form dominated intervals are often thick (up to 12m), and may be too thick to be solely the product of winnowing and sorting, suggesting that there may be an overriding biological imprint on the storm dominated biofabrics.

The more wackestone and packstone B-form nummulite and discocyclinid-rich beds in the upper and lower thirds of the formation are interpreted as representing accumulation in deeper water than the central portion of the reservoir (Beckett, 1998). The central portion of the El Garia Formation may represent moderate energy with removal of fines in shallower waters, possibly with a normal wavebase or alternatively by storm processes sourcing sediment from a more proximal area (Beckett, 1998). The lack of fines may be explained by complete seaward movement of fines/nummulithoclastics or by deep scour by storms removing previous fine-grained deposits. Alternatively this thick unit may represent a major turbidite unit, with derivation from a more proximal source area to that of the upper and lower thirds of the formation (Beckett, 1998). The thin mudstone and wackestone interval encountered near the base of the A-form nummulite-rich interval in Hasdrubal -3 may represent a minor flooding event (Braithewaite, 1998). The uppermost El Garia Formation in Hasdrubal -3 and -4 is interpreted as representing condensed deposition at an omission surface prior to a transgression at the base of the Lutetian and deposition of the Compact Micrite Member (Beckett, 1998).

Compact Micrite Member

The Compact Micrite Member is partly cored in Hasdrubal -3 and -4 (depths 2858.00-2868.90m and 2966.00-2986.70m, respectively). It comprises calcareous mudstones that show varying degrees of lamination. The mudstones are phosphatic and pyritic in parts and also contain bioclastic debris such as bivalves, ostracods, gastropods and foraminifera (rare nummulites, discocyclinids, planktonics and smaller benthics); very rare corals were also noted in Hasdrubal –4 (Braithwaite, 1998). Bioturbation is evident at certain levels and appears to be cf. *Chrondrites* sp. The base of the unit is very phosphatic, pyritic and glauconitic. In Hasdrubal -4, the Compact Micrite Member

displays more platey fissility and is possibly more organic rich at certain intervals (Braithwaite, 1998). **Plates 7.5 and 7.6** show skeletal packstones containing partially silicified bivalves. Fractures are filled with Fe-rich calcite cements.

Petrographic analysis of the Hasdrubal cores indicated that this unit clearly contains a well-preserved assemblage of deep-water benthic and planktonic foraminifera. The Compact Micrite Member is interpreted as having been deposited during a deep-water transgression, following the deposition of the El Garia Formation (Beckett, 1998).



Plate 7.5. H4. Depth: 2966.0m MD. Compact Micrite Member: Calcareous mudstones.

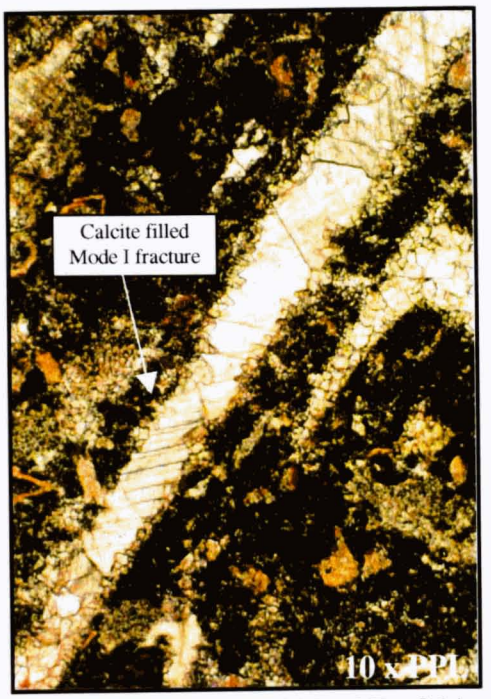

Plate 7.6. H4. Depth: 2986.5m MD. Calcite filled fractures in the Compact Micrite Member:

7.4.4. Regional Depositional Setting of the Metlaoui Group

Many workers have proposed regional depositional models for the Metlaoui Group (Moody, 1987; Moody & Grant, 1989; Loucks et al., 1998). **Figure 7.4** presents a revised interpretation based on previous work and the present study. This model has been refined from the current working BG Group depositional model to incorporate the tectonic style of the area.

Following the shallowing that ended the deposition of the Chouabine limestones in the early Ypresian, a shallow ramp was established over the area during the middle Ypresian, on which the El Garia Formation and its lateral equivalents were deposited (Loucks et al., 1998). Deposition was established in a series of shoreline parallel facies tracts that had irregular margins influenced by local tectonics (**Fig. 3.14**) These facies tracts migrated shorewards or basinwards according to relative changes in sea level.

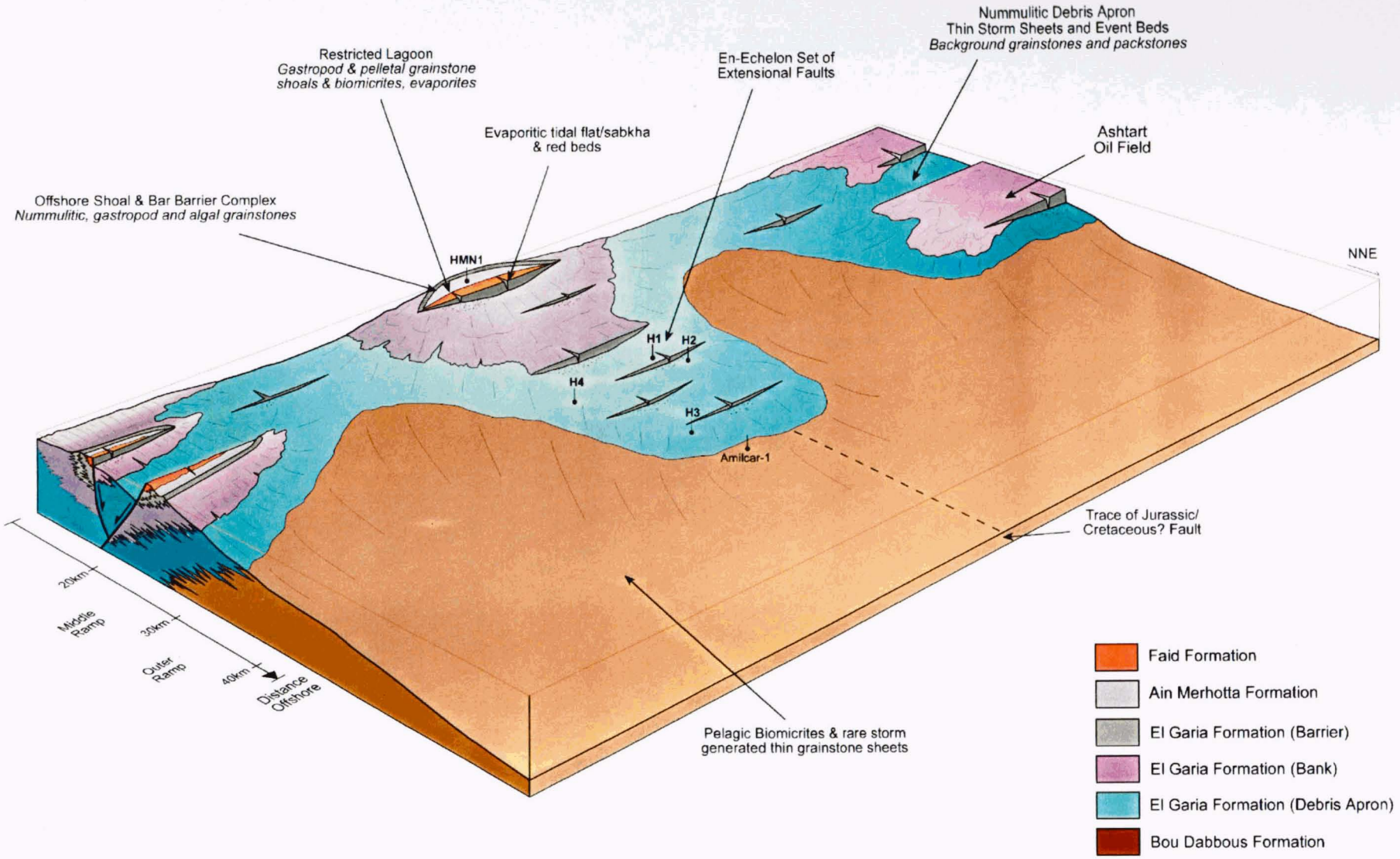

Fig. 7.4. Schematic palaeogeography and depositional model for the Metlaoui Group in and around the Hasdrubal Field (modified from Beckett, 1998)

On the upper inshore reaches of the ramp, the Faid Formation consisting of terrestrial red clays and evaporites was deposited. This was succeeded seawards by evaporitic lagoonal limestones of the Ain Merhotta Formation. The seaward flanks of the low energy Ain Merhotta lagoon might have been protected by hydraulic break constituted by a barrier facies of the El Garia Formation (as recorded onshore by Moody, 1987).

The nummulitic wackestones, packstones and grainstones of the El Garia Formation succeed the upramp facies of the Ain Merhotta Formation. Biostratigraphic analyses indicate that that the El Garia Formation was deposited in a mildly regressive period, which was punctuated by correlatable minor transgressive events (Racey et al., 2001). El Garia deposition was finally terminated by the base Lutetian transgression, during which the overlying Compact Micrite Member was deposited (Racey et al., 2001).

The El Garia facies belt may actually be subdivided into three distinct sub-units comprising a shoreward barrier sub-facies, a mid-ramp sub-facies and an outer mid-ramp sub-facies (Beckett, 1998). The shoreward barrier sub-facies does not appear to be represented in the wells in the Gulf of Gabes, but by analogy with its onshore equivalents, is thought to consist of high-energy gastropod and calcareous algal grainstones (Moody, 1987). This facies would contain a significant constituent of nummulitic material washed shorewards from the mid-ramp. The in situ mid-ramp sub-facies constitutes an environment that was dominated by nummulites forming a series of low amplitude, periodically winnowed banks. This unit is thought to be represented in the area surrounding the Ashtart Oil Field to the northwest (Beckett, 1998). Finally, background sedimentation on the outer part of the mid-ramp was probably dominated by reworking of material derived from further upramp through both storm processes. This produced a 'background' sediment of packstones-wackestones. Storm triggered redeposition periodically introduced thin sheets of nummulitic grainstone-packstones into this environment. These sheets are typically several inches thick and probably extend laterally for several hundred metres. They usually occur in packages, indicating periods of increased storm activity, punctuated by more quiescent periods of reworking and bioturbation in which wackestones with rare planktonic and deeper water smaller benthic foraminifera were deposited (Beckett, 1998). The presence of rare thick intervals of A or B-form dominated grainstones are interpreted as having been deposited by turbidite processes (Beckett, 1998). The Hasdrubal Accumulation as presently delineated appears to lie entirely within this outer mid-ramp environment.

Basinwards of the Hasdrubal Accumulation, the El Garia Formation appears to pass transitionally into the organic rich pelagic biomicrites of the Bou Dabbous Formation. The Ousselat Formation, recognised onshore by Moody (1987) cannot confidently be distinguished in the Hasdrubal area.

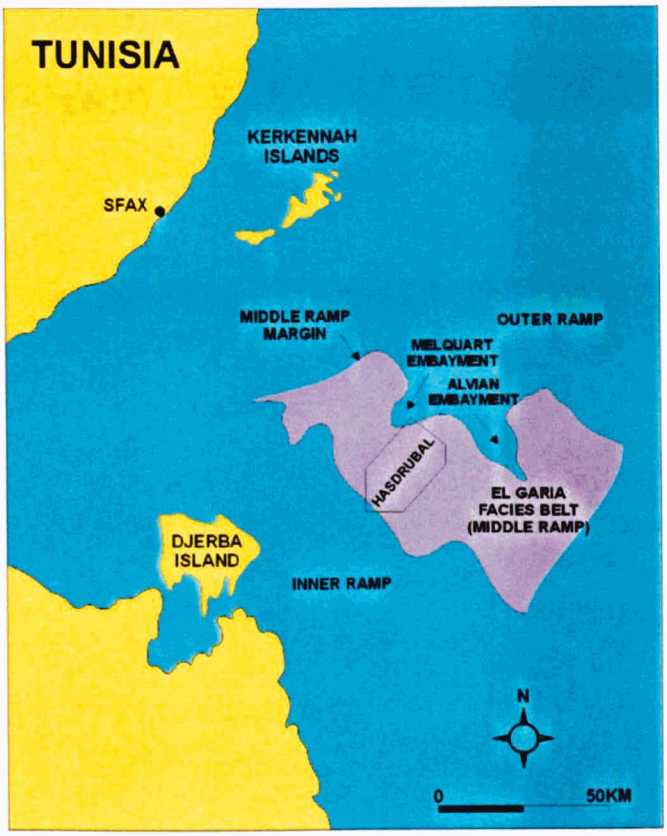

Fig. 7.5. The El Garia facies belt around Hasdrubal, showing a series of small structurally controlled embayments (data taken from the modified Metlaoui Group facies map of Beckett, 2000.

The distribution of facies types described above was locally disrupted by synsedimentary tectonic events. The distribution and relative abundance of planktonic foraminifera within the Upper Cretaceous to Eocene Formations, and the short hydrocarbon migration distance determined by geochemical analyses (McQuilken, 1998) indicates the presence of a structurally controlled deep pelagic embayment on the margin of the reservoir facies tract (**Fig. 7.5**). This embayment appears to coincide with pre-existing N-S trending extensional fault systems. As a result, the dominant NW-SE/NNW-SSE trend of the El Garia facies belt is interrupted around the Hasdrubal and Ashtart areas.

Tectonic control also appears to have been particularly important in the development of Ypresian nummulitic shoals (El Garia Formation) in the Hasdrubal area. Established

tectonic highs would have constituted preferential sites for the formation of nummulitic banks. In Libya and the southern part of the Gulf of Gabes, salt migration during the early Eocene, along and up the footwalls of deep faults caused significant fault block rotation in the Jurassic to Eocene section. The partially emerged crests of these tilted fault blocks would have provided the hydraulic conditions necessary to allow the accumulation of shoaling sandbodies of nummulite grainstones, sourced from offshore nummulitic banks. Subsequent movement of these faults would provide a trigger mechanism for the turbidites invoked as a mechanism for transporting clean nummulitic grainstones to the outer middle ramp. However, salt tectonics do not appear important in the Hasdrubal area and simple fault tectonics may explain the development of the Hammon Palaeohigh. Here the terrigenous and evaporitic Faid Formation is present in the lower part of the Metlaoui interval, succeeded by the Ain Merhotta and the El Garia Formations. From regional facies trends, the presence of mid ramp El Garia facies might be predicted for the Hammon area. The anomalous presence of an isolated succession of terrigenous to nearshore sediments is interpreted to indicate the presence of a locally exposed fault high that gradually subsided during the Metlaoui times, allowing the normal facies succession for the area to be re-established. The apparently abrupt transition from mid ramp El Garia facies to the Bou Dabbous Formation on the northeastern margin of the Ashtart Field may also indicate a local fault control.

7.5. Seismic Stratigraphy & Structure

7.5.1. Introduction

As with Miskar, LandMark™ software was used to interpret the Hasdrubal 3D seismic dataset. TWT structure maps were constructed, and used in conjunction with seismic profiles to determine the main structural elements present, the timing of tectonic events and the influence of these processes on the depositional architecture of the main reservoir.

7.5.2. Seismic Stratigraphy

Ten seismic sequences have been interpreted in the Hasdrubal dataset from the Palaeocene to the present-day. These are shown in Table 3.1. They are also illustrated in **Figure 7.6**. The top of the El Garia Formation (i.e. top reservoir) cannot be resolved

on the seismic dataset, because the reflection is strongly impacted by the overlying Compact Micrite Member (Foster, pers. comm., 1999). Consequently, the Top Metlaoui has been picked (as a trough on this reverse polarity data), and is on average 16m above the top reservoir. Estimated structure maps of the Top El Garia Formation have subsequently been produced by isopaching down from the Top Metlaoui pick. An attempt has been made to map the Top Chouabine Formation (i.e. base reservoir). However, owing to the fact that the reservoir is very close to tuning thickness this was not always possible.

The El Garia Formation actually thins and pinches out to the north. It is possible to estimate the position of the pinch-out by mapping the northerly truncation of the sub-cropping (Chouabine) reflections. On 3D seismic data the truncating reflectors are best seen in a direction that is oblique to the in-line direction. The mapped pinch-out was found to be coincident with a sharp inflexion in the thinning of the total Metlaoui isopach towards the northeast. The Metlaoui isopach thins by approximately 25-30ms (two-way-time) over the length of the accumulation.

7.5.3. Seismic Structure

A total of over 220 seismically resolvable faults were identified over the whole Hasdrubal survey area, over 90 of which cut the El Garia Formation. The geometry and timing of movement on these structures has been analysed through the seismic interpretation and the construction of relevant two-way-time (TWT) structure maps.

Seismic Expression of Hasdrubal Structure

As previously mentioned, the Hasdrubal accumulation is located on an approximately NNW-SSE trending horst block, within a system of left-stepping en-echelon extensional to oblique (?) -slip faults (**Fig 7.2**). It represents one of a linear system of highs that trends approximately NNE-SSW across the Gulf of Gabes region. Other highs along this zone include the Melquart, Hammon, Gabes and Miskar Highs or Horsts. These highs group together to form the Amilcar High, which has a similar trend to the Kerkennah High (Chapter 3). The structural geometry of the Hasdrubal horst block is similar to that of the Miskar structure, and hence only a brief explanation is presented. It is delineated by two approximately NNW-SSE trending faults zones which throw down to the east and west (**Fig. 7.6**). Internally it is sub-divided by numerous NNW-SSE trending extensional faults.

CONTAINS PULLOUTS

Southwestern Fault Zone

The western bounding fault zone is expressed in its lower section by a steeply dipping, concave-westward fault plane that extends up upwards to approximately top Abiod level (*SS-8*) where it kinks sharply, and flattens out into the El Haria Formation (*SS-9*) (**Fig. 7.6**). It then steepens upwards into the Metlaoui Group (SS-10) and Cherahil Formation (SS-11). Unlike the Miskar structure this zone extends across the Oligocene unconformity and up into the Oligocene to present-day section. The extension of this fault zone across this unconformity is probably the result of later reactivation. Hangingwall displacements vary with depth; at Salammbo level throws range between 50m and 80m, whereas at Abiod level displacements can exceed 200m.

Northeastern Fault Zone

The geometry of the northeastern fault zone is very similar to the southwestern horst-bounding fault (**Fig. 7.6**). It is expressed by a steep fault zone in the Upper Cretaceous section that kinks, and flattens out in the El Haria Formation (SS-9). It then steepens up into the Eocene to present-day succession. Minor displacements are observed across the Oligocene unconformity. Hangingwall displacements down to the north-northeast vary with depth; at Salammbo level (SS-12) throws range between 50m and 80m, whereas at Abiod level (SS-8) displacements can exceed 250m. Salt-associated pillow structures under the northeastern bounding fault provide evidence of Late Cretaceous to late Eocene halokinesis (**Fig. 7.6**). Salt migration has caused minor fault block rotation within the Middle/Upper Cretaceous to Upper Eocene sequence and also small scale inversion on some structures.

Intra-Horst Faulting

The central portion of the Hasdrubal horst block is dissected by a series of NNW-SSE trending extensional faults that cut the Upper Cretaceous to Upper Eocene succession. The most important of these is located just west of Hasdrubal -3. It displaces down to the southwest by approximately 40m.

Sequence of Faulting in the Hasdrubal Area

Due to the poorer seismic resolution (than Miskar) of the Hasdrubal dataset, only three of the fault systems identified in the Miskar area are observed. These range from the latest Cretaceous to the present-day, and include: 1) A Campanian to late Maastrichtian

Maastrichtian fault system, 2) A late Thanetian to Priabonian fault system and 3) A Langhian to present-day fault system. The discussion given in Chapter 6 regarding the nature and timing of these fault systems is appropriate for the Hasdrubal structure, and in order to avoid duplication, the reader is referred to Section 6.5.3.

One observation that has been made from the Hasdrubal dataset, which is more difficult to identify in the Miskar accumulation, is the difference in orientation of the late Thanetian-Priabonian and Langhian to present-day fault systems (**Fig. 7.7**). This shift is thought to be controlled by transtensional movements on underlying N-S to NNE-SSW trending basement faults, which have effectively caused a rotation of fault propagation paths in the cover sequence (refer to Section 6.5.4 for an explanation).

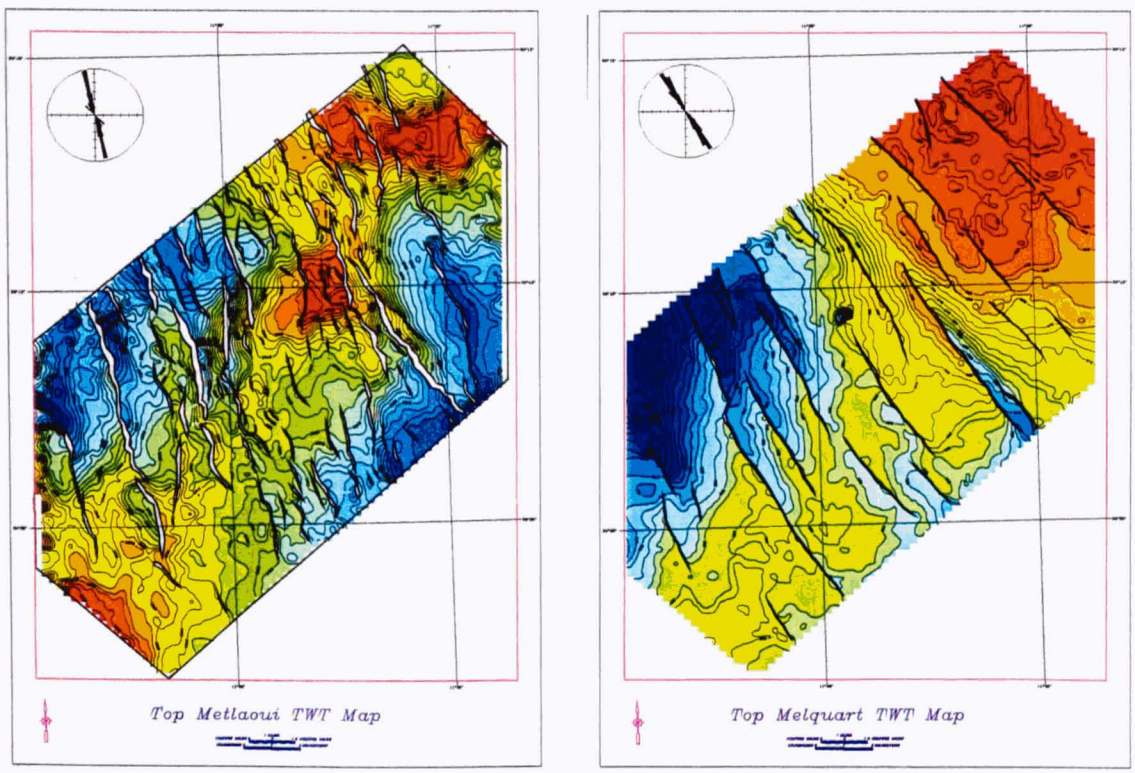

Fig. 7.7. A comparison of two-way-time (TWT) maps for a) the Top Metlaoui (Lower Eocene) and b) the Top Melquart (Miocene) intervals. Rose Diagrams of average fault orientation are given for each two-way-time map. Hot colours indicate highs and cold colours indicate lows.

7.5.4. Structural Evolution of the Hasdrubal Field

As expected, the structural evolution of the Hasdrubal accumulation is very similar to that of the Miskar Structure. The series of reconstructions shown in **Figure 7.8** summarise the development of the accumulation from the early Mesozoic to the present-day. The evolution of this structure is very similar to that of Miskar and the reader is referred to Section 6.5.4, which details the evolution of the Miskar Field.

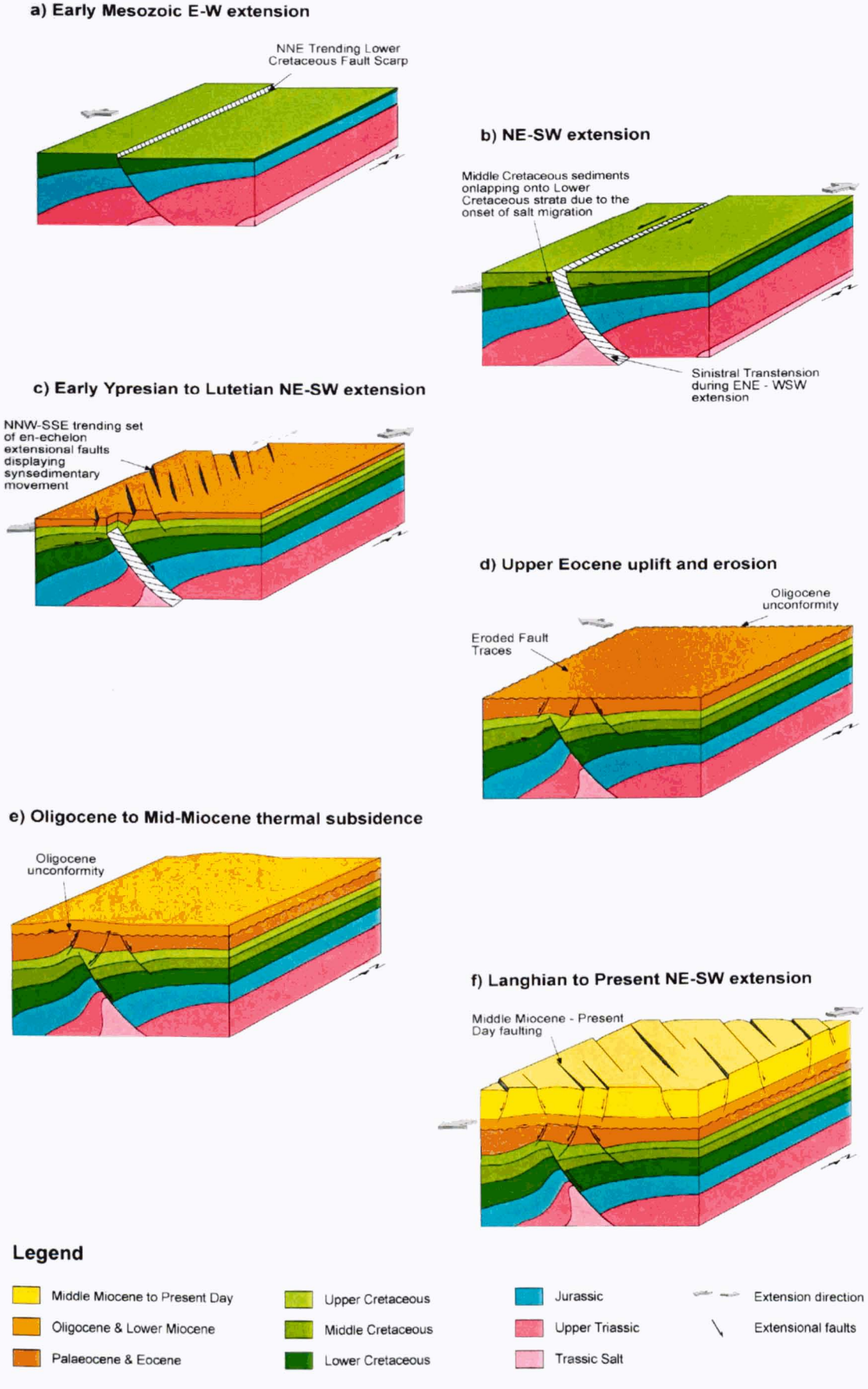

Fig. 7.8. Sequential restoration of the Hasdrubal Structure showing the main tectonic phases that have affected the area during the Mesozoic and Tertiary.

7.6. Structural Analysis of the Hasdrubal -2, -3 & -4 Cores

7.6.1. Introduction

Detailed structural analyses of the available cored intervals from a number of Hasdrubal wells were undertaken in order to ascertain the nature and distribution of fracturing in the principal reservoir zones (**Fig. 7.3**). The results, which have been integrated with the field-scale seismic study and the subsidence modelling (Section 3.7), provide an assessment of the sequence of fracturing in the accumulation. Table 7.2 lists the cored intervals in each well analysed.

Interval	Hasdrubal -2	Hasdrubal -3	Hasdrubal -4
Reineche Member (Cherahil)	✔		
Compact Micrite Member		✔	✔
El Garia Formation	✔	✔	✔
Chouabine Formation	✔	✔	✔

Table 7.2. Cored intervals in Hasdrubal wells under analysis.

All of the wells intersected the El Garia reservoir interval. The Hasdrubal -2 well also cored the Reineche (Vascus) Member of the Cherahil Formation, a secondary exploration target. The upper section of the underlying Chouabine Formation was cored in Hasdrubal -2, -3 and -4, together with the lower part of the Compact Micrite Member in Hasdrubal -3 and -4. This allowed a direct comparison of fracturing between adjacent lithostratigraphic units. Table 7.3 summarises the formation top depths of each lithostratigraphic unit of importance in each well.

Interval	Hasdrubal -2	Hasdrubal -3	Hasdrubal -4
Reineche Member (Cherahil)	2418.0		
Compact Micrite Member	2901.0	2855.0	2970.9
El Garia Formation	2915.2	2872.0	2992.0
Chouabine Formation	2968.0	2913.1	3041.5

Table 7.3. Measured depths (m MD) to lithostratigraphic unit tops in Hasdrubal wells.

In addition to core, image logs were also obtained for the Hasdrubal -2 and -3 wells. These logs (CAST and FMS for Hasdrubal -2 and -3 respectively) have been interpreted using Z & S Recall software (refer to Section 5.3.6 for a discussion). Table

7.4 shows the key intervals in which the imaging tools were run. The results of this study are given in Section 7.6.4.

Interval	Hasdrubal –2 (CAST)	Hasdrubal –3 (FMS)
Reineche Member (Cherahil)		
Compact Micrite Member	✔	✔
El Garia Formation	✔	✔
Chouabine Formation	✔	✔

Table 7.4. Intervals in which CAST and FMS imaging tools were run in Hasdrubal -2 & -3.

7.6.2. Core Quality & Study Limitations

The Hasdrubal -2 and -3 cored intervals were slabbed and resinated. When analysed, the Hasdrubal -4 core had only just been obtained through drilling, and was therefore only slabbed. Core was generally of moderate to good quality apart from occasional rubble zones.

Hasdrubal -2 and -3 cores were not oriented, thus precluding an examination of fracture and bedding orientation. Hasdrubal -4, in contrast was partly oriented. This section was only partly oriented because, due to difficulties in drilling, the orientation assembly had to be removed just prior to the main reservoir section. This meant that only the recovered core in the Compact Micrite Member and the upper parts of the El Garia Formation was oriented. Nevertheless, the orientation data obtained from this interval proved extremely useful.

The main limitations in the core analysis are associated with the lack of orientation data in all wells, and also the angle of the core axis relative to fracturing (i.e. the analysed cores trend sub-parallel to the fracture systems present). An explanation of this issue has already been provided in Chapters 5 and 6.

7.6.3. Core Observations

Summaries of the core observations for each well are provided in the following account. Many observations are similar to those presented in the core analysis of Miskar. An attempt is made to avoid repetition of previous statements. Reference should be made to Appendix B for raw data collected from all wells.

Hasdrubal –2

Hasdrubal -2 was drilled in November 1994. It is located on the western part of the main horst block (**Fig. 7.2**), approximately 2000m from the main western horst-bounding fault, and ~500-600m west of the nearest seismic-scale fault. The well is near vertical, deviated at $2^0/035^0$ over the cored intervals. All data has been corrected for the deviation in the well bore during drilling. A core shift of +2m has been applied to each core. Five cores were recovered during drilling. An account of these in given in Table 7.5. Core 1 is omitted from the analysis.

Core Number	Interval Depth (m)	Lithostratigraphic Unit
1	2422.13 – 2427.75	Reineche Member
2	2916.20 – 2925.30	El Garia Formation
3	2925.70 – 2944.30	El Garia Formation
4	2944.30 – 2972.20	El Garia Formation / Chouabine Formation
5	2972.20 – 3000.1	Chouabine Formation

Table 7.5. Cored intervals in Hasdrubal -2.

Stylolites

Structural analysis identified a total of 40 compactional aggregate stylolites within Cores 2-5 in Hasdrubal -2. As in Miskar, they develop along bed boundaries where there is a distinct variation in the bulk rock composition between two lithological units. Consequently their mean orientation generally parallels that of bedding. Stylolite geometries are almost entirely the 'sutured' type of Park & Schot (1968). This differs from Miskar, where both 'sutured' and 'simple' stylolite occur.

Figure 7.9 and Table 7.6 show the relative distribution of compactional stylolites in each lithofacies. Clearly, there is a predominance of stylolites within the El Garia Formation. Stylolite development in the El Garia Formation occurs preferentially along boundaries between coarse packstone units.

Lithostratigraphic Unit	Number of Stylolites	Stylolite Freq/metre	Average Spacing (m)
Compact Micrite Mbr.	NOT CORED	NOT CORED	NOT CORED
El Garia Formation	37	0.7	1.43
Chouabine Formation	3	0.09	11.1
Total Core	40	0.48	2.08

Table 7.6. Stylolite frequency and spacing in each lithostratigraphic interval (Hasdrubal -2).

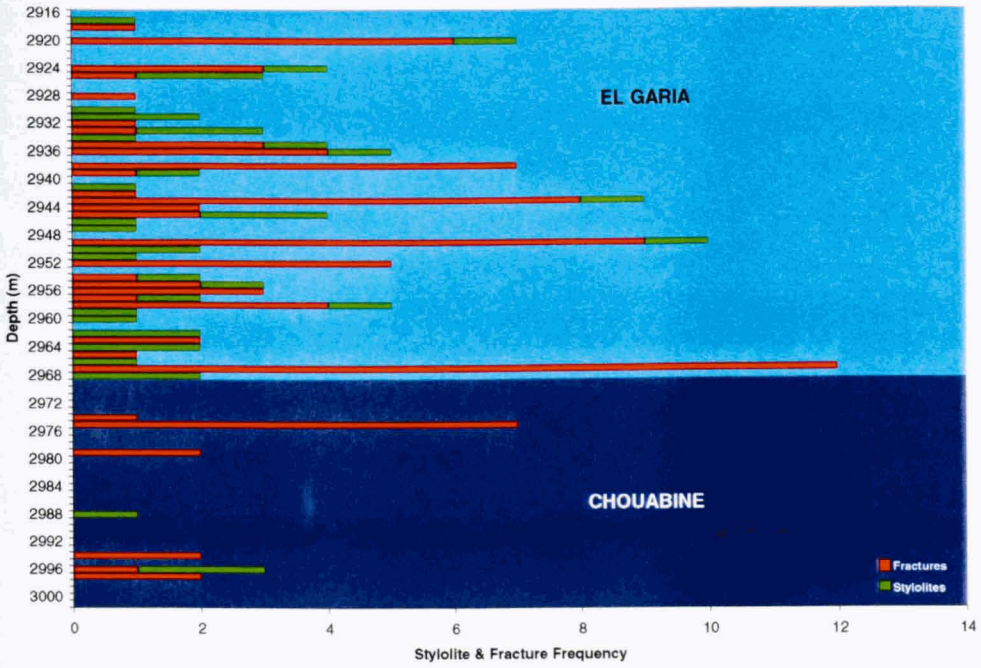

Fig. 7.9. Hasdrubal -2. Stylolite and Fracture Frequency versus depth

As already mention in Chapter 6, the distance between stylolite dentae provides an approximate indication of the amount of fluid generated (or amount of material lost) through the process of pressure solution. Measurements in Hasdrubal -2 have shown that over ~160mm of material has been removed during the formation of some stylolites. Table 7.7 shows that high amplitude stylolites are developed preferentially in the coarse packstone units within the El Garia Formation.

Lithostratigraphic Unit	Material Removed (mm)	Average Removed/Stylolite (mm)
Compact Micrite Mbr.	NOT CORED	NOT CORED
El Garia Formation	1182	33.78
Chouabine Formation	44	14.55
Total Core	1226	32.26

Table 7.7. Material removed through the process of pressure solution (mm) (Hasdrubal -2)

Fractures

A total of 97 fractures were recorded within Cores 2-5 in Hasdrubal -2. **Figure 7.10** and Table 7.8 show the fracture distribution in each lithostratigraphic unit. These data show preferential fracture development in the El Garia Formation. Most fractures are sub-vertical Mode I fractures tipping off stylolite dentae, or sub-vertical Mode I fractures forming en-echelon arrays away from the main stylolite-associated fracture (Table 7.10) (refer to Section 6.6.3 for a detailed explanation of stylolite-associated

fractures) (**Plate 7.7**). Occasional Mode II and III fractures are also present showing both normal and strike-slip displacements. A relatively large (>770mm), sub-vertical, Mode II fracture was observed at a depth of 2968.91m (MD) (**Plate 7.8**). Well-developed slickenside lineations on the fracture walls indicate a pure sinistral strike-slip displacement vector along the fracture plane. These lineations are covered by patchy euhedral calcite cements, which may indicate a late stage of calcite reprecipitation, subsequent to fault movement. Unfortunately, because the core is not oriented, a detailed kinematic study cannot not be undertaken.

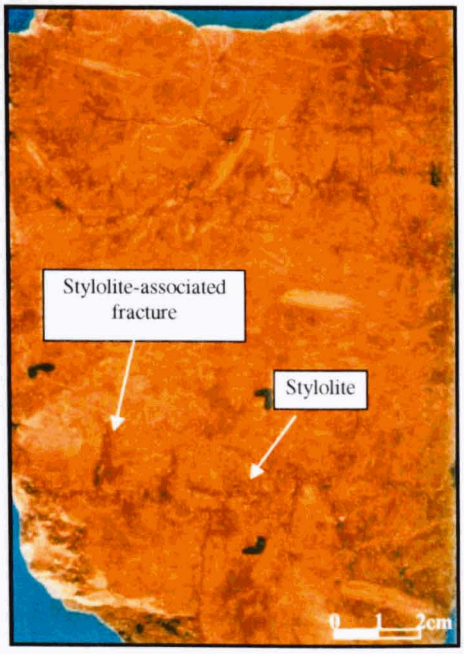

Plate 7.7. H2. Depth: 2422.8m MD. Sutured stylolite with associated Mode I fractures in the El Garia Formation

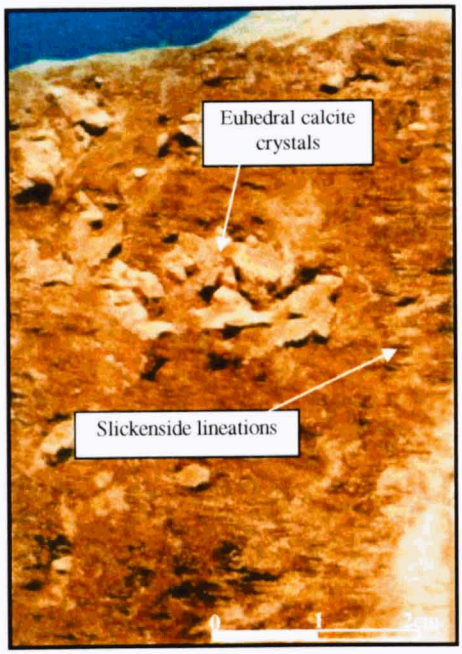

Plate 7.8. H2. Depth: 2968.91m MD. Mode II fracture with well developed slickensides showing sinistral stike-slip displacements

An assessment of fracture frequency suggests that fractures form in regularly spaced clusters (every 1-1.5m) (**Figure 7.10**). Average fracture spacing within these clusters is commonly ~20-50mm. A comparison of stylolite and fracture incidence shows that fracture clustering may be attributed to stylolite presence. Fracture intensity is shown to decrease up the cored interval throughout the El Garia Formation. This could be the result of subtle changes in the mechanical rock properties within the El Garia Formation. As in Miskar, the nature of fracturing (i.e. sub-parallel to the core axis) precludes a direct determination of fracture spacing. Consequently, the average fracture spacing (AFS) methodology of Narr (1996) has been used to obtain fracture spacing estimates. These values (which are based on average fracture apertures of 0.5mm) also show greater fracture intensity in the El Garia Formation (Table 7.8).

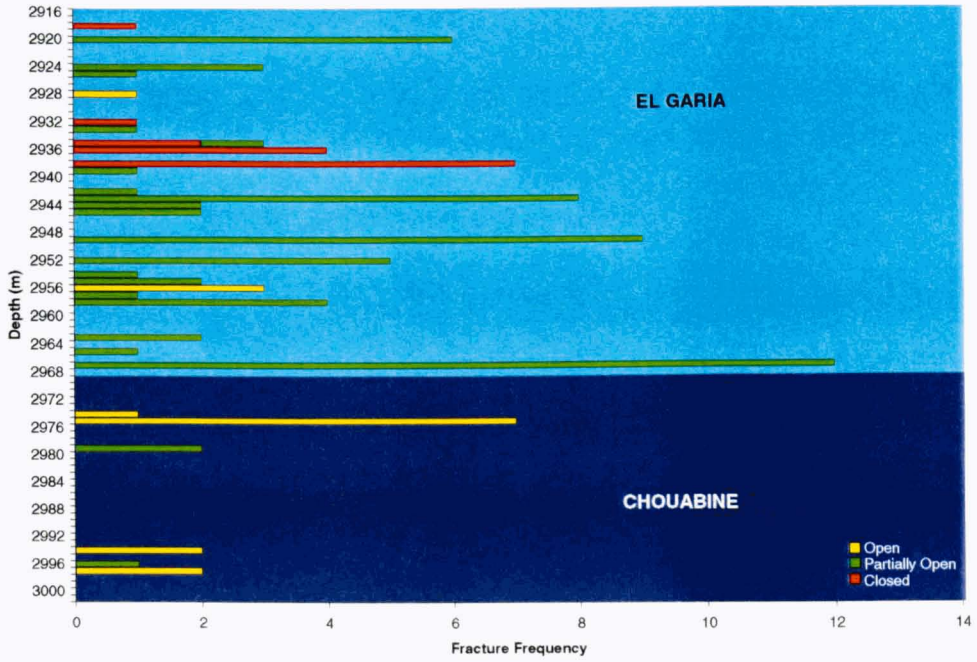

Fig. 7.10. Hasdrubal -2. Fracture frequency versus depth

Lithostratigraphic Unit	No. of Fractures	App. Frac. Freq/metre	Fracture Spacing (m)
Compact Micrite Mbr.	NOT CORED	NOT CORED	NOT CORED
El Garia Formation	82	1.54	0.51
Chouabine Formation	15	0.45	1.42
Total Core	97	1.16	0.86

Table 7.8. Apparent fracture frequency and spacing for each lithostratigraphic interval (Hasdrubal -2).

Known fracture heights from all cored intervals in Hasdrubal -2 have been analysed to determine if the fracture height distribution is power-law (i.e. self-similar). The cumulative frequency distribution given in **Figure 7.11** shows a straight-line segment indicating power-law height distributions over a scale range of 20-105mm.

An examination of the nature and extent of cementation in fractures within Hasdrubal -2 demonstrates that most closed fractures occur in the Chouabine Formation and lowermost parts of the El Garia Formation (**Fig. 7.10** and Table 7.9). In contrast, open and partially open fractures dominate the middle and upper parts of the El Garia Formation. Most closed fractures are filled with late Fe-rich calcite cements (MacCaulay et al., 2001). The large proportion of open and partially open fractures in this well is likely to enhance vertical permeability (K_V) significantly.

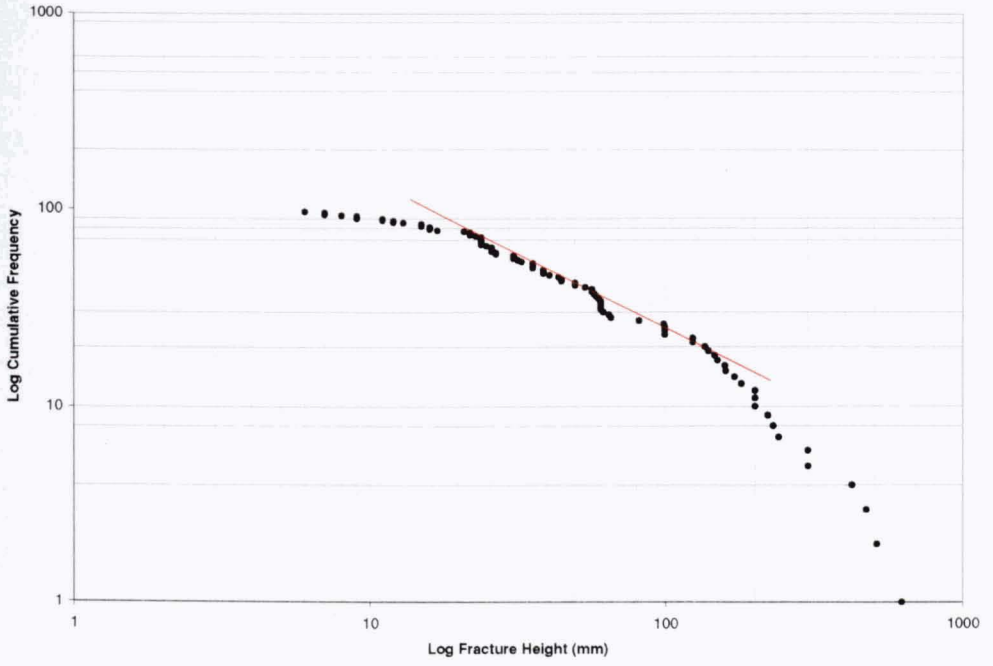

Fig. 7.11. Cumulative frequency distribution of fracture height within the cored intervals in the Hasdrubal -2 well

Lithostratigraphic Unit	Fracture Type				Fracture Fill		
	I (STA)	I	II	III	CL	PO	OP
Compact Micrite Member	NC	NC	NC	NC	NC	NC	NC
El Garia Formation	24	57	1	0	5%	77%	18%
Chouabine Formation	0	15	0	0	80%	20%	0%
Total Core	24	72	1	0	17%	68%	15%

Table 7.9. Distribution of fracture type, and nature of fracture fill/cementation in Hasdrubal -2. Closed (CL), Partially Open (PO) and Open (OP) fractures.

Hasdrubal –3

Hasdrubal -3 was drilled in April 1997. It is located on the eastern side of the main horst block, approximately 2000m west of the eastern bounding fault, within a small cluster of seismically resolvable faults (the nearest identifiable fault is ~200m to the east) (**Fig. 7.2**). The well is near vertical, deviated at $1^0/016^0$ at 2680.00m to $1.5^0/330^0$ at 3180.00m. Four non-oriented cores were obtained within the Chouabine and El Garia Formations and the Compact Micrite Member (2861.00-2944.00m) (Table 7.10). A core shift of +3m has been applied to each core.

Stylolites

A total of 43 compactional stylolites were identified within cores 1-4 in Hasdrubal -3 (**Fig. 7.12** and Table 7.11). Stylolite frequencies show a predominance of stylolites in

the El Garia Formation. No stylolites were identified in the Compact Micrite Member. **Figure 7.12** shows that stylolite spacing in the El Garia Formation in Hasdrubal -3 is quite regular.

Core Number	Interval Depth (m)	Lithostratigraphic Unit
1	2861.00 – 2862.50	Compact Micrite Member
2	2862.50 – 2890.30	Compact Micrite Member / El Garia Formation
3	2890.30 – 2916.20	El Garia Formation / Chouabine Formation
4	2916.50 – 2944.00	Chouabine Formation

Table 7.10. Cored intervals in Hasdrubal -3.

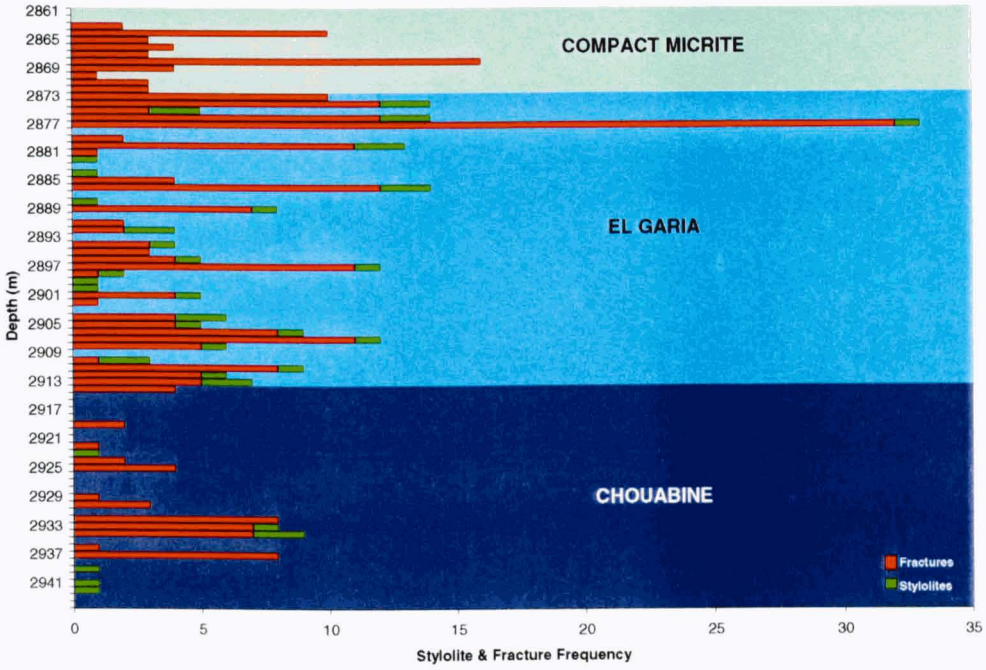

Fig. 7.12. Hasdrubal -3. Stylolite and Fracture Frequency versus depth

Lithostratigraphic Unit	Number of Stylolites	Stylolite Freq/metre	Average Spacing (m)
Compact Micrite Mbr	0	0	∞
El Garia Formation	36	0.88	1.14
Chouabine Formation	7	0.23	4.35
Total Core	43	0.52	1.92

Table 7.11. Stylolite frequency and spacing in each lithostratigraphic interval (Hasdrubal -3).

Table 7.12 shows that the average amount of material that has been removed through the process of stylolitisation within the El Garia Formation is comparable to that in Hasdrubal -2.

Lithostratigraphic Unit	Material Removed (mm)	Average Removed/Stylolite (mm)
Compact Micrite Mbr.	0	0
El Garia Formation	1382	39.48
Chouabine Formation	125	17.89
Total Core	1507	35.05

Table 7.12. Material removed through the process of pressure solution (mm) (Hasdrubal -3)

Fractures and Faults

Structural analysis identified a total of 283 fractures within Cores 1-4 in Hasdrubal -3 (**Fig. 7.13** and Table 7.13). It is apparent that fractures are preferentially developed in the El Garia Formation and the Compact Micrite Member. Many fractures in the El Garia Formation are associated with stylolites. There is a general trend to increasing fracture intensities up through the cored intervals.

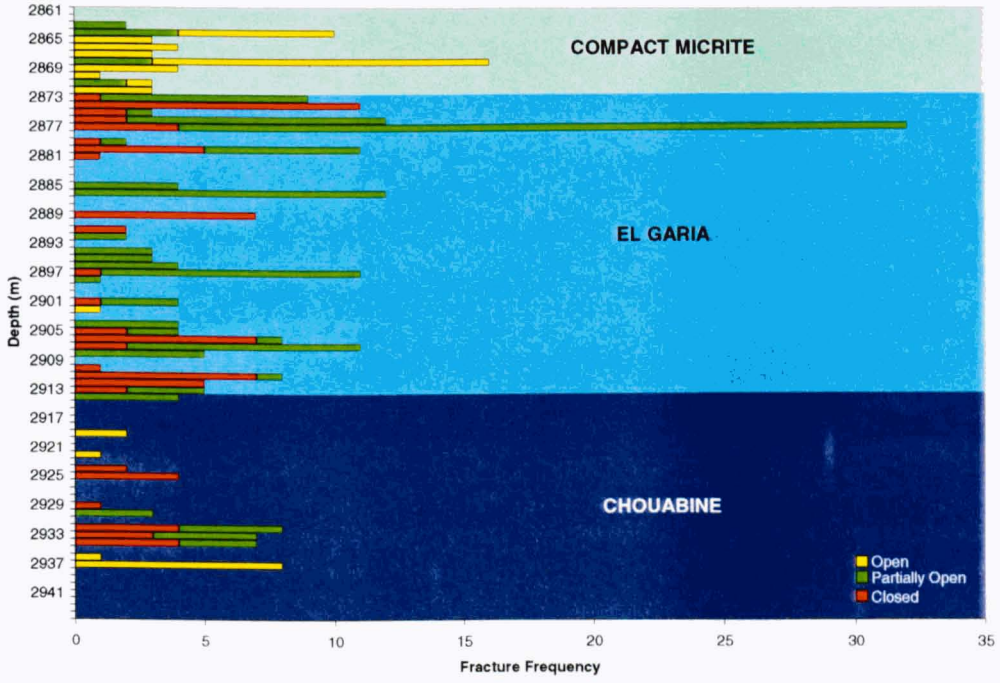

Fig. 7.13. Hasdrubal -3. Fracture frequency versus depth

Lithostratigraphic Unit	No. of Fractures	App. Frac.Freq/metre	Fracture Spacing (m)
Compact Micrite Mbr.	49	4.08	0.14
El Garia Formation	186	4.54	0.23
Chouabine Formation	48	0.65	0.64
Total Core	283	3.41	0.27

Table 7.13. Apparent fracture frequency and spacing for each lithostratigraphic interval (Hasdrubal -3).

The spacing values obtained through Narr's methodology are in close agreement with apparent fracture frequency estimates. These show values between 0.14 and 0.23m within the Compact Micrite Member and El Garia Formation respectively.

The cumulative frequency distribution of fracture height in Hasdrubal -3 is given in **Figure 7.14**. This shows a power-law distribution over a scale range of 40-500 mm.

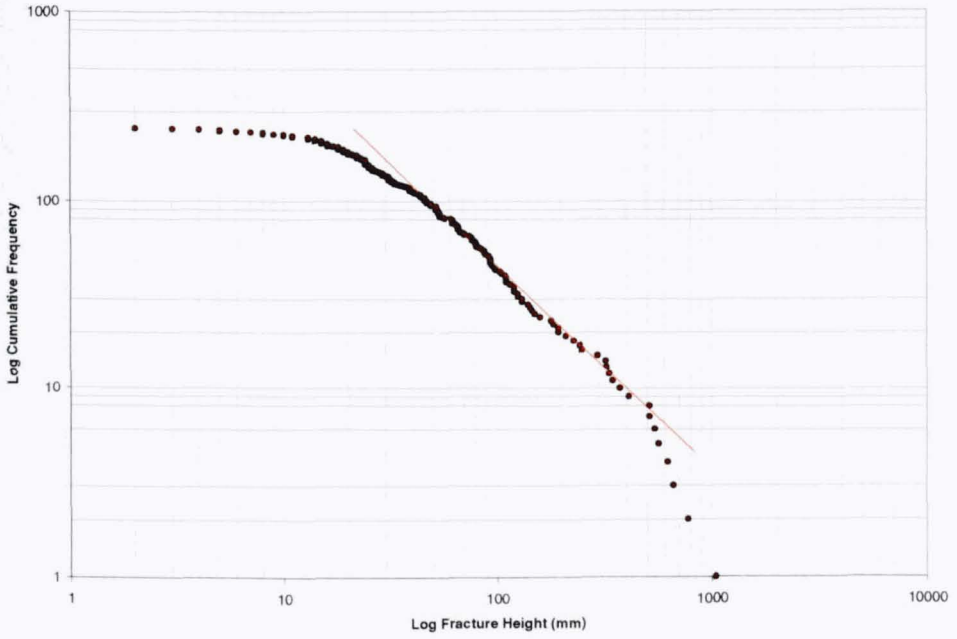

Fig. 7.14. Cumulative frequency distribution of fracture height within the cored intervals in the Hasdrubal -3 well

Most of the recognised fractures are Mode I stylolite-associated fractures that form en-echelon configurations (Table 7.15). These fractures are commonly completely filled with calcite in zones ~40-100mm long, immediately adjacent to the stylolite seam. The remaining fractures present are steeply dipping Mode II features that show minor normal displacements. There may actually be more Mode II fractures present, but they are very difficult to recognise.

An analysis of fracture cementation shows that cemented fractures are located principally within the Compact Micrite Member and the lower parts of the Chouabine Formation, whilst open fractures predominate throughout the Chouabine and El Garia Formation (**Fig. 7.13** and Table 7.15). The Compact Micrite Member contains no open fractures. A model to explain this is given in Section 7.8. Partially cemented fractures are located throughout the cored interval, in particular in the El Garia Formation.

Although accurate measurements of fracture orientation are not obtainable from the Hasdrubal -3 core analysis, it is apparent that most of the fractures measured have a similar strike. An assessment of vertical connectivity indicates that the fracture system in Hasdrubal -3 is moderately connected particularly in areas of intense en-echelon fracture development. These observations are in agreement with Hasdrubal -2.

Lithostratigraphic Unit	Fracture Type				Fracture Fill		
	I (STA)	I	II	III	CL	PO	OP
Compact Micrite Member	0	49	0	0	79%	21%	0%
El Garia Formation	45	139	2	0	1%	65%	34%
Chouabine Formation	0	48	0	0	24%	38%	38%
Total Core	45	236	2	0	18%	53%	29%

Table 7.14. Distribution of fracture type, and nature of fracture fill/cementation in Hasdrubal -3. Closed (CL), Partially Open (PO) and Open (OP) fractures.

Hasdrubal -4

Hasdrubal -4 was drilled in May 1998. It is located on southwestern side of the horst block, approximately 1500m east of the main western bounding normal fault, on a small structurally controlled high (**Fig. 7.2**). The nearest seismically resolvable faults are situated ~100m to the southwest and northeast (i.e. the faults that bound the High). It is near vertical, deviated at 1^0/~280^0 throughout the cored interval. During drilling, the well experienced significant losses to formation, and was finally abandoned within the Chouabine Formation due to a loss of circulation. It is believed that the loss of circulation corresponded to the well intersecting a highly permeable fault zone.

Core Number	Interval Depth (m)	Lithostratigraphic Unit
1	2971.00 – 2977.45	Compact Micrite Member
2	2977.45 – 3004.00	Compact Micrite Member / El Garia Formation
3	3004.00 – 3022.11	El Garia Formation
4	3022.11 – 3045.45	El Garia Formation / Chouabine Formation

Table 7.15. Cored intervals in Hasdrubal -4.

Four cores were obtained during drilling. As previously mentioned, two of these cores were oriented (i.e. Cores 1 and 2: 2971.00m-3003.90m), through the upper part of the El Garia Formation and the Compact Micrite Member. The two non-oriented cores (i.e. Cores 3 and 4: 3004.15m-3045.45m) were taken through the upper section of

Chouabine Formation and the El Garia Formations (Table 7.15). A core shift of +5m has been applied to each core.

Stylolites

A total of 65 compactional stylolites were observed within Cores 1-4 in Hasdrubal -4 (**Fig. 7.15**, and Table 7.16).

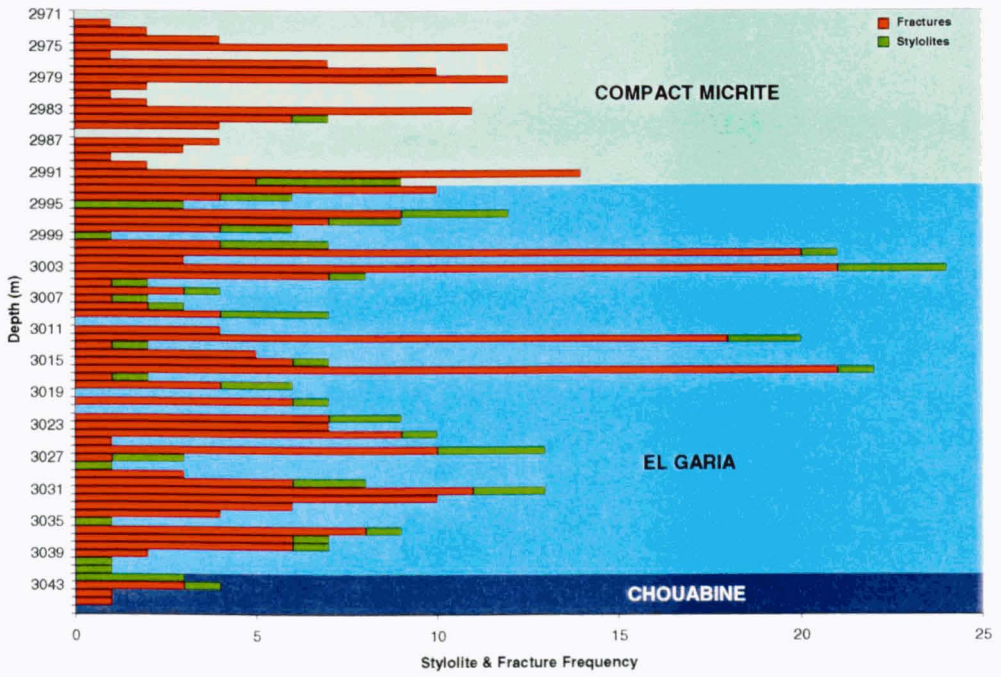

Fig. 7.15. Hasdrubal -4. Stylolite and Fracture Frequency versus depth

Lithostratigraphic Unit	Number of Stylolites	Stylolite Freq/metre	Average Spacing (m)
Compact Micrite Mbr	5	0.23	4.35
El Garia Formation	56	1.14	0.88
Chouabine Formation	4	0.80	1.25
Total Core	65	0.88	1.14

Table 7.16. Stylolite frequency and spacing in each lithostratigraphic interval (Hasdrubal -4).

Most of these are high amplitude aggregate stylolites developed at bed boundaries between packstone units within the El Garia Formation (**Plate 7.9**). Well-defined low amplitude intergranular stylolites have been identified at the boundary between the El Garia Formation and the Compact Micrite Member (**Plate 7.10**).

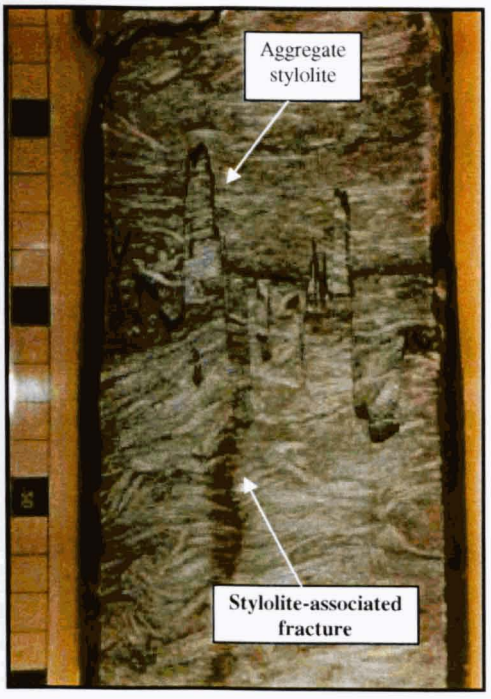

Plate 7.9. H4. Depth: 3036.45m MD. Bedding-parallel sutured stylolite in the El Garia Formation with associated Mode I fractures.

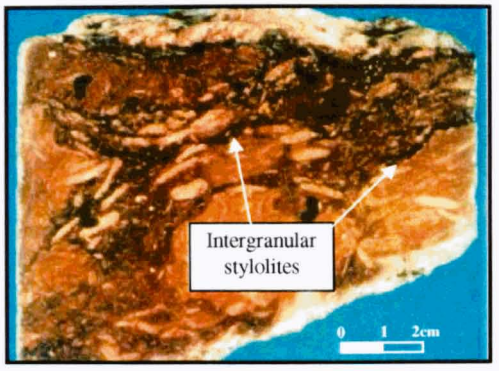

Plate 7.10. H4. Depth: 2991.80m MD. Series of intergranular stylolites at the boundary between the El Garia Formation and the Compact Micrite Member

Thin section analysis of selected samples from the Hasdrubal -4 cores has shown that within the El Garia Formation, intergranular micro-stylolites develop frequently at nummulitic grain/test contacts. **Plate 7.11** shows an example of intergranular stylolitisation between two nummulitic tests. Here, the smaller test protrudes into the larger one. This is in accordance with the theory of Park & Schot (1968), which suggests that when two grains of identical composition pit each other through pressure solution, the smaller grain always tends to protrude into the larger one.

The thin-sections given in **Plates 7.12** to **7.14** clearly show evidence of fluid migration in and adjacent to stylolite seams, in the form of; 1) Pore-fill and fracture-fill calcite cements associated with the pressure solution process (**Plate 7.12 & 7.13**), and 2) Dead oil lining stylolite walls and filling open pores (or chambers) in the nummulitic matrix (**Plate 7.14**). The latter demonstrates that open stylolites acted as conduits to fluid flow during hydrocarbon migration.

Table 7.17 provides a minimum estimate of the amount of material that has been lost through the process of pressure solution, for each of the cored intervals in Hasdrubal -4. These data are similar to those in Hasdrubal -2 and -3, in that a large amount of material has been passed into solution within the El Garia Formation. Occasionally, stylolite seams contain small amounts of dolomitic cements.

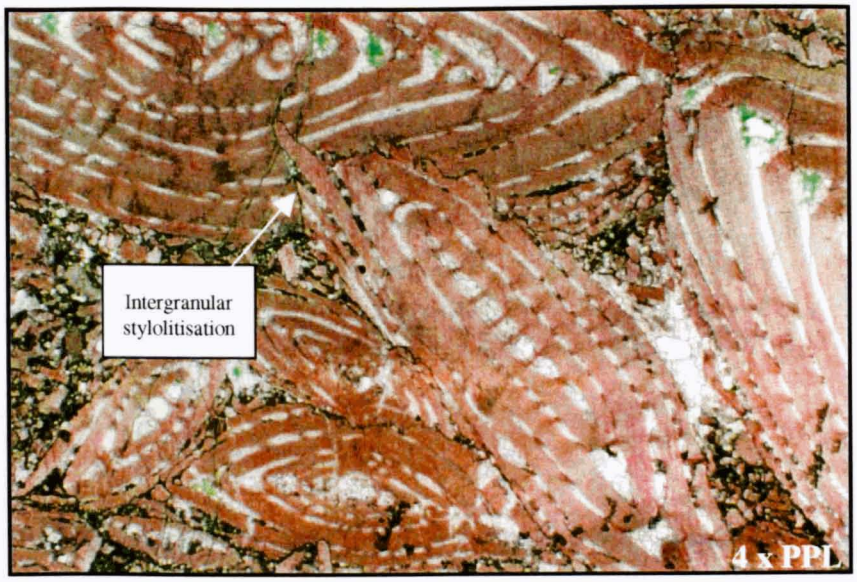

Plate 7.11. H4. Depth: 3011.00m MD. Microgranular stylolites at grain boundaries within a nummultic packstone.

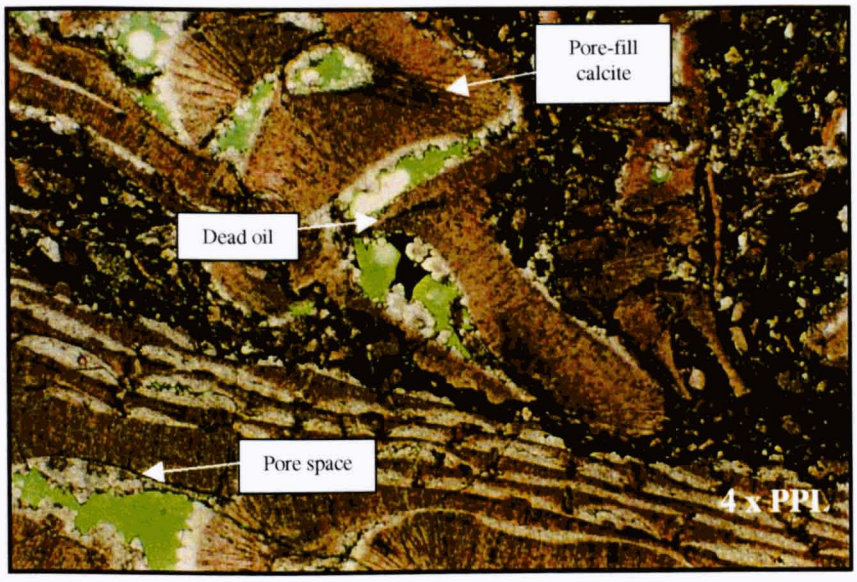

Plate 7.12. H4. Depth: 3029.00m MD. Nummulites with pore-fill calcite cements and dead oil, within a fine-grained oil stained matrix.

Lithostratigraphic Unit	Material Removed (mm)	Average Removed/Stylolite (mm)
Compact Micrite Mbr	27	5.40
El Garia Formation	1797	32.09
Chouabine Formation	30	7.50
Total Core	1854	28.52

Table 7.17. Material removed through the process of pressure solution (mm) (Hasdrubal -4)

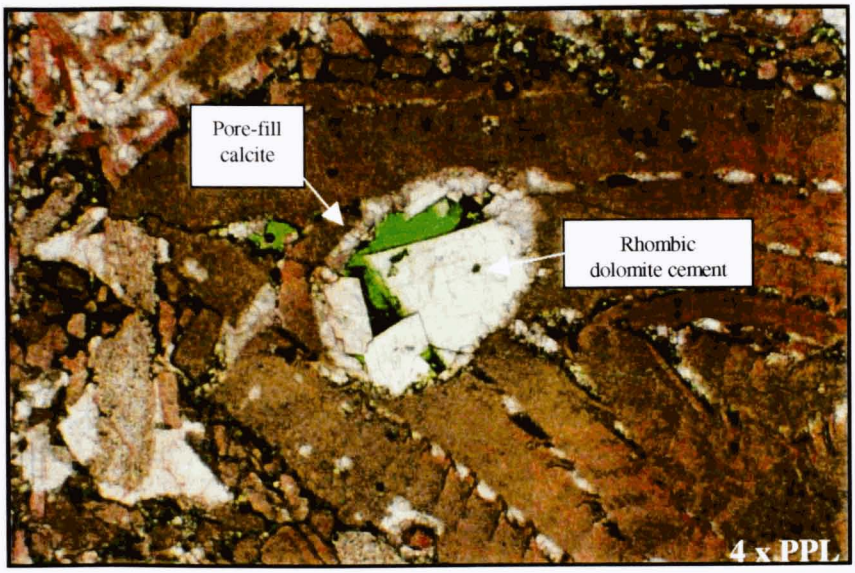

Plate 7.13. H4. Depth: 2998.75m MD. Nummulite containing void (boring?/solution?) containing calcite and rhombic dolomite cements.

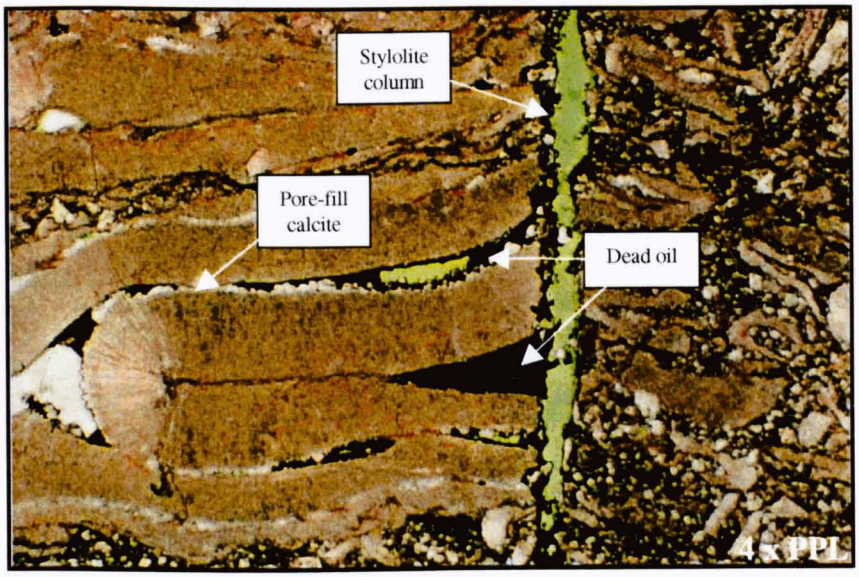

Plate 7.14. H4. Depth: 3030.00m MD. Stylolite column within a nummulitic packstone. Dead oil lines the stylolite walls and fills open chambers within the nummulites test.

Fractures and Faults

A total of 368 fractures were recorded within Cores 1-4 in Hasdrubal -4 (**Fig. 7.16** and Table 7.18). Fractures predominate in the El Garia Formation and the Compact Micrite Member. There is a general trend to increasing fracture intensities from the Chouabine up into the top of the El Garia, with a slight decrease in the Compact Micrite. Fracture spacing estimates correlate very closely with apparent fracture frequency values.

Lithostratigraphic Unit	No. of Fractures	App. Frac. Freq/metre	Fracture Spacing (m)
Compact Micrite Mbr	103	4.90	0.21
El Garia Formation	260	5.25	0.22
Chouabine Formation	5	1.26	0.75
Total Core	368	4.94	0.22

Table 7.18. Apparent fracture frequency and spacing (Hasdrubal -4).

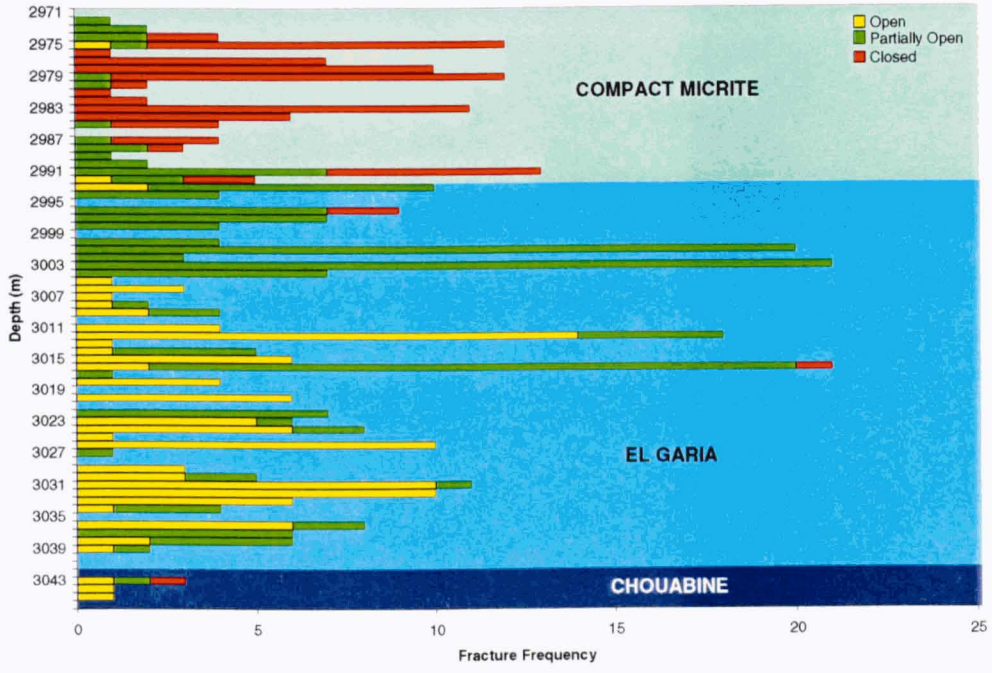

Fig. 7.16. Hasdrubal -4. Fracture frequency versus depth

Lithostratigraphic Unit	Fracture Type				Fracture Fill		
	I (STA)	I	II	III	CL	PO	OP
Compact Micrite Member	2	96	4	0	74%	24%	2%
El Garia Formation	45	197	18	0	2%	55%	43%
Chouabine Formation	0	4	0	0	20%	20%	60%
Total Core	47	297	22	0	22%	46%	32%

Table 7.19. Distribution of fracture type, and nature of fracture fill/cementation in Hasdrubal -4. Closed (CL), Partially Open (PO) and Open (OP) fractures.

The majority of the fractures observed are stylolite-associated fractures (Table 7.19 and **Plates 7.15 & 7.16**), or en-echelon sets leading off from the main stylolite-associated structures (**Plate 7.17**). **Plate 7.16** shows a good example of a partially filled stylolite-associated fracture crosscut and displaced by a moderately dipping Mode II shear fracture. Calcite cementation is visible along most stylolite-associated fractures,

particularly in the zone immediately adjacent to the stylolite seam. The cement (probably anhydrite) lining the fracture wall in **Plate 7.18** is either a diagenetic product or an artefact of the drilling process.

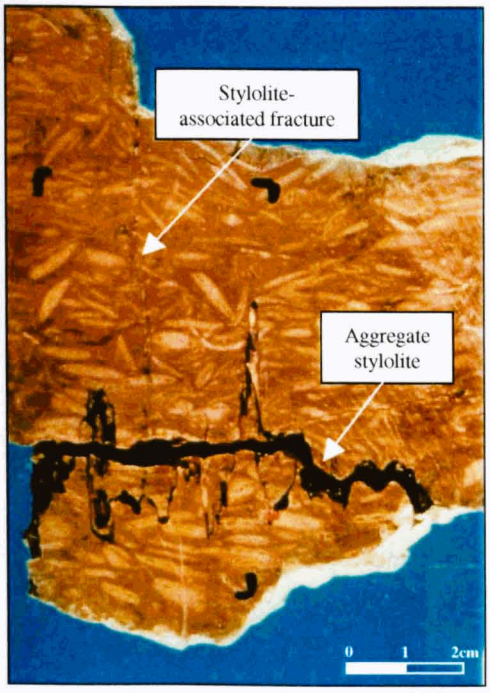

Plate 7.15. H4. Depth: 3000.70m MD. Sutured stylolite and associated Mode I fractures.

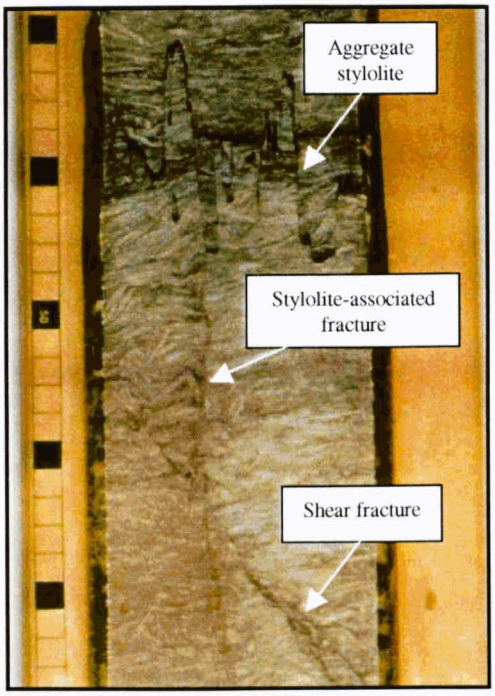

Plate 7.16. H4. Depth: 3036.35m MD. Stylolite associated fracture cross-cut and displaced by a tectonic shear fracture.



Plate 7.17. H4. Depth: 3015.50m MD. En echelon Mode I fractures.

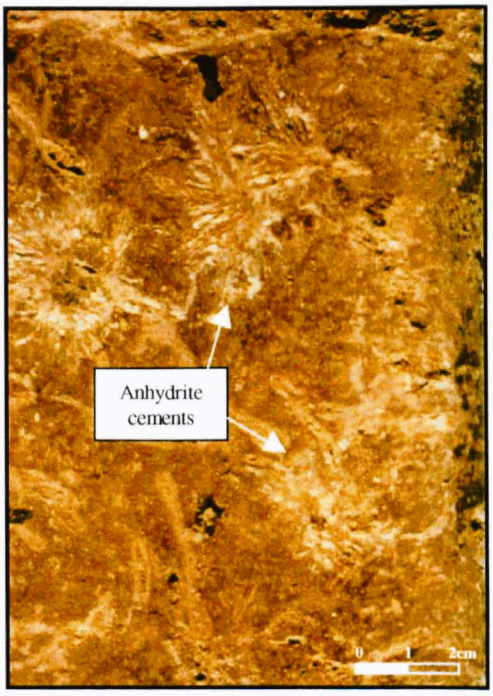

Plate 7.18. H4. Depth: 3001.46m MD. Anhydrite cements on a fracture wall.

Open fractures predominate throughout the Chouabine and lower to middle parts of the El Garia Formation (NB. There is a general decrease in open fracture intensity up through the lower and middle El Garia Formation) (**Fig. 7.16**). Open fractures are very

rare in the Compact Micrite Member. A mechanism to explain this is presented in Section 7.8. Partially open fractures are located throughout the cored interval, although. they are dominant in the El Garia Formation, increasing in frequency towards the top.

The thin-sections shown in **Plates 7.6** and **7.19-7.24** and Table 7.19 illustrate the style of fracturing and the nature of fracture fill within the Hasdrubal -4 core. Fractures in the Compact Micrite Member are usually totally filled with late Fe-rich calcite and minor dolomite cements (**Plate 7.6**). In contrast, fractures in the El Garia and Chouabine Formations are usually partially open to open features that contain fine to medium crystalline calcite and rhombic dolomite cements with associated dead oil.

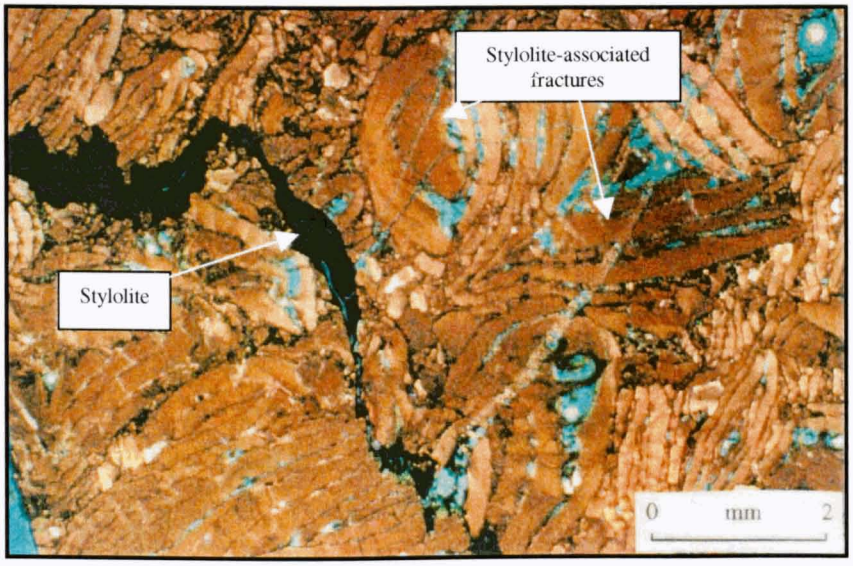

Plate 7.19. H4. Depth: 3021.60m MD. Stylolite seam and partially cemented Mode I stylolite-associated fractures (from Braithwaite, 1998).

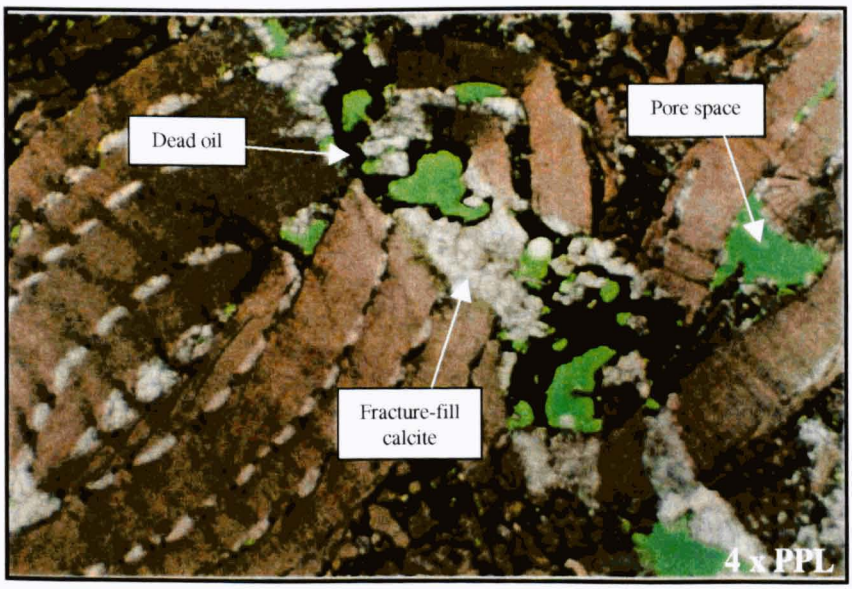

Plate 7.20. H4. Depth: 2989.50m MD. Partially cemented Mode I fracture filled with dead oil.

Plate 7.19 shows the relationship between stylolites and associated fractures in the El Garia Formation. In this example the dark insoluble residue along the seam is clearly identified. The associated fractures are partially filled with fine calcite cements, and also show minor hydrocarbon staining. **Plate 7.20** is a typical example of a partially filled Mode I fracture containing dead oil. **Plate 7.21** shows a Mode I fracture completely filled with fine to medium calcite cements.

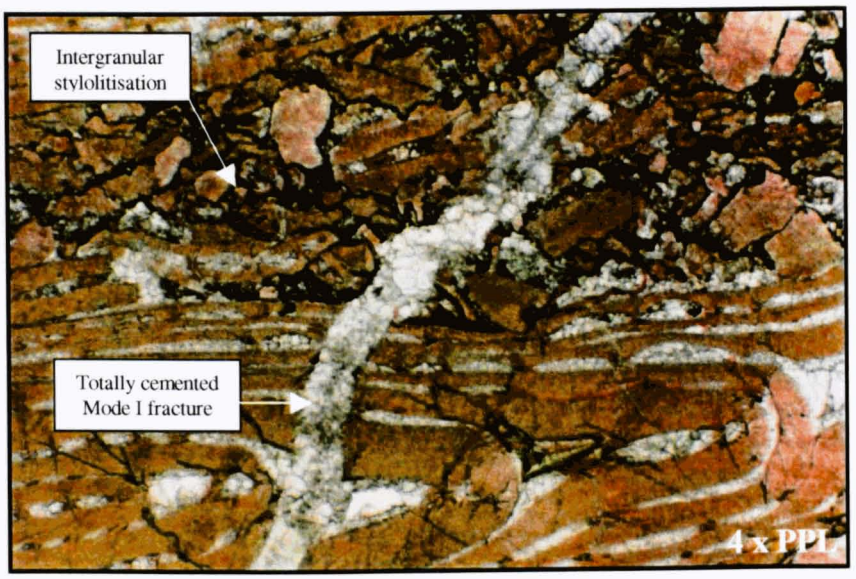

Plate 7.21. H4. Depth: 2989.25m MD. Totally cemented Mode I fracture within a heavily stylolitised nummulitic packstone.

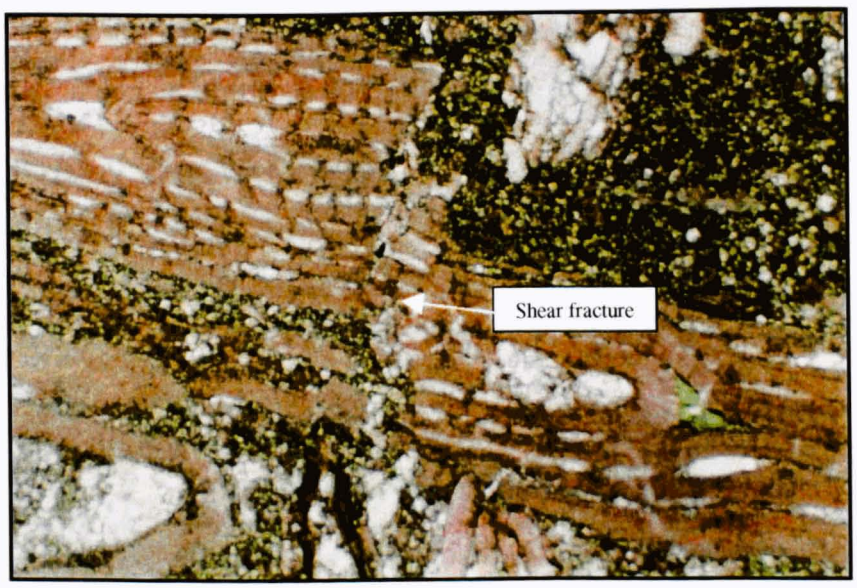

Plate 7.22. H4. Depth: 3005.00m MD. Mechanical compaction and shear fracturing of B-form nummulites within partially dolomitised and porous matrix.

Thin sections have also shown that the El Garia Formation has undergone significant mechanical compaction and fracturing throughout its burial history (**Plates 7.22-7.24**).

Nummulite tests are commonly broken up by numerous Mode I 'micro-fractures' that appear to have formed perpendicular to the overburden stress (σ_v). The process of mechanical compaction through 'micro-fracturing' is believed to have occurred during diagenesis in the early stages of burial. The presence of such fractures is important in that they provide much of the connectivity between hydrocarbon-filled pores.

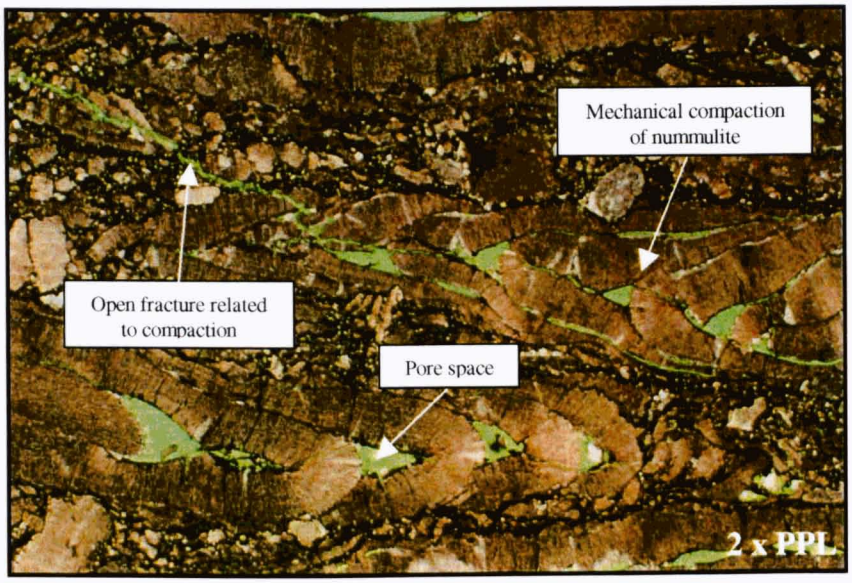

Plate 7.23. H4. Depth: 3024.00m MD. Mechanical compaction and fracturing of B-form nummulites.

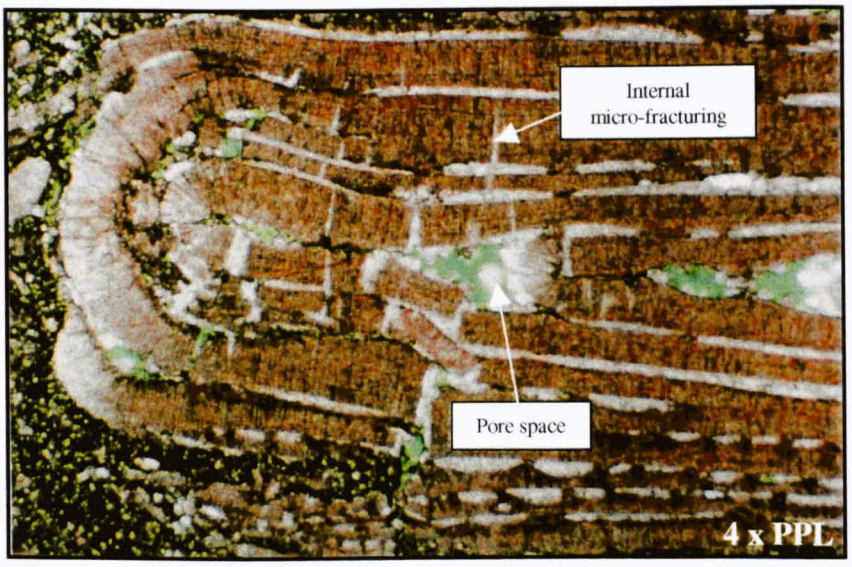

Plate 7.24. H4. Depth: 3005.00m MD. Mechanical compaction and fracturing of a B-form nummulite.

The fracture height distribution for Hasdrubal –4 is given in **Figure 7.17**. This shows a power law distribution over the scale range between 80 and 600mm.

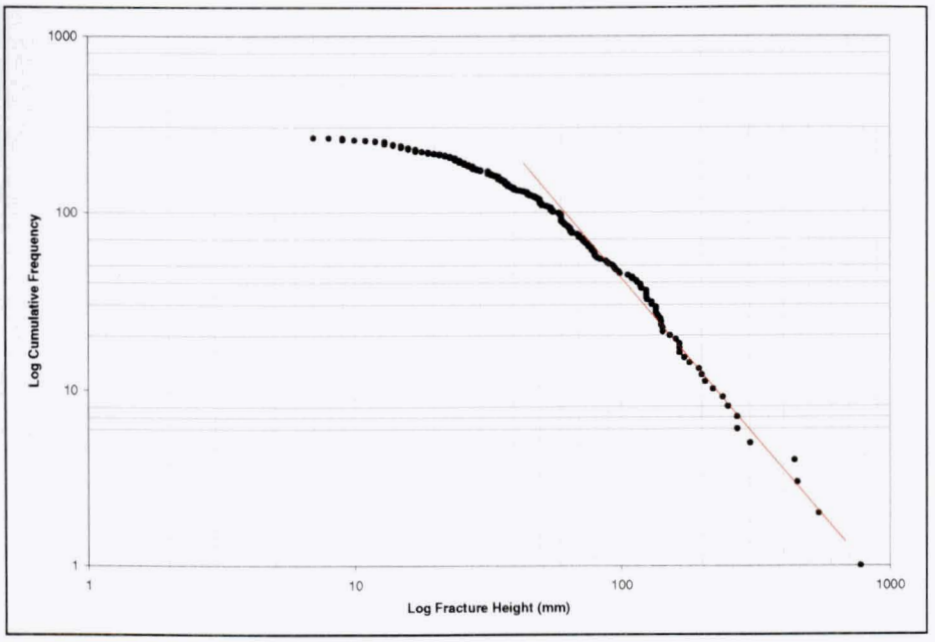

Fig. 7.17. Cumulative frequency distribution of fracture height within the cored intervals in the Hasdrubal -4 well

As previously mentioned, cores 1 and 2 were oriented. Rose diagrams of fracture trend show approximately unimodal (NNW-SSE) and bimodal (NNW-SSE and NE-SW) distributions within the El Garia Formation and the Compact Micrite Member respectively (**Fig. 7.18a-b**). The NNW-SSE trending fractures generally parallel seismic-scale faults (**Fig. 7.2**). Hence, it is inferred that they are attributed to the same stress state that caused faulting. The nature of NE-SW trending fractures is less well constrained. Various mechanisms are discussed in Section 7.8 to explain their origin.

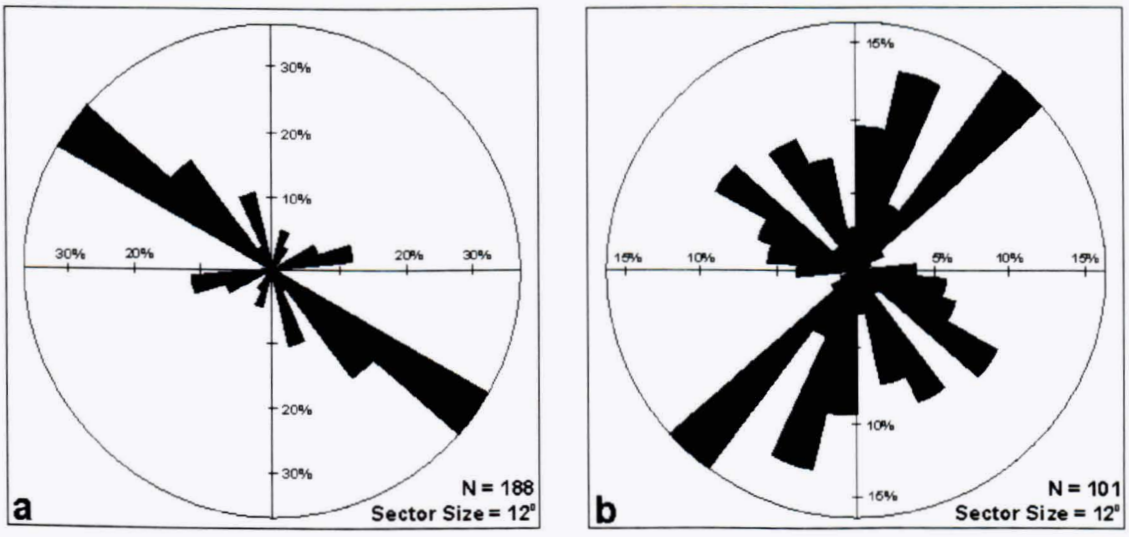

Fig. 7.18. Rose diagrams of fracture orientation within a) the El Garia Formation, and b) the Compact Micrite Member. Note the bimodal orientation distribution within the Compact Micrite Member.

Although useful, the rose diagrams given provide little information on fracture orientation with respect to depth. **Figure 7.19** shows that the upper part of the El Garia Formation comprises a series of layer-bound fracture systems of different orientation. A comparison of these data with lithological logs demonstrates that these layer-bound systems are bounded by high amplitude aggregate stylolites (which probably represent bed boundaries).

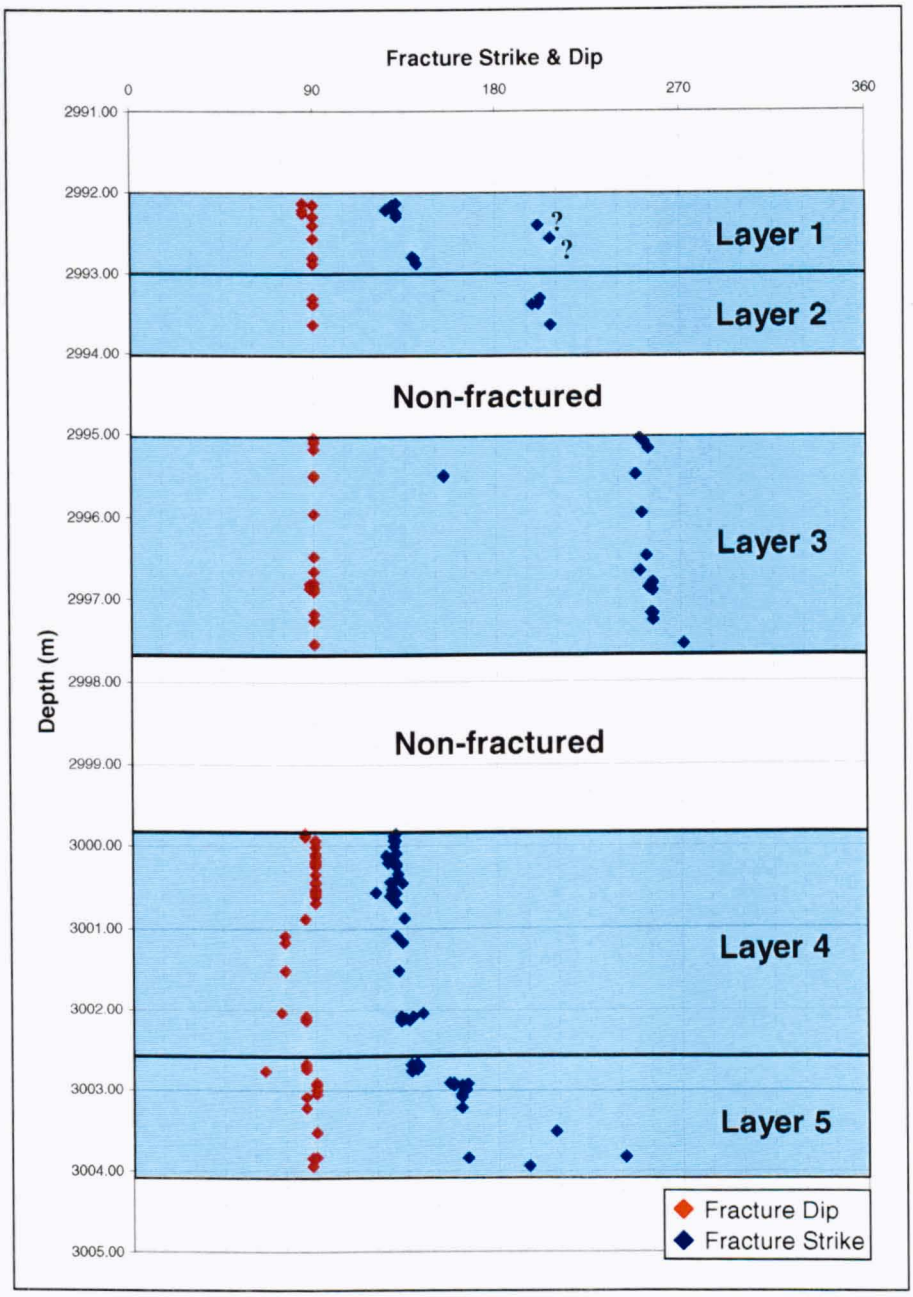

Fig. 7.19. Fracture dip and strike versus depth within the upper part of the El Garia Formation.

Through the analysis of fracture cementation (i.e. type and amount) with respect to fracture strike in this oriented part of the core, it may be argued that, by inference, it

could be possible to differentiate between fracture sets in the unoriented section (below) based on various the fracture fill-fracture strike relationships. However, analyses show that fractures of different orientations do not show distinctly different styles of cementation, and thus cannot be separated by the method proposed. It may therefore only be suggested that this style of layer bound fracturing is common to the entire core interval.

7.7. Analysis of CAST & FMS Image Logs from the Hasdrubal -2 & -3 Wells

7.7.1. Introduction

Raw image data from the Circumferential Acoustic Scanner Tool (CAST) and the Schlumberger Formation Micro-Scanner (FMS) have been processed and interpreted for the Hasdrubal -2 and Hasdrubal -3 wells respectively. This section will briefly summarise the results obtained from this study and integrates some of these results with the core analysis from the Hasdrubal -2 and -3 wells.

CAST and FMS image logs were examined over the following intervals:

- Hasdrubal - 2 (CAST) → 2873 - 3068m
- Hasdrubal - 3 (FMS) → 2680 - 3181m

Image processing and interpretation was mainly undertaken at Z&S Geoscience. Static and dynamic normalised false-colour images were created from processed CAST and FMS data and subsequently interpreted with Z&S RECALL software (refer to Chapter 5 for a discussion). Interpretation focused on structural dip determination, fault and fracture characterisation and in-situ stress evaluation.

7.7.2. Data Quality & Study Limitations

The quality of CAST and FMS images is generally controlled by lithology. FMS image data is usually of higher quality than CAST image data. This is a function of both better tool resolution, and the fact that resistivity variations in the host rock are more sensitive than acoustic amplitude variations. Image artefacts are common to both types of tool. Lofts & Bourke (1999) give a comprehensive account of the most commonly recognised artefacts associated with both image types. A summary of these has been given in Chapter 5.

An inherent problem with all imaging tools is that due to the resolution constraints calculated fracture frequency estimates are significantly smaller than respective core analyses from the same interval. Thus, image log data, although useful in determining a crude approximation of structuration in a well, cannot be used in isolation, and where possible must be integrated with core observations.

7.7.3. Image Log Interpretation

Hasdrubal -2

CAST images show that the nummulitic wackestones of the Chouabine and El Garia Formations generally display lower acoustic amplitudes than the micrites of the Compact Micrite Member and the Cherahil Formation (Styles & McKee, 1998). The nummultic wackestones-packstones have an even log response and show little washout or borehole rugosity. In contrast, the micrites have a speckled appearance, and more commonly correspond to intervals of rugose wellbore. This may reflect porosity variations between lithologies.

Structural Dip

Bed boundaries are reasonably resolved on CAST images, particularly where stylolitisation has occurred. The dip azimuth vector plot of Styles & McKee (1998) for the whole interval shows a mean structural dip of $2^0/316^0$ **(Fig. 7.20)**. This plot separates data into three structural dip-zones, which are thought to be associated with minor unconformities (Table 7.20 and **Fig. 7.20**) (Styles & McKee, 1998).

Structural zone	Interval (m)	Mean orientation	Stratigraphic interval
Zone 1	2875-2968	$2^0/308^0$	Cherahil - Compact Micrite - Upper El Garia
Zone 2	2968-3021	$8^0/223^0$	Lower El Garia - Chouabine Formations
Zone 3	3021-3070	$6^0/325^0$	Chouabine Formation

Table 7.20: Summary of structural dip zonation in Hasdrubal –2, after analysis of dip azimuth vector plot of Styles & McKee (1998)

Stylolites

Only 14 stylolites were identified with confidence over the entire interval. They were primarily located within the El Garia Formation, and show a similar orientation to bedding ($\sim 3^0/309^0$) **(Fig. 7.21)**. Observation of dentae is rare due to image resolution, and the number picked is a significant underestimate of the true stylolite frequency.

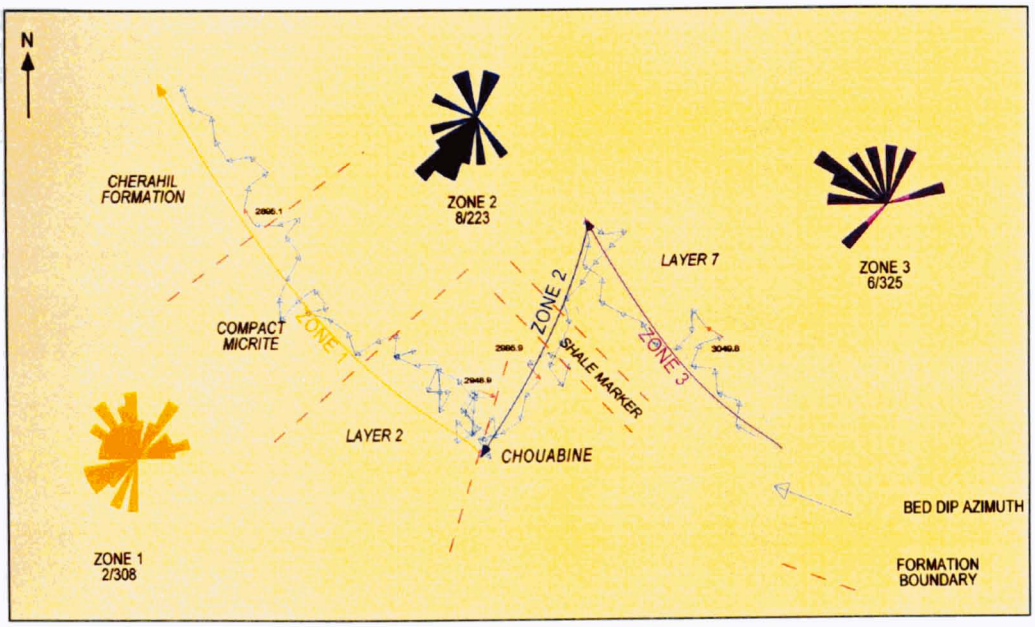

Fig. 7.20. Bedding dip azimuth vector plot for Hasdrubal -2. Dips filtered to remove low confidence picks and stylolites. Rose histograms display azimuth variation by structural dip zone (after Styles & McKee, 1998).

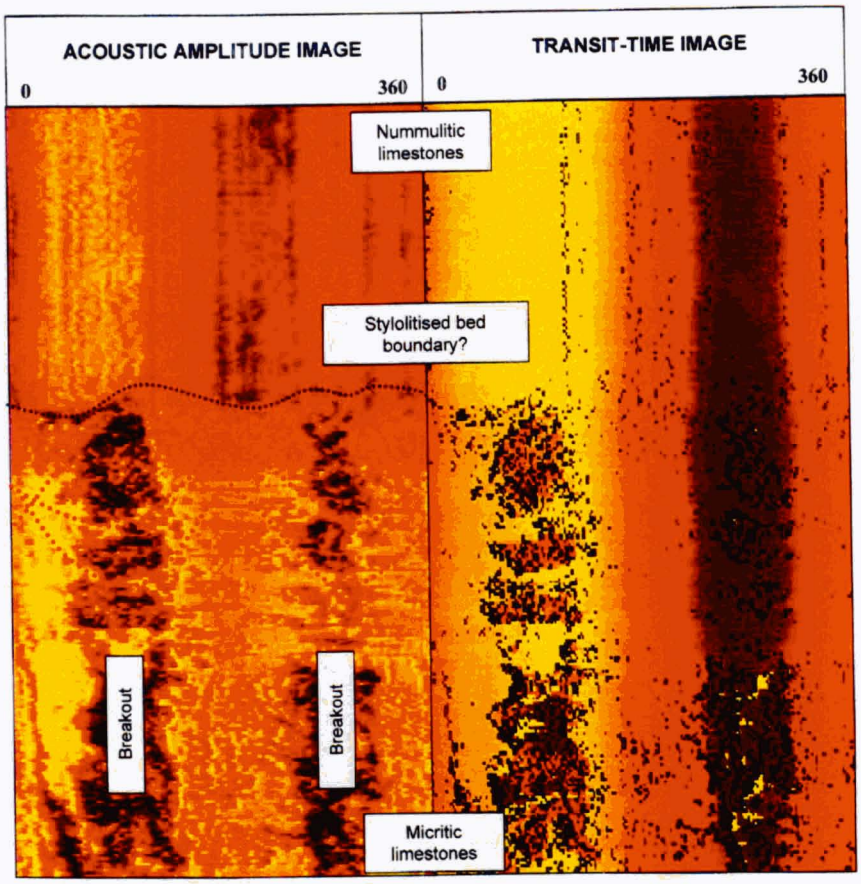

Fig. 7.21. Typical stylolitised bed boundary and associated high amplitude fractures within Hasdrubal –2. The left hand image shows acoustic amplitude response, the right hand image shows transit time. The upper part of the image shows the typical response of nummulitic limestones and the lower part shows the typical response of micritic limestones. They are separated by a stylolitised bed boundary. High amplitude fractures are visible in the micritic limestones as light coloured features which remain visible throughout the breakouts (after Styles & McKee, 1998).

Fractures

Thirteen high amplitude and six low amplitude natural fractures were recorded in the Hasdrubal -2 well (Styles & McKee, 1998) (Table 7.21). High amplitude fractures are generally imaged as indistinct, light coloured, planar features, whereas low amplitude fractures are darker features with decreased transit-time response (**Fig. 7.22**). High amplitude fractures occur in two weak clusters within the Lower El Garia and Chouabine Formations. They dip moderately to steeply, and display a preferred WNW-ESE trend. No apparent offset is observed, and they are thought to represent thin cataclastic or calcite-filled fractures.

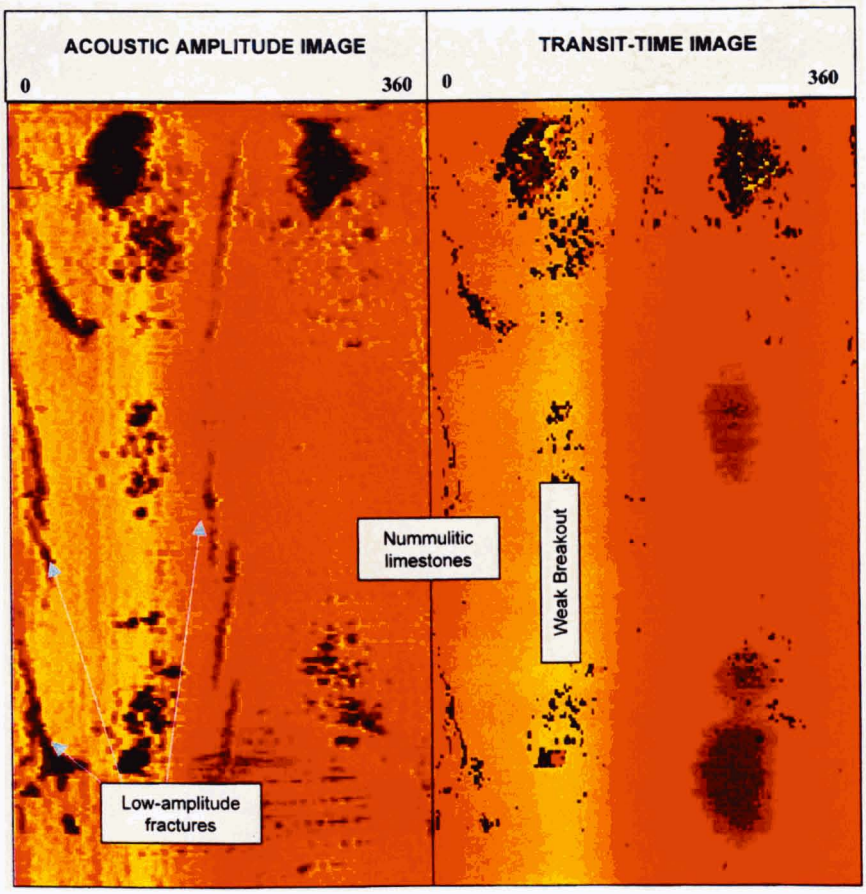

Fig. 7.22. Low amplitude fractures imaged over the interval 2998m to 3000m in Hasdrubal –2. The left hand image shows acoustic amplitude response, the right hand image shows transit time. The full interval images nummulitic limestone. Low amplitude fractures are visible as steep dark features in en-echelon sets in both amplitude and transit time (after Styles & McKee, 1998).

Low amplitude fractures occur in two zones within the basal Cherahil and Upper El Garia Formations (Table 7.21). They are generally sub-vertical/vertical and have an approximately NNW-SSE trend. They are commonly associated with stylolites, either tipping off stylolite dentae or forming en-echelon sets leading from stylolite-associated

fractures. It is important to note that due to similarities in image log characteristics caution must be applied in differentiating between low amplitude natural fractures from drilling-induced tensile fractures. In such cases core observations are vital in assessing fracture type.

Fracture Type	No. of Fractures	Density Fracture/m	Mean Orientation
High Amp. Fracture	13	0.07	$42^0/014^0$
Low Amp. Fracture	6	0.03	$88^0/065^0$

Table 7.21. Fracture statistics in Hasdrubal -2 (after Styles & McKee, 1998).

In-situ stress

CAST images are well suited to in-situ stress analysis due to their 360^0 borehole coverage and the high acoustic contrast of breakouts and induced tension fractures. Table 7.22 shows the relative orientation of in-situ stress within Hasdrubal –2.

Hasdrubal - 2: In -situ Stress Analysis	
Main breakout intervals	Compact Micrite, Lower El Garia, Chouabine
Mean breakout strike	091^0 (E-W)
Mean induced fracture strike	176^0 (N-S)
Interpreted SHmax direction	N-S

Table 7.22. Borehole breakout and induced fracture statistics for Hasdrubal - 2 (after Styles & McKee, 1998).

Hasdrubal -3

Examination of the static FMS images of Styles & McKee (1998) shows little bulk character change between lithological units. The nummulitic wackestones and packstones of the El Garia Formation show little washout or borehole rugosity when compared to the micrites of the Compact Micrite Member and Cherahil Formation.

Structural Dip

The dip azimuth vector plot of Styles & McKee (1998) for the whole interval shows a mean structural dip of $7^0/165^0$ for the whole interval in Hasdrubal -3 (**Fig. 7.23**). Unlike Hasdrubal -2, the entire study interval appears to lie within a single structural dip zone (Table 7.23). A minor dip azimuth change occurs at 2975m where an easterly trend is developed. This coincides with a zone of increased stylolitisation and thus the dip change is likely to be a dissolution effect (Styles & McKee, 1998).

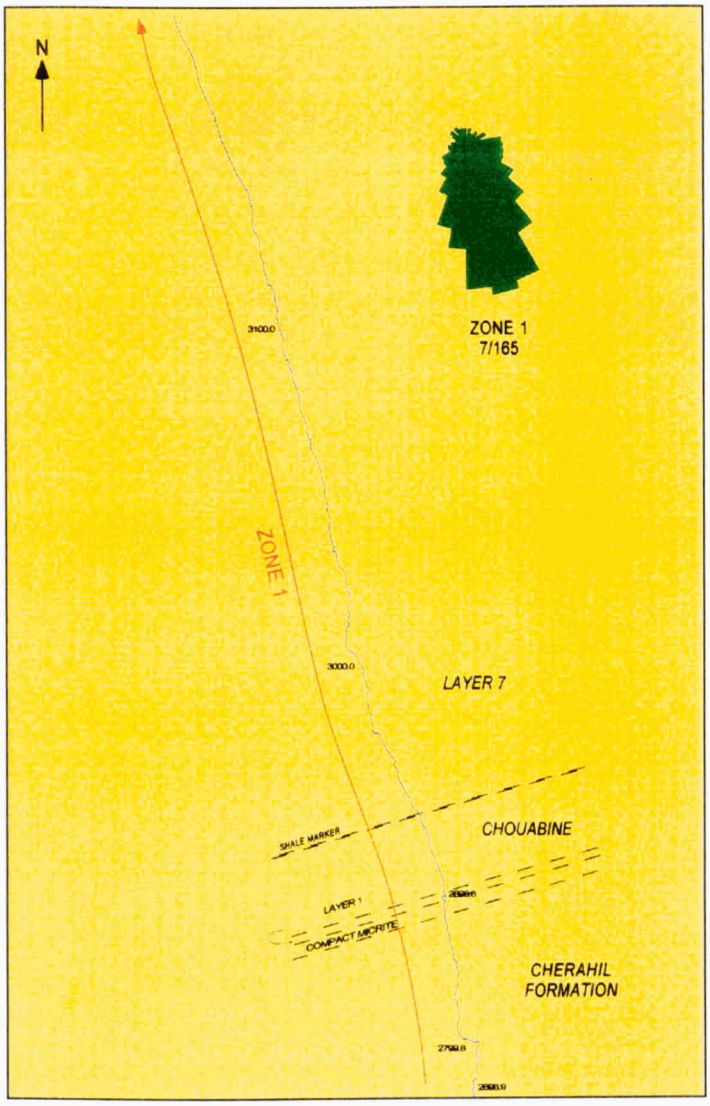

Fig. 7.23. Bedding dip azimuth vector plot for Hasdrubal -3. Dips filtered to remove low confidence picks and stylolites. Rose histograms display azimuth variation over the whole interval (after Styles & McKee, 1998).

Fractures

Fractures were frequently observed on FMS images, with 179 natural fractures observed in the well (Table 7.23).

Fracture Type	No. of Fractures	Density Fracture/m	Mean Orientation
Resistive Fracture	3	<0.01	Scattered
Conductive Fracture	23	0.05	Scattered
Sty. Assoc. Fracture	153	0.3	$85^0/249^0$

Table 7.23. Fracture statistics in Hasdrubal -3 (after Styles & McKee, 1998).

Resistive fractures are uncommon, but where present (i.e. only in the El Garia Formation) they occur as discrete Mode I fractures, highly oblique to bedding (**Fig.**

7.24). Conductive fractures are seen throughout the interval as dark, bedding discordant features that typically dip between 55^0-70^0 and strike N-S, NNW-SSE or NE-SW (**Fig. 7.25**). Differentiation of conductive fractures from stylolite-associated fractures and induced fractures is problematic due to similarities in appearance. Stylolite-associated fractures (STA) are imaged as discontinuous, planar sub-vertical fractures that are constrained by stylolitised bed boundaries (**Fig. 7.26**). They show a strong NNW-SSE trend. It is thought that this fracture type is strongly undersampled using this analysis technique.

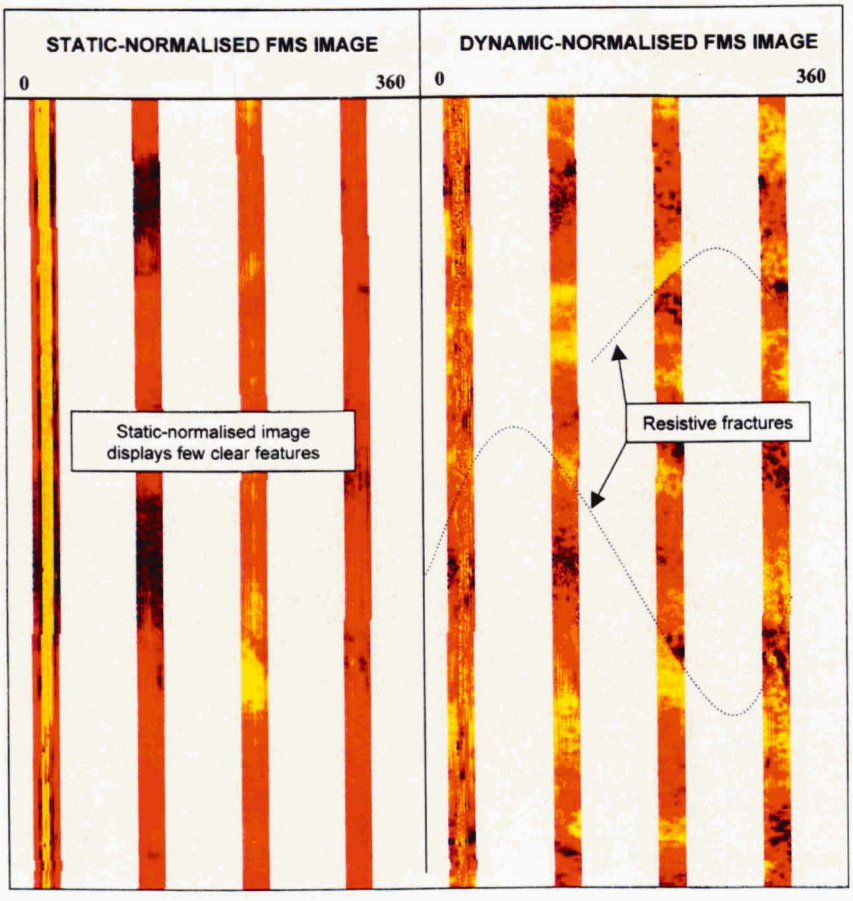

Fig. 7.24. Resistive fractures (indicated) imaged by FMS in Hasdrubal –3. The left hand image shows static-normalised response, the right-hand image shows dynamic-normalised response. Resistive fractures are visible as pale features, oblique to the main bedding trend (sub-horizontal). Images are poorly focused due to poor pad contact and/or gas effect. The left hand data pad is reduced by mud smear (after Styles & McKee, 1998).

In-situ stress

Low borehole area coverage of the FMS tool within Hasdrubal -3, makes borehole breakouts difficult to orient from images. However, induced fracture orientations and ovalisation of the core allow determination of the in-situ stress field (Table 7.24).

Hasdrubal - 3: In -situ Stress Analysis	
Number of breakout segments	None imaged
Number of induced fractures	39
Mean induced fracture strike	169^0 (NNW-SSE)
Interpreted SHmax direction	~N-S

Table 7.24. Induced fracture statistics for Hasdrubal -3.

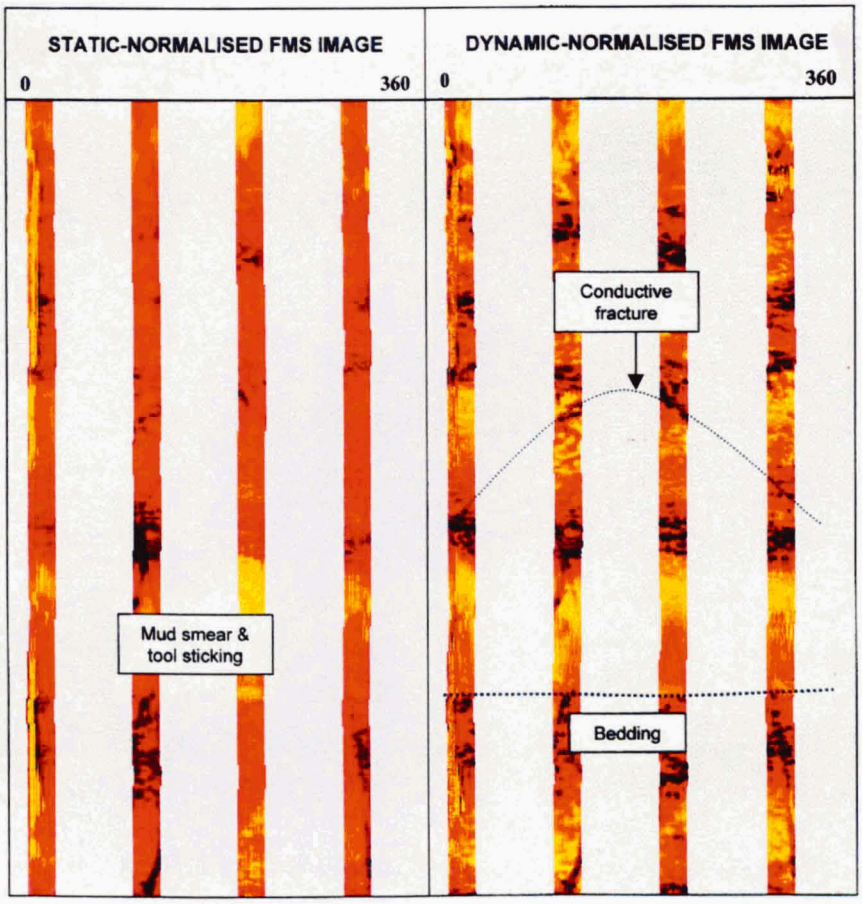

Fig. 7.25. Conductive fractures (indicated) imaged by FMS in Hasdrubal –3. The left hand image shows static-normalised response, the right-hand image shows dynamic-normalised response. Conductive fractures are visible as dark features, oblique to the main bedding trend (sub-horizontal). Images are poorly focused due to poor pad contact and/or gas effect. The left hand data pad is reduced by mud smear (after Styles & McKee, 1998).

7.7.4. Comparison of Core & Image Log Observations

Although image logs provide a reasonable method of gaining a crude approximation of subsurface structuration (particularly when there is no core available), they do significantly undersample structural features, causing large biases in spacing and frequency calculations. A comparison of data (over the same sample length) from the core and image log analyses of the Hasdrubal -2 and -3 wells demonstrates the effect of

image log resolution on sampling (Tables 7.25 to 7.26 and Fig. 7.27). This is particularly apparent in Hasdrubal -2, which is of lower resolution than Hasdrubal -3.

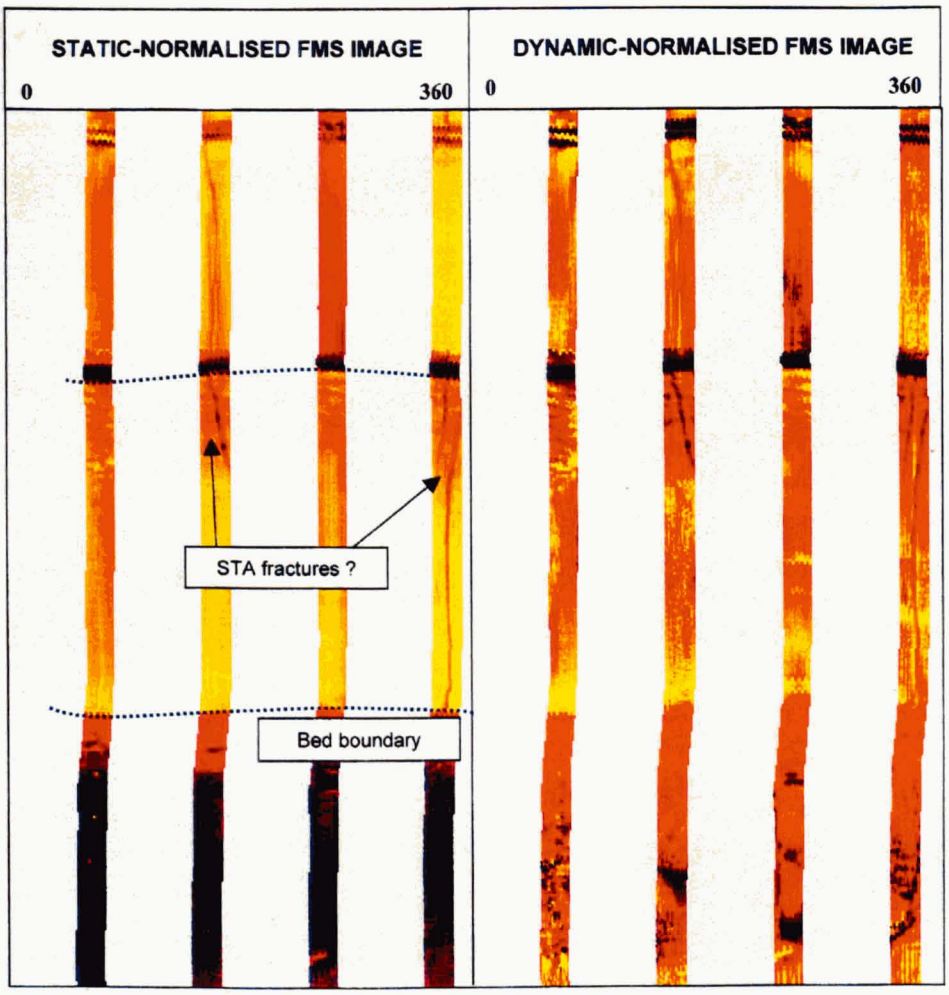

Fig. 7.26. Stylolite-associated fractures imaged by FMS in Hasdrubal –3. The left hand image shows static-normalised response, the right-hand image shows dynamic-normalised response. Stylolite associated fractures are visible as dark features, oblique to the main bedding/stylolite trend. The fractures terminate/nucleate at bed boundaries which show irregularity in form that may suggest stylolitisation. They continue over several decimetres. It is essential that interpretations from image logs are cross-referenced against actual core observations to alleviate sampling biases caused by induced fracturing (after Styles & McKee, 1998).

Lithostratigraphic Unit	Hasdrubal -2		Hasdrubal -3	
	Image Data	Core Data	Image Data	Core Data
Compact Micrite Member	-	-	1 (0.09)	0 (0.00)
El Garia Formation	10 (0.19)	37 (0.7)	8 (0.20)	36 (0.88)
Chouabine Formation	3 (0.09)	3 (0.09)	5 (0.16)	7 (0.23)
Total Sample Length	13 (0.15)	40 (0.40)	14 (0.17)	43 (0.52)

Table 7.25. Comparison of measured stylolite frequencies from image and core data. Values in brackets represent calculated stylolite frequencies.

Lithostratigraphic Unit	Hasdrubal -2		Hasdrubal -3	
	Image Data	Core Data	Image Data	Core Data
Compact Micrite Member	-	-	5 (0.45)	49 (4.08)
El Garia Formation	2 (0.04)	82 (1.54)	20 (0.49)	186 (4.54)
Chouabine Formation	4 (0.12)	15 (0.45)	23 (0.74)	48 (0.65)
Total Sample Length	6 (0.07)	97 (1.00)	48 (0.57)	283 (3.41)

Table 7.26. Comparison of measured fracture frequencies from image and core data. Values in brackets represent calculated fracture frequencies.

Another inherent problem associated with image logs is that in general they provide no quantitative information on fracture aperture and degree and type of cementation, thus precluding an analysis of fracture porosity. Furthermore, particular attention must be placed on the differentiation of induced and natural fractures on processed images. Commonly during image log interpretation, induced fractures are interpreted as natural features, thus introducing sampling biases into calculations.

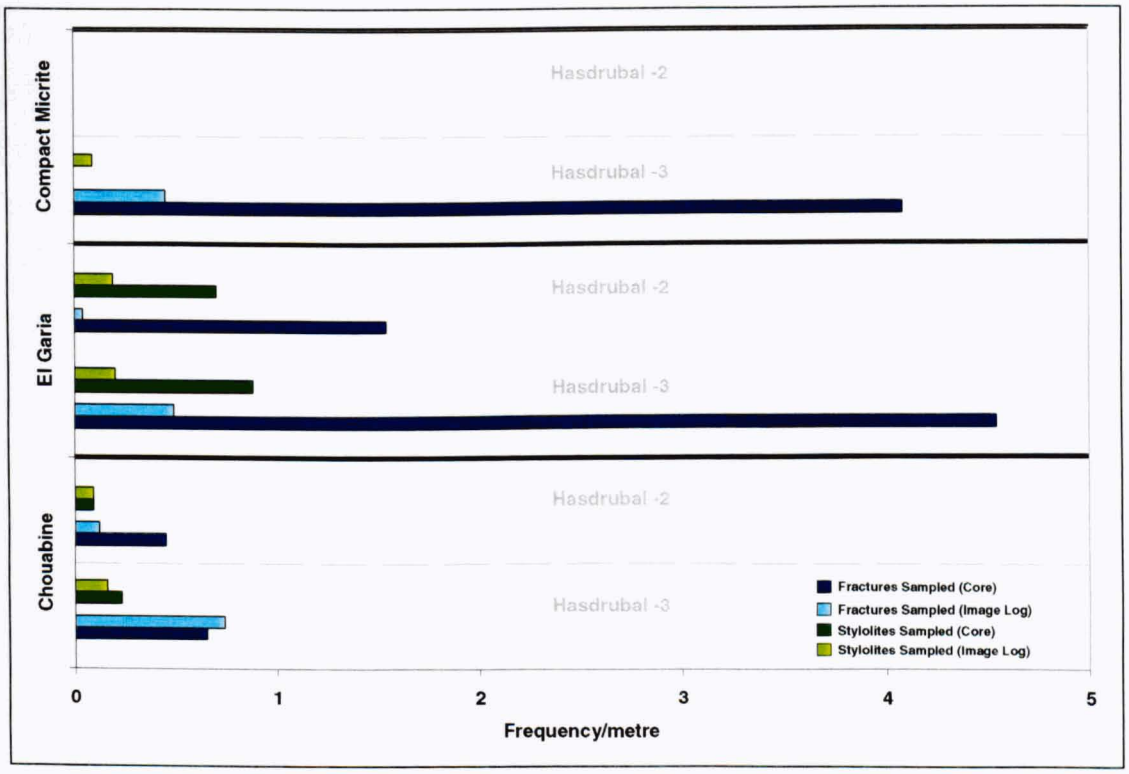

Fig. 7.27. Comparison of stylolite and fracture frequencies from the image and core log analyses showing under-sampling due to the resolution constraints in the imaging tools.

An advantage of imaging tools is that because they are oriented, it is possible to gain an insight into the orientation of imaged structures, and additionally in-situ stress within wells where no core has been cut, or where oriented core is unavailable. This has proved useful in the Hasdrubal -2 and –3 wells, where core is not oriented. Fracture orientation data gained from the image log analyses corresponds closely to the data obtained from the analysis of cores 1 and 2 in Hasdrubal -4 (i.e. both analyses show a strong NNW-SSE fracture trend throughout the sample interval, and a weaker NE-SW trend in the Compact Micrite Member) (**Fig. 7.28**). Thus, in summary, although image log analyses allow a reasonable determination of subsurface structuration, whenever possible they must be integrated with core studies.

7.8. Discussion of Core & Image Log Observations

Because Hasdrubal and Miskar are relatively close together in the same tectonic domain, the structural style within the Hasdrubal wells is very similar to that recognised in Miskar. The following account summarises the most important features identified through the core and image log analyses in Hasdrubal, and also presents a model illustrating the proposed sequence of fracturing in the El Garia Formation. As in Miskar, caution is applied to spacing and frequency calculations, particularly in cored intervals of small sample length. However, it is stressed that the values given in this analysis are based on a larger and higher quality database, and thus are probably a better representation of subsurface structuration.

The results from the core and image log analyses were finally input into a stochastic fracture generation package (FracMan), in an attempt to model the geometry and distribution of fracture systems within the Hasdrubal reservoir. The procedures involved in generating this model, and the final simulation are presented in Appendix C.

7.8.1. Stylolites

All the stylolites present in the Hasdrubal cores are compactional features, which have formed in response to the overburden stress (σ_v). They tend to have been developed along bed boundaries where there is a distinct variation in the bulk rock properties between two lithological units. Image log analyses support this, indicating that stylolite orientation equates to structural dip (i.e. bedding).

Two particular types of stylolites dominate the cored intervals:

- High amplitude, 'sutured' stylolites, which are well developed in the wackestone to packstone lithofacies of the El Garia Formation.
- Low amplitude 'non-sutured' stylolites, which are present in the Compact Micrite Member and Chouabine Formation.

The difference in stylolite geometries between contrasting lithofacies is believed to be related to the relative percentage of clay and 'structurally resistive' material present within the bulk rock volume (Wanless et al., 1979). This relationship is applicable in the Hasdrubal case study. Here, the El Garia Formation, which contains many resistive elements (in the form of nummulitic tests), and only minor amounts of clay material contains many high amplitude 'sutured' stylolites. In contrast, the Compact Micrite Member and the Chouabine Formation, which both contain much more clay material, and do not have as many resistive elements are dominated by low amplitude 'non-sutured' stylolites.

The 'sutured' stylolites observed in the Hasdrubal cores contain variable amounts of fine-grained, dark seam material, which is generally thicker at the apex of stylolite crests and in valleys. Seam material commonly consists of micro-granular clay residues, accompanied by small amounts of quartz, calcite, dolomite and occasional pyrite. Oil and late meteoric dolomitic cements (Macaulay et al., 2001) are also present along some stylolites.

	Stylolite Frequency (Stylolites/m)			Average Amount Rem^d/Stylolite (mm)		
Lithostratigraphic Unit	Has -2	Has -3	Has -4	Has -2	Has -3	Has -4
Compact Micrite Mbr	-	0 (∞)	0.23 (4.35)	-	0 (0.%)	5.4 (0.1%)
El Garia Formation	0.7 (1.43)	0.88 (1.14)	1.14 (0.88)	33.8 (2.3%)	39.5 (3.4%)	32.1 (3.6%)
Chouabine Formation	0.09 (11.1)	0.23 (4.35)	0.80 (1.25)	14.6 (0.1%)	17.9 (0.4%)	7.5 (0.8%)
Total Core	0.40 (2.5)	0.52 (1.92)	0.88 (1.14)	32.3 (1.4%)	35.1 (2.1%)	28.5 (2.5%)

Table 7.27. Comparison of average stylolite frequencies, and the average amount of material removed within each lithostratigraphic interval for each well.

As mentioned previously, stylolite amplitude (i.e. the distance between dentae) gives an indication of the minimum amount of material removed by the pressure solution process (Table 7.27). Stylolite amplitudes are consistently higher in the wackestone to packstone fabrics of the El Garia Formation. Calculations of the amount of

compactional strain for each lithostratigraphic unit, through the process of stylolitisation also show that higher amounts of compactional strain are associated with the El Garia Formation (Table 7.27).

Average stylolite frequencies are fairly consistent in all the wells analysed, although there is a tendency towards higher frequencies in all units in Hasdrubal -4 (Table 7.27). Stylolite frequencies in all wells increase within the El Garia Formation, in comparison to both the Chouabine Formation and the Compact Micrite Member. This suggests that the grainstone/packstone fabrics of the El Garia Formation particularly favour sutured stylolite development.

7.8.2. Fractures

Two particular scales of fractures are observed in the Hasdrubal cores:

- Micro-fractures, which affect individual nummulite tests (visible in thin sections);
- Macro-fractures, which dissect the core width (visible to the naked eye).

Micro-fractures tend to break up nummulitic tests. They are commonly sub-vertical to vertical Mode I fractures that have formed perpendicular to the overburden stress (σ_v) The process of internal micro-fracturing is believed to occur through mechanical compaction during the early stages of diagenesis. This phase of initial compaction is accompanied by dewatering, and the elimination of unsupported pore space.

Fracture Type

Macro-fractures can be classified into two broad groups:

- Sub-vertical Mode I extensional fractures, associated principally with stylolites;
- Moderately dipping Mode II & III fractures, associated with seismic scale faults.

Mode I extensional fractures can be classified into two sub-sets; 1) Stylolite-associated (STA) fractures and, 2) En-echelon Mode I fractures sets that are intimately associated with the STA fractures. These fractures develop contemporaneously with stylolitisation. They are generally filled with a zone of calcite cementation in the region immediately adjacent to the stylolite seam (usually <300mm in length), which represents the first phase of calcite reprecipitation from the initial stages of pressure solution. The en-echelon sets of Mode I fractures that lead off from STA-fractures are believed to have

formed in response to stylolitisation and/or later phases of extension (N.B. the length of some of these fractures could have been enlarged by the coring process). Core and image log analyses show unimodal (NNW-SSE) and bimodal (NNW-SSE and NE-SW) orientation distributions in the El Garia Formation and Compact Micrite Member, respectively for these fracture systems. An analysis of fracture orientation with respect to depth for cores 1 and 2 within Hasdrubal -4 demonstrates that the upper part of the El Garia Formation is composed of a series of layer-bound fracture systems of different orientation (refer to Section 7.6.3 and Appendix D). Most of these fractures are partially filled with calcite cements. Occasionally fractures show strike-slip and dip-slip components of displacement.

Moderately dipping Mode II and III fractures are present, but to a lesser extent. They are generally totally to partially filled with calcite and late meteoric cements (MacCaulay et al., 2001). Core and image log analyses demonstrate that these fractures appear to parallel seismic-scale faults. As in Miskar, these fractures have formed in response to NE-SW to ENE-WSW directed extension, which has been intermittently active throughout the Late Cretaceous to present-day evolution of the area (Westaway, 1990).

Fracture Frequency and Spacing

Table 7.28 shows fracture frequencies and spacing values for the cored lithostratigraphic units in each well. Spacing estimates have been obtained through the methodology of Narr (1996). This summary is believed to represent a reasonable estimate of fracture spacing in the Hasdrubal cores, although as in Miskar, spacing estimates along zones of small sample length must be treated with caution. Frequency and spacing estimates are presented for grouped fracture types.

In general, apparent fracture frequency values and spacing estimates correlate closely. The most consistent results were obtained from the Hasdrubal -3 and -4 wells. These two wells show very similar spacing and frequency values within each lithostratigraphic unit. It is noted that the El Garia Formation tends to show constantly higher frequency values, compared to the other intervals. Considering that most of the fractures in the core are stylolite-associated features, and that the El Garia Formation contains a high percentage of stylolites, it is reasonable to suggest that fracture frequency (in particular STA-fracture frequency) is mainly controlled by stylolite

development. The two curves presented in **Figure 7.28** for Hasdrubal -4, illustrate this relationship, showing that fracture and stylolite frequencies correlate very well. Core observations also support this, showing that STA-fractures tend to form in clusters around stylolites. The spacing of these clusters (~1-1.5m) is intimately associated with the average spacing of stylolites in each interval (N.B. Fracture spacing within clusters is commonly ~20-50mm). For instance, fracture frequencies tend to increase in the upper parts of the El Garia Formation, coinciding with a relative decrease in stylolite spacing (i.e. increase in stylolite presence). This increase is reflected by subtle lithological variations through the upper parts of the El Garia Formation.

	Apparent Fracture Frequency (Fractures/m)			Average Fracture Spacing (m)		
Lithostratigraphic Unit	**H2**	**H3**	**H4**	**H2**	**H3**	**H4**
Compact Micrite Mbr	-	4.08	4.90	-	0.14	0.21
El Garia Formation	1.54	4.54	5.25	0.51	0.23	0.22
Chouabine Formation	0.45	0.65	1.26	1.42	0.64	0.75
Total Core	1.00	3.41	4.94	0.68	0.27	0.22

Table 7.28. Comparison of apparent fracture frequencies, and average fracture spacing values within each lithostratigraphic interval for each well.

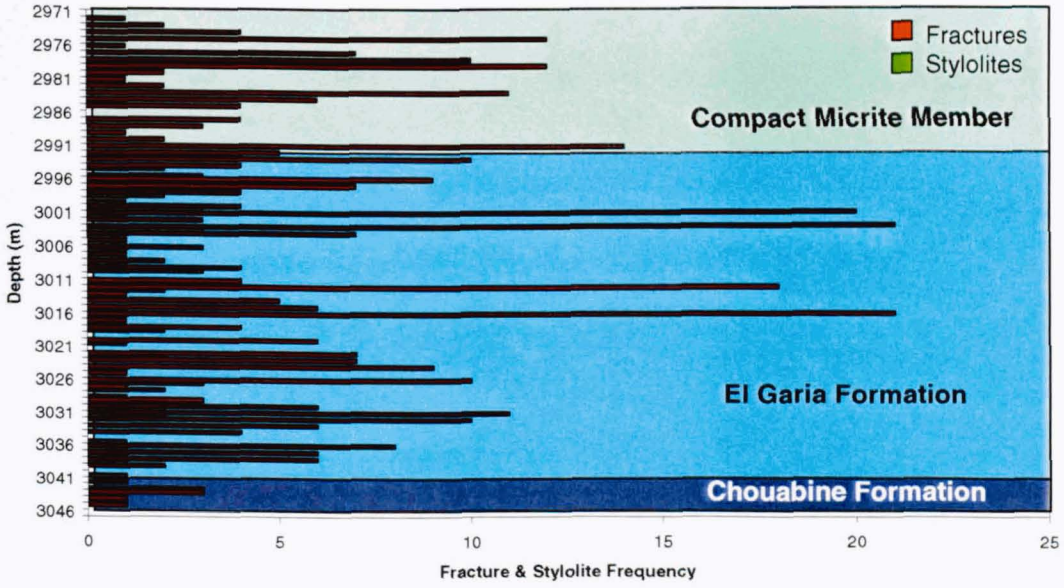

Fig. 7.28. Stylolite and fracture frequencies in Hasdrubal –4, illustrating the close correlation between stylolite presence and fracture intensity.

During this analysis, a number of questions arose with regard to the spacing of STA-fractures. In particular, it is still a matter of debate whether there is a constant spacing relationship of STA-fractures actually tipping off from stylolite dentae. If this could be

understood, it would then be necessary to ascertain whether STA-fracture spacing was controlled by the stylolite type (sutured/non-sutured) and/or size (distance between stylolite dentae). It seems logical to assume that STA-fractures would preferentially be generated along sutured stylolites, in particular at the tips of dentae where the stress concentrations are highest. However, due to the small sample area in the core it has been impossible to make any direct observations on the nature of spacing.

Analyses of fracture height for all fracture types in the Hasdrubal wells show power-law distributions over the scale range 30-600mm. It should be noted that significant biases are observed in this particular analysis due to the small sample area of core (i.e. fractures commonly extend outside the diameter of the core).

The Relationship between Fracture Frequency/Spacing and Proximity to Local Structure

It is widely recognised that the distribution of strain associated with a given fault, increases with proximity to the main fault plane(s). That is, the relative frequency of associated fractures generally increases toward the main fault. This relationship is evident in well data from Hasdrubal. **Figure 7.29** shows the top Metlaoui structure map with the positions of the Hasdrubal -2, -3 and -4 wells. The faults shown on this map are all above the limit of seismic resolution, in that they have displacements that exceed 12 metres. Maximum displacements are given for each fault trace.

From this diagram, it is evident that Hasdrubal -3 and -4 are situated approximately 200m and 100m from the closest seismic-scale faults respectively, whereas Hasdrubal -2 is situated 550m from comparable structures. **Figure 7.30a-d** presents a series of plots (for the Hasdrubal -2, -3 and -4 wells) illustrating the relationship between sub-seismic fracture intensity and proximity to the closest seismically resolvable faults of comparable size. These plots all show a tendency towards higher fracture distributions within the wells closest to interpreted seismic-scale faults (i.e. Hasdrubal -3 and -4). In particular, **Figures 7.30a & c** show an apparently linear relationship.

It should be noted, that although a relationship has been observed in these three wells, more data points (i.e. wells) are required to provide a robust argument. In addition, it must be stressed that a large proportion of fractures observed are interpreted as STA-fractures that are not directly associated with faulting. Hence, from this data alone, it is impossible to make any predictions on the hierarchical distribution of the fault and fracture populations directly associated with 'seismic-scale' faulting. A closer look into

the hierarchical distribution of sub-seismic scale fractures/faults in relation to seismic scale faults is given in Chapter 8.

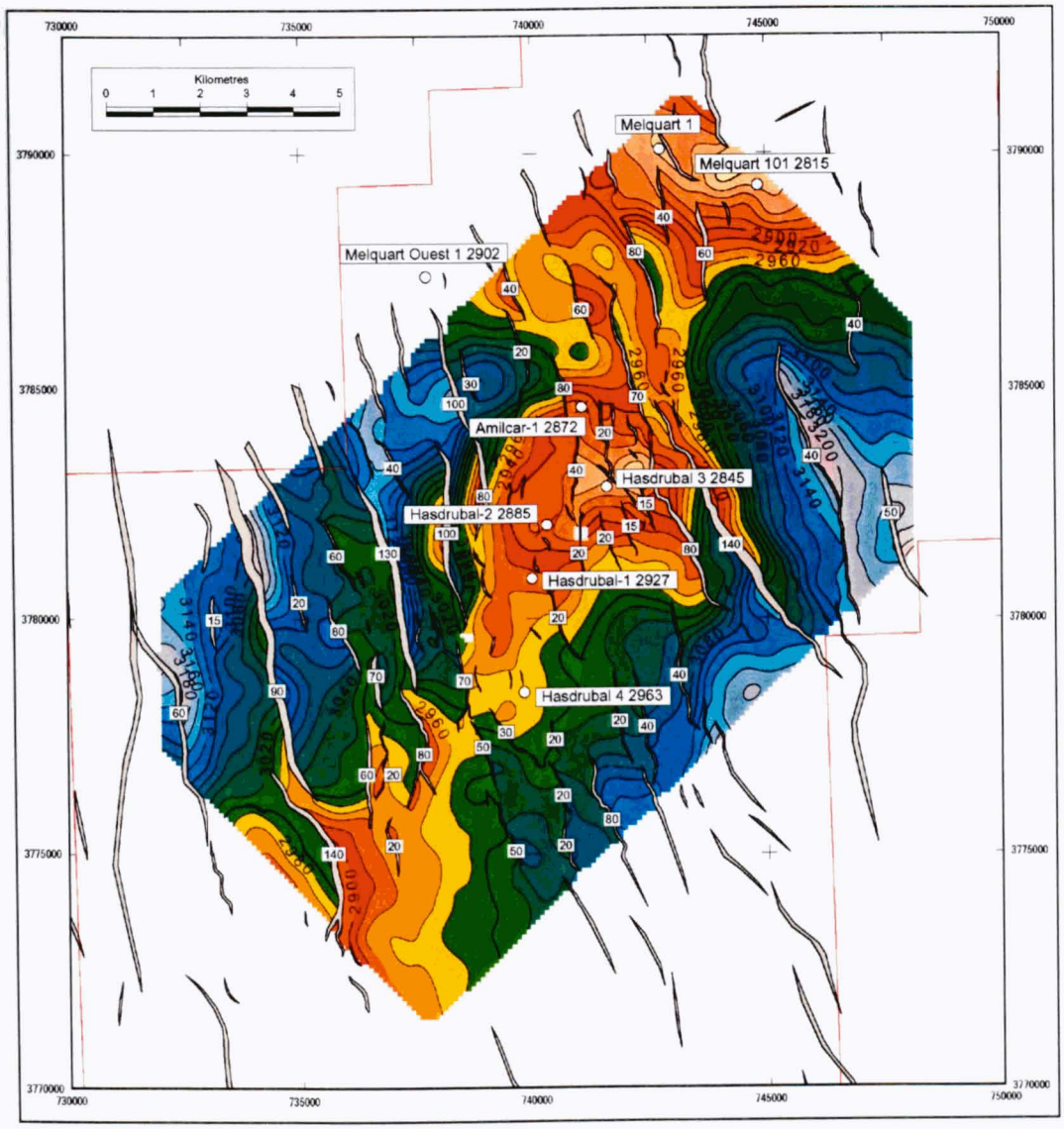

Fig. 7.29. Depth structure map of the top Metaloui Formation over the Hasdrubal acreage. The locations of Hasdrubal –2, -3 and –4 are shown. Maximum fault displacements are also presented, for all the faults interpreted

Fracture and Matrix Cementation

Thin section and core studies demonstrate the presence of calcite and dolomite cements in the main reservoir interval. Conventional stable isotope and fluid inclusion studies suggest that matrix dolomite precipitated at temperatures of 81-88^{0}C, and is therefore of burial diagenetic origin (Macaulay et al., 2001). Matrix dolomitisation has improved reservoir porosity and permeability where secondary porosity has not been filled by later dolomite cement. The highest permeabilities occur along a zone in the middle of

the reservoir, where preferential dolomitisation of finer grained wackestone-mudstone units has occurred. The reason of this fabric-specific dolomitisation is unclear, although it is not an uncommon occurrence (James et al., 1993). Coarser grained baroque cement dolomites, which were precipitated at higher temperatures (and are thus later), fill some of the secondary porosity created by matrix dolomitisation (Macaulay et al., 2001).

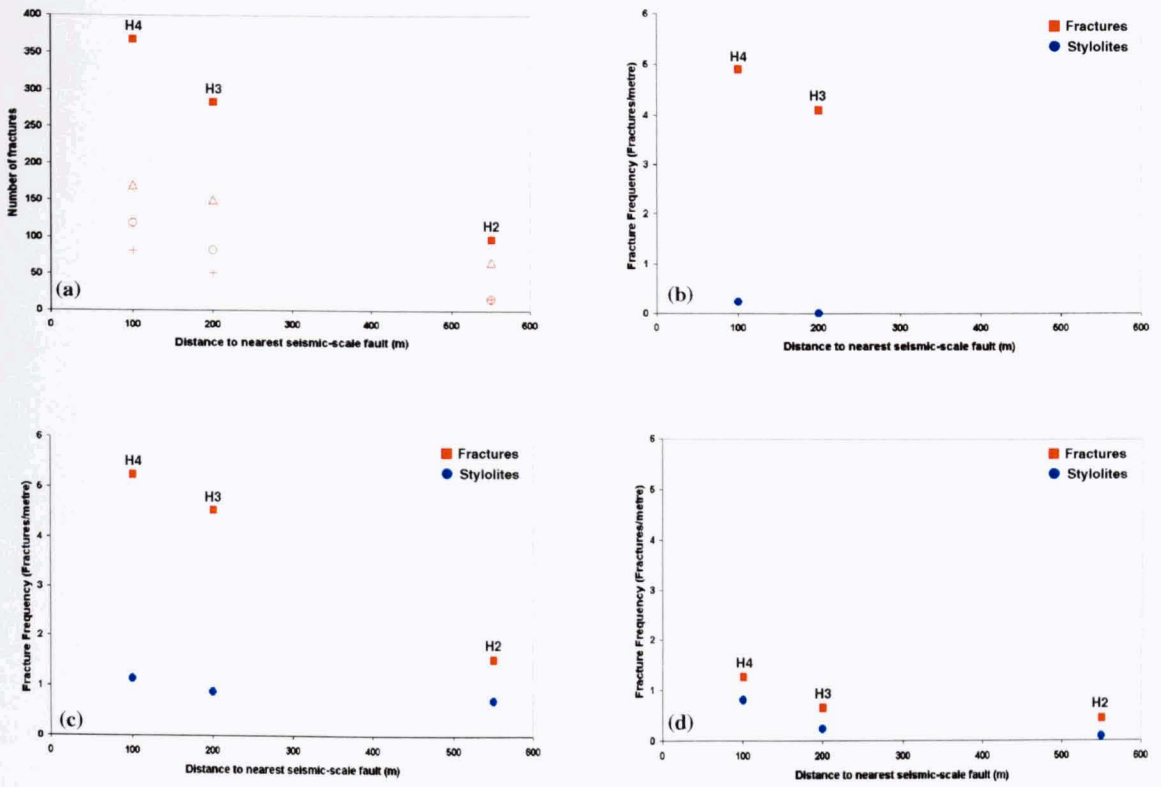

Fig. 7.30a-d. Series of plots showing the relationship between fracture intensity and proximity to seismic-scale faulting. (a) Total number of fractures versus distance to nearest seismic-scale structure, (b) Fracture frequency versus distance to nearest seismic-scale structure (Compact Micrite Member), (c) Fracture frequency versus distance to nearest seismic-scale structure (El Garia Formation), (d) Fracture frequency versus distance to nearest seismic-scale structure (Chouabine Formation).

Stable isotope analyses of calcite cements exhibit wide a range in isotopic composition, reflecting growth over a wide temperature range (Macaulay et al., 2001) (**Fig. 7.31a**). Measured isotope ratios in samples from wells Hasdrubal -2 and -3 were similar, and ranged from $\delta^{13}C$ +1.0‰ to –4.1‰ PDB, and from $\delta^{18}O$ –0.5‰ to -15.3‰ PDB. Samples from well Hasdrubal –4, $\delta^{13}C$ varied from +1.6‰ to –2.7‰ PDB, and $\delta^{18}O$ -1.1‰ to –9.0‰ (refer to Tables 1 & 2 from Macaulay et al., 2001 for a listing).

Overall, the large range in calcite $\delta^{18}O$ values includes calcite infilling fractures and large vuggy pores as well as inter- and intragranular porosity. This implies that

fracturing and calcite cementation has affected the reservoir since early in the burial history. In Hasdrubal -4, oxygen isotope data from fracture-filling cements indicates that fracture cementation occurred at temperatures as low as 68^0C from water with a $\delta^{18}O$ of +4‰ (Macaulay et al., 2001). Compactional stylolitisation and associated fracturing and cementation is the most likely origin for these early fractures. If the calculated temperature (68^0C) of early stylolite associated calcite cementation is integrated with the burial history model of McQuilken (1998), an age for the onset of stylolite associated fracture cementation of 37Ma is established (**Fig. 7.32**).

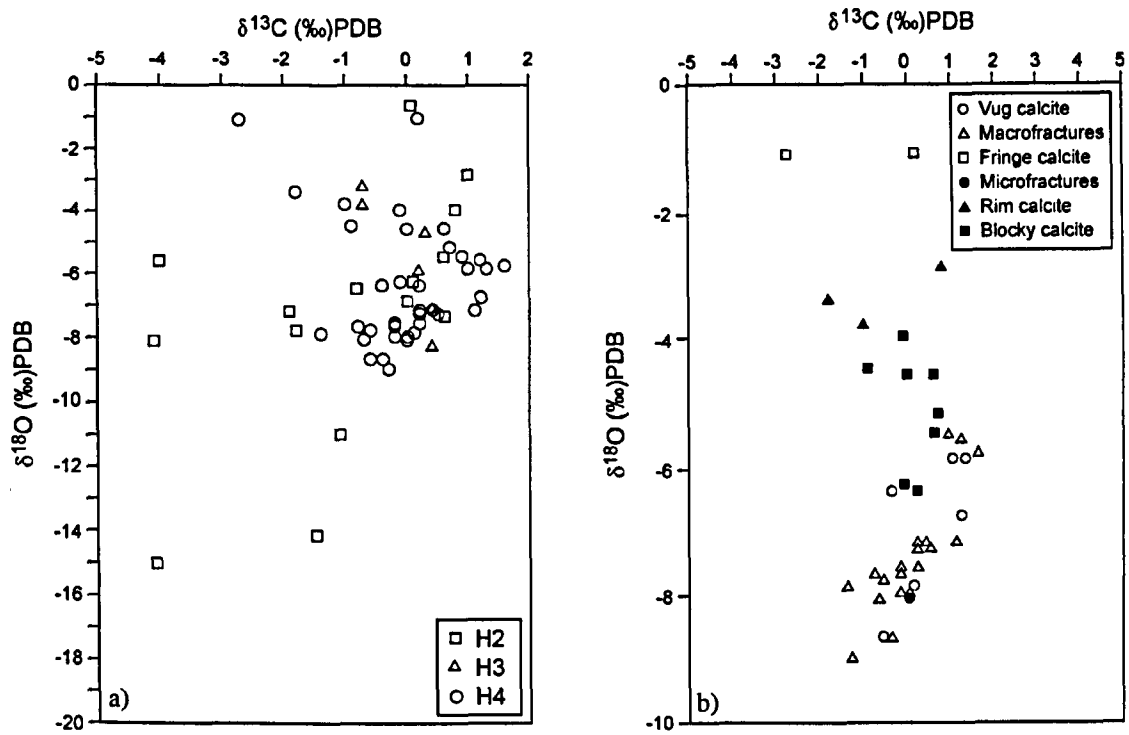

Fig. 7.31. (a) Plot of $\delta^{13}C$ versus $\delta^{18}O$ for diagenitic calcites from Hasdrubal -2, -3 and -4. (b) Plot of $\delta^{13}C$ versus $\delta^{18}O$ for the various types of calcite in Hasdrubal –4 (from Macaulay et al., 2001)

Low $\delta^{18}O$ calcites (**Fig. 7.31b**) with high fluid inclusion temperatures (Th - 147.6^0C) (i.e. hotter than the present-day temperature of 125^0C for the reservoir) were probably precipitated from hot brines that migrated from depth along a pre-existing fracture network (Macaulay et al., 2001). This theory is supported by fluid inclusion salinities that are 1.5 times present formation water salinity (Macaulay et al., 2001). These hot fluids may have also contributed to the formation of vuggy porosity in which some late calcite can be found. Macaulay et al. (2001) interestingly note that in Hasdrubal -4, which drilled through a fault zone in the Chouabine Formation, bottom-hole temperatures were higher than in the other two wells.

In Hasdrubal -4, calcite cements in fractures with fluid inclusion temperatures of around 110^{0}C are observed to contain hydrocarbon inclusions (Macaulay, 2001). This suggests that the fracture network was therefore being exploited by migrating oil at temperatures of about 110^{0}C, which relates to 15-20Ma (**Fig. 7.32**).

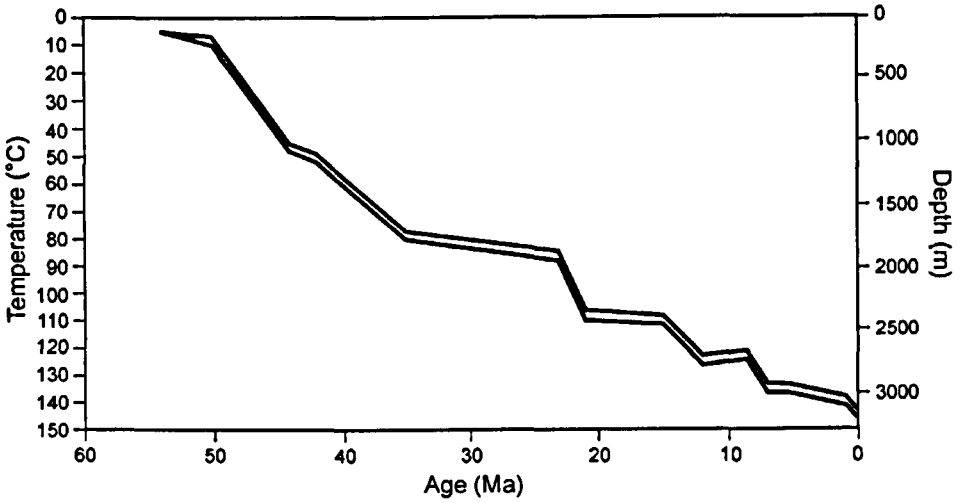

Fig. 7.32. Burial History curve for the El Garia Fm. in Hasdrubal -4 (from McQuilken, 1998).

The extent of fracture cementation varies within different lithostratigraphic intervals, In Hasdrubal -3 and -4, totally occluded fractures dominate the Compact Micrite Member and the uppermost portion of the El Garia Formation (Table 7.29). In contrast, open and partially occluded fractures occur within the Chouabine and El Garia Formations. Table 7.28 summarises the distribution of open, occluded and partially occludded fractures in each lithostratigraphic interval for Hasdrubal -2, -3 and -4.

	Hasdrubal -2			Hasdrubal -3			Hasdrubal -4		
	CL	PO	OP	CL	PO	OP	CL	PO	OP
Compact Micrite Mbr	NC	NC	NC	79%	21%	0%	74%	24%	2%
El Garia Formation	5%	77%	18%	1%	65%	34%	2%	55%	43%
Chouabine Formation	80%	20%	0%	24%	38%	38%	20%	20%	60%
Total Core	17%	68%	15%	18%	53%	29%	22%	46%	32%

Table 7.29. Comparison of apparent fracture frequencies, and average fracture spacing values within each lithostratigraphic interval for each well.

7.8.3. Sequence of Fracturing in the Hasdrubal Reservoir

The following discussion summarises the stages of fracture development in the Hasdrubal Accumulation. A series of sequential restorations are presented which detail the evolution of these fracture systems (**Fig. 7.33a-c**).

During the Ypresian, tectonic subsidence throughout the Gulf of Gabes coincided with the deposition of Chouabine and El Garia Formations, and the Compact Micrite Member. Extension and fault activity, which was prevalent throughout this period created a number of structurally controlled embayments in the Hasdrubal area, and also influenced sedimentation (**Fig. 7.33a**). As the unconsolidated El Garia Formation became buried and compacted, dewatering occurred together with the elimination of unsupported pore space. Internal micro-fracturing took place within individual nummulite tests, in response to the overburden pressure, together with micro-stylolitisation, which occurred at grain-grain contacts.

At a certain stage, the El Garia Formation became lithified and the process of stylolitisation commenced (**Fig. 7.33b**). Stylolites were initiated preferentially at bed boundaries. Fractures associated with the stylolitisation process are observed to nucleate from the tips of 'sutured' stylolite dentae. They are generally filled with coarse, highly twinned calcite, and strike NNW-SSE, following the main trend of seismic-scale faults within the El Garia Formation. The exact timing of stylolite initiation is uncertain, although the results of the stable isotope study demonstrate that initial cementation within stylolite-associated fractures occurred at ~37Ma.

Stylolite amplitudes increased during progressive burial, and significant amounts of calcite were passed into solution. Some of this calcite was re-precipitated in the tensile fractures that had nucleated at stylolite dentae. A large proportion, however, was re-precipitated in the pre-existing fracture sets associated with active faults. The wide range in isotopic composition of calcite cements in fractures (which reflects growth over a wide temperature range), suggests that calcite dissolution and re-precipitation associated with stylolitisation has occurred throughout the history of the reservoir.

Tectonic subsidence and related extension continued throughout much of the Miocene-present-day. This caused increased fracturing within the El Garia Formation (particularly in the near vicinity to faults) and also led to the reactivation and propagation of stylolite-associated fractures (many fractures show evidence of sinistral strike-slip displacements) (**Fig. 7.33c**). Hydrocarbon inclusions in calcite cements with homogenisation temperatures of ~110^{0}C, indicate that oil was migrating through the fracture system at this time (15-20Ma). Occasionally, widespread subsidence was interrupted by minor episodes of uplift and erosion that caused stylolites to crack open and conduct fluids. It may also have been one of these tectonic events that created the

NW-SE trending fracture set formed in the Compact Micrite Member (**Fig. 7.33c**). Recently, the entire fracture system present has acted as a conduit to the flow of hot brines, which originate from deeper parts of the basin. Calcite cements precipitated from these solutions are the latest cements identified. They are particularly prevalent filling the NE-SW trending fracture system in the Compact Micrite Member.

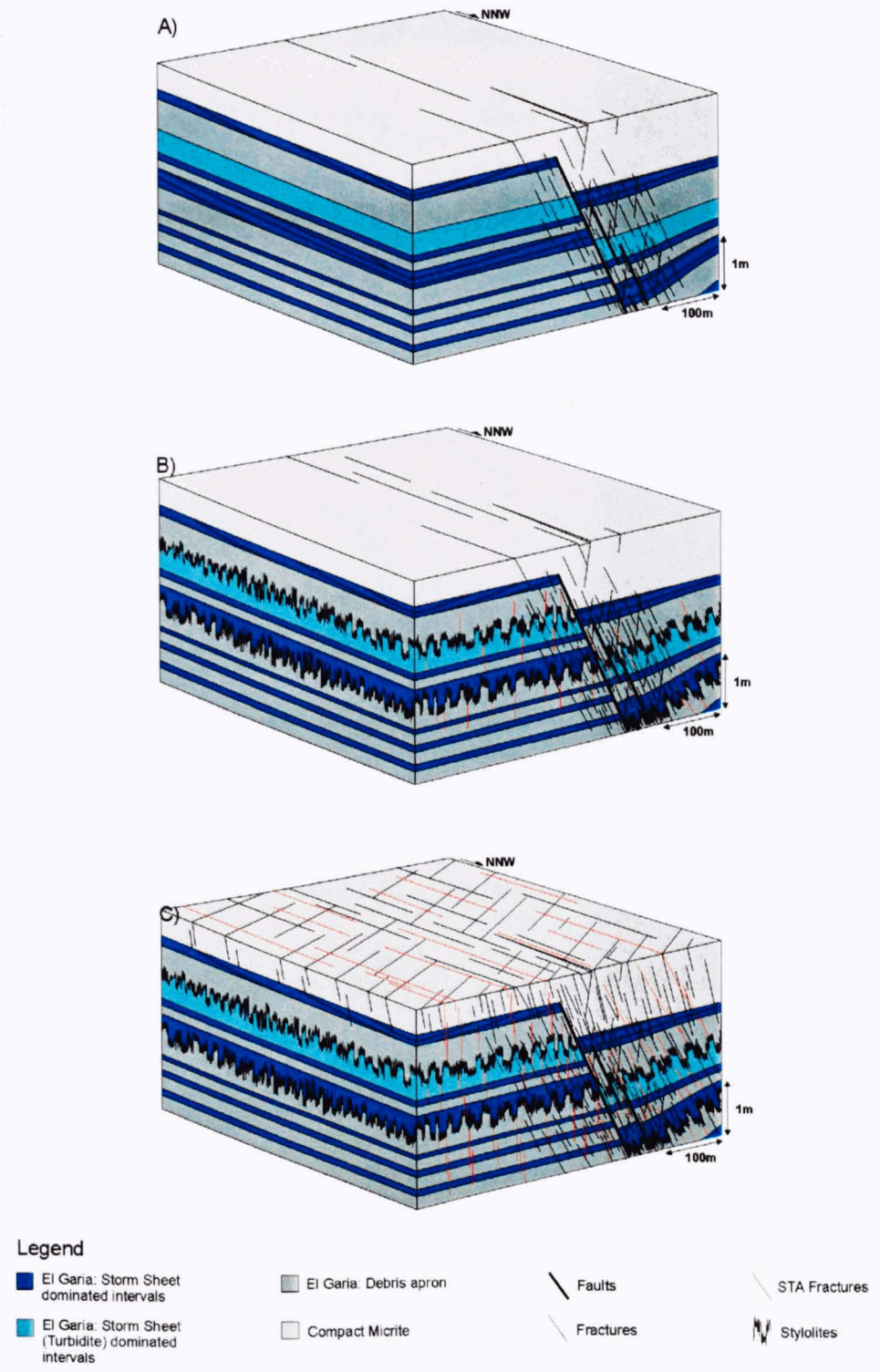

Fig. 7.33. Sequential restoration showing the main phases of fracturing in the primary reservoir interval (i.e. the El Garia Formation) in the Hasdrubal Gas Condensate Field.

7.8.4. Influence on Reservoir Performance

It is apparent from the preceding discussion that there are many similarities with respect to fracturing in the Hasdrubal and Miskar accumulations. Evidently, the better dataset came from the Hasdrubal accumulation, as it allowed the direct determination of fracture orientation through both the core and CAST/FMI image log analyses. In addition larger sample lengths were obtained through core extraction. As a consequence, it is possible to get a better handle of the influence of fracturing on reservoir performance.

In summary, reservoir quality in the Hasdrubal Accumulation has suffered as a result of mechanical and chemical compaction and the precipitation of diagenetic calcites, but was improved as a result of dolomitisation and fracturing. Porosities are often reasonable (7-20%), but corresponding permeabilities are variable (<1-100md) because much of the porosity is ineffective intra-particle porosity. Fringe calcite cements around nummulitic grains have helped to reduce inter-particle permeability and porosity. The contribution of internal micro-fracturing (within nummulitic grains) to bulk rock permeability is unclear, although it is probably negligible.

The highest permeabilities occur as a result of matrix dolomitisation around the middle of the reservoir. The stable isotope and fluid inclusion studies suggest that most dolomite precipitated at temperatures of 80-90^{0}C (i.e. between 20-30Ma) and is therefore of burial diagenetic origin. Remnant rock fabrics in the dolomitised zone suggest that finer-grained or muddy units have been preferentially dolomitised, indicating a matrix-rich facies control on diagenetic permeability improvement. Late coarse-grained baroque dolomite has filled some of the secondary porosity created by matrix dolomitisation.

Where present, fractures appear from well-test data to increase permeability by at least an order of magnitude (Macaulay et al., 2001). From the core analysis, it is reasonable to suggest that K_H increases in the direction parallel to the main fracture trend (i.e. NNW-SSE and NE-SW). Flow data has also demonstrated vertical communication between different reservoir layers. This is most likely to be associated with reservoir-scale fracturing. The connectivity of the NNW-SSE and NE-SW trending fracture systems is unclear due to the small sample area of the core. However, it is noted that many of the fractures in the NE-SW trending set are completely occluded by late calcite cements, and therefore do not represent permeability conduits.

In summary, it is reasonable to classify the Hasdrubal Accumulation as a Type III reservoir, according to the scheme of Nelson (2001), whereby 'fractures partially assist permeability in an producible reservoir'.

Chapter 8

Fault-Related Reservoir Fracturing in Hasdrubal: Outcrop Analogues

8.1. Introduction

It has already been established in Chapter 7, that in the Hasdrubal reservoir, sub-seismic scale fault and fracture populations vary from well to well. In particular, it was illustrated in **Figure 7.27**, that sub-seismic fracture intensities gained from core data generally increase as a function of proximity to 'seismic-scale' faulting. This relationship, although widely studied, still remains poorly defined. This is due to a complex interplay of a number of intimately related parameters.

In this chapter, the relationship between seismic and sub-seismic fault and fracture populations is investigated for the Hasdrubal Accumulation. Outcrop analogue studies from Malta are used to gain a broad insight into subsurface fracture populations below the limit of seismic resolution within the Hasdrubal reservoir (i.e. the El Garia Formation). The size of deformation zones will be analysed for a number of seismic-scale faults of varying size, and estimates on the frequency and spacing of sub-seismic scale structures within these zones will be given. The results of this study were input into the most recent reservoir simulation for the Field (Thompson, 1998).

8.2. Scope & Previous Work

8.2.1. Introduction

Faults and fractures at all scales have a hierarchical distribution of larger and smaller faults and fractures associated with them. The distribution and configuration of these structures within this hierarchy can be complicated. For instance, in a given stratigraphic succession, the nature of fault and fracture populations is controlled by

the structural style (whether in an extensional, strike-slip, thrust related setting), the position in relation to other structures, the bed thickness, and the mechanical properties of the host rock (i.e. composition, grain size, porosity).

8.2.2. Sampling Fracture Populations from Subsurface Data

Faults and fractures in the subsurface are sampled through the use of both seismic and well data. Seismic data only provides information on faults whose displacements are above the limit of seismic resolution (e.g. >12m throw in the Hasdrubal dataset (P. Foster, pers. comm., 1998)). Smaller faults and fractures within the deformation zones associated with these structures cannot be imaged, and are consequently analysed through the use of well data (i.e. core and image logs). This data, although very useful, is limited, in that it provides a spatially isolated, one-dimensional sample of sub-seismic fault and fracture distributions (Narr, 1996). In addition, Yielding et al. (1992) have demonstrated that it generally only provides information on small-scale structures (mm-cm scale displacements). Intermediate-scale faults and fractures (e.g. 1-12m displacement) are harder to sample due to their size.

The constraints mentioned above show that from seismic and well data alone, it is very difficult to make quantitative predictions on the spatial distribution of sub-seismic scale fractures that are associated with seismic-scale faults. Several alternative techniques have been employed to resolve this problem. Where present, field analogue outcrop studies can be used to provide a good understanding of sub-seismic fault and fracture distributions. Information from such studies can then be used to construct detailed reservoir models. In cases where there is a lack of appropriate field analogues, indirect techniques need to be applied. Recently, various workers have recognised that the prediction of sub-seismic fault and fracture populations is feasible (indirectly) because many aspects of faults are scale-invariant (or self-similar) (Walsh & Watterson, 1988; Marrett & Allmendinger, 1991; Cowie & Scholtz, 1992a; Yielding et al., 1992, Gauthier & Lake, 1993; Needham et al., 1996). This scale-invariance, which is a property of fractals is briefly mentioned below.

The Fractal Nature of Faults & Fractures

For a fault or fracture or set of faults or fractures to show scale-invariance, properties such as geometry, frequency, and distribution must remain the same at all scales (Gauthier & Lake, 1993). Mathematically, this requires that the size and frequency distribution of elements is controlled by a power law (Yielding et al., 1992). For

example, if the size of each fault or fracture is defined by a measurement L, the number N of faults/fractures within a size greater than L, is given by:

$$N = aL^{-D} \tag{8.1}$$

where a is a constant that depends on the sample size and D is the fractal dimension of the set (Yielding et al., 1992).

Power-law scaling relationships have been used to describe the size distributions of fault and fracture lengths (or displacements), the relationship between displacement and length, and the spatial pattern of faulting. Data that have been obtained from field studies show that faults and fractures exhibit power-law size distributions (Needham et al., 1996), spatial clustering and branching configurations characteristic of fractal patterns (Cowie et al., 1995), and linear displacement-length relationships (Walsh & Watterson, 1992). Consequently, these scaling relationships have been used to predict (by extrapolation) the relative numbers, the geometry, and the spatial distribution of sub-seismic scale faulting and fracturing (Walsh & Watterson, 1988; Marrett & Allmendinger, 1991; Cowie & Scholtz, 1992a; Needham et al., 1996) (**Fig. 8.1**).

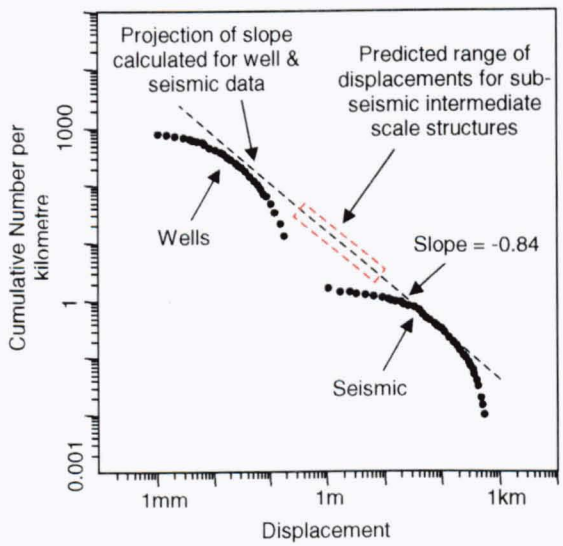

Fig. 8.1. Comparison of top Reservoir seismic scale throw data with well displacement data, for Field A (from Needham et al., 1996). The slope of 0.84 was calculated for seismic data, and is projected to lower displacement values. It is clear from this diagram that the seismic scale faults and well core fractures appear to form part of the same population. From this data it is possible to make predictions on intermediate scale fault and fracture displacements.

It is apparent from the afore-mentioned studies, that this technique can provide a powerful tool in sub-seismic fault and fracture prediction where field outcrop analogues are very limited or unavailable. Fortunately, outcrop analogues were

identified for the Hasdrubal reservoir. Hence this technique did not need to be applied. Broad fieldwork observations were summarised and integrated into the subsurface environment for the Hasdrubal accumulation.

8.3. Outcrop Analogue Identification

Despite an early anticipation that viable reservoir analogues might be found at outcrop in the onshore 'Sahel' region of Tunisia, a map study and reconnaissance trip established that no outcrops of suitable lithology existed within this tectonic regime. As a consequence, fieldwork was mainly focused on Malta. This area provided the closest tectonic analogues (on the Pelagian Platform) within comparable lithologies to the Hasdrubal Accumulation. An initial reconnaissance trip to Malta highlighted various sites that could be evaluated. This was accompanied by aerial photograph interpretation and the analysis of geological maps.

8.4. Fracture Classification & Sampling at Outcrop

Faults and fractures at outcrop were broadly classified according to size. Displacement was used as criteria to characterise structures into distinct groups, which reflected the resolution constraints imposed by seismic and core data (refer to Section 8.2.2). These groups are shown in Table 8.1.

	Seismic Scale (Large)	Sub-seismic Scale (Intermediate)	Sub-seismic Scale (Small)
Displacement (m)	12+	1.0 to 12	0.0001 to 1.0

Table 8.1. Classification scheme for faults and fractures measured at outcrop based on displacement.

The various strategies used to sample fault and fracture systems in the field were summarised in Chapter 5. In this study, basic field maps were constructed, and integrated with scanline data, taken from specific outcrop studies. **Figure 8.2** shows a typical sample log used during scanline sampling procedures. Data requirements were inevitably constrained by the quality of outcrop. Hence at some outcrops the amount of data collected was very limited (i.e. the inaccessibility of many outcrops precluded the construction of scanlines). This field study, nevertheless, makes maximum use of the outcrops available for observation.

Details of Scanline:	**Details of Rock Face:**	Rock Type:
Log. No:	Location:	Condition of Exposure:
Trend:	Dip Direction:	
Plunge:	Dip angle:	Comments:
Trimming level	Non-overhanging/Overhanging	
Logged by:	Height:	
Date Logged:	Width:	

Intersection Distance	Dip Angle	Strike Direction	Throw (m)			Comments
			<1m	1-12m	>12m	

8.5. Outcrop Analogue Studies in Malta

8.5.1. Introduction

Malta, which is the largest of the Maltese Islands (Malta, Gozo and Comino) is located in the central part of the Pelagian Platform, at the northern margin of the Strait of Sicily Rift Zone (SSRZ), (**Fig. 8.3**). It exposes a relatively 'layer-cake' Oligocene to Miocene succession, which is composed predominantly of shallow water carbonates and clays. This sequence has been gently tilted to the northeast. The succession is cut by two major fault sets; the northeast trending set dominates the fault pattern on Malta (examples include the Victoria Lines Faults) (Dart et al., 1993). This set of extensional faults is often cross-cut northwest trending extensional faults that are parallel to the submarine grabens of the SSRZ (e.g. Maghlaq Fault System) (Illies, 1981). The formation of these is discussed in Section 8.5.3.

A number of faults at outcrop (in particular the NW-SE trending set) show similarities to seismic scale structures in Hasdrubal. For example, the Maghlaq Fault System on the southern coast of Malta contains numerous faults that are similar in type (i.e. almost purely dip-slip) and size to those observed from seismic data. In addition, they are also located within broadly comparable lithologies (in terms of composition and fabric) to the main subsurface reservoir interval (refer to Section 8.5.2). Consequently, this outcropping fault system provides a reasonable analogue in which to observe the hierarchical nature of fault and fracture populations at seismic and sub-seismic scales. Other good analogues were identified in various quarries over Malta. The appropriateness of each of these as analogues, and the observations made will be discussed later. Section 8.5.2 and 8.5.3 provide an overview of the stratigraphy and structure of Malta.

8.5.2. Stratigraphy

A detailed lithostratigraphy of the Maltese Islands was first established by Spratt (1843). Later workers including Murray (1890), Pedley (1974; 1987a/b), Pedley et al (1976) changed many of the earlier formational terms and refined the lithostratigraphic framework. This recent lithostratigraphic sub-division of the sequence is currently widely accepted, although the biostratigraphy and chronostratigraphy is a matter of debate. The following account attempts to summarise the main stratigraphy present at outcrop. A generalised stratigraphy of the islands is given in **Figure 8.4**.

CONTAINS PULLOUTS

Oligocene Stratigraphy

Lower Coralline Limestone Formation (Chattian)

This unit is the oldest outcropping formation on the Maltese Islands, correlatable with the Ragusa Formation (Leonardo Member) on the Hyblean Plateau (Pedley, 1981). It is separated into the Maghlaq, Attard, Xlendi and Il-Mara Members (Pedley et al, 1976; Pedley, 1987a/b):

- *The Maghlaq Member*: consists of massive bedded, pale yellow to grey carbonate mudstones rich in planktonic foraminifera (>38m thick) (Pedley et al., 1976; Pedley, 1987a). This unit passes transitionally up into the Attard Member.
- *The Attard Member*: consists of grey wackestones and packstones, with ubiquitous coralline algal rhodoliths (10-15m thick) (Pedley et al., 1976). An extensive N-S trending belt of patch reefs consisting of colonial corals, molluscs and echiniods extend from Wied Maghlaq to Naxxar. These reefs are truncated by one or more major erosion surfaces.
- *The Xlendi Member*: consists of cross-stratified, coarse-grained packstones with abundant coralline algal fragments (0-22m thick) (Pedley et al., 1976). It is best developed in the central and western parts of Malta and Gozo. In the east it passes into the Il-Mara Member. The contact between the Xlendi Member and the Globigerina Limestone Member consists of a marked erosional unconformity.
- *The Il-Mara Member*: consists of thick, tabular beds of cream-grey carbonate mudstones, wackestones and packstones, which are best developed in the eastern areas of Malta and Gozo (0-20m thick) (Pedley et al., 1976). The top of the member is transitional with the overlying Globigerina Limestone Member.

The character of these sequences suggest initial deposition within a shallow gulf area (Maghlaq Member) (Felix, 1973), followed by the development of inter-tidal conditions favouring the development of algal rhodolites (Attard Member). After which, a gradual shallowing prevailed, producing a sub-tidal shoal environment in all areas except southeastern Malta (Pedley et al., 1976).

Miocene Stratigraphy

The Globigerina Limestone Formation (Aquitanian-Langhian)

This unit is so named due to its high planktonic foraminifera content. It is correlatable to the Ragusa Formation (Irminio Member) on the Hyblean Plateau, and may be

separated into the Lower Globigerina Limestone, Middle Globigerina Limestone and Upper Globigerina Limestone Members (Pedley et al., 1976):

- *The Lower Globigerina Limestone*: consists of pale, massive bedded Globigerina-rich packstones which grade into wackestones just above the base (>40m thick). The top of the sequence is represented by a coarse conglomerate containing abundant phosphatic nodules (Pedley et al., 1976). The contact with the overlying Middle Globigerina Limestone Member is formed by a regional unconformity.

- *The Middle Globigerina Limestone*: consists of massive, white, soft carbonate mudstones (rich in Globigerina), which locally pass into pale-grey marly mudstones (5-40m thick) (Pedley et al., 1976). A second conglomeratic unit (0.5m thick) with abundant phosphatic pebbles is located above the mudstones.

- *The Upper Globigerina Limestone*: consists of lower and upper sequences of cream-coloured Globigerina-rich wackestones, and a middle sequence of pale grey marls (2-15m thick) (Pedley et al., 1976). A ubiquitous phosphorite conglomerate bed occurs at the base of the member.

The Blue Clay Formation (Serravallian-early Tortonian)

This unit consists of a banded (medium grey/pale grey) sequence of Globigerina-rich marls (18-75m thick). Pedley et al. (1976) suggest deposition within an open marine environment, envisaging water depths up to 150m for the lower part of the formation.

The Greensand Formation (early Tortonian):

This unit, which is only present on Gozo consists of a variable thickness of poorly cemented, glauconite rich bioclastic wackestones (0-11m thick) (Pedley et al., 1976). The contact with the underlying Blue Clay Formation is generally represented by a marked erosional surface. The intense bioturbation associated with these deposits suggests sedimentation under shallow-water marine conditions.

The Upper Coralline Limestone Formation

This unit is very similar to the Lower Coralline Limestone Formation. It consists of 4 distinct intervals, the Ghajn Melel, Mtarfa, Tal-Pitkal and Gebel Imbark Members:

- *The Ghajn Melel Member*: consists of massive dark to pale brown foraminiferal packstones rich in glauconite (0-16m thick) (Pedley et al., 1976; Pedley, 1987a/b). The base of this sequence is marked by a localised erosional surface.

- *The Mtarfa Member*: consists of massive carbonate mudstones and wackestones which rest unconformably on the Ghajn Melel Member and Greensand Formation (2-16m thick). On Malta west of a N-S line from Rdum il-Hmar to Rdum Dikkiena a prominent coralline algal biostrome is developed (~16m thick) in this unit.

- *The Tal-Pitkal Member*: consists of coarse-grained bioclastic and oolitic wackestones and packstones rich in coralline algae (0-50m thick) (Pedley et al., 1976). The upper part of the unit is dominated by patch reefs and biostromes.

- *The Gebel Imbark Member*: consists of cross-bedded, oolitic, peloidal and bioclastic grainstones and packstones, which lie above a marked erosional unconformity (4-25m thick) (Pedley et al., 1976).

Pedley et al., (1976) suggest that although most of these deposits represent shallow sub-tidal sedimentation, the apparent reduction of microfossil numbers and the absence of microfauna from the highest beds may indicate that inter-tidal and even supra-tidal conditions developed.

Plio-Pleistocene

Quaternary deposits are of local extent, consisting of isolated cave and fissure infills and sediment veneers. The earliest are the Pleistocene bone deposits of various cave systems. Later deposits, include alluvial fan deposits, calcreted breccias and conglomerates, and caliche soil profiles (Pedley et al., 1976).

In terms of lithology and fabric, the closest analogues to the main reservoir interval in Hasdrubal (i.e. the El Garia Formation) are the Maghlaq, Attard and Xlendi Members (Lower Coralline Limestone Formation) and the Lower, Middle and Upper Globigerina Limestone Members of the Globigerina Limestone Formation. These units mainly consist of wackestones and packstones dominated by abundant benthonic and planktonic foraminifera.

8.5.3. Structure

As previously mentioned, the Maltese Islands consists of a relatively 'layer-cake' sequence which is cut by two fault generations (Pedley et al., 1976; Illies, 1980; Reuther & Eisbacher, 1985; Dart et al., 1993)(**Fig. 8.3**). The more dominant fault set trends approximately ENE-WSW ($N50^0$ - $N70^0$) (Reuther & Eisbacher, 1985). Two

important ENE-WSW trending graben are associated with this fault system; 1) the North Gozo Graben, and 2) the North Malta Graben (Dart et al., 1993). The North Gozo Graben is the deepest, with composite vertical displacements in excess of 1600m on its northwestern bounding fault (Dart et al., 1993). The North Malta Graben is flanked by the Victoria Lines Fault to the south, and the South Gozo Fault to the north (**Fig. 8.3**). The Victoria Lines Fault dips about 70^0 to the northwest, with its throw increasing from 90m in the east to 195m in the west (Dart et al., 1993). Similarly, the South Gozo Fault Zone shows a throw of approximately 100m (Pedley et al., 1976). The second system of NW-SE trending extensional faults is particularly well exposed on the southern coast of Malta. Here, composite vertical displacements along the NW-SE trending Maghlaq Fault System are in excess of 200m. The main bounding fault of the Straits of Sicily Rift is located approximately 10km to the SW (Dart et al., 1993).

Various mechanisms detailing the kinematic evolution of the Maltese graben system have been proposed in the literature. Reuther & Eisbacher (1985) amongst others divided the evolution of the Maltese region into three distinct phases; 1) ENE-WSW extensional fault generation, 2) NW-SE extensional fault generation, 3) Reactivation of the pre-existing ENE-WSW structures by dextral strike-slip movements. As a result of this, early models detailing the regional evolution of the entire Straits of Sicily Rift suggested that this zone formed as either a large pull-apart structure within an ~E-W trending dextral wrench zone (Jongsma et al., 1987), or as a large pull-apart structure associated with the NNE-SSW trending Scicli wrench zone (Grasso & Reuther, 1988). However, recent fieldwork studies on Malta (Dart et al., 1993) question the validity of these early models by providing little evidence of strike-slip deformation (which is a pre-requisite of these models). Fault slip data from the study of Dart et al. (1993) does however show an approximately N-S extension axis from both NW-SE and ENE-WSW fault systems, and hence supports the model of Argnani (1990). This model proposes N-S orientated foreland extension in the region of the Straits of Sicily Rift that is coeval and causally related to back-arc extension in the Tyrrhenian Sea, and compression in the Apennine-Maghrebian thrust belt (Argnani, 1990). Importantly, it does not require the influence of substantial strike-slip tectonics.

8.5.4. Observations Along The Maghlaq Fault System

The Maghlaq Fault System, located on the southern coast of Malta between Ix Xwieki and Wied iz-Zurrieq, consists of a series of stepped fault scarps that extend over a

500m wide zone (**Fig. 8.5 & 8.6**). Fault surfaces typically trend approximately NW-SE (~N120^0), dip between 60^0 - 90^0 to the SW, and display slickensides that show almost pure dip-slip movements. Fault size varies, from the seismic scale (where a small number of faults extend over hundreds of metres and display throws in excess of 20m) down to the subseismic scale (where faults extend over tens of metres and possess centimetre to metre scale displacements). Composite vertical displacements across the entire fault zone are in excess of 200m (Pedley et al., 1978; Dart et al., 1993). Map interpretation illustrates that this zone affects the entire Oligocene and Miocene succession (**Fig. 8.5**). Commonly, the Gebel Imbark Member of the Upper Coralline Limestone Formation (early Messinian) is observed to have been downthrown against Attard and Maghlaq Members of the Lower Coralline Limestone Formation (**Fig. 8.5**). In addition, locally, the fault zone is characterised by complex synthetic and antithetic rotation of semi-detached blocks on a scale of several tens of metres (Reuther, 1984). Ongoing activity along the Maghlaq Fault System is evidenced by fresh slickensided surfaces on fault scarps, vertical dislocations of Pleistocene waterlines in karst caverns, and by fault displacements of raised beaches and related beachrocks.

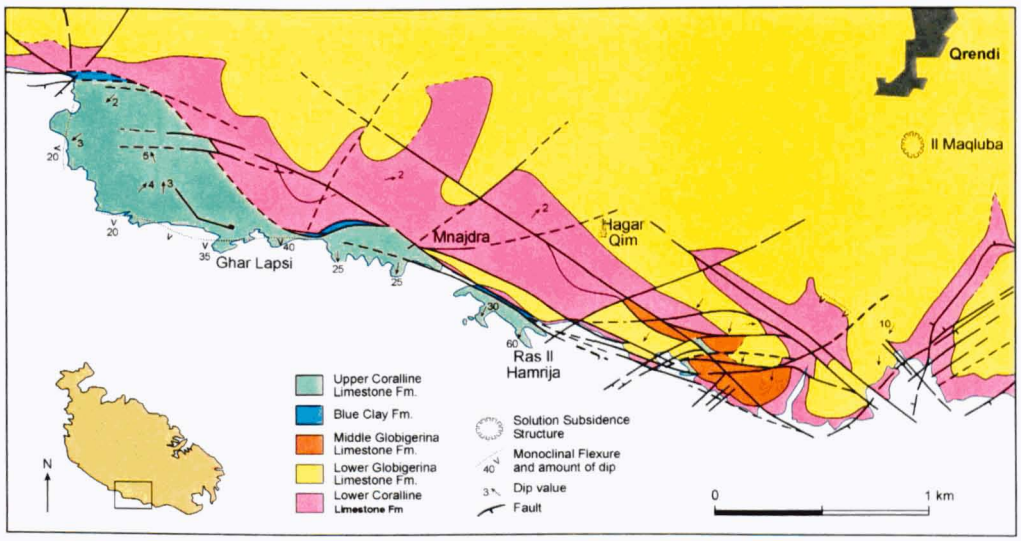

Fig. 8.5. Geological map of the Maghlaq Fault System, on the southern coast of Malta (modified after Pedley et al., 1976).

Quality of Outcrop

The quality of outcrop along the Maghlaq Fault System varies considerably. The neotectonic nature of the fault zone means that in places freshly exposed fault/fracture surfaces were readily visible, and thus easily sampled. However, in certain lithological units, most notably the Tal-Pitkal Member (Upper Coralline Limestone Formation) weathering made it very difficult to identify and sample fractures.

Hierarchical distribution of Faulting & Fracturing along the Maghlaq Fault System

The 1:5000 scale map presented in **Figure 8.6 (Enclosure 4)** summarises the main observations that were made from outcrops along the Maghlaq Fault System. Mappable faults and fractures have been plotted and colour-coded according to size (refer to Table 8.1), and general descriptions on the size and spacing of unmappable structures are given. Scanline locations have been highlighted.

Seismic Scale Fault & Fracture Distribution

The majority of seismic scale faults sampled along this zone trend approximately NW-SE ($N120^0$-$N150^0$), parallel to the main trend of the grabens in the SSRZ (**Fig. 8.6 - Enclosure 4**). Many display well-defined slickensided fault planes and show recent dip-slip displacements (**Plate 8.1 & 8.2**). The largest of these structures is the WNW-ESE trending Ghar Lapsi Fault Zone, which consists of a series of fault segments, which have a composite length in excess of 4km (**Fig. 8.6 - Enclosure 4**). Displacements typically range between 20-150m, throwing the Tal-Pitkal and Gebel Imbark Members (Upper Coralline Limestone Formation) against the Maghlaq, Attard and Xlendi Members (Lower Coralline Limestone Formation). Thin outcrops of the Globigerina Limestone Formation are also evident outcropping along the fault zone. Slickensides generally plunge at ~$88^0/220^0$. At Ras Hanzir (448400mE, 3965150mN), the main fault plane is particularly well exposed, with slickengrooves showing almost pure dip-slip displacements ($72^0/179^0$). A 4-5m wide zone of fault gouge has been identified immediately adjacent to the main fault plane mainly containing blocks of the Globigerina Limestone Formation (**Plate 8.3**). The distribution of sub-seismic scale fractures associated with this zone will be explained in more detail later.

Other large (seismic scale) structures along the Maghlaq Fault System include the WNW-ESE trending Ras il-Hamrija, Hagar Qim, Il-Hnejja Faults, Wied Zurreiq and Blue Grotto Faults which are located at fairly regularly spaced intervals (every 80-200m). They are all located to the north east of the Ghar Lapsi Fault Zone (**Fig. 8.6 - Enclosure 4**). Average fault length on these structures is in the order of several kilometres, and displacements range between 10-80m, commonly throwing the Lower Globigerina Limestone Member (Globigerina Limestone Formation) against the Attard and Xlendi Members (Lower Coralline Limestone Formation). Occasionally it is possible to observe these structures cutting the ENE-WSW trending set associated with the Victoria Lines Fault System (**Plate 8.4**).

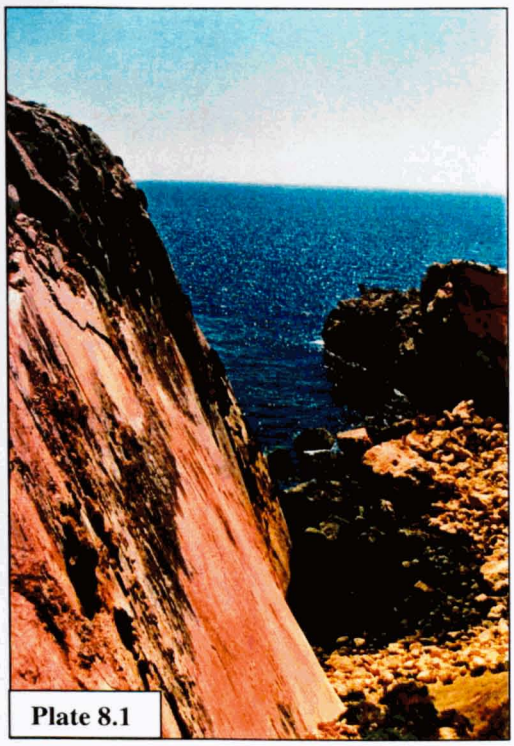

Plate 8.1

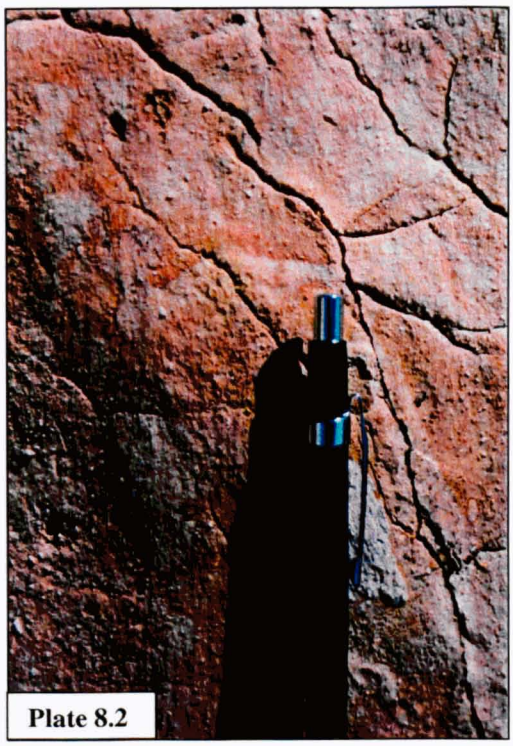

Plate 8.2

Plate. 8.1. Ras il-Hamrija (449400mE, 3964700mN): Well-exposed fault segment within the Maghlaq Fault System - $70^0/124^0$SW. Plate. 8.2. Ras il-Hamrija (449400mE, 3964700mN): Fresh slickensides indicate almost pure dip-slip displacements ($88^0/220^0$).



Plate 8.3

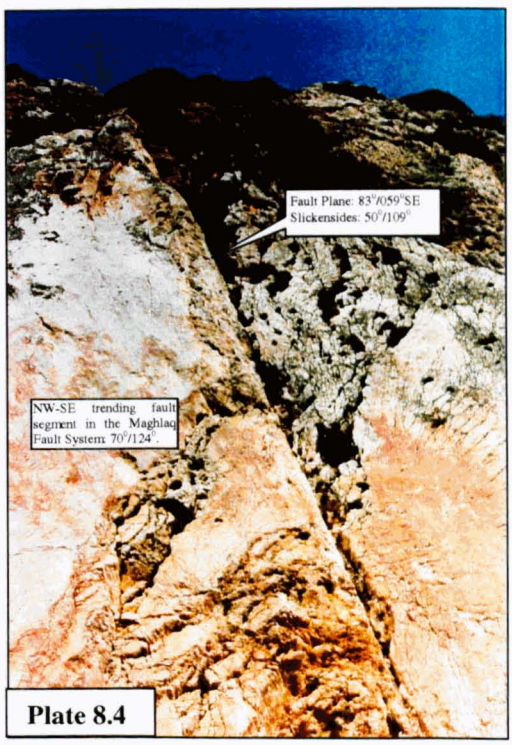

Plate 8.4

Plate 8.3. Ras Hanzir (448400mE, 3965150mN): 2-3m wide zone of fault gouge immediately adjacent to the main Ghar Lapsi fault. The zone contains numerous angular blocks mainly from the Globigerina Limestone Formation. Plate 8.4. Ras il-Hamrija (449400mE, 3964700mN): Well-exposed fault segment within the Maghlaq Fault System cutting an older fault trace that is associated with the Victoria Lines Fault System.

Table 8.2 presents a comparison of the spacing of seismic scale faults mapped along the Maghlaq Fault Complex and the seismically resolvable structures interpreted in the Hasdrubal area (**Fig. 7.29**). Average seismic scale fault spacing estimates were obtained for both the Maghlaq and Hasdrubal datasets by constructing a series of scanlines orthogonal to the main fault trend on the field map and top reservoir structure map respectively (**Figs. 8.6 and 8.7**).

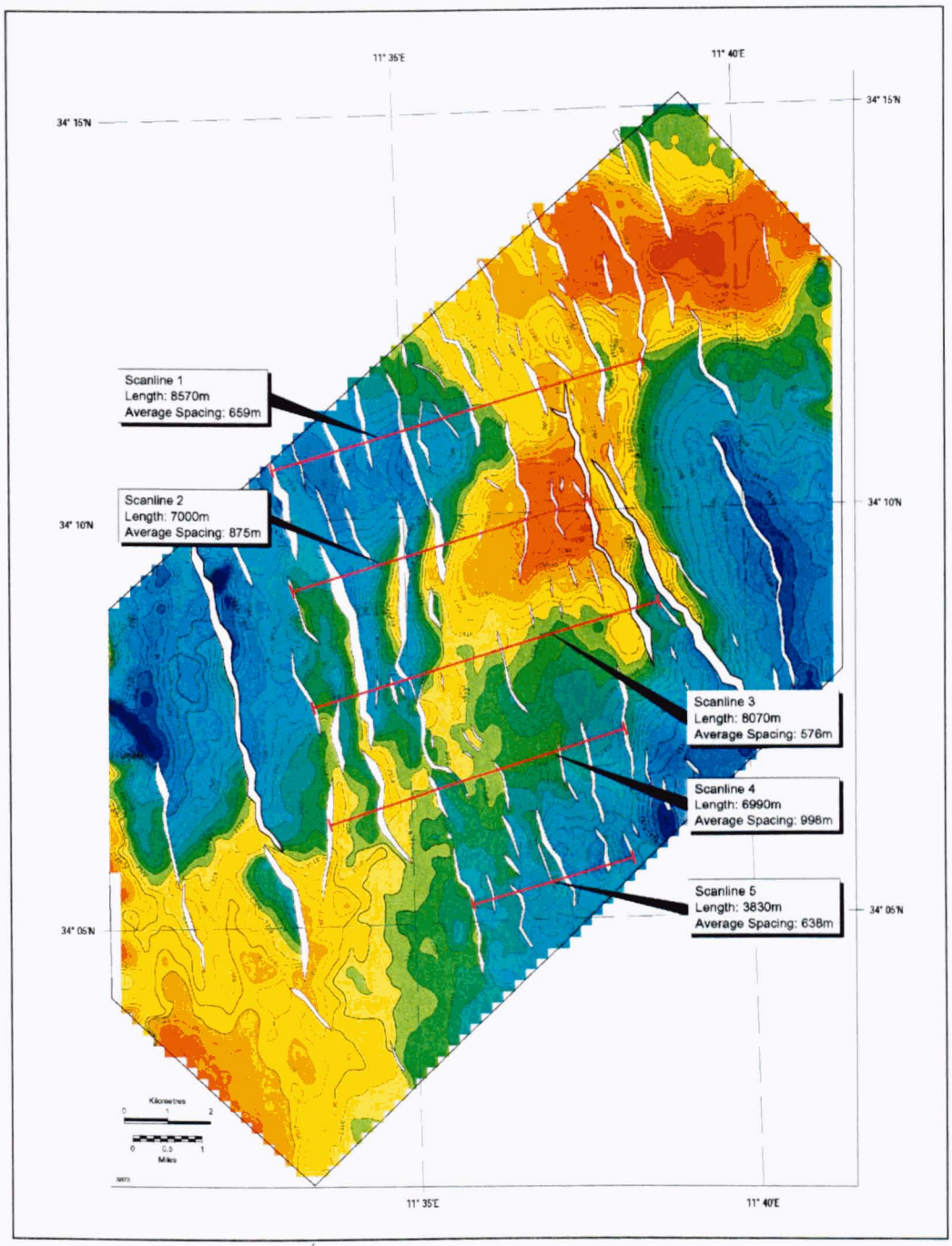

Fig. 8.7. Two-way-time structure map of the top Metlaoui Group over the Hasdrubal area. Five scanlines of specified length were constructed across the dataset, in order to determine the spacing distribution of seismic-scale faults over the study area. Average Spacing Distribution: Scanline 1 - 659m, Scanline 2 - 875m, Scanline 3 - 576m, Scanline 4 - 998m and Scanline 5 - 638m.

It is evident from this table that average spacing estimates are significantly larger in the Hasdrubal Accumulation. However, it should be highlighted that only a few seismic scale faults were actually observed in the Maghlaq Fault System, and that the reliability of the estimates given in Table 8.2 for this area is questionable.

	Average 2nd Order Fault Spacing	
Scanline No.	**Hasdrubal**	**Maghlaq Fault Complex**
1 / A	659*	200
2 / B	875	80
3 / C	576*	160
4	998	-
5	638	-

Table 8.2. Comparison of average 2nd order fault spacing distributions for subsurface structures in the Hasdrubal Accumulation and exposed structures in the Maghlaq Fault System. * Most reliable data in the Hasdrubal dataset based on scanline length.

Sub-Seismic Fault & Fracture Distribution

This section presents a series of individual outcrop studies, which attempt to summarise the nature and distribution of sub-seismic scale fracturing related to the afore-mentioned faults. This work provided an insight into the size of deformation zones associated with seismic-scale faults in Hasdrubal, and also gave an indication of the spacing and frequency of sub-seismic scale fractures within these zones.

Ras Hanzir (448400mE, 3965150mN): Sub-seismic Scale Deformation Associated with the Ghar Lapsi Fault

As previously mentioned, at Ras Hanzir, the Ghar Lapsi Fault is particularly well exposed, showing a freshly slickensided fault surface indicating almost pure dip-slip displacements. This fault zone has a displacement in excess of 150m, throwing the Lower Globigerina Limestone Member (Miocene) against the Maghlaq Member (Oligocene). A location map for this area is presented in **Figure 8.8.**

Plate 8.5 and **Figure 8.9 (Enclosure 5)** provide a detailed overview of the style and intensity of sub-seismic scale deformation associated with the Ghar Lapsi Fault. In summary, the hangingwall section is characterised by:

- A 4-5m wide zone of fault gouge immediately adjacent to the main fault plane, consisting of fine grained cataclastic gouge, which contains angular blocks mainly from the Globigerina Limestone Formation;

- A 25-30m wide, highly deformed zone consisting of the Lower Globigerina Limestone Member. The southern limit of this Miocene outcrop is represented by another fault (i.e. the Ras Hanzir Fault), which has displacements in excess of 60m, and throws the Tal-Pitkal Member against the Lower Globigerina Limestone Member.

- A broad zone of deformation within the Tal-Pitkal Member, which is primarily associated with the Ras Hanzir Fault. Intermediate scale structures associated with this fault zone are regularly spaced, at 20-25m intervals and generally have displacements less than 5m. Small-scale fractures are pervasive throughout this outcrop, increasing in intensity towards intermediate and large-scale structures. Average spacing of these fractures is approximately 0.5-1m. Displacements rarely exceed 0.2m.

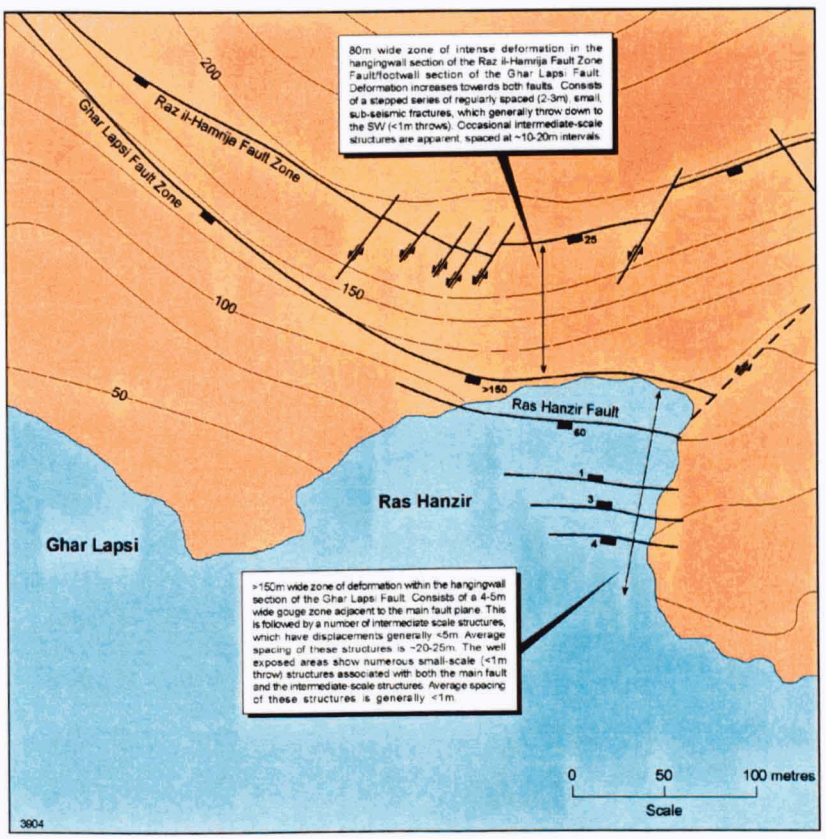

Fig. 8.8. Location map showing the Ghar Lapsi Fault Zone at Ras Hanzir (448400mE, 3965150mN). Fault throws are indicated adjacent to the tick marks.

The overall width of the hangingwall deformation zone associated with the Ghar Lapsi Fault is impossible to determine due to limited outcrop. However, it is reasonable to suggest that the deformation (fracture) 'envelope' is greater than 150m wide (i.e. from the main fault plane down to the coastline).

In the footwall section, deformation is less intense. Data collected from a number of outcrop sites along the fault zone, suggest a footwall deformation (fracture) 'envelope', which is less than 100m wide. This consists predominantly of small-scale structures, spaced at 1-3m intervals, with displacements rarely exceeding 0.5m. Fracture spacing generally increases away from the main fault surface (spacing immediately adjacent to the Ghar Lapsi Fault - 0.5 to1.0m; spacing 30m from the main fault - 2.0 to 3.0m). No scanlines could be obtained at this locality.

Wied Maghlaq (West): (448900mE, 3965200mN): Sub-seismic Scale Deformation Associated with the Ras il-Hamrija Fault

The topographic expression of the Ras il-Hamrija Fault is expressed by a large fault scarp, which throws down to the southwest, displacing the Lower Globigerina Limestone Member (Miocene) against the Attard Member (Oligocene) (~73^0/121^0) (**Fig. 8.10**). Average displacements along the fault zone are approximately 25-40m. The nature of sub-seismic scale deformation in the hangingwall section of this fault zone is summarised in **Plate 8.6** and **Figure 8.11** (**Enclosure 5**). This diagram is accompanied by scanline data from three regularly spaced sections orthogonal to the main fault strike (Table 8.3).

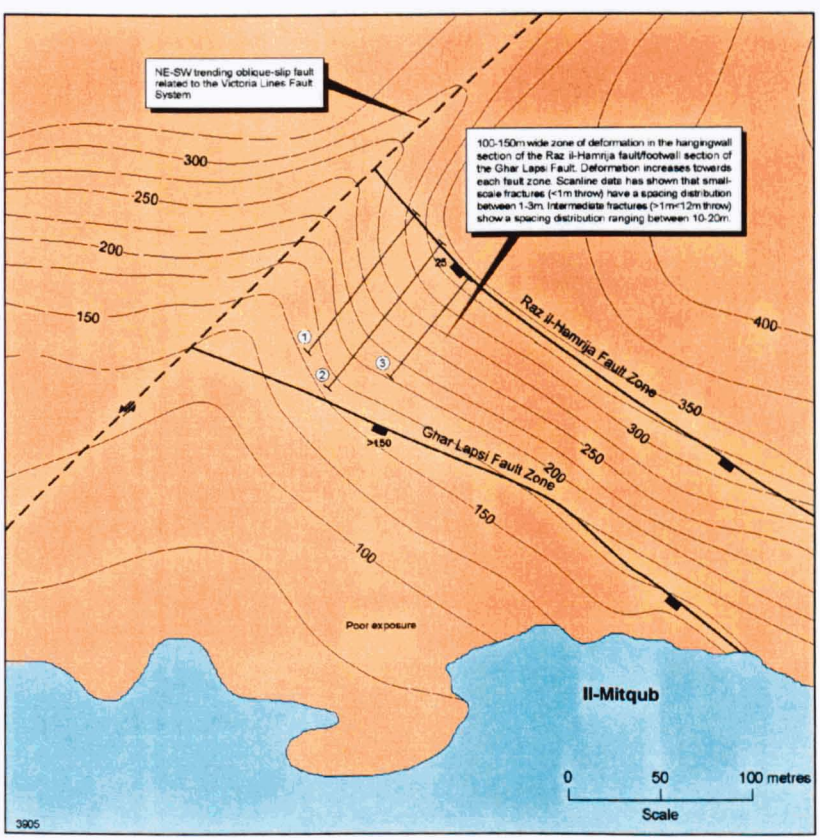

Fig. 8.10. Location map showing the Ras il-Hamrija Fault just west of Wied Babu (448900mE, 3965200mN).

The fieldwork observations and scanline data presented show that intermediate scale faults and fractures in the hangingwall section of the Ras il-Hamrija Fault have spacing distributions between 12-18m. Displacements on these structures generally do not exceed 5m. Smaller scale faults and fractures are more closely spaced (1-3m intervals), and have only minor displacements (commonly <0.2m) (**Plate 8.6**). These spacing estimates are in good agreement with calculations from scanline data (Table 8.3). Although it was difficult to find reasonable exposure in close proximity to the Ras il-Hamrija Fault, general field observations suggest that fracture intensity increases significantly towards the main fault plane (**Fig. 8.6**).

	Scanline 1	Scanline 2	Scanline 3
Sub-seismic Scale Fracture Spacing (all fractures)	2.40m	2.02m	1.56m
Sub-seismic Scale Fracture Spacing (<1m throws)	2.96m	2.34m	1.71m
Sub-seismic Scale Fracture Spacing (>1m throws)	12.70m	15.06m	17.59m

Table 8.3. Summary of sub-seismic scale fracture spacing along three scanlines aligned orthogonal to the main fracture trend in the hangingwall of the Ras il-Hamrija Fault.

Data from the three scanline sections at Wied Maghlaq have been plotted to determine whether there was a spacing relationship between different sized structures within the hangingwall section of the Ras il-Hamrija Fault (**Fig. 8.12a-d**). This follows on from the aforementioned discussion. Each scanline is approximately 100m in length. The data shows that there is a relationship in the spacing of small-, and intermediate-scale structures in the hangingwall section of the Ras il-Hamrija Fault (**Fig. 8.12 a-c**). **Figure 8.12d** plots the data from all of the scanlines. It also incorporates several pseudo-data points for large-scale faults (throws: >12m), to establish whether a relationship exists throughout the whole dataset. The pseudo-data points modelled are based on a spacing distribution between 80-100m, which is a realistic representation of large-scale faulting at this outcrop. The projection of the straight-line segment of each curve, suggests that all the fractures mapped within hangingwall section of the Ras il-Hamrija Fault form part of the same spacing distribution (**Fig 8.12d**). This is significant in that it demonstrates that the data obtained from fieldwork can be directly integrated into the subsurface environment.

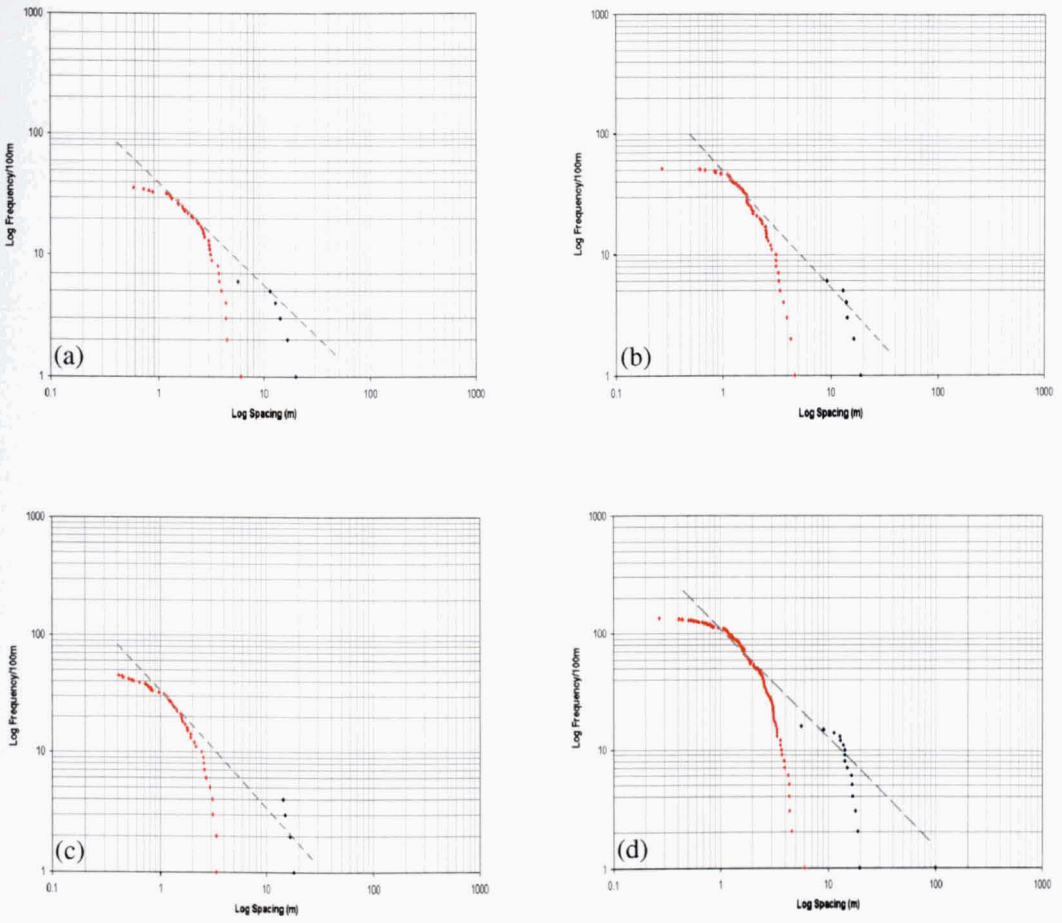

Fig. 8.12. Log-log plots showing the spacing distributions of small and intermediate-scale faults and fractures along the three scanline sections at Wied Maghlaq. (a) Scanline 1, (b) Scanline 2, (c) Scanline 3, and (d) Scanlines 1-3 (all data). The spacing of small- and intermediate-scale structures shows a relationship, which fits on a straight line. Several pseudo-data points have been added to the dataset in Plot (d) in order to establish whether a scaling relationship exists throughout the dataset. The projection of the straight-line segment of each curve (indicated) shows that all the data belongs to the same scaling population.

The size of the hangingwall deformation zone associated with the Ras il-Hamrija Fault is difficult to quantify, due to the interaction of this zone with footwall deformation associated with the Ghar Lapsi Fault. However, the assumption made from fieldwork investigations over the whole area (**Fig. 8.6**) suggests a minimum width of at least 60-70m. Footwall deformation is less intense (approximately 30m).

Blue Grotto: (450900mE, 3964300mN): Sub-seismic Scale Deformation Associated with the Blue Grotto Fault

The Blue Grotto Fault, situated at the eastern end of the study area, throws the Lower Globigerina Limestone Member against the Xlendi Member (~59^0/132^0) (**Fig. 8.13**). Displacements along the outcrop range between 10-15m.

Plate 8.7 and **Figure 8.14** (**Enclosure 5**) provide a detailed overview of the distribution of sub-seismic scale deformation associated with the Blue Grotto Fault. Unfortunately due to the inaccessible nature of the outcrop scanline data could not be obtained. In summary, deformation in the hangingwall section comprises:

- A 0.5-1m zone of fault gouge, which contained sub-angular to angular blocks mainly of the Lower Globigerina Limestone Member (Globigerina Limestone Formation);

- An ~80m wide zone of sub-seismic scale fracturing. Intermediate scale fracture spacing: ~5-20m, Average displacements: <2m; Small-scale fracture spacing: 2-4m, Average displacements: <0.3m. Fracture intensity is greater in the lower Xlendi Member (**Plate 8.7** and **Fig. 8.14**)

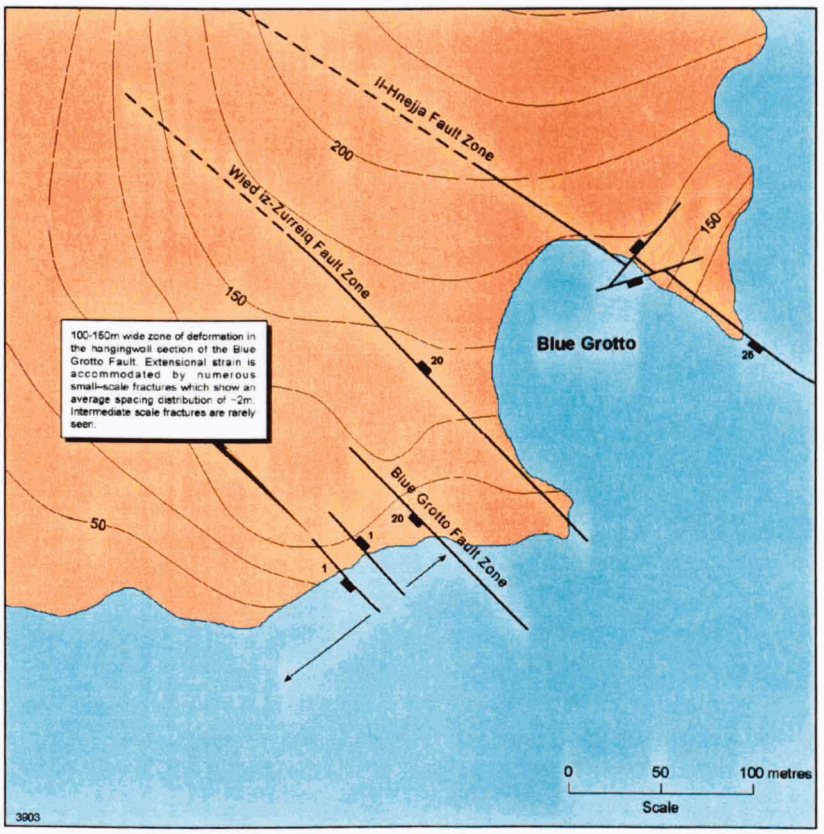

Fig. 8.13. Location map showing the Blue Grotto Fault (450900mE, 3964300mN).

Wied iz-Zurreiq: (450700mE, 3964600mN): Sub-seismic Scale Deformation Associated with the Il-Hnejja Fault

The Il-Hnejja Fault is located at the northern end of Wied iz-Zurreiq. It is expressed by a large fault scarp, which throws down to the southwest. It displaces the Xlendi

Member against the Attard Member (**Fig. 8.15**). Average fault displacements at this locality are approximately 15-20m. **Plate 8.8** and **Figure 8.16** (**Enclosure 5**) summarise the nature of sub-seismic deformation within the hangingwall block of this fault zone. It is accompanied by calculated spacing estimates, which were obtained from two scanline surveys, oriented perpendicular to the main fault strike (Table 8.4). these surveys provide an indication of the intensity of fracturing in the hangingwall section, although there short length (~40m) precludes a detailed examination.

Field observations and scanline data suggest that intermediate-scale structures present have spacing distributions of ~18m, with displacements rarely exceeding 4m. Smaller scale fractures show spacing distributions of 1-1.5m and have only minimal displacements.

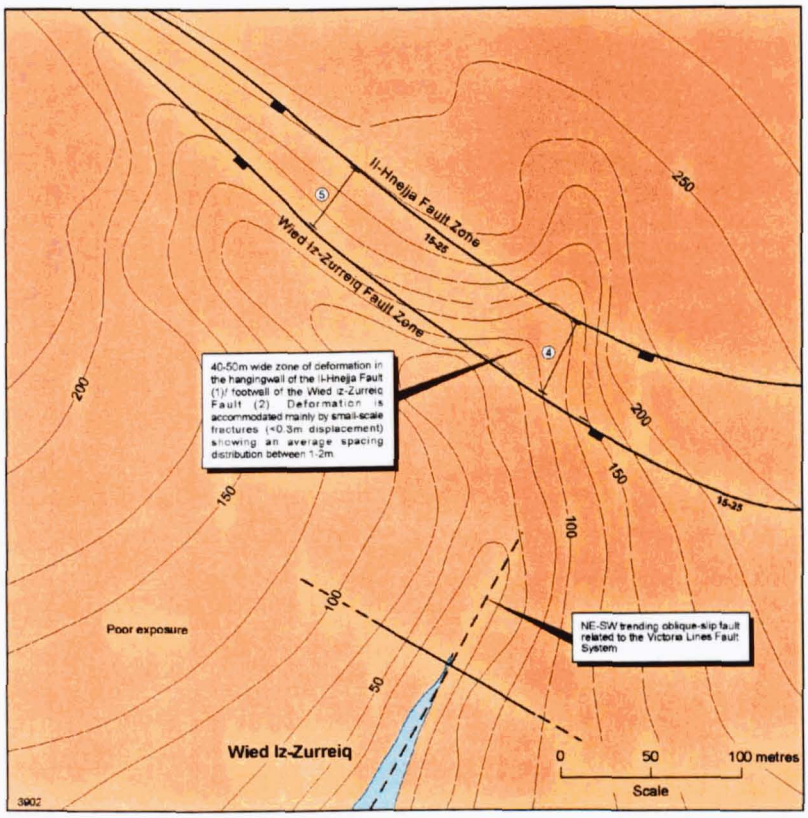

Fig. 8.15. Location map showing the Il-Hnejja and Wied iz-Zurreiq Faults at the northern end of Wied iz-Zurreiq (450700mE, 3964600mN).

	Scanline 4	Scanline 5
Sub-seismic Scale Fracture Spacing (all fractures)	1.13m	1.02m
Sub-seismic Scale Fracture Spacing (<1m throws)	1.20m	1.02m
Sub-seismic Scale Fracture Spacing (>1m throws)	17.53m	-

Table 8.4. Summary of sub-seismic scale fracture spacing along two scanlines aligned orthogonal to the main fracture trend in the hangingwall section of the Il-Hnejja Fault.

8.5.5. Observations from Selected Quarries

A number of quarries were studied within Malta in an attempt to validate the observations that were made along the Maghlaq Fault System. Although some of the examples presented in this section are not ideal, it was felt that the observations made were of some use, and generally supported the main conclusions established from the preceding study. Non-ideal examples included some NE-SW trending structures, which displayed a late component of the dextral strike-slip movement. All of the quarries studied exploit the Attard, Xlendi and Maghlaq Members of the Lower Coralline Limestone Formation. Hence the structures analysed were in comparable lithologies to the sub-surface reservoir in Hasdrubal.

Ix-Xaqqa Quarry

The Ix-Xaqqa quarry (447400mE, 3966000mN) (**Fig. 8.17**) provided good exposure in which to examine the nature of fracturing within the footwall section of the NE-SW trending Ix-Xweiki Fault, and the deformation associated with oblique-slip movements on the Ix-Xaqqa Fault. In this quarry, the Attard and Xlendi Members are extracted for use as building stone. **Plate 8.9** locates the quarry, and shows the two main study areas. The principal observations that were made are presented in **Plates 8.10 & 8.11** and **Figures 8.18 & 8.19** (**Enclosure 6**). Unfortunately, scanline information could not be obtained due to the inaccessibility of the exposure.

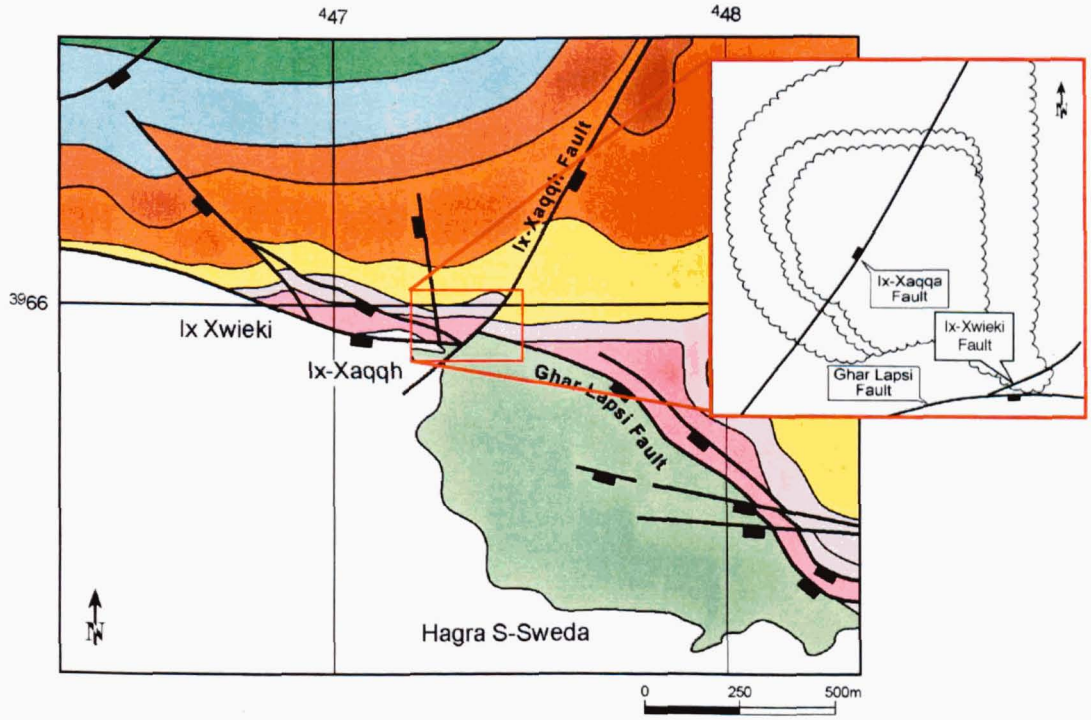

Fig. 8.17. Location map of the Ix-Xaqqa Quarry (447400mE, 3966000mN).

Footwall Deformation Associated with the Ix-Xwieki Fault

The information given in **Plate 8.10** and **Figure 8.18** summarises the intensity and style of fracturing within the footwall section of the NE-SW Ix-Xweiki Fault. This fault is situated approximately 20m south of the southern limit of the outcrop shown in **Plate 8.10**. According to Debono & Xerri (1993) displacements at this locality are ~25m down to the southeast. Slickensided fracture surfaces on antithetic structures associated with this fault show almost pure dip-slip throws ($87^0/278^0$). All the fractures observed in this section trend sub-parallel to the main fault plane ($71^0/037^0$ NW). Most have throws that rarely exceed 0.2m (**Plate 8.10** and **Fig. 8.18**). Spacing estimates across this zone generally are between 1-5m. At the southern limit of the outcrop (i.e. 20m north of the main fault), spacing distributions are ~1-2m. These values increase away from the fault. Footwall deformation associated with this fault appears to die out towards the north of the exposure, giving a total width of ~60m (**Fig. 8.18**). Unfortunately, due to the nature of outcrop, the distribution and intensity of deformation in the hangingwall section deformation could not be determined.

Hangingwall/Footwall Deformation Associated with the Ix-Xaqqa Fault

The Ix-Xaqqa Fault intersects the southwestern face of the quarry (**Fig. 8.17**). It trends approximately NE-SW and consists of a steeply dipping fault plane, which throws down to the southeast ($85^0/016^0$NW). It is characterised by oblique-slip displacements, and a composite vertical throw of approximately 10-15m. The photomontage and field illustration presented in **Plate 8.11** and **Figure 8.19** show the nature and extent of deformation in the hangingwall and footwall sections of the main fault. Hangingwall deformation may be summarised into; 1) A ~4-5m wide zone of intense brecciation, immediately adjacent to the main fault plane, characterised by a fracture spacing distribution between 0.1-0.2m; 2) A ~8m wide zone of small-scale fracturing characterised by spacing distributions of 0.8-1.0m. Average displacements on these structures do not exceed 0.2m; and 3) A ~45m wide zone consisting of regularly spaced small/intermediate-scale fractures which have displacements of ~1m or less. The few intermediate-scale structures that were identified along this zone, were regularly spaced at 10-15m intervals. Hangingwall deformation associated with the Ix-Xaqqa Fault diminishes towards the northeastern part of the quarry, giving a total width of ~60-70m. Footwall deformation is less intense, and is characterised by a few small-scale structures that are spaced at 5-10m intervals. Average displacements on these fractures are no greater than 0.5m.

Lapsi Quarry

The Lapsi Quarry is located to the west of Wied Maghlaq, just north of the main Ghar Lapsi Fault Zone (448700mE, 3965400mN)(**Fig. 8.20**). The northwestern face of the quarry is cut by two NE-SW trending intermediate-scale faults, which are related to the Victoria Lines System ($57^0/019^0$ NW and $55^0/024^0$ NW). These faults have minor displacements (~1-1.5m) and show almost pure dip-slip displacements ($80^0/357^0$). **Plates 8.12, 8.13** & **Figure 8.21** (**Enclosure 7**) summarise the style and intensity small-scale fracturing associated with these structures.

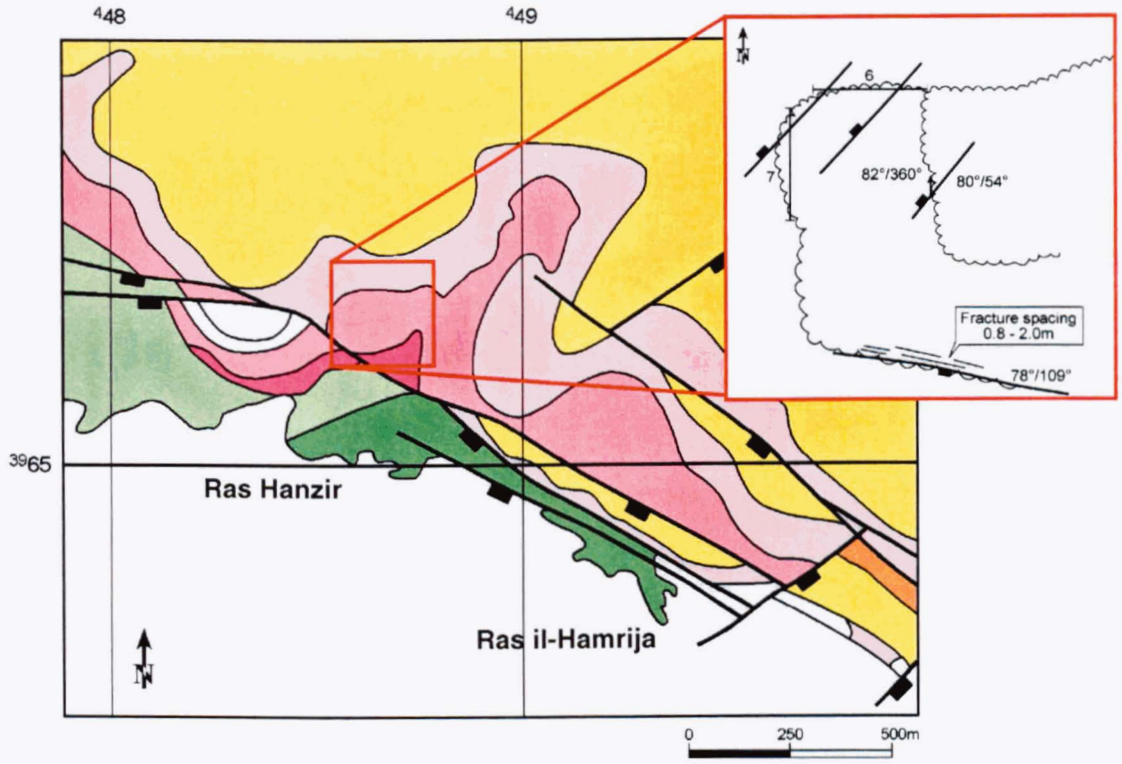

Fig. 8.20. Location map of the Lapsi Quarry (448700mE, 3965400mN).

Scanline data from two orthogonal sections in the quarry face show that the two intermediate-scale faults are spaced between 13-16m (Table 8.5). Small-scale structures across the zone are spaced at 0.4-0.6m intervals. These results correlate very closely to the estimates given for parts of the Maghlaq Fault System. The inset given with **Figure 8.21** shows the spacing of small-scale fractures along this zone.

	Scanline 6	Scanline 7
Sub-seismic Scale Fracture Spacing (all fractures)	0.56m	0.47m
Sub-seismic Scale Fracture Spacing (<1m throws)	0.58m	0.49m
Sub-seismic Scale Fracture Spacing (>1m throws)	13.38m	15.77m

Table 8.5. Summary of sub-seismic scale fracture spacing associated with the fault zone shown in Plate 8.13.

Naxxar Gap Quarries

The Naxxar Gap quarries are located just north of Naxxar (448800mE, 3975700mN)(**Fig. 8.22**). Structurally, they are situated in the footwall of the NE-SW trending Victoria Lines Fault (N.B. the northern limit of the quarry is marked by the main fault plane). This structure has vertical displacements in excess of 100m, and also shows evidence of late, dextral strike-slip overprinting, which has been attributed to the opening of the Straits of Sicily Rift Zone (Reuther & Eisbacher, 1985). The southern limit of the quarry is marked by the St. Margerita Fault, which throws the Xlendi Member down to the NW, against the Attard Member. Debono and Xerri (1993) have shown that it has composite vertical displacement of ~20-30m.

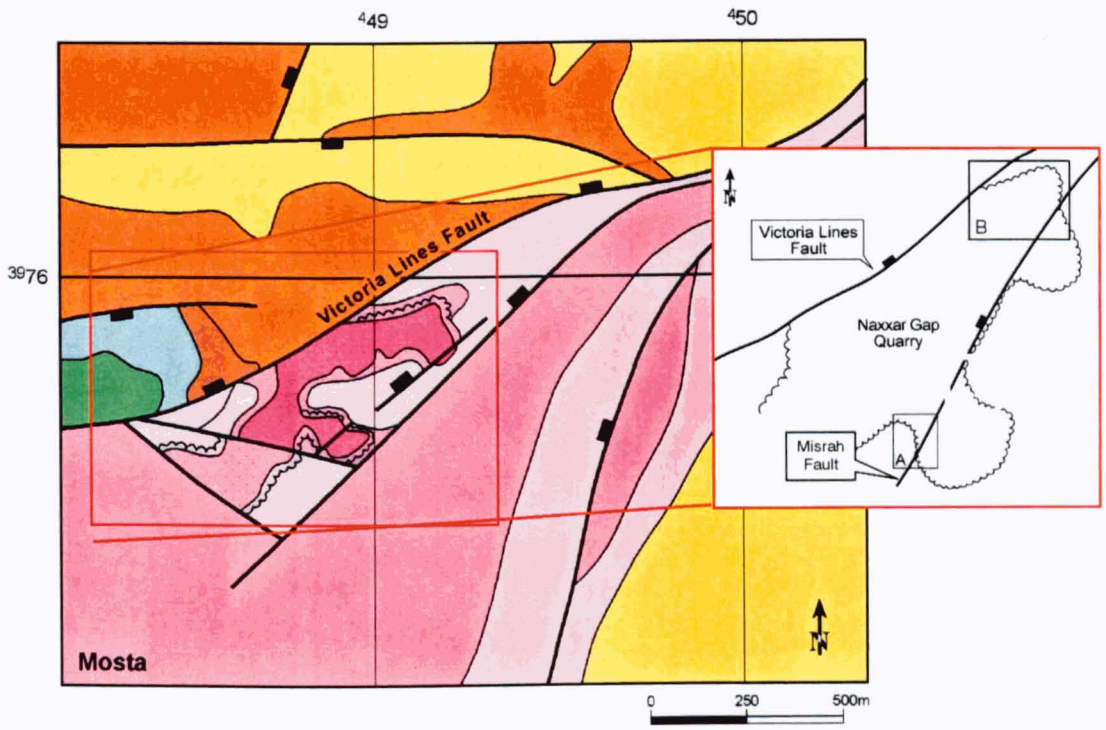

Fig. 8.22. Location map of the Naxxar Gap Quarries (448800mE, 3975700mN).

Within the quarry itself, a number of NE-SW trending intermediate-scale faults have been recognised. The largest of these is the NE-SW trending Misrah Fault ($66^0/058^0$ NW), which has a displacement of ~10-15m, down to the northwest (**Fig. 8.22 & Plate 8.16**). Most of the structures recognised show dip-slip displacements, although late dextral overprinting has been observed on a number of fault planes (refer to the insets in **Figure 8.25**). **Plates 8.14-8.19** and **Figures 8.23-8.25** (**Enclosure 8**) summarise the nature of deformation associated with some of the intermediate structures present.

Intermediate-Scale Fracture Spacing in the Footwall of the Victoria Lines Fault

Plate 8.14 provides an overview of the quarry. This is accompanied by **Plates 8.15-8.16**, which provide enlarged views of the main study areas. **Plate 8.17**, together with the illustration given in **Figure 8.23** summarise the nature of deformation along a 100-150m wide section through the footwall of the Victoria Lines Fault (N.B. the northern end of the outcrop is approximately 100m from the main fault plane). The intermediate-scale structures mapped along this zone only have minor displacements (with the exception of the Misrah Fault) and are generally spaced at 20-40m intervals. This spacing distribution, although slightly larger is not dissimilar to those identified at other localities. **Plate 8.18** and **Figure 8.24** show the nature of deformation associated with one of these intermediate-scale faults. This structure trends ~NE-SW ($69^0/080^0$ SE), and has a displacement ~5-10m down to the southwest. Fractures trend sub-parallel to the fault plane ($85^0/078^0$ SE). Scanline logs from various locations around this fault show the spacing distributions within the hangingwall and footwall sections immediately adjacent to the main fault plane (Table 8.6)(refer to **Figure 8.24** for the position of individual scanlines). The width of hangingwall deformation is difficult to ascertain, although field studies suggest that it is >40m wide.

	Scanline 8	Scanline 9	Scanline 10
Sub-seismic Scale Fracture Spacing (all fractures)	0.53m	0.29m	0.72m
Sub-seismic Scale Fracture Spacing (<1m throws)	0.56m	0.29m	0.83m
Sub-seismic Scale Fracture Spacing (>1m throws)	10.87m	>9.16m	5.54m

Table 8.6. Summary of small/intermediate-scale fracture spacing associated with the Misrah Fault Zone.

Hangingwall Deformation Associated with the Misrah Fault

Plate 8.19 and **Figure 8.25** show the nature of deformation in the hangingwall section of the Misrah Fault ($74^0/041^0$ NW). This fault shows evidence of early dip-slip displacements, with later dextral strike-slip overprinting (refer to insets accompanying **Figure 8.25**). Deformation associated with this fault can be separated into 1) a ~4m wide zone of intense brecciation immediately adjacent to the main fault plane, characterised by a fracture spacing distribution between 0.04-0.2m; 2) a zone >30m wide (limit of outcrop) which consists of regularly spaced small-scale fractures (1-3m) with only minor displacements (generally less than 0.3m). Unfortunately, the exposure was inaccessible, and hence scanline data could not be obtained.

Attard Quarries

The Attard quarries, which are located southwest of Attard (449200mE, 3971400mN), expose two intermediate-scale faults (**Fig. 8.26**). These structures trend $80^0/056^0$ SE and $68^0/140^0$ NE, and show almost pure dip-slip displacements ($76^0/140^0$ for the structure in Study Area A). **Plates 8.20-8.21** and **Figures 8.27-8.28** (**Enclosure 9**) summarise the distribution of deformation associated with each structure. Scanline data from various localities adjacent to the main fault plane in Study Area A is presented in Table 8.7. This data shows average spacing distributions of 1.35m and 0.18m, within the hangingwall and footwall sections respectively. Average displacements across the entire zone, range from 0.01m to 0.4m. Deformation in the hangingwall extends for at least 20m (i.e. the limit of available outcrop). The zone of footwall deformation is smaller (~5-10m). Deformation associated with the fault in Study Area B is concentrated within a 2-3m wide zone within the footwall section of the main fault. Deformation in the hangingwall block is minimal (**Plate 8.21**).



Fig. 8.26. Location map of the Attard Quarries (449200mE, 3971400mN)

	Scanline 11	Scanline 12
Sub-seismic Scale Fracture Spacing (all fractures)	1.35m	0.18m
Sub-seismic Scale Fracture Spacing (<1m throws)	1.35m	0.18m
Sub-seismic Scale Fracture Spacing (>1m throws)	-	-

Table 8.7. Summary of small-scale fracture spacing along two scanlines adjacent to the main fault plane observed in Study Area A. Scanline 11 (Hangingwall); Scanline 12 (Footwall).

8.6. Summary & Discussion of Observations

Faults and fractures at outcrop were classified into three distinct groups reflecting the resolution constraints imposed by seismic and core data:

- Large (seismic scale) faults/fractures: Displacements of 12m or more (i.e. above the limit of seismic resolution);
- Intermediate (sub-seismic scale) faults/fractures: Displacements ranging between 1-12m (i.e. below the limit of seismic resolution but above the limit of core resolution);
- Small (sub-seismic scale) faults/fractures: Displacements less than 1m (i.e. below the limit of seismic resolution and easily resolved in core).

The characterisation of faults and fractures into these groups provided a simple but effective way to gain an insight into the distribution and frequency of all structures identified at outcrop. Maximum use was made from available outcrops. However, it must be stressed that rigorous data collection was often constrained by the quality of exposure. Hence, good quality, unbiased scanline data was frequently hard to obtain.

Observations from various localities along the Maghlaq Fault System were generally fairly consistent. These conclusions were supported by similar structural data from each quarry. The model presented in **Figure 8.29** summarises the main consistencies in observations, and provides a best estimate of the spatial distribution and relationship of seismic and sub-seismic scale fractures in the Maltese analogues (N.B. it provides a section of the Maghlaq Fault System). Table 8.8 accompanies this diagram, and attempts to define a range of numbers which relate to the spacing distribution of various scale structures. Although not definitive, the distributions presented provide the best estimate from available data.

	Throw (m)	Spacing (m)	Hangingwall Deformation Zone (m)	Footwall Deformation Zone (m)
Seismic Scale Fracture Distribution (>12m throw)	12 to 150+	80 to 200+	~60 to 150+	~20 to 70+
Sub-seismic Scale Fracture Distribution (1-12m throw)	1 to 12	5 to 100	-	-
Sub-seismic Scale Fracture Distribution (<1m throw)	0.01-1	0.05 to 5	-	-

Table 8.8. Spatial distribution of seismic and sub-seismic scale faulting and fracturing in the Maghlaq System. The range of values shown, have been approximated from field data.

CONTAINS PULLOUTS

Seismic-scale faults within the Maltese analogues showed displacements ranging from 12m to 150+m. The Ghar Lapsi fault Zone is the largest with over 150m displacement (N.B. that the displacement estimates for most of the seismic scale faults described are a minimum estimate, calculated from the reported thickness of lithostratigraphic units in this area (Debono & Xerri, 1993). All the faults analysed in the Maghlaq Fault System were oriented NW-SE, and showed predominantly dip-slip displacements. Elsewhere, within some of the quarry sections, NE-SW trending faults (associated with the Victoria Lines System), showed evidence of early dip-slip displacements with later dextral strike-slip overprinting. Observations from these structures were treated with caution, as they did not represent good analogues for the subsurface structures in the Hasdrubal acreage.

Along the Maghlaq Fault System, seismic scale faults were generally spaced at regular intervals between 80 to 200+m. The discrepancy between this, and the spacing of similar sized structures in the Hasdrubal area could be attributed to the fact that:

- the small sample width across the Maghlaq Fault System may not be representative of the outcropping fault distribution on Malta;
- this system of faults is located very close to the main bounding fault zone of the Malta Graben, and thus may be more deformed.

The spatial distribution of small- and intermediate-scale fracture populations associated with seismic scale faults was analysed through scanline construction and general field observations. Consistencies in observations for a number similar-sized structures, allowed the prediction of subsurface distribution and frequency for a number of seismic scale faults in the Hasdrubal area. The following paragraphs outline some of generalised observations made from field outcrop studies.

In general, the intermediate-scale structures mapped had displacements of 1-5m. These structures were regularly spaced between 5-25m, generally increasing in frequency towards seismic-scale faults. Intermediate-scale faults with displacements ranging between 5-12m were only occasionally identified. Small-scale structures within the deformation zones associated with large and intermediate-scale faults showed average displacements of less than 0.5m. The spacing of these structures varied from ~0.05m immediately adjacent to intermediate and seismic-scale faults, to up to 5m, away from the main fault plane (refer to **Figure 8.29** for a summary of all the observations made).

Scanlines from the Wied Maghlaq area provided a reasonable dataset in which to quantify the spacing distribution of faults and fractures at all scales. These scanlines were approximately 100m in length, and therefore provided a reasonable sample of intermediate- and small-scale structures. Several realistic pseudo-data points were added to the dataset in order to model the spacing distribution of large-scale faults. The log-log plots presented in **Figure 8.12a-d** showed a spacing relationship for all the fractures mapped along these scanlines (i.e. within hangingwall section of the Ras il-Hamrija Fault). This relationship obviously needs to be tested with more data. However, if it is valid, it provides a powerful tool in which to accurately integrate fieldwork data into the subsurface environment.

It was observed during the field studies that the relative width of deformation associated with seismic-scale structures is controlled by the nature and size of the individual faults themselves. Obviously, larger faults (in terms of displacement and length) possess larger zones of deformation. In addition, the field studies have shown that strike-slip structures generally have narrower zones of deformation than corresponding dip-slip faults. **Figure 8.30** shows the minimum extent of deformation associated with seismic-scale structures mapped along the Maghlaq Fault System. The actual width of the deformation 'envelopes' associated with these structures is often constrained by the size and quality of outcrop. Hence, only minimum estimates are given. Frequently, deformation zones interact with each other, causing complicated spacing relationships. A combination of the data from this map, together with observations from the quarry studies has been used to superimpose likely 'deformation envelopes' (i.e. zones of deformation) around seismic scale faults over the top reservoir depth structure map in the Hasdrubal area (**Fig. 8.31**). This map provides minimum estimates for the extent of deformation associated with these faults.

From **Figure 8.31**, it is possible to identify a relationship between fracture frequency, observed in the Hasdrubal wells, and proximity to seismic scale faulting. Hasdrubal -2 lies outside any recognisable 'deformation envelope', and hence is not significantly fractured. On the other hand Hasdrubal -3 and particularly Hasdrubal -4 lie in very close proximity to, and within zones of deformation. As a consequence, they are more fractured; Hasdrubal -4 showing the highest fracture frequencies (refer to **Figure 7.30**). It is stressed that numerous fractures in the Hasdrubal wells are directly associated with stylolites, and therefore not fault-related. However, it is apparent that a relationship still exists between this style of fracturing and proximity to seismic scale

faulting. It could therefore be argued that the strain associated with movements on a specific fault is accommodated by both reactivation on pre-existing stylolite-associated fractures, and the generation of fault-related fractures.

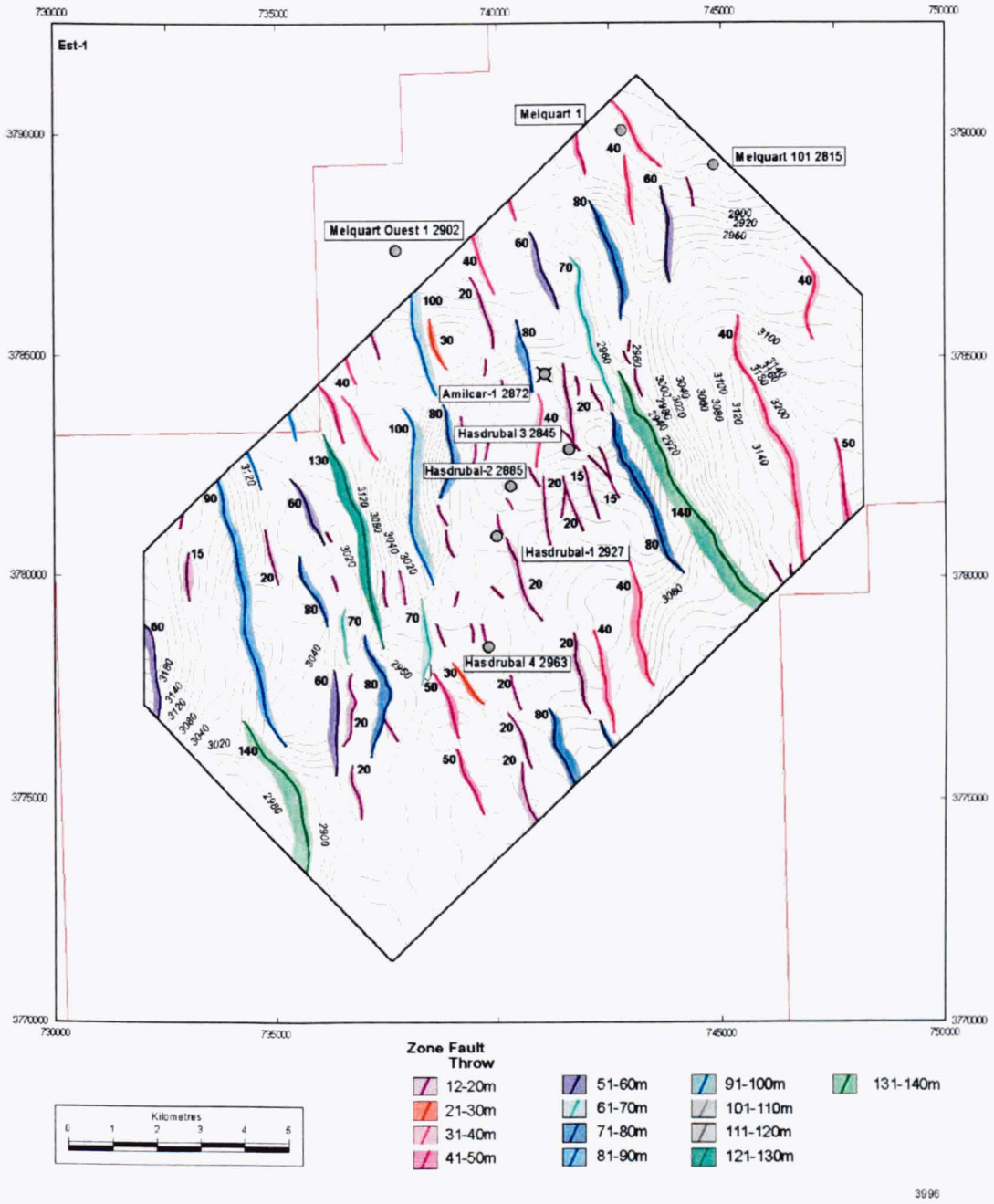

Fig. 8.31. Top reservoir depth structure map over the Hasdrubal area, showing the broad extent of deformation associated with seismic-scale faults within the Hasdrubal accumulation. The size of the deformation zones are constrained by fieldwork evidence.

Chapter 9

Discussion & Conclusions

9.1. Introduction

In this chapter, the structure and evolution of the south-western margin of the Pelagian Platform is summarised, and the tectonic controls on carbonate reservoir development, for the Miskar and Hasdrubal Fields are considered. The main conclusions provide a useful tool for planning well position and orientation in exploration and field development. Suggestions for further study are also introduced.

9.2. Regional Setting of the Pelagian Platform

The Pelagian Platform forms a distinct structural element on the North African continental margin. It is bounded by several deep-seated fault zones: i) the North-South Axis, ii) the Gafsa-Jerrafa Fault, iii) the Malta Escarpment, and iv) the Medina Escarpment.

Field and seismic interpretation undertaken during the course of this thesis have demonstrated that the structural configuration of the Pelagian Platform is characterised by a complicated network of fault-controlled basins and highs (e.g. Gabes-Tripoli Basin, Lampedusa-Medina Plateaux and the graben associated with the Straits of Sicily Rift Zone). It is demonstrated that the evolution of these structures has been controlled in part, by strike-slip deformation processes (refer to Chapters 2 and 3 for a detailed review). A strike-slip model of internal deformation on the Pelagian Platform alleviates the large spatial overlap problems between the Adriatic promontory and the European continental margin when Africa and Europe are restored back through the Mesozoic and Tertiary (Cohen et al., 1980; Jongsma et al., 1985; Reuther & Eisbacher, 1985; Dewey et al., 1989).

9.3. Structure & Evolution of the Gulf of Gabes

The south-western region of the Pelagian Platform is sub-divided into four principal tectonic domains (i.e. the Gabes-Tripoli Basin, the Lampedusa-Medina Plateau, the Kerkennah High and the Jerrafa-Djerba High). The Gabes-Tripoli Basin, which hosts the Miskar and Hasdrubal Fields is characterised by a pervasive system of approximately NW-SE trending extensional faults, which are sub-parallel to the basin axis. This fault system has produced horst and graben topography in the Mesozoic and Tertiary succession. Seismic data indicates that most of the extensional faulting in the Gabes-Tripoli Basin is oblique to the bounding Gafsa-Jerrafa and Mahdia-Medina Fault Zones. This geometry supports a model by which the Gabes-Tripoli Basin developed in a transtensional setting within a large dextral shear zone (i.e. the Gafsa-Medina Shear Zone (GMSZ)). Dextral movements on this shear zone commenced in the middle to late Cretaceous, and were caused by a shift in the relative motion of the African and European plates. The model presented in **Figure 9.1** illustrates the role of strike-slip deformation processes in the development of the Gabes-Tripoli Basin.

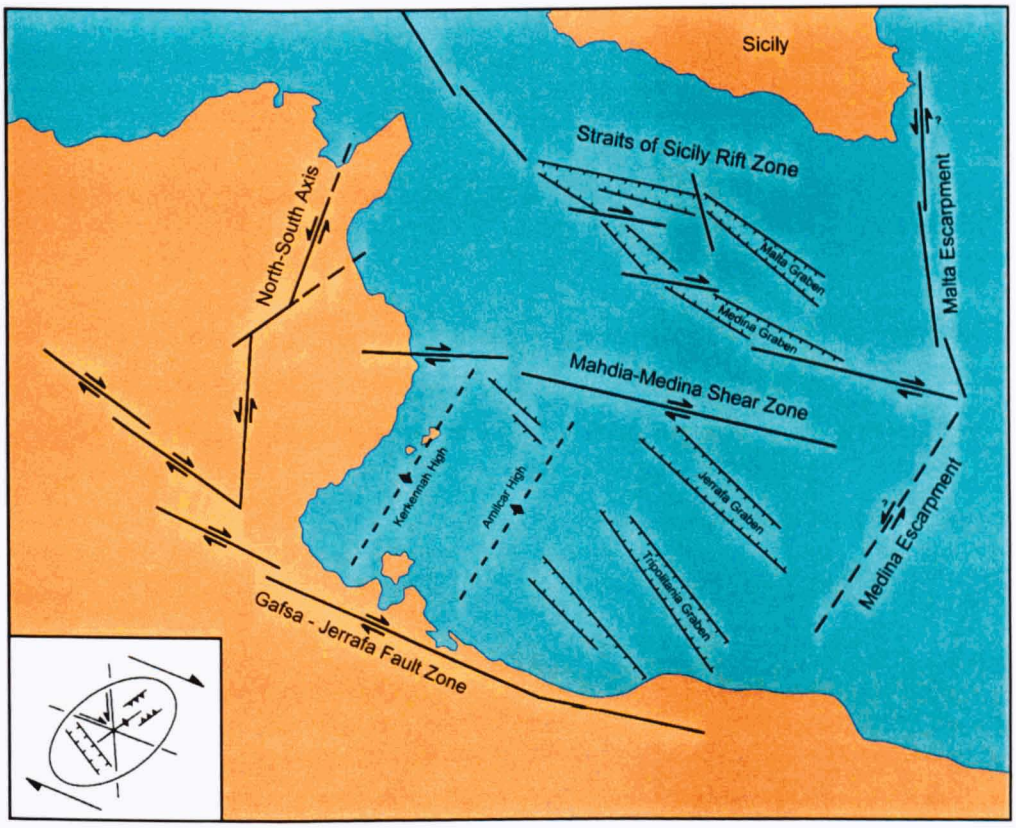

Fig. 9.1. Simplified tectonic map of the Pelagian Platform, showing the role of strike-slip deformation in the development of the Gabes-Tripoli Basin and the Straits of Sicily Rift Zone. Dextral strike-slip reactivation along the Gafsa-Jerrafa and Mahdia-Medina Fault Zones and on various E-W trending structures in the Straits of Sicily has created the Gabes-Tripoli Basin and the Malta, Medina, Linosa and Pantelleria Grabens respectively.

The Kerkennah and Amilcar Highs in the western part of the Gabes-Tripoli Basin are interpreted to have formed by transpressional reactivation of pre-existing basement lineaments during oblique-slip deformation associated with dextral movements on the Gafsa-Medina Shear Zone.

The preceding discussion has shown that the structural evolution of the Gabes-Tripoli Basin is characterised by alternate phases of transtensional and transpressional tectonics (refer to Chapter 3 for a detailed account of the timing and duration of these tectonic processes)(**Fig. 9.2**). This has led to cycles of basin subsidence and inversion. Phases of extension and subsidence may be expected to generate stylolites (and stylolite-associated fractures), in addition to fault-related fractures, at the reservoir scale. Later inversion events would reactivate early fracture and stylolite systems.

While all these cycles throughout the history of the basin are capable of generating tectonic fabrics that contribute to reservoir development, only the phase immediately preceding hydrocarbon emplacement (or associated with the phase of tectonism controlling trap formation) will actively contribute to the present day reservoir system. An exception would be where palaeo-fractures have allowed fluid movements, resulting in diagenetic changes to the reservoir fabric, or where the present day stress state has reactivated ancient fracture systems.

9.4. Tectonic Controls on Reservoir Development

The structure and evolution of the Miskar and Hasdrubal Fields reflect the main tectonic processes affecting the Gabes-Tripoli Basin. The two fields are situated in horst blocks along the Amilcar High. This palaeohigh was established during the middle-late Cretaceous and remained a prominent high into the Tertiary. Throughout this period it was affected by various phases of transpression and transtension. **Figure 9.2** summarises the main tectonic phases in the evolution of each field, and relates these events to the development of the Miskar and Hasdrubal reservoirs.

The tectonic fabric of the Miskar and Hasdrubal reservoirs is dominated by stylolites and fractures. Well test data from each field demonstrates that the occurrence of these features enhance reservoir flow (Thompson, 1998; Pritchard, 2000). An appreciation of the processes that have caused fracturing in these reservoirs is thus critical in field development and management.

CONTAINS PULLOUTS

Stylolitisation

Two types of stylolite have been identified in each reservoir: i) aggregate stylolites and, ii) intergranular stylolites. Aggregate stylolites are divided into, high amplitude 'sutured' stylolites and, low amplitude 'non-sutured' stylolites. High amplitude 'sutured' stylolites tend to develop in packstone to grainstone fabrics (e.g. R1 Superior/Inferior and El Garia reservoirs), whereas low-amplitude 'non-sutured' stylolites form in mudstone to wackestone intervals (e.g. Abiod reservoir). Most stylolites are bedding-parallel, compactional features that have formed in response to the overburden pressure (σ_v). They preferentially develop along bed boundaries where there is a variation in the composition between lithological units. Consequently, stylolite frequency appears to be directly related to bedding surface distribution.

The types of stylolite observed in this study commonly occur in many carbonate reservoirs worldwide. For instance, Nelson (2001) provides good examples of both types of stylolite from the Darius Field, Iran (Yamama Limestone), the Amos Field, Alabama, USA (Smackover Limestone), and the Pineview Field, Wyoming, USA (Twin Creek Limestone). Other documented examples come from the chalk reservoirs (Hod, Tor and Ekofisk Formations) in the Norwegian and Danish sectors of the North Sea (e.g. Ekofisk, Eldfisk, Albusskjell, Kracka and Skjold Fields) (Agarwal et al., 1997; D'Heur, 1990; Watts, 1983; Megson, 1992), the Asmari, Ilam and Sarvak reservoirs of the Ahwaz Field in southwestern Iran (Bordenave & Burwood, 1990; Ala et al., 1980), and the nummulitic Eocene to Oligocene reservoirs of the Kirkuk Field in northern Iraq (Daniel, 1954; Al-Qayim et al., 1980; Majid & Veizer, 1986). From these documented examples, similar comparisons can be drawn to the aforementioned observations made in this study. For instance, Watts (1983) shows a relationship between stylolite distribution and lithology within the Albusskjell Field that agrees with the conclusions in this study. In this example, stylolites are abundant in the more brittle Maastrichtian chalks and absent to weakly developed in the argillaceous or highly porous Danian chalks.

It has been suggested in the literature that stylolites generally have a negative impact on reservoir performance (Nelson, 2001; Priest, 1993). This is valid for many reservoirs documented. However, it has been shown in Hasdrubal and Miskar that stylolite presence can improve reservoir quality. In these fields, high amplitude stylolites typically crack during inversion, and also act as nuclei for stylolite-associated fractures (refer to next section). Alternatively, low amplitude stylolites

frequently develop brittle fabrics after dolomitisation, which may also crack during inversion (and conduct fluids). Based on field studies, it is postulated that the stylolites in the Hasdrubal and Miskar reservoirs would have been reactivated during Late Cretaceous and late Eocene phases of inversion.

Fracturing

Fractures within the Miskar and Hasdrubal reservoirs may be classified into two distinct groups; i) sub-vertical Mode I fractures, predominantly associated with stylolites, and ii) sub-vertical Mode II and III fractures, associated with seismic-scale faults. Mode I 'stylolite-associated' fractures owe their origin to the stress state that caused the stylolite, and hence form parallel to the 'peaks and valleys' of the stylolite seam. In Hasdrubal and Miskar these Mode I fractures trend parallel to the orientation of seismic-scale faulting (i.e. NW-SE to NNW-SSE). Stylolite-associated fractures have been observed in all of the field examples given earlier (e.g. Ekofisk, Albusskjell, Ahwaz and Kirkuk Fields) (Agarwal et al., 1997; Watts, 1983; Bordenave & Burwood, 1990; Al-Qayim et al., 1980). Nelson (2001) has shown that although most stylolites have Mode I fracture associations it is possible to find examples without related fractures. This occurs if the burial process involves only uniaxial compaction.

Mode II and III fractures are intimately related to faults in the Hasdrubal and Miskar Fields. Limited oriented core and image log data shows that the majority of these fractures tend to parallel the orientation of seismic-scale faults (i.e. ~NW-SE to NNW-SSE). Fracturing associated with faulting is evident in zones or 'halos' surrounding the main fault planes. These potentially higher permeability 'halos' reflect early fracture process zones or volumes of fractured rock that immediately predate the creation of the through-going fault slip plane (Stearns & Friedman, 1972; Nelson, 2001). The close proximity and similar orientation of fracture sets indicates that they formed in the same stress state as the fault planes they surround (Shepherd et al., 1982). The width and symmetry of these zones does however vary, and probably reflects the mean stress state during deformation and the mechanical properties of the host rock.

It has been shown in this study that for the faults observed in Hasdrubal, and in particular the outcrop analogues in Malta, fracture zone widths range between ~80m to ~230m. These values are very similar to early analyses, which report fracture zone widths from 1m to 350m, with many in the 61m to 300m range (Piske, 1981; Webber & Bakker, 1981; Shepherd et al., 1982). Recently, Nelson et al. (2000) reported

fracture zone widths (associated with faults) from Cretaceous carbonate reservoirs in the La Paz Field, Venezuela, ranging between 61m to 183m. These ranges are in agreement with production data from the field, which delineate highly elliptical to linear drainage areas surrounding faults (Nelson et al., 2000).

In addition to the previous observations, it has been shown in the Hasdrubal Field, that within these fault halos, fracture intensity increases linearly towards the main fault plane. This relationship has also been borne out by outcrop studies on Malta.

Reservoir Development

The process of fracturing in the Miskar and Hasdrubal reservoirs is intimately associated with the subsidence history of the Gabes-Tripoli Basin (**Fig. 9.2**). For more detailed reconstructions depicting the evolution of each reservoir, the reader is referred to Chapters 6 and 7. However, to briefly summarise, fracturing has occurred at multiple stages in the development of each reservoir. Initial micro-fracturing occurred primarily in packstone-grainstone fabrics as each reservoir was buried and compacted. Following lithification, pressure solution commenced and stylolites developed. This was accompanied by stylolite-associated fracture growth. These fractures developed perpendicular to the main extension direction in the Gabes-Tripoli Basin (i.e. approximately NE-SW). Whilst this was occurring, NE-SW extension in the basin was also being accommodated by extensional fault growth. These fault systems trend approximately NW-SE and have their own fracture associations. With successive phases of extension in the basin, stylolite- and fault-related fractures were continuously reactivated and extended. Occasionally, extension in the basin was interrupted by minor episodes of inversion, which, i) created systems of sub-vertical stylolites, ii) reactivated certain fractures (in strike-slip), and, iii) caused some bedding-parallel stylolites to crack open (and conduct fluids).

9.5. Influence on Reservoir Performance

Although the Miskar and Hasdrubal reservoirs have differing diagenetic and structural histories, the impact of fracturing on reservoir quality is broadly comparable. It has already been stated that well test data from each field shows that both fractures and occasionally sub-horizontal stylolites contribute to enhance reservoir performance by more than an order of magnitude (Thompson, 1998; Pritchard, pers comm., 2000).

This effect would be particularly enhanced in a direction parallel to the main fracture trend (i.e. NW-SE to NNW-SSE).

Based on production data it is interpreted that the Hasdrubal and Miskar reservoirs can be classified as Type III reservoirs according to the scheme of Nelson (2001), whereby matrix porosity supplies the bulk of the hydrocarbon storage capacity and fractures significantly enhance production rates. Other field examples where fractures provide a permeability assist include the Kirkuk Field, Iraq (Daniel, 1954; Majid & Veizer, 1986), the Dukhan Field, Qatar (Nelson, 2001), the Gachsaran Field, Iran (McQuillan, 1974), and the Ekofisk and Albusskjell Fields in the North Sea (Agarwal et al., 1997).

The fractured chalk reservoirs of Ekofisk and Albusskjell amongst others provide broadly comparable analogues for the Abiod Formation in Miskar. Tectonic and stylolite-associated fractures are present in each field. Tectonic fractures have the greatest impact on reservoir enhancement in Ekofisk, whereas stylolite-associated fractures have the most influence on reservoir quality in Albusskjell (Agarwal et al., 1997; Watts, 1983). In Ekofisk, the fracture system provides only ~0.5% of the hydrocarbon pore volume (Christian et al., 1993). However, its presence significantly increases permeability (permeabilities from well test data are as high as 150md (i.e. two orders of magnitude greater than the matrix permeability)) (Brown, 1987).

Analogues (in addition to the La Paz Field) where fracturing associated with faulting is seen to enhance reservoir performance include the Sidi El Kilani, Belli and Ashtart Fields in Tunisia (Smaoui et al., 1998; Corbett & Crevello, 1998; Hornby et al., 1998). The Bou Dabbous reservoirs in the Sidi El Kilani and Belli Fields form good analogues for the Abiod Formation in Miskar, whereas the El Garia reservoir in Ashtart is the same as that in Hasdrubal. Although there are similarities between these analogues and the two fields analysed in this study, the contribution of fractures to reservoir performance does differ. For instance, the Sidi El Kilani Field is classified as a Type I reservoir whereby fault-associated fractures contribute significantly to hydrocarbon storage capacity and the bulk rock permeability (Ben Brahim, pers. comm., 2000). In contrast, the La Paz Field is a Type II reservoir, in which fractures provide essential reservoir permeability. Nelson (2001) has shown that in the case of Type III reservoirs, like Hasdrubal and Miskar an early recognition of the fracture systems present is essential in reservoir management.

9.6. Implications for Field Development

The conclusions presented in this thesis provide valuable information for optimising well position and orientation in field development. In the Miskar and Hasdrubal Fields, two potential development scenarios may be applied. The first approach considers drilling vertical to low angle deviated wells to cross-cut fault zones and their associated fracture 'envelopes' or 'halos'. Nelson (1990) shows that in order for this approach to be truly successful, wells need to be placed in fault and/or fracture zones that have not been drilled or severely depleted below virgin pressure. This technique although valid, would not optimise the number of wellbore fracture intersections in Hasdrubal and Miskar, because most of the fractures observed are sub-vertical.

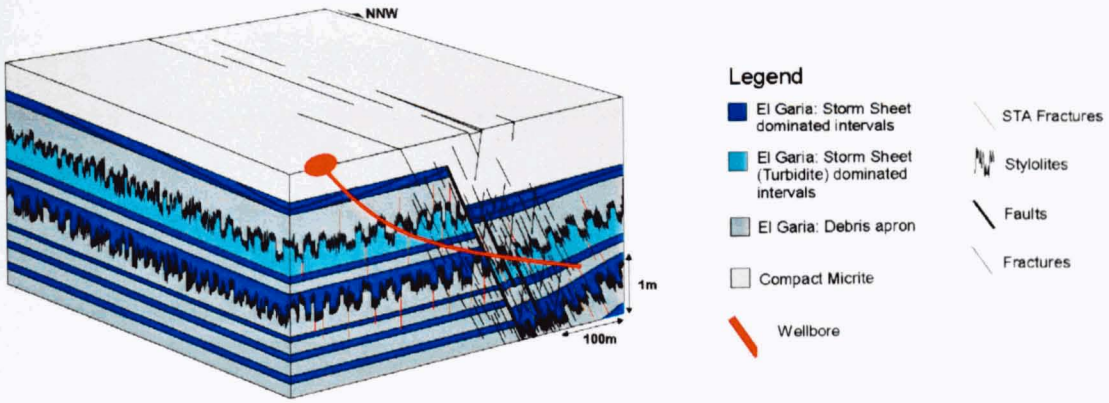

Fig. 9.3. Schematic diagram showing optimum wellbore approach angles to intersect an extensional fault zone within the Hasdrubal reservoir. The well path attempts to maximise the number of fractures intersected per foot and retain the length of the well in the fractured zone. Note that the optimum well path enters the fracture zone from the footwall (modified after Nelson et al., 2000).

The second development scenario involves drilling high angle deviated wells within each reservoir to exploit the sub-vertical fracture systems present. In this approach wells are drilled perpendicular to the dominant fracture trend (i.e. ~NE-SW). Besides communicating with sub-vertical fracture systems, this strategy may also expose poorly or undrained pore volume (Nelson et al., 2000). **Figure 9.3** shows the optimum wellbore approach angles to intersect an extensional fault zone within the Hasdrubal reservoir. Although it is probable that a horizontal drilling strategy would enhance productivity, the overall rate may not increase enough to justify the expenditure.

A major concern in developing of any type of fractured reservoir is that water breakthrough will occur too soon after the start of production. This phenomenon occurs if initial production from the fracture system is too rapid to allow replacement

of oil produced from the matrix. In such circumstances the channelling of water along fractures blocks the free movement of oil from the adjacent matrix, causing a marked decline in hydrocarbon production. As a consequence, a considered approach must be employed when utilising each drilling strategy.

These two drilling methods are currently being evaluated for each field development, and it is anticipated that development drilling will commence in within the next few years.

9.7. Future Work

- This study has demonstrated a relationship between faulting and fracture intensity within a transtensional setting. Further studies could be conducted in other tectonic environments and with faults of different magnitude in a variety of lithologies to establish whether or not a similar relationship develops;

- The models proposed in this study should be validated against additional test data as more wells are drilled on Miskar and Hasdrubal.

References

Abbate, E., Bortolotti, V., & Principi, G., 1980, Apennine ophiolite: a peculiar oceanic crust. *In* Tethyan Ophiolites (Rocci, G. (ed)). Ofiolitti, v. 1, p. 59-96.

Agarwal, B., Allen, L. R., Farrell, H. E., 1997, Ekofisk Field reservoir characterisation; mapping permeability through facies and fracture intensity. SPE Formation Evaluation, v. 12, p. 227-233.

Aguilera, R., 1988, Determination of subsurface distance between vertical parallel natural fractures based on core data. AAPG Bull., v. 72, p. 845-851.

Al-Qayim, B. A. J., Khaiwka, M. H., and Ronca, L. B., 1980, Depositional environment and diagenesis of the Oligocene reef cycles, Kirkuk oil field, northern Iraq. Modern Geology, v. 7, p. 177-190.

Ala, M. A., Kinghorn, R. R. F., and Rahman, M., 1980, Organic geochemistry and source rock characteristics of the Zagros petroleum province, Southwest Iran: J. Pet. Geol., v. 3, p. 61-89.

Alvarez, W., Cocozza, T., & Wezel, F. C., 1974, Fragmentation of the Alpine orogenic belt by microplate dispersal. Nature, v. 248, p. 309-314.

Anderson, J. 1996, The Neogene structural evolution of the western margin of the Pelagian Platform, central Tunisia. J. Struct. Geol., v. 18, p. 819-833.

Anderson, J., 1991, The subsidence history and structural evolution of the western margin of the Pelagian Platform, Central Tunisia. Unpub. PhD Thesis. 267p.

Anketell, J. M., 1995, Structural history of the Sirte Basin and its relationships to the Sabratah Basin and Cyrenaican Platform, Northern Libya. *In* The Geology of Libya (Salem, M. J. El-Hawat, A. S. & Sbeta, A. M. (eds)). Elsevier, Amsterdam, p. 57-87.

Anketell, J. M., & Ghellali, S. M., 1991, A palaeogeographic map of the Pre-Tertiary surface in the region of the Jiffarah Plain and its implication to the structural history of northern Libya. *In* The Geology of Libya (Salem, M. J., Sbeta, A. M., & Bakbak, M. R. (eds)). Elsevier, Amsterdam, p. 2381-2406.

Antonelli, M., Franciosi, R., Pezzi, G., Querci, A., Ronco, G. P., & Vezzani, F., 1988, Paleogeographic evolution and structural setting of the northern side of the Sicily Channel. Proc. 74th Congr. Soc. Geol. It., p. 79-86.

Auzende, J. M., Bonnin, J., & Olivet, J. L., 1973, The origin of the western Mediterranean Basin. J. Geol. Soc. Lond., v. 129, p. 607-620.

Argand, E., 1924, La tectonique de l'Asie, XIIIe Congr. Geol. Intern., Brussels, Compt. Rend., p. 171-372.

Argnani, A., 1990, The Strait of Sicily Rift Zone: Foreland deformation related to the evolutionof a back-arc basin. J. Geodyn., v. 12, p. 311-331.

Argnani, A., Cornini, S., Torelli, L., & Zitellini, N., 1987, Diachronous Neogene-Quaternary Foredeep system in the Strait of Sicily. Mem. Soc. Geol. It., v. 36, p. 46-61.

Attewell, P. B., & Farmer, I. W., 1976, Principles of engineering geology. Chapman & Hall, London.

Bailey, H. W., Dungworth, G., Hardy, M., Scull, D., & Vaughan, R. D., 1989, A fresh approach to the Metlaoui. *In* Ileme Journees de Geologie Tunisienne Appliquee a la Recherche des hydrocarbures, Tunis, 2-3 November 1989, p. 281-307.

Baecher, G. B., Lanney, N. A., & Einstein, H. H., 1977, Statistical description of rock properties and sampling. Proc. 18th U.S. Symposium on Rock Mech. Am. Instit. Min. Eng., 5C1-8.

Barenblatt, G., Zheltov, I., & Kochina, I., 1960, Basic concepts in the theory of seepage of homogeneous liquids in fissured rocks. Prikl. Mat. Mekh., v. 24, p. 852-864.

Barrier, E., 1992, Tectonic analysis of a flexed foreland: the Ragusa Platform. Tectonophys., v. 206, p. 91-111.

Barton, C. A., Moos, D., Peska, P., & Zoback, M. D., 1997. Utilising wellbore image data to determine the complete stress tensor: application to permeability anisotropy and wellbore stability. The Log Analyst, Nov/Dec, p. 21-33.

Barton, P., & Wood, R., 1984, Tectonic evolution of the North Sea basin: crustal stretching and subsidence. Geophys. J. R. Astr. Soc., v. 79, p. 987-1022.

Beckett, D., 1998, Hydrocarbon system and petroleum geology of the Hasdrubal Gas Condensate Field. *In*: Tunisia, Hasdrubal Field: An integrated sub-surface description with hydrocarbons in place and reserves. BG Group Internal Report.

Bedir, M., Zargouni, F., Tlig, S., Bobier, C., 1992, Subsurface geodynamics and petroleum geology of transform basin margins in the Sahel of Mahdia and El Jem (Eastern Tunisia). Am. Assoc. Pet. Geol. Bull., v. 76, p. 1417-1442.

Bellingham, P., 1999. Extension and subsidence in one and two dimensions, north of 60 degrees north. Unpublished PhD thesis. University of Cambridge, UK.

Ben Fergani, A., Burollet, P. F., and Mejri, M., 1990, Petroleum Geology of Tunisia. Enterprise Tunisienne d'Activities Petrolieres. Tunis. 194p.

Ben-Avraham, Z., Nur, A & Cello, G., 1987, Active transcurrent fault system along the North African passive margin. Tectonophys., v. 141, p. 249-260.

Ben-Avraham, Z., & Grasso, M., 1990, Collisional zone segmentation in Sicily and surrounding areas in the Central Mediterranean. Ann. Tectonicae, v. 4, p. 131-139.

Ben-Avraham, Z., Lyakhovsky, V., Grasso, M., 1995, Simulation of collisional zone segmentation in the central Mediterranean. Tectonophys., v. 243, p. 57-68.

Berggren, W.A., Kent, D.V., Swisher, C.C. & Aubrey, M., 1995. A revised Cenozoic geochronology and chronostratigraphy. In Geochronology, time scales and global stratigraphic correlation (Berggren, W. A., Kent, D. V., Aubry, M-P., & Hardenbol, J. (eds)). SEPM Special Publication No. 54. p. 129-212.

Bernoulli, D., & Jenkyns, H. C., 1974, Alpine, Meditteranean and central Atlantic Mesozoic facies in relation to the early evolution of the Tethys. *In* Modern and ancient geosynclinal sedimentation (Dott, R. H., & Shaver, R.H. (eds)), p. 129-160.

Bianca, M., Monaco, C., & Tortorici, L., 2000, Quaternary normal faulting in south-eastern Sicily (Italy): a seismic source for the 1693 earthquake. Tectonophys. *In press*

Biju- Duval, B., Letouzey, J., & Montadert, L., 1977, Structure and evolution of the Mediterranean Basins. Intitial Rep. Deep Sea drill. Proj. XLII(1), p. 951-984.

Bishop, W., 1988, Petroleum Geology of east-central Tunisia. Bull. Am. Assoc. Pet. Geol., v. 72, p. 1033-1058.

Bishop, W., 1985, Eocene and Upper Cretaceous carbonate reservoirs in east0central Tunisia. Oil & Gas Journal 83, v. 48, p. 137-142.

Bishop, W., 1975, Geology of Tunisia and adjacent parts of Algeria and Libya. Bull. Am. Assoc Pet Geol., v. 59, p. 413-450.

Boccaletti, M., Cello, G. & Tortorici, L. 1990. First order kinematic elements in Tunisia and the Pelagian block. Tectonophys., v. 176, p. 215-228.

Boccaletti, M., Cello, G., & Tortorici, L., 1987, Transtensional tectonics in the Sicily channel. J. Struct. Geol., v. 9, p. 869-876.

Bordenave, M. L., and Burwood, R., 1990, Source rock distribution and maturation in the Zagros orogenic belt - provenance of the Asmari and Bangestan reservoir oil accumulation. Organic Geochemistry, v. 16, p. 365-387.

Braithwaite, K., 1998, Sedimentology of the El Garia Formation. *In*: Tunisia, Hasdrubal Field: An integrated sub-surface description with hydrocarbons in place and reserves. BG Group Internal Report.

Brown, D.A., 1987, The flow of water and displacement of hydrocarbons in fractured chalk reservoirs. *In* Fluid Flow in Sedimentary Basins and Aquifers (Goff, J. C., & Williams, B. P. J., (eds)). Geol. Soc. Lond. Spec. Pub., p. 210-218.

Bullard, E. C., Everett, J. E., & Smith, A. G., 1965, The fit of the continents around the Atlantic. Roy. Soc. Lond. Phil. Trans. (A), v. 258, p. 41-51.

Burollet, P. F. 1991. Structures and tectonics of Tunisia. Tectonophysics, v. 195, p. 359-369.

Burollet, P., Mugniot, J. & Sweeney, P. 1978. The geology of the Pelagian block, the margins and basins off southern Tunisia and Tripolitania. *In*: Nairn, A., Kanes, W, and Stelhi, F (eds) The Oceans Basins and Margins 4B, The Western Mediterranean. Plenum Press, New York, p. 331-339.

Burollet, P. F., 1956, Contribution a l'etude stratigraphique de la Tunisie centrale. Ann. Mines Geol., v. 18, 352p.

Butler, R. W. H., Grasso, M., Gardiner, W., & Sedgeley, D., 1997, Depositional patterns and their tectonic controls within the Plio-Quaternary carbonate sands and muds of onshore and offshore SE Sicily (Italy). Mar. Pet. Geol., v. 14, p. 879-892.

Camoin, G. F., 1991, Sedimentologic and paleotectonic evolution of carbonate platforms on a segmented continental margin: example of the African Tethyan margin during Turonian and Early Senonian times. Palaeog. Palaeoclim. Palaeoecol., v. 87, p. 29-52.

Carey, S. W., & Vine, F. J., 1990, Global Tectonics. Blackwell Scientific Publishers. P. 97-107.

Carey, S. W., 1958, A tectonic approach to continental drift – a symposium. Hobart, Australia, Univ. Tasmania, p. 177-355.

Casero, P., Roure, F., & Vially, R., 1991, Tectonic framework and petroleum potential of the southern Apennines. *In* Generation, accumulation and production of Europe's hydrocarbons (Spencer, A. M., (ed)). Special Publication of the European Association of Petroleum Geoscientists No. 1, p. 369-380.

Cavallin, A., & Tornaghi, M.-E., 1986, The evolution of the Mediterranean Area: Kinematics. Mem. Soc. Geol. It., v. 35, p. 221-228.

Cello, G., 1987, Structure and deformation processes in the Strait of Sicily "rift zone". Tectonophys., v. 141, p. 237-247.

Cello, G., Crisci, G., Marabini, S., and Tortorici, L., 1985, Transtensive tectonics in the strait of Sicily: Structural and volcanic evidence from the island of Pantelleria. Tectonics, v. 4, p. 311-322.

Chaabouni, A., 2000, Regional evaluation of the Gulf of Gabes area. Poster. Proc. 8th Tunisian. Pet. Exp. Prod. Conf. Tunis, 5th – 9th May 2000.

Channell, J.E.T., & Mareschal, J.C., 1989, Delamination and asymmetric lithospheric thickening in the development of the Tyrrhenian Rift. In Alpine Tectonics (Coward, M.P., Dietrich, D., & Park, R.G., (eds.)). Geol. Soc. Spec. Pub., p. 285-302.

Channell, J.E.T., D'Argenio, B., & Horváth, F., 1979, Adria, the African Promontory, in Mesozoic Mediterranean Palaeogeography. Earth-Sci. Rev., v. 15, p. 213-292.

Christian, T. M., Currie, J. C., Lantz, T. G., Rismyhr, O., & Snow, S. E., 1993, Reservoir management at Ekofisk Field: Proc. 68th SPE Annual Technical Conference, Houston, SPE 26623, 10 p.

Cogan, J., Rigo, L., Grasso, M., Lerche, I., 1989, Flexural tectonics of southeastern Sicily. J. Geodyn., v. 11, p. 189-241.

Cohen, C.R., Schamel, S., and Boyd-Kaygi, P., 1980, Neogene deformation in northern Tunisia: Origin of the eastern Atlas by microplate-continental margin collision. Geol. Soc. Am. Bull., v. 91, p. 225-237.

Cook, S. E., & Wright, V. P., 1998, The Miskar Gas Condensate Field. Proc. 6th Tunisian Petroleum Exploration and Production Conference, Tunis, May, p. 97-122.

Corbett, K. P., & Crevello, P. D., 1998, Fractal modelling of a fractured reservoir: Belli Field, Tunisia. Proc. 6th Tunisian Petroleum Exploration and Production Conference, Tunis, May, p. 123-128.

Coward, M. P., Dietrich, D., 1989, Alpine tectonics; an overview. In Conference on Alpine tectonics (Coward, M. P., Dietrich, D., & Park, R. G. (eds.). Geol. Soc. Spec. Pub., v. 45, p. 1-29.

Cowie, P. A., & Scholtz, C. H., 1992a, Physical explanation for the displacement-length relationship of faults using a post-yield fracture mechanics model. J. Struct. Geol., v. 14, p. 1133-1148.

Cowie, P. A., Vanneste, C., & Sornette, D., 1993, Statistical physics model for the spatio-temporal evolution of faults. J. Geophys. Res., v. 98, p. 809-821.

D'Heur, M., 1990, Eldfisk Field - Norway, Central Graben, North Sea. *In* Structural Traps IV (Beaumont, E. A., & Foster, N. H., (eds)). AAPG Treatise of Petroleum Geology, Atlas of Oil and Gas Fields, p. 27-56.

Daniel, E. J., 1954, Fractured reservoirs of Middle East: AAPG Bull., v. 38, p. 774-815.

Darcy, H., 1856, Les fontaines publiques de la Ville de Dijon. Paris, V. Dalmont.

Dart, C. J., Bosence, D. W. J., & McClay, K. R., 1993, Stratigraphy and structure of the Maltese graben system. J. Geol. Soc. Lond., v. 150, p. 1153-1166.

Das Gupta, U., & Currie, J. B., 1983, An application to photoelastic models to explain microfractures and joints in carbonate strata. Can. Jour. Earth Sci., v. 20, p. 1682-1693.

Debono, G., & Xerri, S., 1993, Geological map of the Maltese Islands – Sheet 1 (1:25 000). Oil Exploration Dictorate, Office of the Prime Minister, Malta.

De Rosa, R., Mazzuoli, R., & Trua, T., 1992, A petrogenetic model for the co-existence of alkali basalts and tholeiites in the Plio-Pliestocene volcanism of the Iblean Plateau (South-East Sicily, Italy). Acta Vulcanologica Marinelli, v. 2, p. 199-207.

Dercourt, J., Zonenshain, L. P., Ricou, L.-E., Kasmin, V. G., Le Pichon, X., Knipper, A. L., Grandjacquet, C., Sbortshikov, I. M., Geyssant, J., Lepvrier, C., Pechersky, D. H., Boulin, J., Sibuet, J.-C., Savostin, L. A., Sorokhtin, O., Westphal, M., Bazhenov, M. L., Lauer, J.-P & Biju-Duval, B., 1986, Geological evolution of the Tethys belt from the Atlantic to the Pamirs since the Lias. Tectonophys., v. 123, p. 241-315.

Dershowitz, W., Lee, G., Geier, J., Foxford, T., La Pointe, P., & Thomas, A., 1998, FracMan: Interactive discrete feature data analysis, geometric modelling and exploration simulation. User documentation, Version 2.6. Golder Associates Inc.

Dewey, J.F., Helman, M.L., Turco, E., Hutton, D.H.W., and Knott, S.D., 1989, Kinematics of the western Mediterranean. In Alpine Tectonics (Coward, M.P., Dietrich, D., & Park, R.G. (eds.)). Geol. Soc. Spec. Pub. No. 45, p 265-283.

Dewey, J.F., Pitman, W.C., Ryan, W.B.F., and Bonnin, J., 1973, Plate tectonics and evolution of the Alpine system. Geol. Soc. Am. Bull., v. 84, p. 137-180.

Di Grande, A., & Raimondo, W., 1982, Linee di costa plio-pleistoceniche eschema litostratigraphico del Quaternario siracusano. Geol. Romana, v. 21, p. 279-309.

Drummond, J. M., 1964, An appraisal of fracture porosity. Bull. Can. Pet. Geol., v. 12, p. 226-245.

Du Toit, A. L., 1937, Our Wandering Continents. Edinburgh. Oliver & Boyd. 366p.

Dunnington, H. V., 1954, Stylolite development postdates rock induration. J. Sed. Pet., v. 24, p. 27-49.

El Ghoul, A., 1991, Geohistory analysis mapping in central and southern Tarabulus Basin, Northwestern Offshore of Libya. *In* The Geology of Libya (Salem, M. J. El-Hawat, A. S. & Sbeta, A. M. (eds)). Elsevier, Amsterdam, p. 1637-1656.

Engelder, T., 1993, Stress regimes in the lithosphere. Princeton University Press, Princeton, New Jersey. 457pp.

Engelder, T., 1985, Loading paths to joint propogation during a tectonic cycle: an example from the Appalachian Plateau, USA. J. Struct. Geol., v. 7, p. 459-476.

Engelder, T., and Geiser, P., 1980, On the use of regional joint sets as trajectories of paleostress fields during the development of the Appalachian Plateau, New York. J. Geophys. Res., v. 85, p. 6319-6341.

Erickson, A. J., Simmons, G., Ryan, W. B. F., 1977, Review of heat-flow data from the Mediterranean and Aegean Seas. *In* Structural History of the Mediterranean Basins (Biju-Duval, B., & Montadert, L. (eds)). Editions Technip, Paris, p. 263-280.

Faulkner, P.A., 2000. Tectonic and thermal evolution of South Atlantic marginal basins. Unpublished PhD thesis. University of Cambridge, UK.

Farrugia, P., Apopei, I., Bonjer, K. P., 1989, Observation on the Seismicity of the Sicily Channel. Mem. Soc. Geol. It., v. 38, p. 1153-1172.

Ferrucci, F., Gaudiosi, G., Hirn, A., & Nicolich, R., 1991, Ionian Basin and Calabrian Arc. Some new elements from DSS data. Tectonophys., v. 195, p. 411-419.

Finetti, I., 1985, Structure and evolution of the Central Mediterranean (Pelagian and Ionian Seas). In Geological Evolution of the Mediterranean Basin (Stanley, D. J & Wezel, F.-C (eds)). Springer-Verlag, New York, p. 215-230.

Finetti, I., 1984, Geophysical study of the Sicily Channel Rift Zone. Boll. Geofis. Teor. Appl., v. 101-102, p. 3-28.

Fournie, D., 1978, Nomenclature stratigraphique des series du Cretace superieur au Tertiare de Tunisie. Bull. Centr. Rech. Expl. Prod, Elf-Aquitaine, 2, 1, p. 97-148.

Gauthier, B. D. M., & Lake, S. D., 1993, Probabilistic modeling of faults below the limit of seismic resolution in Pelical Field, North Sea, Offshore United Kingdom. AAPG Bull., v. 77, p. 761-777.

Geier, J. E., Lee, K., & Dershowitz, W. S., 1989, Field validation of conceptual models for fracture geometry. Rock Mech & Rock Engineering.

Ghisetti, F., & Vezzani, L., 1980, The structural features of the Iblean Plateau and of the Mount Judica Area (Southeastern Sicily): a micro-tectonic contribution to the deformational history of the Calabrian Arc. Boll. Soc. Geol. It., v. 99, p. 57-102.

Gilbert, C. M., 1949, Cementation of some Californian Tertiary reservoir sands. J. Sed. Petrology, v. 35, p. 643-655.

Guiraud, R., 1998, Mesozoic rifting and basin inversion along the northern African Tethyan margin: an overview. *In* Petroleum Geology of North Africa (Macgregor, D. S., Moody, R. T. J. & Clarke-Lowes, D. D. (eds)). Geol. Soc. Lond. Spec. Pub. No. 132, p. 217-229.

Gardiner, W., Grasso., M., & Sedgeley, D., 1995, Plio-Pleistocene fault movement as evidence for megablock kinematics within the Hyblean-Malta Plateau, Central Mediterranean. J. Geodyn., v. 19, p. 35-51.

Gradstein, F. M., Agterberg, F, P., Ogg, J. G., Hardenbol, J., Van Veen, P, Thierry, J., & Huang, Z., 1995, A Triassic, Jurassic and Cretaceous time scale. In Geochronology, time scales and global stratigraphic correlation (Berggren, W. A., Kent, D. V., Aubry, M-P., & Hardenbol, J. (eds)). SEPM Special Publication No. 54, p. 95-128.

Grasso, M., De Dominicus, A., & Mazzoldi, G., 1990a, Structures and tectonic setting of the western margin of the Hyblean-Malta shelf, Central Mediterranean. Ann. Tectonicae, v. 4/2, p. 140-154.

Grasso, M., & Reuther, C.D., 1988, The western margin of the Hyblean Plateau. A neotectonic transform system on the S. E. Sicilian foreland. Ann. Tectonicae, v. 11, p. 107-120.

Grasso, M., Reuther, C. D., Baumann, H., & Becker, A., 1986, Shallow crustal stress and neotectonic framework of the Malta Platform and the southeastern Pantelleria Rift. Geol. Romana, v. 25, p. 191-212.

Grasso, M., Pedley, H. M., & Reuther, C. D., 1985, The geology of the Pelagian Islands and their structural setting related to the Pantelleria Rift (Central Mediterranean Sea). Centro, v. 1 (2), p. 1-19.

Grasso, M., Lentini, F., Nairn, A. E. M., & Vigliotti., L., 1983, A geologic and palaeomagnetic study of the Hyblean volcanic rocks, Sicily. Tectonophys., v. 98, p. 271-295.

Grasso, M., & Lentini, F., 1982, Sedimentary and tectonic evolution of the eastern Hyblean Plateau (Southeast Sicily) during Late Cretaceous to Quaternary time. Palaeogeogr., Palaeoclimatol., Palaeoecol., v. 39, p. 261-280.

Griffith, A. A., 1925, The theory of rupture. 1st Int. Cong. App. Mech. Proc. Delft, p. 55-63.

Griggs, D., and Handin, J., 1960, Observations on fracture and a hypothesis of earthquakes, in Griggs,D.T., and Handin, J.H., eds., Rock deformation. Geol. Soc. America Mem. 79, p. 347-364.

Haile, N. S., 1987, Time and age in geology: the use of Upper/Lower, late/early in stratigraphic nomenclature. Marine & Petroleum Geology, v. 4, p. 255-257.

Halliburton, 1995, CAST Borehole imaging. Brochure EL 1100.

Hall, B. D., 1995, Early Tertiary tectonics and igneous activity adjacent to the N. W. European continental margin. Unpub. Ph.D thesis. 248p.

Hammuda, O. S., Van Hinte, J. E., & Nederbragt, S., 1991, Geohistory analysis mapping in the central and southern Tarabulus Basin, northwestern offshore Libya. *In* The Geology of Libya (Salem, M. J. (ed)). Elsevier, Amsterdam, p. 1657-1680.

Hancock, P.L., 1985, Brittle microtectonics: principles and practice. J. Struct. Geol., v. 7, p. 437-457.

Hanks, C. L., Lorenz, J. C., & Krumhardt, A. P., 1994, Origin, distribution and character of fractures within the Lisburne Group, northeastern Sadlerochit Mountains, northeastern Alaska (abs.). AAPG/SEG Annual Meeting Abstracts, p. 162.

Harland, W. B., Armstrong, R. C., Craig, L., Smith, A. G., & Smith, D. G., 1990, A Geologic Time Scale 1989. Cambridge University Press, Cambridge.

Hill, K. C., & Hayward, A. B., 1988, Tertiary plate tectonic evolution of Italy. Marine and Petroleum Geol., v. 5, p. 2-16.

Hobbs, B.E., 1967, The formation of tension joints in sedimentary rocks: an explanation. Geol. Mag., v. 104, p. 550-556.

Hornby, B. E., Loucks, R. G., Sovich, P., & Williams, R., Integrated interpretation of fracture conductivity using electrical borehole scans and full-waveform sonic data. Proc. 6th Tunisian Petroleum Exploration and Production Conference, Tunis, May, p. 179-194.

Howard, J.H., and Nolen-Hoeksema, R.C., 1990, Description of natural fracture systems for quantitative use in petroleum geology. AAPG Bull., v. 74, p. 151-162.

Hsü, K.J., 1977, Tectonic evolution of the Mediterranean Sea basins. *In* The ocean basins and margins, 4A, The eastern Mediterranean (Nairn, A.E.M., Kanes, W.H., & Stehli, F.G. (eds.)). Plenum Press, New York, p. 29-75.

Hsü, K. J., 1977, Tectonic evolution of the Mediterranean Sea basins. *In* The ocean basins and margins, 4A, The eastern Mediterranean (Nairn, A.E.M., Kanes, W.H., & Stehli, F.G. (eds.)). Plenum Press, New York, p. 29-75.

Hsü, K. J., & Bernoulli, D., 1975, Genesis of the Tethys and the Mediterranean. Intitial Rep. Deep Sea drill. Proj. XLII (1), p. 943-949.

Hsü, K. J., 1971, Origin of the Alps and western Mediterranean. Nature, v. 233, p. 44-48.

Huang, Q., and Angelier, J., 1989, Fracture spacing and it's relation to bed thickness. Geol. Mag., v. 126, p. 355-362.

Hubbert, M.K., and Willis, D.G., 1957, Mechanics of hydraulic fracturing. Am. Inst. Min. Metall. Engineers, Petroleum Br. Trans., v.210, p. 153-168.

Hubbert, M. K., & Willis, D. G., 1955, Important fractured reservoirs in the United States. 45th World Pet. Cong. Proc, Sec. I/A-1, p. 58-81.

Hubbert, M. K., 1940, The theory of ground-water motion. Jour. Geol., v. 48, p. 785-944.

Huitt, J. L., 1955, Fluid flow in simulated fractures. Amer. Inst. Chen. Eng. Jour., v. 2, p. 259-264.

Jarvis, G. T., & McKenzie, D. P., 1980, Sedimentary basin formation with finite extension rates. Earth Planet. Sci. Letts., v. 48, p. 42-52.

Jongsma, D., 1991, The Medina and Sirte wrenches: A quantitative estimate of strike-slip deformation within the Sirte Rise over the past 5 Ma. In The Geology of Libya (Salem, M. J., Sbeta, A. M., & Bakbak, M. R. (eds)). Elsevier, Ansterdam, VI, p. 2331-2352.

Jongsma, D., Van Hinte, J., & Woodside, J. M., 1985, Geologic structure and neotectonics of the North African continental margin south of Sicily. Mar. Petrol. Geol., v. 2., p. 156-179.

Keary, P., & Brooks, M, 1991, An introduction to geophysical exploration. Oxford Blackwell Scientific Publications. 2nd Edition. 254p.

Keeley, M. L., & Messoud, M. S., 1998, Tectonic controls on the petroleum geology of NE Africa. *In* Petroleum Geology of North Africa (Macgregor, D. S., Moody, R. T. J. & Clarke-Lowes, D. D. (eds)). Geol. Soc. Lond. Spec. Pub. No. 132, p. 265-282.

Keller, J., 1990, Apennine compressional deformation and Tyrrhenian extension on the island of Elba, Italy. Unpub. Ph.D. Thesis. Imperial College, London. 346 pp.

Key, S. C., Argawal, B., Soiland, G. V., & Hielsen, H. H., 1999, Ekofisk Field redevelopment; improved reservoir management through cross-discipline technology and integration of three-dimensional models. *In* Petroleum Geology of Northwest Europe: proceedings of the 5th conference (Fleet, A. J., Boldy, S. A. R (eds))., p. 1147-1155.

Kulander, B. R., Dean, S. L., & Ward, B. J., Fractured Core Analysis: interpretation, logging and the use of natural and induced fractures in core. AAPG Methods in Exploration Series, No. 88p.

La Point, P.R., and Hudson, J.A., 1985, Characterisation and interpretation of rock mass joint patterns. Geol. Soc. Am. Spec. Paper 199, p. 1-25.

Lacazette, A., 1991, A new stereographic technique for the reduction of scanline survey data of geologic fractures. Computers and Geosciences, v. 17, p. 445-463.

Ladiera, F.L., and Price, N.J., 1981, Relationship between fracture spacing and bed thickness. J.Struct. Geol., v. 3, p. 179-183.

Lamb, H., 1957, Hydrodynamics. Cambridge University Press (6th Edition).

Laubscher, H. P., & Bernoulli, D., 1977, Mediterranean and Tethys. *In* The ocean basins and margins, 4A, The eastern Mediterranean (Nairn, A.E.M., Kanes, W.H., & Stehli, F.G. (eds.)). Plenum Press, New York, p. 72-94.

Lawn, B. R., & Wilshaw, T. R., 1975, Fracture of brittle solids. Cambridge University Press, Cambridge. 204p.

Lerche, I., & Narr, W., 1986, Estimating subsurface fracture density in core: effects resulting from variable fracture spacing: Soc. Pet. Eng. Form. Eval., June, p. 249-258.

Livermore, R. A., & Smith, A.G., 1985, Some boundary conditions for the evolution of the Mediterranean. In Geological evolution of the Mediterranean sea (Stanley, D.G., & Wezel, F.C. (eds.)). Springer-Verlag, New York, p. 89-105.

Lofts, J., & Bourke, L., 1999, Atlas of artefacts from acoustic and resistivity borehole imaging devices. Baker Atlas Poster.

Lorenz, J. C., & Hill, R. E., 1994, Subsurface fracture spacing: comparison of inferences from slant/horizontal and vertical cores. Soc. Pet. Eng. Form. Eval., March, p. 66-72.

Lorenz, J. C., Teufel, L. W., & Warpinski, N. R., 1991, Regional fractures I: a mechanism for the formation of regional fractures at depth in flat lying reservoirs. AAPG Bull., v. 75, p. 1714-1737.

McCrossan, R. G., 1989, Regional offshore assessment. Unpublished SOC Study

McKenzie, D. P., 1978a, Some remarks on the development of sedimentary basins. Earth Planet. Sci. Letts., v. 40, p. 25-32.

McKenzie, D. P., 1978b, Active tectonics of the Alpine-Himalayan belt: the Aegean Sea and surrounding regions. Geophys. J. R. Astr. Soc., v. 55, p. 217-254.

Mc Phail, H. E., 1995, Essentials of fractured reservoirs. OGCI Course Notes, Tulsa, Oklahoma.

McQuilken, J., 1998, Thermal maturity modeling of the Bou Dabbous Formation: a potential source rock to the El Garia reservoir. *In*: Tunisia, Hasdrubal Field: An integrated sub-surface description with hydrocarbons in place and reserves. BG Group Internal Report.

McQuillan, H., 1985, Gachsaran and Bibi Hakimeh Fields. *In* Carbonate Petroleum Reservoirs (Roehl, P. O. & Choquette, P.W., (eds)). Springer-Verlag, New York, p. 513-523.

McQuillan, H., 1974, Fracture patterns on Kuh-e Asmari Anticline, southwest Iran. AAPG Bull., v. 58, p. 236-246.

M'Rabat, A., Mejri, F., Burollet, P. F., Memmi, L., & Chandoul, H., 1995, Catalog of type sections in Tunisia "Cretaceous". ETAP Memoir, v. 84, Tunis, 123p.

Macgregor, D.S., & Moody, R. T. J., 1998, Mesozoic and Cenozoic petroleum systems of North Africa. *In* Petroleum Geology of North Africa (Macgregor, D. S., Moody, R. T. J. & Clarke-Lowes, D. D. (eds)). Geol. Soc. Lond. Spec. Pub. No. 132, p. 201-216.

Macaulay, C. I., Beckett, D., Braithwaite, K., Bliefnick, D., & Philps, B. R., 2001, Constraints on diagenesis and reservoir quality in the fractured Hasdrubal Field, offshore Tunisia. J. Pet. Geol., v. 24, p. 55-78.

Mahood, G., & Hildreth, W., 1983, Nested calderas and trapdoor uplift at Pantelleria, Strait of Sicily. Geology, v. 11, p. 722-726.

Majid, A. H., and Veizer, J., 1986, Deposition and chemical diagenesis of Tertiary carbonates, Kirkuk oil field, Iraq: AAPG Bull., v. 70, p. 898-913.

Makris, J., Nicolich, R., & Weigel, W., 1986, A seismic study in the Western Ionian Sea. Ann. Geophys. 4B, p. 665-678.

Makris, J., 1985, Geophysics and geodynamic implications for the evolution of the Hellenides. *In* Geological Evolution of the Mediterranean Sea (Stanley, D. G., & Wezel, F. C., (eds)). Springer-Verlag, New York, p. 231-248.

Maldanado, A., & Stanley, D. J., 1976, Late Quaternary sedimentation and stratigraphy in the Strait of Sicily. Smithsonian contributions to the earth sciences, v. 16 Smithsonian institute, Washington DC.

Marrett, R., & Allmendinger, R. W., 1991, Estimates of strain due to brittle faulting: sampling of fault populations. J. Struct. Geol., v. 13, p. 735-737.

Megson, J. B., 1992, The North Sea chalk - examples from the Danish Central Graben. *In* Exploration Britain - Geological Insights for the Next Decade (Hardman, R. F. P., (ed)). Geol. Soc. Spec. Pub., no. 67, p. 247-282.

Moody, R. T. J., 1987, The Ypresian carbonates of Tunisia – a model of foraminiferal facies distribution. In Micropaleontology of Carbonate Environments (Hart, M. B (ed)). British Micropalaeontology Society Series, p. 82-92.

Morelli, C., Gantar, C., & Pisani, M., 1975a, Bathymetry, gravity and magnetism in the Strait of Sicily and the Ionian Sea. Boll. Geof. Teor. Appl., v. 17, p. 39-58.

Morelli, C., Pisani, M., & Gantar, C., 1975c, Geophysical anomalies and tectonics in the Western Mediterranean. Boll. Geof. Teor. Appl., v. 18, p. 211-249.

Morgan, M. A., Grocott, J., & Moody, R. T. J., 1998, The structural evolution of the Zaghouan-Ressas Structural Belt, Northern Tunisia. . *In* Petroleum Geology of North Africa (Macgregor, D. S., Moody, R. T. J. & Clarke-Lowes, D. D. (eds)). Geol. Soc. Lond. Spec. Pub. No. 132, p. 405-422.

Morgan, W. J., 1981, Hotspot tracks and the opening of the Atlantic and Indian Oceans. *In* The Sea (Emiliani, C. (ed)). J. Wiley & Sons, New York, p. 443-487.

Morgan, W. J., 1983, Hotspot tracks and the early rifting of the Atlantic. Tectonophys., v. 94, p. 123-139.

Murrell, S. A. F., 1958, The strength of coal under triaxial compression. Mech. Prop. Non-metallic brittle material (Walton, W., (ed)), p. 123-153. Butterworth.

Narr, W., 1996, Estimating average fracture spacing in subsurface rocks. AAPG Bull., v. 80, p. 1565-1586.

Narr, W., 1991, Fracture density in the deep subsurface: Techniques with application to Point Arguello oil field. AAPG Bull., v. 75, p. 1300-1323.

Narr, W., and Suppe, J., 1991, Joint spacing in sedimentary rocks. J. Struct. Geol., v. 13, p. 1037-1048.

Narr, W., and Lerche, I., 1984, A method for estimating subsurface fracture density in core. AAPG Bull., v. 68, p. 637-648.

Narr, W., and Currie, J.B., 1982, Origin of fracture porosity- Example from Altamont Field, Utah. AAPG Bull., v. 66, p. 1231-1247.

Needham, T., Yielding, G., & Fox, R., 1996, Fault population description and prediction using examples from the offshore U.K. J. Struct. Geol., v. 18, p. 155-167.

Nelson, R.A., 2001, Geologic analysis of naturally fractured reservoirs. 2nd Edition. Gulf Publishing Company, Houston. 332p.

Nelson, R. A., Moldovanyi, E. P., Matcek, C. C., Azpiritxaga, I., & Bueno, E., 2000, Production characteristics of fractured reservoirs of the La Paz Field, Maracaibo Basin, Venezuela. AAPG Bull., v. 84, p. 1791-1809.

Nelson, R.A., 1985, Geologic analysis of naturally fractured reservoirs. 1st Edition. Gulf Publishing Company, Houston. 320p.

Nelson, R. A., 1979, Natural fracture systems: description and classification. AAPG Bull., v. 63, p. 2214-2232.

Neumayr, M., 1883, Klimatische Zonen wahrend der Jura-and Kreidezeit, Denkschr. math.-naturw. kl., v. 47, p. 277-210.

Norman, A. V. J., 1994, A structural interpretation of the Miskar Field, Golfe de Gabes, Tunisia. Unpub. M.Sc. Thesis. 65p.

Norris, D.K., 1966, Structural analysis of the Queensway folds, Ottawa, Canada. Can. J. Earth Sci., v. 4, p. 299-321.

Odling, N. E., Gillespie, P., Bourgine, B., Castaing, C., Chiles, J. –P., Christensen, N. P., Fillion, E., Genter, A., Olsen, C., Thrane, L., Trice, R., Aarseth, E., Walsh, J. J., & Watterson, J., 1999, Variations in fracture system geometry and their implications for fluif flow in fractured hydrocarbon reservoirs. Pet. Geoscience, v. 5, p. 373-384.

Olivet, J. –L., Bonnin, J., Beuzart, P., & Auzende, J. –M., 1984, Cinematique de l'Atlantique nord et central. *In* Rapports scientifiques. CNEXO, Paris. 108p.

Ord, A & Cheung, C. C., 1991, Image analysis techniques for determining the fractal dimensions of rock joint and fragment size distributions. *In* Proc. Int. Conf. Rock. Mech. Joint. & Fault. Rock, Vienna, Austria, (Beer, G., Booker, J. R., & Carter, J. P., (eds)), Balkema, Rotterdam, p. 87-91.

Ouali, J., 1985, Structure et evolution geodynamique du chainon Nara-Sidi Khalif (Tunisie Centrale). Bull. Cent. Rech. Explor. Prod. Elf Aquitaine, v. 9, p. 155-182.

Pahl, P. J., 1981, Estimating the mean length of discontinuity traces. Int. Jour. Rock Mech. Min. Sci. Geomech. Abs., v. 18, p. 221-228.

Park, W. C., & Schot, E. H., 1968, Stylolites: their nature and origin. J. Sed. Petrology, v. 38, p. 175-191.

Parsons, R. W., 1966, Permeability of idealized fractured rock. Soc. Petrol. Eng. Jour., p. 126-136.

Patacca, E., Scandone, P., Giunta, G. & Liguori, V., 1979, Mesozoic paleotectonic evolution of the Ragusa Zone (Southeastern Sicily). Geol. Romana, v. 18, p. 331-369.

Pedley, H. M., 1987a, The Ghar Lapsi limestones: Sedimentology of a Miocene intra-shelf graben. Centro, v. 1, p. 1-14.

Pedley, H. M., 1987b, Controls on Cenozoic carbonate deposition in the Maltese islands: Review and reinterpretation. Mem. Soc. Geologica. It., v. 38, p. 81-94.

Pedley, H. M., 1981, Sedimentology and palaeoenvironment of the southeast Sicilian Tertiary platform carbonates. Sediment. Geol., v. 28, p. 273-291.

Pedley, H. M., 1974, Miocene sea floor subsidence and later sub aerial solution subsidence structures in the Maltese Islands. Proc. Geol. Assoc., v. 85, p. 533-547.

Pedley, H. M., & Grasso, M., 1991, Sea-level change around the margins of the Catania-Gela Trough and Hyblean Plateau, southeast Sicily (African-Eurpean plate convergence zone): a problem of the Plio-Quaternary plate buoyancy?. Int. Assoc. Sedimentol. Spec. Publ. v. 12, p. 451-464.

Pedley, H. M., House, M. R., & Waugh, B., 1976, The geology of Malta and Gozo. Proc. Geol. Assoc., v. 87, p. 325-341.

Phillips, W.J., 1972, Hydraulic fracturing and mineralisation. J. Geol. Soc London, v. 128, p. 337-359.

Philps, B. R., Structural history and fracturing of the Hasdrubal Gas Accumulation. *In*: Tunisia, Hasdrubal Field: An integrated sub-surface description with hydrocarbons in place and reserves. BG Group Internal Report.

Philps, B.R, 2000, Structural evaluation of the Hasdrubal Gas Condensate Accumulation. Proc. 8th Tunisian. Pet. Exp. Prod. Conf. Tunis, 5th – 9th May 2000.

Piske, J., 1981, Fracture investigations as a contribution to representation of trap models for Zechstein carbonates. Geologische Wissenschaften, Berlin, v. 9, p. 965-982.

Pitman, W.C., III & Talwani, M., 1972, Seafloor spreading in the North Atlantic. Geol. Soc. Am. Bull., v. 83, p. 619-43.

Pompilio, M., & Scribano, V., 1992, Nature and evolution of crystalline basement beneath the Hyblean Plateau (Sicily) inferred from xenoliths in volcanic rocks. Contrib.

Geol. It. (Carmignani, L., & Sassi, F. P. (eds)). IGCP No. 276, Newsletter, v. 5, p. 381-390.

Press, W.H., Flannery, B.P., Teukolsky, S.A. & Vetterling, W.T., 1992, Numerical recipes in Fortran 77, Cambridge University Press, 933pp.

Price, N.J., and Cosgrove, J.W., 1990, Analysis of geological structures. Cambridge University Press, Cambridge, UK.

Price, N.J., 1966, Fault and joint development in brittle and semi-brittle rock. Perganom Press, Oxford, England, 176p.

Priest, S. D., 1993, Discontinuity analysis for rock engineering. Chapman & Hall, London, 1993.

Price, N. J., 1974, The development of stress systems and fracture patterns in undeformed sediments. Proc. Third Cong. Int. Rock Mech., TA p. 487-496.

Price, N.J., 1959, Mechanics of jointing in rocks. Geol. Mag., v. 96, p. 149-167.

Priest, S. D., 1985, Hemispherical projection methods in rock mechanics. George Allen & Unwin, London.

Priest, S. D., & Hudson, J. A., 1981, Estimation of discontinuity spacing and trace length using scanline surveys. Int. J. Rock. Mech. Min. Sci., v. 18, p. 183-197.

Priest, S. D., & Hudson, J.A., 1976, Discontinuity spacings in rock. Int. J. Rock. Mech. Min. Sci & Geomech. Abstr., v. 13, p. 135-148.

Racey, A., Bailey, H. W., Beckett, D., Gallagher, L. T., Hampton, M. J., & McQuilken, J., 2001, The petroleum geology of the Early Eocene El Garia Formation, Hasdrubal Field, offshore Tunisia. J. Pet. Geol., v. 24, p. 29-53.

Rehault, J-P., Boillet, G., Mauffret, A., 1985, The Western Mediterranean Basin. *In* Geological Evolution of the Mediterranean Sea (Stanley, D. G., & Wezel, F. C., (eds)). Springer-Verlag, New York, p. 101-129.

Reuther, C. D., Ben-Avraham, Z., & Grasso, M., 1993, Origin and role of major strike-slip transfers during plate collision in the Central Mediterranean. Terra Nova, v. 249-257.

Reuther, C. D., 1987, Extensional tectonics within the central Mediterranean segment of the Afro-European zone of convergence. Mem. Soc. Geol. It., v. 38, p. 69-80.

Reuther, C. D., & Eisbacher, G. H., 1985, Pantelleria Rift – crustal extension in a convergent intraplate setting. Geol. Rundsch., v. 74, p. 585-597.

Richard, P., 1991, Experiments on faulting in a two-layer cover sequence overlying a reactivated basement fault with oblique-slip. J. Struct. Geol., v. 13, p. 459-469.

Rives, T., Razack, M., Petit, J.-P., and Rawnsley, K.D., 1992, Joint spacing: analogue and numerical simulations. J. Struct. Geol., v. 14, p. 925-937.

Rowley, E.J., 1998. Quantifying Cenozoic exhumation across the British Isles. Unpublished PhD thesis. University of Cambridge, UK.

Salaj, J., 1978, The geology of the Pelagian Block: The Eastern Tunisian Platform. *In* The Ocean Basins and Margins, 4B The eastern Mediterranean (Nairn, A.E.M., Kanes, W.H., & Stehli, F.G. (eds.)). Plenum Press, New York, p. 361-416.

Sattarov, S. S., Vaksler, Y. U. A., & Shesnokov, S. A., 1990, Holographic methods in evaluating rock mass structure. *In* Proc. Int. Conf. Rock. Mech. Joint. & Fault. Rock, Vienna, Austria, (Rossmanith, H. P. R (ed)), Balkema, Rotterdam, p. 323-327.

Savostin, L.A., Sibuet, J.-C., Zonenshain, L.P., Le Pichon, X., & Roulet, M.-J., 1986, Kinematic evolution of the Tethys belt from the Atlantic Ocean to the Pamirs since the Triassic. Tectonophys., v. 123, p. 1-35.

Sclumberger, 1992, FMI Fullbore Formation MicroImager. Brochure, SMP 9210.

Schminke, H.-U., Behncke, B., Grasso, M., & Raffi, S., 1997, Evolution of the northwestern Iblean Mountains, Sicily: uplift, Piocene/Pleistocene sea-level changes, paleoenvironment, and volcanism. Geol. Rundsch., v. 86, p. 637-669.

Sclater, J. G., & Christie, P. A. F., 1980, Continental stretching: An explanation of the post-mid-Cretaceous subsidence of the Central North Sea Basin. J. Geophys. Res., v. 85, p. 3711-3739.

Scribano, V., 1987, Deep-seated xenoliths in alkaline volcanic rocks form the Hyblean Plateau (SE-Sicily). Mem. Soc. Geol. It., v. 38, p. 475-482.

Selli, R., 1985, Tectonic evolution of the Tyrrhenian Sea. *In* Geological Evolution of the Mediterranean Sea (Stanley, D. G., & Wezel, F. C., (eds)). Springer-Verlag, New York, p. 131-151.

Sengor, A.M.C, 1979, Mid-Mesozoic closure of the Permo-Triassic Tethys and its implications. Nature, v.279, p. 590-593.

Shepherd, J., Creasey, J. W., & Rixon, L. K., 1982, Comment on joint spacing as a method for locating faults. Geology, v. 10, p. 282.

Smaoui, J., Masmoudi, N., M'Rad, R., & Gharieni, N., 1998, Fractured carbonate reservoirs and petroleum systems in northeastern Tunisia. Proc. 6th Tunisian Petroleum Exploration and Production Conference, Tunis, May, p. 337-342.

Smith, A.G., & Woodcock, N.H., 1982, Tectonic syntheses of the Alpine-Mediterranean region: a review. In Alpine Mediterranean Geodynamics (Berckhemer and Hsü (eds.). Geodynamics Ser. 7, Am.geophys. Un. and Geol. Soc. Am., pp. 15-38.

Smith, A.G., & Woodcock, N.H., 1976, Emplacement model for some Tethyan ophiolites. Geology, v. 4, p. 653-656.

Smith, A.G., 1971, Alpine deformation and the oceanic areas of the Tethys, Mediterranean, Atlantic. Geol. Soc. Am. Bull., v. 82, p. 2039-2070.

Stearns, D.W., and Friedman, M., 1972, Reservoirs in fractured rock, *in* Stratigraphic oil and gas fields- classification, exploration methods, and case histories. AAPG Mem. 16, p. 82-106.

Stearns, D.W., 1968b, Certain aspects of fracture in naturally deformed rocks. National Science Foundation advanced seminar in rock mechanics (R.F. Riecker, Ed.). Air Force Cambridge Research Laboratory, Special Report 1, p. 97-116.

Stearns, D.W., 1964, Macrofracture patterns on Teton anticline, northwest Montana. Am. Geophys. Union Trans., v. 45, p. 107-108.

Styles & McKee, 1998, Processing, structural interpretation and integration with core images of CAST and FMS data from Hasdrubal –2 and –3. Report prepared for BG Group by Z&S Geoscience. Report Ref. ZSL-98-562.

Suess, E., 1893, Are great oceans depth permanent?: Nat. Sci., v. 2, p. 180-187.

Terzaghi, R. D., 1965, Sources of error in joint surveys. Geotechnique, v. 15, p. 287-304.

Teufel, L. W., Farrell, H. E., 1990, Distribution of in-situ stress and natural fractures in the Ekofisk Field, North Sea; implications for reservoir permeability. AAPG Bull, v. 74, p. 777.

Thompson, P., 1998, Reservoir modelling of the Hasdrubal Gas Condensate Field. *In*: Tunisia, Hasdrubal Field: An integrated sub-surface description with hydrocarbons in place and reserves. BG Group Internal Report.

Torelli, L., Grasso, M., Mazzoldi, G & Peis, D., 1998, Plio-Quaternary tectonic evolution and structure of the Catania foredeep, the northern Hyblean Plateau and the Ionian shelf (SE Sicily). Tectonophys., v. 298, p. 209-221.

Torelli, L., Grasso, M., Mazzoldi, G., Peis, D & Gori, D., 1995, Cretaceous to Neogene structural evolution of the Lampedusa Shelf (Pelagian Sea, Central Mediterranean). Terra Nova, v. 7, p. 200-212.

Tsoutrelis, C. E., Exadactylos, G. E., & Kapenis, A. P., 1990, Study of the rock mass discontinuity system using photoanalysis. *In* Proc. Int. Conf. Rock. Mech. Joint. & Fault. Rock, Vienna, Austria, (Rossmanith, H. P. R (ed)), Balkema, Rotterdam, p. 103-112.

Wagner, G., 1913, Stylolithen und Drucksuturen. Geol. Palaont. Abhandlungen, v. 11, p. 101-128.

Walsh, J. J. & Watterson, J., 1988, Analysis of the relationship between displacement and the dimension of faults. J. Struct Geol., v. 10, p. 239-247.

Wanless, H., 1979, Pervasive pressure solution and associated dolomitisation, Paleozoic limestones. Abs. from 1st AAPG Conf. on deep burial diagenesis in limestones, Tulsa, Oklahoma, p. 21-23.

Watts, A. B., & Steckler, M. S., 1979, Subsidence and eustacy at the continental margin of eastern North America. Am. Geophys. Union Ser., v. 3, p. 218-234.

Watts, L., 1983, Microfractures in chalks of the Albuskjell Field, Norwegian sector, North Sea - possible origin and distribution. AAPG Bulletin, v. 67, p. 201-234.

Weber, K. J., & Bakker, M., 1981, Fracture and vuggy porosity. Proc. 56th Annual Meeting of the Society of Petroleum Engineers of the American Institute of Mechanical Engineers, Preprint SPE 10332, 11p.

Westaway, R., 1995, Active tectonic deformation in the Sirte Basin and its surroundings. *In* The Geology of Libya (Salem, M. J. El-Hawat, A. S. & Sbeta, A. M. (eds)). Elsevier, Amsterdam, p. 89-100.

Westaway, R., 1990, Present-day kinematics of the plate boundary zone between Africa and Europe, from the Azores to the Aegean. Earth & Planetary Sci. Let., v. 96, p. 393-406.

Wezel, F. C., 1985, Structural features and basin tectonics of the Tyrrhenian Sea. *In* Geological Evolution of the Mediterranean Sea (Stanley, D. G., & Wezel, F. C., (eds)). Springer-Verlag, New York, p. 153-194.

Wilson, M., & Guiraud, R., 1998, Late to recent magmatic activity on the African-Arabian margin of the Tethys. *In* Petroleum Geology of North Africa (Macgregor, D. S., Moody, R. T. J. & Clarke-Lowes, D. D. (eds)). Geol. Soc. Lond. Spec. Pub. No. 132, p. 231-263.

Wheeler, P.J., 2000. Cenozoic basin formation in SE Asia. Unpublished PhD thesis. University of Cambridge, UK.

White, N., 1994, An inverse method for determining lithospheric strain rate variation on geologic timescales. Earth & Planetary Science Letters, v. 122, p. 351-371.

White, N., 1993, Recovery of strain rate variation from inversion of subsidence data. Nature, v. 366, p. 449-452.

Whittaker, A., Cope, J. W. C., Cowie, J. W., Gibbons, W., Hailwood, E. A., House, M. R., Jenkins, D. G., Rawson, P. F., Rushton, W. A., Smith, D. G., Thomas, A. T., & Wimbledon, W. A., 1991, A guide to stratigraphical procedure. J. Geol. Soc. Lond., v. 148, p. 813-824.

Winnock, E., 1981, Structure du Bloc Pelagien. In Sedimentary Basins and Margins (Wezel, F. C. (ed)). Bologna, p. 445-464.

Wooler, D. A., Smith, A. G., & White, N., 1992, Measuring lithospheric stretching on Tethyan passive margins. J. Geol. Soc. Lond., v. 149, p. 517-532.

Wu, H., and Pollard, D.D., 1995, An experimental study of the relationship between joint spacing and layer thickness. J. Struct. Geol., v. 17, p. 887-905.

Yielding, J., Walsh, J. J., Watterson, J., 1992, The prediction of small-scale faulting in reservoirs. First Break, v. 10, p. 449-460.

Zaier, A., Beji-Sassi, A., Sassi, S., & Moody, R. T. J., 1998, Basin evolution and deposition during the Early Paleogene in Tunisia. . *In* Petroleum Geology of North Africa (Macgregor, D. S., Moody, R. T. J. & Clarke-Lowes, D. D. (eds)). Geol. Soc. Lond. Spec. Pub. No. 132, p. 375-393.

Ziegler, P. A., 1978, North Sea rift and basin development. In Tectonics and geophysics of continental rifts (Ramberg, I. B., & Neumann, E. –R. (eds)). Reidel, Hingham, Mass., p. 249-277.

Zoback, M. D., 1995, Compressive and tensile failure of inclined well bores and determination of in situ stress and rock strength. J. Geophys. Res., v. 100, p. 12791-12811.

Appendix A

Miskar: Raw Core Data

Miskar A-3 Raw Data

Well/Core	Structural	Non-centreline (m)	Centreline Intersection	Centreline Intersection	Termination		Length	Width	Fracture Type	Open/Closed	Fill	Dip	Strike	Slickensides		Stylolites		Vug	Comments
	Feature	Fract. Mid-point Depth (m)	Depth (m)	Fract. Mid-point Depth (m)	Upper	Lower	(mm)	(mm)	(1, 2, 3)					Plunge/Dir.	Sense	Dentae (mm)	Fill	Size	
Miskar A-3																			
3305.45 (START CORE 1)																			
ABIOD	DSB		3305.62		CW	CW	103	3				25							
ABIOD	STY		3305.705		CW	STY	80	0.5				24				1			Deformation Band
ABIOD	STY		3305.715		CW	CW	108	0.5				26				1			Whole series of stylolites - micro features
ABIOD	STY		3305.74		CW	INT	66	0.5				24				1			
ABIOD	VUG		3306.625															5x5	
ABIOD	STY		3306.89		INT	INT	21	0.5				0				1			
IZ 3307.09-3307.15																			Series of small stylolites
ABIOD	FRACT		3307.31		CW	STY	293	0.5	1	PART. OPEN	CALC	74							Zone of intense stylolitisation (horiz.)
ABIOD	STY		3307.32		CW	CW	100	1.5				0				1			Large Fracture assoc. with Sty
ABIOD	STY		3307.35		CW	CW	100	0.5				3				1			
ABIOD	FRACT	3307.42			INT	INT	56	0.5	1	PART. OPEN	CALC	79							
ABIOD	STY		3307.47		CW	CW	105	0.5			?	23				1			
ABIOD	STY		3307.49		CW	CW	103	0.5				23				1			
ABIOD	FRACT	3307.51			CW	INT	80	0.5	1	PART. OPEN	?	88							
ABIOD	STY		3307.55		CW	CW	150	0.5				59							
ABIOD	FRACT		3307.66		CW	CW	120	1	2	PART. OPEN	CALC	80			NORM				LARGE CLOSED FRACTURES
ABIOD	FRACT		3307.69		CW	CW	143	7	2	CLOSED	CALC	52			NORM				LARGE CLOSED FRACTURES
ABIOD	FRACT		3307.7		CW	CW	145	9	2	CLOSED	CALC	51			NORM				LARGE CLOSED FRACTURES
ABIOD	FRACT		3307.75		CW	CW	135	10	2	CLOSED	CALC	40			NORM				
ABIOD	FRACT		3307.8		CW	CW	129	20	2	CLOSED	CALC	45		39	NORM				
MISSING 3307.80-3307.97																			
IZ 3308.10-3308.15																			
ABIOD	FRACT		3308.13		CW	CW	103	1	2	PART. OPEN	CALC	15			NORM				HEAVILY BRECCIATED ZONE. NO PREF. ORIENT
ABIOD	FRACT		3308.15		FRACT	CW	90	2	2	CLOSED	CALC	40			NORM				
ABIOD	FRACT		3308.43		CW	STY	256	1	2	PART. OPEN	CALC	80			NORM				
ABIOD	STY		3308.5		FRACT	CW	75					0				3			DISPLACES STY. BELOW BY 5MM
ABIOD	STY		3308.515		CW	CW	100	1				0				1			
ABIOD	FRACT	3308.53			STY	STY	19	0.5	1	PART. OPEN	CALC	90							DISPLACED 2X BY FRACTURES. DISP. = 5-15MM
ABIOD	FRACT	3308.53			STY	STY	17	0.5	1	PART. OPEN	CALC	88							FRACT CONNECTED TO STY
ABIOD	FRACT	3308.53			STY	STY	15	0.5	1	PART. OPEN	CALC	88							FRACT CONNECTED TO STY
ABIOD	FRACT		3308.56		CW	INT	115	1.5	2	PART. OPEN	CALC	67			NORM				FRACT CONNECTED TO STY
ABIOD	STY		3308.565		CW	CW	103	3				2				3			DISPLACES LARGE STY. BY 20MM
ABIOD	FRACT	3308.57			STY	INT	22	0.5	1	PART. OPEN	CALC	78							MANY STA FRACTURES LEADING OFF BASE
ABIOD	FRACT	3308.575			STY	INT	24	0.5	1	PART. OPEN	CALC	79							MICROFRACT LEADING FROM ABOVE STY
ABIOD	FRACT		3308.575		STY	STY	12	0.5	1	PART. OPEN	CALC	83							MICROFRACT LEADING FROM ABOVE STY
ABIOD	FRACT	3308.575			STY	INT	16	0.5	1	PART. OPEN	CALC	88							MICROFRACT LEADING FROM ABOVE STY
ABIOD	FRACT	3308.58			STY	INT	32	0.5	1	PART. OPEN	CALC	72							MICROFRACT LEADING FROM ABOVE STY
ABIOD	FRACT		3308.58		STY	INT	23	0.5	1	PART. OPEN	CALC	88							MICROFRACT LEADING FROM ABOVE STY
ABIOD	FRACT		3308.59		CW	STY	73	1	2	PART. OPEN	CALC	56			NORM				LARGE FRACT. NB. DIFF. FROM ABOVE SET
ABIOD	FRACT		3308.59		STY	STY	33	1	2	PART. OPEN	CALC	58			NORM				LARGE FRACT. NB. DIFF. FROM ABOVE SET
ABIOD	STY		3308.595		CW	CW	100	0.5				0				2			
ABIOD	STY		3308.597		CW	CW	100	0.5				0				3			
ABIOD	STY		3308.6		CW	STY	65	0.5				55				4			DIFF. STY. SET TO ABOVE. YOUNGER. NON-COMPACT. CUT BY FRACT. B45
ABIOD	STY		3308.615		CW	CW	103	0.5				0				1			CUT BY ABOVE STY
ABIOD	STY		3308.3		CW	CW	100	0.5				0				1			
ABIOD	FRACT		3308.65		CW	STY	167	0.5	2	PART. OPEN	?	54			NORM				CUTS LOWER STYLOLITES AND ALSO UPPER YOUNGER STY
ABIOD	STY		3308.67		CW	CW	100	0.5				0				1			
ABIOD	STY		3308.675		CW	CW	100	0.5				0				1			
ABIOD	STY		3308.73		CW	CW	102	0.5				0				1			
ABIOD	FRACT		3308.76		INT	CW	90	0.5	2	PART. OPEN	CALC	63			NORM				
ABIOD	STY		3309.2		CW	CW	100	0.5				0				3			
ABIOD	STY		3309.205		CW	CW	100	0.5				0				1			
ABIOD	FRACT		3309.25		CW	INT	125	0.5	2	PART. OPEN	CALC	56			NORM				
ABIOD	VUG	3309.31			INT	INT					CALC							10X2	
ABIOD	VUG	3309.48			INT	INT					CALC							21X3	
ABIOD	FRACT		3309.635		CW	CW	104	1	2	PART. OPEN	CALC	28			NORM?				
RUBBLE 3309.90-3310.39																			
ABIOD	FRACT		3310.47		CW	CW	203	1	2	PART. OPEN	CALC	61			NORM				
IZ 3310.59-3310.61																			
RUBBLE 3310.77-3311.31																			ZONE OF MICRO STYLOLITES
ABIOD	STY		3311.32		CW	CW	115	13				32							
ABIOD	STY		3311.39		CW	CW	116	5				33							LARGE PRESSURE SOLUTION SEAM
ABIOD	STY		3311.46		CW	CW	105	10				23							LARGE PRESSURE SOLUTION SEAM
ABIOD	FRACT		3312.56		CW	CW	110	6	2	PART. OPEN	CALC	26			NORM				LARGE PRESSURE SOLUTION SEAM
ABIOD	STY		3312.566		CW	CW	103	0.5											FRACT. WITH BRECC. ZONE BENEATH IT BOUNDED BY STY AT BASE. PROB. MINOR FAULT
ABIOD	FRACT		3312.6		CW	CW	113	0.5	2	PART. OPEN	CALC	35			NORM		1		STY AT BASE OF FAULT ZONE
RUBBLE 3313.48-3314.15																			
ABIOD	STY		3314.17		CW	CW	176	3				55							
ABIOD	FRACT		3315.08		INT	INT	37	0.5	2	PART. OPEN	?	51			NORM				LARGE TECTONIC STY
ABIOD	FRACT		3315.09		CW	INT	60	0.5	2	PART. OPEN	?	48			NORM				ZONE OF CALC FILLED MICRO FRACTS. INTERSECT EACHOTHER, 2 SETS
ABIOD	FRACT		3315.095		INT	CW	94	0.5	2	PART. OPEN	?	54			NORM				ZONE OF CALC FILLED MICRO FRACTS. INTERSECT EACHOTHER, 2 SETS
ABIOD	FRACT		3315.48		CW	INT	104	0.5	2	PART. OPEN	CALC	49			NORM				ZONE OF CALC FILLED MICRO FRACTS. INTERSECT EACHOTHER, 2 SETS
ABIOD	FRACT		3315.53		CW	INT	110	0.5	2	PART. OPEN	CALC	68			NORM				ZONE OF CALC FILLED MICRO FRACTS. INTERSECT EACHOTHER, 2 SETS
ABIOD	FRACT		3315.55		INT	CW	94	0.5	2	PART. OPEN	CALC	62			NORM				ZONE OF CALC FILLED MICRO FRACTS. INTERSECT EACHOTHER, 2 SETS
RUBBLE 3316.14-3316.33																			
ABIOD	FRACT		3316.35		CW	CW	118	1.5	2	PART. OPEN	CALC	38			NORM				
ABIOD	FRACT		3316.4		CW	CW	138	2	2	PART. OPEN	CALC	53			NORM				THESE TWO FRACTS. REPRES. SAME TECTONIC STRESS FIELD. CONJUGATES THAT INTERSECT
ABIOD	FRACT	3316.41			FRACT	INT	54	0.5	2	PART. OPEN	CALC	35			NORM				THESE TWO FRACTS. REPRES. SAME TECTONIC STRESS FIELD. CONJUGATES THAT INTERSECT
ABIOD	FRACT		3316.45		FRACT	CW	198	0.5	2	PART. OPEN	CALC	62			NORM				
ABIOD	FRACT	3316.48			CW	CW	213	0.5	2	PART. OPEN	CALC	73			NORM				
ABIOD	FRACT	3316.49			INT	CW	130	0.5	2	PART. OPEN	CALC	74			NORM				INTERSECTS ABOVE FRACT (B84)
ABIOD	FRACT	3316.495			INT	CW	174	0.5	2	PART. OPEN	CALC	73			NORM				INTERSECTS ABOVE FRACT (B84)
IZ 3316.55-3316.58																			INTERSECTS ABOVE FRACT (B84)
ABIOD	STY		3316.585		CW	CW	101	0.5				6				15			STY. ACCUMULATION. MANY MICRO STY
ABIOD	FRACT	3316.66			CW	INT	141	0.5	2?	PART. OPEN	CALC	74			NORM?				
ABIOD	STY		3316.92		CW	CW	106	20				23							
ABIOD	FRACT	3316.945			INT	CW	65	0.5	2?	PART. OPEN	CALC	69			NORM				AMALGAMATION OF MANY MICRO STY. COMPACTIONAL
ABIOD	FRACT	3316.955			INT	INT	61	0.5	2	PART. OPEN	CALC	68			NORM				HIGH ANGLE CALC-FILLED FRACTS CUTTING STY. SEAM. THEREFORE YOUNGER THAN SEAM
ABIOD	FRACT	3316.98			CW	INT	73	0.5	2	PART. OPEN	CALC	61			NORM				HIGH ANGLE CALC-FILLED FRACTS CUTTING STY. SEAM. THEREFORE YOUNGER THAN SEAM
ABIOD	FRACT		3317.06		CW	CW	316	0.5	2	PART. OPEN	CALC	72			NORM				HIGH ANGLE CALC-FILLED FRACTS CUTTING STY. SEAM. THEREFORE YOUNGER THAN SEAM

Miskar A-3 Raw Data

ABIOD	STY		3317.13		CW	CW	114	4				31				1			AMALGAMATION OF MANY MICRO-STY. COMPACTIONAL
ABIOD	STY		3317.14		CW	CW	114	0.5				33				1			
ABIOD	STY		3317.147		CW	CW	114	0.5				31				1			
ABIOD	STY		3317.16		CW	CW	114	0.5				30				1			
IZ 3317.33-3317.35																			ZONE OF INTENSE MICROSTYLOLITISATION
ABIOD	STY		3318		CW	CW	158	9				55				20			AMALGAMATION OF MANY MICRO-STY. COMPACTIONAL. LONG WAVELENGTH
ABIOD	STY		3318.26		CW	CW	116	11				46				10			AMALGAMATION OF MANY MICRO-STY. COMPACTIONAL. LONG WAVELENGTH
RUBBLE 3318.48-3318.88																			
ABIOD	STY		3319.69		CW	CW	110	4				28							AMALGAMATION OF MANY MICRO-STY. COMPACTIONAL. LONG WAVELENGTH
RUBBLE 3319.80-3321.47																			
ABIOD	STY		3321.48		CW	CW	100	6				0							AMALGAMATION OF MANY MICRO-STY. COMPACTIONAL. LONG WAVELENGTH
RUBBLE 3321.58-3322.87																			
ABIOD	STY		3322.87		CW	CW	124	6											AMALGAMATION OF MANY MICRO-STY. COMPACTIONAL. LONG WAVELENGTH
RUBBLE 3322.92-3324.38																			
3324.50 (END CORE 1)																			
3324.50 (START CORE 2)																			
RUBBLE 3325.00-3325.63																			
ABIOD	STY		3325.66		CW	CW	107	5				32				5			AMALGAMATION OF MANY MICRO-STY. COMPACTIONAL. LONG WAVELENGTH
RUBBLE 3325.68-3327.65																			
ABIOD	STY		3327.72		CW	CW	107	4				33				15			AMALGAMATION OF MANY MICRO-STY. COMPACTIONAL. LONG WAVELENGTH
ABIOD	STY		3328.25		STY	STY	26	0.5				3				1			OLDER. CUT BY B115
ABIOD	STY		3328.255		CW	CW	115	2.5				28				32			AMALGAMATION OF MANY MICRO-STY. COMPACTIONAL. LONG WAVELENGTH
ABIOD	FRACT		3328.26		STY	CW	40	0.5	??	PART OPEN	CALC	63			NORM				STA FRACTURES. POSS MODE 1
ABIOD	FRACT		3328.3		STY	INT	99	0.5	??	PART OPEN	CALC	62			NORM				STA FRACTURES. POSS MODE 1
ABIOD	STY		3328.455		CW	CW	104	0.5				24				5			
ABIOD	STY		3328.46		CW	CW	106	1				30				5			
ABIOD	STY		3328.52		CW	CW	132	0.5				60				7			
RUBBLE 3328.55-3329.22																			
RUBBLE 3331.75-3332.36																			POSSIBLE FAULT ZONE/ZONE OF INTENSE STY
ABIOD	FRACT	3332.665			INT	INT	41	0.5	1	RE-SEALED	CHALK	69							MANY MICRO-FRACTS. POSSIBLY INDUCED AL THOUGH DOUBTFUL STA ASSOC ?
ABIOD	FRACT	3332.665			INT	INT	22	0.5	1	RE-SEALED	CHALK	64							MANY MICRO-FRACTS. POSSIBLY INDUCED AL THOUGH DOUBTFUL STA ASSOC ?
ABIOD	FRACT	3332.67			INT	INT	35	0.5	1	RE-SEALED	CHALK	61							MANY MICRO-FRACTS. POSSIBLY INDUCED AL THOUGH DOUBTFUL STA ASSOC ?
ABIOD	FRACT	3332.67			INT	INT	47	0.5	1	RE-SEALED	CHALK	59							MANY MICRO-FRACTS. POSSIBLY INDUCED AL THOUGH DOUBTFUL STA ASSOC ?
ABIOD	FRACT	3332.67			INT	INT	15	0.5	1	RE-SEALED	CHALK	64							MANY MICRO-FRACTS. POSSIBLY INDUCED AL THOUGH DOUBTFUL STA ASSOC ?
ABIOD	FRACT	3332.675			INT	INT	23	0.5	1	RE-SEALED	CHALK	63							MANY MICRO-FRACTS. POSSIBLY INDUCED AL THOUGH DOUBTFUL STA ASSOC ?
ABIOD	FRACT	3332.675			INT	INT	33	0.5	1	RE-SEALED	CHALK	64							MANY MICRO-FRACTS. POSSIBLY INDUCED AL THOUGH DOUBTFUL STA ASSOC ?
ABIOD	FRACT	3332.68			INT	INT	36	0.5	1	RE-SEALED	CHALK	57							MANY MICRO-FRACTS. POSSIBLY INDUCED AL THOUGH DOUBTFUL STA ASSOC ?
ABIOD	FRACT	3332.68			INT	INT	42	0.5	1	RE-SEALED	CHALK	62							MANY MICRO-FRACTS. POSSIBLY INDUCED AL THOUGH DOUBTFUL STA ASSOC ?
ABIOD	FRACT	3332.685			INT	INT	54	0.5	1	RE-SEALED	CHALK	58							MANY MICRO-FRACTS. POSSIBLY INDUCED AL THOUGH DOUBTFUL STA ASSOC ?
ABIOD	FRACT	3332.685			INT	INT	16	0.5	1	RE-SEALED	CHALK	60							MANY MICRO-FRACTS. POSSIBLY INDUCED AL THOUGH DOUBTFUL STA ASSOC ?
ABIOD	STY		3332.77		CW	CW	138	1				45				24			COMPACTIONAL
ABIOD	FRACT	3332.8			STY	INT	43	0.5	1	RE-SEALED	CHALK	49							MANY MICRO-FRACTS. POSSIBLY INDUCED AL THOUGH DOUBTFUL STA ASSOC ?
ABIOD	FRACT	3332.805			STY	INT	56	0.5	1	RE-SEALED	CHALK	52							MANY MICRO-FRACTS. POSSIBLY INDUCED AL THOUGH DOUBTFUL STA ASSOC ?
ABIOD	FRACT	3332.81			STY	INT	70	0.5	1	RE-SEALED	CHALK	48							MANY MICRO-FRACTS. POSSIBLY INDUCED AL THOUGH DOUBTFUL STA ASSOC ?
ABIOD	FRACT	3332.815			STY	CW	44	0.5	1	RE-SEALED	CHALK	51							MANY MICRO-FRACTS. POSSIBLY INDUCED AL THOUGH DOUBTFUL STA ASSOC ?
ABIOD	FRACT	3332.815			INT	CW	86	0.5	1	RE-SEALED	CHALK	63							MANY MICRO-FRACTS. POSSIBLY INDUCED AL THOUGH DOUBTFUL STA ASSOC ?
ABIOD	FRACT	3332.82			INT	CW	82	0.5	1	RE-SEALED	CHALK	42							MANY MICRO-FRACTS. POSSIBLY INDUCED AL THOUGH DOUBTFUL STA ASSOC ?
ABIOD	FRACT	3332.82			INT	CW	43	0.5	1	RE-SEALED	CHALK	89							MANY MICRO-FRACTS. POSSIBLY INDUCED AL THOUGH DOUBTFUL STA ASSOC ?
ABIOD	FRACT	3332.89			INT	CW	20	0.5	1	RE-SEALED	CHALK	50							MANY MICRO-FRACTS. POSSIBLY INDUCED AL THOUGH DOUBTFUL STA ASSOC ?
ABIOD	FRACT	3332.9			INT	CW	96	0.5	1	RE-SEALED	CHALK	52							MANY MICRO-FRACTS. POSSIBLY INDUCED AL THOUGH DOUBTFUL STA ASSOC ?
ABIOD	FRACT	3332.905			INT	CW	65	0.5	1	RE-SEALED	CHALK	60							MANY MICRO-FRACTS. POSSIBLY INDUCED AL THOUGH DOUBTFUL STA ASSOC ?
ABIOD	STY	3333.12			CW	CW	103	0.5				28							COMPACTIONAL
ABIOD	STY	3333.13			CW	CW	103	0.5				28							COMPACTIONAL
ABIOD	STY		3333.135		CW	CW	103	0.5				28							COMPACTIONAL
ABIOD	FRACT	3333.16			STY	INT	71	0.5	1	RE-SEALED	CHALK	88							MANY MICRO-FRACTS. POSSIBLY INDUCED AL THOUGH DOUBTFUL STA ASSOC ?
ABIOD	FRACT	3333.17			STY	INT	63	0.5	1	RE-SEALED	CHALK	90							MANY MICRO-FRACTS. POSSIBLY INDUCED AL THOUGH DOUBTFUL STA ASSOC ?
ABIOD	FRACT		3333.175		STY	INT	71	0.5	1	RE-SEALED	CHALK	87							MANY MICRO-FRACTS. POSSIBLY INDUCED AL THOUGH DOUBTFUL STA ASSOC ?
ABIOD	FRACT	3333.18			INT	CW	52	0.5	1	RE-SEALED	CHALK	86							MANY MICRO-FRACTS. POSSIBLY INDUCED AL THOUGH DOUBTFUL STA ASSOC ?
RUBBLE 3333.00-3333.74																			
IZ 3333.74-3333.96																			MANY REHEALED MICRO-FRACTURES. -45. WITHIN CHALK
RUBBLE 3332.96-3334.58																			
IZ 3334.76-3335.99																			MANY REHEALED MICRO-FRACTURES. -45. WITHIN CHALK
ABIOD	STY		3335.39		CW	CW	116	0.5				36				5			COMPACTIONAL
ABIOD	FRACT		3335.41		INT	CW	60	0.5	1?	RE-SEALED	CHALK	68							RESEALED MICRO-FRACTURE
ABIOD	FRACT	3335.47			INT	INT	56	0.5	1?	RE-SEALED	CHALK	65							RESEALED MICRO-FRACTURE
ABIOD	FRACT	3335.49			INT	INT	24	0.5	1?	RE-SEALED	CHALK	64							RESEALED MICRO-FRACTURE
ABIOD	FRACT	3335.525			CW	INT	86	0.5	1?	RE-SEALED	CHALK	67							RESEALED MICRO-FRACTURE
ABIOD	STY		3335.575		CW	CW	116	1				33				14			COMPACTIONAL
ABIOD	FRACT	3335.685			INT	STY	38	0.5	1	RE-SEALED	CHALK	90							
ABIOD	STY		3335.69		CW	CW	123	2								29			COMPACTIONAL. ZONE OF MICRO-FRACTURES AT BASE OF STY
ABIOD	FRACT		3335.87		INT	CW	135	0.5	1	RE-SEALED	CHALK	78							
ABIOD	FRACT		3335.91		INT	INT	17	0.5	1	RE-SEALED	CHALK	86							
ABIOD	FRACT		3335.92		CW	INT	97	0.5	1	RE-SEALED	CHALK	76							
ABIOD	FRACT	3335.99			INT	INT	57	0.5	1	RE-SEALED	CHALK	74							
ABIOD	FRACT		3336.63		INT	CW	123	0.5	1	RE-SEALED	CHALK	67							
IZ 3336.21-3336.27																			ZONE OF INTENSE COMPACTIONAL STY.
ABIOD	FRACT	3336.57			INT	INT	48	0.5	1	RE-SEALED	CHALK	90							
ABIOD	FRACT		3336.58		INT	INT	94	0.5	1	RE-SEALED	CHALK	88							CUT THROUGH STY
ABIOD	FRACT		3336.59		INT	STY	15	0.5	1	RE-SEALED	CHALK	90							
ABIOD	FRACT		3336.61		INT	INT	32	0.5	1	RE-SEALED	CHALK	90							
ABIOD	STY		3336.615		CW	CW	115	0.5				32				1			COMPACTIONAL
ABIOD	FRACT	3336.72			INT	INT	26	0.5	1	RE-SEALED	CHALK	90							
ABIOD	FRACT	3336.73			INT	INT	44	0.5	1	RE-SEALED	CHALK	90							
ABIOD	STY		3337.19		CW	CW	109	1				26				11			COMPACTIONAL
ABIOD	STY		3337.205		CW	CW	109	0.5				24				1			COMPACTIONAL
ABIOD	STY		3337.575		CW	CW	110	0.5				28				1.5			COMPACTIONAL
ABIOD	STY		3337.58		CW	CW	110	0.5				28				1			COMPACTIONAL
ABIOD	STY		3338.15		CW	CW	108	2				27				33			COMPACTIONAL
RUBBLE 3338.67-3352.96																			LARGE CALC. FILLED FRACTS AT 3344.80
3353.00 (END CORE 2)																			
3353.00 (START CORE 3)																			
ABIOD	STY		3353.45		CW	CW	115	1.5				41				6			COMPACTIONAL. POSSIBLY TECTONIC. APPEARS TO CUT ACROSS SED. LAYERING
ABIOD	STY		3353.67		CW	CW	114	1				46				7			COMPACTIONAL. POSSIBLY TECTONIC. APPEARS TO CUT ACROSS SED. LAYERING
IZ 3353.68-3353.79							116	0.5				40				5			ZONE OF PRESS. SOL. SEAMS/STYLOLITE S/COMPACTIONAL
IZ 3354.00-3354.05							104	0.5				21				4			ZONE OF PRESS. SOL. SEAMS/STYLOLITE S/COMPACTIONAL

Miskar A-3 Raw Data

IZ 3354.05-3354.64																		DISCRETE ZONES OF STYLOLITE DEVELOPMENT. 4 ZONES. 50MM WIDE
ABIOD	STY		3354.645		CW	CW	101	0.5				15				5		COMPACTIONAL
ABIOD	STY		3354.65		STY	CW	125	0.5				19				1		COMPACTIONAL
IZ 3354.68-3354.78							100	0.5				42				3		TECTONIC
ABIOD	STY		3354.8		CW	CW	104	0.5				10				2		DISCRETE ZONES OF STYLOLITE DEVELOPMENT. 4 ZONES. 50MM WIDE
ABIOD	STY		3354.815		CW	CW	100	1				29				1		COMPACTIONAL
ABIOD	STY		3354.83		CW	STY	57	0.5				2				4		COMPACTIONAL
IZ 3354.92-3355.09												26				3		POSSIBLY TECTONIC/ POSSIBLE THAT A LOT OF THESE STYLOLITES ARE STICKOLITES. I.E. SHEAR FRACTS.
IZ 3356.11-3357.12																		DISCRETE ZONE OF STYLOLITES. BOTH COMP & TECT. TECT - HIGH ANGLE TO BEDDING
ABIOD	STY		3357.17		CW	CW	101	1				14				2		DISCRETE ZONES OF STYLOLITE DEVELOPMENT.
ABIOD	STY		3357.65		CW	CW	102	17				3				11		COMPACTIONAL
ABIOD	STY		3357.665		CW	CW	102	1				7				2		AMALGAMATION OF STY
ABIOD	STY		3357.685		CW	CW	102	0.5				7				2		COMPACTIONAL
RUBBLE 3357.83-3358.83																		COMPACTIONAL
ABIOD	STY		3358.94		CW	CW	105	0.5				34				1		COMPACTIONAL
ABIOD	STY		3358.98		CW	CW	105	38				34				1		COMPACTIONAL
IZ 3358.99-3360.11																		3-4 ZONES OF INCREASED STY. DEVELOPMENT
RUBBLE 3360.19-3360.75																		
ABIOD	STY		3360.775		CW	CW	110	19				24				1		ZONE OF STY. 5-6 STY. SPACING - 5MM
ABIOD	FRACT		3360.8		STY	CW	75	2.5	2	CLOSED	CHALK	62			NORM			SMALL FAULT ZONE
ABIOD	STY		3360.83		CW	CW	114	0.5				34				1		COMPACTIONAL
ABIOD	STY		3361.095		CW	CW	113	1				34						COMPACTIONAL
ABIOD	STY		3361.116		CW	CW	113	3				30						COMPACTIONAL
RUBBLE 3361.30-3362.32																		
IZ 3362.32-3364.03																		DISCRETE ZONES OF HEAVY STYLOLITISATION
RUBBLE 3364.03-3365.17																		
MAJOR LITH CHANGE 3365.17																		
NOTHING 3365.17-3372.16																		
ABIOD	FRACT		3372.93		CW	INT	200	0.5	2	CLOSED	CALC	74			NORM			HIGH ANGLE FRACT.
IZ 3375.09-3375.35																		HEAVILY STY. ZONE. 23MM THICK
ABIOD	FRACT		3375.63		CW	CW	105	0.5	2?	PART. OPEN	CALC	29			NORM			
ABIOD	FRACT		3375.72		CW	CW	127	0.5	2?	PART. OPEN	CALC	45			NORM			
ABIOD	FRACT		3375.78		CW	CW	184	0.5	2?	PART. OPEN	CALC	54			NORM			
ABIOD	FRACT	3376.04			CW	INT	130	0.5	1?	PART. OPEN	CALC	78			NORM			
ABIOD	FRACT	3376.04			STY	CW	165	0.5	1?	PART. OPEN	CALC	80						
ABIOD	FRACT		3376.08		INT	INT	83	0.5	1?	PART. OPEN	CALC	77						
ABIOD	FRACT		3376.115		CW	INT	125	0.5	1?	PART. OPEN	CALC	69						
ABIOD	FRACT		3376.12		INT	INT	196	0.5	1?	PART. OPEN	CALC	90						
IZ 3376.54-3376.69																		HEAVILY STY. ZONE
ABIOD	FRACT	3376.73			CW	INT	101	0.5	1	CLOSED	CALC	77						
ABIOD	FRACT	3376.75			CW	INT	72	0.5	1	CLOSED	CALC	76						
ABIOD	FRACT		3376.85		INT	INT	126	0.5	1	CLOSED	CALC	76						
ABIOD	FRACT		3376.875		INT	INT	107	0.5	1	CLOSED	CALC	76						
ABIOD	STY		3376.925		CW	CW	109	8				31				2		ZONE OF MICROSTY. COMP.
ABIOD	STY		3376.955		CW	CW	110	6				30				2		ZONE OF MICROSTY. COMP.
ABIOD	STY		3377.09		CW	CW	100	3				0				1		ZONE OF MICROSTY. COMP.
ABIOD	STY		3377.13		CW	CW	156	50				0				2		ZONE OF MICROSTY. COMP.
ABIOD	STY		3377.42		CW	CW	149	1				51				1		
ABIOD	FRACT	3377.82			CW	INT	98	0.5	1	CLOSED	CALC	83						
ABIOD	STY		3377.86		CW	CW	105	20				10						ZONE OF MICROSTY. COMP.
ABIOD	STY		3377.92		CW	CW	109	0.5				19						ZONE OF MICROSTY. COMP.
ABIOD	FRACT		3378.27		CW	INT	342	0.5	1	CLOSED	CALC	74						
ABIOD	FRACT		3378.51		CW	CW	142	0.5	2	PART. OPEN	CALC	51			NORM			
ABIOD	FRACT		3378.76		CW	INT	70	0.5	2	OPEN		43						
ABIOD	STY		3378.85		CW	CW	108	49				19						AMALGAMATION OF MANY MICROSTY. COMP.
ABIOD	FRACT		3378.91		INT	CW	296	0.5	1	CLOSED	CALC	82						
ABIOD	STY		3379.69		CW	CW	121	63				42				6		AMALGAMATION OF MANY MICROSTY. COMP.
ABIOD	FRACT		3379.92		INT	INT	75	0.5	1	OPEN		63						
ABIOD	STY		3380.57		CW	CW	109	17				28						AMALGAMATION OF MANY MICROSTY. COMP.
ABIOD	STY		3380.66		CW	CW	100	43				20						AMALGAMATION OF MANY MICROSTY. COMP.
3380.63 (END CORE 3)																		
3631.50 (START CORE 4)																		
IZ 3631.58-3632.81																		VERY HARD TO IDENTIFY FRACTS. PROBABLY A LOT PRESENT. APPEARS TO BE A BRECCIA.
LITH CHANGE 3632.81)																		
R-1	FRACT		3636.61		INT	CW	102	0.5	3	OPEN		61						POSS. INDUCED
R-1	FRACT		3636.68		INT	CW	92	0.5	3	OPEN		58						POSS. INDUCED
R-1	FRACT		3637.08		INT	INT	37	0.5	3	OPEN		59						POSS. INDUCED
R-1	FRACT	3637.11			INT	INT	32	0.5	3	OPEN		61						POSS. INDUCED
R-1	FRACT		3637.14		INT	INT	66	0.5	3	OPEN		58						POSS. INDUCED
R-1	VUG		3640.48								CALC						1702	
R-1	FRACT	3640.57			INT	INT	32	0.5	3	PART. OPEN	CALC	90						
R-1	FRACT	3640.65			INT	INT	78	0.5	3	PART. OPEN	CALC	88						
R-1	FRACT	3640.66			INT	INT	52	0.5	3	PART. OPEN	CALC	88						
R-1	FRACT	3640.75			INT	INT	93	0.5	3	PART. OPEN	CALC	90						
R-1	STY		3641.03		CW	CW	108	1				29				4		COMP. STY. RECRACKED
R-1	FRACT	3641.08			INT	STY	26	0.5	3	PART. OPEN	CALC	59						
R-1	STY		3641.09		CW	CW	121	0.5				37						COMP. STY.
R-1	FRACT	3641.1			INT	STY	17	0.5	3	PART. OPEN	CALC	59						
R-1	VUG	3642.09									CALC						20X15	
R-1	STY		3647.68		CW	CW	130	3								39		
R-1	FRACT	3647.68			CW	INT	92	0.5	3	PART. OPEN	CALC	88						EN-ECHELON SET ASSOC. WITH STY BELOW
R-1	FRACT	3647.73			INT	INT	34	0.5	3	PART. OPEN	CALC	88						EN-ECHELON SET ASSOC. WITH STY BELOW
R-1	FRACT		3647.81		INT	INT	94	0.5	3	PART. OPEN	CALC	88						EN-ECHELON SET ASSOC. WITH STY BELOW
R-1	FRACT		3647.82		INT	INT	30	0.5	3	PART. OPEN	CALC	88						EN-ECHELON SET ASSOC. WITH STY BELOW
R-1	FRACT	3647.835			INT	INT	19	0.5	3	PART. OPEN	CALC	89						EN-ECHELON SET ASSOC. WITH STY BELOW
R-1	FRACT		3647.865		INT	STY	86	0.5	3	PART. OPEN	CALC	89						EN-ECHELON SET ASSOC. WITH STY BELOW
R-1	FRACT	3647.95			CW	CW	888	1	3	PART. OPEN	CALC	88						MAJOR CALC FILLED FRACT. ASSOC. WITH STY (PROB. UPPER STY.). CUTS STRAIGHT THROUGH LOW. STY. GOOD SLICKS SHOWING OBLIQUE SHEAR
R-1	FRACT		3647.97		INT	STY	125	0.5	3	PART. OPEN	CALC	85						EN-ECHELON SET ASSOC. WITH STY BELOW
R-1	STY		3647.98		CW	CW	160	2				30				76		STY. WITH EN ECHELON FRACT. SET
R-1	FRACT	3648.01			INT	STY	36	0.5	3	PART. OPEN	CALC	88						EN-ECHELON SET ASSOC. WITH STY ABOVE
R-1	STY		3653.41		CW	CW	130	2				40				65		
R-1	STY		3654.64		CW	CW	124	2				102						
R-1	STY		3655.46		CW	CW	132	5				35				62		
IZ 3655.87-3656.63																		ZONE OF STYLOLITES. GOOD RELATIONSHIPS.
R-1	STY		3656.79		CW	CW	132	5				43				56		

Miskar A-3 Raw Data

R-1	FRACT	3657.11			OW	INT	109	0.5	3	PART OPEN	CALC	88							EN-ECHELON SET
R-1	FRACT	3657.19			OW	INT	106	0.5	3	PART OPEN	CALC	88							EN-ECHELON SET
R-1	STY		3657.3		OW	OW	121	3				44			58				
3658.23 (END CORE 4)																			
3659.40 (START CORE 5)																			
R-1	FRACT		3659.87		OW	INT	74	0.5	1?	PART OPEN	?	55							
R-1	STY		3661.53		OW	OW	128	1				37			33				
R-1	STY		3661.64		OW	OW	108	0.5				26			16				
R-1	STY		3661.95		OW	OW	113	0.5				28			14				
R-1	STY		3662.59		OW	OW	114	2				25			43				
R-1	STY		3665.31		OW	OW	129	1				31			38				
R-1	FRACT	3672.68			INT	INT	97	0.5	1	PART OPEN	CALC	88							EN-ECHELON SET
R-1	FRACT	3672.78			INT	INT	121	0.5	1?	PART OPEN	CALC	88							EN-ECHELON SET
R-1	FRACT		3672.78		INT	INT	227	0.5	1?	PART OPEN	CALC	90							EN-ECHELON SET
R-1	FRACT	3672.86			INT	INT	96	0.5	1?	PART OPEN	CALC	88							EN-ECHELON SET
R-1	FRACT		3672.93		INT	INT	92	0.5	1?	PART OPEN	CALC	88							EN-ECHELON SET
R-1	FRACT	3684.18			INT	INT	93	0.5	1?	PART OPEN	CALC	90							
R-1	FRACT		3685.41		INT	OW	121	1	1?	PART OPEN	CALC	88							
R-1	FRACT		3685.49		INT	OW	145	0.5	1?	PART OPEN	CALC	88							
R-1	FRACT		3685.59		INT	OW	55	0.5	1?	PART OPEN	CALC	88							
R-1	FRACT		3685.6		OW	OW	146	0.5	1?	PART OPEN	CALC	88							
3685.53 (END CORE NO. 5)																			
3687.3 (START CORE NO. 6)																			
R-1	FRACT	3688.63			INT	INT	19	0.2	1?	OPEN		54							CONFINED TO V. BRITTLE SHALEY UNIT POSS. INDUCED
R-1	FRACT	3688.635			INT	INT	9	0.2	1?	OPEN		56							CONFINED TO V. BRITTLE SHALEY UNIT POSS. INDUCED
R-1	FRACT		3688.65	3688.66	INT	INT	11	0.2	1?	OPEN		53							CONFINED TO V. BRITTLE SHALEY UNIT POSS. INDUCED
R-1	FRACT	3688.655			INT	INT	27	0.2	1?	OPEN		56							CONFINED TO V. BRITTLE SHALEY UNIT POSS. INDUCED
R-1	FRACT		3688.95	3688.95	INT	INT	31	0.2	1?	OPEN		57							CONFINED TO V. BRITTLE SHALEY UNIT POSS. INDUCED
R-1	FRACT	3689.01			INT	INT	17	0.2	1?	OPEN		54							CONFINED TO V. BRITTLE SHALEY UNIT POSS. INDUCED
R-1	FRACT	3689.015			INT	INT	12	0.2	1?	OPEN		56							CONFINED TO V. BRITTLE SHALEY UNIT POSS. INDUCED
R-1	FRACT		3689.02	3689.03	INT	INT	37	0.2	1?	OPEN		49							CONFINED TO V. BRITTLE SHALEY UNIT POSS. INDUCED
R-1	FRACT	3689.035			INT	INT	12	0.2	1?	OPEN		56							CONFINED TO V. BRITTLE SHALEY UNIT POSS. INDUCED
R-1	FRACT	3689.04			INT	INT	13	0.2	1?	OPEN		51							CONFINED TO V. BRITTLE SHALEY UNIT POSS. INDUCED
R-1	FRACT	3689.245			INT	INT	22	0.2	1?	OPEN		72							FRACT. RELATED TO FAULT ZONE BETWEEN 3689.23-3689.64. ALL FAULT BRECCIA
R-1	FRACT	3689.28			INT	INT	22	0.2	1?	OPEN		51							FRACT. RELATED TO FAULT ZONE BETWEEN 3689.23-3689.64. ALL FAULT BRECCIA
R-1	FRACT	3689.285			INT	INT	56	0.2	1?	OPEN		65							FRACT. RELATED TO FAULT ZONE BETWEEN 3689.23-3689.64. ALL FAULT BRECCIA
R-1	FRACT	3689.325			INT	INT	16	0.2	1?	OPEN		69							FRACT. RELATED TO FAULT ZONE BETWEEN 3689.23-3689.64. ALL FAULT BRECCIA
R-1	FRACT	3689.33			INT	OW	56	0.2	1?	OPEN		72							FRACT. RELATED TO FAULT ZONE BETWEEN 3689.23-3689.64. ALL FAULT BRECCIA
R-1	FRACT		3689.42	3689.4	INT	INT	51	0.2	1?	OPEN		48							FRACT. RELATED TO FAULT ZONE BETWEEN 3689.23-3689.64. ALL FAULT BRECCIA
R-1	FRACT		3689.45	3689.47	INT	INT	96	0.2	1?	OPEN		86							FRACT. RELATED TO FAULT ZONE BETWEEN 3689.23-3689.64. ALL FAULT BRECCIA
R-1	FRACT	3689.455			INT	INT	14	0.2	1?	OPEN		82							FRACT. RELATED TO FAULT ZONE BETWEEN 3689.23-3689.64. ALL FAULT BRECCIA
R-1	FRACT	3689.49			INT	INT	12	0.2	1?	OPEN		74							FRACT. RELATED TO FAULT ZONE BETWEEN 3689.23-3689.64. ALL FAULT BRECCIA
R-1	FRACT	3689.5			INT	INT	17	0.2	1?	OPEN		76							FRACT. RELATED TO FAULT ZONE BETWEEN 3689.23-3689.64. ALL FAULT BRECCIA
R-1	FRACT	3689.53			INT	INT	19	0.2	1?	OPEN		46							FRACT. RELATED TO FAULT ZONE BETWEEN 3689.23-3689.64. ALL FAULT BRECCIA
R-1	FRACT	3689.535			INT	INT	13	0.2	1?	OPEN		73							FRACT. RELATED TO FAULT ZONE BETWEEN 3689.23-3689.64. ALL FAULT BRECCIA
R-1	FRACT		3689.54	3689.55	INT	OW	66	0.2	1?	OPEN		29							FRACT. RELATED TO FAULT ZONE BETWEEN 3689.23-3689.64. ALL FAULT BRECCIA
R-1	FRACT		3689.56	3689.575	INT	OW	63	0.2	1?	OPEN		63							FRACT. RELATED TO FAULT ZONE BETWEEN 3689.23-3689.64. ALL FAULT BRECCIA
R-1	FRACT	3689.62			INT	INT	35	0.2	1?	OPEN		34							FRACT. RELATED TO FAULT ZONE BETWEEN 3689.23-3689.64. ALL FAULT BRECCIA
R-1	FRACT	3691.03			INT	INT	42	1.5	1?	PART OPEN	CALC	88							
R-1	FRACT		3691.06	3691.08	INT	INT	39	0.5	1?	PART OPEN	CALC	61							
R-1	FRACT	3691.29			INT	INT	26	0.2	1?	OPEN		56							
R-1	FRACT		3695.8	3695.795	INT	INT	17	0.2	1?	OPEN		55							
R-1	FRACT	3695.8			INT	INT	11	0.2	1?	OPEN		56							CONFINED TO V. BRITTLE SHALEY UNIT POSS. INDUCED
R-1	FRACT	3695.81			INT	INT	18	0.2	1?	OPEN		55							CONFINED TO V. BRITTLE SHALEY UNIT POSS. INDUCED
R-1	FRACT	3695.815			INT	INT	29	0.2	1?	OPEN		56							CONFINED TO V. BRITTLE SHALEY UNIT POSS. INDUCED
R-1	FRACT	3695.84			INT	OW	36	0.2	1?	OPEN		54							CONFINED TO V. BRITTLE SHALEY UNIT POSS. INDUCED
R-1	FRACT		3695.84	3695.855	INT	INT	37	0.2	1?	OPEN		55							CONFINED TO V. BRITTLE SHALEY UNIT POSS. INDUCED
R-1	FRACT		3695.855	3695.6	INT	INT	14	0.2	1?	OPEN		59							CONFINED TO V. BRITTLE SHALEY UNIT POSS. INDUCED
R-1	FRACT	3695.865			INT	INT	17	0.2	1?	OPEN		51							CONFINED TO V. BRITTLE SHALEY UNIT POSS. INDUCED
R-1	FRACT		3697.56	3697.56	INT	INT	45	1.5	?	PART OPEN	CALC	45							MAYBE TOTALLY CLOSED
R-1	FRACT		3698.32	3698.34	INT	INT	60	0.5	?	PART OPEN	CALC	60							MAYBE TOTALLY CLOSED
R-1	FRACT	3698.33			INT	INT	37	0.5	1	PART OPEN	CALC	88							MAYBE TOTALLY CLOSED
R-1	FRACT	3698.35			INT	OW	29	0.5	1	PART OPEN	CALC	88							MAYBE TOTALLY CLOSED
R-1	FRACT		3698.36	3698.38	INT	OW	27	0.5	1	PART OPEN	CALC	88							MAYBE TOTALLY CLOSED
R-1	FRACT	3698.48			INT	OW	385	0.5	1	PART OPEN	CALC	88							MAYBE TOTALLY CLOSED
R-1	FRACT		3699.685	3699.72	OW	OW	141	0.5	1	CLOSED	CALC	85							COULD BE MODE 3 FRACTURES
R-1	FRACT		3699.88	3699.89	OW	OW	102	0.5	1	PART OPEN	CALC	86							COULD BE MODE 3 FRACTURES
R-1	FRACT		3699.95	3699.97	INT	OW	76	0.5	1	PART OPEN	CALC	85							COULD BE MODE 3 FRACTURES
R-1	FRACT		3700	3700	OW	OW	534	2	1	CLOSED	CALC	88							COULD BE MODE 3 FRACTURES
R-1	FRACT	3700.025			INT	INT	43	0.5	1	PART OPEN	CALC	88							COULD BE MODE 3 FRACTURES
R-1	STY		3700.04	3704.04	OW	OW	102	2				29			13				REGRACKED STY. CALC CEMENTATION ALONG OLD STY. WALLS
R-1	FRACT	3700.07			OW	INT	94	0.5	1	PART OPEN	CALC	88							PROB. ASSOC WITH STY BELOW
R-1	FRACT	3700.2			INT	INT	66	0.5	1	PART OPEN	CALC	88							PROB. ASSOC WITH STY BELOW
R-1	FRACT		3700.21	3700.24	TOP	INT	133	0.5	1	PART OPEN	CALC	88							PROB. ASSOC WITH STY BELOW
R-1	FRACT	3700.22			TOP	INT	96	0.5	1	PART OPEN	CALC	90							PROB. ASSOC WITH STY BELOW
R-1	FRACT		3700.29	3700.29	INT	INT	54	0.5	1	PART OPEN	CALC	88							PROB. ASSOC WITH STY BELOW
R-1	STY		3700.4	3700.4	OW	OW	102	2				0			>100				FILLED WITH CALC (SAMPLE)
R-1	FRACT		3700.7	3700.7	OW	OW	570	2	1	PART OPEN	CALC	88							RUNS ALONG CORE FACE. VERY LARGE CUTS STY. ANOTHER FRACT. BEHIND IT (SPACING = 3MMM)
R-1	FRACT	3701.22			TOP	OW	250	1	1	CLOSED	CALC	88							PROB. ASSOC WITH STY BELOW
R-1	FRACT	3701.24			OW	OW	82	0.5	1	CLOSED	CALC	85							DISPLACES ABOVE FRACTURE. NORMAL SENSE
R-1	STY	3701.26			OW	STY	110	0.5				88			5				VERTICAL STY. INDICATES COMP.
R-1	STY		3701.3	3701.3	OW	OW	108	0.5				4			11				COMP. STY
R-1	FRACT		3701.44	3701.385	OW	INT	134	0.5	2?	PART OPEN	CALC	66							
R-1	FRACT		3701.45	3701.45	INT	INT	24	0.5	2?	PART OPEN	CALC	58							
R-1	FRACT		3701.5	3701.48	INT	INT	72	0.5	1	CLOSED	CALC	88							DIFF. FRACT. TYPE TO ABOVE 2 FRACTS.
R-1	FRACT	3701.57			INT	INT	66	0.5	1	CLOSED	CALC	90							
R-1	FRACT	3701.61			INT	STY	23	0.5	1	PART OPEN	CALC	58							STY ASSOC FRACT. VERTICAL WHEN ROTATED BACK TO ACCOUNT FOR WELL DEVIATION
R-1	FRACT	3701.63			INT	STY	32	0.5	1	PART OPEN	CALC	53							STY ASSOC FRACT. VERTICAL WHEN ROTATED BACK TO ACCOUNT FOR WELL DEVIATION
R-1	FRACT	3701.65			INT	STY	21	0.5	1	PART OPEN	CALC	52							STY ASSOC FRACT. VERTICAL WHEN ROTATED BACK TO ACCOUNT FOR WELL DEVIATION
R-1	FRACT		3701.86	3701.835	INT	STY	53	0.5	1	PART OPEN	CALC	51							STY ASSOC FRACT. VERTICAL WHEN ROTATED BACK TO ACCOUNT FOR WELL DEVIATION
R-1	STY		3701.868	3701.865	OW	OW	117	2				29			11				STY WITH MANY STA FRACTS.
R-1	FRACT	3701.875			OW	STY	19	0.5	1	PART OPEN	CALC	51							RELATED TO STY ABOVE
R-1	FRACT	3701.875			STY	OW	55	0.5	1	PART OPEN	CALC	56							RELATED TO STY ABOVE
R-1	FRACT	3701.875			STY	OW	42	0.5	1	PART OPEN	CALC	56							RELATED TO STY ABOVE
R-1	FRACT		3701.89	3701.905	STY	BASE	65	0.5	1	PART OPEN	CALC	51							RELATED TO STY ABOVE

Miskar A-3 Raw Data

R-1	FRACT	3701.895			STY	INT	25	0.5	1	PART. OPEN	CALC	52							EN ECHELON SET - RELATED TO STY ABOVE
R-1	FRACT	3701.915			INT	INT	10	0.5	1	PART. OPEN	CALC	51							EN ECHELON SET - RELATED TO STY ABOVE
R-1	FRACT	3701.925			INT	INT	10	0.5	1	PART. OPEN	CALC	51							EN ECHELON SET - RELATED TO STY ABOVE
R-1	FRACT	3701.93			STY	BASE	62	0.5	1	PART. OPEN	CALC	54							EN ECHELON SET - RELATED TO STY ABOVE
R-1	FRACT	3701.91			TOP	STY	23	0.5	1	PART. OPEN	CALC	59							RELATED TO STY BELOW
R-1	FRACT	3701.94			TOP	STY	48	0.5	1	PART. OPEN	CALC	58							RELATED TO STY BELOW
R-1	STY		3701.95	3701.95	CW	CW	126	1				33				12			
R-1	FRACT		3701.99	3701.975	STY	INT	42	0.5	1	PART. OPEN	CALC	58							
3701.22 (END CORE 6)																			
3703.00 (START CORE 7)																			
R-1	FRACT		3707.23	3707.23	INT	INT	61	0.5	?	PART. OPEN	CALC	76							
R-1	STY		3710.24	3710.24	CW	CW	104	0.5				17				4			
R-1	FRACT	3710.26			CW	STY	50	1	1	PART. OPEN	CALC	82							STY ASSOC FRACT. EN ECHELON. RELATED TO STY BELOW
R-1	FRACT	3710.3			INT	INT	54	0.5	1	PART. OPEN	CALC	83							STY ASSOC FRACT. EN ECHELON. RELATED TO STY BELOW
R-1	FRACT		3710.37	3710.36	INT	INT	69	0.5	1	PART. OPEN	CALC	80							STY ASSOC FRACT. EN ECHELON. RELATED TO STY BELOW
R-1	FRACT		3710.42	3710.4	INT	INT	76	0.5	1	PART. OPEN	CALC	80							STY ASSOC FRACT. EN ECHELON. RELATED TO STY BELOW
R-1	STY		3710.51	3710.51	CW	CW	105	0.5				13				9			
R-1	FRACT		3710.52	3710.53	STY	INT	65	0.5	1	PART. OPEN	CALC	80							STY ASSOC FRACTS RELATED TO ABOVE STY. EN ECHELON
R-1	FRACT	3710.61			INT	INT	81	0.5	1	PART. OPEN	CALC	82							STY ASSOC FRACTS RELATED TO ABOVE STY. EN ECHELON
R-1	FRACT		3710.63	3710.62	STY	INT	44	0.5	1	PART. OPEN	CALC	84							
R-1	FRACT		3710.67	3710.7	INT	INT	66	0.5	1	PART. OPEN	CALC	83							
R-1	FRACT	3710.75			INT	INT	67	0.5	1	PART. OPEN	CALC	80							
R-1	STY		3712.34	3712.34	CW	CW	110	1				22				21			
R-1	FRACT																		
R-1	FRACT		3713.04	3713.07	INT	INT	480	0.5	1	CLOSED	CALC	82							HAIRLINE
R-1	FRACT		3713.1	3713.02	INT	INT	453	0.5	1	CLOSED	CALC	82							HAIRLINE
R-1	FRACT	3713.11			INT	INT	213	0.5	1	CLOSED	CALC	82							HAIRLINE
3714.83 (END CORE 7)																			
3728.00 (START CORE 8)																			
R-1	FRACT		3729.64	3729.625	CW	INT	77	0.5	2	OPEN		43							SIMILAR TO SHEAR BANDS. FILLED WITH OIL
R-1	FRACT		3729.8	3729.8	CW	INT	176	0.5	2	OPEN		71							SIMILAR TO SHEAR BANDS. FILLED WITH OIL
R-1	FRACT	3729.99			INT	INT	53	1	1	OPEN		80							PROB EXT. FRACT. MODE 1. FILLED WITH OIL
R-1	FRACT		3730.1	3730.08	CW	INT	222	1	2	OPEN		75							SIMILAR TO SHEAR BANDS. FILLED WITH OIL
R-1	FRACT	3730.11			INT	CW	197	1	2	OPEN		78							INTERSECTS PREVIOUS FRACT. TWO DIFF. TRENDS
R-1	FRACT	3730.24			INT	CW	66	1	2	OPEN		75							SIMILAR TO SHEAR BANDS. FILLED WITH OIL
R-1	FRACT		3731.42	3731.42	CW	CW	121	1	2	OPEN		34							SHEAR BAND FILLED WITH OIL (SAMPLE)
IZ 3732.04-3732.19	STY		3732.11	3732.11	CW	CW	100	2				15				44			LARGE STY. WITHIN HEAVILY FRACT. CHERT LAYER
R-1	FRACT		3732.28	3732.28	CW	CW	111	1	2	OPEN		43							SHEAR BAND FILLED WITH OIL (SAMPLE)
RUBBLE 3732.65-3733.35																			
IZ 3733.35-3736.90																			MARKED CHANGE OF LITH. APPEARS TO BE HEAVILY FRACTURED. LIKE RUDISTIC BRECCIA (AS SEEN ON THE MAIELLA)
R-1	FRACT		3737.49	3737.47	CW	INT	71	1	2	OPEN		48							
IZ 3737.67-3737.84																			V. LARGE ZONE OF STYLOTISATION (SAMPLE). APPEARS HEAVILY DOLOMITISED
R-1	FRACT		3738.84	3738.86	INT	INT	54	0.5	1	PRED. OPEN	CALC	88							EN ECHELON SET ASSOC WITH STY. BELOW
R-1	FRACT	3738.875			INT	INT	49	0.5	1	PRED. OPEN	CALC	88							EN ECHELON SET ASSOC WITH STY. BELOW
R-1	FRACT	3739.04			INT	STY	271	0.5	1	PRED. OPEN	CALC	88							EN ECHELON SET ASSOC WITH STY. BELOW
R-1	STY		3739.17	3739.17	CW	CW	100	2				0				19			HEAVILY DOLOMITISED BENEATH STY. OIL IN STY
R-1	STY		3739.86	3739.86	CW	CW	109	2				27				32			HEAVILY DOLOMITISED IN SECTION ABOVE STY. OIL IN STY
R-1	STY		3740.19	3740.19	CW	CW	114	1				27				96			HEAVILY DOLOMITISED IN SECTION ABOVE STY. OIL IN STY
R-1	FRACT		3740.79	3740.79	CW	CW	117	0.5	2	PRED. OPEN	CALC	38							FILLED WITH OIL (SHEAR BAND)
R-1	FRACT		3740.89	3740.89	CW	CW	122	0.5	2	PRED. OPEN	CALC	42							FILLED WITH OIL (SHEAR BAND)
R-1	STY		3741.42	3741.42	CW	CW	136	1				53				54			CALC FILL
R-1	FRACT		3741.46	3741.47	INT	INT	33	0.5	1	CLOSED	CALC	36							PROB ASSOC. WITH ABOVE STY.
R-1	FRACT		3741.53	3741.53	CW	CW	121	0.5	1	CLOSED	CALC	36							PROB ASSOC. WITH ABOVE STY.
R-1	FRACT		3741.54	3741.54	CW	CW	66	0.5	1	CLOSED	CALC	37							PROB ASSOC. WITH ABOVE STY.
R-1	STY		3742.035	3742.035	CW	CW	136	1.5				46							CALC FILL
R-1	FRACT		3742.035	3742.06	STY	CW	82	1	1	CLOSED	CALC	51							STA FRACT
R-1	FRACT		3742.095	3742.125	STY	INT	61	1	1	PRED. OPEN	CALC	52							STA FRACT. EN ECHELON SET. INTERESTING. FRACTS COME OFF STY. NOT VERTICAL IF ROTATE BACK TO NORMAL
R-1	FRACT	3742.105			STY	INT	44	0.5	1	CLOSED	CALC	56							DIFF. STA FRACT
R-1	FRACT	3742.16			INT	BASE	25	1	1	PRED. OPEN	CALC	52							STA FRACT - EN ECHELON SET TO 8433
R-1	FRACT		3742.81	3742.81	CW	CW	119	0.5	2	OPEN		46							SHEAR FRACT. FILLED WITH OIL
R-1	FRACT		3743	3743	TOP	STY	11	1	1	PRED. OPEN	CALC	88							ASSOC. WITH STY BELOW
R-1	STY		3743.02	3743.02	CW	CW	105	0.5				5							
R-1	FRACT		3743.055	3743.06	STY	INT	34	0.5	1	PART. OPEN	CALC	88							ASSOC. WITH STY ABOVE
R-1	FRACT		3743.075	3743.09	INT	INT	46	0.5	1	PRED. OPEN	CALC	88							ASSOC. WITH STY ABOVE
R-1	FRACT	3743.28			INT	CW	301	0.5	1	PRED. OPEN	CALC	88							ASSOC. WITH STY ABOVE
3743.56 (END CORE 8)																			
3743.56 (START CORE 9)																			
R-1	STY		3743.73	3743.73	CW	CW	149	2				42				81			
R-1	FRACT		3744.73	3743.7	CW	BASE	96	1	2	OPEN		48							FILLED WITH OIL
R-1	FRACT		3745.46	3745.46	CW	CW	104	1	2	OPEN		32							FILLED WITH OIL
R-1	STY		3745.54	3745.54	CW	CW	104	1				24				74			
R-1	FRACT		3746.41	3746.41	CW	CW	124	0.5	2	OPEN		45							FILLED WITH OIL
RUBBLE 3746.80-3750.91																			
3750.91 (END CORE 9)																			

Miskar A-6 Raw Data

Well	Structural	Non-centreline (m)	Centreline Intersection	Centreline Intersection	Termination		Length	Width	Fracture Type	Open/Closed	Fill	Dip	Strike	Slickensides		Stylolites		Vug	Comments
	Feature	Fract. Mid-point Depth (m)	Depth (m)	Fract. Mid-point Depth (m)	Upper	Lower	(mm)	(mm)	(1, 2, 3)					Plunge/Dir	Sense	Dentae (mm)	Fill	Size	
Miskar A-6																			
4877.70 (Miskar A-6, Core 1)																			
R-1 SUPERIOR	FRACT		4888.63	4888.63	CW	CW	150	1	2	PRED. CLOSED	CALC	65							LARGE FAULT ZONE. MANY FRACTURES. VERY RANDOM ORIENTATION. ZONE APPROX. 150MM WIDE. HEAVILY BRECCIATED
R-1 SUPERIOR	FRACT		4890.91	4891.92	INT	CW	80	0.5	2	PART. CLOSED	CALC	40							
R-1 SUPERIOR	FRACT		4891.965	4891.965	CW	CW	106	0.5	2	PRED. CLOSED	CALC	35							
R-1 SUPERIOR	FRACT		4891.968	4891.968	CW	CW	106	0.5	2	PRED. CLOSED	CALC	37							
R-1 SUPERIOR	FRACT		4891.97	4891.97	CW	CW	106	0.5	2	PRED. CLOSED	CALC	36							
R-1 SUPERIOR	STY		4894.65	4894.65	CW	CW	144	20				51				1.5			ZONE OF COMP. MICRO STYLOLITES. 20MM WIDE. APPROX. 7 STYS.
R-1 SUPERIOR	STY		4895.35	4895.35	CW	CW	155	0.1				53				1			COMP. STY
R-1 SUPERIOR	STY		4895.64	4895.64	CW	CW	155	2				59				55			COMP. STY
R-1 SUPERIOR	STY		4898.06	4898.06	CW	CW	145	1				46				36			COMP. STY
R-1 SUPERIOR	STY		4899.7	4899.7	CW	CW	140	1.5				45				37			COMP. STY
R-1 SUPERIOR	STY		4900.23	4900.23	CW	CW	134	0.5				51				14			COMP. STY
R-1 SUPERIOR	STY		4900.26	4900.26	CW	CW	139	1				52				9			COMP. STY
4900.37 (END CORE 1)																			
4901.00 (START CORE 2)																			
R-1 SUPERIOR	FRACT	4901.41			INT	INT	26	1	2	CLOSED	CALC	39							POSS. MODE 1 PERPENDICULAR TO BEDDING
R-1 SUPERIOR	FRACT		4901.425	4901.425	INT	INT	44	1	2	CLOSED	CALC	41							POSS. MODE 1 PERPENDICULAR TO BEDDING
R-1 SUPERIOR	FRACT	4901.445			INT	CW	12	1	2	CLOSED	CALC	39							POSS. MODE 1 PERPENDICULAR TO BEDDING
R-1 SUPERIOR	FRACT	4901.455			INT	CW	15	1	2	CLOSED	CALC	39							POSS. MODE 1 PERPENDICULAR TO BEDDING
R-1 SUPERIOR	FRACT		4901.76	4901.76	CW	CW	156	0.5	?	CLOSED	CALC	45							POSS. MODE 1 PERPENDICULAR TO BEDDING
R-1 SUPERIOR	FRACT		4901.765	4901.765	CW	CW	156	0.5	?	CLOSED	CALC	47							POSS. MODE 1 PERPENDICULAR TO BEDDING
R-1 SUPERIOR	FRACT		4901.77	4901.77	CW	CW	158	0.5	?	CLOSED	CALC	46							POSS. MODE 1 PERPENDICULAR TO BEDDING
R-1 SUPERIOR	FRACT		4901.875	4901.875	INT	CW	99	0.5	?	PRED. CLOSED	CALC	46							POSS. MODE 1 PERPENDICULAR TO BEDDING
R-1 SUPERIOR	FRACT		4901.91	4901.91	CW	INT	99	0.5	?	PRED. CLOSED	CALC	47							POSS. MODE 1 PERPENDICULAR TO BEDDING
R-1 SUPERIOR	FRACT		4902	4902	TOP	CW	67	0.5	1	PRED. CLOSED	CALC	42							POSS. MODE 1 PERPENDICULAR TO BEDDING
R-1 SUPERIOR	FRACT		4902.15	4902.15	TOP	CW	89	0.5	1	PRED. CLOSED	CALC	42							POSS. MODE 1 PERPENDICULAR TO BEDDING
R-1 SUPERIOR	STY		4902.26	4902.26	CW	CW	170	1				61				12			COMP. STY
R-1 SUPERIOR	STY		4902.68	4902.68	CW	CW	148	1				54				1			COMP. STY
R-1 SUPERIOR	STY		4903.63	4903.63	CW	CW	149	0.5				56				14			COMP. STY
R-1 SUPERIOR	FRACT		4904.19	4904.19	CW	STY	108	1	1	PART. CLOSED	CALC	33							STY ASSOC FRACT. MODE 1. ASSOC WITH FRACT BELOW
R-1 SUPERIOR	FRACT		4904.27	4904.27	INT	STY	56	1	1	PART. CLOSED	CALC	39							STY ASSOC FRACT. MODE 1. ASSOC WITH FRACT BELOW
R-1 SUPERIOR	STY		4904.31	4904.31	CW	CW	155	2				56				85			COMP. STY
R-1 SUPERIOR	FRACT		4904.37	4904.38	STY	INT	40	0.5	1	PART. CLOSED	CALC	38							EN ECHELON FRACT. SET. STA FRACTS.
R-1 SUPERIOR	FRACT	4904.385			INT	INT	36	0.5	1	PART. CLOSED	CALC	39							EN ECHELON FRACT. SET. STA FRACTS.
R-1 SUPERIOR	FRACT	4904.4			INT	CW	22	0.5	1	PART. CLOSED	CALC	37							EN ECHELON FRACT. SET. STA FRACTS.
R-1 SUPERIOR	STY		4904.8	4904.8	CW	CW	135					36				16			COMP. STY
R-1 SUPERIOR	FRACT		4905.53	4905.53	CW	CW	122	0.5	1	PART. CLOSED	CALC	35							SERIES OF HAIRLINE FRACTS AND ONE LARGE CALC FILLED FRACT.
R-1 SUPERIOR	STY		4905.87	4905.87	CW	BASE	136	1.5				54				11			COMP. STY
R-1 SUPERIOR	FRACT	4906.13			STY	INT	26	1	1	PRED. CLOSED	CALC	48							STA FRACTS ASSOC. WITH STY ABOVE. EH ECHELON.
R-1 SUPERIOR	FRACT		4906.16	4906.165	INT	INT	54	1	1	PRED. CLOSED	CALC	59							STA FRACTS ASSOC. WITH STY ABOVE. EH ECHELON.
R-1 SUPERIOR	FRACT	4906.17			INT	CW	33	1	1	PRED. CLOSED	CALC	47							STA FRACTS ASSOC. WITH STY ABOVE. EH ECHELON.
R-1 SUPERIOR	STY		4906.89	4906.89	CW	CW	147	1				56				15			COMP. STY
R-1 SUPERIOR	STY		4907.15	4907.15	CW	CW	145	1.5				46				12			COMP. STY
IZ 4906.76-4906.84																			ZONE OF MANY STY
R-1 SUPERIOR	FRACT		4908	4908.02	CW	CW	12	1	1	PRED. CLOSED	CALC	36							COMP. STY
R-1 SUPERIOR	FRACT		4909.15	4909.14	CW	INT	89	1	1	PRED. CLOSED	CALC	60							PERPENDICULAR TO BEDDING. MODE 1
R-1 SUPERIOR	FRACT	4909.155			INT	INT	26	1	1	PRED. CLOSED	CALC	61							PERPENDICULAR TO BEDDING. MODE 1
R-1 SUPERIOR	FRACT		4909.16	4909.18	INT	CW	102	1	1	PRED. CLOSED	CALC	39							PERPENDICULAR TO BEDDING. MODE 1
IZ 4916.50-4919.00																			ODD UNIT. POSS. LARGE FAULT ZONE. HEAVILY BRECC. MIXTURE OF ROCK TYPES. HOWEVER, IMBRIACTION PARALLEL TO BEDDING?
IZ 4926.00-4926.82																			FAULT ZONE? SIMILAR TO ABOVE BUT MORE MESSED UP. ACTUALLY PROBABLY TWO DEBRIS FLOWS.
4926.82 (END CORE 2)																			
4928.00 (START CORE 3)																			
IZ 4928.00-4928.20																			
IGNEOUS IN R-1	FRACT		4928.76	4928.76	CW	CW	109	0.75	2	PRED. CLOSED	DOL	19							MANY VUGS. PART. OPEN. CALC. 15X15MM
IGNEOUS IN R-1	FRACT		4929.24	4929.24	CW	CW	188	2	2	PRED. CLOSED	DOL	56							DOL FILLED SHEAR FRACT.
IGNEOUS IN R-1	FRACT		4929.275	4929.275	FRACT	CW	83	1	2	PRED. CLOSED	DOL	61							DOL FILLED SHEAR FRACT.
IGNEOUS IN R-1	FRACT		4929.48	4929.48	CW	CW	129	1	2	CLOSED	DOL	40							CONJUGATE TO ABOVE FRACT. TREND
IGNEOUS IN R-1	FRACT		4929.905	4929.92	TOP	CW	71	2	2	CLOSED	DOL	39							CONJUGATE TO ABOVE FRACT. TREND
IGNEOUS IN R-1	FRACT		4930.56	4930.56	CW	CW	102	1.5	2	CLOSED	DOL	31							DOL FILLED SHEAR FRACT.
IGNEOUS IN R-1	FRACT		4930.985	4930.99	INT	CW	71	0.5	2	CLOSED	CALC	17							DOL FILLED SHEAR FRACT.
IGNEOUS IN R-1	FRACT		4931	4931	CW	CW	102	0.5	2	CLOSED	CALC	17							DIFF. FRACT SET
4931.00 (END CORE 3)																			DIFF. FRACT SET
4931.60 (START CORE 4)																			
IGNEOUS IN R-1	FRACT		4931.76	4931.76	CW	CW	122	4	2	CLOSED	DOL	39							DOL FILLED FRACT.
IGNEOUS IN R-1	FRACT		4932.11	4932.11	CW	CW	110	3	2	CLOSED	DOL	38							DOL FILLED FRACT.
IGNEOUS IN R-1	FRACT	4932.32			CW	INT	49	1	2	PRED. CLOSED	CALC	39							DIFF. SET TO ABOVE
IGNEOUS IN R-1	FRACT		4932.34	4932.335	INT	CW	43	1	2	PRED. CLOSED	CALC	38							DIFF. SET TO ABOVE
IGNEOUS IN R-1	FRACT		4932.36	4932.36	CW	CW	129	1	2	PRED. CLOSED	CALC	39							DIFF. SET TO ABOVE
IGNEOUS IN R-1	FRACT		4932.66	4932.66	CW	CW	121	4	2	CLOSED	DOL	26							DOL FILLED FRACT.
IGNEOUS IN R-1	FRACT		4932.74	4932.74	CW	CW	127	0.5	2	PRED. CLOSED	CALC	40							CALC FILLED FRACT.
IGNEOUS IN R-1	FRACT		4932.75	4932.75	CW	CW	127	0.5	2	PRED. CLOSED	CALC	40							CALC FILLED FRACT.
IGNEOUS IN R-1	FRACT		4933.31	4933.31	CW	CW	121	2	2	CLOSED	DOL	26							DOL FILLED FRACT.
IGNEOUS IN R-1	FRACT		4933.38	4933.38	CW	CW	122	0.5	2	PRED. CLOSED	CALC	35							CALC FILLED FRACT.
IGNEOUS IN R-1	FRACT		4933.4	4933.4	CW	CW	122	0.5	2	PRED. CLOSED	CALC	37							CALC FILLED FRACT.
IGNEOUS IN R-1	FRACT		4933.42	4933.42	CW	CW	121	0.5	2	PRED. CLOSED	CALC	35							CALC FILLED FRACT.
IGNEOUS IN R-1	FRACT		4933.61	4933.61	CW	CW	146	1	2	CLOSED	DOL	59							DOL FILLED FRACT.
IGNEOUS IN R-1	FRACT		4933.78	4933.78	CW	CW	160	3	2	CLOSED	DOL	57							
IGNEOUS IN R-1	FRACT		4933.81	4933.81	CW	CW	114	0.5	2	PRED. CLOSED	CALC	35							INTERSECTS AND DISPLACES ABOVE FRACT.
IGNEOUS IN R-1	FRACT		4933.875	4933.875	FRACT	CW	101	1.5	2	CLOSED	DOL	21							
IGNEOUS IN R-1	FRACT		4933.92	4933.92	CW	CW	116	0.5	2	PRED. CLOSED	CALC	39							DIFF. 2 SETS OF FRACTS. EARLIER DOL FILLED SET (TOT CLOSED) CUT BY LATER CALC FILLED SET. CALC FILLED FRACTS. SYSTEMATIC. DOL FILLED FRACTS. NON SYSTEMA
IGNEOUS IN R-1	FRACT		4934.16	4934.16	CW	CW	129	3	2	CLOSED	DOL	45							DOL FILLED FRACT.
IGNEOUS IN R-1	FRACT		4934.32	4934.32	CW	CW	126	2	2	CLOSED	DOL	39							DOL FILLED FRACT.
IGNEOUS IN R-1	VUG		4934.47	4934.47	INT	INT					DOL							5X10D	
IGNEOUS IN R-1	FRACT		4934.96	4934.96	CW	CW	115	1	2	PRED. CLOSED	CALC	34							CALC FILLED FRACT.
IGNEOUS IN R-1	FRACT		4934.99	4934.99	CW	CW	333	5	2	CLOSED	DOL	76							DISPLACED BY ABOVE SYSTEMATIC FRACT.
IGNEOUS IN R-1	FRACT		4935.38	4935.38	CW	INT	136	1	2	CLOSED	DOL	58							
IGNEOUS IN R-1	FRACT		4935.69	4935.69	CW	CW	109	4	?	CLOSED	DOL	1							
IGNEOUS IN R-1	FRACT		4935.79	4935.79	INT	INT	94	0.5	2	CLOSED	DOL	72							
IGNEOUS IN R-1	FRACT		4936.04	4936.04	CW	CW	121	2.5	?	CLOSED	DOL	59							SOME OF THESE DOL FILLED FRACTS MAY BE RECRACKED STYLOLITES WHICH HAVE THEN BEEN FILLED WITH DOL CEMENTS.

Miskar A-6 Raw Data

IGNEOUS IN A-1	FRACT		4936.34	4936.34	CW	CW	110	5	?	CLOSED	DOL	4							
IGNEOUS IN A-1	FRACT		4936.55	4936.55	CW	CW	105	1.5	?	CLOSED	DOL	0							
IGNEOUS IN A-1	FRACT		4936.71	4936.75	INT	CW	130	0.5	2	CLOSED	DOL	61							
IGNEOUS IN A-1	FRACT	4937.09			CW	INT	94	0.5	2	CLOSED	DOL	62							
IGNEOUS IN A-1	FRACT		4937.43	4937.43	CW	CW	144	2	?	CLOSED	DOL	59							
IGNEOUS IN A-1	FRACT		4937.52	4937.49	CW	INT	81	1	2	CLOSED	DOL	51							
IGNEOUS IN A-1	FRACT		4937.56	4937.56	CW	CW	96	1	?	CLOSED	DOL	0							
IGNEOUS IN A-1	FRACT		4937.76	4937.76	CW	CW	110	2	?	CLOSED	DOL	19							
IGNEOUS IN A-1	FRACT		4937.97	4937.97	CW	CW	109	3	2?	CLOSED	DOL	24							
IGNEOUS IN A-1	VUG		4938.17	4938.17	INT	INT				CLOSED	CALC						30X20		
IGNEOUS IN A-1	FRACT		4938.22	4938.22	CW	CW	140	1.5	2	CLOSED	CID	45							
IGNEOUS IN A-1	FRACT		4938.24	4938.27	CW	CW	190	9	2	CLOSED	CID	58						DISPLACES ABOVE FRACT. BOTH FILLED WITH CALC IN FIMS AND DOL IN MIDDLE	
IGNEOUS IN A-1	FRACT		4938.45	4938.47	CW	CW	315	3	2	CLOSED	CID	75							
IGNEOUS IN A-1	FRACT		4938.61	4938.61	CW	CW	186	5	2	CLOSED	CID	56							
IGNEOUS IN A-1	FRACT		4938.87	4938.87	CW	CW	150	1	2	CLOSED	CID	46							
IGNEOUS IN A-1	FRACT		4940.27	4940.27	CW	CW	166	3	2	CLOSED	CID	58							
IGNEOUS IN A-1	FRACT		4940.54	4940.54	CW	FRACT	95	2	2	CLOSED	CID	36							
IGNEOUS IN A-1	FRACT		4940.6	4940.6	CW	CW	159	2	2	CLOSED	CID	45							
IGNEOUS IN A-1	FRACT	4940.69			FRACT	BASE	580	1.5	1?	CLOSED	CID	88							
IGNEOUS IN A-1	FRACT		4941	4941	CW	BASE	116	2	2	CLOSED	CID	34							
4942.00 (END CORE 4)																			
4954.00 (START CORE 5)																			
LZ 4964.78 - 4964.80																		ZONE OF INTENSE STY. MANY MICROSTY	
R-1 SUPERIOR	FRACT		4964.88	4964.88	INT	INT	92	0.5	1	PRED. CLOSED	CALC	48						PROB. STY ASSOC	
R-1 SUPERIOR	FRACT		4964.91	4964.91	CW	CW	152	0.5	1	PRED. CLOSED	CALC	48						PROB. STY ASSOC	
R-1 SUPERIOR	FRACT		4965.91	4965.91	CW	CW	137	0.5	1	PRED. CLOSED	CALC	48							
R-1 SUPERIOR	FRACT		4966.35	4966.35	CW	CW	119	8	2?	PART. OPEN	CALC	25						V. LARGE CALC. FILLED FRACT.	
4969.19 (END CORE 5)																			
4968.90 (START CORE 6)??																		NOTHING IN THIS SECTION OF CORE	
4995.63 (END CORE 6)																			
4997 (START CORE 7)																			
R-1SUPERIOR/INFERIOR	STY		4996.94	4996.94	CW	CW	166	0.5				55				5		COMP. STY	
R-1SUPERIOR/INFERIOR	STY		4997.95	4997.95	CW	CW	147	0.5				59				22		COMP. STY	
R-1SUPERIOR/INFERIOR	STY		4998.86	4998.86	CW	CW	153	0.5				58				12		COMP. STY	
R-1SUPERIOR/INFERIOR	FRACT		4999.49	4999.49	CW	CW	121	1	1	PART. OPEN	CALC	36							
R-1SUPERIOR/INFERIOR	FRACT		4999.74	4999.74	CW	INT	66	0.5	1	PART. OPEN	CALC	39							
5009.00 (END CORE 7)																			
5009.00 (START CORE 8)																			
R-1 INFERIOR	BEDDING											-99							
R-1 INFERIOR	STY		5011.7	5011.7	CW	CW	235	0.5				82				18		COMP. STY	
R-1 INFERIOR	STY		5011.78	5011.78	CW	CW	129	0.1				39				5		PROB. COMP. STY. HOWEVER AT LARGE ANGLE TO BEDDING	
R-1 INFERIOR	FRACT		5013.68	5013.68	CW	CW	185	0.1	1?	OPEN		57						HIGH ANGLE FRACTURE FILLED WITH OIL. PERPENDICULAR TO BEDDING	
R-1 INFERIOR	STY		5014.23	5014.23	CW	CW	121	0.5				32				9		COMP. STY	
R-1 INFERIOR	STY		5014.93	5014.93	CW	CW	124	2				34				26		COMP. STY	
R-1 INFERIOR	STY		5017.3	5017.3	CW	CW	99	0.5				0				31		TECTONIC STY	
R-1 INFERIOR	STY		5017.4	5017.4	CW	CW	149	0.5				54				6		COMP. STY	
R-1 INFERIOR	VUG	5018.25									CALC						20X10		
R-1 INFERIOR	VUG	5018.32									CALC						20X10		
R-1 INFERIOR	STY		5020.31	5020.31	CW	CW	146	0.5				54				8		COMP. STY	
R-1 INFERIOR	STY		5020.38	5020.38	CW	CW	172	1				63				9		COMP. STY	
R-1 INFERIOR	STY		5020.44	5020.44	CW	CW	139	1				53				7		COMP. STY	
R-1 INFERIOR	FRACT		5021.105	5021.105	CW	CW	111	0.5	1	PART. OPEN	CALC	32						STA FRACTS. ASSOC WITH STY BELOW	
R-1 INFERIOR	FRACT		5021.13	5021.13	INT	CW	87	0.5	1	PART. OPEN	CALC	33						STA FRACTS. ASSOC WITH STY BELOW	
R-1 INFERIOR	FRACT		5021.135	5021.135	CW	CW	112	0.5	1	PART. OPEN	CALC	33						STA FRACTS. ASSOC WITH STY BELOW	
R-1 INFERIOR	FRACT		5021.185	5021.185	CW	CW	111	0.5	1	PART. OPEN	CALC	32						STA FRACTS. ASSOC WITH STY BELOW	
R-1 INFERIOR	FRACT		5021.195	5021.195	CW	CW	111	1.5	1	PART. OPEN	CALC	32						STA FRACTS. ASSOC WITH STY BELOW	
R-1 INFERIOR	STY		5021.26	5021.26	CW	CW	178	0.5				63				7		COMP. STY	
R-1 INFERIOR	STY		5022.2	5022.2	CW	CW	201	1.5				63				64		COMP. STY	
R-1 INFERIOR	FRACT		5022.34	5022.38	STY	CW	94	0.5	1	PRED. OPEN	CALC	33						STA FRACTS. ASSOC WITH STY ABOVE	
R-1 INFERIOR	FRACT		5022.38	5022.38	CW	CW	115	0.5	1	PRED. OPEN	CALC	34						STA FRACTS. ASSOC WITH STY ABOVE	
R-1 INFERIOR	FRACT	5022.38			CW	INT	84	0.5	1	PRED. OPEN	CALC	33						STA FRACTS. ASSOC WITH STY ABOVE	
R-1 INFERIOR	FRACT		5022.41	5022.415	INT	INT	42	0.5	1	PRED. OPEN	CALC	32						STA FRACTS. ASSOC WITH STY ABOVE	
R-1 INFERIOR	FRACT		5022.415	5022.41	CW	INT	72	0.5	1	PRED. OPEN	CALC	34						STA FRACTS. ASSOC WITH STY ABOVE	
R-1 INFERIOR	STY		5022.98	5022.98	CW	CW	179	1				64				11		COMP. STY	
R-1 INFERIOR	FRACT		5023.13	5023.13	CW	CW	135	0.5	1	PRED. OPEN	CALC	52						STA FRACTS. ASSOC WITH STY ABOVE	
R-1 INFERIOR	FRACT		5023.145	5023.145	CW	CW	166	0.5	1	PRED. OPEN	CALC	56						STA FRACTS. ASSOC WITH STY ABOVE	
R-1 INFERIOR	FRACT	5023.2			FRACT	CW	98	0.5	1	PRED. OPEN	CALC	54						STA FRACTS. ASSOC WITH STY ABOVE	
5025.55 (END CORE 8)																			
5026.00 (START CORE 9)																			
R-1 INFERIOR	STY		5027.535	5027.535	CW	CW	119	0.5				33				27		COMP. STY	
R-1 INFERIOR	STY		5029.92	5029.92	CW	CW	101	0.5				14				4		COMP. STY	
R-1 INFERIOR	STY		5029.94	5029.94	CW	CW	131	0.5				46				4		COMP. STY	
R-1 INFERIOR	STY		5029.45	5029.45	CW	CW	187	0.5				57				5		COMP. STY	
R-1 INFERIOR	FRACT		5038.49	5038.49	CW	CW	113	2	?	PART. OPEN	CALC	33						STA FRACT. POSS. UNDERSAMPLED HERE SUBSTANT. BECAUSE STA FRACTS LOOK V. SIMILAR TO INDUCED. COULD BE UP TO 6.7 OPEN FRACTS PER METRE (5028.00-5040.00	
R-1 INFERIOR	STY		5038.9	5038.9	CW	CW	180	1				76				14		COMP. STY	
R-1 INFERIOR	FRACT		5039.04	5039.04	CW	INT	83	0.5	1?	PART. OPEN	CALC	35						STA FRACTS.	
R-1 INFERIOR	FRACT		5039.105	5039.105	CW	CW	113	2	1?	PART. OPEN	CALC	36						STA FRACTS.	
R-1 INFERIOR	STY		5040.61	5040.61	CW	CW	140	0.5				49				17		COMP. STY	
R-1 INFERIOR	FRACT		5040.615	5040.64	STY	CW	52	0.5	1	PART. OPEN	CALC	42						STA FRACTS. ASSOC WITH STY ABOVE	
R-1 INFERIOR		5040.645			CW	STY	23	0.5	1	PART. OPEN	CALC	43						STA FRACTS. ASSOC WITH STY ABOVE	
R-1 INFERIOR	FRACT		5040.685	5040.685	CW	CW	104	0.5	1	PART. OPEN	CALC	42						STA FRACTS. ASSOC WITH STY ABOVE	
R-1 INFERIOR	FRACT		5041.77	5041.77	CW	CW	131	0.5	1	PART. OPEN	CALC	57						ASSOC. WITH STY BELOW	
R-1 INFERIOR	FRACT		5041.88	5041.88	CW	STY	167	0.5	1	PART. OPEN	CALC	68						ASSOC. WITH STY BELOW	
R-1 INFERIOR	STY		5041.96	5041.96	CW	CW	111	0.5				36				15		COMP. STY	
R-1 INFERIOR	STY		5042.15	5042.15	CW	CW	119	0.5				29				22		COMP. STY	
R-1 INFERIOR	FRACT		5045.19	5045.19	CW	CW	105	2	2?	PART. OPEN	CALC	6						SHEAR FRACT?	
R-1 INFERIOR	STY		5051.17	5051.17	CW	CW	121	0.5				59				29		COMP. STY	
R-1 INFERIOR	STY		5051.74	5051.74	CW	CW	126	0.5				59				19		COMP. STY	
5053.5 (END CORE 9)																			
5053.56 (START CORE 10)																			
R-1 INFERIOR, ALEG	STY		5054.42	5054.42	CW	CW	?	2			CALC	?				LARGE		PROB COMP. STY RECRACKED AND FILLED WITH CALC. APPEARS APPROX VERTICAL	
R-1 INFERIOR, ALEG	FRACT		5055.235	5055.235	CW	CW	113	0.5	1?	PRED. CLOSED	CALC	19						SERIES OF FRACTS FILLED WITH CALC. STA FRACTS???? DEFINITELY UNDERSAMPLED BEFORE	
R-1 INFERIOR, ALEG	FRACT		5055.25	5055.25	CW	CW	113	0.5	1?	PRED. CLOSED	CALC	20						SERIES OF FRACTS FILLED WITH CALC. STA FRACTS???? DEFINITELY UNDERSAMPLED BEFORE	

Miskar A-6 Raw Data

R-1 INFERIORI, ALEG	FRACT		5055.26	5055.26	CW	CW	115	0.5	1?	PRED. CLOSED	CALC	19							SERIES OF FRACTS FILLED WITH CALC. STA FRACTS???? DEFINITELY UNDERSAMPLED BEFORE
R-1 INFERIORI, ALEG	FRACT		5055.28	5055.28	CW	CW	113	0.5	1?	PRED. CLOSED	CALC	20							SERIES OF FRACTS FILLED WITH CALC. STA FRACTS???? DEFINITELY UNDERSAMPLED BEFORE
R-1 INFERIORI, ALEG	FRACT		5055.61	5055.61	CW	CW	114	0.5	1?	PRED. CLOSED	CALC	20							SERIES OF FRACTS FILLED WITH CALC. STA FRACTS???? DEFINITELY UNDERSAMPLED BEFORE
R-1 INFERIORI, ALEG	FRACT		5055.615	5055.615	CW	CW	115	0.5	1?	PRED. CLOSED	CALC	20							SERIES OF FRACTS FILLED WITH CALC. STA FRACTS???? DEFINITELY UNDERSAMPLED BEFORE
R-1 INFERIORI, ALEG	FRACT		5055.63	5055.63	CW	CW	113	0.5	1?	PRED. CLOSED	CALC	19							SERIES OF FRACTS FILLED WITH CALC. STA FRACTS???? DEFINITELY UNDERSAMPLED BEFORE
R-1 INFERIORI, ALEG	FRACT		5055.84	5055.84	CW	CW	113	0.5	1?	PRED. CLOSED	CALC	19							SERIES OF FRACTS FILLED WITH CALC. STA FRACTS???? DEFINITELY UNDERSAMPLED BEFORE
R-1 INFERIORI, ALEG	FRACT		5055.93	5055.93	CW	CW	115	0.5	1?	PRED. CLOSED	CALC	20							SERIES OF FRACTS FILLED WITH CALC. STA FRACTS???? DEFINITELY UNDERSAMPLED BEFORE
R-1 INFERIORI, ALEG	FRACT		5056.075	5056.075	CW	CW	115	0.5	1?	PRED. CLOSED	CALC	23							SERIES OF FRACTS FILLED WITH CALC. STA FRACTS???? DEFINITELY UNDERSAMPLED BEFORE
R-1 INFERIORI, ALEG	FRACT		5056.085	5056.085	CW	CW	115	0.5	1?	PRED. CLOSED	CALC	22							SERIES OF FRACTS FILLED WITH CALC. STA FRACTS???? DEFINITELY UNDERSAMPLED BEFORE
R-1 INFERIORI, ALEG	FRACT		5056.285	5056.285	CW	CW	114	0.5	1?	PRED. CLOSED	CALC	23							SERIES OF FRACTS FILLED WITH CALC. STA FRACTS???? DEFINITELY UNDERSAMPLED BEFORE
R-1 INFERIORI, ALEG	FRACT		5056.29	5056.29	CW	CW	114	0.5	1?	PRED. CLOSED	CALC	23							SERIES OF FRACTS FILLED WITH CALC. STA FRACTS???? DEFINITELY UNDERSAMPLED BEFORE
R-1 INFERIORI, ALEG	FRACT		5056.825	5056.825	CW	CW	115	0.5	1?	PRED. CLOSED	CALC	23							SERIES OF FRACTS FILLED WITH CALC. STA FRACTS???? DEFINITELY UNDERSAMPLED BEFORE
R-1 INFERIORI, ALEG	FRACT		5056.9	5056.9	CW	CW	115	3	1?	PRED. CLOSED	CALC	22							SERIES OF FRACTS FILLED WITH CALC. STA FRACTS???? DEFINITELY UNDERSAMPLED BEFORE
R-1 INFERIORI, ALEG	FRACT		5056.91	5056.91	CW	CW	115	0.5	1?	PRED. CLOSED	CALC	23							SERIES OF FRACTS FILLED WITH CALC. STA FRACTS???? DEFINITELY UNDERSAMPLED BEFORE
R-1 INFERIORI, ALEG	FRACT		5056.93	5056.93	CW	CW	113	0.5	1?	PRED. CLOSED	CALC	24							SERIES OF FRACTS FILLED WITH CALC. STA FRACTS???? DEFINITELY UNDERSAMPLED BEFORE
R-1 INFERIORI, ALEG	STY		5057.58	5057.58	CW	CW	133	1.5			CALC	31				29			PROB COMP. STY RECRACKED AND FILLED WITH CALC. APPEARS APPROX VERTICAL
R-1 INFERIORI, ALEG	FRACT		5057.65	5057.65	STY	CW	111	0.5	1?	PRED. CLOSED	CALC	31							SERIES OF FRACTS FILLED WITH CALC. STA FRACTS???? DEFINITELY UNDERSAMPLED BEFORE
R-1 INFERIORI, ALEG	FRACT		5057.66	5057.66	STY	CW	86	0.5	1?	PRED. CLOSED	CALC	31							SERIES OF FRACTS FILLED WITH CALC. STA FRACTS???? DEFINITELY UNDERSAMPLED BEFORE
R-1 INFERIORI, ALEG	FRACT		5057.78	5057.78	CW	CW	115	1	1?	PART. CLOSED	CALC	24							SERIES OF FRACTS FILLED WITH CALC. STA FRACTS???? DEFINITELY UNDERSAMPLED BEFORE
R-1 INFERIORI, ALEG	FRACT		5057.79	5057.79	CW	CW	116	0.5	1?	PRED. CLOSED	CALC	24							SERIES OF FRACTS FILLED WITH CALC. STA FRACTS???? DEFINITELY UNDERSAMPLED BEFORE
R-1 INFERIORI, ALEG	FRACT		5057.825	5057.825	CW	CW	115	0.5	1?	PRED. CLOSED	CALC	25							SERIES OF FRACTS FILLED WITH CALC. STA FRACTS???? DEFINITELY UNDERSAMPLED BEFORE
R-1 INFERIORI, ALEG	FRACT		5057.89	5057.89	CW	CW	115	0.5	1?	PRED. CLOSED	CALC	24							SERIES OF FRACTS FILLED WITH CALC. STA FRACTS???? DEFINITELY UNDERSAMPLED BEFORE
R-1 INFERIORI, ALEG	FRACT		5058.09	5058.09	CW	CW	124	0.5	1?	PART. CLOSED	CALC	32							SERIES OF FRACTS FILLED WITH CALC. STA FRACTS???? DEFINITELY UNDERSAMPLED BEFORE
R-1 INFERIORI, ALEG	FRACT		5058.24	5058.24	CW	CW	125	0.5	1?	PART. CLOSED	CALC	32							SERIES OF FRACTS FILLED WITH CALC. STA FRACTS???? DEFINITELY UNDERSAMPLED BEFORE
R-1 INFERIORI, ALEG	FRACT		5058.39	5058.39	CW	CW	125	0.5	1?	PART. CLOSED	CALC	33							SERIES OF FRACTS FILLED WITH CALC. STA FRACTS???? DEFINITELY UNDERSAMPLED BEFORE
R-1 INFERIORI, ALEG	FRACT		5058.92	5058.92	CW	CW	125	0.5	1?	PART. CLOSED	CALC	32							SERIES OF FRACTS FILLED WITH CALC. STA FRACTS???? DEFINITELY UNDERSAMPLED BEFORE
R-1 INFERIORI, ALEG	FRACT		5059.01	5059.01	TOP	CW	73	0.5	1?	PRED. CLOSED	CALC	27							SERIES OF FRACTS FILLED WITH CALC. STA FRACTS???? DEFINITELY UNDERSAMPLED BEFORE
R-1 INFERIORI, ALEG	FRACT	5059.055			FRACT	CW	110	0.5	1?	PRED. CLOSED	CALC	71							SERIES OF FRACTS FILLED WITH CALC. STA FRACTS???? DEFINITELY UNDERSAMPLED BEFORE
R-1 INFERIORI, ALEG	FRACT		5059.565	5059.565	CW	CW	124	0.5	1?	PRED. CLOSED	CALC	27							SERIES OF FRACTS FILLED WITH CALC. STA FRACTS???? DEFINITELY UNDERSAMPLED BEFORE
R-1 INFERIORI, ALEG	FRACT		5059.58	5059.58	CW	CW	124	0.5	1?	PRED. CLOSED	CALC	26							SERIES OF FRACTS FILLED WITH CALC. STA FRACTS???? DEFINITELY UNDERSAMPLED BEFORE
R-1 INFERIORI, ALEG	FRACT		5059.645	5059.645	CW	CW	124	0.5	1?	PRED. CLOSED	CALC	27							SERIES OF FRACTS FILLED WITH CALC. STA FRACTS???? DEFINITELY UNDERSAMPLED BEFORE
R-1 INFERIORI, ALEG	FRACT		5059.68	5059.68	INT	CW	97	0.5	1?	PRED. CLOSED	CALC	36							SERIES OF FRACTS FILLED WITH CALC. STA FRACTS???? DEFINITELY UNDERSAMPLED BEFORE
R-1 INFERIORI, ALEG	FRACT		5059.69	5059.69	CW	CW	126	0.5	1?	PRED. CLOSED	CALC	27							SERIES OF FRACTS FILLED WITH CALC. STA FRACTS???? DEFINITELY UNDERSAMPLED BEFORE
R-1 INFERIORI, ALEG	FRACT		5059.725	5059.725	CW	CW	124	3	1?	PRED. CLOSED	CALC	26							SERIES OF FRACTS FILLED WITH CALC. STA FRACTS???? DEFINITELY UNDERSAMPLED BEFORE
R-1 INFERIORI, ALEG	FRACT		5059.73	5059.715	CW	INT	71	0.5	1?	PRED. CLOSED	CALC	22							SERIES OF FRACTS FILLED WITH CALC. STA FRACTS???? DEFINITELY UNDERSAMPLED BEFORE
R-1 INFERIORI, ALEG	FRACT		5059.91	5059.91	CW	CW	124	0.5	1?	PRED. CLOSED	CALC	26							SERIES OF FRACTS FILLED WITH CALC. STA FRACTS???? DEFINITELY UNDERSAMPLED BEFORE
R-1 INFERIORI, ALEG	STY		5061.53	5061.53	CW	CW	162	0.5				54							COMP. STY
R-1 INFERIORI, ALEG	FRACT		5061.67	5061.65	CW	INT	83	0.5	1	OPEN		48							RELATED TO ABOVE STY
R-1 INFERIORI, ALEG	FRACT		5061.73	5061.73	CW	CW	162	0.5	1	OPEN		56							RELATED TO ABOVE STY
R-1 INFERIORI, ALEG	FRACT	5062.38			INT	CW	81	0.5	1?	PRED. CLOSED	CALC	34							SERIES OF FRACTS FILLED WITH CALC. STA FRACTS???? DEFINITELY UNDERSAMPLED BEFORE
R-1 INFERIORI, ALEG	FRACT		5062.39	5062.39	INT	INT	72	0.5	1?	PRED. CLOSED	CALC	36							SERIES OF FRACTS FILLED WITH CALC. STA FRACTS???? DEFINITELY UNDERSAMPLED BEFORE
R-1 INFERIORI, ALEG	FRACT	5062.43			CW	INT	41	0.5	1?	PRED. CLOSED	CALC	34							SERIES OF FRACTS FILLED WITH CALC. STA FRACTS???? DEFINITELY UNDERSAMPLED BEFORE
R-1 INFERIORI, ALEG	FRACT		5062.46	5062.45	CW	CW	126	0.5	1?	PRED. CLOSED	CALC	39							SERIES OF FRACTS FILLED WITH CALC. STA FRACTS???? DEFINITELY UNDERSAMPLED BEFORE
R-1 INFERIORI, ALEG	FRACT		5062.49	5062.48	CW	INT	43	4.5	1?	PRED. CLOSED	CALC	34							SERIES OF FRACTS FILLED WITH CALC. STA FRACTS???? DEFINITELY UNDERSAMPLED BEFORE
R-1 INFERIORI, ALEG	FRACT	5062.51			INT	CW	54	4.5	1?	PRED. CLOSED	CALC	31							SERIES OF FRACTS FILLED WITH CALC. STA FRACTS???? DEFINITELY UNDERSAMPLED BEFORE
R-1 INFERIORI, ALEG	FRACT	5062.52			CW	INT	39	0.5	1?	PRED. CLOSED	CALC	42							SERIES OF FRACTS FILLED WITH CALC. STA FRACTS???? DEFINITELY UNDERSAMPLED BEFORE
R-1 INFERIORI, ALEG	FRACT		5062.525	5062.525	CW	CW	125	0.5	1?	PRED. CLOSED	CALC	34							SERIES OF FRACTS FILLED WITH CALC. STA FRACTS???? DEFINITELY UNDERSAMPLED BEFORE
R-1 INFERIORI, ALEG	FRACT		5062.525	5062.525	CW	CW	129	0.5	1?	PRED. CLOSED	CALC	34							SERIES OF FRACTS FILLED WITH CALC. STA FRACTS???? DEFINITELY UNDERSAMPLED BEFORE
R-1 INFERIORI, ALEG	FRACT		5062.525	5062.525	CW	CW	126	0.5	1?	PRED. CLOSED	CALC	34							SERIES OF FRACTS FILLED WITH CALC. STA FRACTS???? DEFINITELY UNDERSAMPLED BEFORE
R-1 INFERIORI, ALEG	FRACT		5062.525	5062.525	CW	CW	126	0.5	1?	PRED. CLOSED	CALC	39							SERIES OF FRACTS FILLED WITH CALC. STA FRACTS???? DEFINITELY UNDERSAMPLED BEFORE
R-1 INFERIORI, ALEG	FRACT		5063.2	5063.2	CW	CW	124	0.5	1?	PRED. CLOSED	CALC	34							SERIES OF FRACTS FILLED WITH CALC. STA FRACTS???? DEFINITELY UNDERSAMPLED BEFORE
R-1 INFERIORI, ALEG	FRACT		5063.27	5063.27	CW	CW	125	0.5	1?	PRED. CLOSED	CALC	36							SERIES OF FRACTS FILLED WITH CALC. STA FRACTS???? DEFINITELY UNDERSAMPLED BEFORE
R-1 INFERIORI, ALEG	FRACT		5063.29	5063.29	CW	CW	125	0.5	1?	PRED. CLOSED	CALC	34							SERIES OF FRACTS FILLED WITH CALC. STA FRACTS???? DEFINITELY UNDERSAMPLED BEFORE
R-1 INFERIORI, ALEG	FRACT		5063.46	5063.46	CW	CW	125	0.5	1?	PRED. CLOSED	CALC	33							SERIES OF FRACTS FILLED WITH CALC. STA FRACTS???? DEFINITELY UNDERSAMPLED BEFORE
R-1 INFERIORI, ALEG	FRACT		5063.53	5063.53	CW	CW	129	0.5	1?	PRED. CLOSED	CALC	34							SERIES OF FRACTS FILLED WITH CALC. STA FRACTS???? DEFINITELY UNDERSAMPLED BEFORE
R-1 INFERIORI, ALEG	FRACT		5063.545	5063.545	CW	CW	125	0.5	1?	PRED. CLOSED	CALC	35							SERIES OF FRACTS FILLED WITH CALC. STA FRACTS???? DEFINITELY UNDERSAMPLED BEFORE
R-1 INFERIORI, ALEG	FRACT		5064.245	5064.245	CW	CW	117	0.5	1?	PRED. CLOSED	CALC	35							SERIES OF FRACTS FILLED WITH CALC. STA FRACTS???? DEFINITELY UNDERSAMPLED BEFORE
R-1 INFERIORI, ALEG	FRACT		5064.34	5064.34	CW	CW	120	0.5	1?	PRED. CLOSED	CALC	35							SERIES OF FRACTS FILLED WITH CALC. STA FRACTS???? DEFINITELY UNDERSAMPLED BEFORE
R-1 INFERIORI, ALEG	FRACT		5064.38	5064.38	CW	CW	121	0.5	1?	PRED. CLOSED	CALC	35							SERIES OF FRACTS FILLED WITH CALC. STA FRACTS???? DEFINITELY UNDERSAMPLED BEFORE
R-1 INFERIORI, ALEG	FRACT		5064.39	5064.38	CW	CW	118	0.5	1?	PRED. CLOSED	CALC	34							SERIES OF FRACTS FILLED WITH CALC. STA FRACTS???? DEFINITELY UNDERSAMPLED BEFORE
R-1 INFERIORI, ALEG	FRACT		5064.69	5064.68	CW	CW	125	0.5	1?	PRED. CLOSED	CALC	35							SERIES OF FRACTS FILLED WITH CALC. STA FRACTS???? DEFINITELY UNDERSAMPLED BEFORE
R-1 INFERIORI, ALEG	FRACT		5064.75	5064.75	CW	CW	126	0.5	1?	PRED. CLOSED	CALC	35							SERIES OF FRACTS FILLED WITH CALC. STA FRACTS???? DEFINITELY UNDERSAMPLED BEFORE
R-1 INFERIORI, ALEG	FRACT	5064.85			CW	INT	54	0.5	1?	PRED. CLOSED	CALC	38							SERIES OF FRACTS FILLED WITH CALC. STA FRACTS???? DEFINITELY UNDERSAMPLED BEFORE
R-1 INFERIORI, ALEG	FRACT		5064.91	5064.89	CW	INT	73	0.5	1?	PRED. CLOSED	CALC	38							SERIES OF FRACTS FILLED WITH CALC. STA FRACTS???? DEFINITELY UNDERSAMPLED BEFORE
R-1 INFERIORI, ALEG	FRACT		5064.925	5064.925	FRACT	INT	49	1	1?	PRED. CLOSED	CALC	49							SERIES OF FRACTS FILLED WITH CALC. STA FRACTS???? DEFINITELY UNDERSAMPLED BEFORE
R-1 INFERIORI, ALEG	FRACT		5064.94	5064.94	CW	CW	129	3	1?	PRED. CLOSED	CALC	38							SERIES OF FRACTS FILLED WITH CALC. STA FRACTS???? DEFINITELY UNDERSAMPLED BEFORE
R-1 INFERIORI, ALEG	FRACT		5064.98	5064.98	CW	CW	128	1	1	PRED. CLOSED	CALC	37							SERIES OF FRACTS FILLED WITH CALC. STA FRACTS???? DEFINITELY UNDERSAMPLED BEFORE
R-1 INFERIORI, ALEG	STY		5065	5065	CW	CW	185				CALC	57				57			COMP. STY ABOVE FRACTS ARE STA
R-1 INFERIORI, ALEG	FRACT		5065.03	5065.06	INT	STY	75	0.5	1	PRED. CLOSED	CALC	31							SERIES OF FRACTS FILLED WITH CALC. STA FRACTS???? DEFINITELY UNDERSAMPLED BEFORE
R-1 INFERIORI, ALEG	FRACT		5065.12	5065.13	INT	STY	83	0.5	1	PRED. CLOSED	CALC	33							SERIES OF FRACTS FILLED WITH CALC. STA FRACTS???? DEFINITELY UNDERSAMPLED BEFORE
R-1 INFERIORI, ALEG	FRACT		5065.185	5065.165	CW	CW	129	0.5	1	PRED. CLOSED	CALC	34							SERIES OF FRACTS FILLED WITH CALC. STA FRACTS???? DEFINITELY UNDERSAMPLED BEFORE
R-1 INFERIORI, ALEG	FRACT		5065.17	5065.17	CW	CW	130	2.5	1	PRED. CLOSED	CALC	31							SERIES OF FRACTS FILLED WITH CALC. STA FRACTS???? DEFINITELY UNDERSAMPLED BEFORE
R-1 INFERIORI, ALEG	FRACT		5065.265	5065.265	CW	CW	129	1	1	PRED. CLOSED	CALC	32							SERIES OF FRACTS FILLED WITH CALC. STA FRACTS???? DEFINITELY UNDERSAMPLED BEFORE
R-1 INFERIORI, ALEG	FRACT		5065.29	5065.29	CW	CW	129	0.5	1	PRED. CLOSED	CALC	24							SERIES OF FRACTS FILLED WITH CALC. STA FRACTS???? DEFINITELY UNDERSAMPLED BEFORE
R-1 INFERIORI, ALEG	FRACT		5065.3	5065.3	CW	CW	129	3	1	PRED. CLOSED	CALC	33							SERIES OF FRACTS FILLED WITH CALC. STA FRACTS???? DEFINITELY UNDERSAMPLED BEFORE
R-1 INFERIORI, ALEG	FRACT		5065.33	5065.33	CW	CW	129	0.5	1	PRED. CLOSED	CALC	30							SERIES OF FRACTS FILLED WITH CALC. STA FRACTS???? DEFINITELY UNDERSAMPLED BEFORE
R-1 INFERIORI, ALEG	FRACT		5065.38	5065.38	CW	CW	129	1.5	1	PRED. CLOSED	CALC	33							SERIES OF FRACTS FILLED WITH CALC. STA FRACTS???? DEFINITELY UNDERSAMPLED BEFORE
R-1 INFERIORI, ALEG	STY		5065.75	5065.75	CW	CW	210	1.5				54							COMP. STY
R-1 INFERIORI, ALEG	FRACT		5066.19	5066.19	CW	CW	129	1	1	PRED. CLOSED	CALC	38							STA FRACT
R-1 INFERIORI, ALEG	FRACT		5066.38	5066.38	CW	CW	129	0.5	1	PRED. CLOSED	CALC	37							STA FRACT
R-1 INFERIORI, ALEG	FRACT		5066.48	5066.48	CW	CW	130	1	1	PRED. CLOSED	CALC	36							STA FRACT
R-1 INFERIORI, ALEG	FRACT		5066.49	5066.49	CW	CW	129	1	1	PRED. CLOSED	CALC	38							STA FRACT
R-1 INFERIORI, ALEG	FRACT	5067.085			INT	CW	33	0.5	1	PRED. CLOSED	CALC	24							STA FRACT
R-1 INFERIORI, ALEG	FRACT		5067.105	5067.105	CW	CW	88	1	1	PRED. CLOSED	CALC	26							STA FRACT
R-1 INFERIORI, ALEG	FRACT		5067.23	5067.23	CW	CW	88	0.5	1	PRED. CLOSED	CALC	26							STA FRACT
R-1 INFERIORI, ALEG	FRACT		5067.245	5067.24	CW	INT	88	1.5	1	PRED. CLOSED	CALC	24							STA FRACT
R-1 INFERIORI, ALEG	FRACT	5067.24			INT	CW	36	1.5	1	PRED. CLOSED	CALC	29							STA FRACT
R-1 INFERIORI, ALEG	FRACT		5067.345	5067.345	INT	CW	34	1.5	1	PRED. CLOSED	CALC	28							STA FRACT
R-1 INFERIORI, ALEG	FRACT		5067.85	5067.85	CW	CW	109	1	1	PRED. CLOSED	CALC	32							STA FRACT
R-1 INFERIORI, ALEG	FRACT		5068.4	5068.4	CW	CW	107	1	1	PRED. CLOSED	CALC	29							STA FRACT
R-1 INFERIORI, ALEG	STY		5075.38	5075.38	CW	CW	110	4	1		CALC	29				26			V. GOOD EXAMPLE OF COMP. STY INFILLED WITH CALC.
R-1 INFERIORI, ALEG	FRACT		5075.74	5075.74	CW	CW	114	0.5	1	PRED. CLOSED	CALC	31							STA FRACT
R-1 INFERIORI, ALEG	FRACT		5075.78	5075.78	CW	CW	115	0.5	1	PRED. CLOSED	CALC	34							STA FRACT

Miskar A-6 Raw Data

R 1 INFERIORM_ALEG	FRACT		5075.79	5075.79	CW	CW	114	0.5	1	PRED_CLOSED	CALC	30							STA FRACT
R 1 INFERIORM_ALEG	FRACT		5075.86	5075.86	CW	CW	114	0.5	1	PRED_CLOSED	CALC	32							STA FRACT
R 1 INFERIORM_ALEG	FRACT		5075.89	5075.89	CW	CW	114	0.5	1	PRED_CLOSED	CALC	30							STA FRACT
R 1 INFERIORM_ALEG	FRACT		5076.05	5076.05	CW	CW	115	0.5	1	PRED_CLOSED	CALC	31							STA FRACT
R 1 INFERIORM_ALEG	FRACT		5076.11	5076.11	CW	CW	114	0.5	1	PRED_CLOSED	CALC	30							STA FRACT
R 1 INFERIORM_ALEG	FRACT		5076.12	5076.12	CW	CW	114	0.5	1	PRED_CLOSED	CALC	30							STA FRACT
R 1 INFERIORM_ALEG	FRACT		5076.21	5076.21	CW	CW	115	0.5	1	PRED_CLOSED	CALC	28							STA FRACT
R 1 INFERIORM_ALEG	FRACT		5076.29	5076.29	CW	CW	115	0.5	1	PRED_CLOSED	CALC	30							STA FRACT
R 1 INFERIORM_ALEG	FRACT		5076.39	5076.39	CW	CW	105	0.5	1	PRED_CLOSED	CALC	9							STA FRACT
R 1 INFERIORM_ALEG	FRACT		5076.405	5076.405	CW	CW	100	0.5	1	PRED_CLOSED	CALC	10							DIFF_FRACT_SET
R 1 INFERIORM_ALEG	FRACT		5076.46	5076.46	CW	CW	100	0.5	1	PRED_CLOSED	CALC	5							DIFF_FRACT_SET
R 1 INFERIORM_ALEG	FRACT		5076.74	5076.74	CW	CW	300	0.5	?	PRED_CLOSED	CALC	72							DIFF_FRACT_SET?
R 1 INFERIORM_ALEG	FRACT		5076.87	5076.87	CW	CW	134	0.5	?	PRED_CLOSED	CALC	41							DIFF_FRACT_SET?
R 1 INFERIORM_ALEG	FRACT		5077.26	5077.26	CW	CW	126	10	?	PRED_CLOSED	CALC	40							DIFF_FRACT_SET?
R 1 INFERIORM_ALEG	FRACT		5077.32	5077.32	CW	CW	122	0.5	?	PRED_CLOSED	CALC	36							DIFF_FRACT_SET?
R 1 INFERIORM_ALEG	FRACT		5077.4	5077.4	CW	CW	112	0.5	?	PRED_CLOSED	CALC	37							
R 1 INFERIORM_ALEG	FRACT		5077.59	5077.59	CW	CW	119	0.5	?	PRED_CLOSED	CALC	36							
R 1 INFERIORM_ALEG	FRACT		5078.28	5078.28	INT	INT	46	0.5	?	PRED_CLOSED	CALC	70							
R 1 INFERIORM_ALEG	FRACT																		
5081.00 (END CORE 19)																			

Miskar A-7 Raw Data

Well	Structural	Non-centreline (m)	Centreline Intersection	Centreline Intersection	Termination		Length	Width	Fracture Type	Open/Closed	Fill	Dip	Strike	Slickensides		Stylolites		Vug	Comments
	Feature	Fract. Mid-point Depth (m)	Depth (m)	Fract. Mid-point Depth (m)	Upper	Lower	(mm)	(mm)	(1, 2, 3)					Plunge/Dir.	Sense	Dentae (mm)	Fill	Size	
Miskar A-7																			
3511.00 (TOP CORE 1)																			
EL HARIA	FRACT	3529.2			INT	CW	133	0.5	1	OPEN		78							REHEALED FRACT.
RUBBLE 3524.63-3525.50																			
ABIOD	FRACT		3525.79	3525.79	CW	CW	105	1.5	?	CLOSED		28							REHEALED FRACT. THIS INTERVAL PROB. UNDERSAMPLED
ABIOD	FRACT		3525.84	3525.84	CW	CW	105	3	?	CLOSED		28							REHEALED FRACT. THIS INTERVAL PROB. UNDERSAMPLED
ABIOD	FRACT		3525.885	3525.885	CW	CW	105	3	?	CLOSED		30							REHEALED FRACT. THIS INTERVAL PROB. UNDERSAMPLED
	STY		3527.38	3527.38	CW	CW	100	6				15				70			VERY DIFF. MORPHOLOGY OF STY. NOT AS SHARP, VERY SMOOTH, SIGMOIDAL
	STY		3528.4	3528.4	CW	CW	100	5				0				55			VERY DIFF. MORPHOLOGY OF STY. NOT AS SHARP, VERY SMOOTH, SIGMOIDAL
RUBBLE 3528.63-3529.42																			
ABIOD	FRACT		3529.84	3529.83	CW	CW	557	2	1?	OPEN		88							FRACT FILLED WITH DRILLING MUD, NOT INDUCED
	STY		3530.31	3530.31	CW	CW	102	4				2				27			VERY DIFF. MORPHOLOGY OF STY. NOT AS SHARP, VERY SMOOTH, SIGMOIDAL
ABIOD	FRACT		3523.23	3523.23	CW	CW	140	0.5	2?	OPEN		42							REHEALED FRACT. THIS INTERVAL PROB. UNDERSAMPLED
	STY		3534.49	3534.49	CW	CW	100	4				0				5			
	STY		3535.955	3535.955	CW	CW	100	2				0				9			
	STY		3537.9	3537.9	CW	CW	104	0.5				4				5			

Miskar A-9 Raw Data

Well	Structural	Non-centreline (m)	Centreline Intersection	Centreline Intersection	Termination		Length	Width	Fracture Type	Open/Closed	Fill	Dip	Strike	Slickensides		Stylolites		Vug	Comments
	Feature	Fract. Mid-point Depth (m)	Depth (m)	Fract. Mid-point Depth (m)	Upper	Lower	(mm)	(mm)	(1, 2, 3)					Plunge/Dir.	Sense	Dentae (mm)	Fill	Size	
Miskar A-9																			
3880.00 (TOP CORE 1)																			
RUBBLE 3880.00-3880.55																			
R-1	FRACT		3881.57	3381.68	INT	INT	263	0.5	1	PRED. CLOSED	CALC	81							SERIES OF EN ECHELON FRACTURES
R-1	FRACT	3881.61			INT	INT	42	0.5	1	PRED. CLOSED	CALC	83							SERIES OF EN ECHELON FRACTURES
R-1	FRACT	3881.62			INT	INT	43	0.5	1	MAINLY OPEN	CALC	85							SERIES OF EN ECHELON FRACTURES
R-1	FRACT		3881.7	3881.74	INT	INT	316	0.5	1	PRED. CLOSED	CALC	82							SERIES OF EN ECHELON FRACTURES
R-1	FRACT	3881.8			INT	INT	26	0.5	1	PRED. CLOSED	CALC	84							SERIES OF EN ECHELON FRACTURES
R-1	FRACT	3881.83			INT	INT	37	0.5	1	PRED. CLOSED	CALC	82							SERIES OF EN ECHELON FRACTURES
R-1	FRACT	3881.84			INT	INT	26	0.5	1	PRED. CLOSED	CALC	84							SERIES OF EN ECHELON FRACTURES
R-1	FRACT	3881.85			INT	CW	55	0.5	1	PRED. CLOSED	CALC	89							SERIES OF EN ECHELON FRACTURES
R-1	FRACT	3881.89			INT	INT	66	0.5	1	PRED. CLOSED	CALC	83							SERIES OF EN ECHELON FRACTURES
R-1	FRACT	3881.965			INT	INT	76	0.5	1	PRED. CLOSED	CALC	87							SERIES OF EN ECHELON FRACTURES
R-1	FRACT		3882	3882.025	TOP	INT	46	0.5	1	PRED. CLOSED	CALC	86							SERIES OF EN ECHELON FRACTURES
R-1	FRACT		3882.04	3882.085	INT	INT	102	0.5	1	PRED. CLOSED	CALC	87							SERIES OF EN ECHELON FRACTURES
R-1	FRACT	3882.145			INT	INT	19	0.5	1	MAINLY OPEN	CALC	86							SERIES OF EN ECHELON FRACTURES
R-1	FRACT	3882.165			INT	INT	33	0.5	1	PRED. CLOSED	CALC	86							SERIES OF EN ECHELON FRACTURES
R-1	FRACT	3882.215			INT	INT	12	0.5	1	PRED. CLOSED	CALC	88							SERIES OF EN ECHELON FRACTURES
R-1	FRACT	3885.42			INT	INT	44	0.5	1	MAINLY OPEN	CALC	88							SERIES OF EN ECHELON FRACTURES
IZ 3889.65-3889.85																			
3889.85-3904.44 (NOTHING)																			STRANGE ZONE. ALMOST A MARBLE. MANY STY + FRACTS
R-1	FRACT		3904.44	3904.44	CW	CW	202	2	2	OPEN		63							OIL FILLED SHEAR BAND - VERY SIMILAR TO MISKAR A3
R-1	STY		3904.9	3904.9	CW	CW	100	2				0				122			
R-1	STY		3906.23	3906.23	CW	CW	100	1				4				18			
R-1	STY		3908.84	3908.84	CW	CW	105	1				4				36			
R-1	STY		3912.94	3912.94	CW	CW	104	2				2				13			
R-1	FRACT		3913	3913.1	STY	CW	330	2	1	PART. OPEN	CALC	89							LARGE STA FRACT.
R-1	STY		3915.18	3915.18	CW	CW	110	1				25				15			FILLED WITH PYRITE
3917.00 (BASE CORE)																			

Miskar A-10 Raw Data

Well	Structural	Non-centreline (m)	Centreline Intersection	Centreline Intersection	Termination		Length	Width	Fracture Type	Open/Closed	Fill	Dip	Strike	Slickensides		Stylolites		Vug	Comments
	Feature	Fract. Mid-point Depth (m)	Depth (m)	Fract. Mid-point Depth (m)	Upper	Lower	(mm)	(mm)	(1, 2, 3)					Plunge/Dir.	Sense	Dentae (mm)	Fill	Size	
Miskar A-10																			
4356.00 (START CORE 1)	BEDDING											54							
	STY		4358.86	4358.86	CW	CW	124	0.5				48				5			COMP. STY
	STY		4359.39	4359.39	CW	CW	174	6				57				19			COMP. STY
	FRACT		4363.33	4363.33	CW	STY	124	0.5	1	PRED. OPEN	CALC	56							STA FRACT
	STY		4363.41	4363.41	CW	CW	116	4				39				31			COMP. STY
	STY		4364.17	4364.17	CW	CW	136	0.5			CALC	45				12			CALC FILLED STY
	STY		4364.81	4364.81	CW	CW	126	0.5				40				13			COMP. STY
	FRACT		4372.63	4372.63	CW	CW	145	0.5	2?	OPEN		45							? FRACT OR BEDDING
4389.00 (END CORE 1)																			
4640.00 (START CORE 2)																			
	FRACT		4641.18	4641.18	CW	CW	159	0.5	1	PRED. OPEN	CALC	48							APPEAR AS INDUCED. FILLED WITH CALC. AND DRILLING MUD. STA FRACT
	FRACT		4641.24	4641.24	CW	CW	158	0.5	1	PRED. OPEN	CALC	48							APPEAR AS INDUCED. FILLED WITH CALC. AND DRILLING MUD. STA FRACT
	FRACT		4641.3	4641.3	CW	CW	159	0.5	1	PRED. OPEN	CALC	48							APPEAR AS INDUCED. FILLED WITH CALC. AND DRILLING MUD. STA FRACT
	STY		4642.03	4642.03	CW	CW	139	0.7				46				64			COMP. STY
	FRACT		4642.135	4642.135	CW	CW	171	1	1	PART. OPEN	CALC	52							STA FRACT
	FRACT		4643.16	4643.16	CW	CW	161	0.5	1	PART. OPEN	CALC	53							STA FRACT
	FRACT		4643.56	4643.56	CW	CW	156	0.5	1	PART. OPEN	CALC	56							STA FRACT
4645.00 (END CORE 2)																			
4645.00 (START CORE 3)																			
	STY		4645.76	4645.76	CW	CW	151	6				49				30			COMP. STY
	STY		4647.27	4647.27	CW	CW	155	0.5				47				70			COMP. STY
	STY		4647.55	4647.55	CW	CW	148	7				47				47			COMP. STY
	FRACT		4647.555	4647.555	STY	CW	35	1	1	PART. OPEN	CALC	46							STA FRACT
	STY		4648.67	4648.67	CW	CW	142	2			CALC	47				30			COMP. STY. FILLED WITH CALC.
	STY		4650.23	4650.23	CW	CW	168	5			CALC	48				69			COMP. STY. FILLED WITH CALC.
	STY		4651.825	4651.825	CW	CW	139	0.5				47				15			COMP. STY.
	STY		4653.635	4653.635	CW	CW	131	0.5			CALC	39				22			COMP. STY.
	STY		4654.35	4654.35	CW	CW	149	1			CALC	42				51			COMP. STY.
	FRACT	4654.375			CW	STY	18	0.5	1	PART. OPEN	CALC	54							STA FRACT
	FRACT	4654.375			CW	STY	20	0.5	1	PART. OPEN	CALC	54							STA FRACT
	FRACT	4654.38			CW	STY	21	0.5	1	PART. OPEN	CALC	53							STA FRACT
	FRACT		4654.54	4654.54	CW	CW	149	1	1	PART. OPEN	CALC	54							STA FRACT
	FRACT		5654.545	5654.545	CW	CW	151	0.5	1	PART. OPEN	CALC	54							STA FRACT
	FRACT		4655.23	4655.23	CW	CW	152	1	1	PART. OPEN	CALC	55							STA FRACT
	STY		4658.34	4658.34	CW	CW	105	5			CALC	11				12			COMP. STY. FILLED WITH CALC.
	FRACT		4660.77	4660.77	CW	CW	127	0.5	1	PART. OPEN	CALC	41							STA FRACT
	FRACT		4661	4661	CW	CW	117	0.5	1	PART. OPEN	CALC	30							STA FRACT
	FRACT		4661.075	4661.075	CW	CW	119	0.5	1	PART. OPEN	CALC	30							STA FRACT
	FRACT		4661.095	4661.095	CW	CW	118	0.5	1	PART. OPEN	CALC	30							STA FRACT
	FRACT		4661.14	4661.14	CW	CW	122	0.5	1	PART. OPEN	CALC	31							STA FRACT
	FRACT		4661.17	4661.17	CW	CW	116	0.5	1	PART. OPEN	CALC	30							STA FRACT
	FRACT		4661.22	4661.22	CW	CW	118	0.5	1	PART. OPEN	CALC	31							STA FRACT
	FRACT		4661.34	4661.34	CW	CW	118	0.5	1	PART. OPEN	CALC	30							STA FRACT
	STY		4661.63	4661.63	CW	CW	126	2			CALC	38				104			COMP. STY. FILLED WITH CALC.
	FRACT		4662.67	4662.67	CW	CW	129	0.5	1	PART. OPEN	CALC	29							STA FRACT
	FRACT		4662.675	4662.675	CW	CW	119	0.5	1	PART. OPEN	CALC	31							STA FRACT
	FRACT		4662.68	4662.68	CW	CW	118	0.5	1	PART. OPEN	CALC	34							STA FRACT
	FRACT		4662.69	4662.69	CW	CW	121	0.5	1	PART. OPEN	CALC	30							STA FRACT
	STY		4662.84	4662.84	CW	CW	162	3			CALC	51				26			COMP. STY. FILLED WITH CALC.
	STY		4663	4663	CW	CW	167	4			CALC	54				72			COMP. STY. FILLED WITH CALC.
	FRACT		4663.37	4663.37	CW	CW	137	0.5	1	PART. OPEN	CALC	38							STA FRACT
	FRACT		3663.38	3663.38	CW	CW	136	0.5	1	PART. OPEN	CALC	37							STA FRACT
	FRACT		4663.39	4663.39	CW	CW	138	0.5	1	PART. OPEN	CALC	42							STA FRACT
	FRACT		4663.405	4663.405	CW	CW	137	1.5	1	PART. OPEN	CALC	38							STA FRACT
	FRACT		4663.42	4663.42	CW	CW	137	0.5	1	PART. OPEN	CALC	38							STA FRACT
	FRACT		4663.45	4663.45	CW	CW	136	0.5	1	PART. OPEN	CALC	38							STA FRACT
	FRACT		4663.6	4663.6	CW	CW	134	0.5	1	PART. OPEN	CALC	38							STA FRACT
	FRACT		4663.76	4663.76	CW	CW	134	0.5	1	PART. OPEN	CALC	38							STA FRACT
	STY		4664.28	4664.28	CW	CW	152	2.5			CALC	51				94			COMP. STY. FILLED WITH CALC.
	FRACT		4665.95	4665.93	CW	INT	137	1	1	PART. OPEN	CALC	45							STA FRACT. EN ECHELON
	FRACT	4665.98			INT	CW	25	1	1	PART. OPEN	CALC	45							STA FRACT. EN ECHELON
	FRACT	4665.99			INT	CW	18	1	1	PART. OPEN	CALC	44							STA FRACT. EN ECHELON
	STY		4666.21	4666.21	CW	CW	139	0.5				43				22			COMP. STY. FILLED WITH CALC.
	FRACT	4666.4			CW	INT	66	0.5	1	PART. OPEN	CALC	52							STA FRACT
	FRACT		4666.44	4666.44	CW	CW	138	1	1	PART. OPEN	CALC	52							STA FRACT
	FRACT		4666.55	4666.55	CW	CW	138	2	1	PART. OPEN	CALC	51							STA FRACT
	FRACT		4666.56	4666.56	CW	CW	162	1	1	PART. OPEN	CALC	52							STA FRACT
	STY		4667.08	4667.08	CW	CW	156	0.5			CALC	50				21			COMP. STY. FILLED WITH CALC.
	FRACT		4667.085	4667.085	CW	CW	156	1	1	PART. OPEN	CALC	47							STA FRACT. CUTS STRAIGHT THROUGH STY.
	STY		4669.74	4669.74	CW	CW	119	1			CALC	17				20			COMP. STY. FILLED WITH CALC.
4672.50 (END CORE 3)																			

Miskar A-11 Raw Data

Well / Lithology	Structural	Non-centreline (m)	Centreline Intersection	Centreline Intersection	Termination		Length	Width	Fracture Type	Open/Closed		Dip	Strike	Slickensides		Stylolites		Vug	Comments
	Feature	Fract. Mid-point Depth (m)	Measured Depth (m MD)	Fract. Mid-point Depth (m)	Upper	Lower	(mm)	(mm)	(1, 2, 3)					Plunge/Dir.	Sense	Dentae (mm)	Fill	Size	
Miskar A-11																			
4851.00 (START CORE 1)	FRACT	4851.53			INT	INT	175	0.2	1?	OPEN		90							REHEALED FRACT PROB EXT
ABIOD	STY		4851.57	4851.57	TOP	STY	1380	0.5				88				2			VERTICAL STY. TECTONIC. FILLED WITH PYRITE
ABIOD	FRACT	4851.695			INT	STY	51	0.2	1?	OPEN		90							REHEALED FRACT PROB EXT
ABIOD	STY		4852.27	4852.27	CW	STY	165	2				55				22			COMP. STY
ABIOD	STY		4852.33	4852.33	STY	STY	91	0.5				88				4			TECTONIC STY
ABIOD	STY		4852.34	4852.34	STY	STY	102	0.5				88				5			TECTONIC STY
ABIOD	STY		4852.37	4852.37	CW	CW	177	3				47				25			COMP. STY
ABIOD	STY		4852.77	4852.77	CW	CW	143	0.2				40				2			COMP. STY
ABIOD	STY		4852.94	4852.94	CW	CW	149	0.5				42				6			COMP. STY
ABIOD	STY		4853.62	4853.62	CW	CW	163	0.5				46				20			COMP. STY
ABIOD	STY		4854.045	4854.045	CW	CW	113	1				12				9			COMP. STY
ABIOD	FRACT	4854.815			INT	STY	22	0.5	1	PRED. CLOSED	CALC	51							STA FRACTS, HOWEVER, SLIGHTLY OBLIQUE TO STY. BELOW
ABIOD	FRACT	4854.815			INT	STY	9	0.5	1	PRED. CLOSED	CALC	49							STA FRACTS, HOWEVER, SLIGHTLY OBLIQUE TO STY. BELOW
ABIOD	FRACT	4854.82			INT	STY	22	0.5	1	PRED. CLOSED	CALC	48							STA FRACTS, HOWEVER, SLIGHTLY OBLIQUE TO STY. BELOW
ABIOD	FRACT	4854.82			INT	STY	14	0.5	1	PRED. CLOSED	CALC	50							STA FRACTS, HOWEVER, SLIGHTLY OBLIQUE TO STY. BELOW
ABIOD	STY		4854.825	4854.825	CW	CW	112	1				11				12			COMP. STY
ABIOD	STY		4855.26	4855.26	CW	CW	191	1				47				10			COMP. STY
ABIOD	STY		4855.54	4855.54	CW	CW	162	1				45				8			COMP. STY
ABIOD	STY		4855.83	4855.83	CW	CW	162	1				45				5			COMP. STY
ABIOD	FRACT	4856			INT	STY	105	0.5	1?	PRED. CLOSED	CALC	90							STA FRACTS, HOWEVER, SLIGHTLY OBLIQUE TO STY. BELOW
ABIOD	STY		4856.01	4856.01	CW	CW	164	1				47				8			COMP. STY
ABIOD	STY		4856.07	4856.07	CW	CW	166	3				51				74			COMP. STY
ABIOD	STY		4856.28	4856.28	CW	CW	150	0.5				40				5			COMP. STY
ABIOD	STY		4856.6	4856.6	CW	CW	153	0.5				42				1			COMP. STY
ABIOD	STY		4857.03	4857.03	CW	CW	155	2				47				24			COMP. STY
ABIOD	FRACT	4857.28			INT	STY	364	0.5	1?	PART CLOSED	CALC	88							STA FRACTS, HOWEVER, SLIGHTLY OBLIQUE TO STY. BELOW
ABIOD	FRACT	4857.4			INT	STY	96	0.5	1?	PART CLOSED	CALC	88							STA FRACTS, HOWEVER, SLIGHTLY OBLIQUE TO STY. BELOW
ABIOD	FRACT	4857.46			INT	STY	38	0.5	1?	PART CLOSED	CALC	88							STA FRACTS, HOWEVER, SLIGHTLY OBLIQUE TO STY. BELOW
ABIOD	FRACT	4857.48			INT	STY	107	0.5	1?	PART CLOSED	CALC	88							STA FRACTS, HOWEVER, SLIGHTLY OBLIQUE TO STY. BELOW
ABIOD	STY		4857.5	4857.5	CW	CW	179	0.5				53				7			COMP. STY
ABIOD	STY		4857.53	4857.53	CW	CW	181	3				53				10			COMP. STY
ABIOD	FRACT	4857.6			STY	INT	175	0.5	1?	PART CLOSED	CALC	88							MORE STA FRACTS, HOWEVER, SLIGHTLY OBLIQUE TO STY
ABIOD	FRACT	4857.71			INT	INT	66	0.5	1?	PART CLOSED	CALC	88							MORE STA FRACTS, HOWEVER, SLIGHTLY OBLIQUE TO STY
ABIOD	STY		4857.955	4857.955	CW	CW	172	0.5				55				2			COMP. STY
ABIOD	FRACT	4858.07			STY	STY	130	0.5	1?	PART CLOSED	CALC	88							MORE STA FRACTS, HOWEVER, SLIGHTLY OBLIQUE TO STY
ABIOD	STY		4858.13	4858.13	CW	CW	112	1				20				16			COMP. STY
ABIOD	FRACT	4858.165			STY	STY	64	0.5	1?	PART CLOSED	CALC	88							MORE STA FRACTS, HOWEVER, SLIGHTLY OBLIQUE TO STY
ABIOD	STY		4858.19	4858.19	CW	CW	133	0.5				21				15			COMP. STY
ABIOD	STY		4859.29	4859.29	CW	CW	114	1				20				12			COMP. STY
ABIOD	STY		4858.44	4858.44	CW	CW	114	1				20				4			COMP. STY
ABIOD	STY		4858.635	4858.635	CW	CW	114	0.5				20				12			COMP. STY
ABIOD	STY		4858.66	4858.66	CW	CW	114	0.5				20				13			COMP. STY
ABIOD	STY		4858.67	4858.67	CW	CW	114	0.5				20				20			COMP. STY
ABIOD	STY		4858.69	4858.69	CW	CW	114	1				20				5			COMP. STY
ABIOD	STY		4858.7	4858.7	CW	CW	114	1				20				4			COMP. STY
ABIOD	STY		4858.94	4858.94	CW	CW	114	1				20				1			COMP. STY
ABIOD	STY		4859.145	4859.145	CW	CW	178	1				53				10			COMP. STY
ABIOD	STY		4859.6	4859.6	CW	CW	174	1				51				9			COMP. STY
ABIOD	STY		4860.725	4860.725	CW	CW	115	1				21				11			COMP. STY
ABIOD	STY		4861.01	4861.01	CW	CW	115	1				21				34			COMP. STY
ABIOD	STY		4861.3	4861.3	CW	CW	115	0.5				21				1			COMP. STY
ABIOD	STY		4862.01	4862.01	CW	CW	112	2				22				19			COMP. STY
ABIOD	STY		4862.1	4862.1	CW	CW	113	2				22				31			COMP. STY
ABIOD	STY		4862.89	4862.89	CW	CW	115	4				23				42			FILLED WITH PYRITE. COMP. STY
ABIOD	FRACT	4863.17			INT	STY	15	0.5	1	PART CLOSED	CALC	85							MORE STA FRACTS, HOWEVER, SLIGHTLY OBLIQUE TO STY
ABIOD	FRACT	4863.17			INT	STY	13	0.5	1	PART CLOSED	CALC	85							MORE STA FRACTS, HOWEVER, SLIGHTLY OBLIQUE TO STY
ABIOD	STY		4863.17	4863.17	CW	CW	141	0.5				43				5			COMP. STY
ABIOD	STY		4863.205	4863.205	CW	CW	142	0.5				43				5			COMP. STY
ABIOD	FRACT	4863.21			STY	INT	79	0.5	1	PART CLOSED	CALC	86							MORE STA FRACTS, HOWEVER, SLIGHTLY OBLIQUE TO STY
ABIOD	STY		4863.62	4863.62	CW	CW	136	2				37				22			COMP. STY
ABIOD	STY		4863.77	4863.77	CW	CW	114	1				13				9			COMP. STY
ABIOD	STY		4863.915	4863.915	CW	CW	118	2				13				11			COMP. STY
ABIOD	STY		4865.51	4865.51	CW	CW	136	3				29				29			COMP. STY
ABIOD	STY		4865.66	4865.66	CW	CW	115	2.5				19				9			COMP. STY
ABIOD	STY		4866.73	4866.73	CW	CW	145	0.5				44				11			COMP. STY
ABIOD	STY		4866.78	4866.78	CW	CW	153	1				48				9			COMP. STY
ABIOD	STY		4867.74	4867.74	CW	CW	129	0.5				27				7			COMP. STY
ABIOD	STY		4867.8	4867.8	CW	CW	128	2				27				14			COMP. STY
ABIOD	STY		4868.13	4868.13	CW	CW	157	4				46				1			COMP. STY
ABIOD	STY		4869.35	4869.35	CW	CW	178	1				53				2			COMP. STY
ABIOD	STY		4869.86	4869.86	CW	CW	120	1				24				16			COMP. STY
ABIOD	STY		4870.29	4870.29	CW	CW	175	2				51				9			COMP. STY
ABIOD	STY		4870.39	4870.39	CW	CW	225	4				69				53			COMP. STY
ABIOD	STY		4871.34	4871.34	CW	CW	153	1				44				7			COMP. STY
ABIOD	STY		4871.36	4871.36	CW	CW	192	0.5				54				7			COMP. STY
ABIOD	STY		4871.71	4871.71	CW	CW	134	1				33				8			COMP. STY
ABIOD	STY		4872.015	4872.015	CW	CW	153	1				49				7			COMP. STY
ABIOD	STY		4872.035	4872.035	CW	CW	155	1				49				7			COMP. STY
ABIOD	STY		4872.055	4872.055	CW	CW	153	1				48				19			COMP. STY
ABIOD	STY		4872.07	4872.07	CW	CW	153	1				49				13			COMP. STY
ABIOD	STY		4872.16	4872.16	CW	CW	153	1				47				7			COMP. STY
ABIOD	STY		4872.69	4872.69	CW	CW	168	0.5				47				3			COMP. STY
ABIOD	STY		4872.76	4872.76	CW	CW	163	1				46				2			COMP. STY
ABIOD	STY		4873.64	4873.64	CW	CW	178	0.5				55				7			COMP. STY
ABIOD	STY		4873.69	4873.69	CW	CW	171	0.5				54				4			COMP. STY
ABIOD	STY		4873.72	4873.72	CW	CW	176	1				55				1			COMP. STY
ABIOD	STY		4874.05	4874.05	CW	CW	155	0.5				46				9			COMP. STY
ABIOD	STY		4874.22	4874.22	CW	CW	164	0.5				49				9			COMP. STY
ABIOD	STY		4874.46	4874.46	CW	CW	158	0.5				49				15			COMP. STY
ABIOD	STY		4874.52	4874.52	CW	CW	156	0.5				50				12			COMP. STY

Miskar A-11 Raw Data

ABIOD	STY		4874.54	4874.54	OW	OW	156	0.5				49				7			COMP. STY
ABIOD	STY		4874.65	4874.65	OW	OW	150	0.5				40				19			COMP. STY
ABIOD	STY		4874.78	4874.78	OW	OW	155	0.5				37				7			COMP. STY
ABIOD	STY		4875.13	4875.13	OW	OW	158	0.5				44				2			COMP. STY
ABIOD	STY		4875.18	4875.18	OW	OW	209	0.5				54				5			COMP. STY
ABIOD	STY		4875.7	4875.7	OW	OW	155	0.5				43				4			COMP. STY
ABIOD	STY		4876.01	4876.01	OW	OW	152	0.5				45				1			COMP. STY
ABIOD	STY		4876.28	4876.28	OW	OW	153	0.5				45				2			COMP. STY
ABIOD	STY		4876.7	4876.7	OW	OW	155	0.5				45				1			COMP. STY
ABIOD	STY		4876.72	4876.72	OW	OW	155	0.5				45				1			COMP. STY
4877.00 4878.50 RUBBLE																			
4878.50 (END CORE 1)																			
4878.50 (START CORE 2)																			
ABIOD	STY		4878.53	4878.53	OW	OW	115	0.5				21				2			COMP. STY
ABIOD	STY		4878.54	4878.54	OW	OW	113	0.5				21				2			COMP. STY
ABIOD	STY		4878.69	4878.69	OW	OW	117	0.5				22				2			COMP. STY
ABIOD	STY		4878.71	4878.71	OW	OW	119	0.5				22				2			COMP. STY
ABIOD	STY		4879.05	4879.05	OW	OW	170	0.5				46				2			COMP. STY
ABIOD	STY		4879.23	4879.23	OW	OW	167	1				46				2			COMP. STY
ABIOD	STY		4879.41	4879.41	OW	OW	168	0.5				45				2			COMP. STY
ABIOD	STY		4879.46	4879.46	OW	OW	170	1				46				2			COMP. STY
ABIOD	STY		4879.55	4879.55	OW	OW	169	0.5				46				2			COMP. STY
ABIOD	STY		4880.49	4880.49	OW	OW	127	0.5				37				2			COMP. STY
ABIOD	STY		4880.62	4880.62	OW	OW	134	0.5				38				2			COMP. STY
ABIOD	STY		4881.27	4881.27	OW	OW	210	0.5				59				2			COMP. STY
ABIOD	STY		4881.85	4881.85	OW	OW	179	0.5				53				2			COMP. STY
ABIOD	STY		4882.13	4882.13	OW	OW	169	0.5				48				1			COMP. STY
IZ 4882.13 4886.00																			MANY MICROSTY. APPROX 40MM SPACING
RUBBLE 4886.00 4891.20																			
ABIOD	STY		4891.36	4891.36	OW	OW	170	8				55				1			COMP. STY
ABIOD	STY		4891.4	4891.4	OW	OW	165	0.5				53				10			COMP. STY
ABIOD	STY		4891.53	4891.53	OW	OW	169	0.5				55				4			COMP. STY
ABIOD	STY		4891.54	4891.54	OW	OW	169	0.5				55				2			COMP. STY
ABIOD	STY		4892.12	4892.12	OW	OW	156	0.5				45				2			COMP. STY
ABIOD	STY		4892.69	4892.69	OW	OW	154	0.5				44				2			COMP. STY
ABIOD	STY		4892.73	4892.73	OW	OW	156	7				44				2			COMP. STY
ABIOD	STY		4892.92	4892.95	OW	OW	156	0.5				44				7			COMP. STY
ABIOD	STY		4894.85	4894.85	OW	OW	149	0.5				44				3			COMP. STY
ABIOD	STY		4897.57	4897.57	OW	OW	140	62				41				1			ZONE OF MANY MICROSTY
ABIOD	STY		4898.9	4898.9	OW	OW	185	15				52				1			ZONE OF MANY MICROSTY
ABIOD	STY		4900.09	4900.09	OW	OW	183	141				55				1			ZONE OF MANY MICROSTY
ABIOD	STY		4901.21	4901.21	OW	OW	179	61				57				1			ZONE OF MANY MICROSTY
ABIOD	STY		4902.52	4902.52	OW	OW	162	49				44				1			ZONE OF MANY MICROSTY
ABIOD	STY		4904	4904	OW	OW	159	92				44				1			ZONE OF MANY MICROSTY
ABIOD	STY		4905.5	4905.5	OW	OW	160	73				43				1			ZONE OF MANY MICROSTY
4906.30 (END CORE 2)																			
5254.00 (START CORE 3)																			
R-1 SUPERIOR	FRACT	4252.93			INT	INT	40	3	1	CLOSED	CALC	90							ISOLATED CALC. FILLED FRACT.
R-1 SUPERIOR	STY		5263.42	5263.42	OW	OW	146	1				44				22			COMP. STY
R-1 SUPERIOR	STY		5263.66	5263.66	OW	OW	155	0.5				47				13			COMP. STY
R-1 SUPERIOR	STY		5264.92	5264.92	OW	OW	145	1				40				5			COMP. STY
R-1 SUPERIOR	STY		5268.4	5268.4	OW	OW	155	9				46				1			ZONE OF MANY MICROSTY
5270.37 (END CORE 3)																			
5270.80 (START CORE 4)																			
R-1 SUPERIOR	STY		5273.96	5273.96	OW	OW	108	1				16				12			PROB. COMP. STY
RUBBLE 5274.00 5284.00																			
R-1 SUPERIOR	STY		5284.61	5284.61	OW	OW	188	0.5				51				5			PROB. COMP. STY.
5288.70 (END CORE 4)																			
5288.75 (START CORE 5)																			
R-1 SUPERIOR	STY		5289.825	5289.825	OW	OW	185	1			PYR	51				9			COMP. STY
R-1 SUPERIOR	FRACT		5289.05	5289.07	INT	STY	105	1	1	PART. OPEN	CALC	41							STA FRACT.
R-1 SUPERIOR	FRACT		5289.18	5289.19	INT	STY	56	1	1	PART. OPEN	CALC	42							STA FRACT.
R-1 SUPERIOR	STY		5294.27	5294.27	OW	OW	224	2			CALC	59				125			VERY LARGE STY FILLED WITH CALC.
R-1 SUPERIOR	FRACT		4295.45	4295.45	OW	OW	273	0.5	1	PART. OPEN	CALC	68							STA FRACT.
R-1 SUPERIOR	FRACT		4295.47	4295.47	OW	OW	275	0.5	1	PART. OPEN	CALC	68							STA FRACT.
R-1 SUPERIOR	STY		4295.59	4295.59	OW	OW	129	0.5				34				15			COMP. STY
RUBBLE 5298.00 5303.44																			
R-1 SUPERIOR	STY		5305.55	5305.55	OW	OW	149	0.5				42				47			COMP. STY
RUBBLE 5306.00 5307.50																			
5307.50 (END CORE 5)																			
5307.50 (START CORE 6)																			
R-1 SUPERIOR	STY		5307.94	5307.94	OW	OW	128	0.5				33				29			COMP. STY
5318.00 (END CORE 6)																			
5318.15 (START CORE 7)																			
R-1 SUPERIOR	STY		5324.81	5324.81	OW	OW	177	1				48				15			COMP. STY
R-1 SUPERIOR	STY		5327.35	5327.35	OW	OW	118	0.5				24				39			COMP. STY
R-1 SUPERIOR	STY		5327.43	5327.43	OW	OW	112	0.5				29				27			COMP. STY
5331.98 (END CORE 7)																			
5331.98 (START CORE 8)																			
R-1 SUPERIOR/INFERIOR	STY		5334.71	5334.71	OW	OW	187	0.5				54				8			COMP. STY
R-1 SUPERIOR/INFERIOR	STY	5334.72			OW	OW	145	0.5				90				15			TECT. STY.
R-1 SUPERIOR/INFERIOR	STY		5342.33	5342.33	OW	OW	163	0.5				44				8			COMP. STY
R-1 SUPERIOR/INFERIOR	STY		5346.05	5346.05	OW	OW	190	2				54				4			COMP. STY
IZ 5351.53-5354.94																			
R-1 SUPERIOR/INFERIOR	STY		5355.14	5355.14	OW	OW	189	1				55				6			COMP. STY
R-1 SUPERIOR/INFERIOR	STY		5358.97	5358.97	OW	OW	129	3				46				31			COMP. STY
5359.80 (END CORE 8)																			
5359.80 (START CORE 9)																			
IZ 5363.31 5363.51																			ZONE OF INTENSE FRACT. CALC FILLED FRACTS. SMALL FAULT ZONE
R-1 INFERIOR	STY		5363.71	5363.71	OW	OW	210	0.5				58							
5397.56 (END CORE 9)																			
5397.56 (START CORE 10)																			
R-1 INFERIOR	STY		5394.86	5394.86	OW	OW	149	1				44				89			COMP. STY
R-1 INFERIOR	STY		5398.42	5398.42	OW	OW	133	1				34				13			COMP. STY

Miskar A-11 Raw Data

R 1 INFERIOR	FRACT	5,399.4	5398.87	5398.87	OW	OW	117	1	17	CLOSED	CALC	21			22			CALC FILLED FRACT	
R 1 INFERIOR	STY				OW	BASE	570	2				88						TECT STY	
5,400.10 (END CORE 10)																			

Appendix B

Hasdrubal: Raw Core Data

Hasdrubal-2 Raw Data

Well/Core	Depth	Fracture No.	Fracture Type	Open/Closed	Fill	Term (Upper)	Term (Lower)	Dip	Strike	Length	Width	Displacement	Slick-Orient	Stylolite Height	Stylolite Fill	Comments
H2 / Core # 1																
	2420.13	1				CW	CW	0						8.63	0.24	
IZ 2420.38 - 2420.44																Intensely styolitised zone
	2420.59	2	1	PRED. OPEN	CALC	I	STY	90		57	0.2					Could be induced
	2420.59	3	1	PRED. OPEN	CALC	I	STY	90		61	0.2					*Could be induced*
	2420.59	4	1	PRED. OPEN	CALC	I	STY	90		60	0.2					
IZ 2420.62 - 2420.66																4-5 styolites - all with low amplitude
	2420.85	5				CW	CW	0						12.00	0.26	
	2421.06	6				CW	CW	0						14.13	0.30	
	2422.37	7				CW	CW	0						5.44	0.20	
	2422.38	8				CW	CW	0						11.28	0.21	
	2422.47	9				CW	CW	0						3.53	0.19	
	2422.48	10	1	PRED. OPEN	CALC	STY	I	90		7	0.3					
	2422.48	11	1	PRED. OPEN	CALC	STY	I	90		6	0.3					
	2422.78	12	1	PRED. OPEN	CALC	I	STY	85		147	0.3					
	2422.85	13	1	PRED. OPEN	CALC	I	STY	85		24	0.2					
	2422.85	14	1	PRED. OPEN	CALC	I	STY	85		15	0.2					
	2422.86	15				CW	CW	0						9.32	0.23	
	2422.87	16	1	PRED. OPEN	CALC	STY	I	90		16	0.3					
	2422.87	17	1	PRED. OPEN	CALC	STY	I	90		11	0.3					
	2422.93	18	1	PRED. OPEN	CALC	I	STY	90		9	0.2					
	2422.94	19				CW	CW	0						8.39	0.43	
	2422.98	20	1	O		STY	I	88		61	0.2					
	2423.06	21				CW	CW	0						7.12	0.34	
IZ 2425.54 - 2425.72																Intensely styolitised zone
H2 / Core # 2	2914.20															
IZ 2914.20 - 2914.42																Rubble
	2914.42	22				CW	CW	0						29.52	0.21	
	2915.24	23	1	O		I	IF	88		50	0.2					*Could be induced*
IZ 2915.26 - 2916.00																Rubble
IZ 2916.00 - 2917.00																Intensely styolitised zones - 200mm spacing between zone
	2917.04	24				CW	CW	0						5.12	0.27	
	2917.05	25	1	PRED. OPEN	CALC	STY	I	90		15	0.2					
	2917.08	26	1	PRED. OPEN	CALC	STY	I	90		36	0.2					
	2917.08	27	1	PRED. OPEN	CALC	STY	I	90		9	0.2					
	2917.47	28	1	PO	CALC	I	I	85		150	0.3					
	2917.53	29	1	PO	CALC	I	CB	85		>155	0.3					
	2917.59	30	1	PO	CALC	I	CB	85		>76	0.3					
IZ 2918.00 - 2919.00																Rubble. Possibly two small extensional fractures at *bottom of zone*
IZ 2919.00 - 2920.00																Rubble. Large extensional fracture - 2920.77. Calcite cement ~ 200mm
	2921.10	31	1	PO	CALC	I	STY	85		26	0.3					Calcite within fracture in close proximity to styolite
	2921.11	32				CW	CW	0						8.21	0.21	
	2921.14	33	1	PO	CALC	STY	CW	85		86	0.3					
	2921.15	34	1	PO	CALC	STY	I	85		41	0.3					
IZ 2921.18 - 2922.00																*Rubble*
	2922.09	35	1	PO	CALC	CT	?	85		>>120	0.3					
	2922.33	36				CW	CW	0						4.78	0.15	
	2922.66	37				CW	CW	0						6.27	0.22	
IZ 2922.70 - 2923.30																Rubble
H2 / Core #3																
IZ 2923.70 - 2925.00																Rubble
	2925.28	38	1	C	CALC	I	I	80		31	0.2					
	2927.13	39				CW	CW	0						32.98	0.89	
	2928.24	40				CW	CW	0						8.13	0.41	
	2928.55	41				CW	CW	0						27.32	2.06	
	2929.25	42	1	O		I	I	88		45	0.2					

Hasdrubal-2 Raw Data

	2930.47	43				CW	CW	0						10.15	0.72	
	2930.51	44				CW	CW	0						53.18	0.68	
	2930.57	45	1	PO	CALC	STY	I	90		99	0.3					
	2931.51	46				CW	CW	0						40.37	0.56	
	2932.02	47	1	O		CT	I	90		33	0.2					
	2932.17	48	1	O		I	CW	90		221	0.2					
	2932.62	49	1	PO	CALC	I	STY	90		26	0.2					
	2932.63	50				CW	CW	0						31.68	0.61	
	2933.19	51	1	O		I	NF	88		24	0.2					
	2933.21	52	1	O		NF	NF	88		22	0.2					
	2933.29	53	1	O		NF	NF	88		124	0.2					
	2933.36	54	1	O		NF	I	88		39	0.2					
	2933.70	55				CW	CW	0						22.52	1.68	
	2935.15	56	1	O		CT	IF	85		>>94	0.2					Could be induced
	2935.16	57	1	O		CT	IF	85		>>106	0.2					Could be induced
	2935.15	58	1	O		CT	I	85		>55	0.2					Could be induced
IZ 2935.27 - 2935.31																Small zone of styolites
IZ 2935.50 - 2935.56																Small zone of styolites
	2935.58	59	1	O		I	NF	90		25	0.2					En echelon fracture set
	2935.62	60	1	O		NF	I	90		62	0.2					En echelon fracture set
	2935.66	61	1	O		I	I	90		31	0.2					En echelon fracture set
	2935.70	62	1	O		NF	I	90		58	0.2					En echelon fracture set
	2936.41	63	1	PO	CALC	CT	STY	90		770	0.3					
	2936.79	64				CW	CW	0						51.86	1.73	
IZ 2938.35		65														Vugs < 20mm in diameter
	2938.79	66				CW	CW	0						23.79	0.55	
	2939.80	67	1	PO	CALC	IF	CB	90		>274	?					Could be induced
	2940.40	68	1	PRED.OPEN	CALC	I	NF	90		24	0.2					
	2940.45	69	1	PRED.OPEN	CALC	NF	I	90		54	0.2					
	2940.51	70	1	PRED.OPEN	CALC	I	I	90		59	0.2					
	2940.57	71	1	PRED.OPEN	CALC	I	I	89		24	0.2					
	2940.63	72				CW	CW							13.77	0.52	
	2940.65	73	1	PO	CALC	STY	I	90		16	0.2					
	2940.65	74	1	PO	CALC	STY	I	90		12	0.2					
	2940.65	75	1	PO	CALC	STY	I	90		9	0.2					
	2940.82	76	1	PO	CALC	I	I	90		27	0.2					
IZ 2941.12 - 2941.18																Intensely styolitised zone
	2941.19	77	1	PO	CALC	STY	I	86		27	0.2					
	2941.22	78	1	PO	CALC	I	I	86		>29	0.2					
H2 / Core #4																
	2942.40	79				CW	CW	0						15.32	0.37	
	2942.41	80	1	PO	CALC	STY	I	90		21	0.2					
	2942.41	81	1	PO	CALC	STY	I	90		26	0.2					
	2942.51	82				CW	CW	0						14.97	0.54	
	2943.58	83				CW	CW	0						29.91	1.00	
	2944.28	84				CW	CW	0						24.63	1.02	
	2946.10	85	1	PRED. OPEN	CALC	I	I	90		22	0.2					
	2946.10	86	1	PRED. OPEN	CALC	I	I	90		17	0.2					
	2946.11	87	1	PRED. OPEN	CALC	I	I	90		36	0.2					
	2946.12	88	1	PRED. OPEN	CALC	I	I	90		12	0.2					
	2946.12	89	1	PRED. OPEN	CALC	I	I	90		8	0.2					
	2946.41	90	1	PO	CALC	I	I	90		470	0.4					En echelon fracture set
	2946.48	91	1	PO	CALC	I	NF	80		159	0.8					En echelon fracture set
	2946.63	92	1	PO	CALC	NF	STY	80		171	0.8					En echelon fracture set
	2946.71	93				CW	CW	0						19.9	0.36	
	2946.69	94	1	PO	CALC	I	STY	90		36	0.4					
IZ 2946.75 - 2947.00																Rubble
	2947.07	95				CW	CW	0						12.47	0.52	
	2947.74	96				CW	CW	0						20.97	0.29	
IZ 2948.00 - 2948.60																Vertical pressure solution seams - sheared?

Hasdrubal-2 Raw Data

	2948.73	97				CW	CW	0						42.94	1.07	
	2949.30	98	1	PO	CALC	CT	I	90		620	0.4					
	2949.19	99	1	PO	CALC	CT	I	90		380	0.4					
	2949.53	100	1	PC	CALC	I	I	90		240	0.4					
	2949.49	101	1	PC	CALC	I	I	90		160	0.3					
	2949.50	102	1	PC	CALC	I	I	90		140	0.3					
IZ 2949.80 - 2951.00																Rubble
	2951.33	103				CW	CW	0						92.00	0.51	
	2951.54	104	1	PC	CALC	STY	?	90		322	0.4					
	2952.40	105				CW	CW	0						28.78	0.38	
	2952.42	106	1	PO	CALC	STY	I	89		32	0.4					
	2952.60	107	1	PO	CALC	STY	I	90		>>160	0.3					
	2953.43	108	1	C	CALC	CW	I	90		>51	0.6					
	2953.50	109	1	C	CALC	I	I	90		22	0.3					Could be vertical solution seams
	2953.54	110	1	C	CALC	I	I	90		16	0.3					Could be vertical solution seams
	2954.35	111	1	PO	CALC	I	I	90		180	?					Could be vertical solution seams
	2954.70	112				CW	CW	0						73.41	0.81	
	2955.53	113	1	PO	CALC	I	STY	88		>140	0.4					
	2955.60	114				CW	CW	0						23.57	1.09	
	2955.77	115	1	PO	CALC	STY	I	90		>270	0.4					
	2955.64	116	1	PO	CALC	STY	I	90		82	0.4					
	2955.63	117	1	PO	CALC	STY	I	90		44	0.3					
	2956.72	118				CW	CW	0						?	?	
	2957.61	119				CW	CW	0						?	?	
	2959.14	120				CW	CW	0						43.88	1.30	
	2959.49	121				CW	CW	0						60.00	0.36	
	2960.84	122	1	PO	CALC	I	NF	85		65	0.4					
	2960.93	123	1	PO	CALC	NF	I	85		>50	0.4					
	2961.21	124				CW	CW	0						101.66	2.77	
	2962.00	125				CW	CW	0						162.13	2.94	
	2962.83	126	1	PO	CALC	I	CW	90		1030	0.8					
	2964.00	127				CW	CW	0						21.15	0.24	
	2964.07	128	1	PO	CALC	I	I	88		45	0.4					
	2964.10	129	1	PO	CALC	I	I	88		24	0.4					
	2964.13	130	1	PO	CALC	CW	I	88		24	0.4					
	2964.37	131	1	PO	CALC	I	NF	88		11	0.4					
	2964.39	132	1	PO	CALC	NF	NF	88		7	0.4					
	2964.38	133	1	PO	CALC	NF	NF	90		7	0.4					
	2964.37	134	1	PO	CALC	I	NF	90		26	0.6					
	2964.39	135	1	PO	CALC	NF	NF	90		13	0.6					
	2964.41	136	1	PO	CALC	NF	I	90		24	0.6					
	2964.46	137	1	PO	CALC	I	I	90		15	0.6					
	2964.45	138	1	PO	CALC	I	I	90		31	0.7					
	2964.91	139	2	PO	CALC	CW	CW	90		>770	1.2	? (Large)	90			Pure strike slip movement. Calcite growth - crystals ~ 7-8mm
	2965.24	140				CW	CW	0						9.60	1.38	
	2965.55	141				CW	CW	0						15.52	1.19	
IZ 2966.47 - 2966.54																Small zone of styolites
	2971.41	142	1	C	CALC	I	I	88		24	1.2					Could just be a shell
	2972.37	143	1	C	CALC	I	I	90		510	0.4					
	2972.22	144	1	C	CALC	I	I	90		230	1.1					
	2972.37	145	1	C	CALC	I	I	85		124	1.1					
	2972.42	146	1	C	CALC	I	I	90		66	0.4					
	2972.72	147	1	C	CALC	I	I	90		136	0.5					
	2972.80	148	1	C	CALC	I	I	90		57	0.4					
	2972.83	149	1	C	CALC	I	I	90		36	0.4					
	2976.21	150	1	PO	CALC	I	I	90		421	2.3					
	2976.70	151	1	PO	CALC	I	CW	90		>165	3.5					En echelon fracture. Lots of vugs present.
IZ 2977.90 - 2978.95																Lots of vugs present throughout section
	2985.70	152				CW	CW	0						23.54	0.93	
IZ 2989.45 - 2989.51																Intensely styolitised zone
IZ 2989.85 - 2989.89																Intensely styolitised zone
IZ 2991.54 - 2991.63																Intensely styolitised zone

Hasdrubal-2 Raw Data

	2991.80	153	1	C	CALC	I	I	90		23	0.3					
	2991.84	154	1	C	CALC	I	I	90		39	0.3					
	2993.05	155				CW	CW	0						1.10	3.67	
	2993.29	156	1	PO	CALC	I	I	90		61	0.4					
	2993.97	157				CW	CW	0						19.00	3.91	
	2994.69	158	1	C	CALC	I	I	90		39	0.3					
	2994.83	159	1	C	CALC	I	I	90		61	0.3					
IZ 2995.00 - 2997.55																Rubble
	2998.10															

Hasdrubal-3 Raw Data

Well/Core	Depth	Fracture No.	Fracture Type	Open/Closed		Fill	Term (Upper)	Term (Lower)	Dip	Strike	Length	Width	Displacement	Slick-Orient	Stylolite Height	Stylolite Fill	Comments
H3 / Core #1	2858																
IZ 2858.00 - 2859.00																	Rubble
H3 / Core #2																	
	2860.00	1	1	PRED. C		CALC	I	I	88		14	0.2					From FMI all these fractures could have a strike of 140
	2860.00	2	1	PRED. C		CALC	I	I	88		7	0.2					From FMI all these fractures could have a strike of 140
	2860.02	3	1	PRED. C		CALC	I	CW	88		45	0.2					From FMI all these fractures could have a strike of 140
	2860.02	4	1	PRED. C		CALC	I	CW	88		29	0.2					From FMI all these fractures could have a strike of 140
	2860.22	5	1	PRED. C		CALC	I	I	90		>40	0.5					From FMI all these fractures could have a strike of 140
	2860.23	6	1	PRED. C		CALC	I	I	90		>40	0.9					From FMI all these fractures could have a strike of 140
	2860.64	7	1	C		CALC	I	I	90		24	0.4					From FMI all these fractures could have a strike of 140
	2860.65	8	1	C		CALC	I	I	90		36	0.4					From FMI all these fractures could have a strike of 140
	2860.77	9	1	C		CALC	I	I	90		120	0.4					From FMI all these fractures could have a strike of 140
	2860.86	10	1	C		CALC	I	NF	90		45	0.5					From FMI all these fractures could have a strike of 140
	2860.85	11	1	C		CALC	I	I	90		18	0.2					From FMI all these fractures could have a strike of 140
	2860.90	12	1	C		CALC	NF	IF	90		76	0.2					From FMI all these fractures could have a strike of 140
	2861.05	13	1	C		CALC	I	IF	90		510	0.6					From FMI all these fractures could have a strike of 140
	2861.95	14	1	C		CALC	CW	NF	90		102	0.3					From FMI all these fractures could have a strike of 140
	2861.92	15	1	C		CALC	NF	I	90		62	0.3					From FMI all these fractures could have a strike of 140
	2862.21	16	1	C		CALC	I	I	90		19	0.2					From FMI all these fractures could have a strike of 140
	2862.22	17	1	C		CALC	I	I	90		66	0.2					From FMI all these fractures could have a strike of 140
	2862.27	18	1	C		CALC	I	IF	90		>29	0.2					From FMI all these fractures could have a strike of 140
	2862.31	19	1	C		CALC	IF	IF	90		>31	0.2					From FMI all these fractures could have a strike of 140
	2863.13	20	1	CO (C)		CALC	CW	CW	90		470	0.6					From FMI all these fractures could have a strike of 140
	2863.18	21	1	C		CALC	I	?	90		150	0.3					From FMI all these fractures could have a strike of 140
	2863.18	22	1	C		CALC	I	?	90		146	0.3					From FMI all these fractures could have a strike of 140
IZ 2863.24																	Core probably wrong way up. Evidence for two intersecting fracture sets
	2864.07	23	1	C		CALC	I	I	80		87	0.3					
	2864.10	24	1	C		CALC	I	I	80		62	0.3					
	2864.14	25	1	C		CALC	I	I	80		103	0.3					
	2864.27	26	1	C		CALC	I	I	90		110	0.3					
	2864.27	27	1	C		CALC	I	I	90		85	0.3					
	2864.62	28	1	C		CALC	I	I	80		11	0.3					Cluster of small extensional fractures
	2864.64	29	1	C		CALC	I	I	85		24	0.2					Cluster of small extensional fractures
	2864.64	30	1	C		CALC	I	I	85		29	0.3					Cluster of small extensional fractures
	2864.65	31	1	C		CALC	I	I	85		16	0.3					Cluster of small extensional fractures
	2864.66	32	1	C		CALC	I	I	85		31	0.3					Cluster of small extensional fractures
	2864.71	33	1	C		CALC	I	I	85		47	0.3					Cluster of small extensional fractures
	2864.72	34	1	C		CALC	I	I	85		22	0.3					Cluster of small extensional fractures
	2864.73	35	1	C		CALC	I	I	85		41	0.3					Cluster of small extensional fractures
	2864.91	36	1	PO		CALC	I	I	88		11	0.3					Cluster of small extensional fractures
	2864.92	37	1	PO		CALC	I	NF	88		13	0.3					
	2864.93	38	1	PO		CALC	NF	IF	88		>60	0.4					
	2865.48	39	1	C		CALC	CW	IF	85		>82	0.2					
	2865.50	40	1	C		CALC	I	I	85		62	0.2					
	2865.57	41	1	C		CALC	I	I	88		66	0.2					
	2865.83	42	1	C		CALC	I	I	88		67	0.2					
	2867.75	43	1	CO (PO)		CALC	I	CW	90		3021	0.7					
	2866.97	44	1	C		CALC	NF	I	90		93	0.4					Average spacing ~ 200mm
	2867.41	45	1	C		CALC	I	IF	90		88	0.3					Average spacing ~ 200mm
	2867.71	46	1	CO (PO)		CALC	I	I	88		621	0.4					Average spacing ~ 200mm
	2868.33	47	1	C		CALC	I	NF	85		34	0.2					
	2868.34	48	1	C		CALC	NF	I	85		26	0.2					
	2868.37	49	1	C		CALC	NF	I	85		46	0.2					
	2869.26	50	1	O			I	I	89		93	0.2					
	2869.27	51	1	O	PO?		I	NF	87		32	0.2					En echelon set - similar in character, but different spatially to Fr.28-Fr.36
	2869.29	52	1	O	PO?		NF	I	87		33	0.2					En echelon set - similar in character, but different spatially to Fr.28-Fr.36
	2869.79	53	1	O			I	I	88		52	0.3					En echelon set - similar in character, but different spatially to Fr.28-Fr.36
	2869.89	54	1	O	PO?		I	NF	90		39	0.2					En echelon set - similar in character, but different spatially to Fr.28-Fr.36
	2869.91	55	1	O	PO?		I	NF	90		19	0.3					En echelon set - similar in character, but different spatially to Fr.28-Fr.36
	2869.92	56	1	O	PO?		NF	I	90		14	0.3					En echelon set - similar in character, but different spatially to Fr.28-Fr.36
	2869.93	57	1	O	PO?		I	I	90		10	0.3					En echelon set - similar in character, but different spatially to Fr.28-Fr.36
	2869.94	58	1	O	PO?		I	I	90		10	0.2					En echelon set - similar in character, but different spatially to Fr.28-Fr.36
	2869.91	59	1	O	PO?		I	I	90		39	0.2					
	2870.01	60	1	O			I	STY	85		125	0.3					
	2870.01	61	1	O			I	STY	88		98	0.2					
	2870.07	62					CW	CW	0						21.07	0.86	
	2870.16	63	1	O			I	I	87		87	0.2					
	2870.21	64	1	O			I	I	90		37	0.2					
	2870.22	65	1	O			I	I	90		28	0.3					
	2870.60	66	1	O			I	NF	90		143	0.3					En echelon fracture set
	2870.65	67					NF	I	90		49	0.3					En echelon fracture set

Hasdrubal-3 Raw Data

	2870.65	68	1	O			I	NF	90		31	0.3					En echelon fracture set
	2870.66	69	1	O			NF	I	90		16	0.3					En echelon fracture set
	2870.68	70	1	O			NF	I	90		14	0.3					En echelon fracture set
	2870.68	71	1	O			I	NF	90		38	0.3					En echelon fracture set
	2870.70	72	1	O			NF	I	90		24	0.2					En echelon fracture set
	2870.85	73					CW	CW	0					36.23	0.90		
	2871.28	74					CW	CW	0					50.79	1.51		
	2871.78	75					CW	CW	0					11.76	0.32		
	2871.97	76	1	PRED. OPEN		CALC	I	STY	86		321	0.3					Calcite within fracture in close proximity to stylolite. Open further away
	2871.95	77	1	O			I	NF	90		22	0.2					
	2871.97	78	1	O			NF	I	90		16	0.2					
	2872.08	79	1	O			I	I	90		109	0.2					
	2872.15	80					CW	CW	0					20.47	0.47		
	2872.18	81	1	O			STY	CW	88		91	0.2					
	2872.61	82	1	PRED. OPEN		CALC	CT	STY	90		>219	0.4					
	2872.58	83	1	PRED. OPEN		CALC	I	I	90		26	0.2					
	2872.68	84	1	PRED. OPEN		CALC	I	I	90		26	0.3					
	2872.70	85	1	PRED. OPEN		CALC	I	STY	90		57	0.3					
	2872.75	86					CW	CW	0					36.65	0.38		
	2872.84	87	1	PRED. OPEN		CALC	I	I	90		30	0.2					
	2872.86	88	1	PRED. OPEN		CALC	I	NF	90		6	0.2					
	2872.87	89	1	PRED. OPEN		CALC	NF	I	90		15	0.2					
	2872.88	90	1	PRED. OPEN		CALC	I	I	90		14	0.2					
	2872.89	91	1	PRED. OPEN		CALC	I	NF	90		26	0.2					
	2872.91	92	1	PRED. OPEN		CALC	NF	I	90		5	0.2					
	2873.13	93	1	O			I	I	90		54	0.2					
	2873.17	94	1	O			I	CW	80		104	0.3					Series of small en echelon fractures
	2873.26	95	1	PRED. OPEN		CALC	I	I	90		131	0.3					Series of small en echelon fractures
	2873.22	96	1	O	PO?		I	NF	90		25	0.3					Series of small en echelon fractures
	2873.23	97	1	O	PO?		NF	I	90		10	0.3					Series of small en echelon fractures
	2873.23	98	1	O	PO?		I	I	90		20	0.3					Series of small en echelon fractures
	2873.28	99	1	O	PO?		I	NF	90		24	0.3					Series of small en echelon fractures
	2873.30	100	1	O	PO?		NF	I	90		16	0.3					Series of small en echelon fractures
	2873.28	101	1	O	PO?		I	I	90		13	0.3					Series of small en echelon fractures
	2873.29	102	1	O	PO?		I	NF	90		8	0.3					Series of small en echelon fractures
	2873.28	103	1	O	PO?		NF	I	90		16	0.3					Series of small en echelon fractures
	2873.28	104	1	O	PO?		I	NF	90		15	0.3					Series of small en echelon fractures
	2873.29	105	1	O	PO?		NF	I	90		13	0.3					Series of small en echelon fractures
	2873.31	106	1	O	PO?		NF	I	90		15	0.3					Series of small en echelon fractures
	2873.43	107	1	O	PO?		I	I	88		54	0.3					
	2873.46	108	1	O	PO?		NF	I	88		20	0.3					
	2873.45	109	1	O	PO?		I	NF	88		24	0.3					
	2873.46	110	1	O	PO?		NF	I	88		16	0.3					
	2873.59	111	1	O	PO?		CT	NF	90		151	0.3					
	2873.66	112	1	O	PO?		NF	I	90		52	0.2					
	2873.61	113	1	O	PO?		I	I	90		67	0.2					
	2873.60	114	1	O	PO?		CT	CW	89		180	0.3					
	2873.62	115	1	O	PO?		I	I	89		53	0.2					
	2873.75	116	1	O	PO?		NF	CW	88		245	0.3					
	2873.63	117	1	O	PO?		I	NF	88		11	0.3					Large cluster of minor fractures
	2873.65	118	1	O	PO?		NF	I	88		31	0.3					Large cluster of minor fractures
	2873.67	119	1	O	PO?		I	NF	90		6	0.3					Large cluster of minor fractures
	2873.68	120	1	O	PO?		NF	I	90		15	0.3					Large cluster of minor fractures
	2873.69	121	1	O	PO?		I	I	90		18	0.3					Large cluster of minor fractures
	2873.71	122	1	O	PO?		I	I	90		13	0.3					Large cluster of minor fractures
	2873.72	123	1	O	PO?		I	I	90		19	0.3					Large cluster of minor fractures
	2873.73	124	1	O	PO?		I	I	90		>21	0.2					Large cluster of minor fractures
	2873.87	125					CW	CW	0					18.32	1.18		
IZ 2874.56																	Intensely stylolitised zone
IZ 2875.30 - 2875.50																	Cluster of v. small en echelon fractures (~40) ~8-10mm in length. Drilling induced
	2875.92	126	1	O			IF	I	90		32	0.2					
	2875.98	127	1	PO		CALC	I	STY	88		17	0.3					
	2876.04	128	1	PO		CALC	I	I	90		42	0.3					
	2876.07	129	1	PO		CALC	I	I	90		25	0.3					
IZ 2876.04 - 2876.10																	Intensely stylolitised zone. Many partially / totally filled vugs
	2876.14	130					CW	CW	0					25.65	1.69		
	2876.15	131	1	PC		CALC	STY	I	90		33	0.2					
	2876.16	132	1	PC		CALC	STY	I	90		61	0.2					
	2876.21	133	1	PC		CALC	I	I	90		70	0.3					
	2876.25	134	1	PC		CALC	CW	CW	90		104	0.2					
	2876.72	135					CW	CW	0					40.18	0.64		
	2876.77	136	1	O			STY	NF	89		47	0.3					
	2876.79	137	1	O			I	I	88		5	0.2					

Hasdrubal-3 Raw Data

	2876.83	138	1	O			NF	I	88		80	0.3					
	2876.87	139	1	O			I	I	90		46	0.3					
	2876.89	140	1	O			I	PS	88		>50	0.4					
PS 2876.89 - 2877.10																	Obviously something interesting - seems to intersect a calcite filled fracture set.
	2877.10	141	1	O			PS	STY	90		>46	0.3					
	2878.30	142					CW	CW	0						66.51	2.64	
IZ 2878.50 - 2880.50																	Highly dolomitised zone - Heavily fractured (Drilling induced?). 2 styolite generations
	2880.51	143					CW	CW	0						42.44	0.61	
	2881.80	144	1	PC		CALC	I	STY	90		1040	0.5					Partially filled - v.small calcite crystals
	2881.28	145	1	PC		CALC	I	W	90		59	0.2					Partially filled - v.small calcite crystals
	2881.63	146	1	PC		CALC	CT	I	90		280	0.3					Partially filled - v.small calcite crystals
	2881.85	147	1	PC		CALC	I	I	90		372	0.3					Partially filled - v.small calcite crystals
	2882.14	148	1	PC		CALC	I	I	90		92	0.3					Partially filled - v.small calcite crystals
	2882.26	149					CW	CW	0						57.43	0.52	
	2882.29	150	1	PC		CALC	STY	NF	90		29	0.3					En echelon fracture set
	2882.28	151	1	PC		CALC	STY	NF	90		26	0.3					En echelon fracture set
	2882.30	152	1	PC		CALC	NF	NF	90		15	0.3					En echelon fracture set
	2882.33	153	1	PC		CALC	NF	I	90		39	0.3					En echelon fracture set
	2882.34	154	1	PC		CALC	I	NF	90		120	0.3					En echelon fracture set
	2882.42	155	1	PC		CALC	NF	I	90		97	0.3					En echelon fracture set
	2882.35	156	1	PC		CALC	I	I	90		23	0.4					En echelon fracture set
	2882.36	157	1	PC		CALC	I	I	90		18	0.3					En echelon fracture set
	2882.43	158	1	PC		CALC	I	I	90		244	0.3					En echelon fracture set
	2882.39	159	1	PC		CALC	STY	I	90		228	0.3					En echelon fracture set
	2882.39	160	1	PC		CALC	STY	CW	90		>245	0.3					En echelon fracture set
	2882.94	161					CW	CW	0						49.10	0.95	
	2884.82	162					CW	CW	0						44.45	0.55	
	2885.31	163	1	O			I	I	90		20	0.4					
	2885.31	164	1	O			I	NF	90		31	0.3					
	2885.35	165	1	O			NF	STY	90		95	0.3					
	2885.34	166	1	O			I	STY	90		110	0.4					
	2885.36	167	1	O			I	NF	90		56	0.4					
	2885.38	168	1	O			CW	STY	90		>70	0.4					
	2885.39	169	1	O			I	STY	90		52	0.4					
	2885.40	170					CW	CW	0						21.77	0.75	
IZ 2885.75 - 2887.3																	Highly dolomitised. Core / Handling induced fracture ~400mm. No calcite
H3 / Core #3																	
	2887.94	171	1	O			I	NF	88		17	0.8					
	2887.96	172	1	O			NF	I	88		24	0.9					
	2888.30	173					CW	CW	0						31.81	0.60	
	2888.62	174					CW	CW	0						38.10	1.23	
	2888.71	175	1	PO		CALC	STY	I	87		159	0.4					
	2888.74	176	1	PO		CALC	STY	I	88		194	0.4					
	2890.28	177					CW	CW	0						7.40	1.10	
	2890.30	178	1	PO		CALC	STY	I	90		76	0.4					
	2890.34	179	1	PO		CALC	STY	I	90		110	0.4					
	2890.30	180	1	PO		CALC	STY	I	90		22	0.4					
	2891.65	181	1	PRED.OPEN		CALC	I	I	90		29	0.3					Probably Induced
	2891.66	182	1	PRED.OPEN		CALC	I	I	90		21	0.3					Probably Induced
	2891.67	183	1	PRED.OPEN		CALC	I	I	90		19	0.3					Probably Induced
	2892.27	184	1	PO		CALC	CW	I	90		>86	0.3					
	2892.36	185	1	PO		CALC	I	STY	90		75	0.3					
	2892.40	186					CW	CW	0						42.70	0.59	
	2892.69	187	1	PRED.OPEN		CALC	STY	I	90		539	1					
	2892.70	188	1	PRED.OPEN		CALC	I	I	90		509	0.7					
	2893.36	189	1	PO		CALC	I	NF	90		24	0.3					En echelon fracture set
	2893.37	190	1	PO		CALC	NF	NF	90		8	0.3					En echelon fracture set
	2893.38	191	1	PO		CALC	NF	I	90		8	0.3					En echelon fracture set
	2893.38	192	1	PO		CALC	I	NF	90		4	0.3					En echelon fracture set
	2893.39	193	1	PO		CALC	NF	NF	90		4	0.3					En echelon fracture set
	2893.39	194	1	PO		CALC	NF	NF	90		3	0.3					En echelon fracture set
	2893.39	195	1	PO		CALC	NF	NF	90		5	0.3					En echelon fracture set
	2893.41	196	1	PO		CALC	I	I	90		46	0.3					
	2893.45	197	1	PO		CALC	I	NF	86		39	0.3					
	2893.62	198	1	PO		CALC	NF	STY	86		324	0.6					
	2893.80	199					CW	CW	0						?	?	
	2893.85	200	1	O			I	I	89		31	0.3					
	2894.40	201					CW	CW	0						31.10	0.80	
	2894.42	202	1	PO		CALC	STY	I	88		49	0.3					
	2895.32	203					CW	CW	0						36.10	1.10	
	2896.39	204					CW	CW	0						39.30	0.80	
	2897.09	205	1	PRED.OPEN		CALC	I	STY	90		770	0.9					

Hasdrubal-3 Raw Data

	2897.30	206	1	PRED.OPEN	CALC	I	STY	90	331	0.9						
	2897.29	207	1	PRED.OPEN	CALC	I	I	90	344	0.9						
	2897.45	208				CW	CW	0					55.05	0.30		
	2897.64	209	1	O		STY	I	90	409	0.8						
	2898.08	210	3	C	CALC	CW	CW	45	170	0.6						
IZ 2898.35 - 2898.45																Zone of v. small en echelon micro-fractures ~20mm in length. Possibly induced.
	2900.23	211				CW	CW	0					80.30	2.38		
	2900.50	212	1	PRED.OPEN	CALC	STY	I	90	562	0.4						Possibly induced
	2900.79	213	1	PRED.OPEN	CALC	I	I	90	31	0.2						Possibly induced
	2900.91	214				CW	CW	0					50.92	0.69		
	2900.95	215	1	PRED.OPEN	CALC	STY	NF	90	79	0.4						
	2900.96	216	1	PRED.OPEN	CALC	I	I	90	27	0.4						
	2901.03	217	1	PRED.OPEN	CALC	NF	I	90	93	0.4						
	2901.61	218				CW	CW	0					35.67	0.57		
	2901.65	219	1	PRED.OPEN	CALC	STY	I	88	44	0.2						
PS 2901.72 - 2901.95																
	2901.96	220	1	O		I	I	90	>38	0.2						En echelon fracture set
	2902.00	221	1	O		I	I	90	47	0.2						En echelon fracture set
	2902.01	222	1	O		I	I	90	62	0.2						En echelon fracture set
	2902.03	223	1	O		I	I	90	70	0.2						En echelon fracture set
	2902.06	224	1	O		I	I	90	39	0.2						En echelon fracture set
	2902.10	225	1	O		I	I	90	53	0.2						
	2902.19	226	1	O		I	I	88	194	0.2						
	2902.30	227				CW	CW	0					43.53	1.46		
	2902.49	228	1	O		IF	CW	80	36	0.2						Possibly induced
	2902.50	229	1	O		I	I	80	294	0.2						Possibly induced
	2902.92	230	1	PO	CALC	I	STY	89	249	0.3						
	2903.03	231				CW	CW	0					11.21	1.11		
	2903.05	232	3	PO	CALC	STY	NF	80	65	0.4						
	2903.09	233	1	PO	CALC	NF	NF	80	22	0.4						
	2903.11	234	1	PO	CALC	NF	CW	80	20	0.4						
	2903.07	235	1	PO	CALC	STY	I	80	120	0.4						
	2903.08	236	1	PO	CALC	STY	I	80	131	0.4						
	2903.12	237	1	PO	CALC	STY	I	80	184	0.4						
	2903.21	238	1	PO	CALC	CW	CW	80	207	0.4						
	2903.23	239	1	PO	CALC	CW	CW	75	166	0.4						
	2903.62	240	1	O		I	I	90	9	0.2						
	2903.65	241	1	O		I	I	90	27	0.2						
	2904.00	242	1	PO	CALC	CW	STY	90	348	0.4						
	2904.07	243	1	PO	CALC	I	NF	90	33	0.3						
	2904.09	244	1	PO	CALC	I	NF	90	23	0.3						
	2904.12	245	1	PO	CALC	I	STY	90	25	0.3						
	2904.13	246				CW	CW	0					74.99	2.10		
	2904.17	247	1	PO	CALC	I	I	90	66	0.3						
	2904.20	248	1	PO	CALC	STY	I	90	115	0.3						
	2906.04	249				CW	CW						97.06	2.17		
	2906.69	250	1	O		I	STY	90	54	0.2						
	2906.73	251											63.53	1.51		
	2907.43	252	1	O		CT	I	90	>155	0.2						
	2907.51	253	1	O		I	I	90	46	0.2						
	2907.58	254				CW	CW						47.99	1.12		
	2907.61	255	1	PO	CALC	STY	I	89	53	0.4						En echelon fracture set
	2907.96	256	1	O		I	I	90	8	0.2						En echelon fracture set
	2907.97	257	1	O		I	NF	90	13	0.2						En echelon fracture set
	2907.98	258	1	O		NF	I	90	3	0.2						En echelon fracture set
	2907.98	259	1	O		I	I	90	2	0.2						En echelon fracture set
	2907.99	260	1	O		I	I	90	15	0.2						En echelon fracture set
	2908.02	261	1	O		I	I	90	52	0.2						En echelon fracture set
	2908.06	262	1	O		I	I	90	35	0.2						En echelon fracture set
	2908.08	263	1	O		I	NF	90	40	0.2						En echelon fracture set
	2908.11	264	1	O		I	NF	90	25	0.2						En echelon fracture set
	2908.14	265	1	O		NF	I	90	25	0.2						En echelon fracture set
	2908.25	266				CW	CW	0					29.41	0.45		
	2909.42	267				CW	CW	0					12.72	0.30		
	2909.43	268				CW	CW	0					10.01	1.10		
	2909.58	269	1	O		I	I	90	18	0.2						
	2909.60	270	1	O		I	I	90	14	0.2						
	2909.65	271	1	PRED.OPEN	CALC	I	I	90	28	0.4						
	2909.70	272	1	PRED.OPEN	CALC	I	I	90	64	0.4						
	2909.74	273	1	PRED.OPEN	CALC	I	I	90	5	0.4						
	2910.55	274	1	PO	CALC	CT	I	90	510	0.4						En echelon fracture set
	2910.64	275	1	PO	CALC	I	I	90	105	0.4						En echelon fracture set
	2910.75	276	1	PO	CALC	I	I	90	94	0.4						En echelon fracture set

Hasdrubal-3 Raw Data

	2910.96	277	1	PO		CALC	I	CW	90		613	0.4					En echelon fracture set
H3 / Core #4																	
	2915.03	278	1	C		CALC	I	I	?		15	0.4					
	2915.03	279	1	C		CALC	I	I	?		22	0.4					
	2918.02	280	1	C		CALC	I	I	?		23	1					
	2919.83	281													4.40	0.45	
	2920.42	282	1	O			I	I	?		19	0.2					
	2920.44	283	1	O			I	I	?		30	0.2					
IZ 2920.50 - 2920.65																	Intensely styolitised zone
	2921.03	284	1	O			I	NF	90		29	0.2					Possibly induced
	2921.09	285	1	O			NF	NF	90		125	0.2					Possibly induced
	2921.16	286	1	O			NF	I	90		24	0.2					Possibly induced
	2921.26	287	1	O			I	I	90		80	0.2					Possibly induced
	2925.93	288	1	O			I	I	90		79	0.2					
	2926.59	289	1	PC		CALC	I	I	80		210	0.2					
	2926.55	290	1	PC		CALC	I	I	88		25	0.2					
	2926.58	291	1	PC		CALC	I	I	88		44	0.2					
	2928.39	292	1	PC		CALC	I	I	90		22	0.3					
	2928.43	293	1	PC		CALC	I	I	90		8	0.3					
	2928.44	294	1	PC		CALC	I	NF	90		11	0.3					
	2928.49	295	1	PC		CALC	NF	I	90		49	0.3					
IZ 2928.60 - 2928.71																	Zone of v. small en echelon micro-fractures (?) - 15-40mm in length - open
	2928.84	296	1	O			CW	CW	88		251	0.2					
	2928.91	297	1	O			I	I	88		52	0.2					
	2928.91	298	1	O			I	I	88		21	0.2					
	2928.92	299	1	O			I	I	88		>11	0.2					
	2929.02	300	1	O			I	I	89		>56	0.2					
	2929.02	301	1	O			I	I	90		>30	0.2					
	2929.05	302	1	O			I	I	90		32	0.2					
	2929.09	303	1	PO			CW	I	86		65	0.4					
	2929.14	304	1	PO			I	I	88		74	0.4					
	2929.20	305					CW	CW	0						28.39	1.79	
	2929.87	306	1	PO			I	NF	90		24	0.2					
	2929.90	307	1	PO			NF	I	90		18	0.2					
	2930.15	308	1	PO			I	NF	90		20	0.2					
	2930.16	309	1	PO			NF	I	90		18	0.2					
	2930.21	310	1	PO			I	I	90		78	0.2					
	2930.30	311					CW	CW	0						34.41	2.69	
	2930.59	312	1	O			I	NF	90		54	0.2					
	2930.66	313	1	O			NF	I	90		83	0.2					
	2930.71	314	1	O			I	I	90		24	0.2					
	2930.71	315	1	O			I	I	90		20	0.2					
	2930.92	316					CW	CW	0						26.64	1.98	
	2932.95	317	1	C			CW	I	90		526	0.6					
	2933.12	318	1	C			I	I	90		66	0.6					
	2933.51	319	1	C			I	I	90		661	0.6					
	2933.46	320	1	C			I	I	90		140	0.6					
	2933.63	321	1	C			I	I	90		179	0.6					
	2933.85	322	1	C			I	I	90		41	0.4					
	2933.83	323	1	C			I	I	90		44	0.4					
	2933.86	324	1	C			NF	I	90		43	0.4					
	2933.87	325	1	C			I	I	90		19	0.4					
	2935.76	326					CW	CW	0						14.70	4.19	
	2937.34	327					CW	CW	0						7.98	1.07	
	2938.86	328					CW	CW	0						8.70	6.07	
	2941																

Hasdrubal-4 Raw Data

Well/Core	Depth	Fracture No.	Fracture Type	Open/Closed	Fill	Term (Upper)	Term (Lower)	Dip	Strike	Length	Width	Displacement	Slick-Orient	Styolite Height	Styolite Fill	Comments
H4/Core #1	2966															
	2966.83	1	1	PO	CALC	CW	CW	90	157	760	1.5					
	2967.82	2	1	PO	CALC	CW	CW	90	20	550	1.5					
	2967.90	3	1	PO	CALC	CW	CW	90	21	460	1.5					
	2968.60	4	1	PO	CALC	CW	CW	90	19	39	1.5					
	2968.83	5	1	C	CALC	?	I	86	161	78	0.5					
	2968.86	6	1	C	CALC	I	I	88	162	16	0.6					
	2968.96	7	1	PO	CALC	I	IF	90	178	110	0.6					
	2969.08	8	1	C	CALC	CW	I	90	176	6	0.6					En echelon fracture set
	2969.10	9	1	C	CALC	I	I	90	176	13	0.6					En echelon fracture set
	2969.11	10	1	C	CALC	I	I	90	177	24	0.6					En echelon fracture set
	2969.12	11	1	C	CALC	I	IF	90	176	10	0.6					En echelon fracture set
	2969.12	12	1	C	CALC	I	IF	90	178	13	0.6					
	2969.38	13	1	C	CALC	I	I	90	131	28	0.6					
	2969.39	14	1	C	CALC	I	IF	90	134	35	0.6					
	2969.82	15	1	C	CALC	I	I	90	130	9	0.6					
	2969.82	16	1	C	CALC	I	I	90	128	15	0.6					
	2969.82	17	1	C	CALC	I	I	90	131	19	0.6					
	2969.97	18	1	PO	CALC	I	I	90	166	110	0.8					Two intersecting fracture sets
	2969.98	19	1	O		CW	CW	85	72	?	0.1					Two intersecting fracture sets (This one has no infill)
	2970.65	20	1	C	CALC	IF	IF	85	118	>25	0.9					
	2971.62	21	1	C	CALC	I	I	90	55	80	0.2					
	2971.63	22	1	C	CALC	I	I	80	53	65	0.2					
	2971.64	23	1	C	CALC	I	I	90	58	56	0.2					
	2971.65	24	1	C	CALC	I	I	80	56	44	0.2					
	2971.70	25	1	C	CALC	CW	I	80	57	64	0.2					
	2971.70	26	1	C	CALC	IF	IF	80	55	55	0.2					
	2971.77	27	1	C	CALC	I	I	90	55	60	0.2					
H4 Core #2	2972.46	28	1	C	CALC	I	I	90	62	70	0.4					
	2972.45	29	1	C	CALC	I	I	90	63	65	0.4					
	2972.48	30	1	C	CALC	I	I	90	65	22	0.4					
	2972.52	31	1	C	CALC	IF	IF	90	63	95	0.4					
	2972.52	32	1	C	CALC	IF	CW	90	61	130	0.4					
	2972.50	33	1	C	CALC	IF	IF	90	62	140	0.4					
	2972.55	34	1	C	CALC	IF	IF	90	128	>44	0.6					
	2972.59	35	1	C	CALC	IF	IF	90	130	>80	0.6					
	2972.59	36	3	C	CALC	IF	IF	90	128	>400	1.1					Two more fractures present (do not intersect slabbed face) ~ spacing 15mm - oblique fibre growth
	2972.78	37	1	C	CALC	I	IF	90	159	>25	0.4					
	2973.13	38	1	C	CALC	CW	I	90	80	70	0.2					
	2973.21	39	1	C	CALC	I	I	90	85	35	0.2					
	2973.26	40	1	C	CALC	I	I	90	84	45	0.1					
	2973.53	41	1	C	CALC	I	IF	85	160	>48	0.5					
	2973.54	42	1	C	CALC	I	I	85	158	14	0.4					
	2973.54	43	1	C	CALC	I	I	85	161	16	0.4					
	2973.54	44	1	C	CALC	I	I	85	160	>10	0.4					
	2973.52	45	1	C	CALC	I	I	85	163	20	0.4					
	2973.58	46	1	C	CALC	I	I	90	151	49	0.4					
	2973.58	47	1	C	CALC	I	I	90	153	70	0.4					
	2973.60	48	1	PO	CALC	I	I	90	151	250	0.2					Two fracture sets - this one later than Fr.49
	2973.61	49	1	C	CALC	I	CW	90	69	90	1.1					Two fracture sets - this one later than Fr.48
	2974.08	50	1	CO (PO)	CALC	CT	I	90	120	>80	1					Large calcite filled fractures ~3-3.5mm wide. Strike 60. Spacing 40-50mm. Vugs also present
IZ 2974.26																
	2974.92	51	1	C	CALC	IF	IF	80	125	60	0.5					
	2975.42	52	1	C	CALC	CW	I	75	129	67	1.0					
	2976.20	53	1	C	CALC	I	I	80	131	60	0.5					
	2976.83	54	1	C	CALC	I	CW	80	121	>71	0.4					
	2977.24	55	1	C	CALC	I	I	88	90	45	0.5					
	2977.25	56	1	C	CALC	I	I	88	90	51	0.5					
	2977.25	57	1	C	CALC	I	CW	88	90	54	0.5					
	2977.41	58	1	C	CALC	I	I	90	128	50	0.6					Series of parallel fractures
	2977.42	59	1	C	CALC	I	NF	90	128	66	0.4					Series of parallel fractures
	2977.41	60	1	C	CALC	I	I	90	100	50	0.2					Possibly a different set (on cross cutting relationships)
	2977.45	61	1	C	CALC	I	NF	90	60	80	1.0					
	2977.46	62	1	C	CALC	I	I	90	62	60	0.6					
	2977.46	63	1	C	CALC	I	I	90	60	35	0.1					
	2977.68	64	1	C	CALC	I	I	90	?	>50	0.2					
	2977.87	65	1	C	CALC	IF	IF	90	80	>40	0.2					
	2978.45	66	1	C	CALC	I	CW	88	65	>65	1.5					
	2978.50	67	1	C	CALC	CW	CW	90	90	>300	2.0					
	2978.53	68	1	C	CALC	I	CW	90	90	>150	3.5					

Hasdrubal-4 Raw Data

	2978.59	69	1	C	CALC	IF	IF	85	50	50	1.3					
	2978.58	70	1	C	CALC	I	I	90	37	25	0.7					
	2978.60	71	1	C	CALC	I	I	90	39	30	0.8					
	2978.71	72				CW	CW	0						3.00	0.20	
	2979.73	73	3	PO	CALC	IF	I	90	95	50	0.9					
	2979.75	74	1	C	CALC	I	I	90	25	60	0.2					
	2979.80	75	1	C	CALC	IF	IF	90	155	>>40	0.8					
	2979.83	76	1	C	CALC	IF	IF	75	160	>>40	0.7					
2980.00 - 2981.00 (Rubble)																
	2981.58	77	1	C	CALC	CW	CW	85	90	>35	0.5					
	2981.58	78	1	PO	CALC	CW	CW	86	90	>80	3.13					Calcite crystals are up to 3mm in length
	2981.95	79	1	C	CALC	CW	?	89	73	>50	0.2					
	2981.95	80	1	C	CALC	I	?	89	75	>51	0.4					
	2982.07	81	1	C	CALC	I	I	?	?	30	0.3					
	2982.70	82	1	PO	CALC	CW	I	90	85	>>70	1.46					One more fracture present (does not intersect slabbed face) - spacing 40mm, 15mm wide
	2982.72	83	1	PO	CALC	I	I	90	178	302	0.2					This fracture intersects Fr.83. Unsure on relationship.
	2983.30	84	1	CO (PO)		I	I	90	80	>200	0.3					
2983.30 - 2984.25 (Oil Core)																
	2984.57	85	2	CO (PO)		I	I	65	108	>500	?					
	2984.04	86	1	PO	CALC	I	CW	90	101	70	1.2					
	2985.05	87	1	PO	CALC	I	I	80	71	39	>1.8					
	2985.06	88	1	PO	CALC	I	I	80	73	21	>1.8					
	2985.03	89	1	PO	CALC	I	I	80	70	17	>1.8					
	2985.07	90	1	PO	CALC	I	I	80	73	32	>1.8					
	2985.04	91	1	PO	CALC	I	I	80	71	>55	>1.8					
	2985.07	92	1	PO	CALC	I	I	80	72	50	>1.8					
	2985.07	93	1	C	CALC	CW	I	90	93	200	0.4					
	2985.08	94	1	C	CALC	I	I	85	71	15	1					
IZ 2985.32 (Abundant Vugs)																Many calcite filled vugs
	2985.33	95	1	C	CALC	I	NF	90	155	72	0.3					En echelon fracture set
	2985.37	96	1	C	CALC	NF	NF	90	154	43	0.3					En echelon fracture set
	2985.39	97	1	C	CALC	NF	NF	90	150	15	0.3					En echelon fracture set
	2985.45	98	1	C	CALC	NF	I	90	155	99	0.3					En echelon fracture set
	2985.26	99	2	PO		CW	I	75	70	>>90	0.2					Good slickensides
	2985.84	100	1	C	CALC	I	I	90	150	24	0.4					
	2986.40	101	1	PC	CALC	CW	I	80	94	35	1.2					
	2986.43	102				CW	CW	0						2.23	0.40	
	2986.51	103	1	PC	CALC	I	CW	80	60	70	0.6					One more fracture present (does not intersect slabbed face) - spacing 50mm
	2986.64	104	1	C	CALC	I	I	90	64	50	0.6					
IZ 2986.71-2986.8 (Styolites)																
	2986.74	105	1	O	O	STY	I	80	?	84	0.5					
	2986.84	106	1	C	CALC	I	STY	90	90	33	0.7					
	2986.86	107				CW	CW	0						1.37	0.60	
	2986.88	108				CW	CW	0						17.55	0.86	
	2986.91	109				CW	CW	0						2.62	0.20	
	2987.14	110	1	PC	CALC	CW	CW	85	140	170	1.27					En echelon fracture set. Spacing ~ 15-20mm
	2987.16	111	1	PC	CALC	CW	I	90	142	11	0.6					
	2987.22	112	1	PC	CALC	I	I	85	145	37	0.6					
	2987.26	113	1	PC	CALC	I	I	85	140	36	0.5					
	2987.30	114	1	PC	CALC	I	I	90	140	26	0.2					
	2987.41	115	1	O		CW	I	90	70	70	0.5					
	2987.57	116	1	PO	CALC	I	I	90	64	130	1					Intersecting fracture sets. Both open
	2987.81	117	1	PO	CALC	IF	I	90	131	64	0.5					Intersecting fracture sets. Both open
	2987.80	118	1	PO	CALC	IF	I	90	132	25	0.4					
	2987.88	119	1	O		I	IF	90	130	70	0.4					
	2988.31	120	1	PO	CALC	I	I	90	70	40	0.5					
	2988.38	121	1	PO	CALC	I	I	90	71	54	?					
	2988.39	122	1	PO	CALC	I	I	90	74	33	?					
	2988.64	123	1	PO	CALC	I	I	90	65	30	0.4					
	2988.82	124				CW	CW	0						6.23	0.43	
	2988.94	125				CW	CW	0						17.26	0.63	
	2989.27	126				CW	CW	0						18.11	0.99	
	2989.37	127				CW	CW	0						28.52	0.52	
	2989.87	128				CW	CW	0						34.15	1.09	
	2990.47	129				CW	CW	0						20.14	0.60	
	2990.50	130	1	PO	CALC	STY	I	90	120	60	0.9					
	2990.50	131	1	PO	CALC	STY	I	90	26	60	0.8					
	2990.51	132	1	PO		STY	I	90	120	40	0.4					
	2990.62	133				CW	CW	0						9.00	0.30	
	2990.63	134	1	C	CALC	STY	NF	90	?	37	0.4					
	2990.67	135	1	C	CALC	NF	I	90	?	36	0.4					
	2990.80	136				CW	CW	0						43.55	0.80	
	2990.05	137	1	PC	CALC	STY	STY	90	24	440	1.3					Spacing - 10mm
	2990.96	138	1	PC	CALC	STY	I	90	23	270	1.1					Spacing - 10mm

Hasdrubal-4 Raw Data

	2990.10	139	1	PC	CALC	STY	I	90	22	165	1.74					Spacing ~10mm
	2990.18	140	1	PC	CALC	I	STY	90	20	135	1.1					Spacing ~10mm
	2991.25	141				CW	CW	0						2.90	0.50	
	2991.48	142	1	PO	CALC	I	I	90	22	165	0.8					
	2991.66	143	1	PO	CALC	I	I	90	25	130	0.7					
	2991.80	144	1	PO	CALC	I	I	90	19	12	0.5					En echelon fracture set - associated with styolite
	2991.81	145	1	PO	CALC	I	NF	88	19	13	0.5					En echelon fracture set - associated with styolite
	2991.86	146	1	PO	CALC	I	NF	88	21	47	0.5					En echelon fracture set - associated with styolite
	2991.90	147	1	PO	CALC	NF	STY	90	19	51	0.5					En echelon fracture set - associated with styolite
	2991.93	148				CW	CW	0						3.90	0.33	
	2991.86	149	1	PO	CALC	I	I	90	21	32	0.4					
	2992.02	150												2.20	0.50	
	2992.18	151	1	PO	CALC	CW	CW	90	20	130	0.57					
	2992.18	152	1	PO	CALC	I	I	90	21	124	0.6					
	2992.26	153	1	PO	CALC	I	I	90	20	81	0.5					
	2992.52	154				CW	CW	0						13.3	0.70	
	2992.55	155	1	PO	CALC	STY	I	90	5	61	0.4					
	2993.49	156				CW	CW	0						32.98	1.75	
	2994.16	157				CW	CW	0						34.00	1.24	
	2994.48	158				CW	CW	0						8.35	0.42	
	2994.77	159				CW	CW	0						9.74	0.48	
	2994.86	160	1	PO	CALC	I	I	85	149	29	0.3					
	2994.89	161	1	PO	CALC	I	CW	85	150	74	0.3					
	2994.94	162	1	PO	CALC	I	I	90	150	65	0.3					
	2994.95	163	1	PO	CALC	I	I	90	149	55	0.3					
	2995.02	164	1	PO	CALC	I	NF	90	151	200	0.8					
	2995.10	165	1	PO	CALC	NF	NF	90	150	160	0.8					
	2995.20	166	1	PO	CALC	NF	NF	90	152	29	0.6					
	2995.22	167	1	PO	CALC	NF	I	90	150	26	0.6					
	2995.13	168	1	PO	CALC	NF	NF	90	155	32	0.7					
	2995.18	169	1	PO	CALC	NF	NF	90	151	124	0.6					
	2995.21	170	1	PO	CALC	NF	NF	90	154	49	0.6					
	2995.25	171	1	PO	CALC	NF	NF	90	150	45	0.6					
	2995.35	172	1	PO	CALC	NF	CW	90	149	158	0.6					
	2995.45	173	1	PO	CALC	I	NF	90	153	23	0.37					En echelon fracture set
	2995.44	174	1	PO		I	I	90	151	9	0.4					En echelon fracture set
	2995.46	175	1	PO	CALC	NF	NF	90	147	17	0.4					En echelon fracture set
	2995.58	176	1	PO	CALC	NF	I	90	150	206	0.5					En echelon fracture set
	2995.53	177	1	PO	CALC	I	NF	90	152	14	0.3					En echelon fracture set
	2995.55	178	1	PO	CALC	NF	NF	90	151	18	0.3					En echelon fracture set
	2995.57	179	1	PO	CALC	NF	NF	90	160	26	0.3					En echelon fracture set
	2995.58	180	1	PO	CALC	NF	NF	90	152	24	0.3					En echelon fracture set
	2995.61	181	1	PO	CALC	NF	NF	90	153	88	0.6					En echelon fracture set
	2995.69	182	1	PO	CALC	NF	STY	90	150	90	0.9					En echelon fracture set
	2995.76	183				CW	CW	0						36.58	1.61	
	2995.88	184	1	PRED.O	CALC	STY	I	85	146	180	?					
	2996.09	185	3	PRED.P	CALC	CW	CW	75	151	170	0.4					
	2996.17	186	3	PRED.Q	CALC	CW	CW	75	148	192	0.4					
	2996.52	187	3	PRED.R	CALC	CW	CW	75	150	130	0.4					
	2997.04	188	1	PRED.S	CALC	I	I	73	139	56	0.2					En echelon fracture set
	2997.08	189	1	PO	CALC	I	I	85	144	39	0.2					En echelon fracture set
	2997.10	190	1	PO	CALC	I	NF	85	148	35	0.2					En echelon fracture set
	2997.13	191	1	PO	CALC	NF	I	85	146	27	0.2					En echelon fracture set
	2997.14	192	1	PO	CALC	I	STY	85	150	33	0.2					En echelon fracture set
	2997.08	193	1	PO	CALC	I	NF	85	150	24	0.2					
	2997.12	194	1	PO	CALC	NF	I	85	150	59	0.2					
	2997.19	195				CW	CW	0						67.77	1.08	
	2997.61	196				CW	CW	0						12.35	0.34	
	2997.67	197	1	PO	CALC	I	I	85	142	23	0.3					En echelon fracture set
	2997.68	198	1	PO	CALC	I	I	85	145	16	0.3					En echelon fracture set
	2997.69	199	1	PO	CALC	I	I	85	144	46	0.3					En echelon fracture set
	2997.71	200	1	PO	CALC	I	NF	85	142	28	0.3					En echelon fracture set
	2997.74	201	1	PO	CALC	NF	I	85	142	32	0.3					En echelon fracture set
	2997.70	202	1	PO	CALC	I	I	85	141	62	0.3					En echelon fracture set
	2997.76	203	3	PO	CALC	CW	STY	65	145	66	0.4					En echelon fracture set
	2997.83	204				CW	CW	0						33.19	4.13	
	2997.91	205	1	PO	CALC	I	CW	90	124	101	0.3					
	2997.91	206	1	PO	CALC	I	NF	90	126	72	0.3					Good zone of open fractures. Average spacing ~40mm
	2997.94	207	1	PO	CALC	I	NF	90	124	65	0.3					Good zone of open fractures. Average spacing ~40mm
	2998.00	208	1	PO	CALC	I	I	90	119	115	0.3					Good zone of open fractures. Average spacing ~40mm
	2997.92	209	1	PO	CALC	I	I	90	117	14	0.2					Good zone of open fractures. Average spacing ~40mm
	2997.94	210	1	PO	CALC	NF	NF	90	120	16	0.4					Good zone of open fractures. Average spacing ~40mm
	2997.99	211	1	PO	CALC	I	CW	90	118	375	0.5					Good zone of open fractures. Average spacing ~40mm
	2998.05	212	1	PO	CALC	NF	I	90	121	76	0.5					

Hasdrubal-4 Raw Data

	2998.09	213	1	PO	CALC	I	CW	85	121	92	0.5					
	2998.22	214	1	PO	CALC	CW	CW	85	121	290	0.5					Different orientation - could be styolite associated
	2998.52	215	1	PO	CALC	?	CW	90	75	>140	>1.16					
	2998.64	216				CW	CW	0						24.83	1.28	
	2998.83	217	1	PO	CALC	STY	CB	90	41	>320	0.3					Two different sets - can see intersection
	2998.84	218	1	PO	CALC	CW	CW	88	118	140	0.5					Two different sets - can see intersection
	2998.94	219	1	PO	CALC	I	CB	88	88	120	0.5					Two different sets - can see intersection
H4/CORE #3	2999.24	220	1	O		CW	I	90		320	0.2					Possibly induced
IZ 2999.09 - 2999.62																
	2999.69	221				CW	CW	0						24.71	0.40	
	3000.15	222				CW	CW	0						16.16	1.23	
	3000.84	223	1	O		I	STY	90		80	0.2					
	3000.82	224	1	O		I	I	90		23	0.3					
	3000.87	225	1	O		I	STY	90		28	0.3					
	3001.33	226						0						39.8	1.86	
	3001.66	227	1	?		I	I	90		220	0.3					Could be a vertical styolite
	3002.31	228	1	O		I	I	85		46	0.3					
	3002.63	229	1	PO	CALC	CW	I	85		99	0.3					
	3002.71	230				CW	CW	0						26.99	1.79	
	3003.05	231				CW	CW	0						9.97	0.70	
	3003.07	232	1	O		STY	I	90		38	0.3					
	3003.12	233	1	O		CW	I	85		84	0.3					
	3003.41	234	1	PO	CALC	CW	STY	80		130	0.5					
	3003.48	235				CW	CW	0						15.34	1.41	
PS 3003.55 - 3003.75																
	3003.77	236	1	PO	CALC	CW	PS	45		64	0.2					Possibly induced
	3003.86	237				CW	CW	0						44.72	0.60	
	3005.21	238	1	O		I	I	90		25	2					
	3005.35	239	1	O		I	I	90		26	2					
	3005.4	240	1	O		I	I	90		19	2					
	3005.4	241	1	O		I	I	90		17	2					
	3006.11	242	1	O		I	STY	80		37	0.3					
	3006.15	243				CW	CW	20						57.04	0.55	
	3006.2	244				CW	CW	20						5.17	0.65	
	3006.2	245	1	PO	CALC	I	STY	90		13	0.2					
	3006.19	246	1	PO	CALC	I	STY	90		28	0.7					
	3006.19	247	1	PO	CALC	STY	STY	90		24	1.7					
	3006.18	248	1	PO	CALC	STY	STY	88		35	0.7					
	3006.64	249	1	O		I	?	85		>350	0.3					En echelon fracture set - open. Highly permeable zone
	3006.73	250	1	O		I	?	86		>80	0.3					En echelon fracture set - open. Highly permeable zone
	3006.74	251	1	O		I	I	90		141	0.2					En echelon fracture set - open. Highly permeable zone
	3006.86	252	1	O		I	I	90		195	0.3					En echelon fracture set - open. Highly permeable zone
	3006.85	253	1	O		NF	NF	90		56	0.1					En echelon fracture set - open. Highly permeable zone
	3006.86	254	1	O		I	I	85		24	0.5					En echelon fracture set - open. Highly permeable zone
	3006.91	255	1	O		NF	NF	85		62	0.6					En echelon fracture set - open. Highly permeable zone
	3006.88	256	1	O		NF	NF	85		19	0.4					En echelon fracture set - open. Highly permeable zone
	3006.95	257	1	O		NF	CW	85		110	0.5					En echelon fracture set - open. Highly permeable zone
	3006.92	258	1	O		I	I	85		26	0.3					En echelon fracture set - open. Highly permeable zone
	3006.96	259	1	O		I	CW	80		62	0.4					En echelon fracture set - open. Highly permeable zone
	3006.98	260	1	O		I	I	90		>150	0.4					En echelon fracture set - open. Highly permeable zone
	3007	261	1	O		I	I	90		>100	1.5					
	3007.04	262	1	O		I	I	90		>70	0.3					
	3007.17	263				CW	CW	0						20.93	0.95	
	3008.15	264	1	PO	CALC	STY	I	90		17	0.6					
	3008.14	265	1	PO	CALC	I	STY	90		7	0.2					
	3008.16	266	1	PO	CALC	I	I	90		9	0.3					
	3008.19	267	1	PO	CALC	I	I	90		60	0.3					
	3008.8	268	1	O		I	I	80		13	0.2					
	3009.2	269				CW	CW	0						75.63	1.12	
	3009.72	270	1	O		I	I	88		124	0.2					
	3009.84	271	1	O		I	I	88		34	0.2					
	3009.89	272	1	O		I	CW	85		52	0.3					
	3009.92	273	1	O		I	I	85		12	0.3					
	3009.93	274	1	O		I	I	85		13	0.3					
	3009.98	275	1	O		I	I	85		74	0.3					
	3010.03	276	1	O		I	I	90		25	0.1					
	3010.05	277	1	PO	CALC	NF	I	90		17	0.2					
	3010.1	278	1	PO	CALC	I	NF	90		98	1					
	3010.18	279	1	PO	CALC	NF	STY	90		124	0.9					
	3010.25	280				CW	CW	0						35.90	1.15	
	3010.29	281	1	C	CALC / SADDLE DOL	STY	CW	85		73	0.3					
	3010.43	282	3	PO	CALC / SADDLE DOL	?	I	90		>51	0.5					J. Hendry - possibly saddle dolomite

Hasdrubal-4 Raw Data

	3010.44	283	1	PO	CALC / SADDLE DOL	I	I	90		38	0.4					En echelon set - all v. well connected
	3010.5	284	1	PO	CALC / SADDLE DOL	I	I	90		27	0.1					En echelon set - all v. well connected
	3010.57	285	1	PO	CALC / SADDLE DOL	I	NF	90		37	0.2					En echelon set - all v. well connected
	3010.66	286	1	PO	CALC / SADDLE DOL	NF	I	90		137	0.4					En echelon set - all v. well connected
	3010.75	287	1	PO	CALC / SADDLE DOL	I	I	90		37	0.3					En echelon set - all v. well connected
	3010.71	288	1	PO	CALC / SADDLE DOL	I	I	90		89	0.4					En echelon set - all v. well connected
	3010.71	289	1	PO	CALC / SADDLE DOL	I	NF	88		118	0.4					En echelon set - all v. well connected
	3010.81	290	1	PO	CALC / SADDLE DOL	NF	I	85		141	0.6					En echelon set - all v. well connected
	3010.85	291	1	O		I	CW	80		78	0.5					En echelon set - all v. well connected
	3010.83	292	1	PO	CALC	I	NF	85		42	0.2					En echelon set - all v. well connected
	3010.91	293	1	PO	CALC	NF	NF	85		118	1.6					En echelon set - all v. well connected
	3010.96	294	1	PO	CALC	NF	I	85		63	1					En echelon set - all v. well connected
	3010.95	295	1	PO	CALC	I	NF	85		27	0.4					En echelon set - all v. well connected
	3010.99	296	1	PO	CALC	NF	NF	85		69	0.4					En echelon set - all v. well connected
	3010.99	297	1	PO	CALC	I	I	85		66	0.2					En echelon set - all v. well connected
	3011.04	298	1	PO	CALC	I	STY	85		24	0.6					En echelon set - all v. well connected
	3011.12	299				CW	CW	0						52.83	1.95	
	3012.65	300	1	O	DRILLING MUD	I	NF	85		106	0.2					En echelon set. Spacing ~7mm
	3012.71	301	1	O	DRILLING MUD	NF	I	85		8	0.2					En echelon set. Spacing ~7mm
	3012.72	302	1	O	DRILLING MUD	I	I	85		18	0.2					En echelon set. Spacing ~7mm
	3012.77	303	1	O	DRILLING MUD	I	IF	85		73	0.2					En echelon set. Spacing ~7mm
	3012.84	304				CW	CW	0						25.99	1.20	
	3012.86	305				CW	CW	0						8.51	0.82	
	3014.3	306				CW	CW	0						51.06	1.47	
	3014.66	307	1	O		I	NF	80		78	0.2					
	3014.73	308	1	O		NF	NF	80		38	0.2					
	3014.75	309	1	O		I	I	85		34	0.2					
	3014.76	310	1	O		I	I	85		9	0.3					
	3014.77	311	1	O		I	I	85		11	0.2					
	3014.79	312	1	O		I	I	85		>35	0.2					
	3016.23	313				CW	CW	0						59.00	1.22	
PS 3016.30 - 3016.53																
	3016.61	314	1	PO	CALC	I	NF	85		23	0.2					
	3016.64	315	1	PO	CALC	NF	STY	85		40	0.2					
	3016.66	316	1	PO	CALC	I	I	85		21	0.2					
	3016.67	317	1	PO	CALC	I	I	85		20	0.3					
	3016.74	318	1	PO	CALC	I	I	85		>27	0.3					
	3016.77	319	1	PO	CALC	I	STY	85		41	0.3					
	3016.8	320				CW	CW	0						19.00	0.57	
	3016.83	321	1	PO	CALC	STY	I	85		>62	0.4					
H4/Core #4	3017.28	322	1	PO	CALC	I	IF	87		93	0.5					
	3017.27	323	1	CO	CALC	I	IF	88		73	?					Abundance of induced fractures?
	3017.60	324	1	O		CW	CW	81		20	?					
	3017.75	325	1	O		CW	CW	71		51	?					
	3017.84	326	1	O		I	IF	20		15	0.4					Possibly Induced - but unlike other induced features
	3017.84	327	1	O		I	IF	21		21	0.4					Possibly Induced - but unlike other induced features
	3017.84	328	1	O		I	IF	24		13	0.4					Possibly Induced - but unlike other induced features
PS 3018.00 - 3018.20																
	3018.24	329	1	O		IF	I	75		76	0.8					
	3018.58	330	1	O		CW	STY	78		81	0.3					Lower termination at styolite tip
	3018.60	331				CW	CW	29						27.67	2.34	Possibly not a compactional styolite
	3018.64	332	1	O		STY	I	60		28	0.4					Upper termination at styolite tip
	3018.66	333	1	O		CW	I	80		38	0.4					
	3018.68	334	1	O		I	I	81		32	0.4					
	3018.72	335	3	PC	CALC	CW	IF	76		94	1.1	?	?			Large amount of cementation. Fracture cluster - spacing ~15mm
	3018.74	336	1	PC		I	CW	85		91	0.4					
	3018.81	337	1	C	CALC	I	CW	85		80	0.4					
	3018.83	338	1	O		I	CW	75		215	0.4					
PS 3019.64 - 3019.85																
	3019.97	339	1	O	CALC	CW	STY	66		70	0.4					
	3020.04	340				CW	CW	0						26.79	0.85	
	3020.14	341	1	O		STY	CW	76		132	0.7					
	3020.15	342	1	O		I	I	80		40	0.3					
	3020.22	343	1	O		IF	CW	80		137	0.5					Series of minor extensional faults coalescing
	3020.26	344	?	O		CW	I	76		180	?					Intersects F24 at bottom - no displacement
	3020.28	345	?	O		CW	I	80		120	0.3					Intersects F23 at bottom - no displacement
	3020.44	346	1	O		I	I	90		13	0.2					En echelon fracture set
	3020.46	347	1	O		I	I	90		15	0.2					En echelon fracture set
	3020.47	348	1	O		I	I	90		9	0.2					En echelon fracture set
	3020.5	349	1	O		I	I	90		32	0.2					En echelon fracture set
	3020.59	350	1	O		I	CW	85		104	0.3					
	3020.86	351				CW	CW	0						0.74	0.30	Small cluster of styolites

Hasdrubal-4 Raw Data

	3020.94	352				CW	CW	0						13.76	0.84	
	3021.12	353				CW	CW	0						6.89	0.80	
	3021.22	354	1	PO	CALC	CW	CW	75		86	2.0					
	3021.64	355				CW	CW	0						28.36	0.66	
IZ 3021.75 - 3021.90																Zone of very small microfractures - spacing - 10-22mm. Tipping off styolite peaks
	3022.81	356				CW	CW	0						61.66	0.45	
	3023.23	357	2?	O		CW	CW	70		93	?	?				Probably pur shear although hard to identify
	3023.73	358	1	O		IF	IF	90		114	0.4					
	3023.91	359	1	O		IF	IF	90		165	0.1					
IZ 3024.00 - 3024.13																3 very small vertical microfractures - 110mm, 45mm, and 30mm -0.1mm thick
	3024.22	360	1	PC	CALC	I	STY	80		55	0.4					
	3024.25	361				CW	CW	0						72.00	0.65	
	3024.48	362	1	CO	CALC	CW	CW	90		416	>1.2					
	3024.47	363	1	O		I	I	90		25	0.3					Fracture growth by tip linkage
	3024.49	364	1	PO	CALC	I	I	90		28	0.3					
	3024.52	365	1	O		I	IF	90		55	0.3					This may be recracked styloite
	3024.66	366	2	O		I	STY	70		96	0.4					Many drilling induced fractures
	3024.93	367				CW	CW	0						18.61	0.32	Fractures propagating from tips in styolite
	3025.05	368				CW	CW	0						20.57	0.70	
	3025.10	369				CW	CW	0						7.55	0.22	Only the initail stages of formation
	3025.14	370	1	O		STY	I	85		38	0.4					
	3025.15	371	1	O		STY	I	85		17	0.4					
	3025.17	372	1	O		STY	I	85		22	0.4					
	3025.27	373	1	O		I	CW	75		74	0.3					Series of very small anatomising tensile fractures
	3025.28	374	1	O		I	I	79		9	0.3					Series of very small anatomising tensile fractures
	3025.29	375	1	O		I	I	80		14	0.3					Series of very small anatomising tensile fractures
	3025.43	376	1	O		CW	I	75		269	0.3					Long anastomising sub-vertical fractures
	3025.68	377	1	O		I	I	82		125	0.3					Long anastomising sub-vertical fractures
	3025.73	378	1	O		I	CW	80		44	0.3					
	3025.73	379	1	PO	CALC	CW	IF	80		65	0.4					
	3025.81	380	1	O		I	I	90		119	0.1					
	3026.05	381	1	O		CW	I	90		110	0.2					
	3026.12	382	3	O		CW	CW	70		113	?	39	?			Shear fracture - displaced other vertical tensile fractures
	3026.17	383	1	O		NF	I	85		50	0.2					
	3026.12	384	1	O		I	I	85		59	0.2					
	3026.19	385	3	O		CW	I	80		182	0.8	2	?			Mixed mode fracture
	3026.26	386	3	O		I	I	90		11	0.5	0.5	?			Smaller mixed mode fracture associated with F64
	3026.27	387	3	O		I	I	90		22	0.5	0.5	?			Smaller mixed mode fracture associated with F65
	3026.19	388	1	O		I	I	90		48	0.2					Displaced by F61 ~39mm displacement.
	3026.22	389	1	O		I	I	90		61	0.2					En echelon with F67
	3026.60	390	3	O		CW	CW	82		210	?	50				
	3027.32	391	1	O		I	I	90		75	0.3					Extensional fracture propagated from tip of a nummulite
	3027.29	392	1	O		I	I	90		16	0.3					Cluster of small microfractures
	3027.81	393	1	O		I	I	88		53	0.1					Cluster of small microfractures
	3027.87	394	1	O		I	I	85		143	0.1					Cluster of small microfractures
	3027.88	395	1	O		CW	CW	88		132	0.1					
	3027.90	396	1	O		I	I	88		135	0.1					
	3028.22	397	1	PO	CALC	I	I	88		450	>2.0					Large open extensional fracture. Abundant crystal growth of fracture walls
	3028.15	398	1	O		I	I	90		48	0.1					
	3028.45	399	1	PO	CALC	IF	PS	90		270	>2.0					Large open extensional fracture. Abundant crystal growth of fracture walls
PS 3028.58 - 3028.76																
	3028.80	400	1	PO	CALC	PS	I	89		776	1.1					Large open extensional fracture. Abundant crystal growth of fracture walls
IZ 3028.80 - 3028.92																Intense pressure solution around nummulitic clasts
	3029.22	401				CW	CW	0						113.30	1.64	
	3030.05	402				CW	CW	0						144.00	2.83	
	3030.12	403	1	O		CW	CW	90		114	0.2					Extensional fracture propagating from styolite tip
	3030.18	404	1	O		CW	CW	90		36	0.2					Series of en echelon micro-fractures - no fill
	3030.19	405	1	O		STY	I	90		13	0.2					Series of en echelon micro-fractures - no fill
	3030.21	406	1	O		I	I	90		15	0.2					Series of en echelon micro-fractures - no fill
	3030.23	407	1	O		I	I	90		38	0.2					Series of en echelon micro-fractures - no fill
	3030.20	408	1	O		I	I	90		51	0.2					Series of en echelon micro-fractures - no fill
	3030.83	409	2	PO	CALC	IF	I	85		143	0.5	20				Two shear fractures with differing orientations
	3030.83	410	2	PO	CALC	IF	I	85		135	0.5	5				Two shear fractures with differing orientations
	3031.44	411				CW	CW	0						74.27	1.71	
	3031.52	412	1	PO	CALC	STY	I	90		94	0.5					Series of en echelon fractures - crystal growth on walls
	3031.58	413	1	PO	CALC	I	I	90		64	0.5					Series of en echelon fractures - crystal growth on walls
	3031.65	414	1	PO	CALC	I	I	90		35	0.5					Series of en echelon fractures - crystal growth on walls
	3031.72	415	1	PO	CALC	I	I	90		152	0.5					Series of en echelon fractures - crystal growth on walls
	3031.59	416	2	PO	CALC	CW	CW	80		151	0.2	>40				
	3031.78	417	1	PO	CALC	I	I	88		79	0.3					Extensional fractures of differing orientation - connectivivity
	3032.05	418	1	PO	CALC	I	I	88		540	>0.3					Extensional fractures of differing orientation - connectivivity
PS 3032.07 - 3032.27																
	3032.71	419	1	PO	CALC	I	STY	89		239	1.0					Styolite associated fracture - filled with calcite
	3032.73	420	2	O		CW	CW	76		150	0.2	?				

Hasdrubal-4 Raw Data

	3032.85	421				CW	CW	0						79.14	2.77	
	3032.76	422	1	PO	CALC	I	STY	90		82	0.2					
	3032.85	423	1	PO	CALC	I	I	90		45	0.2					
	3032.86	424	1	O		STY	I	90		60	0.3					
	3033.12	425	2	PO	CALC	CW	IF	70		102	0.1	>15				May be induced
	3033.20	426	1	O		IF	IF	90		78	0.1					Series of v. small calcite filled fracturesall about 25mm in length. 2 orientations
IZ 3034.05 - 3034.30														30.95	3.13	
	3034.83	427				CW	CW	0						22.99	3.22	
	3035.19	428				CW	CW	0						9.21	1.02	
	3036.62	429				CW	CW	0						5.01	0.18	
	3036.69	430				CW	CW	0						4.05	0.42	
	3036.89	431				CW	CW	0								May be induced
	3037.03	432	1	C	CALC	CW	I	50		52	0.1					
PS 3037.06 - 3037.32														11.93	1.89	
	3037.38	433				CW	CW	0								
	3037.55	434	1	O		CW	I	80		237	0.1					
	3037.55	435	1	PO	CALC	I	I	85		27	0.2					Intensely styolitised. Presence of a lot of small calcite vugs
IZ 3037.50 - 3038.17																
	3038.93	436	1	O		I	I	85		36	0.1					Very thin system of micro-fractures
	3039.20	437	1	?	?	I	I	90		172	0.1					
	3040.45															

Appendix C

Discrete Fracture Modelling of the Hasdrubal Reservoir

C.1. Introduction

Raw fracture data from the core and image log analyses has been input into FracMan, an MS-DOS™ PC software package developed by Golder Associates in order to model the geometry of fractures in the Hasdrubal reservoir. This software provides an integrated environment for the entire process of discrete fracture data analysis and modelling. FracMan incorporates six modules: 1) FracSys - fracture data analysis, 2) FracWorks - Stochastic fracture generation and sampling, 3) MeshMaker/MeshView - Mesh control and visualisation, 4) PAWorks/LTG - Transport and pathway analysis, 5) FraCluster - Analysis of compartmentalisation and dual porosity behaviour, and 6) RockBlock - Key block stability of rock blocks (**Fig. C.1**). For the purpose of the thesis and also due to time constraints only the FracSys and FracWorks modules were utilised.

In order to visualise the discrete fracture model generated in FracMan more effectively, the final output model was input into FRED, a "Fractured Reservoir Evaluation & Development" package also developed by Golder Associates Inc. This software package provided the front-end graphical output for FracMan. Individual fracture set distributions could be colour coded, and the viewer could essentially 'fly' through the generated model, identifying areas of particular interest.

C.2. Fracture & Stylolite Data Analysis

ISIS (Interactive Set Identification System): Fracture data analysis was undertaken in the ISIS (Interactive Set Identification System) sub-module of FracSys. ISIS provides a tool for defining fracture sets from raw data using an adaptive, probabilistic pattern

recognition algorithm. ISIS allows the user to select the fracture properties of concern and define their relative significance for the analysis. Unlike conventional approaches to fracture set definition, which define sets by contouring orientations on stereoplots, ISIS is as powerful for overlapping fracture sets as for clearly defined fracture sets (as will be shown). The premise on the ISIS approach for the definition of fracture sets is that the sets should be groups of fractures with similar properties. Orientation does not need to be the only property defining sets; size, termination, fillings and other properties can identify sets as well.

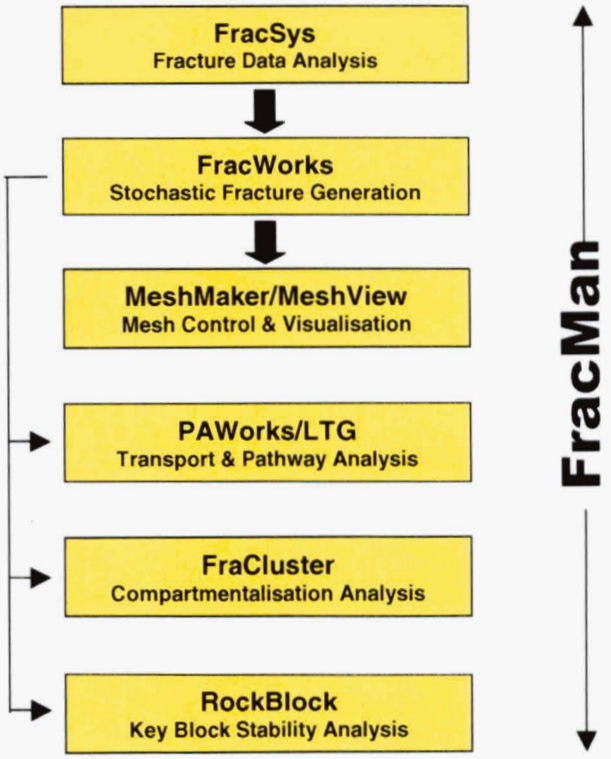

Fig. C.1. The FracMan modelling package.

ISIS identifies fracture sets using multiple fracture properties. It calculates the distribution of properties for the fractures assigned to each set, then re-assigns fractures to sets according to probabilistic weights proportional to their similarity to other fractures in the set. The properties of the sets are then recalculated and the process is repeated until the set assignment is optimised. Thus the aim of the ISIS technique is to assign groups of fractures that are similar geologically to sets that are statistically homogeneous. This is achieved by deriving the statistical properties of each set from the statistical properties of the fractures assigned to the set and then removing and reassigning fractures which have a low probability of being a part of that set (**Fig. C.2**).

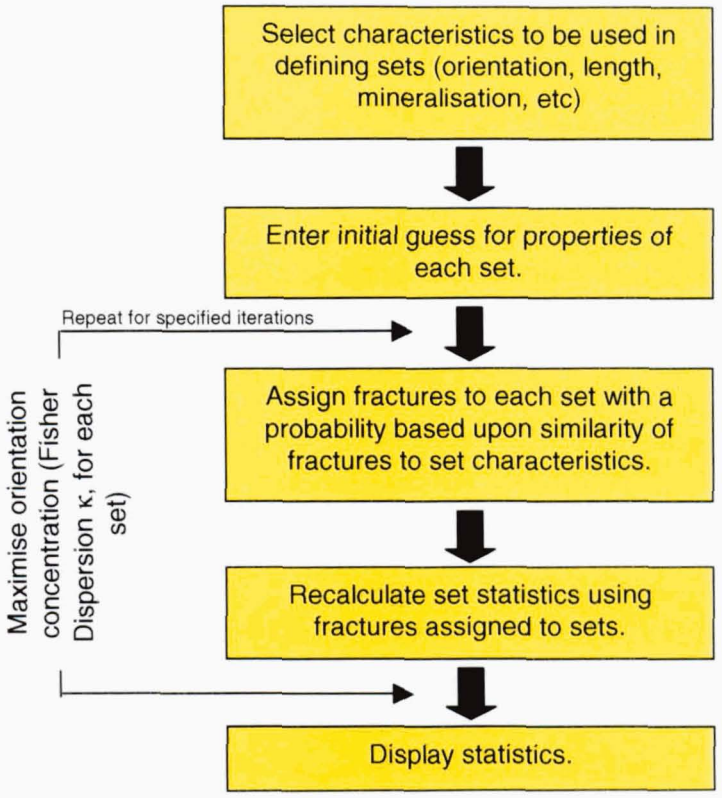

Fig. C.2. Overview of the ISIS approach.

Although ISIS allows the identification of fracture sets through the use of multiple fracture properties, due to time constraints in this study, fracture and stylolite sets were characterised principally by orientation. The nature and extent of cementation within fractures was analysed with a view to incorporating this data into the model, to aid differentiation of fracture distributions. However, it became apparent that partial to total cementation was a relatively pervasive feature in all the fracture sets observed, and that it would not significantly assist fracture set identification. This was also the case for fracture size, which varied markedly within individual fracture distributions. The following discussion attempts to briefly summarise the procedures involved in analysing the raw data, prior to generating a discrete fracture model in FracWorks. The example used is for Hasdrubal -4. The procedures used for Hasdrubal -2 and -3 are identical.

Stylolite Data Analysis (Hasdrubal –4)

Stylolite orientation data from the analysis of cores 1 and 2 was input into ISIS to identify the mean orientation of stylolites within the El Garia Formation and Compact Micrite Member. Unfortunately the cored section within the Chouabine Formation was un-oriented, precluding an analysis of stylolite and fracture trend. **Figure C.3** presents

two contoured steroenets for the Compact Micrite Member and the El Garia Formation, showing the mean dip and dip direction of stylolites within both lithostratigraphic units.

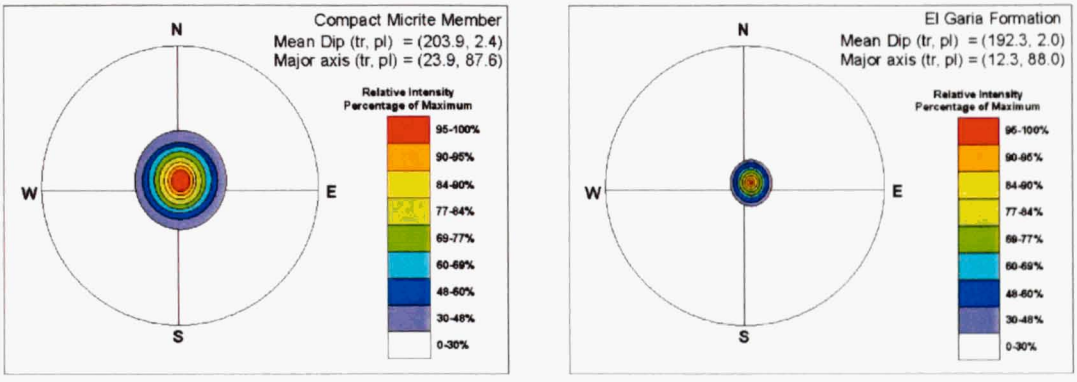

Fig. C.3. Contoured stereonet of stylolite orientation in the Compact Micrite Member and El Garia Formation.

Fracture Data Analysis (Hasdrubal –4)

Fracture orientation data from the Compact Micrite Member and the upper part of the El Garia Formation was also input into ISIS to distinguish and calculate the mean orientation of different fracture sets. This analysis, which follows on from that given earlier in Section 7.6 demonstrated that the Compact Micrite Member contains two different fracture distributions (~NW-SE and NE-SW), and that the upper part of the El Garia Formation is comprised of a series of five layer-bound fracture systems of different orientation (refer to **Figs. 7.18-7.19**). As previously mentioned high amplitude stylolites tend to bound these five fracture systems. **Figures C.4 & C.5** present a series of contoured steroenets for the Compact Micrite Member and the El Garia Formation, showing the mean dip and dip direction of individual fracture sets within both lithostratigraphic units. The plots generally show univariant to bivariant Fisher distributions in the El Garia Formation and Compact Micrite Member.

C.3. Stochastic Fracture Generation & Modelling

FracWorks (Fracture Geometric Modelling): Once the raw core data from Hasdrubal -4 had been analysed within FracSys, it was then manipulated and input into the FracWorks module of FracMan™, in order to generate a stochastic fracture model of the cored interval. The process of stochastic fracture generation within the FracWorks is summarised in the following discussion.

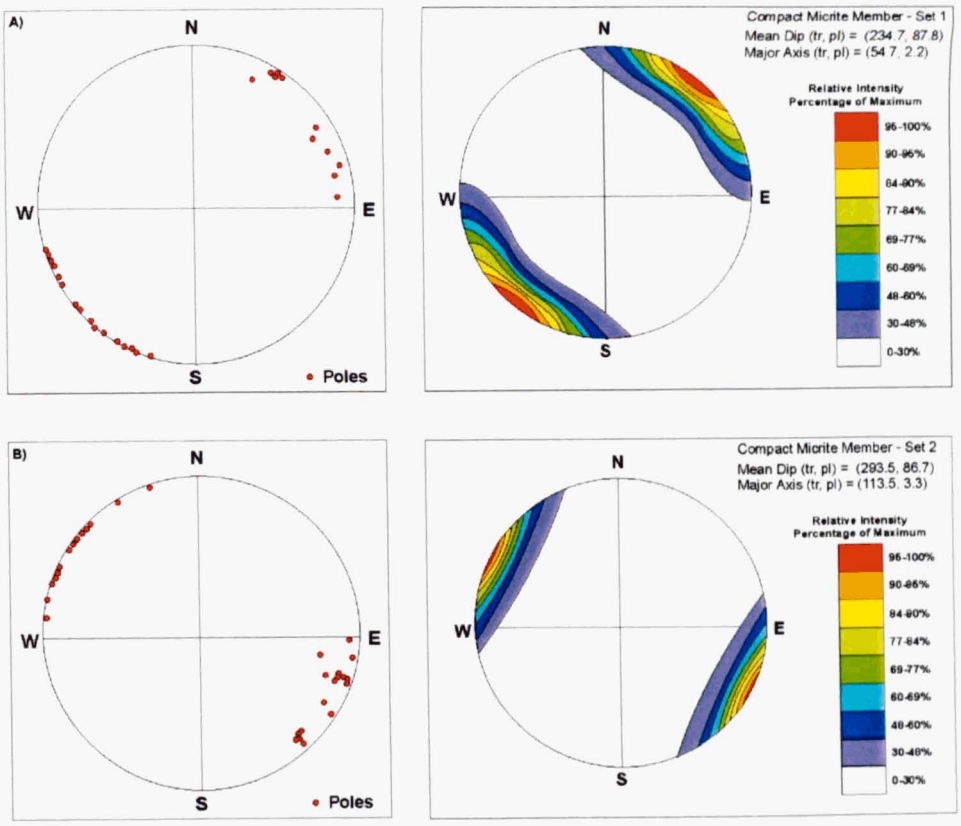

Fig. C.4. Equal area projection and respective contour plot showing poles to fractures within the Compact Micrite Member. Two fracture sets are clearly defined.

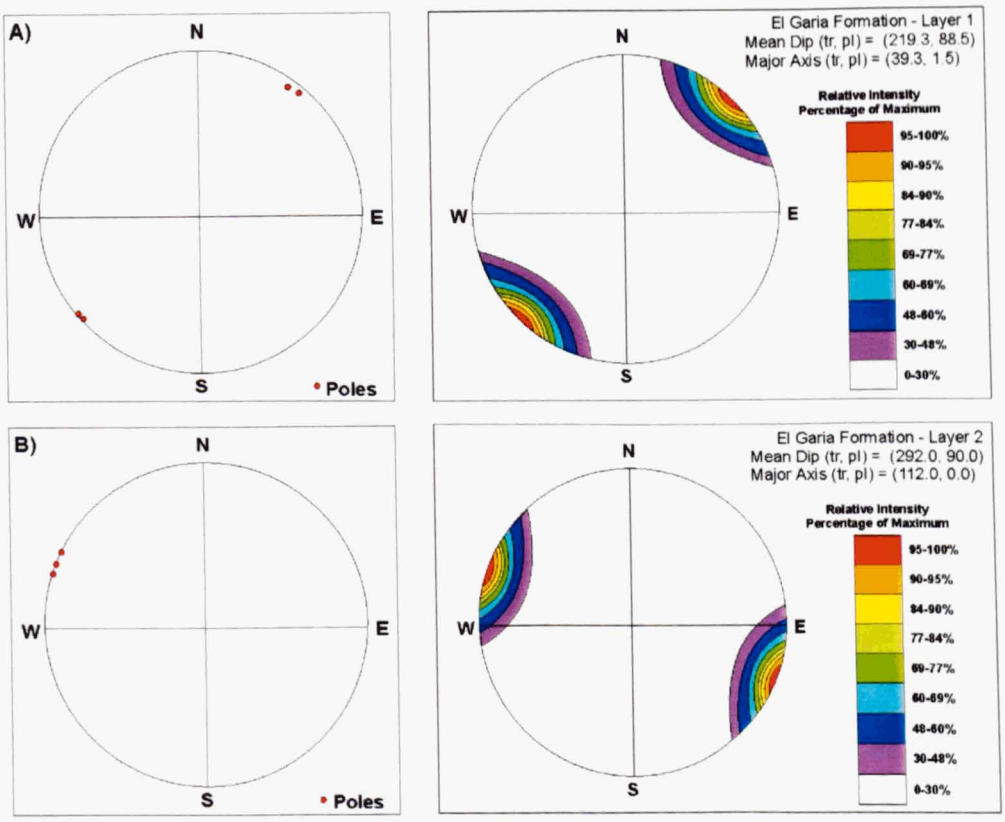

Fig. C.5a-b. Equal area projections and respective contour plots showing poles to fractures within the El Garia Formation. Five well-defined layers have been defined (refer to Fig. 7.19).

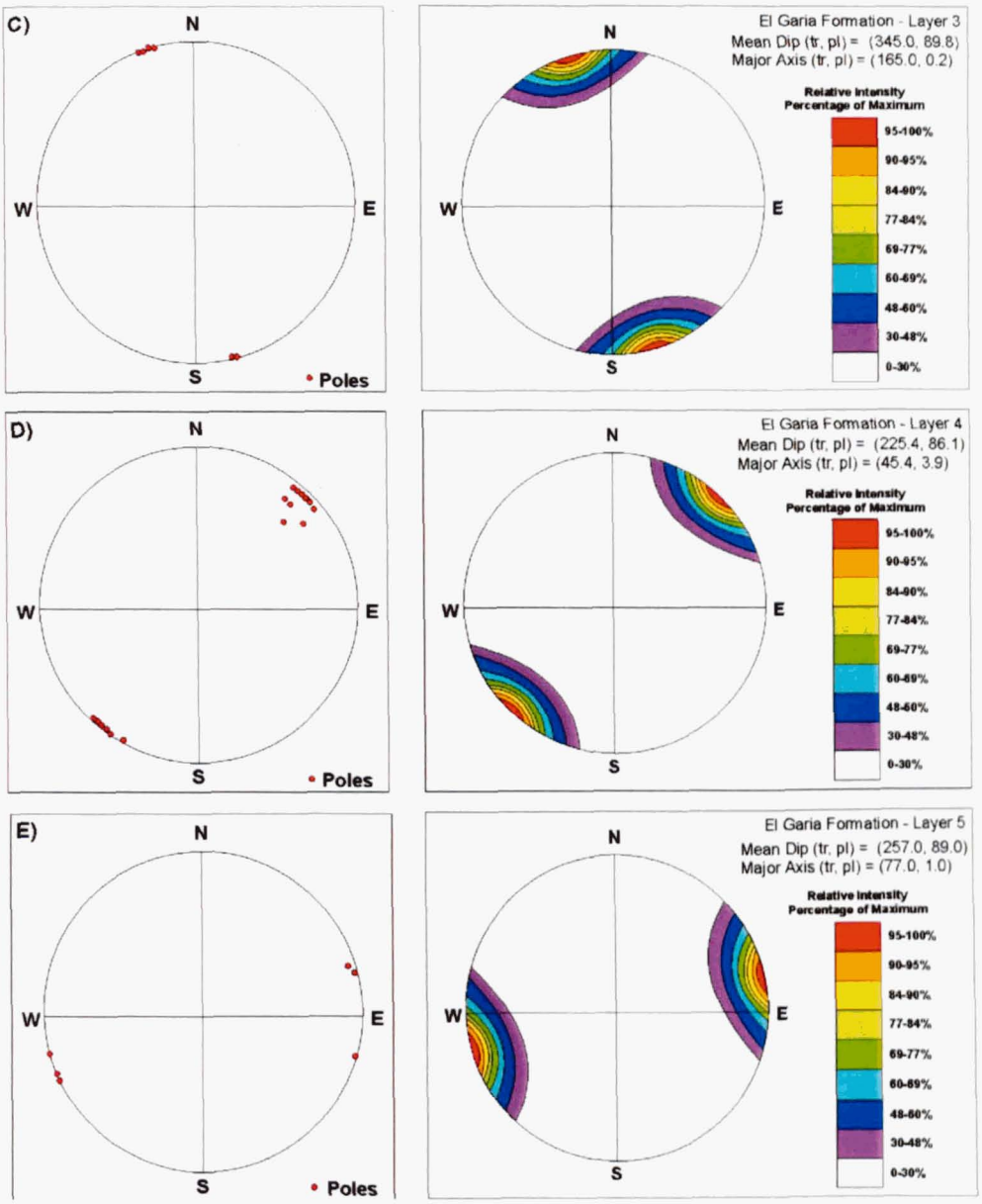

Fig. C.5c-e. Equal area projections and respective contour plots showing poles to fractures within the El Garia Formation. Five well-defined layers have been defined (refer to Fig. 7.19).

Creation of a Fracture Generation Region

The initial task in building a three-dimensional stochastic fracture model of the cored interval in Hasdrubal –4 involved creating a fracture generation region. The FracWorks program uses a three-dimensional system of co-ordinates (x, y, z), where the x, y and z axes point in the southward, eastward and upward directions respectively, as shown in **Figure C.6**. Directions in the FracWorks program are stated in terms of their trend and plunge, where trend is the positive angle from North as shown in **Figure C.7** and plunge is measured in downward from horizontal. Upward directions are stated as having negative plunge. All angles are measured in degrees, and all lengths in metres. For the purpose of this study the generation region was a cube 100m x 100m x 100m.

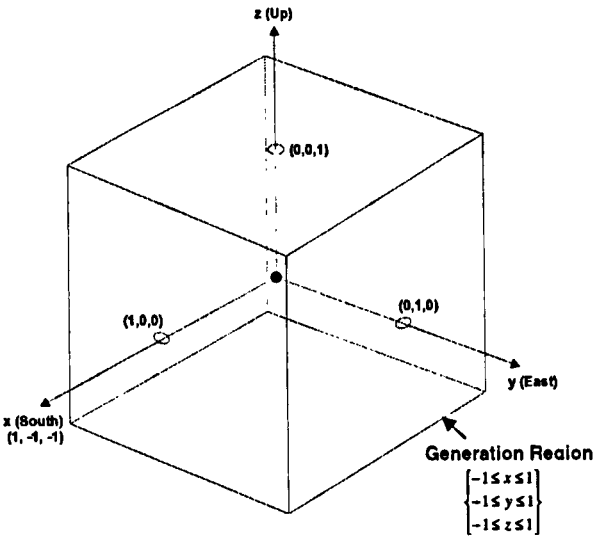

Fig. C.6. FracWorks generation region (after Dershowitz et al., 1998).

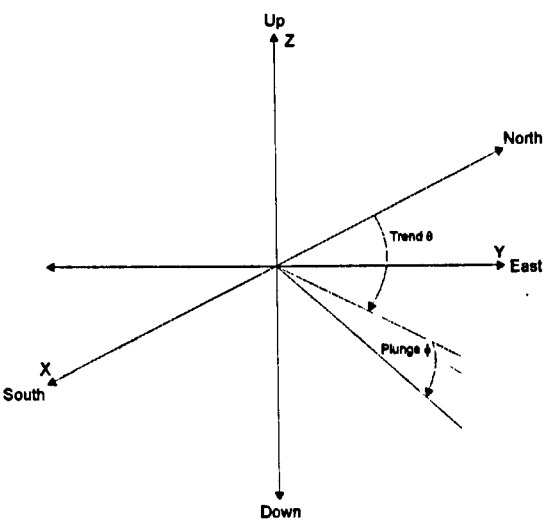

Fig. C.7. Specifications of directions in FracMan in terms of trend and plunge (after Dershowitz et al., 1998).

Layer Input

The lithostratigraphic boundaries separating the Tselja, Chouabine, El Garia, Compact Micrite, and Cherahil intervals in Hasdrubal -4 were input into the model by generating four bedding-parallel surfaces (at specific depths) that extended beyond the FracWorks generation region (**Fig. C.8**).

Trace Plane/Borehole Input

In order to ensure that the number of stochastically generated fractures and stylolites within the FracWorks generation region resembled that of the subsurface in the vicinity of Hasdrubal -4, it was necessary to introduce a pseudo-borehole into the model, from

which statistical data could be obtained and compared with the actual core observations (**Fig. C.9**). This pseudo-borehole or sampling program essentially represented the Hasdrubal -4 well. Typical statistical displays for pseudo-borehole samples provided information on the number of fracture intersections (i.e. fracture intensity), orientation and spacing. On comparison with actual borehole data, it was then possible to alter input parameters in order to gain a close fit between real and modelled fracture and stylolite distributions.

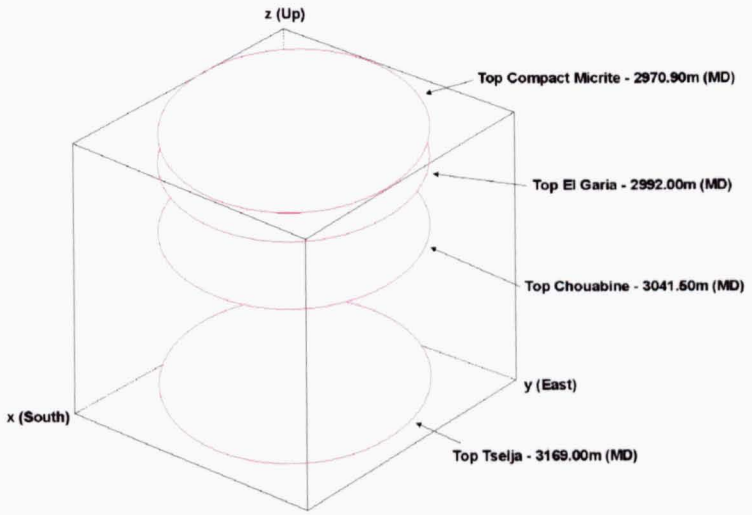

Fig. C.8. Schematic diagram showing the FracWorks generation region with the layer boundaries between the Tselja, Chouabine, El Garia, Compact Micrite, and Cherahil intervals.

Given that the geometric data (ie. orientation, length, width etc.) that was input into the model is correct, the main parameter that needs to be altered during simulations is intensity. The FracWorks program models areal intensity (P_{32}). This is defined as the total area of features per unit volume (Dershowitz et al., 1998):

$$P_{32} = \frac{A_f}{V_t} \tag{7.1}$$

where A_f is the total area of features, and V_t is the total volume. P_{32} values are dimensional (in units of 1/meters or 1/km), but scale independent (i.e. they do not depend on the volume studied, the orientation of the measurement or the distribution of fracture size).

It is clear that variations in the initial P_{32} value input into the simulation control the intensity of generated fractures, and hence influence the number of fracture intersections on a pseudo-borehole. Thus in order to gain a 'best fit' between actual and

model data along a pseudo-borehole, it may be necessary to run numerous simulations, varying the input P_{32} value until model results and real data closely match.

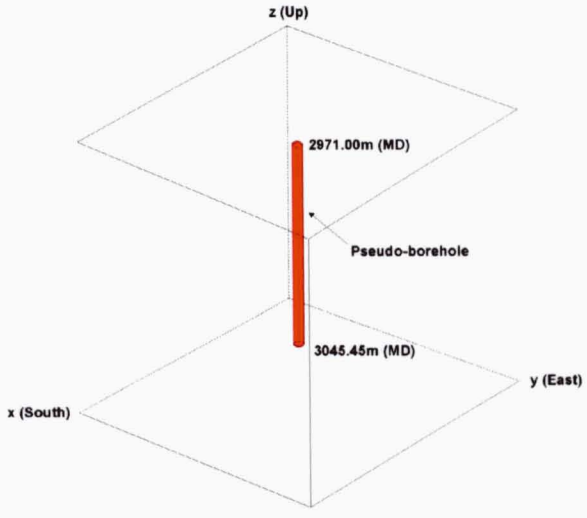

Fig. C.9. Schematic diagram showing the FracWorks generation region with the introduction of a pseudo-borehole resembling the Hasdrubal -4 well.

Fracture and Stylolite Input

The FracMan package idealizes fractures as planar and polygonal. The planarity simplification is adopted for three reasons: firstly, because little field and core data is available on non-planar fractures; secondly, because planar fractures are computationally far more tractable than undulating fractures; and thirdly, because for problems of concern the effects of fracture undulation can be approximated in a more tractable manner, e.g., as an increased coefficient of friction for mechanical problems, or as an adjusted transmissivity for hydrological problems.

The assumption of polygonal fractures is both realistic and useful, as it allows the approximate representation of a wide variety of fracture shapes by a single mathematical form. Considerations from fracture mechanics suggest that in a homogeneous rock the general shape of an isolated fracture should be elliptical, as it is assumed in the Baecher model (Baecher et al., 1977). However, since rock is generally heterogeneous, perfectly elliptical fractures are unlikely, and in a practical sense no error is introduced by representing the ideal, elliptical fracture by a many sided polygon of equivalent area. Dershowitz (1984) has noted, moreover, that observed fractures are generally polygonal due to terminations of the fractures at intersections with other fractures.

FracWorks defines nine 'conceptual models' that form the basis of fracture and stylolite simulations (**Fig. C.10**):

- *The Enhanced Baecher (BART) Model* is an extension of the Baecher model in which fracture centres are located uniformly in space, using a poisson process and the fractures are generated as disks with a given radius and orientation. The Enhanced Baecher model (Dershowitz et al., 1989) extends the Baecher model by providing a provision for fracture terminations and more general fracture shapes. The BART (Baecher Algorithm, revised Terminations) generalises the Baecher model further by allowing termination modes which result in non-uniform fracture locations;
- *The Poisson Rectangle Model* is a simplified version of the Enhanced Baecher Model, in which fractures are represented by rectangles with prescribed length and width, rather than as polygonal disks with an 'effective' radius. Location and termination are treated in the same way as in the Enhanced Baecher model;
- *The Levy-Lee Model* is a stochastic model, which uses a Levy Flight fractal process to produce clusters of smaller fractures around widely scattered, larger fractures;
- *The Nearest Neighbour Model* is a semi-stochastic, pattern-based model which simulates the tendency of fractures to be clustered around major joints and faults by preferentially producing new fractures in the vicinity of earlier fractures;
- *The Probabilistic War Zone Model* is a semi-stochastic, pattern-based model which imitates the geometry of shear zones by preferentially producing fractures in the regions between large, sub-parallel, neighbouring fractures;
- *The Non-Planar Fracture Zone Model* is semi-stochastic model which generates fractures with location and orientation varying according to a user defined non-planar surface;
- *The Fractal Box Model* uses a self-similar fractured field to define fracture initiation points, which may be either centres or random surface points;
- *The Fractal POCS (Projection Onto Convex Sets) Model* generates a random field of fracture initiation points (centres or surface points) which are (a) consistent with a user specified fractal dimension, (b) consistent with a user specified variogram, and (c) conditioned to intensities at specified locations.

➢ The Geostatistical Model generates a random field of fracture initiation points (centre or surface points) according to a specified spherical, exponential, or null variogram.

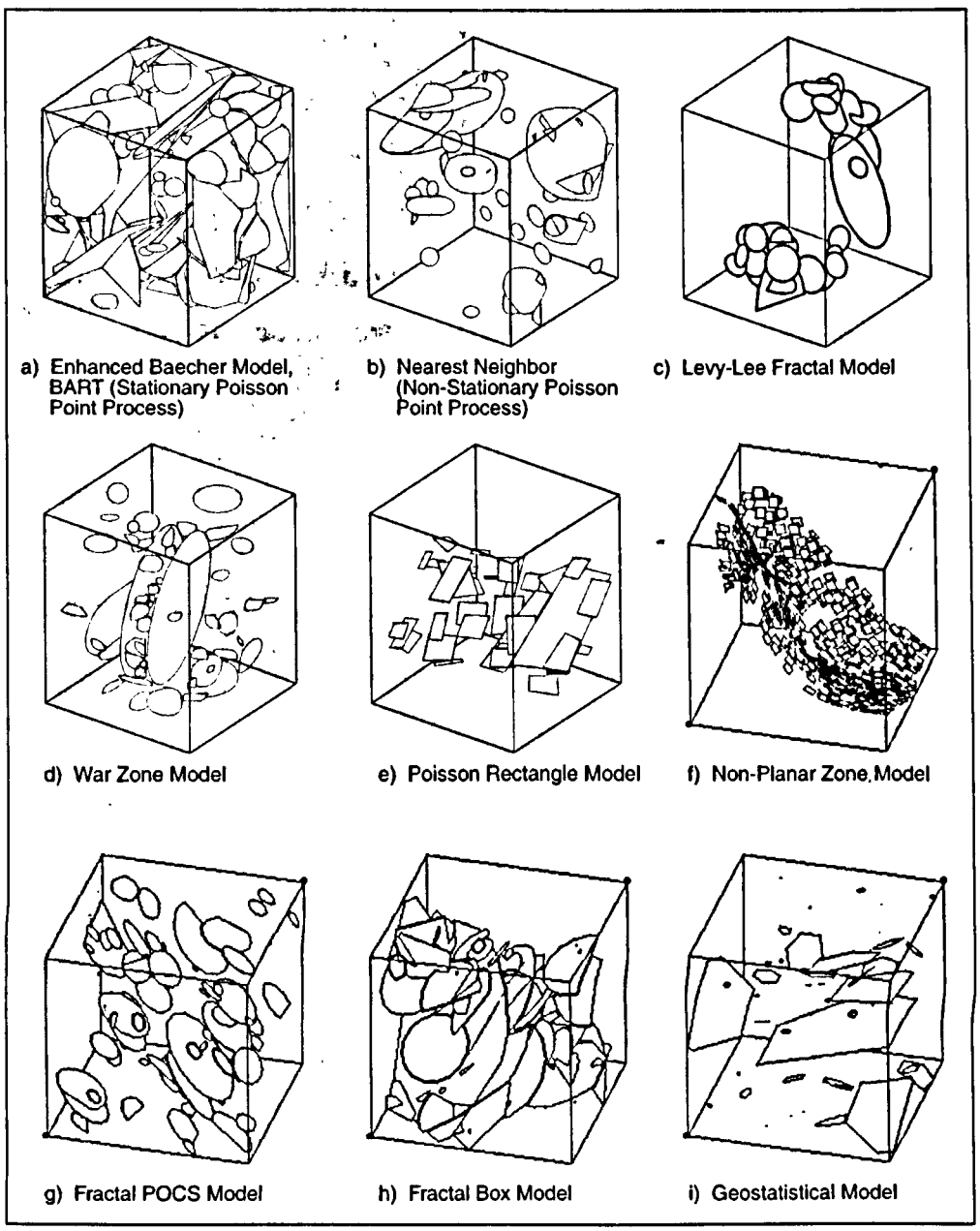

Fig. C.10. Diagram illustrating the nine 'conceptual models' that form the basis of fracture simulations in FracMan (Dershowitz, 1984).

The Enhanced Baecher, Levy-Lee fractal, Nearest Neighbour and War Zone models are described in more detail by Geier et al. (1989). These models all generate polygonal fractures that may or may not terminate at intersections with other fractures. The models differ from one another only with regard to the spatial distribution of the fractures, and the interrelationship of fracture size and fracture location.

It is essential that the right conceptual model is utilised in a specific simulation in order to correctly model subsurface distributions. This is, in part accomplished through the FracSys analysis, which identifies appropriate models that provide a best fit to the observed data. In the Hasdrubal case study, the Poisson Rectangle Model was used because it provided the most appropriate fit to the output results from the FracSys analysis.

Once this conceptual model had been identified, a generation shape was selected within which geological features were simulated. For the purpose of this study, a cylindrical shape was selected that effectively modelled distributions radially away from the borehole axis. Cylinder dimensions are defined by axial length (i.e. the sample length in Hasdrubal -4) and cylindrical radius, which was taken as 10m for the purpose of this study (**Fig. C.11**). The cylindrical radius could have been enlarged, although confidence in the model data at large distances from the borehole is reduced. In addition to this, as one increases the size of the generation volume, the number of fractures created increases, thus impacting file size.

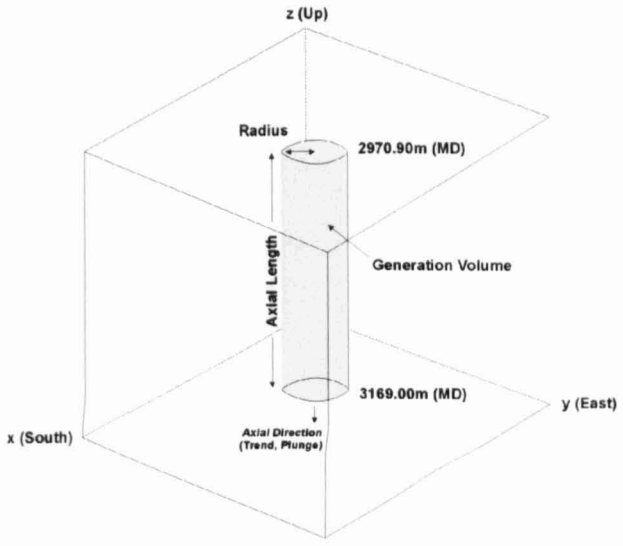

Fig. C.11. Schematic diagram showing the generation volume within which geological features were simulated. The generation volume traces the trend of the pseudo-borehole.

Various parameters derived from the FracSys analysis are incorporated into each simulation. Table C.1 shows the main input parameters and data formats that were incorporated into simulations on the Hasdrubal -4 well. The following discussion attempts to summarise the procedures used in generating stylolites and fractures within the FracWorks module.

Main Input Parameters/Data Formats	Options/Formats Utilised
Conceptual Model	Enhanced Baecher/Poisson Rectangle
Generation Mode (Centre Point/Surface Point)	Fracture Centre Points
Generation Region Truncation Mode (On/Off)	Off
Orientation Vectors (Pole/Dip)	Pole vectors
No. of Fracture/Stylolite sides	Four
Generation Volume Shape (Cube/Cylinder/Slab)	Cylinder (10m Radius)
Fracture/Stylolite Orientation (Pole/Dip Direction)	Mean Pole (for each fracture set)
Distribution Type for Orientation	Fisher/Bivariate Fisher/Bivariate Bingham
Fracture/Stylolite Size	Length/Width (for Poisson Rectangle only)
Distribution Type for Fracture Length	Power Law/Negative Exponential
Standard Deviation for Fracture Length	Constant/Power Law
Intensity (P_{32}/P_{33})	Areal Intensity (P_{32})
Distribution Type for Intensity	Constant

Table C.1. Main input parameters within FracWorks for the particular distributions identified in the Hasdrubal wells. The various options selected are shown.

Stylolite Input

Stylolites were modelled for each lithostratigraphic interval by randomly generating a number of sub-horizontal surfaces within the generation region using the 'Enhanced Baecher' conceptual model of Dershowitz et al. (1998). Stylolites were generated around a single point as polygons with 10 sides.

As it was assumed that the stylolites modelled were laterally extensive features, they were given an 'effective radius' that extended outside the FracWorks generation volume (i.e. >10m diameter). Orientation data was gained from the FracSys analysis. Numerous simulations were run for each lithostratigraphic interval until an appropriate P_{32} value was identified, which provided a 'best fit' between the model data and actual core observations (**Fig. C.12**).

As previously mentioned, only the first two cores in Hasdrubal -4 were oriented (2971.00m-3003.90m (MD)). These cores provided orientation information for structures in the Compact Micrite Member and the upper part of the El Garia Formation. For the purpose of this study orientation data from the El Garia Formation has been extrapolated down into the Chouabine Formation. This seems to be a reasonable procedure given that stylolite orientation does not vary significantly between the Compact Micrite Member and the Chouabine Formation, and that the Tertiary sequence is relatively 'layer cake'. Table C.2 details the parameters input into stylolite realisations within FracWorks for each of the Hasdrubal wells.

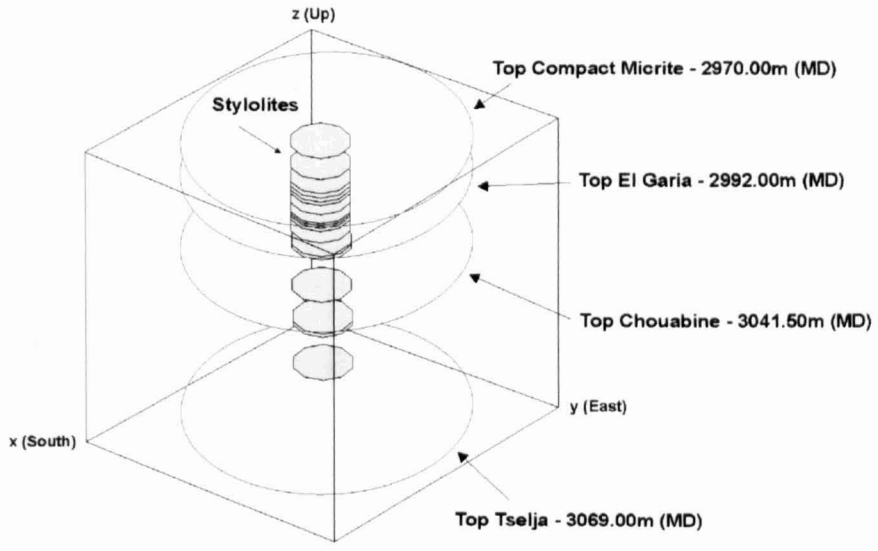

Fig. C.12. Schematic diagram showing the layer boundaries between the Tselja, Chouabine, El Garia, Compact Micrite, and Cherahil intervals and stylolites generated.

Input Parameter	Hasdrubal -2			Hasdrubal -3			Hasdrubal -4		
	CM	EG	CH	CM	EG	CH	CM	EG	CH
Conceptual Model	-	En. Ba	En. Ba	En. Ba	En. Ba	En. Ba	En. Ba	En. Ba	En. Ba
Generation Mode	-	Centre	Centre	Centre	Centre	Centre	Centre	Centre	Centre
No. of sides (polygon)	-	10	10	10	10	10	10	10	10
Mean Dip/Dip Dir.	-	$2^0/192^0$	$2^0/192^0$	$2^0/204^0$	$2^0/192^0$	$2^0/192^0$	$2^0/204^0$	$2^0/192^0$	$2^0/192^0$
Polygonal Radius	-	10m	10m	10m	10m	10m	10m	10m	10m
Size Distribution	-	Const.	Const.	Const.	Const.	Const.	Const.	Const.	Const.
Areal Intensity (P_{32})	-	0.36	0.045	-	0.43	0.13	0.128	0.6	0.6
Intensity Distribution	-	Const.	Const.	Const.	Const.	Const.	Const.	Const.	Const.

Table C.2. Input parameters for stylolite realisations for each of the Hasdrubal wells. Orientation information for Hasdrubal -2 and -3 was taken from Hasdrubal -4

Fracture Input

Fracture distributions have been simulated within FracWorks using the 'Poisson Rectangle' conceptual model of Dershowitz et al. (1998). In this model, the fracture centres are located uniformly in space, using a Poisson process and the fractures are generated as rectangles with a prescribed length and width.

Based on the data output from FracSys, where numerous different fracture distributions were identified within the cored interval, a number of fracture sets have been generated within each lithostratigraphic unit. For example, in the Compact Micrite Member, two fracture systems have been modelled trending ~NW-SE and ~NE-SW over the entire

interval. In contrast, within the upper part of the El Garia Formation where oriented core was available, it has been possible to model five layer-bound fracture systems.

Fracture lengths (in the direction of the dip vector) were calculated for each system based on average fracture height values from the core analysis. The length distribution of fractures for each of these sets has also been analysed (Section 7.6.3) and input into the model. Fracture widths (in the direction orthogonal to both the dip and pole vectors) are the correlated with respect to length. As in the stylolite simulations, numerous models were run until an appropriate P_{32} value (i.e. areal intensity) was identified, which provided a 'best fit' between the model data and actual core observations. Table C.3 details the fracture data input into FracWorks.

Input Parameter	Hasdrubal -2			Hasdrubal -3			Hasdrubal -4		
	CM	EG	CH	CM	EG	CH	CM	EG	CH
Conceptual Model	P. Rec	P. Rec	P. Rec	P. Rec	P. Rec	P. Rec	P. Rec	P. Rec	P. Rec
Generation Mode	Centre	Centre	Centre	Centre	Centre	Centre	Centre	Centre	Centre
No. of sides	4	4	4	4	4	4	4	4	4
Mean Dip/Dip Dir.	1)88/234	1)89/219	1)89/219	1)88/234	1)89/219	1)89/219	1)88/234	1)89/219	1a) 89/219
	2)87/294	2)90/292	2)90/292	2)87/294	2)90/292	2)90/292	2)87/294	2)90/292	1b) 90/292
		3)90/345	3)90/345		3)90/345	3)90/345		3)90/345	1c) 90/345
		4)86/225	4)86/225		4)86/225	4)86/225		4)86/225	1d) 86/225
		5)89/257	5)89/257		5)89/257	5)89/257		5)89/257	1e) 89/257
								6a)89/219	2a) 89/219
								6b)90/292	2b) 90/292
								6c)90/345	2c) 90/345
								6d)86/225	2d) 86/225
								6e)89/25	2e) 89/257
Length Distribution	Neg. Ex	P. Law	P. Law	Neg. Ex	P. Law	P. Law	Neg. Ex	P. Law	P. Law
Fracture Width	Corr.	Corr.	Corr.	Corr.	Corr.	Corr.	Corr.	Corr.	Corr.
Areal Intensity (P_{32})	-	1) 0.07	1) 0.02	1) 0.38	1) 0.1	1) 0.045	1) 0.34	1) 2.5	1a) 0.018
	-	2) 0.03	2) 0.018	2) 0.395	2) 0.05	2) 0.03	2) 0.34	2) 0.5	1b) 0.013
		3) 0.1	3) 0.031		3) 0.18	3) 0.065		3) 1.7	1c) 0.042
		4) 0.255	4) 0.04		4) 0.42	4) 0.13		4) 2.35	1d) 0.028
		5) 0.08	5) 0.03		5) 0.14	5) 0.065		5) 3.14	1e) 0.014
								6a) 0.25	2a) 0.018
								6b) 0.05	2b) 0.013
								6c) 0.2	2c) 0.042
								6d) 0.45	2d) 0.028
								6e) 0.26	2e) 0.014
Intensity distribution	Const.	Const.	Const.	Const.	Const.	Const.	Const.	Const.	Const.

Table C.3. Main input parameters for fracture realisations for each of the Hasdrubal wells.

Unfortunately, the cored interval in the lower part of the El Garia Formation and the entire Chouabine Formation was not oriented, thus precluding fracture set differentiation on orientation data. Consequently, data from the upper part of the El Garia Formation has been merged and extrapolated down into this non-oriented section. P_{32} values were scaled down in accordance, in order to fit observed

measurements. Although it is unclear whether fracture distributions within the Chouabine Formation are the same as those in the El Garia Formation, it seems a reasonable assumption that they are at least similar, given the similar tectonic conditions. This limitation in the three-dimensional fracture model is inevitable, due to the lack of data available, and thus where necessary a best estimate must be proposed.

C.4. Three-Dimensional Visualisation of FracWorks Realisations

FRED (Fractured Reservoir Evaluation & Development)

Fracture and stylolite realisations developed in FracWorks were input into FRED (Fractured Reservoir Evaluation & Development) in order to visualise the final three-dimensional model more effectively. The following discussion attempts to briefly summarise the final realisation for the Hasdrubal -4 well. Output models for Hasdrubal -2 and -3 were also generated and a movie of the output model from all three wells is presented on the disk provided.

Prior to integrating the model data into FRED, it was necessary to construct a visualisation region that incorporated the spatial co-ordinates of the Hasdrubal -4 well. This is shown in **Figure C.13a-b** (N.B. for ease in visualising model data, the depths in metres given on the well bore are an order of magnitude less than real depths).

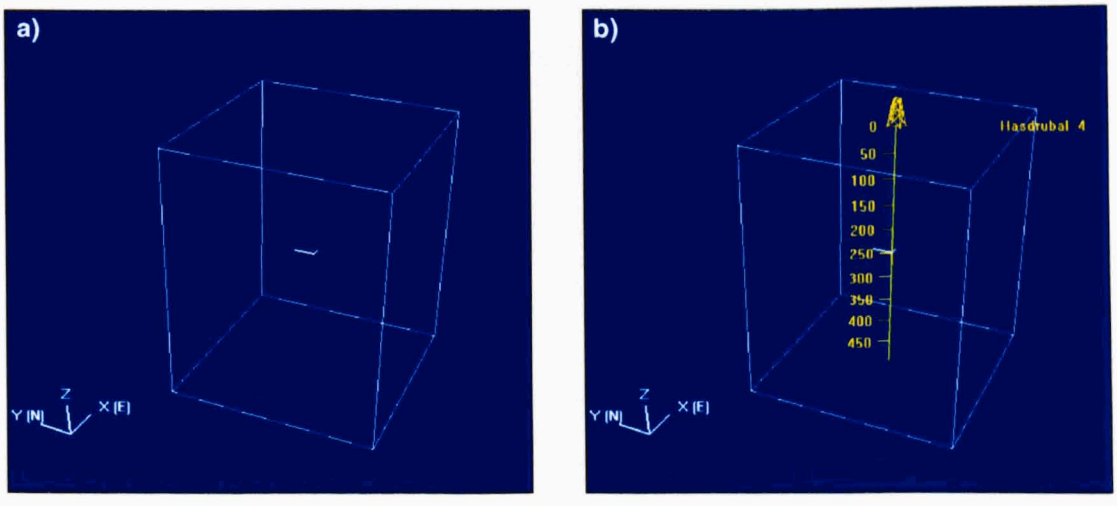

Fig. C.13. FRED Visualisations. a) Visualisation region, b) Visualisation region incorporating the well bore for Hasdrubal –4.

Compact Micrite Member

Figure C.14a-d shows the model output for stylolite and fracture realisations in the Compact Micrite Member within Hasdrubal -4. In accordance with the core analysis

only two compactional stylolites were modelled within this lithostratigraphic unit. A mean stylolite orientation of $2.4^0/203.9^0$ was gained from the FracSys analysis.

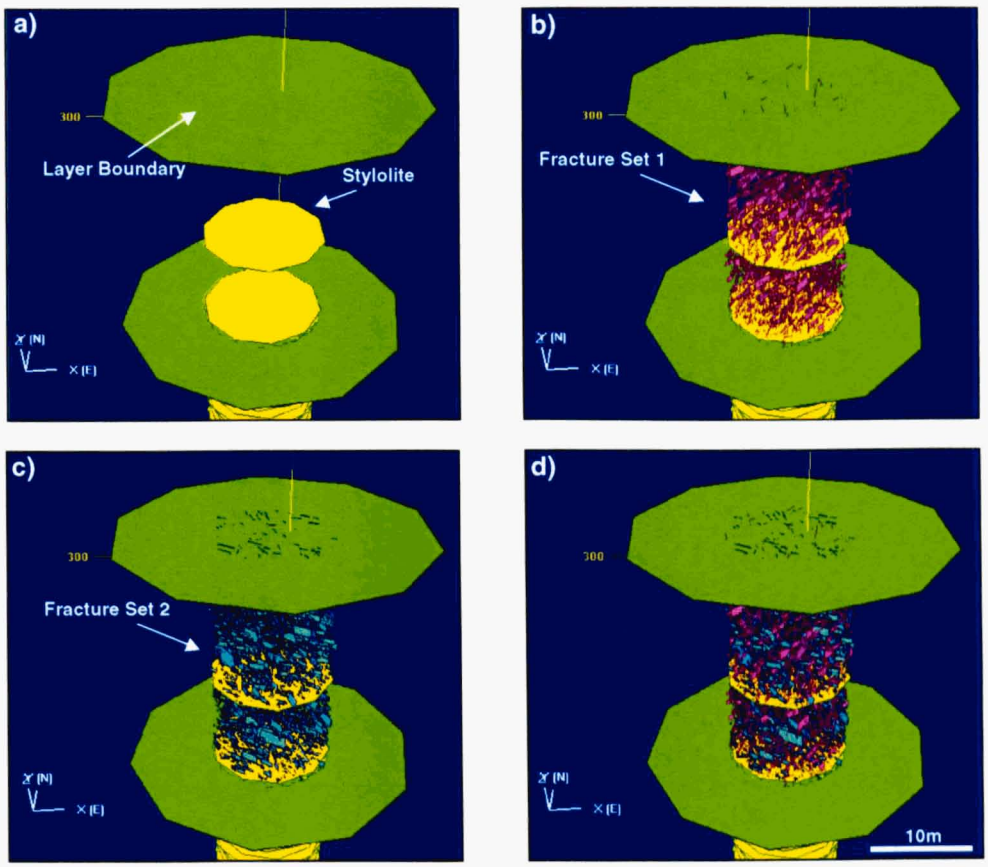

Fig. C.14. Stylolite and fracture realisations for the Compact Micrite Member in Hasdrubal -4. a) Stylolite realisation, b) Fracture Set 1 realisation (Mean trend = 203.5^0), c) Fracture Set 2 realisation (Mean trend = 144.7^0), and d) Combined stylolite and fracture realisations.

Two sets of fractures were generated for the Compact Micrite Member with mean trends of 203.5^0 and 144.7^0. These fracture systems form pervasive interconnected networks throughout the entire cored interval (**Fig. C.15a-c**).

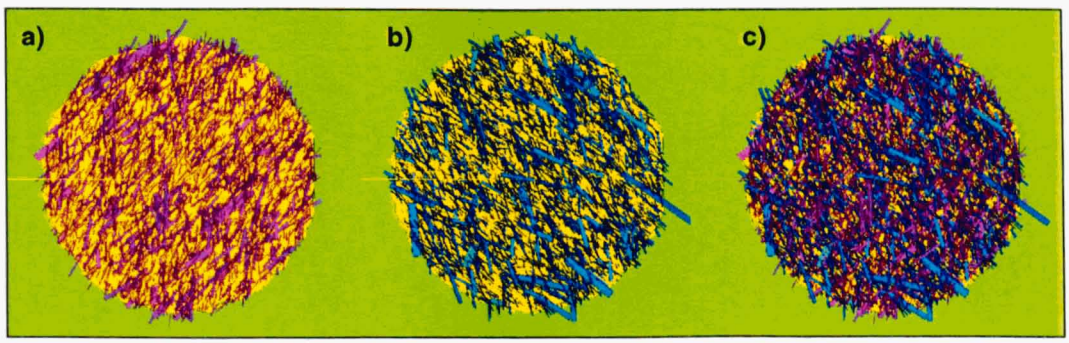

Fig. C.15a-c. Plan view of fracture realisations for the Compact Micrite Member in Hasdrubal - 4. a) Fracture Set 1 (Mean trend = 203.5^0), b) Fracture Set 2 (Mean trend = 144.7^0), and c) Combined realisation of fracture Sets 1 and 2. Stylolite Diameter = 10m.

El Garia & Chouabine Formations

Figure C.16a-f shows stylolite and fracture realisations for the El Garia Formation where oriented core was available. Fifty-six stylolites have been generated within the El Garia Formation using a P_{32} value of 0.6. A sample of these is shown in **Figure C.16a**.

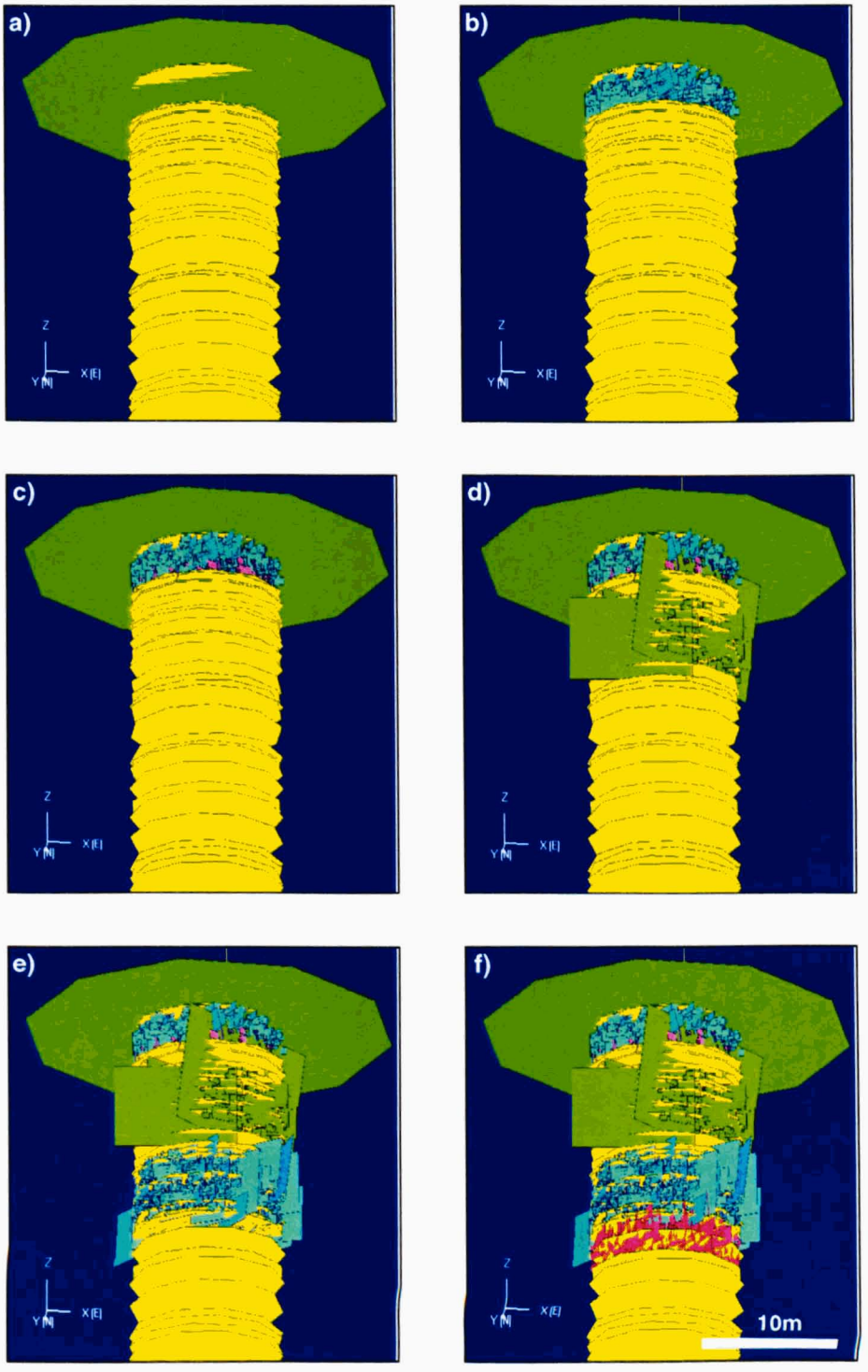

Fig. C.16a-f. Stylolite and fracture realisations for the upper (oriented) part of the El Garia Formation in Hasdrubal -4. a) Stylolite realisation, b) Fracture Set 1, c) Fracture Sets 1 to 2, d) Fracture Sets 1 to 3, e) Fracture Sets 1 to 4, and f) Fracture Sets 1 to 5. Stylolite Diameter = 10m.

Based on the data output from the FracSys analysis of the oriented section of core from Hasdrubal -4, five layer-bound fracture systems have been modelled within the upper part of the El Garia Formation (**Fig. C.16b-f**). Mean trends of each of these fracture sets (from top to bottom) are 309.3^0, 202.3^0, 255.0^0, 315.4^0 and 347.0^0 respectively (**Fig C.17a-f**).

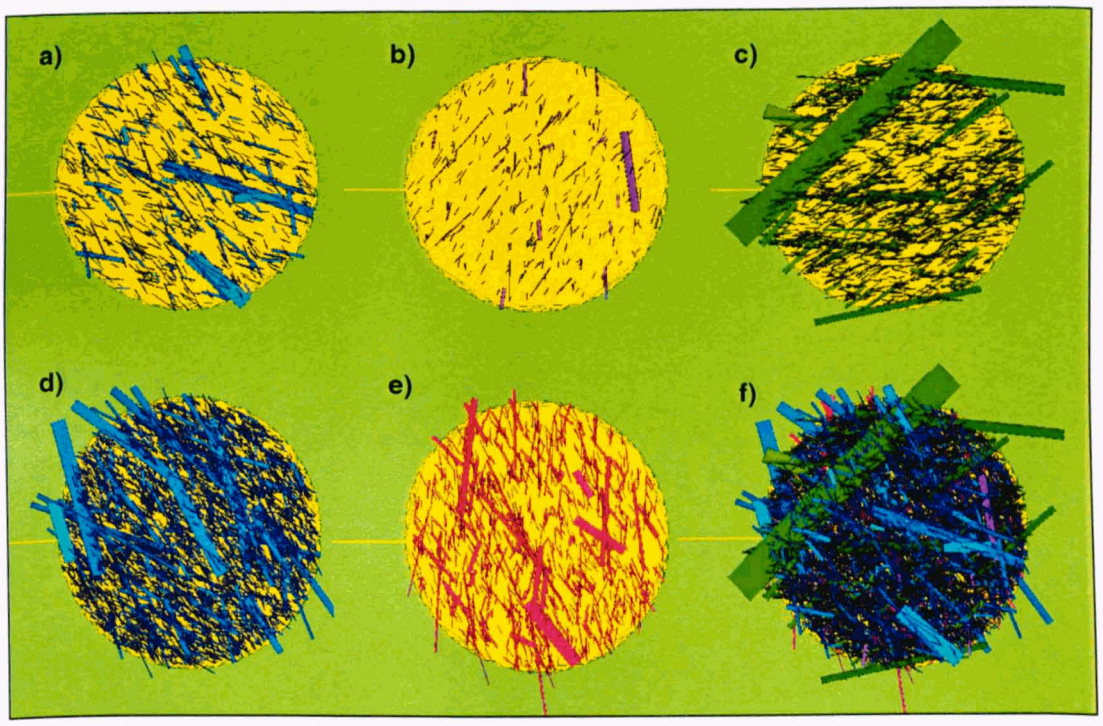

Fig. C.17a-f. Plan view of fracture realisations for the upper (oriented) part of the El Garia Formation in Hasdrubal -4. a) Fracture Set 1 realisation (Mean trend = 309.3^0), b) Fracture Set 2 realisation (Mean trend = 202.3^0), c) Fracture Set 3 realisation (Mean trend = 255.0^0), d) Fracture Set 4 realisation (Mean trend = 315.4^0), e) Fracture Set 5 realisation (Mean trend = 347.0^0), and f) Combined realisation of fracture Sets 1 to 5. Stylolite Diameter = 10m.

In contrast to the upper part of the El Garia Formation where orientation information from core allows the direct differentiation of individual fracture sets, the lack of sufficient data in the lower part of the El Garia Formation has meant that the nature of fracturing is largely unresolved. As a consequence, the fracture simulations in this section of Hasdrubal -4 have been highly simplified.

Although it is assumed that layer-bound fracture systems probably do exist in this section, it has not been feasible (given the available data) to make any direct comparisons. Therefore, it has been treated as a single layer (i.e. 3003.90m to 3045.45m (MD)). In an attempt to use as much of the data that is available, orientation data from the upper part of the El Garia Formation has been extrapolated down into

this section, and P_{32} values scaled accordingly to fit observed intensites. **Figures C.18 & C.19** show the distribution of modelled fractures in this section of the cored interval.

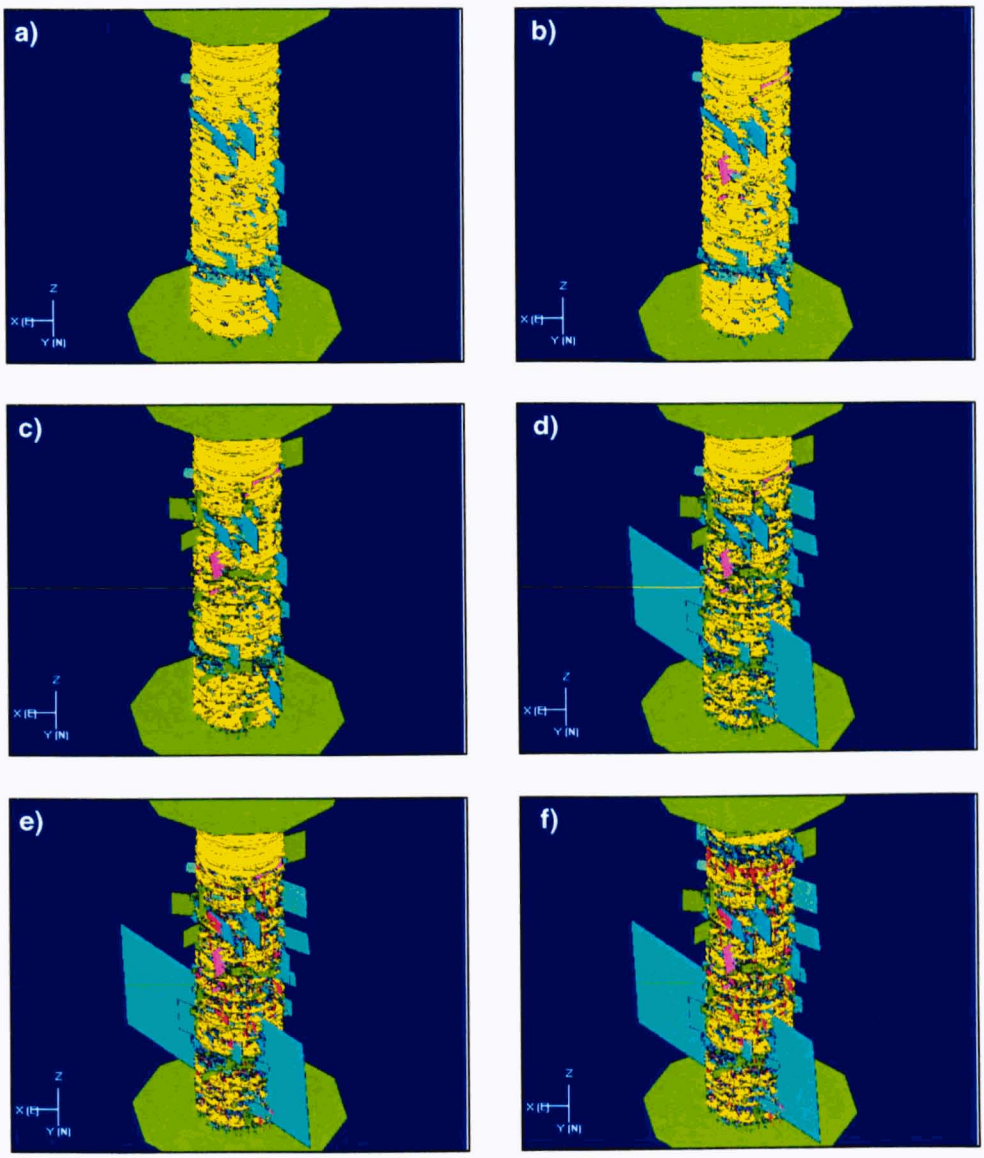

Fig. C.18. Stylolite and fracture realisations for the lower (un-oriented) part of the El Garia Formation in Hasdrubal -4. Fracture trends have been extrapolated into this section and P_{32} values have been scaled down to match observed data. a) Fracture Set 1, b) Fracture Sets 1 to2, c) Fracture Sets 1 to 3, d) Fracture Sets 1 to 4, e) Fracture Sets 1 to 5, and f) Combined upper and lower parts of the El Garia Formation.

Fracture and stylolite simulations within the Chouabine Formation have been treated in much the same way as those in the lower part of the El Garia Formation. Again, this interval has been treated as a single layer, and simulations are based on the orientation information that was gained from the upper part of the El Garia Formation. **Figure C.20** show the relative distribution of stylolites and fractures within the Chouabine Formation.

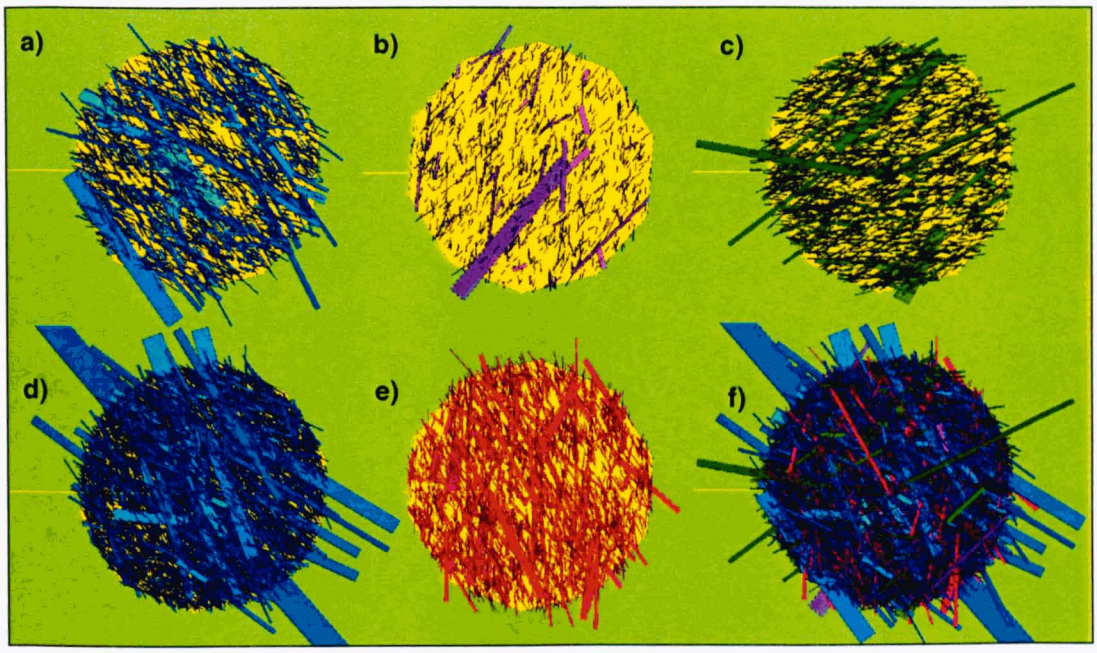

Fig. C.19. Plan view of fracture realisations for the lower (un-oriented) part of the El Garia Formation in Hasdrubal -4. a) Fracture Set 1 realisation (Mean trend = 309.3^0), b) Fracture Set 2 realisation (Mean trend = 202.3^0), c) Fracture Set 3 realisation (Mean trend = 255.0^0), d) Fracture Set 4 realisation (Mean trend = 315.4^0), e) Fracture Set 5 realisation (Mean trend = 347.0^0), and f) Combined realisation of fracture Sets 1 to 5.

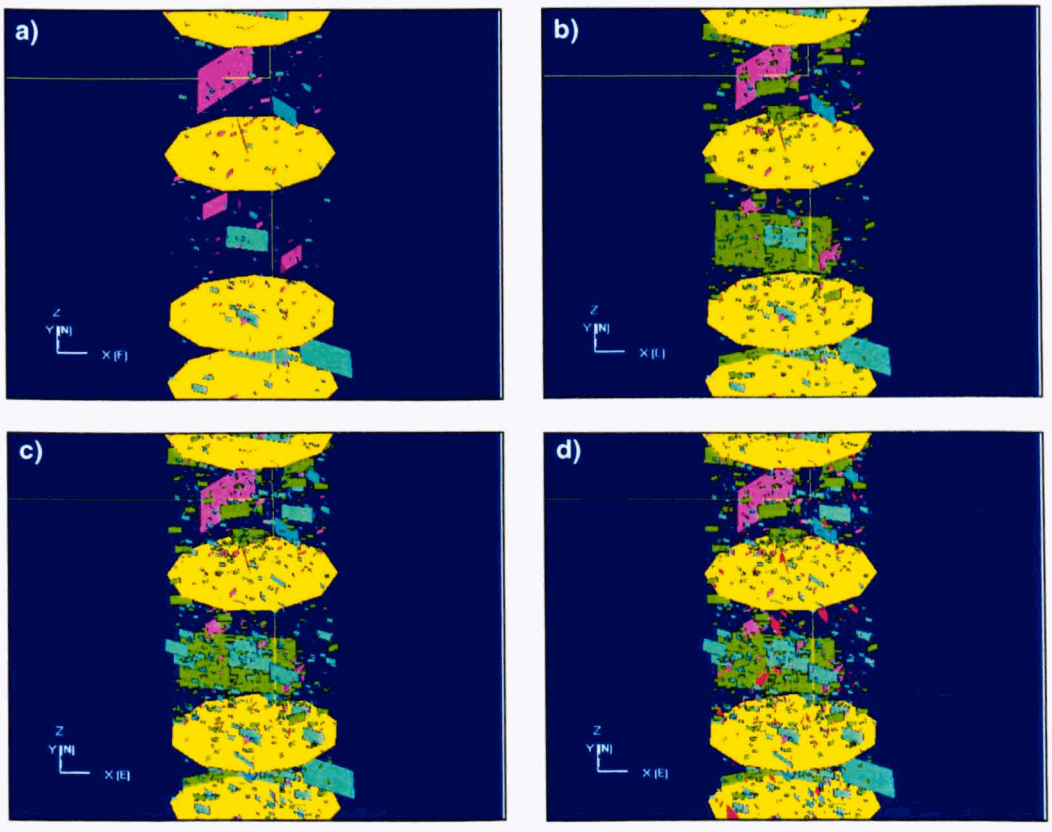

Fig. C.20 Plan view of fracture realisations for the Chouabine Formation. a) Fracture Sets 1 to 2, b) Fracture Sets 1 to 3, c) Fracture Set 1 to 4, d) Fracture Sets 1 to 5, and f) Fracture Sets 1 to 5.

C.5. Discussion

It is apparent from this analysis that the creation of a detailed three-dimensional fracture model of a given reservoir interval is entirely dependant on the quality and quantity of data available. Although the current database for the Hasdrubal reservoir is reasonably good, the current study has shown that there are still many limitations and shortcomings in data collection. In an ideal situation, one would have a full suite of image logs together with oriented core over the entire reservoir interval. However, this is generally expensive and thus may not prove economically viable. In such instances, such as this it is essential to extract as much information out of the available data for use in reservoir simulations.

Appendix D

Field Logs

Details of Scanline			**Details of Rock Face**			Rock Type: Attard Member
Log No. 1			Location: East of Wied Maghlaq			Condition of exposure: Moderate
Trend: 020			Dip Direction: 033			
Plunge: 32 S			Dip Angle: 12			Comments:
Trimming Level:			Non-overhanging/~~overhanging~~			
Logged by: B.Philps			Height: 30m			
Date Logged: 20/04/99			Width: 300m			

Intersection Distance	Dip (deg)	Strike (deg)	Throw (m)	Semi-trace Length (l)	Semi-trace Length (r)	Comments
0	66	099 SW				
0.58	64	101 SW				
1.3	76	124 NE				
2.11	69	116 SW				
3.65	77	139 SW				Intermediate-scale fracture
6.71	64	115 SW				
9.32	66	112 SW				
11.62	60	107 SW				
13.32	59	114 NE				
16.51	59	100 NE				Intermediate-scale fracture
18.9	72	132 SW				
22.01	60	123 SW				
23.52	71	130 SW				
27.91	52	121 SW				Intermediate-scale fracture
32.31	79	129 SW				
33.58	88	060 SW				Intermediate-scale fracture
36.31	86	118 SW				
40.11	66	131 SW				
46.18	71	132 SW				
50.16	62	130 SW				Intermediate-scale fracture
52.83	67	131 SW				
57.3	56	116 SW				
59.4	68	109 NE				
62.41	62	111 NE				
66.15	64	132 NE				
68.21	51	099 NE				
69.96	69	108 SW				Intermediate-scale fracture
71.14	68	116 SW				
74.12	65	122 SW				
76.01	78	114 SW				
77.32	69	120 SW				
79.01	71	120 SW				
80.53	62	107 SW				
84.21	74	111 SW				Intermediate-scale fracture
85.08	68	121 SW				
86.41	65	124 SW				
88.92	59	108 SW				

Details of Scanline	**Details of Rock Face**	Rock Type: Attard Member
Log No. 2	Location: East of Wied Maghlaq	Condition of exposure: Moderate
Trend: 021	Dip Direction: 033	
Plunge: 27 S	Dip Angle: 12	Comments: 75m east of Scaline 1
Trimming Level:	Non-overhanging/~~overhanging~~	
Logged by: B.Philps	Height: 30m	
Date Logged: 20/04/99	Width: 300m	

Intersection Distance	Dip (deg)	Strike (deg)	Throw (m)	Semi-trace Length (l)	Semi-trace Length (r)	Comments
0	71	123 SW				
0.97	65	101 SW				
1.24	53	097 SW				
3.1	66	122 SW				
4.28	69	118 SW				
6.8	81	116 SW				
9.12	84	121 SW				
9.97	51	124 SW				Intermediate-scale fracture
12.04	62	131 SW				
13.78	66	110 SW				
15.06	82	108 NE				
17.56	74	092 NE				
19.17	72	101 SW				
21.01	84	115 SW				
23.81	71	101 SW				Intermediate-scale fracture
25.04	68	035 NW				
26.97	69	038 NW				
30.11	65	111 SW				
33.4	72	109 SW				
36.79	83	107 SW				Intermediate-scale fracture
40.44	74	114 SW				
42.67	69	123 SW				
45.23	70	126 SW				
49.89	68	141 SW				
53.21	52	162 SW				Intermediate-scale fracture
57.17	63	136 SW				
58.04	67	120 NE				
59.47	67	119 SW				
62.33	65	114 NE				Intermediate-scale fracture
64.02	71	119 SW				
65.27	80	120 SW				
65.88	76	123 SW				
67.07	81	118 SW				
68.61	76	136 SW				
69.76	74	117 NE				
72.09	70	108 SW				
73.21	68	110 SW				
74.89	73	113 SW				
76.57	80	112 SW				
78.1	64	119 SW				
81.23	56	127 SW				Intermediate-scale fracture
83.15	63	102 SW				
86.29	65	104 SW				
87.98	71	112 SW				
89.34	82	116 NE				
90.03	63	118 SW				
92.67	64	131 SW				
93.86	59	125 SW				

Details of Scanline	**Details of Rock Face**	Rock Type: Attard Member
Log No. 2	Location: East of Wied Maghlaq	Condition of exposure: Moderate
Trend: 021	Dip Direction: 033	
Plunge: 27 S	Dip Angle: 12	Comments: 75m east of Scaline 1
Trimming Level:	Non-overhanging/~~overhanging~~	
Logged by: B.Philps	Height: 30m	
Date Logged: 20/04/99	Width: 300m	

Intersection Distance	Dip (deg)	Strike (deg)	Throw (m)	Semi-trace Length (l)	Semi-trace Length (r)	Comments
95.45	57	116 SW				Intermediate-scale fracture
97.14	61	123 SW				
101.43	64	121 SW				
104	63	120 SW				
105.47	68	117 SW				

Details of Scanline	**Details of Rock Face**	Rock Type: Attard Member
Log No. 3	Location: East of Wied Maghlaq	Condition of exposure: Moderate
Trend: 024	Dip Direction: 030	
Plunge: 22 S	Dip Angle: 15	Comments: 100m east of Scaline 2
Trimming Level:	Non-overhanging/~~overhanging~~	
Logged by: B.Philps	Height: 30m	
Date Logged: 20/04/99	Width: 300m	

Intersection Distance	Dip (deg)	Strike (deg)	Throw (m)	Semi-trace Length (l)	Semi-trace Length (r)	Comments
0.00	64	113 SW				Intermediate-scale fracture
1.22	67	123 SW				
3.15	65	119 NE				
4.28	71	117 SW				
5.03	69	134 SW				
7.14	66	136 SW				
8.56	65	122 SW				
10.34	58	116 SW				
12.89	81	118 SW				
14.47	83	101 NE				
15.03	67	107 NE				Intermediate-scale fracture
17.21	73	104 NE				
19.67	77	111 SW				
20.31	79	154 NE				
22.11	81	122 SW				
24.81	84	124 SW				
27.92	76	097 SW				
28.43	68	099 SW				
29.98	61	101 SW				
32.56	62	104 SW				
33.01	82	106 SW				Intermediate-scale fracture
33.78	79	117 SW				
34.62	61	109 SW				
35.34	64	119 NE				
35.88	61	114 SW				
37.07	59	109 SW				
38.24	57	123 SW				
39.21	57	120 SW				
40.78	73	134 SW				
41.59	69	141 SW				
43.29	56	152 NE				
45.89	64	143 SW				
47.32	66	121 SW				*Intermediate-scale fracture*
47.76	63	116 SW				
48.57	69	110 NE				
49.87	71	112 SW				
53.01	70	114 SW				
55.96	71	125 SW				
59.37	72	119 NE				
62.76	74	121 SW				
64.03	68	125 SW				Intermediate-scale fracture
65.37	67	118 SW				
66.45	81	108 NE				
66.86	74	113 SW				
68.78	68	112 SW				
70.39	72	114 SW				

Details of Scanline	**Details of Rock Face**	Rock Type: Attard Member
Log No. 4	Location: North of Wied Iz-Zurrieq	Condition of exposure: Moderate
Trend: 036	Dip Direction: 026	
Plunge: 00	Dip Angle: 04	Comments: Northen end of Wied Iz-Zurreiq
Trimming Level:	Non-overhanging/~~overhanging~~	
Logged by: B.Philps	Height: 0m	
Date Logged: 22/04/99	Width: 60m	

Intersection Distance	Dip (deg)	Strike (deg)	Throw (m)	Semi-trace Length (l)	Semi-trace Length (r)	Comments
0.00	61	118 SW				
0.62	72	111 SW				
0.92	76	103 SW				
1.81	68	119 SW				
3.41	64	126 SW				
3.82	90	103 SW				
5.95	72	112 SW				
7.11	81	106 SW				
8.04	71	111 SW				Intermediate-scale fracture
9.14	60	62 NW				
11.70	68	131 SW				
14.50	76	115 SW				
16.53	80	054 SE				
19.20	80	070 SE				Intermediate-scale fracture
20.32	72	110 SW				
20.79	81	104 SW				
21.52	90	154 SW				
22.61	78	113 SW				
24.45	79	111 SW				
25.16	79	111 SW				
26.27	86	095 SW				
27.43	79	109 SW				
27.80	79	109 SW				
28.43	76	110 SW				
29.66	78	107 SW				
30.86	68	120 SW				
32.06	69	118 SW				
32.86	66	106 SW				
33.69	67	116 SW				
35.06	60	93 NE				

Details of Scanline	**Details of Rock Face**	Rock Type: Attard Member
Log No. 5	Location: North of Wied iz-Zurrieq	Condition of exposure: Moderate
Trend: 030	Dip Direction: 022	
Plunge: 45	Dip Angle: 08	Comments: Northen end of Wied iz-Zurreiq
Trimming Level:	Non-overhanging/~~overhanging~~	
Logged by: B.Philps	Height: 25m	
Date Logged: 22/04/99	Width: 100m	

Intersection Distance	Dip (deg)	Strike (deg)	Throw (m)	Semi-trace Length (l)	Semi-trace Length (r)	Comments
0.00	78	121 SW				
0.31	74	122 SW				
1.02	68	115 SW				
2.83	66	128 SW				
3.56	71	131 SW				
6.06	68	120 SW				
7.01	68	115 SW				
8.22	64	114 SW				

Details of Scanline	**Details of Rock Face**	Rock Type: Attard Member
Log No. 6	Location: Lapsi Quarry	Condition of exposure: Good
Trend: 080	Dip Direction: 009	
Plunge: 00	Dip Angle: 02	Comments: First of two scanlines orthogonal to eachother.
Trimming Level:	Non-overhanging/~~overhanging~~	
Logged by: B.Philps	Height: 15m	
Date Logged: 27/04/99	Width: 30m	

Intersection Distance	Dip (deg)	Strike (deg)	Throw (m)	Semi-trace Length (l)	Semi-trace Length (r)	Comments
0.30	62	049 NW				
0.72	49	029 NW				
1.42	56	051 NW				
1.95	64	041 SE				
2.11	51	053 NW				
2.41	48	042 NW				
2.93	75	054 NW				
3.42	64	184 W				
3.56	89	031 SE				
3.65	79	016 NW				
3.93	54	029 NW				
4.10	74	012 SE				
5.05	56	044 NW				
5.67	56	021 NW				
6.04	45	054 NW				
7.00	57	019 NW				Intermediate-scale fracture
7.13	66	004 NW				
7.18	50	124 NW				
7.32	63	018 NW				
7.56	66	019 NW				
8.02	54	047 NW				
8.15	60	052 NW				
8.25	58	052 NW				
8.39	81	022 SE				
9.72	63	025 NW				
9.86	61	012 NW				
12.40	62	039 NW				
12.62	61	039 NW				
14.91	64	042 NW				
15.18	77	056 NW				
15.62	68	012 NW				
15.91	58	007 NW				
16.25	83	056 NW				
16.71	61	048 NW				
16.92	66	025 NW				
17.32	54	030 NW				
18.28	63	141 SW				
19.59	46	040 SW				
19.75	62	024 NW				
19.95	49	184 W				
20.20	51	030 NW				
20.70	69	022 NW				
20.91	86	023 SE				
23.05	56	028 NW				
24.62	58	027 NW				
26.21	56	026 NW				
26.53	62	031 NW				
26.76	55	024 NW				Intermediate-scale fracture

Details of Scanline	**Details of Rock Face**	Rock Type: Attard Member
Log No. 7	Location: Lapsi Quarry	Condition of exposure: Good
Trend: 025	*Dip Direction*: 099	
Plunge: 0	Dip Angle: 0	Comments: Second of two scanlines orthogonal to eachother.
Trimming Level:	Non-overhanging/~~overhanging~~	
Logged by: B.Philps	Height: 15m	
Date Logged: 28/04/99	Width: 40m	

Intersection Distance	Dip (deg)	Strike (deg)	Throw (m)	Semi-trace Length (l)	Semi-trace Length (r)	Comments
0.00	78	006 NW				
0.78	83	044 NW				Intermediate-scale fracture
0.80	82	023 NW				
0.95	80	043 NW				
1.29	76	028 SE				
1.48	72	141 NE				
1.76	85	053 NW				
1.88	88	050 NW				
2.32	68	150 NW				
2.33	80	028 NW				
2.70	89	029 NW				
2.81	88	020 NW				
3.71	86	022 SE				
4.15	80	032 SE				
4.41	89	030 SE				
5.11	86	043 NW				
5.79	80	024 NW				
7.31	74	018 NW				
8.20	84	033 NW				
8.81	75	030 NW				
9.09	76	030 NW				
9.40	82	029 NW				
10.85	83	078 SE				
12.20	86	033 NW				Intermediate-scale fracture
15.90	75	021 NW				
16.18	71	017 NW				
16.22	75	025 NW				
16.26	70	037 NW				
16.30	86	056 SE				
16.40	74	034 NW				
16.53	64	063 NW				
16.64	69	065 NW				
17.07	74	024 NW				
17.13	84	026 NW				
17.21	85	024 NW				
17.28	83	024 NW				
17.4	84	026 NW				
18.31	72	010 SE				
18.76	68	046 NW				
19.2	65	027 NW				
19.40	64	047 NW				
20.10	61	069 NW				
20.22	64	067 NW				
20.40	82	008 NW				
22.30	69	010 NW				
23.15	72	038 NW				
23.91	89	016 NW				
25.25	74	053 SE				

Details of Scanline	**Details of Rock Face**	Rock Type: Attard Member
Log No. 7	Location: Lapsi Quarry	Condition of exposure: Good
Trend: 025	Dip Direction: 099	
Plunge: 0	Dip Angle: 0	Comments: Second of two scanlines orthogonal to eachother.
Trimming Level:	Non-overhanging/~~overhanging~~	
Logged by: B.Philps	Height: 15m	
Date Logged: 28/04/99	Width: 40m	

Intersection Distance	Dip (deg)	Strike (deg)	Throw (m)	Semi-trace Length (l)	Semi-trace Length (r)	Comments
25.79	77	061 NW				
25.96	76	039 SE				
26.05	84	038 NW				
26.55	89	080 NW				
26.64	89	057 SE				
26.78	86	075 SE				
27.05	64	088 NW				
27.29	69	107 SW				
27.34	74	063 NW				
27.69	75	064 NW				
27.98	79	057 NW				
28.13	78	061 NW				
28.70	89	046 SE				
29.05	79	056 NW				
29.43	84	053 NW				
29.51	84	057 NW				
29.91	60	038 NW				
30.21	66	040 NW				
31.05	67	049 NW				
31.49	88	069 NW				
31.91	80	051 NW				
32.25	76	048 NW				
33.21	78	043 NW				
33.70	84	048 NW				
34.20	83	044 NW				
34.50	88	069 SE				
34.81	89	046 NW				
35.11	86	042 NW				Intermediate-scale fracture

Details of Scanline	**Details of Rock Face**	Rock Type: Attard Member
Log No. 8	Location: Naxxar Gap Quarry	Condition of exposure: Good
Trend: 033	Dip Direction: 293	
Plunge: 0	Dip Angle: 3	Comments: Scanline within the hangingwall of a large fault
Trimming Level:	~~Non-overhanging~~/overhanging	
Logged by: B.Philps	Height: 15m	
Date Logged: 05/05/99	Width: 40m	

Intersection Distance	Dip (deg)	Strike (deg)	Throw (m)	Semi-trace Length (l)	Semi-trace Length (r)	Comments
0.00	78	069 NW				Intermediate-scale fracture
0.31	51	172 SW				
0.69	76	061 SE				
1.51	85	121 NE				
1.85	82	061 NW				
2.23	84	074 NW				
2.30	86	151 NE				
2.71	64	057 NW				
3.14	71	081 SE				
3.33	76	062 SE				
4.72	89	044 NW				
4.89	72	176 SW				
						Poor Exposure
7.22	83	050 NW				
7.92	82	065 NW				
8.14	86	182 NW				
9.76	78	065 SE				
9.91	76	065 SE				
10.01	80	066 SE				
10.08	81	064 SE				
10.09	78	126 SW				
10.11	84	129 SW				
10.16	86	127 SW				
10.24	86	124 SW				
10.40	59	161 SW				
						Zone of V. Intense Brecciation
13.11	80	051 NW				Intermediate-scale fracture
						Zone of V. Intense Brecciation
16.30	58	070 SE				
16.44	72	069 SE				
16.45	88	116 SW				
16.51	86	118 SW				
16.7	72	069 SE				
17.22	86	084 NW				
17.9	89	084 NW				
18.12	76	072 SE				
19.06	67	060 SE				
19.14	67	062 SE				
19.61	89	122 NE				
19.64	88	124 NE				
19.92	82	073 NW				
19.95	84	076 SE				
20.09	79	076 NW				
						Zone of V. Intense Brecciation
21.73	72	068 SE				Main Fault Plane
						Poor Exposure. Overview: Series of dm-scale fractures spaced at ~5-10m intervals

Details of Scanline	**Details of Rock Face**	Rock Type: Attard Member
Log No. 9	Location: Naxxar Gap Quarry	Condition of exposure: Good
Trend: 080	Dip Direction: 099	
Plunge: 0	Dip Angle: 0	Comments: Scanline in the footwall section immediately adjacent to the main fault in Scanline 8
Trimming Level:	~~Non-overhanging~~/overhanging	
Logged by: B.Philps	Height: 15m	
Date Logged: 05/05/99	Width: 10m	

Intersection Distance	Dip (deg)	Strike (deg)	Throw (m)	Semi-trace Length (l)	Semi-trace Length (r)	Comments
0.00	80	096 NE				
0.12	79	087 NW				
0.16	64	123 NE				
0.86	72	091 NE				
1.24	78	095 NE				
2.04	81	098 NE				
2.61	82	176 SW				
2.72	65	131 NE				
2.84	78	089 NW				
3.61	82	086 NW				
3.82	76	165 SW				
3.94	80	094 NE				
4.04	79	165 SW				
4.21	82	094 NE				
4.39	86	086 NW				
4.64	72	124 SW				
5.01	79	090 N				
5.42	84	096 NE				
5.64	80	127 SE				
6.08	87	086 SE				
6.42	83	100 NE				
6.51	79	097 NW				
7.21	62	184 NW				
7.36	71	169 SW				
7.44	82	099 NE				
7.92	86	106 NE				
8.14	79	095 NE				
8.36	68	101 NE				
8.42	80	178 SW				
8.72	80	098 NE				
9.01	82	098 NE				
9.16	78	104 NE				

Details of Scanline			**Details of Rock Face**			Rock Type: Attard Member
Log No. 10			Location: Naxxar Gap Quarry			Condition of exposure: Good
Trend: 140			Dip Direction: 329			
Plunge: 0			Dip Angle: 03			Comments: Scanline in the footwall section immediately adjacent to the main fault in Scanline 8
Trimming Level:			~~Non-overhanging~~/overhanging			
Logged by: B.Philps			Height: 15m			
Date Logged: 05/05/99			Width: 10m			
Intersection Distance	Dip (deg)	Strike (deg)	Throw (m)	Semi-trace Length (l)	Semi-trace Length (r)	Comments
0.00	68	062 NW				Intermediate-scale structure
						Zone of intense brecciation
2.10	72	064 NW				
2.51	88	188 NW				
3.12	88	044 NW				
3.71	64	059 NW				
4.40	65	060 NW				
4.60	65	060 NW				
4.79	66	059 NW				
						Poor Exposure
7.70	69	059 SE				
7.95	76	060 SE				
						Zone of intense brecciation
11.65	78	075 NW				
11.80	72	066 NW				
12.07	82	088 NW				
						Zone of intense brecciation
13.01	81	052 SE				Intermediate-scale structure
13.71	86	053 SE				
13.96	84	054 SE				
13.99	68	068 NW				
14.41	88	044 SE				
14.81	86	053 SE				
15.43	80	062 SE				
15.54	82	064 SE				
15.83	82	053 SE				
16.63	88	067 SE				Main Fault Plane

Details of Scanline			**Details of Rock Face**			Rock Type: Attard Member
Log No. 11			Location: Naxxar Gap Quarry			Condition of exposure: Good
Trend: 180			Dip Direction: 336			
Plunge: 0			Dip Angle: 02			Comments:
Trimming Level:			~~Non-overhanging~~/overhanging			
Logged by: B.Philps			Height: 15m			
Date Logged: 05/05/99			Width: 10m			
Intersection Distance	Dip (deg)	Strike (deg)	Throw (m)	Semi-trace Length (l)	Semi-trace Length (r)	Comments
0.00	75	084 NW				
0.11	81	084 NW				
0.41	80	074 NW				
0.53	81	092 NW				
0.54	80	092 NW				
0.60	88	085 SE				
0.63	88	086 SE				
0.69	89	074 SE				
0.85	80	073 SE				dm-scale fracture
0.87	82	074 SE				
0.90	79	081 NW				
1.10	76	071 SE				
1.68	84	077 SE				dm-scale fracture
1.89	85	076 NW				
2.20	68	090 N				
2.60	71	091 NE				
2.72	87	075 SE				
2.89	79	090 N				
2.95	64	081 NW				
3.61	81	071 SE				dm-scale fracture
3.82	85	066 SE				
3.95	86	098 NE				
4.12	60	091 NE				
4.45	64	054 NW				
5.11	88	050 NW				
5.50	60	098 NE				
6.05	88	100 SW				

Details of Scanline	**Details of Rock Face**	Rock Type: Attard Member
Log No. 12	Location: Attard Quarry	Condition of exposure: Good
Trend: 164	Dip Direction: 029	
Plunge: 0	Dip Angle: 10	Comments: Scanline in the footwall section of the main fault.
Trimming Level:	~~Non-overhanging~~/overhanging	
Logged by: B.Philps	Height: 8m	
Date Logged: 06/05/99	Width: 25m	

Intersection Distance	Dip (deg)	Strike (deg)	Throw (m)	Semi-trace Length (l)	Semi-trace Length (r)	Comments
0.00	82	056 SE				Main Fault Plane
0.21	84	046 SE				
0.26	86	049 SE				
0.31	88	050 SE				
0.40	89	046 SE				
0.55	89	059 SE				
0.91	85	068 SE				
0.94	89	080 SE				
1.01	89	074 SE				
1.07	89	073 SE				
1.21	86	084 SE				
1.29	83	083 SE				Intermediate-scale structure
1.52	85	073 SE				
						Zone of intense brecciation
2.42	81	050 SE				
2.55	85	078 NW				
2.76	74	082 NW				
3.08	84	074 SE				
3.20	65	118 SW				
3.31	74	082 NW				
3.47	82	076 NW				
3.54	78	079 NW				
						Poor exposure
4.00	77	056 NW				

Vol 2.

List of Enclosures

Enclosure 1: Principal tectonic elements in the Mediterranean region

Enclosure 2: Principal tectonic elements in the Central Mediterranean region

Enclosure 3: Main structural elements on the Pelagian Platform and surrounding areas

Enclosure 4: General overview of the main field observations made along the Maghlaq Fault System

Enclosure 5: Summary of observations from specific localities along the Maghlaq Fault System

Enclosure 6: Summary of observations made in the Ix-Xaqqa Quarry

Enclosure 7: Summary of observations made in the Lapsi Quarry

Enclosure 8: Summary of observations made in the Naxxar Gap Quarries

Enclosure 9: Summary of observations made in the Attard Quarries

BIBL. LOCAL UNIV.